LHCb-ANA-2018-022
January 4, 2021

Angular analysis of the decay $B^+ \to K^{*+}\mu^+\mu^-$ with $K^{*+} \to K^0_S\pi^+$ using $9\,\text{fb}^{-1}$

Martino Borsato[1], Michel De Cian[1,2], David Gerick[1], Renata Kopečná[1].

[1] *Physikalisches Institut, Heidelberg University, Germany*
[2] *École polytechnique fédérale de Lausanne, Lausanne, Switzerland*

Abstract

An angular analysis of the rare decay $[B^+ \to K^{*+}\mu^+\mu^-\,]_{\text{CC}}$, using $K^{*+} \to K^0_S\pi^+$, is performed, exploiting a data-set of $9\,\text{fb}^{-1}$ integrated luminosity, corresponding to the full Run I and Run II data of the LHCb experiment. A five dimensional fit in the three decay angles and the invariant masses of the B^+ meson and the K^{*+} meson systems is performed in intervals of the dimuon invariant mass, q^2, in order to extract the angular observables.

The candidate selection yields 737 ± 34 signal candidates over the full q^2 spectrum without the resonant-dimuon regions. Two sets of angular observables (S_x and $P_i^{(\prime)}$) are measured in ten q^2 intervals.

Contents

Version history

The following versions of this document have been published:

Table 1: Overview of the version history of this document

version	status or comments	date
0r1	First draft including Introduction, Selection, Decay kinematics and FCNCfitter. Send out to WG conveners	Friday, 14.06.2019
0r2	Second draft with Fitter, MoM, FCNCfitter and some systematic studies. WG convener comments implemented. Asking for pre-approval and WG circulation.	Friday, 29.11.2019
0r3	Third version with WG comments implement. Still missing final toy studies and F_S systematics	Monday, 20.01.2020
0r4	Referee's comments included	Friday, 28.02.2020
0r5	Second round of referee's comments included	Friday, 08.05.2020
0r6	All comments included. Feldman-Cousins and unblinding strategy updated. Completed systematic studies	Tuesday, 21.07.2020
1	Final results are added to the document. The analysis is approved and paper draft is ready	Friday, 16.10.2020
1r1	Updated final result plots and tables. Included remark on usage of F_{L} and A_{FB}.	Monday, 04.01.2021

1 Introduction

This note presents an angular analysis of the decay $B^+ \to K^{*+}\mu^+\mu^-$ with the goal to extract the angular observables of the differential angular decay rate. This decay proceeds via flavour-changing neutral currents with a W, γ or Z exchange, see Fig. 1, and is heavily suppressed in the Standard Model (SM). The differential decay rate and isospin asymmetry has been measured before by the LHCb collaboration [1], while in addition the angular distributions have been measured by the Belle and BaBar collaborations, although with a limited statistical precision [2] [3]. This analysis therefore presents the first measurement of the angular distribution of $B^+ \to K^{*+}\mu^+\mu^-$ in LHCb, as well as the most precise one.

Additionally, in the angular analysis of the decay $B^0 \to K^{*0}\mu^+\mu^-$, the isospin partner of this decay, a tension between Standard Model predictions and measurement results have been observed by the LHCb collaboration [4]. The decay $B^+ \to K^{*+}\mu^+\mu^-$ provides an ideal complementary measurement in helping to understand the tension observed in the B^0 channel and the underlying physical phenomena in these decays. All data used for the analysis was taken during proton-proton (pp) collisions in the years 2011, 2012, 2015, 2016, 2017 and 2018 and corresponds to about $9.1\,\text{fb}^{-1}$. The center of mass energy of the colliding protons increased during this period from $\sqrt{s} = 7\,\text{TeV}$ in 2011, over $\sqrt{s} = 8\,\text{TeV}$ in 2012 up to $\sqrt{s} = 13\,\text{TeV}$ in 2015 – 2018.

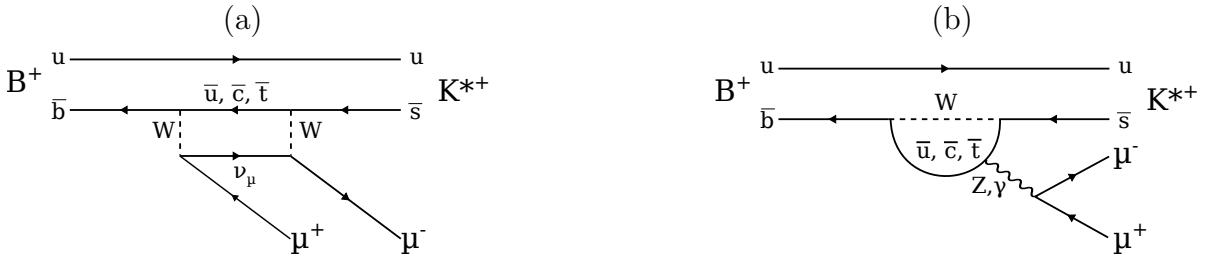

Figure 1: Feynman diagrams of the matrix elements contributing most to the total decay amplitude of the decay $B^+ \to K^{*+}\mu^+\mu^-$. The box diagram (a) and the loop diagram (b). The latter is also referred to as penguin diagram.

1.1 Analysis strategy

The analysis is split up in two main parts: the selection of events containing signal candidates, which is described thoroughly in Section 2, and the fit of the angular distributions, described in Section 4. The decay kinematics of a $b \to s\ell^+\ell^-$ transition is introduced in Section 3, including the angular decay rates and resulting PDF as well as the angular acceptance corrections that have to be performed. The extraction of the angular observables using a 4D-fitter or the method of moments are discussed in Section 4. Systematic effects are evaluated in Section 5. Finally, the results of the angular observables are presented and discussed in Section 7.

1.2 Blinding

The total signal yield over the integrated q^2 region, and especially the signal yield in each q^2 bin (see Table 15) is blinded. For tests of the fitter, we use signal yield estimations, as

described in Section 4.4.2.
Throughout the optimisation and stabilization of the fitter and during the studies of systematic uncertainties, the absolute values of the angular observables S_i are blinded. The unblinding of the yields and the angular observables of the fit to the signal channel events will only be performed after the analysis is reviewed. The results are shown in Section 7.2 after the unblinding.

1.2.1 Unblinding strategy

For the unblinding of the final results, the following strategy is foreseen:

1) Comparison to Method of Moments

2) Comparison of the final results from individual sub-sets:

   a) magnet *up* versus magnet *down* samples

   b) *Run I versus Run II*, if statistic in Run I is sufficient

   c) `DD` tracks versus `LL` tracks samples

3) Inspect the B^+ mass dimension fits and unblind the signal yields per q^2 bin

4) Unblinding of the final values from the likelihood fits

The comparisons from point 1) and 2) are given in Section 7.1, with point 3) to follow in the same section. Point 4) is then given in Section 7.2.

2 Selection

This analysis is based on data recorded in proton-proton collisions by the LHCb experiment in the years 2011, 2012, 2015, 2016, 2017 and 2018. In this time, LHCb recorded data equivalent to a total integrated luminosity of $9.09\,\text{fb}^{-1}$, with $1.11\,\text{fb}^{-1}$ (2011), $2.08\,\text{fb}^{-1}$ (2012), $0.33\,\text{fb}^{-1}$ (2015), $1.67\,\text{fb}^{-1}$ (2016), $1.71\,\text{fb}^{-1}$ (2017) and $2.19\,\text{fb}^{-1}$ (2018) in the different years. The proton beam energy increased from 3.5 TeV in 2011 over 4.0 TeV in 2012 to 6.5 TeV in 2015 - 2018.
Throughout the selection, data from the years 2011 and 2012 is often referred to as Run I[1] and data from the years 2015 to 2018 is referred to as Run II
In the following, the selection process can be divided into a five step process:

(1) Stripping decision using `B2XMuMu` stripping line

(2) Trigger line decision requirements

(3) 1D cut in various particle and event variables

(4) *sWeights* of data and re-weighting of simulated events

(5) Multi-variate analysis to suppress combinatorial background

As a baseline, the selection process of $B^0 \to K^{*0}\mu^+\mu^-$ (`LHCb-ANA-2013-090`, Ref. [5]) was considered and modified in many ways throughout the different selection steps. Changes in the selection process are due to the different hadronic final state and to different conditions in Run II compared to Run I. Some major changes can be seen in the input variables of the multi-variate analysis, as the distributions of some variables used in Ref. [5] do not agree adequately for simulated events and data.
The resulting selection process is presented in the following, starting with details about the stripping line which are given in Section 2.2. All trigger decisions are introduced in Section 2.3. The reduction of background contributions due to misidentified particles and resonant structures is described in Section 2.4. Monte Carlo (MC) events are used to understand efficiencies of the selection procedure as well as to provide a suitable signal-like sample for the multi-variate analysis. The selection and re-weighting of the MC sample is presented in Section 2.7. Finally, the multi-variate analysis is trained on a signal MC sample and a background data sample from the mass region above the B^+ peak. Training and testing, as well as the resulting efficiency and separation power of this final step of selection is shown in Section 2.8.

2.1 Splitting the data sample

Both data and simulation samples are split into four sub-samples. Events are sorted depending on whether the K^0_S decays inside (`LL` tracks) or outside of the VELO (`DD` tracks) and whether they belong to Run I or Run II. Table 2 lists the four samples.

[1] Even thought this is technically incorrect due to the omission of data from 2010...

Table 2: The four samples, into which all data and simulation events are split. The final fit to the events is performed simultaneously in all samples, with common parameters for the physical observables.

#	sample name
1	Run I `DD` tracks
2	Run I `LL` tracks
3	Run II `DD` tracks
4	Run II `LL` tracks

2.2 Reconstruction and Stripping

Proton-proton collisions inside the LHCb detector are reconstructed using Brunel. For events recorded in the years 2011 and 2012, reconstruction version `Reco14c` is used, while for 2015 to 2018 `Reco15` to `Reco18` is used. The simulated MC events are reconstructed with the same reconstruction versions as in data for all years.
Events are processed by the LHCb stripping line `B2XMuMu` which consists of the selection criteria shown in Table 3.

A total of 10.2 million data events pass the stripping line, with 2.8 million and 7.4 million events from Run I (2011 & 2012) and Run II (2015, 2016, 2017 & 2018), respectively. Further numbers on the sub-samples divided by the magnet polarity or the track type of the events are found in the summary Table 4.

2.3 Trigger

Events at the LHCb detector are selected online using a multi-level trigger system, starting with the L0 hardware trigger. The accepted events are then processed by the HLT, which is split up into two stages, HLT1 and HLT2. Events accepted by all three stages are stored for offline processing, including the information from the trigger decision of all levels.
Only events that were selected by the trigger lines listed in Table 5 are used for this analysis. Any event is required to pass at least one of the listed trigger lines for each trigger level. Offline, the signal candidate is required to be directly responsible for triggering these lines by using the *triggered on signal* (TOS) tag related to the B meson.
The trigger selection in Run II is kept as similar as possible to Run I. However, as shown in Table 5, some trigger lines were renamed for Run II and two more were added. The signal yield of each trigger line is given in Table 6 by using the *sWeighted* event yield after the cut based selection (see Section 2.4 for more information). A detailed description of the trigger lines and their requirements is presented in Ref. [6].

2.3.1 Hlt1TrackMVA 2D cut

In 2016, a two dimensional cut in χ^2_{IP} and p_{T} of the B meson was introduced, which can be described by

$$\log\left(\chi^2_{\text{IP}}\right) = \frac{1.0}{\left(p_{\text{T}}[\,\text{GeV}] - 1.0\right)^2} + \frac{b}{25.0} \times \left(25.0 - p_{\text{T}}[\,\text{GeV}]\right) + \log(7.4) \qquad (1)$$

Table 3: Selection criteria of the stripping line `B2XMuMu`. These have been used for all recorded and simulated data. The versions of the stripping differ between the years: 2011 (*S21r1p1*), 2012 (*S21r0p1*), 2015 (*S24r1*), 2016 (*S28r1*), 2017 (*S29r2*) and 2018 (*S34*).

candidate	selection
$B^\pm$	$4700\,\text{MeV}/c^2 < \text{m}(B^\pm) < 7000\,\text{MeV}/c^2$ (*S21r(0/1)p1*)
	$4900\,\text{MeV}/c^2 < \text{m}(B^\pm) < 7000\,\text{MeV}/c^2$ (*S24r1,S28r1,S29r2 & S34*)
$B^\pm$	$\chi^2_{\text{IP}} < 16$ (best PV)
$B^\pm$	DIRA angle $< 14\,\text{MRad}$
$B^\pm$	flight distance $\chi^2 > 121$
$B^\pm$	$\chi^2_{\text{vtx}}/\text{ndf} < 8$
$\mu^+\mu^-$	$\text{m}(\mu^+\mu^-) < 7100\,\text{MeV}/c^2$
$\mu^+\mu^-$	$\chi^2_{\text{vtx}}/\text{ndf} < 12$
$\mu^\pm$	track *ghost prob* < 0.5
$\mu^\pm$	flight distance $\chi^2 > 6$
$\mu^\pm$	$\text{DLL}_{\mu\pi} >$ -3
$\mu^\pm$	`isMuon`
$K^{*\pm}$	$\text{m}(K^{*\pm}) < 6200\,\text{MeV}/c^2$
K^0_S	$\tau_{K^0_\text{S}} > 2\,\text{ps}$
K^0_S	$467\,\text{MeV}/c^2 < \text{m}(K^0_\text{S}) < 527\,\text{MeV}/c^2$
$\pi^\pm$	track *ghost prob* < 0.5
$\pi^\pm$	flight distance $\chi^2 > 6$
$\pi^\pm$	`hasRich`
$\pi^\pm$ from K^0_S	$\text{p}(\pi^\pm) > 2\,\text{GeV}/c$
event	SPD Multiplicity < 600 (*S21r(0/1)p1*)
	SPD Multiplicity < 450 (*S24r1,S28r1,S29r2 & S34*)

as taken from Equation 9 in Ref. [7]. The parameter b is configured with different values (1.1, 1.6 and 2.3) for different TCK throughout the data taking in 2016. As MC uses only one TCK configuration per year, there should be only one value for b. Solving Eq. (1) for b one gets

$$b = \left[\log\left(\frac{\chi^2_{\text{IP}}}{7.4}\right) - \frac{1}{(p_\text{T}[\,\text{GeV}] - 1)^2}\right] \times \frac{25}{25 - p_\text{T}[\,\text{GeV}]}. \tag{2}$$

This parameter was plotted with reweighted MC events and *sWeighted* data events for 2016 `DD` tracks and `LL` tracks samples and is shown in Fig. 2. No significant difference where found, especially since the region of interest (larger 1.0) is very poorly occupied. Therefore, no further measures are considered for this issue.

2.3.2 Hlt2DiMuonDetached bug

For 2015 & 2016 data, a bug in the trigger line *Hlt2DiMuonDetached* was found after data acquisition (DAQ). This bug resulted in a cut of the invariant mass spectrum of the $\mu^+\mu^-$ system, rejecting events below $2900\,\text{MeV}/c^2$ [8]. Tests with 2017 data have shown, that the

Table 4: Total statistics after stripping of the events with stripping line `B2XMuMu`.

Year	track type	magnet down	magnet up	combined
2011	DD	388036	264746	652782
	LL	120005	82327	202332
	total	508041	347073	855114
2012	DD	712096	815428	1527524
	LL	201635	230618	432253
	total	913731	1046046	1959777
2015	DD	143389	110853	254242
	LL	46084	35663	81747
	total	189473	146516	335989
2016	DD	1039721	606637	1646358
	LL	374974	219603	594577
	total	1414695	826240	2240935
2017	DD	894466	835997	1730463
	LL	280844	266437	547281
	total	1175310	1102434	2277744
2018	DD	1402618	1398665	2801283
	LL	1188165	1182087	2370252
	total	2590783	2580752	5171535

Table 5: List of the trigger requirements for Run I + II. All trigger lines within the same trigger level are used in a logical *OR*. The trigger decision is TOS in all cases.

Trigger level	Run I	Run II
L0	L0Muon	L0Muon
HLT1	TrackAllL0	TrackMVA
	TrackMuon	TrackMuon
HLT2	DiMuonDetached	DiMuonDetached
	TopoMu2BodyBBDT	TopoMu2Body
	TopoMu3BodyBBDT	TopoMu3Body
	Topo2BodyBBDT	Topo2Body
	Topo3BodyBBDT	Topo3Body
		TopoMuMu2Body (2016 – 2018 only)
		TopoMuMu3Body (2016 – 2018 only)

fraction of events below 2900 MeV/c^2 and exclusively triggered by *Hlt2DiMuonDetached* relative to all events (passing the nominal trigger) is approximately 10 %: In 2017 magnet down (up) 10.33% (7.95%) of all triggered events had an exclusive HLT2 trigger from *Hlt2DiMuonDetached* and had an invariant $\mu^+\mu^-$ mass below 2900 MeV/c^2. 2017 `DD` tracks samples show a lower fraction of 9.75% (7.49%) than 2017 `LL` tracks samples with 12.24%

Table 6: Signal event statistics for each trigger line in Run I and Run II after the cut based selection (see Section 2.4 is applied. The complete q^2 range is considered as signal, including the charmonium resonance regions. For these numbers, the sum of *sWeights* for each trigger line is added up. Note that each event can be triggered by multiple lines and, hence, is counted into the statistics of each trigger line. The naming convention of Run II is used in this table. The Run I equivalent names can be seen in Table 5.

Stripping line	Run I	Run II
L0Muon	30973.9	99195.3
Hlt1TrackMVA	26109.8	94874.2
Hlt1TrackMuon	30522.5	97339.3
Hlt2DiMuonDetached	27229.6	94259.6
Hlt2TopoMu2Body	25326.4	90274.6
Hlt2TopoMu3Body	19760.2	86467.9
Hlt2Topo2Body	21070.1	81828.6
Hlt2Topo3Body	17984.4	84264.2
Hlt2TopoMuMu2Body	0.0	73589.7
Hlt2TopoMuMu3Body	0.0	82188.7

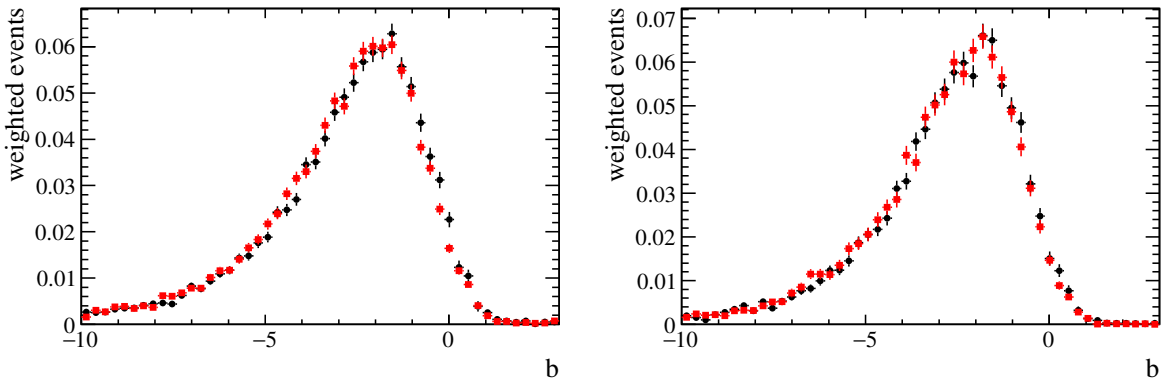

Figure 2: Parameter b (Eq. (2)) is plotted for *sWeighted* data (black) and reweighted MC (red) for `DD` tracks (left) and `LL` tracks (right) samples of 2016. The perfect agreement of both distributions indicates no issues with different values of b in 2016 MC events. This means, an indirect cut in the two-dimensional plane of χ^2_{IP} and p_{T} does not affect this analysis. See Section 2.7.4 for information about the applied MC reweighting.

(9.42%) for magnet down (up). The bug well represented in MC and hence the only effect of this bug is a reduction of event yield.

2.3.3 ALLSAMEPV bug

The impact of the `ALLSAMEPV` [9] [10] bug on the analysis was investigated. The stripping line `B2XMuMu` does not make use of the `ALLSAMEPV` LoKi functor. And despite that the use of *Topo*-trigger-lines in a logical *OR* for the trigger selection, the `ALLSAMEPV` bug has only a minor impact on the event yield, as the `ALLSAMEPV` LoKi functor is used in a *OR*

configuration in those lines as well. The distribution of primary vertices per event also is in good agreement in MC and data, as shown in the appendix, Appendix A.3.

2.3.4 TISTOS bug

Due to a bug in the trigger decision making (*TISTOSing* [11] [12]), the data sample is updated to incremental stripping versions of *S24r1*,*S28r1* and *S29r2* for 2015, 2016 and 2017, respectively, in which the bug has been fixed.

2.4 Cut-based Selection

In a further step, cuts in particle identification variables and kinematics are applied to remove background events.
Veto regions in invariant mass spectra of different combinations of the daughter particles are used to remove partially reconstructed background events.

2.4.1 Invariant mass and DecayTreeFitter

The mass of the B^+ meson is given from the invariant mass of all five daughter particles

$$m(B^+) = m_{inv}(\pi^+\pi^-\pi^+\mu^+\mu^-) \tag{3}$$

However, the mass of the K^0_S is constrained to the world averaged value [13] using DecayTreeFitter [14], resulting in

$$m(B^+) = m_{inv}(K^0_S\pi^+\mu^+\mu^-). \tag{4}$$

In addition to this mass constrain, the primary vertex (PV) and all particles momenta are included into the DecayTreeFitter with constrains equal to their measurement uncertainties. This improves the resolution on the invariant mass of the B^+ slightly by approximately $1\,\mathrm{MeV}/c^2$. All kinematic variables in the selection and the determination of the angles (see Section 3) are using the values from the DecayTreeFitter. We require the fit of the DecayTreeFitter to converge and cut away events with a χ^2 larger than 200 and require the fit status to be equal to 0. The cut on the χ^2 is very soft and lies at the upper end of the DecayTreeFitter χ^2 distribution.
As a first step in the cut-based selection, the reconstructed invariant mass of the B meson is required to lie within the region, $5150\,\mathrm{MeV}/c^2 < m_{B^+} < 6000\,\mathrm{MeV}/c^2$. This cut removes background events left to the mass peak of the B^+ at $m^{(\mathrm{PDG})}_{B^+} = 5279.32\,\mathrm{MeV}/c^2 \pm 0.14\,\mathrm{MeV}/c^2$, the global mean value obtained by the Particle Data Group (PDG) [13]. The low mass cut at $5150\,\mathrm{MeV}/c^2$ is loose enough to not cut into the low mass tail of the signal peak. At the same time, the high upper mass limit of $6000\,\mathrm{MeV}/c^2$ leaves enough background events right to the mass peak as a background proxy for the training of the multi-variate analysis.
A window of $\pm 100\,\mathrm{MeV}/c^2$ is applied around the peak position of the K^{*+} at $m^{(\mathrm{PDG})}_{K^{*+}} = 891.76\,\mathrm{MeV}/c^2 \pm 0.25\,\mathrm{MeV}/c^2$ in the $K^0_S\pi^+$ invariant mass spectrum.

2.4.2 Veto against peaking background structure

A peaking background in the mass-region above the B^+ mass peak originates from the rare decay $B^0 \to K^0_S \mu^+\mu^-$ combined with a (slow) random pion. As shown in Figs. 3 and 4, a cut around the invariant mass of $B^0 \to K^0_S \mu^+\mu^-$ is therefore applied and events with $\left\| m(K^0_S \mu^+\mu^-) - m^{(\mathrm{PDG})}_{B^0} \right\| < 50\,\mathrm{MeV}/c^2$ are dismissed. Tested on the MC samples, the signal efficiency of this veto is found to be 99.8% and larger. Also, the background efficiency in the angular distributions of the background is evaluated, as presented exemplary for the 2017 magnet up sample in the appendix, Appendix A.4. Unlike in previous analysis (of the B^0 decay), the remaining spectrum of the angular distributions does not see edges or spikes in the $\cos\theta_K$ distribution as a result of this cut. A polynomial description of the angular background is possible. The agreement of the angular background in the lower and upper mass side-band will be further investigated and discussed in Section 3.3.4. Hence, a further systematic study of the effect on the angular distributions in signal data is not performed.

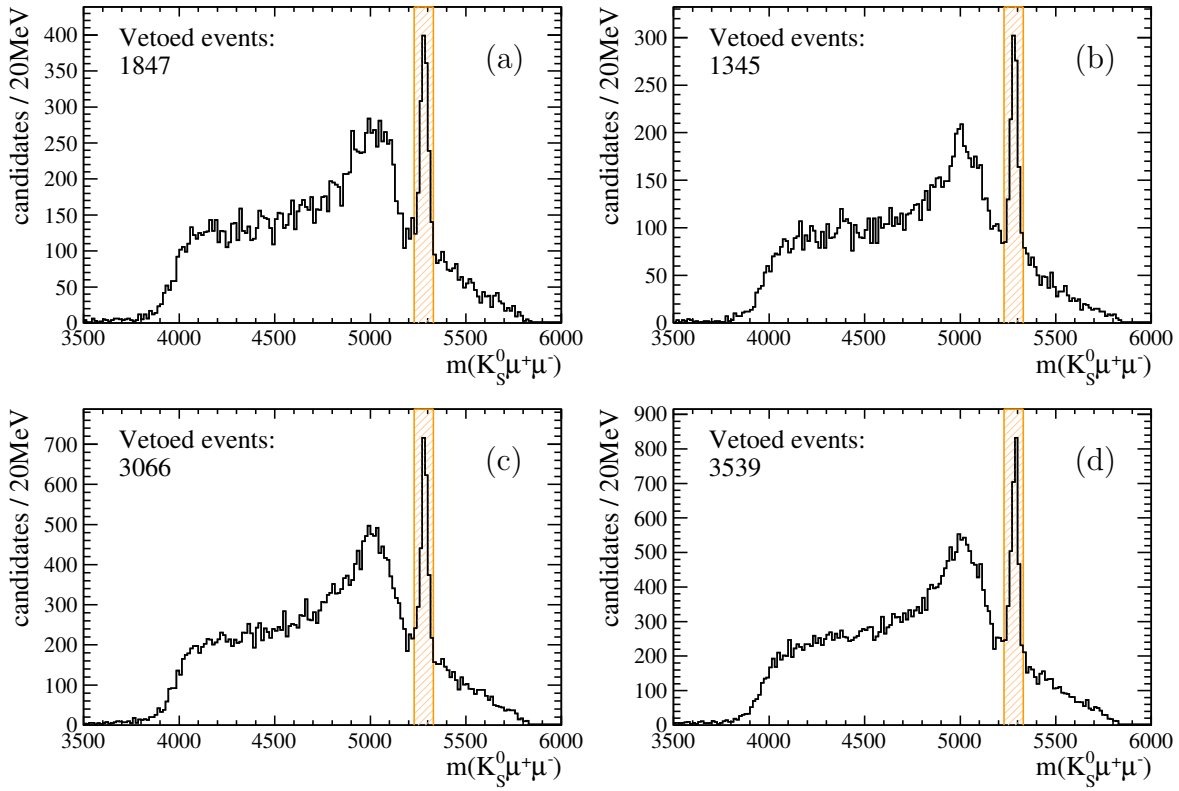

Figure 3: Invariant mass of $K^0_S \mu^+\mu^-$ with the veto around the B^0 mass indicated in orange. Data from Run I is shown for 2011 (a)+(b) and 2012 (c)+(d) with magnet polarity down and up, respectively. The number of rejected events is given in each histogram.

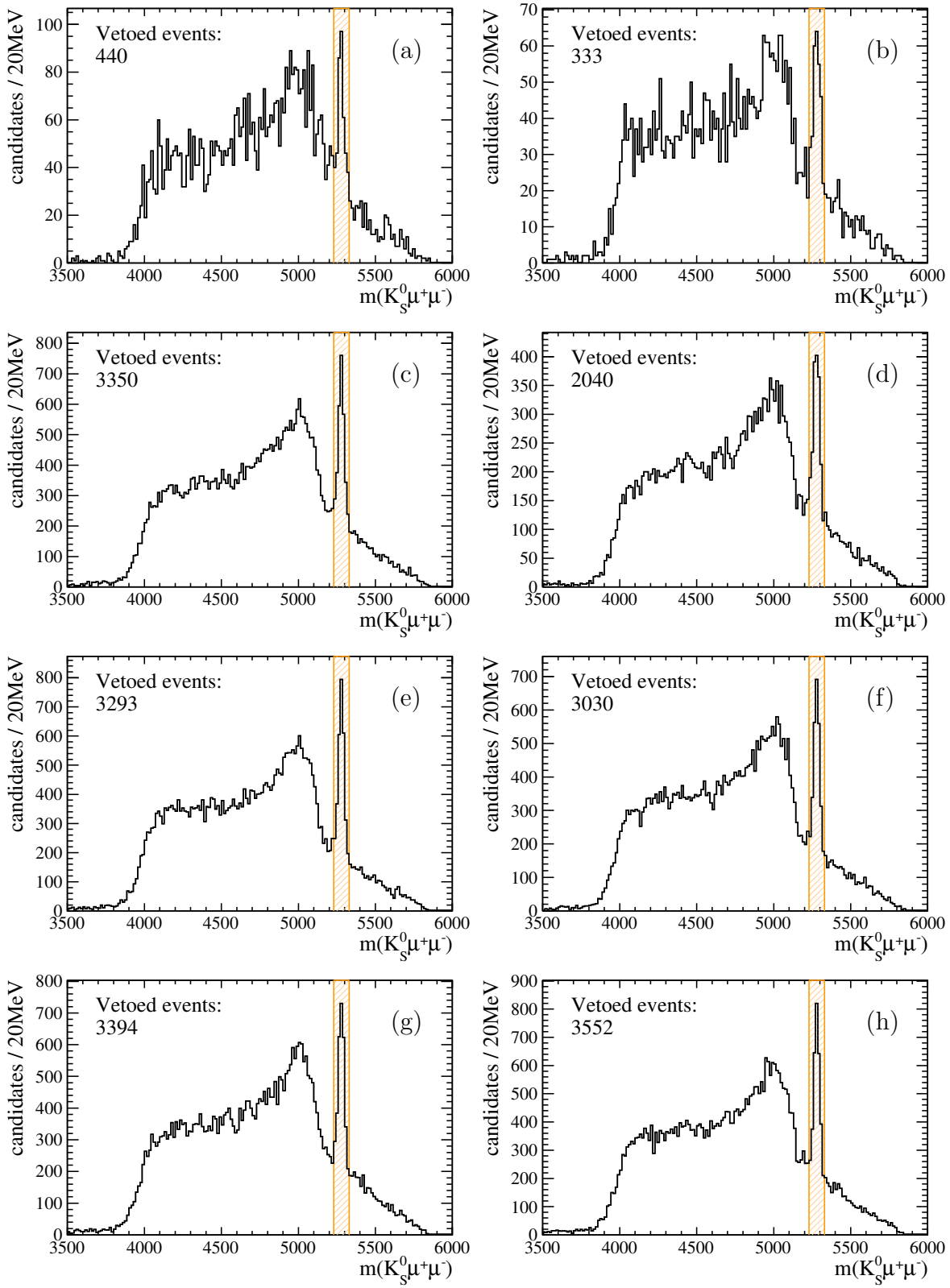

Figure 4: Invariant mass of $K^0_S\mu^+\mu^-$ with the veto around the B^0 mass indicated in orange. Data from Run II is shown for 2015 (a)+(b), 2016 (c)+(d), 2017 (e)+(f) and 2018 (g)+(h) with magnet polarity down and up, respectively. The number of rejected events is given in each histogram.

2.4.3 Decay kinematics

To avoid modelling the reconstruction efficiency of tracks that are close to the outer edge of the detector active region, all signal candidate tracks are required to have an opening angle from the beam-pipe, θ, smaller than 400.0 mrad. Furthermore, to ensure a significant spacial separation of the their VELO hits, the track pairs of $\mu^+\mu^-$ and the three track pairs of the three final state pions must all have a minimum opening angle of $\theta_{\text{pair}} > 1\,\text{mrad}$ with respect to each other.

2.4.4 Particle identification

Particle identification (PID) requires the combined information from different sub-detector systems. Pions are required to have information from the RICH systems (the `hasRich` flag has to be true) and muon candidates are required to be tagged as muons by the muon system (the `isMuon` flag has to be true). Both muons are cut by a global particle identification classifier: $\text{ProbNN}_\mu > 0.25$.
For simulated MC events, the PID variables are corrected before applying the selection. This process will be explained in more details in Section 2.7.2.

2.4.5 Double misidentification

As a last step in the cut-based selection, the possibility of double misidentification of a muon and a pion, coming from $B^+ \to J/\psi\, K^{*+}$, with the PID hypotheses of the μ^+ from the J/ψ and the π^+ from the K^{*+} being swapped. This would result in an invariant mass of the $\mu^+\mu^-$ system outside of the vetoed charmonium q^2-regions, while keeping the $\mu^+\mu^- K^{*+}$ invariant mass consistent with a B^+ decay hypothesis. To reduce the impact from double misidentification pollution in the sample, the mass hypotheses of the π^+ and μ^+ are swapped and a two dimensional cut in the plane of the two invariant masses $\text{m}(\mu^-[\pi^+]_{m_\mu})$ and $\text{m}(K^0_\text{S}[\mu^+]_{m_\pi})$ is performed:

$$\left\| m(\mu^-[\pi^+]_{m_\mu}) - m^{(\text{PDG})}_{J/\psi} \right\| > 50\,\text{MeV}/c^2 \text{ and}$$

$$\left\| m(K^0_\text{S}[\mu^+]_{m_\pi}) - m^{(\text{PDG})}_{K^{*+}} \right\| > 30\,\text{MeV}/c^2.$$

The signal efficiency of this cut was determined on signal MC events (see Section 2.7) to be above 99.9%.
The exited $c\bar{c}$ resonance ($\psi(2S)$) has been tested for a potential pollution into the signal region, but due to a smaller branching fraction (with respect to the J/ψ resonance), no events have been found and therefore no veto is applied.

2.5 Mass fit

A fit to the $K^0_\text{S}\pi^+\mu^+\mu^-$ invariant mass is crucial for many aspects of the analysis, including the optimisation of the selection (Section 2.8), the matching of MC and data (Section 2.7) and the final fit to extract the physical observables (Section 4). The fit-model comprises a component for the B^+ mass peak as well as a component for the combinatorial background. The B^+ mass peak is modelled by a Crystal Ball [15] functions. Crystal Ball (CB) functions are empirical descriptions of a mass spectrum peaking at x_{peak}, using a Gaussian bell

function of width σ. In the presented case, both sides of the Gaussian are cut off at $\alpha_{1,2}$ and described by an exponential tail of power $n_{1,2}$. With these parameters, the Crystal Ball is defined mathematically by

$$\mathcal{P}_{CB}(x; x_{peak}, \sigma, n_1, n_2, \alpha_1, \alpha_2) = N \cdot \begin{cases} A_1 \cdot (B_1 - \frac{x - x_{peak}}{\sigma})^{-n_1} & \text{for } \frac{x-x_{peak}}{\sigma} \leq -\alpha_1 \\ exp(\frac{-(x-x_{peak})^2}{2\sigma^2}) & \text{for } -\alpha_1 \leq \frac{x-x_{peak}}{\sigma} \leq \alpha_2 \\ A_2 \cdot (B_2 - \frac{x - x_{peak}}{\sigma})^{-n_2} & \text{for } \alpha_2 \leq \frac{x-x_{peak}}{\sigma} \end{cases},$$

with the normalisation, N, and the two coefficients $A_{1,2}$ and $B_{1,2}$, defined as

$$\begin{aligned} A_{1,2} = & \ (\frac{n_{1,2}}{\|n_{1,2}\|})^{n_{1,2}} \cdot exp(\pm\frac{\alpha_{1,2}^2}{2}), \\ B_{1,2} = & \ \frac{n_{1,2}}{\|\alpha_{1,2}\|} - \|\alpha_{1,2}\| \,. \end{aligned}$$

The shape of the of the signal peak is obtained from a fit to the corresponding simulated event sample (see Section 2.7) and the parameters $n_{1,2}$ and $\alpha_{1,2}$ are fixed to the obtained values. The mean position and the width, σ, of the Crystal Ball functions are floating in the fit. In the appendix, Appendix A.2, all fits to simulated events are shown, from which the mass shapes are obtained.

The combinatorial background model is a single exponential using only one free parameter. Always, the exponent of all exponential functions have negative signs.

In total twelve samples are fitted individually, separated by `DD` tracks and `LL` tracks as well as by years. In Figs. 5 and 6 the results of fits to the reference channel $B^+ \to J/\psi\, K^{*+}$ for Run I and Run II are shown.

We see some remaining discrepancy in the upper mass side-band of 2016–2018 `DD` tracks tracks. The larger statistics in these samples highlight the veto cut against B^0 plus random π^+ (see Section 2.4), which cuts away some combinatorial in the mass region between 5400 and 5600 MeV/c^2. This small residual in the pull histograms is however negligible for the usage of *sWeights* for MC reweighting.

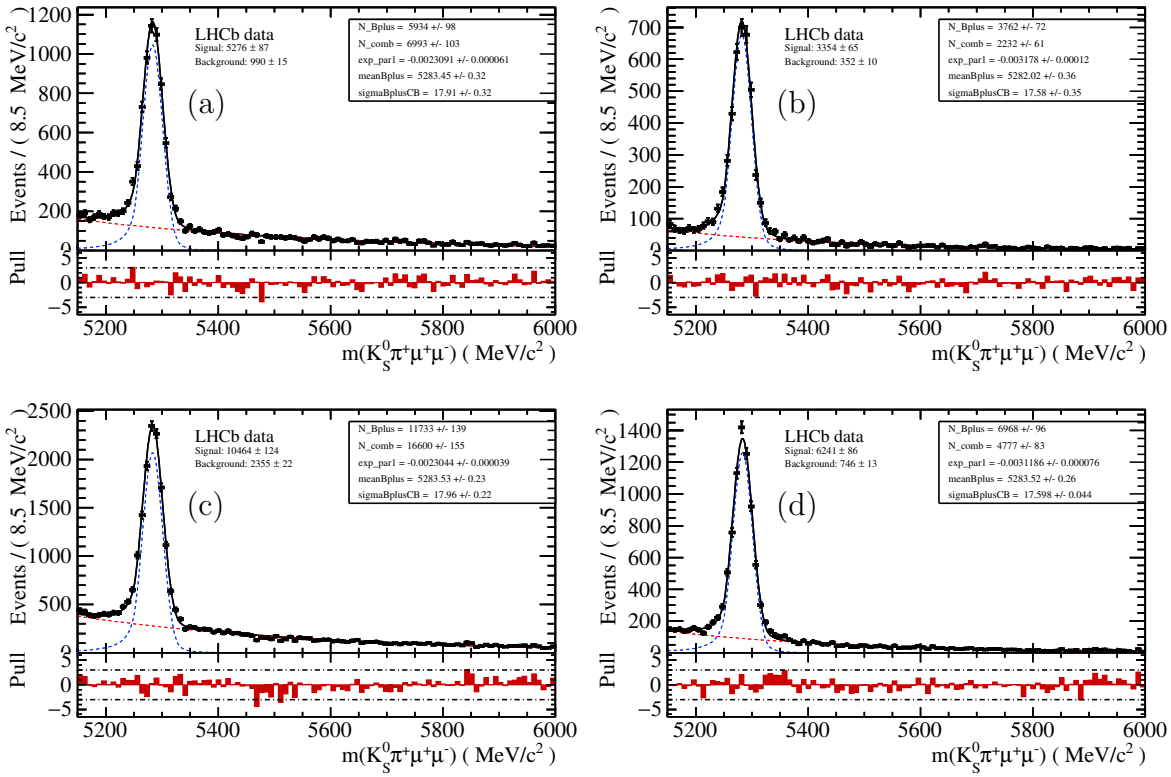

Figure 5: B^+ mass distribution of events from 2011 DD (a) and LL (b) track events and 2012 DD (c) and LL (d) track events. These data samples consist almost entirely of $\mu^+\mu^-$ decays coming from a J/ψ by filtering the invariant mass squared to $8.68\,\mathrm{GeV}^2/c^4 < q^2 < 10.09\,\mathrm{GeV}^2/c^4$. The B^+ mass peak is modelled by a two tailed Crystal Ball (one tail to low mass region and one towards high mass region). The remaining background is described by an exponential function.

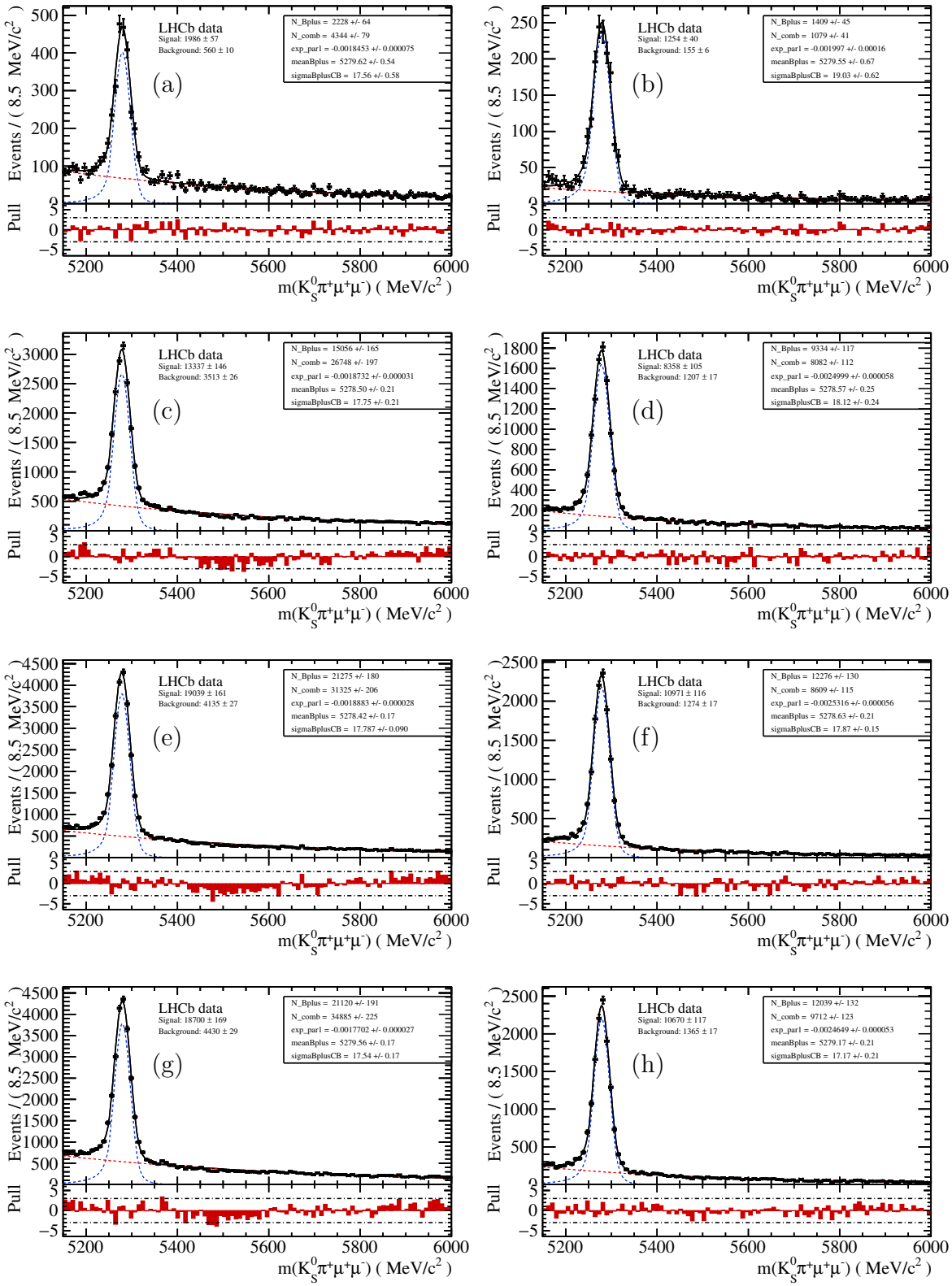

Figure 6: B^+ mass distribution of events from 2015 DD (a) and LL (b), 2016 DD (c) and LL (d), 2017 DD (e) and LL (f) and 2018 DD (g) and LL (h) track events. These data samples consist almost entirely of $\mu^+\mu^-$ decays coming from a J/ψ by filtering the invariant mass squared to $8.68\,\mathrm{GeV}^2/c^4 < q^2 < 10.09\,\mathrm{GeV}^2/c^4$. The B^+ mass peak is modelled by a two tailed Crystal Ball (one tail to low mass region and one towards high mass region). The remaining background is described by an exponential function.

2.6 Signal estimation

For the optimisation of the multi-variate analysis, the estimation of signal events in the sample is essential. To avoid biasing the optimisation on upward fluctuations of the signal, the yield of the reference channel $B^+ \to J/\psi K^{*+}$ is used to determine the number of events with signal signature.

The expected yield of the signal channel, $Y^{(\mathrm{cbs})}_{K^{*+}\mu^+\mu^-}$, is therefore determined by scaling the yield of the reference channel $B^+ \to J/\psi K^{*+}$ $Y^{(\mathrm{cbs})}_{J/\psi K^{*+}}$ via the different branching fractions and assuming the selection efficiency is the same for the reference and signal channels:

$$Y^{(\mathrm{cbs})}_{K^{*+}\mu^+\mu^-} = \frac{\mathcal{B}_{eff}(B^+ \to K^{*+}\mu^+\mu^-)}{\mathcal{B}(B^+ \to J/\psi K^{*+}) \cdot \mathcal{B}(J/\psi \to \mu^+\mu^-)} \cdot Y^{(\mathrm{cbs})}_{J/\psi K^{*+}} \tag{5}$$

with PDG values used for the branching fractions $\mathcal{B}\,(B^+ \to J/\psi K^{*+})$ and $\mathcal{B}\,(J/\psi \to \mu^+\mu^-)$. This method assumes the selection efficiency of both reference and rare channel to be identical. Ref. [5] measured the ratio of the total selection efficiencies for the two channels to be compatible with 1.0 within a 10% uncertainty. For Run I [2] we determined the selection efficiencies (to the point after the cut-based selection) to be 1.80% (1.98%) in 2011 for the rare (reference) channel. In 2012, the same efficiency is 1.66% (1.81%) for the rare (reference) channel. These values have been calculated from the MC event samples and are is agreement with the ratios of Ref. [5].

The yields of the reference channel are obtained with the fits described in Section 2.5 and are shown in Table 7. The branching fraction of the signal channel, $\mathcal{B}_{\,eff}(B^+ \to K^{*+}\mu^+\mu^-)$ is calculated from the results of the measurement of the differential branching fraction [16]. Table 6 in this publication contains the resulting values of $\frac{\mathrm{d}\mathcal{B}}{\mathrm{d}q^2}$, which are summed up over the q^2 region introduced in Section 3.1.

The resulting value is

$$\mathcal{B}_{eff}(B^+ \to K^{*+}\mu^+\mu^-) = 6.096 \pm^{0.650}_{0.578} (stat.) \pm 0.171(sys.) \times 10^{-7}. \tag{6}$$

Non-resonant $\mu^+\mu^-$ with $8.0\,\mathrm{GeV}^2/c^4 < \sqrt{s} < 11.0\,\mathrm{GeV}^2/c^4$ are polluting the q^2 region of the reference channel and cannot be voted, however, the number of events for this case is negligible compared to the large number of $B^+ \to J/\psi K^{*+}$ decays.

Identically to the paragraph before, the B^+ invariant mass spectrum is modelled using a two tailed Crystal Ball function for the signal component and a single exponential function for the combinatorial background. The signal window is defined to be two times the sigma σ of the Crystal Ball functions around the central mean value of the signal component.

2.7 Monte Carlo

For all simulated events, official LHCb simulation [17] data was used. All available simulated – Monte Carlo (MC) – data is based on simulations using Pythia [18] version 8 and events are reconstructed using DaVinci version v39r1p1 (2011 & 2012), v38r1p3 (2015), v41r4p2 (2016), v42r7p3 (2017) and v44r7 (2018).

A set of three different MC samples is produced, namely signal decay MC describing the signal decay $B^+ \to K^{*+}\mu^+\mu^-$, the reference decay $B^+ \to J/\psi K^{*+}$ and so called phase-space MC of the signal decay, in which no physical couplings are included but the

[2] For Run II no reference channel MC was available, as listed in Table 11.

Table 7: Raw event numbers after the application of the cut-based selections. These numbers contain signal and background events over the full invariant mass range of the B meson.

Year	track type	number of events
2011	DD	19841
	LL	7775
	total	27616
2012	DD	43438
	LL	15413
	total	58851
2015	DD	6572
	LL	2488
	total	9060
2016	DD	41804
	LL	17415
	total	59219
2017	DD	52600
	LL	20884
	total	73484
2018	DD	56006
	LL	21751
	total	77757

Table 8: Estimated signal yield after the cut-based selection. The value is determined from the event yield of the reference channel $B^+ \to J/\psi K^{*+}$. The corresponding mass distributions are shown in Figs. 5 and 6. This signal event yield is scaled by the different branching ratios. The background yield is taken from signal channel directly, by counting all events in the mass region and subtracting the signal yield estimations.

Run	track type	signal estimation	background events
Run I	DD tracks	158	2035
	LL tracks	97	451
Run II	DD tracks	492	4813
	LL tracks	291	1016
Run I + II	DD tracks	650	6848
	LL tracks	388	1467

decay has the pure kinematics of phase-space distribution. In addition, the phase-space MC request has a flat q^2 distribution.

Due to different reconstruction efficiencies for K^0_S in the trigger throughout the data taking in 2012, the MC phase-space request is separated in early 2012 and late 2012 with different trigger configurations. The differences in the HLT1 trigger lines *Hlt1TrackMuon* and *Hlt1TrackAllL0* are shown in Table 9. After testing the sub-samples showed no differences

Table 9: The different cuts for HLT1 trigger lines *Hlt1TrackMuon* and *Hlt1TrackAllL0* between the early and late 2012 data-taking period. All further cuts, which are identical in the early and late period are not mentioned. All other trigger lines from Table 5 do not show differences between early and late

Data taking periode in 2012	early	late
Hlt1TrackMuon:		
Track momentum	$> 8000\,\text{MeV}/c$	$> 3000\,\text{MeV}/c$
Hlt1TrackAllL0:		
Track trans. momentum	$> 1700\,\text{MeV}/c$	$> 1600\,\text{MeV}/c$
Track momentum	$> 10000\,\text{MeV}/c$	$> 3000\,\text{MeV}/c$
Track χ^2_{IP}	< 1.5	< 2.0
`ValidateWithTT`	false	true

Table 10: List of all used DECfiles in the production of simulated events.

number	class	sub-decay	name
12115102	signal	$K^{*+} \to K^0_S \pi^+$	`Bu_Kstmumu,KSpi=DecProdCut`
12115179	phase-space	$K^{*+} \to K^0_S \pi^+$	`Bu_Kstmumu,KSpi=PHSP,flatq2,DecProdCut,TightCut`
12145102	reference	$K^{*+} \to K^0_S \pi^+$	`Bu_JpsiKst,mm,pipipi=DecProdCut`

in their angular distributions, the mixture of different TCK configurations in 2012 with the approximately same fraction of events from early/late in data and MC are combined into a single 2012 sample.

2.7.1 DECfiles

To describe the B^+ decay in simulation, DECfiles describe all included particles and define the coupling in the decay. An overview of the used DECfiles used for this analysis is presented in Table 10. Simulated data with a phase-space like kinematic distribution is used to correct for angular acceptance effects. This simulation data is filtered by the stripping line (`B2XMuMu`) before saving the data to disk and undergoes generator level cuts at the production step to reduce the use of computation power. Therefore, the numbers for the phase-space MC in Table 10 are given after the application of the filter.

The incorrect use of DecayDescriptor arrows in the DECfiles for filtered phase-space resulted in an incorrect asymmetry in the angular distribution of $\cos\theta_L$ [19]. The phase-space MC sets for the years 2011-2016 had to be redone, while the error was found just before the 2017 & 2018 production had started. DECfile numbers 12115178 and 12113445 have been declared obsolete in the process.

Table 11: Statistics of the number of produced simulation events with signal-like events with sub-decay $K^{*+} \to K^0_S \pi^+$. The DECfile numbers are 12115102 (signal), 12115179 (phase-space) and 12145102 (reference). The numbers of phase-space MC are given after the filter. See text for details on these numbers.

Year	signal		phase-space		reference	
	MagDown	*MagUp*	*MagDown*	*MagUp*	*MagDown*	*MagUp*
2011	1M	1M	75k	75k	1M	1M
2012	1M	1M	50k+125k	50k+125k	1M	1M
2015	500k	500k	40k	40k	–	–
2016	1M	1M	210k	210k	–	–
2017	1.15M	1.15M	240k	240k	–	–
2018	1.15M	1.15M	290k	290k	–	–

2.7.2 Correction of particle identification variables

Particle identification (PID) variables are poorly described in simulated event generation. All PHSP MC samples are corrected using the PIDGEN [20] toolkit.

2.7.3 Monte Carlo truth-matching

All simulated events are checked for their reconstructed accordingly to their true information, which is saved in the process of generating simulated events. From the tool `BackgroundCategory` [21] events with category 10 and 50 are excepted for the signal channel. This counts for signal MC as well as PHSP MC. While for the reference channel, categories 0 and 50 are excepted.
Category 0 and 10 mark events, where no background category as defined in Ref. [21] was found, with the only difference, that in category 10 further resonances may be in the decay chain. This is by definition the case, as the di-muons are always reconstructed as a J/ψ first. Events from category 50 mostly make up the lower mass tail of the B meson peak, as due to partial reconstructed radiative decays.
Ghosts in category 60 are rejected. The events from category 60 peak slightly at the B^+ mass, but contain a large fraction of high mass background which would then later be considered as signal. Also the angular distributions of category 60 only warp the angular distributions marginally and are therefore rejected.

2.7.4 Monte Carlo re-weighting

Simulation in LHCb is constantly developing and aiming for a perfect agreement with data. However, some differences and decay specific features result in discrepancies in the distributions of some variables. MC events are used as training sample in the multi-variate analysis and to model the angular acceptance and therefore need to match data in the variables relevant to these procedures. Studies have shown that the agreement between MC and data is good enough after reweighting in the following two dimensions:

- `nLongTracks`: Number of long tracks in an event

- `B_plus_PT`: the transverse momentum of the B^+

As shown in Figs. 7 and 8 the correlation between the two variables in data is small and lies below 7.5% for all sub-samples.
Therefore, a two-step one-dimensional re-weighting is performed, first in the dimension of track multiplicity and second in the transverse momentum of the B^+. The ratio of *sWeighted* data events and MC events yield in the (re-)weights for all MC samples. For all years, the *sWeighted* data from the q^2 region of the resonant decay is used as the signal distribution, while the MC sample used for the ratios differs between Run I and Run II: In Run I, weights are determined by using the reference channel MC distributions compared to *sWeighted* data. Whereas in Run II rare-channel MC is considered. The very similar decay kinematics of the reference channel allow a re-weighting of signal channel MC event to *sWeighted* reference channel data. This option is not optimal, since the reference channel does not accommodate any q^2 dependencies. However, since reference channel MC samples were available only up to 2012, signal channel MC samples are used for the re-weighting in Run II.
To account for any possible incorrect weights, the effect of weights on the final fit are investigated in the final systematic studies in Section 5.1.
Weights for Monte Carlo are determined in bins, with bin widths of 1.5 for track multiplicity and 500 MeV/c for the transverse momentum of B^+.

After the first weighting in the track multiplicity, the resulting weights are used for the second step of re-weighting. These intermediate weights are shown in Figs. 9 and 10. The resulting weights for the Monte Carlo sample are shown as a function of the transverse momentum of the B^+ in Figs. 11 and 12 and are applied to the sample for the comparison plots in Section 2.7.5 as well as for the training of the multi-variate analysis in Section 2.8.

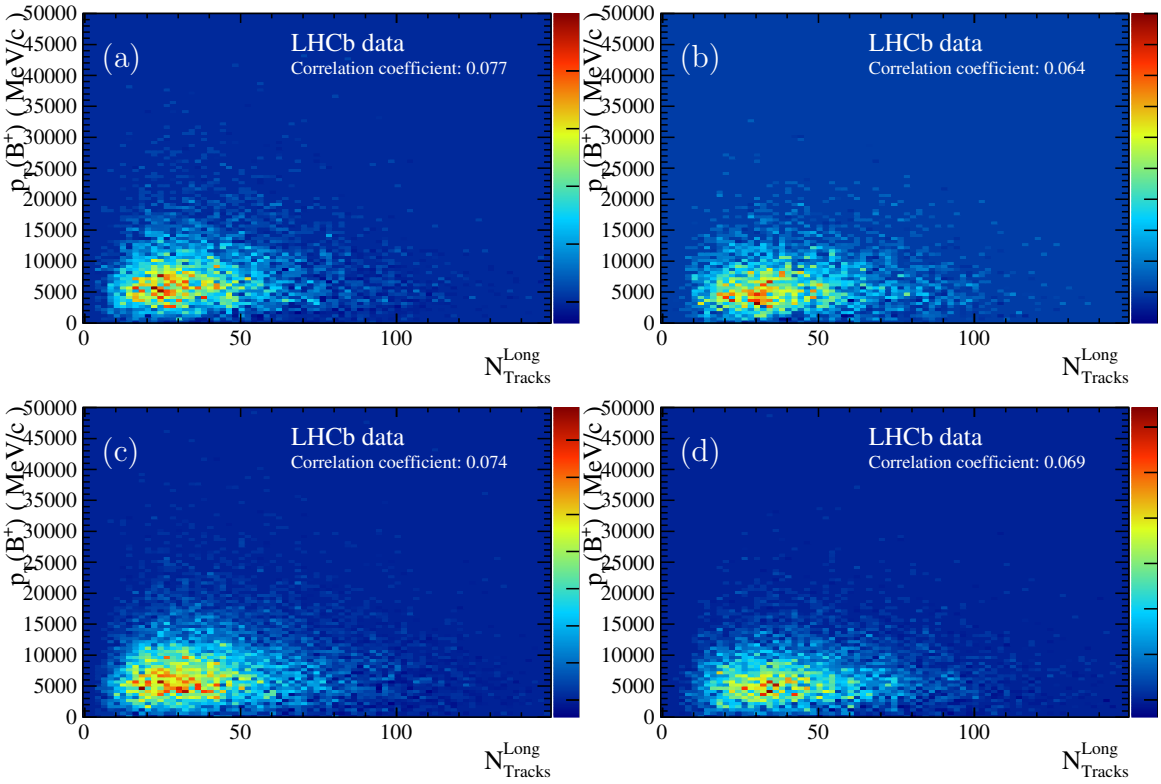

Figure 7: Correlation between the track multiplicity and the transverse momentum of the B^+ for 2011 (a) + (b) and 2012 (c) and (d) with DD tracks events in the left column and LL tracks events in the right column.

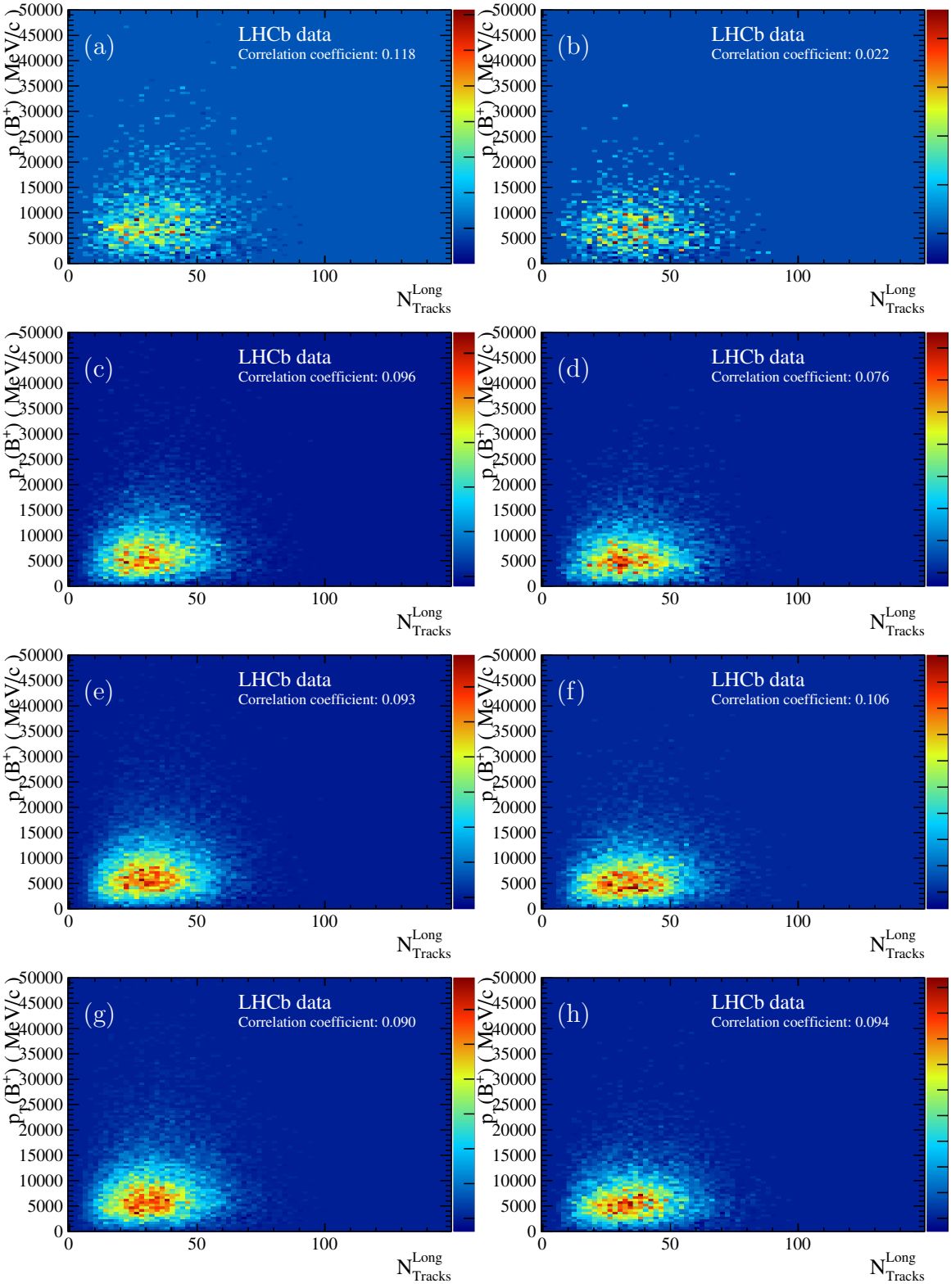

Figure 8: Correlation between the track multiplicity and the transverse momentum of the B^+ for 2015 (a) + (b), 2016 (c) and (d), 2017 (e) and (f) and 2018 (g) and (h), with DD tracks events in the left column and LL tracks events in the right column.

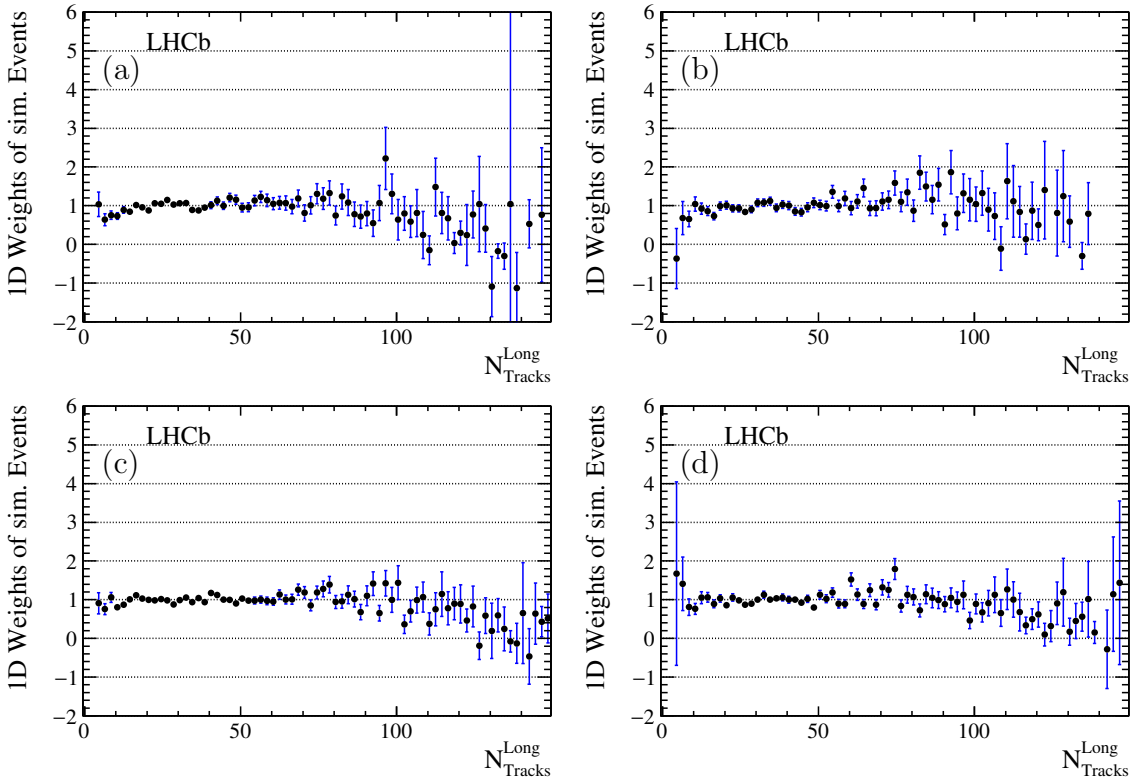

Figure 9: Intermediate weights for simulated events of Run I split in DD tracks and LL tracks events. Re-weights are obtained from the ratio of track multiplicity (*long tracks*) distributions of *sWeighted* data over simulated events. The data is shown for 2011 (a) and (b) and 2012 (c) and (d), with DD tracks events in the left column and LL tracks events in the right column.

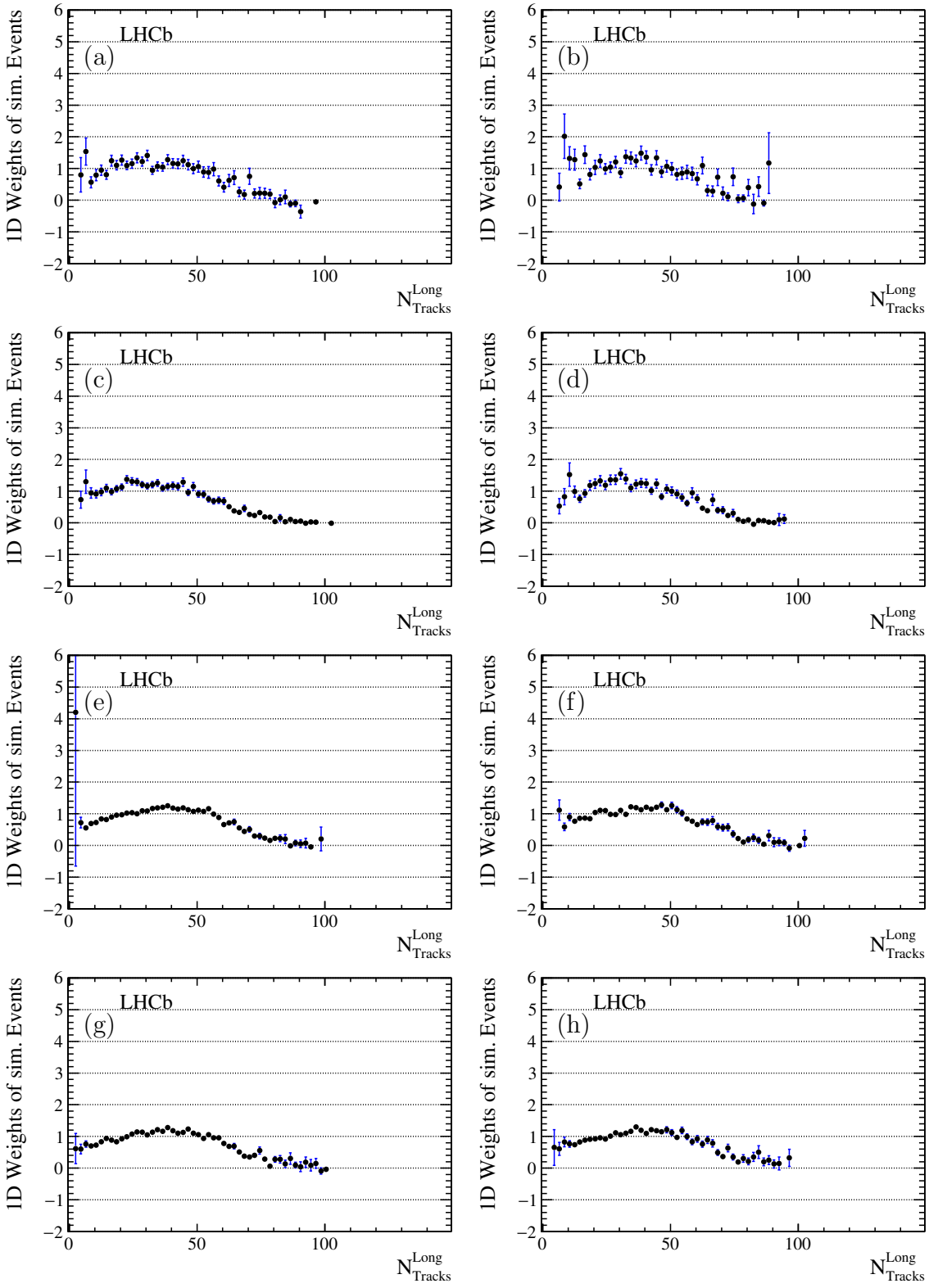

Figure 10: Intermediate weights for simulated events of Run II split in DD tracks and LL tracks events. Re-weights are obtained from the ratio of track multiplicity (*long tracks*) distributions of *sWeighted* data over simulated events. The data is shown for 2015 (a) and (b), 2016 (c) and (d), 2017 (e) and (f) and 2018 (g) and (h), with DD tracks events in the left column and LL tracks events in the right column.

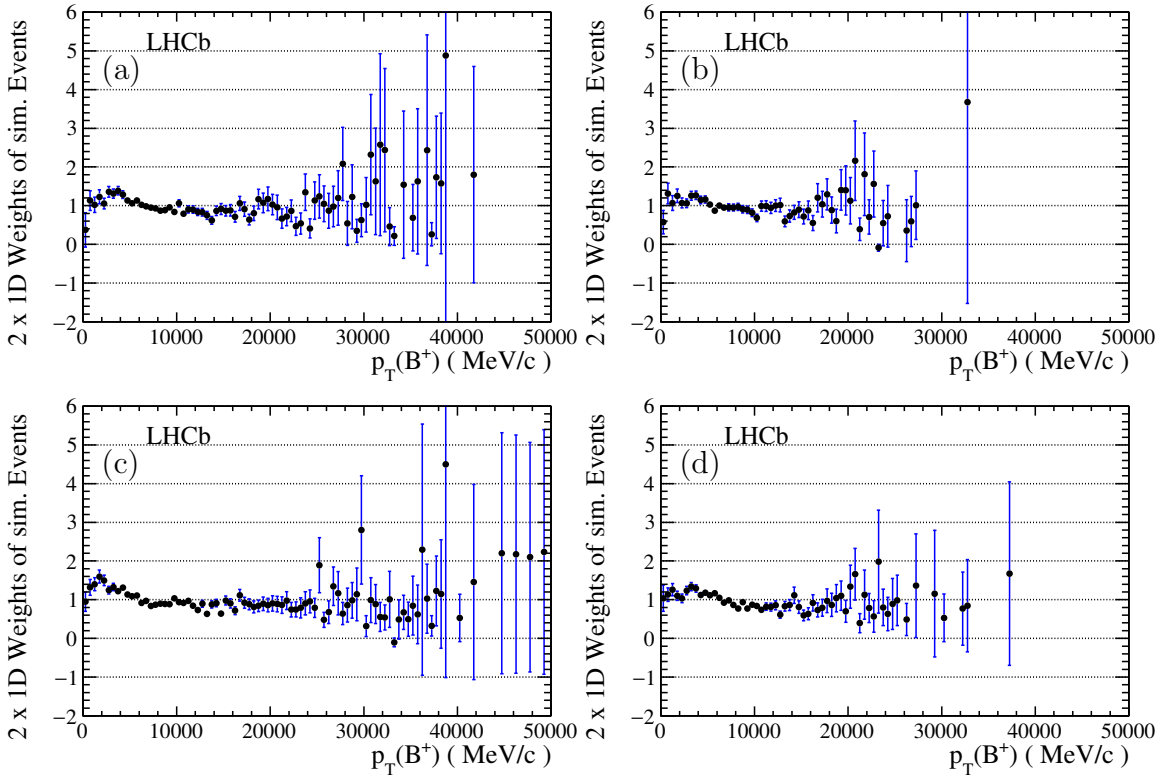

Figure 11: Resulting weights for simulated events of Run I split in DD tracks and LL tracks events. Re-weights are obtained by applying a 1D reweight in track multiplicity and a second step 1D reweight in the transverse momentum of the B^+. The data is shown for 2011 (a) and (b) and 2012 (c) and (d), with DD tracks events in the left column and LL tracks events in the right column.

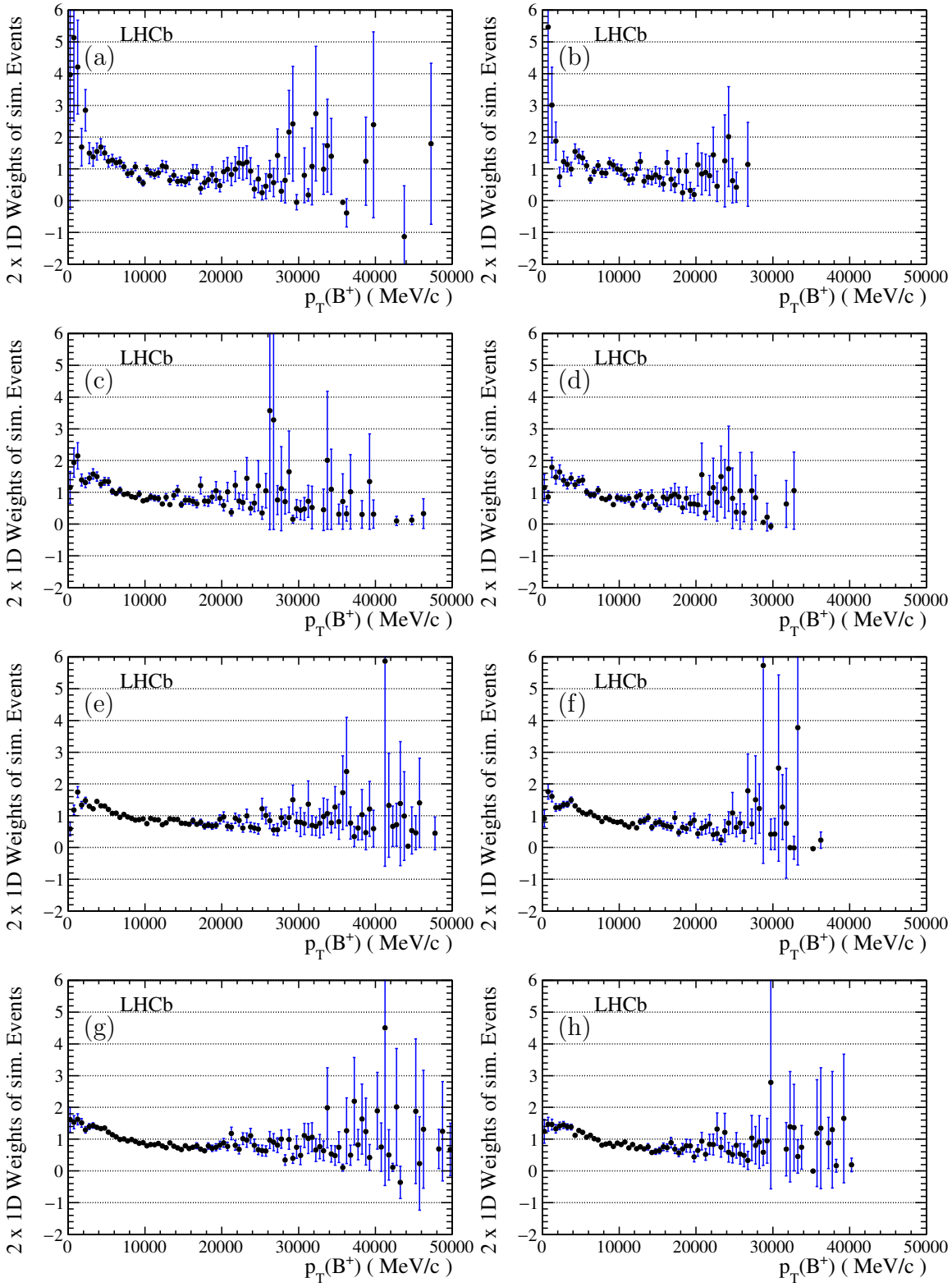

Figure 12: Resulting weights for simulated events of Run II split in DD tracks and LL tracks events. Re-weights are obtained by applying a 1D reweight in track multiplicity and a second step 1D reweight in the transverse momentum of the B^+. The data is shown for 2015 (a) and (b), 2016 (c) and (d), 2017 (e) and (f) and 2018 (g) and (h), with DD tracks events in the left column and LL tracks events in the right column.

2.7.5 Comparison between Monte Carlo and data

sWeights are calculated for experimental data and the Monte Carlo data is re-weighted in two steps in the the number of long tracks track and transverse momentum of the B^+, the distribution of all variables feeding the multi-variate analysis (and the track multiplicity distribution) are displayed in their normalised overlap and as a ratio between data and simulation. The sample is again split up into `DD` tracks and `LL` tracks events and into the individual years. For all years and split into `DD` tracks and `LL` tracks, the comparison plots of data events and simulated MC events can be found in the appendix, in Appendix A.3. All variables[3] show a satisfying agreement, with the exception of $\chi^2_{\text{IP}}(B^+)$, which shows some non-perfect agreement especially for the latest years (2017 + 2018). The effect was tested to be independent of q^2 and re-weighting in this variable has no effect on the angular distributions. It is therefore decided to keep this variable with strong separation power for the multi-variate analysis despite the small deviations between simulation and data.

The input variables of the multi-variate analysis will be summarized in Tables 12 and 13 and non-familiar variables will be explained in the accompanying text in Section 2.8.

2.7.6 L0Muon efficiency differences between Monte Carlo and data

Trigger efficiencies are not guaranteed to match well in data and MC events. For this matter, the L0 trigger efficiency is determined for data and PHSP MC events in all six years to investigate potential effects of this difference on the angular acceptance. Following the study of the B^0 angular analysis (see Section 9.10 in Ref [7]), the usual `TISTOS` method is used to determine the L0Muon efficiencies for both samples. For this method, the sample is required `TIS` of L0Global as well as a cut on track multiplicity: nSPDhits smaller 600 (450) for Run I (Run II) to obtain unbiased samples for the efficiency measurement. The the `TOS` requirement on L0MuonDecision is applied to obtain the efficiency.
In Fig. 13 the L0Muon efficiency is determined in the explained way and as a function of the maximum transverse momenta of the two muons. The ratio of both efficiencies is used to reweight PHSP MC events and the effect on final angular observables is discussed in a systematic study in Section 5.10.

[3]The full set of variables used in Section 2.8 for the training and testing of the multi-variate analysis are compared.

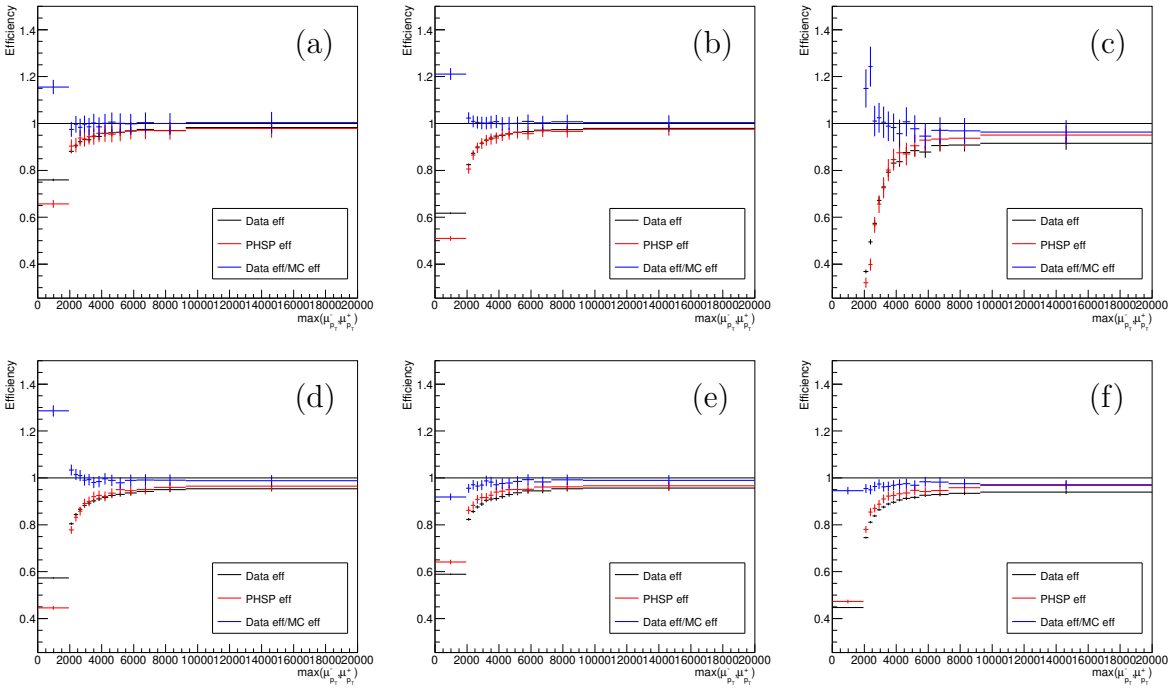

Figure 13: L0Muon efficiency in data (black) and PHSP MC (red). The six plots are showing the full data set of each year: 2011 (a) to 2018 (f). The usual `TISTOS` method is used and the ratio of both efficiencies is determined (blue). The ratios are used for the systematic study of this effect. The mis-match between data and MC is most prominent in the region of low muon momenta and in years up to 2016.

2.7.7 VELO error determination difference in 2017+18

The problem with the discrepancy in the determination of the VELO error between simulated and recorded event samples during the years 2017 and 2018 [22] is investigated. Some IPχ^2 variables are used in the multi-variate analysis, but no direct cut is applied to these variables. A test by taking the normalized ratios of the angular distributions with direct strong cuts in the logarithmic IPχ^2 variable for K^{*+} (smaller 4, 6 or 8) and B^+ (smaller -1, 0, 1 or 2) have shown no significant hints of any distribution being warped. From these tests we conclude that this issue does not impact this angular analysis.

2.8 Multi-Variate Analysis

A multi-variate analysis (MVA) is performed to remove remaining combinatorial background. For this method, the build-in-ROOT tool-kit TMVA [23] is used to optimize the separation power between background and signal. Multi-dimensional decision trees are formed from the given set of input variables. These trees are trained on two defined samples containing only background and signal, respectively. Details about the samples are given in the next paragraph. By iterating these decision trees and applying weights to each branch of the trees for each iteration, the significance in separation is tremendously increased throughout the iteration process. This iterative weighting is called *boost*, therefore the used methods are also referred to as *boosted decision tree* (BDT). As a second method, the slightly different approach of *boosted decision tree - gradient boost* (BDTG) is used. The later method is thought to be less sensitive to statistical fluctuations in the training process. After the training process, the resulting classifier are tested on a test sample; usually the total available sample is split into two halves, one for training and one for testing. This testing ensures the prevention of over-training, in which the boosted decision tree large would show discrepancies in the training sample that are not representative for the total sample. The boosting might run into small statistical fluctuations of the training sample, which are critically enhanced due to the iterative weighting. Results for all sub-samples for training and testing of the method are presented in the corresponding paragraph in the following.

2.8.1 Input variables

Run I and Run II are trained individually but use the exact same set of input variables for the MVA, while `DD` tracks and `LL` tracks use different sets of variables. Between `DD` tracks and `LL` tracks events, different variables are suitable for the input into the MVA due to their agreement between experimental data and simulation data as discussed in Section 2.7.5. Also the discrimination power of variables varies between `DD` tracks and `LL` tracks, and influences the impact of variables on the total separation ability. As a baseline, the input variables from the previous selection in Ref. [5] are used. Suitable variables are added to maximise the separation. Those final selections of variables for the `DD` tracks and `LL` tracks MVA training are listed in order of their separation power inside the MVA in Tables 12 and 13.

Almost all variables are standard LHCb variables and therefore assumed to be well known by the reader. The one exception is p_{T} ConeAsym(B^+). The transverse momentum asymmetry in a cone around the flight direction of the B meson is defined following Ref. [24]

Table 12: List of all input variables for the MVA training in Run I. The list is ordered from most to least significant separation power as determined by the BDTG method for Run I. The variable importance is given in percent.

Run I DD tracks	[%]	Run I LL tracks	[%]
$\ln(\mu^+ \text{ IP}\chi^2)$	9.64	Vertexχ^2 (B^+)	14.86
$\ln(\pi^+ \text{ IP}\chi^2)$	9.51	FlightDistance(K^0_S)	12.48
$\ln(1\text{-}B^+ \text{ DIRA})$	9.40	$\ln(B^+ \text{ IP}\chi^2)$	12.33
$\ln(\mu^- \text{ IP}\chi^2)$	8.88	$\ln(\mu^- \text{ IP}\chi^2)$	12.06
$\eta(\pi^+)$	8.85	$\ln(\mu^+ \text{ IP}\chi^2)$	10.80
p_T ConeAsym(B^+)	8.52	p_T (B^+)	10.58
FlightDistance(K^0_S)	8.48	p_T ConeAsym(B^+)	9.84
$\ln(B^+ \text{ IP}\chi^2)$	8.36	FlightDistance(B^+)	8.69
p_T (K^0_S)	8.32	p_T (K^0_S)	8.36
p_T (B^+)	8.02		
IP(B^+)	6.13		
$\ln(K^{*+} \text{ IP}\chi^2)$	5.89		

Table 13: List of all input variables for the MVA training in Run II. The list is ordered from most to least significant separation power as determined by the BDTG method for Run II. The variable importance is given in percent.

Run II DD tracks	[%]	Run II LL tracks	[%]
$\ln(B^+ \text{ IP}\chi^2)$	10.52	Vertexχ^2 (B^+)	14.07
$\ln(\mu^+ \text{ IP}\chi^2)$	10.20	$\ln(\mu^+ \text{ IP}\chi^2)$	12.29
$\ln(1\text{-}B^+ \text{ DIRA})$	9.96	$\ln(B^+ \text{ IP}\chi^2)$	11.89
$\ln(\mu^- \text{ IP}\chi^2)$	9.19	$\ln(\mu^- \text{ IP}\chi^2)$	11.52
p_T (B^+)	8.58	FlightDistance(K^0_S)	11.51
FlightDistance(K^0_S)	8.53	FlightDistance(B^+)	10.94
p_T (K^0_S)	8.42	p_T (B^+)	10.80
$\eta(\pi^+)$	8.28	p_T ConeAsym(B^+)	9.28
$\ln(\pi^+ \text{ IP}\chi^2)$	8.22	p_T (K^0_S)	7.69
p_T ConeAsym(B^+)	8.09		
$\ln(K^{*+} \text{ IP}\chi^2)$	5.34		
IP(B^+)	4.66		

as

$$p_T ConeAsym(B^+) = \frac{\sum_i p_{Ti} - \sum_j p_{Tj}}{\sum_i p_{Ti} + \sum_j p_{Tj}} \tag{7}$$

with i and j running over the final state particles of the B meson and all particle tracks in the cone, respectively. The opening angle of the cone used in this analysis is 1.0 rad in the η-ϕ-plane.

Correlations between the input variables are tested by the TMVA framework and the

results show satisfyingly independent variables for all four subsets as shown in Figs. 14 and 15 for Run I and Run II, respectively. For variables with a correlation close to 100%, the one with weaker separation power was dismissed from the MVA to keep the training as simple as possible while preserving the maximal separation power. LL tracks event samples show almost no correlation throughout all nine input variables for the MVA training, as seen by the green correlation matrix in Fig. 15. This counts for both, signal and background sample. The DD tracks event samples some variables show significant correlations of above 50%. Due to the fact, that the correlations are different in signal and background samples, the correlations are of no concern.

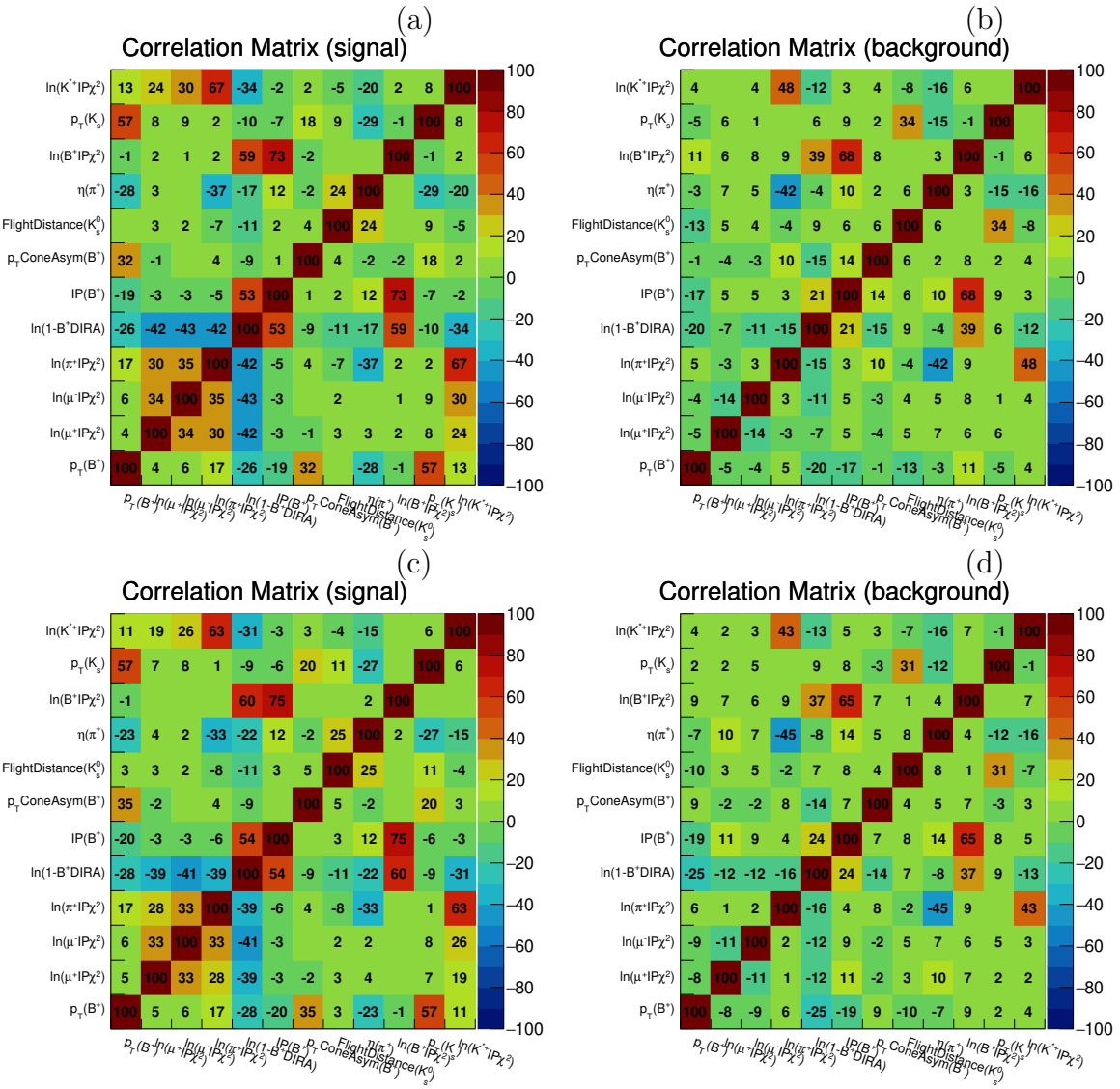

Figure 14: Correlation of input variables for the training and testing of the MVA for DD tracks events. Signal and background candidates for Run I (a) and (b) and Run II (c) and (d), respectively.

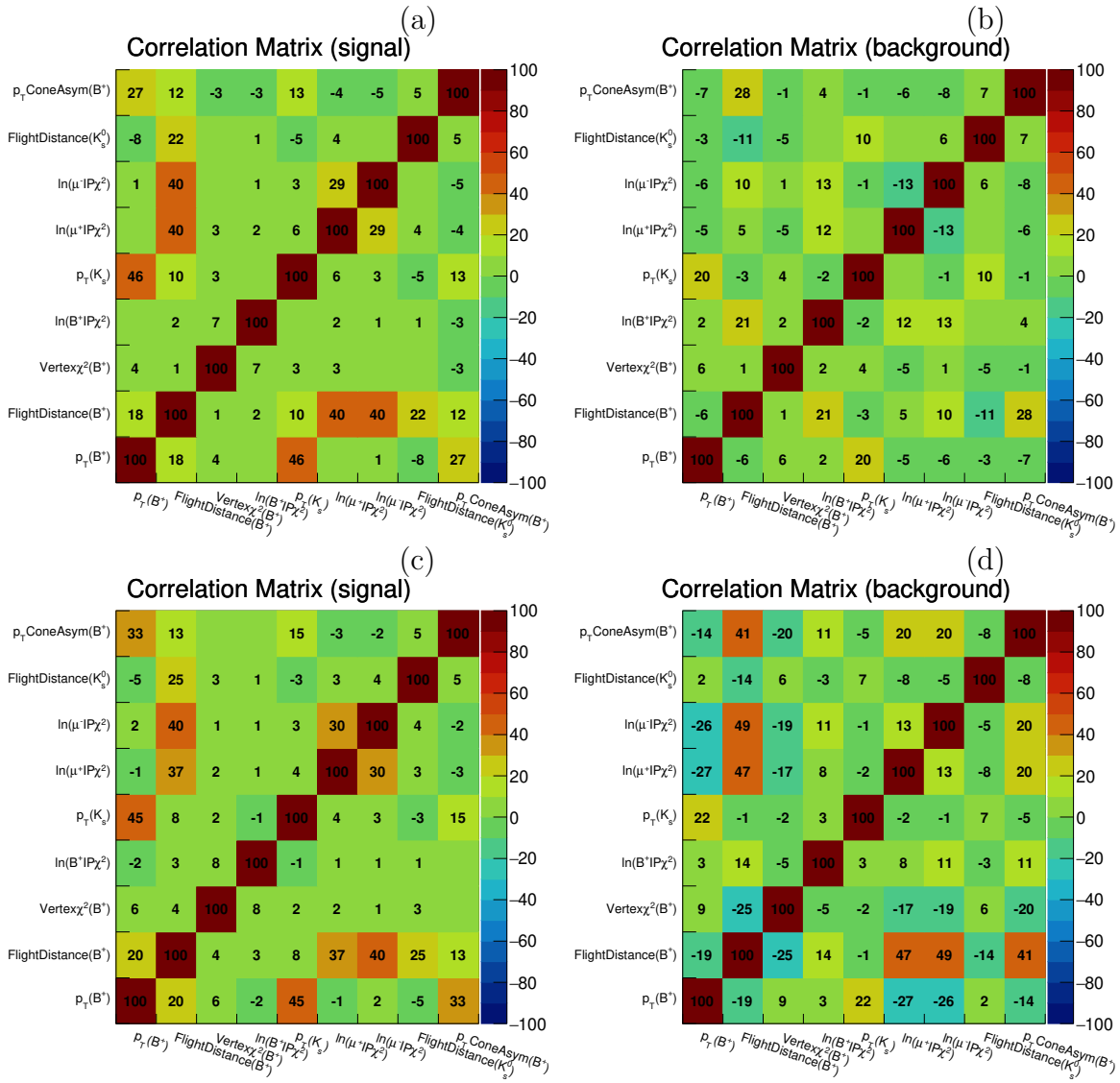

Figure 15: Correlation of input variables for the training and testing of the MVA for LL tracks events. Signal and background candidates for Run I (a) and (b) and Run II (c) and (d), respectively.

No single input variables shows a clear separation between the signal and background sample. If this would be the case, a simple cut selection in this variable should be performed to reduce the selection complexity. Furthermore, a single clear separating variable would dominate the multi-variate analysis and reduce the effect of the combination of *multiple* variables into this framework.

This is the case for all samples and all variables, as shown in distributions in Figs. 16 to 19.

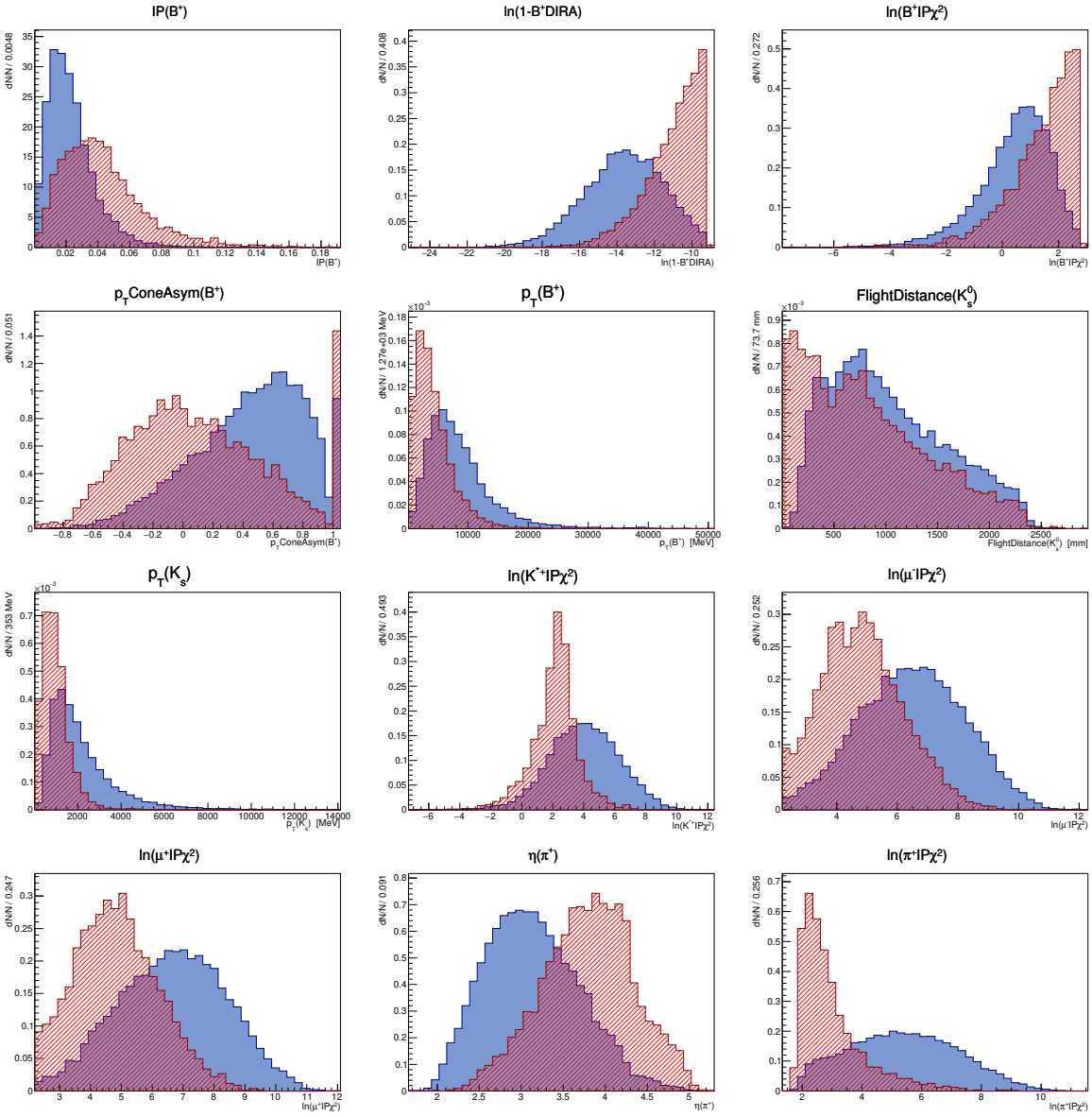

Figure 16: Distributions of all input variables used for the training and testing of the MVA in Run I data for DD tracks events. Signal decays from simulated events are drawn in blue by data events from the upper-mass-sideband in red.

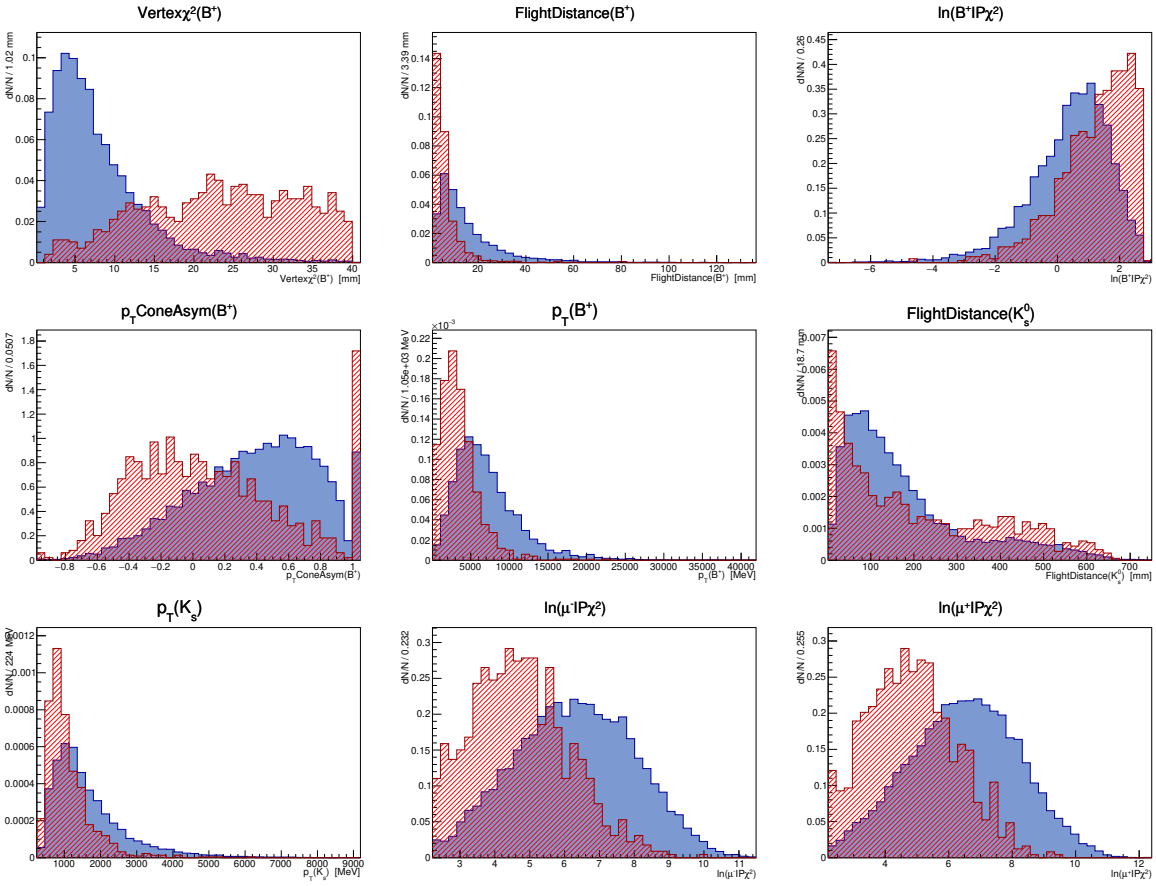

Figure 17: Distributions of all input variables used for the training and testing of the MVA in Run I data for LL tracks events. Signal decays from simulated events are drawn in blue by data events from the upper-mass-sideband in red.

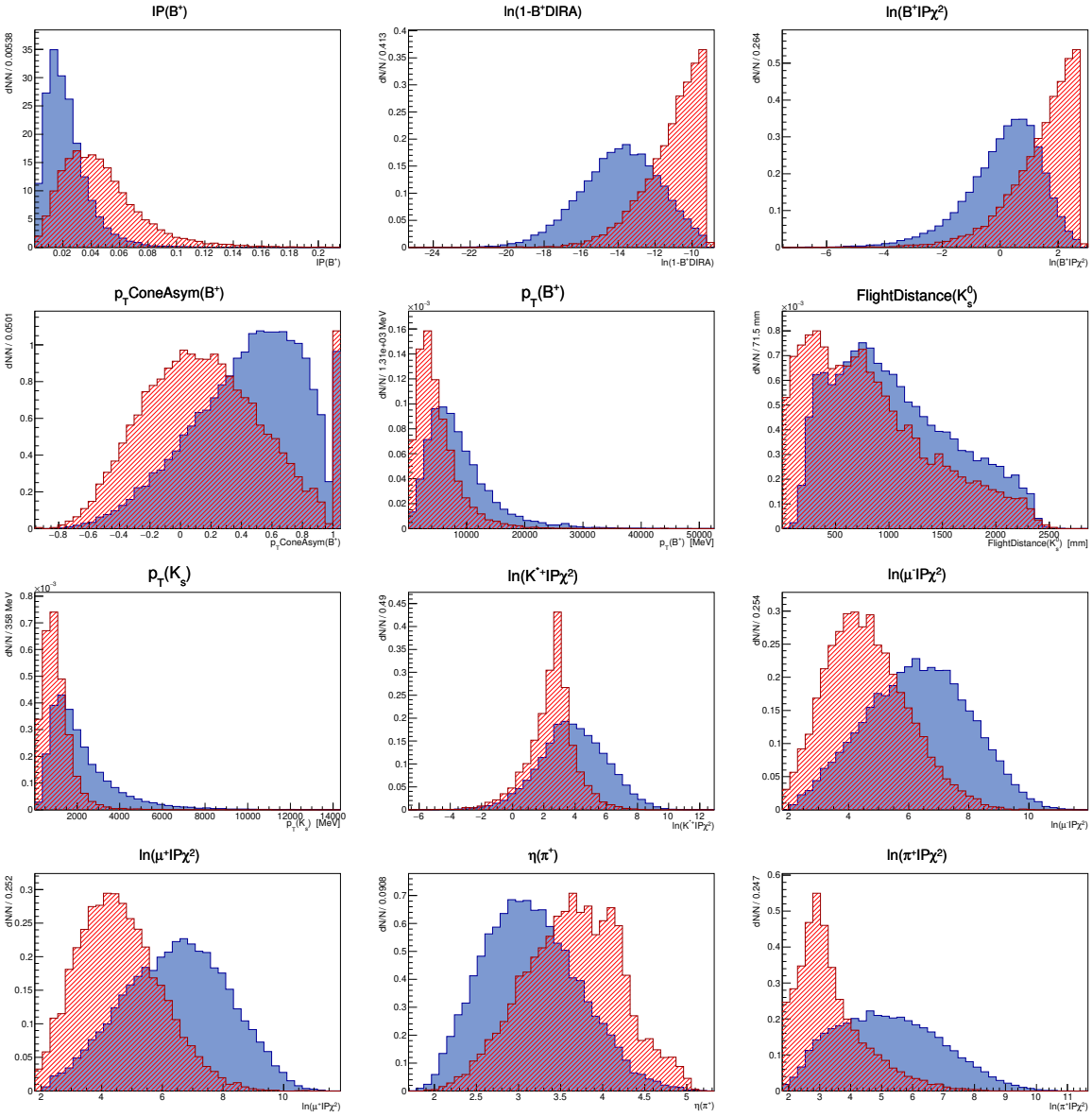

Figure 18: Distributions of all input variables used for the training and testing of the MVA in Run II data for DD tracks events. Signal decays from simulated events are drawn in blue by data events from the upper-mass-sideband in red.

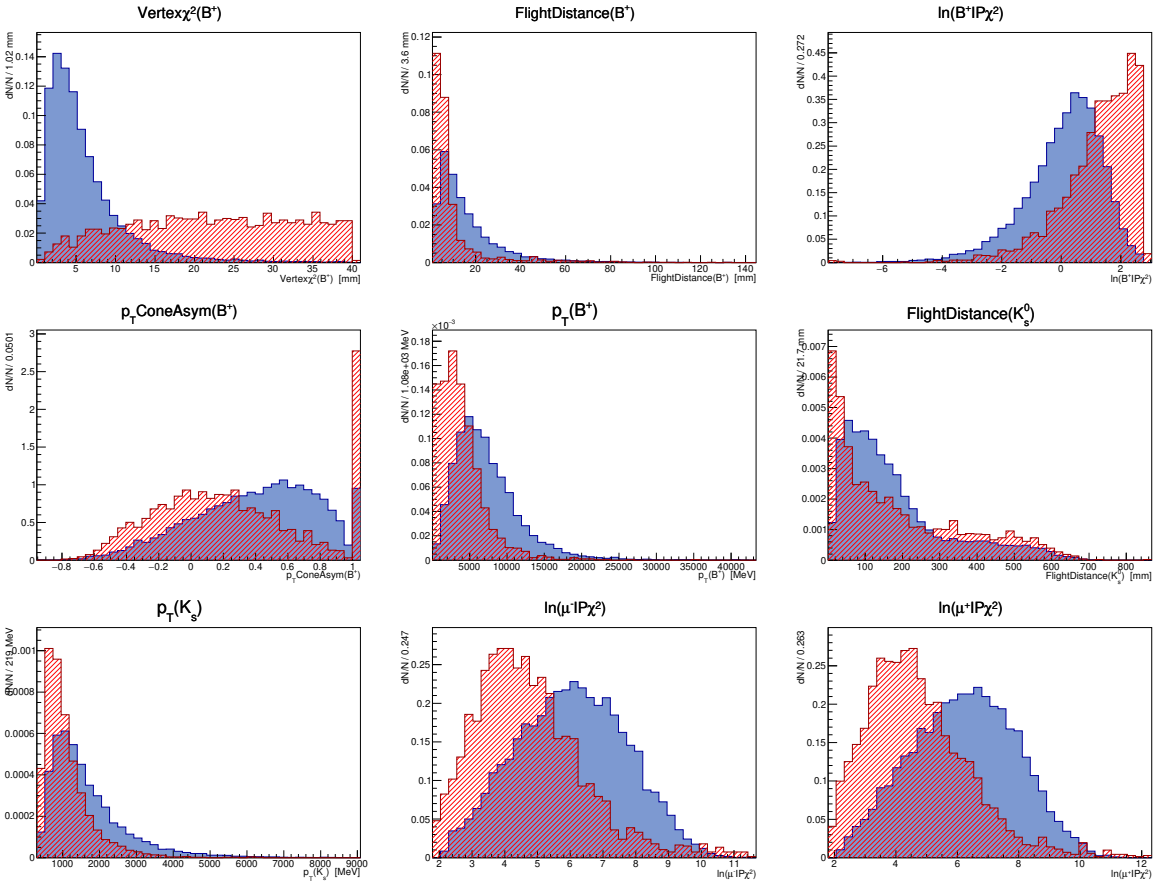

Figure 19: Distributions of all input variables used for the training and testing of the MVA in Run II data for LL tracks events. Signal decays from simulated events are drawn in blue by data events from the upper-mass-sideband in red.

Table 14: After cutting in the B meson mass and q^2, the following number of events are available for the MVA training and testing. The numbers are split equally in half for testing and training.

	Run I DD tracks	Run I LL tracks	Run II DD tracks	Run II LL tracks
Signal	32680	16306	61296	33670
Background	9015	1892	21456	5105

2.8.2 MVA training and testing

As a signal sample, data from simulation with the according weights from Section 2.7 is used to train the MVA. The invariant mass is required to be within $100\,\mathrm{MeV}/c^2$ around the known B meson mass.
The background sample is taken from combinatorial background events in the upper-mass sideband of the B^+ with invariant masses greater than $5400\,\mathrm{MeV}/c^2$. The lower mass limit for the background sample is chosen as such, that the training sample of the MVA is as large as possible while at the same point being high enough to guarantee not to include signal events as a background proxy. Both, signal and background proxy, are cut in q^2: The resonant regions of the J/ψ (8.68-10.09 GeV^2/c^2) and the $\psi(2S)$ (12.9-14.4 GeV^2/c^2) are excluded.
In Table 14 the statistics of background and signal input samples are given. Each sample is split half-half into training and testing samples.

The boosted decistion tree (BDT) method uses 300 trees with a maximal depth of 3 layers. The BDT with gradiant boost (BDTG) method uses 450 trees and a maximal depth of 2 layers.

The ROC curve is shown in Figs. 20 and 21 for DD tracks and LL tracks events, respectively. The two shown curve differ slightly with the red line of the BDTG method being at least as good as the basic BDT method (black line).
Due to this and the stronger agreement of training and testing sample, the BDTG method was chosen for the analysis. The overlays of training and testing distributions for the BDTG method for all four background and four signal for Run I and Run II with DD tracks and LL tracks in Figs. 22 and 23 show no signs of over-training.

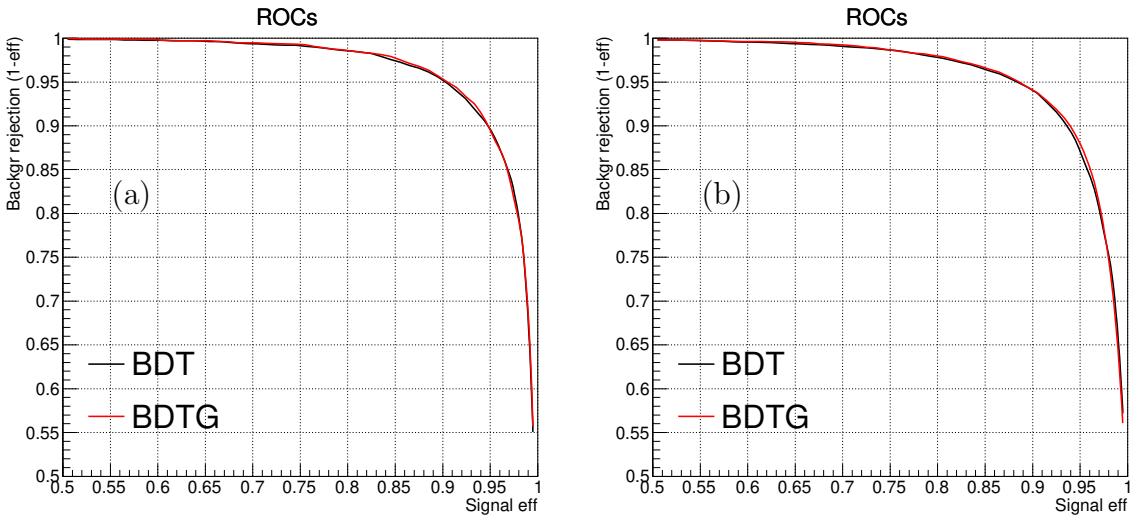

Figure 20: Background rejection efficiency over the resulting signal yield curve for the trained BDT and BDTG for DD tracks events of Run I and Run II in (a) and (b), respectively.

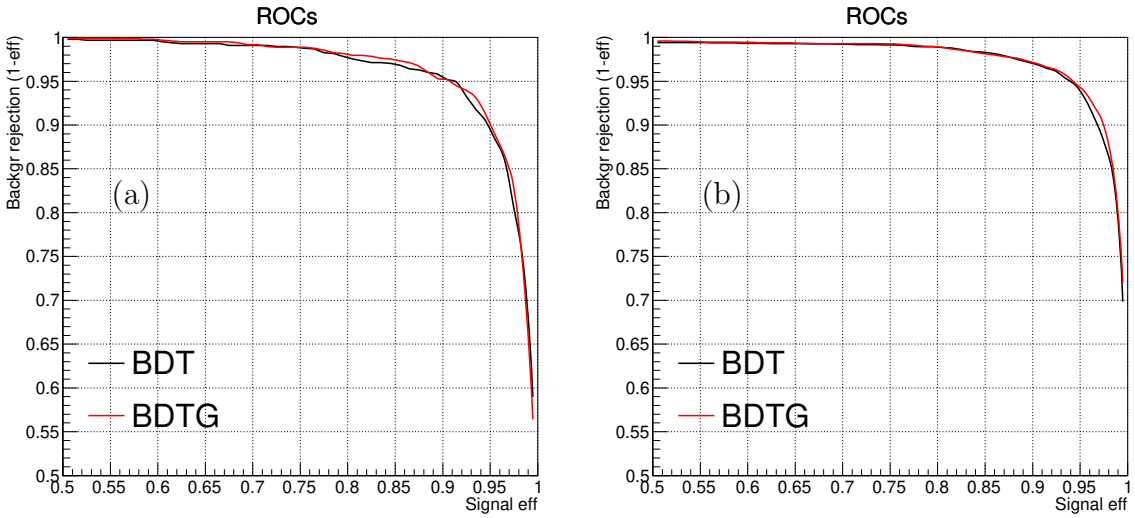

Figure 21: Background rejection efficiency over the resulting signal yield curve for the trained BDT and BDTG for LL tracks events of Run I and Run II in (a) and (b), respectively.

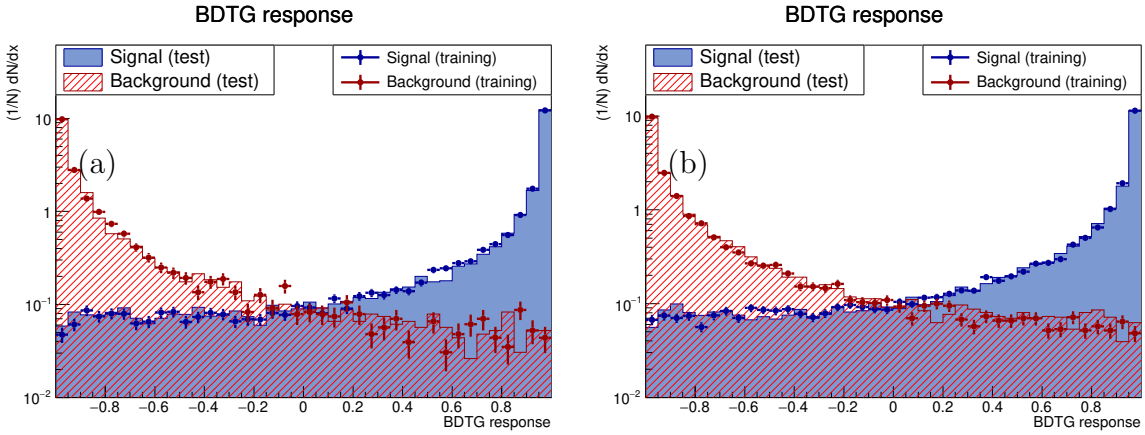

Figure 22: Output of DD tracks events BDTG response for training and testing sample overlayed in logarithmic scale (a) and (b) from Run I and Run II, respectively. The agreement of training (markers) and test (filled area) for both signal (blue) and background (red) shows no signs of over-training.

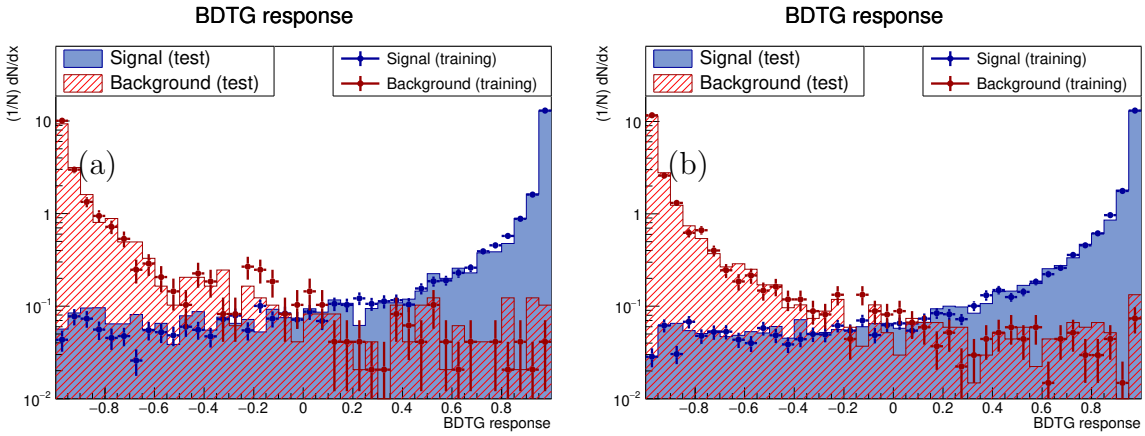

Figure 23: Output of LL tracks events BDTG response for training and testing sample overlayed in logarithmic scale (a) and (b) from Run I and Run II, respectively. The agreement of training (markers) and test (filled area) for both signal (blue) and background (red) shows no signs of over-training.

2.8.3 MVA cut value optimisation

The estimated event statistics from the reference channel presented in Table 8. Using those event numbers and the signal and background efficiencies of the MVA, a figure of merit $S/\sqrt{S+B}$ can be determined for a given BDTG response cut. By scanning over the BDTG response cut, this figure of merit can be optimized and the maximal statistical power of the sample is given at the point with maximum figure of merit.
From the MVA efficiencies in Fig. 24, the optimum cut values are chosen to be 0.8 (0.65) for DD tracks and 0.5 (0.4) for LL tracks in Run I (Run II).

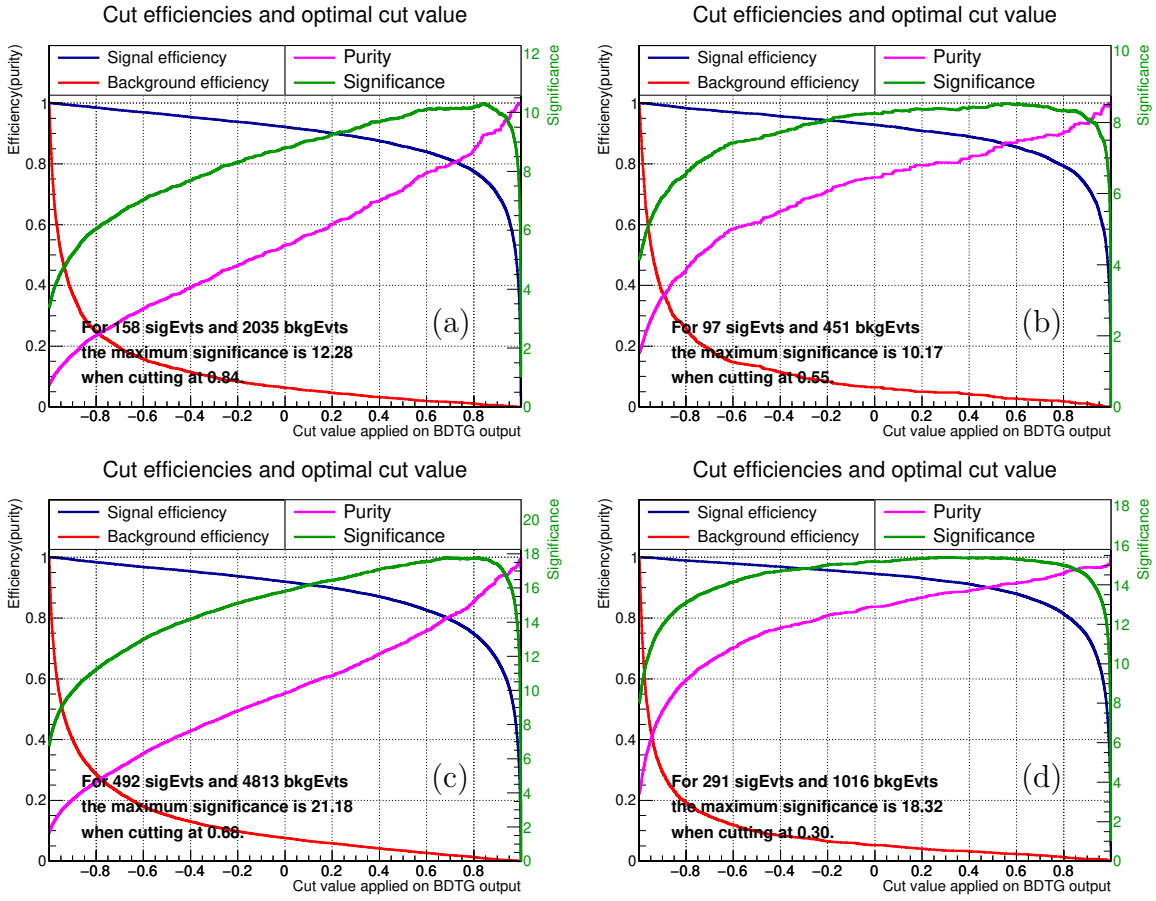

Figure 24: Scan through all possible cut values of the BDTG response variable in order to optimise the figure of merit with the trained BDTG and input of the signal yield estimation taken from Table 8 for Run I DD tracks (a) and LL tracks (b) as well as Run II DD tracks (c) and LL tracks (d).

2.8.4 MVA efficiency q^2 dependence

The optimization of the cut value of the multi-variate analysis uses the yield and efficiency from the reference channel. To justify this scaling of event yields, as explained in Eq. (5) and using the relative branching fraction (Eq. (6)), the efficiency of the MVA should not vary significantly as a function of q^2 and should be in agreement with the signal efficiency determined by the TMVA toolkit as presented in Fig. 24. This test is performed using the signal channel MC and the BDTG cut as stated in the previous section. The efficiency is

given as a function of q^2 in Fig. 25. The distributions are fairly flat and the values are in agreement with values in Fig. 24.

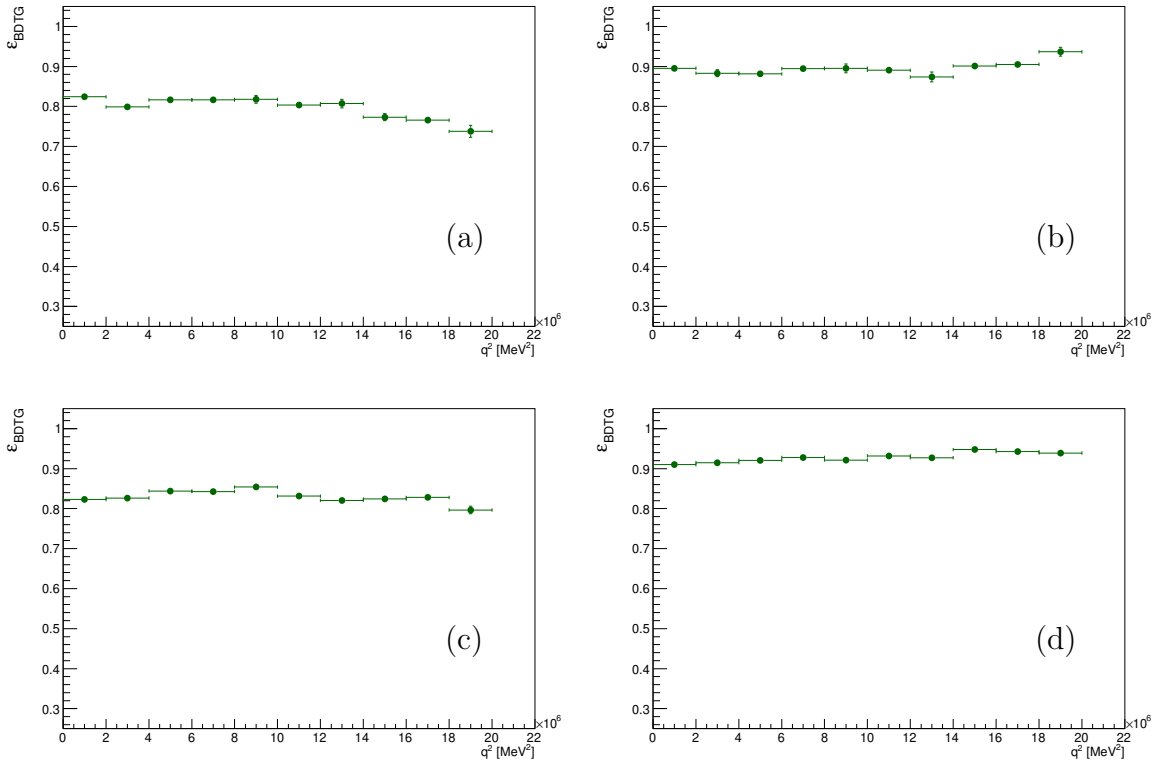

Figure 25: The BDTG cut efficiency for the given cut values (see Section 2.8.3) in ten bins of q^2 for Run I `DD` tracks (a) and `LL` tracks (b) as well as Run II `DD` tracks (c) and `LL` tracks (d). The distribution are fairly flat and hence justify the usage of signal yield estimations from the reference channel as given in Eq. (5).

2.9 Signal yield after selection

The signal event yield is part of the blinding strategy, as explained in more details in Section 1.2. Therefore, the signal yield after the application of the MVA is not given at this point, but is given in the last paragraph of Section 7.1.
However, to show the significant improvements of the data-set in terms of purity from the stripping selection to the final selection with the BDTG, a normalised two dimensional presentation of the data samples is given at different steps of the selection process. In Figs. 26 and 27, all events of Run I and Run II, respectively, are shown in the two dimensional plane of the invariant mass of the B^+ and the q^2 value. The region marked in red represents the signal region in which events are considered for the angular analysis. After `stripping` (first row) and cut-based selection (second row) no clear accumulation of events above background level is visible. Only after the application of the BDTG training and cut in the output variable, a significant clustering of events in the region of interest (indicated by the red striped boxes) is clearly visible by eye for both Run I and Run II.

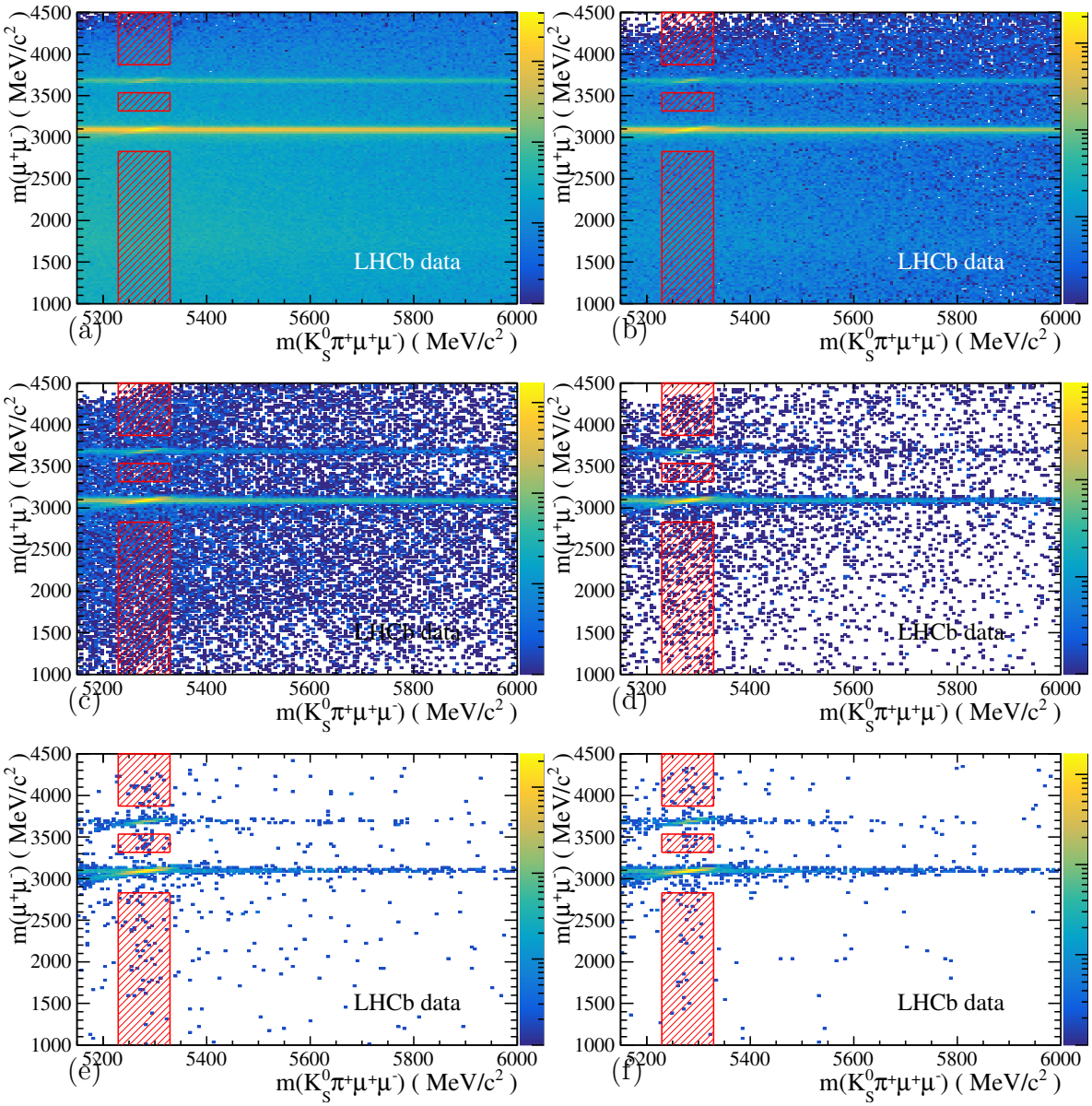

Figure 26: Invariant mass of the two muon system and the invariant mass of the B-meson at three different stages of the selection process. The combined data of Run I is displayed after the stripping (a) and (b), after the cut based selection (c) and (d) and after the cut in the multi-variate analysis output variable (e) and (f). The two columns separate the data sample into DD tracks (left) and LL tracks (right) track events. The color scheme is normalized to the total number of events in each histogram. In all plots the B-meson and charmonium resonances are visible as vertical and horizontal band structures, respectively. At the end of the selection process, the structure in the signal region (indicated by overlaying boxes) is becoming visible.

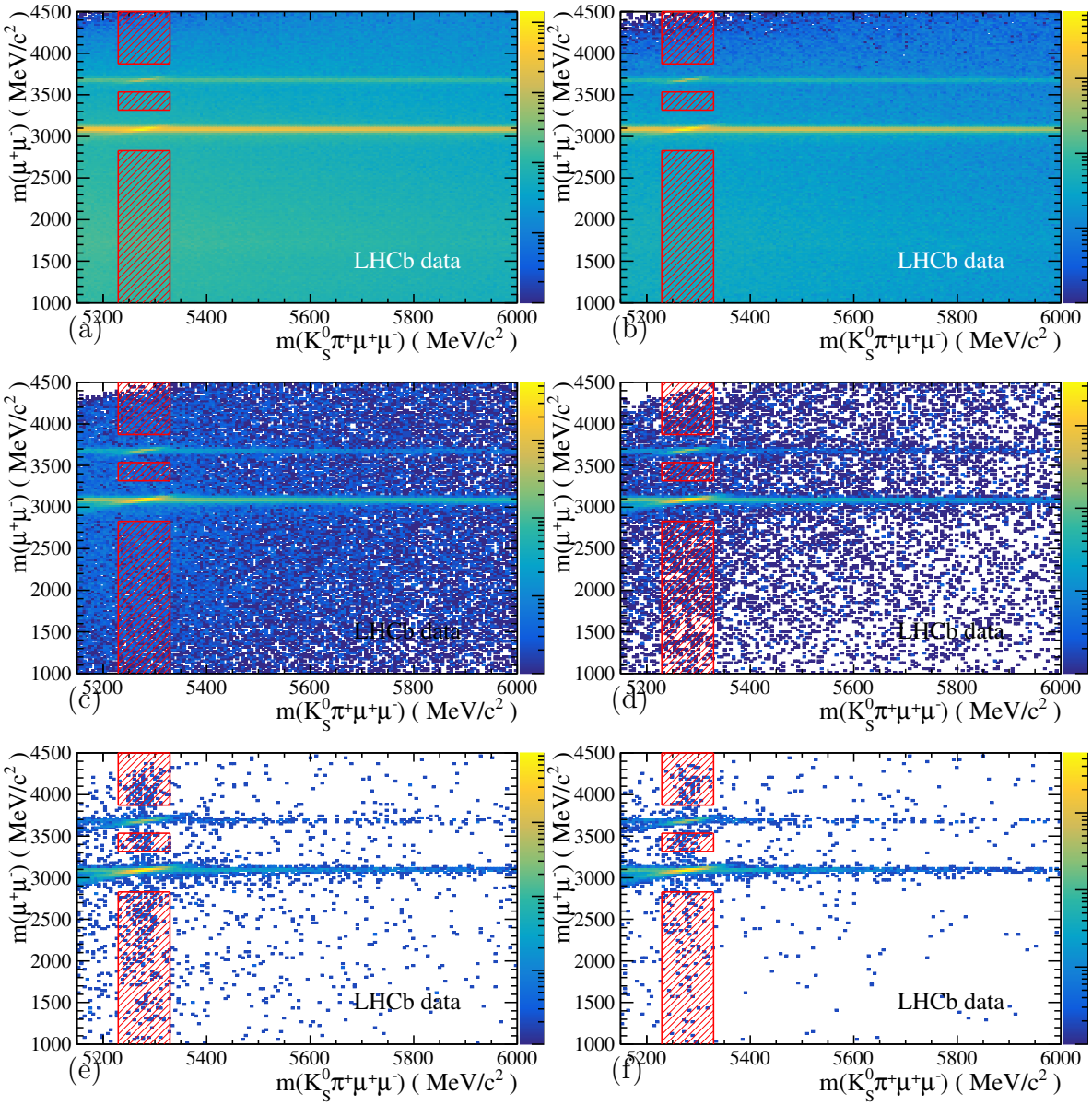

Figure 27: Invariant mass of the two muon system and the invariant mass of the B-meson at three different stages of the selection process. The Run II data is displayed after the stripping (a) and (b), after the cut based selection (c) and (d) and after the cut in the multi-variate analysis output variable (e) and (f). The two columns separate the data sample into `DD` tracks (left) and `LL` tracks (right) track events. The color scheme is normalized to the total number of events in each histogram. In all plots the B-meson and charmonium resonances are visible as vertical and horizontal band structures, respectively. At the end of the selection process, the structure in the signal region (indicated by overlaying boxes) is becoming visible.

3 Decay kinematics

The decay kinematics of the decay $B^+ \to K^{*+}\mu^+\mu^-$ can be parametrized using the three angles ($\cos\theta_L$, $\cos\theta_K$ and ϕ) together with the invariant mass of the di-muon system, q^2. The data-set will be split up into eight bins in q^2 (see Section 3.1 for the binning scheme), in which the individual values of the angular observables will be extracted by the fit.

The three angles, $\cos\theta_L$, $\cos\theta_K$ and ϕ, will be defined from the daughter particle's momenta in Section 3.2, followed by the differential angular decay rate in this angular basis in Section 3.3.

The angular acceptance and the required corrections on this effect are discussed in Section 3.4. Furthermore the angular folding, a technique to reduce the number of free parameters in the fit and stabilize the fit for low statistic samples, is introduced in Section 3.5.

3.1 q^2-Binning

The invariant mass squared of the $\mu^+\mu^-$ system (q^2) is segmented into eight signal regions plus three vetoed region of $\mu^+\mu^-$ resonances. From the decay kinematics, the phase-space is limited to low q^2 by the mass of the two muons. The limit towards large q^2 is given by the squared of the mass differences of the B meson and K^{*+}:

$$q^2{}_{\max} = (m_{B^+} - m_{K^{*+}})^2 \approx 19.25\,\mathrm{GeV}^2/c^2 \tag{8}$$

Due to the expected number of signal candidates, the bins are kept as large as possible and to keep final fit results comparable, we follow the notation of the Run I analysis of the angular analysis of the B^0. The binning scheme is taken from Table 9 in Ref. [25]. The q^2 binning is therefore equal to previous angular analysis of B^0. All q^2 bins are introduced in Table 15.

The resonant decays $B^+ \to K^{*+}\phi$, $B^+ \to K^{*+}J/\psi$ and $B^+ \to K^{*+}\psi(2S)$ with the ϕ, J/ψ and $\psi(2S)$ decaying further into $\mu^+\mu^-$ create the identical final state and due to the short life-time of ϕ, J/ψ and $\psi(2S)$, their decay vertex is not displaced from the decay vertex of the B^+ leaving the decays indistinguishable from the signal decay by any selection criteria. Therefore, the corresponding q^2 regions are vetoed for the analysis. In Table 15 these q^2 regions are marked including their corresponding resonant particle.

In addition to the fine binning scheme with eight q^2 bins, two larger q^2 regions have been used in analyses with comparable statistics:

- $[1.1, 6.0]$ GeV$^2/c^4$
- $[15.0, 19.0]$ GeV$^2/c^4$

3.1.1 Pollution of resonant events into non-resonant regions

The branching ratios of the resonant decays $B^+ \to J/\psi K^{*+}$ or $B^+ \to \psi(2S)K^{*+}$ are significantly higher then the non-resonant decay of the signal channel. Long tails of the mass peak are reaching (down) into non-resonant regions and can have a sizable contribution of a few percent compared to number of events from the rare mode. However, this *pollution* is considered and taken into the central value of the theoretical predictions, as stated explicitly in Ref. [26].

Table 15: Designated binning scheme in q^2 for the angular analysis including the veto regions of $\mu^+\mu^-$ decay resonances.

bin	q^2 (GeV^2/c^4)	veto
1	[0.1, 0.98]	
	[0.98, 1.1]	ϕ
2	[1.1, 2.5]	
3	[2.5, 4.0]	
4	[4.0, 6.0]	
5	[6.0, 8.0]	
	[8.0, 11.0]	J/ψ
6	[11.0, 12.5]	
	[12.5, 15.0]	$\psi(2S)$
7	[15.0, 17.0]	
8	[17.0, 19.0]	

3.2 Angular description

A total of three angles, $\cos\theta_L$, $\cos\theta_K$ and ϕ, describe the kinematics of a pseudo-scalar $B^\pm$ decaying into vector boson $K^{*\pm}$ plus two leptons $\mu^+\mu^-$. The $K^{*\pm}$ further decays into two pseudo-scalar mesons K^0_S and $\pi^\pm$, with their (squared) invariant mass $m_{K\pi}$ (p^2). In the same way, the two leptons $\mu^+\mu^-$ have the squared invariant mass, q^2.

The angle θ_L is defined as the angle between the direction of the $\mu^\pm$ in the dimuon rest frame and the direction of the dimuon system in the $B^\pm$ rest frame. In the same manner, θ_K is defined as the angle between the K^0_S in the $K^{*\pm}$ rest frame and the direction of the $K^{*\pm}$ system in the $B^\pm$ rest frame. Finally, ϕ describes the angle between the two decay planes given by the dimuon system on one side and by the $K^0_\mathrm{S}\pi^+$ system on the other side, all in the rest frame of the $B^\pm$.

The mathematical description of the angles, used for this analysis and the LHCb analysis on $B^0 \to K^{*0}\mu^+\mu^-$ [25] and former publications [27, 28] is given by

$$\cos\theta_L = \left(\hat{p}_{\mu^\pm}^{(\mu^+\mu^-)}\right)\cdot\left(\hat{p}_{\mu^+\mu^-}^{(B^\pm)}\right) = \left(\hat{p}_{\mu^\pm}^{(\mu^+\mu^-)}\right)\cdot\left(-\hat{p}_{(B^\pm)}^{\mu^+\mu^-}\right) \tag{9}$$

$$\cos\theta_K = \left(\hat{p}_{K^0_\mathrm{S}}^{(K^{*\pm})}\right)\cdot\left(\hat{p}_{K^{*\pm}}^{(B^\pm)}\right) = \left(\hat{p}_{K^0_\mathrm{S}}^{(K^{*\pm})}\right)\cdot\left(-\hat{p}_{(B^\pm)}^{K^{*\pm}}\right) \tag{10}$$

$$\cos\phi = \left[\left(\hat{p}_{\mu^\pm}^{(B^\pm)}\right)\times\left(\hat{p}_{\mu^\mp}^{(B^\pm)}\right)\right]\cdot\left[\left(\hat{p}_{K^0_\mathrm{S}}^{(B^\pm)}\right)\times\left(\hat{p}_{\pi^\pm}^{(B^\pm)}\right)\right] \tag{11}$$

$$\sin\phi = \left[\left(\hat{p}_{\mu^\pm}^{(B^\pm)}\right)\times\left(\hat{p}_{\mu^\mp}^{(B^\pm)}\right)\right]\times\left[\left(\hat{p}_{K^0_\mathrm{S}}^{(B^\pm)}\right)\times\left(\hat{p}_{\pi^\pm}^{(B^\pm)}\right)\right]\cdot\left(\hat{p}_{K^{*\pm}}^{(B^\pm)}\right) \tag{12}$$

with $\hat{p}_X^{(Y)}$, the normalised vector of a particle or multi-particle system, X, in the rest frame of system Y. The angles are illustrated in a decay sketch shown in Fig. 28.

3.3 Angular differential decay rate

In the angular basis, which was introduced in the previous chapter, the differential angular decay rate of the decay $B^+ \to K^{*+}\mu^+\mu^-$ with CP-averaged angular observables, S_i,

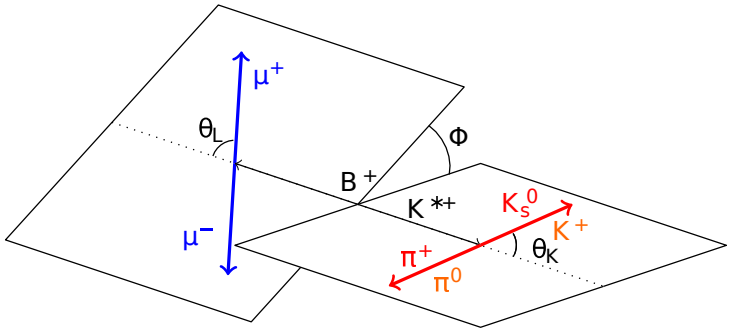

Figure 28: Sketch of the angular description of the decay $B^+ \to K^{*+}\mu^+\mu^-$. The three angles θ_K, θ_L and ϕ describe the full decay kinematics. The sketch is not complete and for illustration purpose only, as angles are defined in rest-frames of different particles. A complete picture of the angles can be found in Sections 3.2 to 3.2 or in Reference [25]

consists of two parts: a P-wave contribution, where the K π system originates from the K^{*+} (892) resonance, and the S-wave contribution, with K π originating from different K π resonances, such as the K^{*+} (1400). The S-wave component is non-distinguishable in the mass dimension of the B^+ meson. It however as a different angular decay rate with respect to the P-wave and therefore different angular distributions in $\cos\theta_L$, $\cos\theta_K$ and ϕ. In the invariant mass dimension of the K π, the S-wave component has a rather flat distribution in the region of interest around the K^{*+} (892) resonance. Since the S-wave component cannot be separated by the event selection, it has to be taken into account in the fit model used for the extraction of (P-wave) angular observables.

3.3.1 ... of the P-wave contribution

The signal component of the angular decay rate is derived in details in the analysis note of $B^0 \to K^{*0}\mu^+\mu^-$ for Run I [25] and is given by

$$\begin{aligned}\frac{1}{(\Gamma+\bar{\Gamma})}\frac{\mathrm{d}(\Gamma+\bar{\Gamma})}{\mathrm{d}\cos\theta_L\,\mathrm{d}\cos\theta_K\,\mathrm{d}\phi}\bigg|_{\mathrm{P}} = \frac{9}{32\pi}\Big[&S_{1s}\sin^2\theta_K && + S_{1c}\cos^2\theta_K \\ &+S_{2s}\sin^2\theta_K\cos 2\theta_L && + S_{2c}\cos^2\theta_K\cos 2\theta_L \\ &+S_3\sin^2\theta_K\sin^2\theta_L\cos 2\phi && + S_4\sin 2\theta_K\sin 2\theta_L\cos\phi \\ &+S_5\sin 2\theta_K\sin\theta_L\cos\phi && + S_{6s}\sin^2\theta_K\cos\theta_L \\ &+S_7\sin 2\theta_K\sin\theta_L\sin\phi && + S_8\sin 2\theta_K\sin 2\theta_L\sin\phi \\ &+S_9\sin^2\theta_K\sin^2\theta_L\sin 2\phi\Big].\end{aligned} \tag{13}$$

In this equation, the q^2 dependence is already integrated out, as the observables are determined for each of the eight q^2 bins (see Section 3.1) independently. Further, the $\mu^+\mu^-$ system neglects contributions from scalar configurations and the formula operates in the limits of $q^2 \gg 4m(\mu)^2$.

Eq. (13) can be simplified to

$$\frac{1}{(\Gamma+\bar{\Gamma})}\frac{\mathrm{d}(\Gamma+\bar{\Gamma})}{\mathrm{dcos}\theta_L\,\mathrm{dcos}\theta_K\,\mathrm{d}\phi} = \frac{9}{32\pi}\sum_i S_i f_i(\cos\theta_L,\cos\theta_K,\phi), \tag{14}$$

with the angular moments $f_i(\cos\theta_L,\cos\theta_K,\phi)$. The angular terms f_3, f_4, ..., f_9 are all orthogonal to each other, theoretically making the angular observables S_3 – S_9 uncorrelated. S_{1s}, S_{1c}, S_{2s} and S_{2c} are not independent and follow the normalisation conditions and correlations:

$$\begin{aligned}\frac{3}{4}(2S_{1s}+S_{1c})-\frac{1}{4}(2S_{2s}+S_{2c}) =& 1\\ S_{2c} =& -S_{1c}\\ S_{2s} =& \frac{1}{3}S_{1s}\end{aligned} \tag{15}$$

With these normalisation conditions on the four non-orthogonal observables, the introduction of the longitudinal polarisation fraction, $F_L = S_{1c}$, and the forward-backward asymmetry, $A_{FB} = \frac{3}{4}S_{6s}$, the angular decay rate for the P-wave component reduces to

$$\begin{aligned}\frac{1}{(\Gamma+\bar{\Gamma})}\frac{\mathrm{d}(\Gamma+\bar{\Gamma})}{\mathrm{dcos}\theta_L\,\mathrm{dcos}\theta_K\,\mathrm{d}\phi}\bigg|_{\mathrm{P}} = \frac{9}{32\pi}\Big[&\tfrac{3}{4}(1-F_L)\sin^2\theta_K && + F_L\cos^2\theta_K\\ &+\tfrac{1}{4}(1-F_L)\sin^2\theta_K\cos 2\theta_L && - F_L\cos^2\theta_K\cos 2\theta_L\\ &+S_3\sin^2\theta_K\sin^2\theta_L\cos 2\phi && + S_4\sin 2\theta_K\sin 2\theta_L\cos\phi\\ &+S_5\sin 2\theta_K\sin\theta_L\cos\phi && + \tfrac{3}{4}A_{FB}\sin^2\theta_K\cos\theta_L\\ &+S_7\sin 2\theta_K\sin\theta_L\sin\phi && + S_8\sin 2\theta_K\sin 2\theta_L\sin\phi\\ &+S_9\sin^2\theta_K\sin^2\theta_L\sin 2\phi\Big].\end{aligned} \tag{16}$$

3.3.2 ... of the S-wave contribution

Lower angular momentum of the $K\,\pi$ resonance other than the K^{*+} (892) are present in the angular distributions of the decay.

Therefore, the angular differential decay rate of the P-wave has to be extended by the angular momenta of the S-wave. The details about the determination of these angular terms is again discussed in more detail in [25]. Here, only the resulting formula is given:

$$\frac{1}{(\Gamma+\bar{\Gamma})}\frac{\mathrm{d}(\Gamma+\bar{\Gamma})}{\mathrm{dcos}\theta_L\,\mathrm{dcos}\theta_K\,\mathrm{d}\phi}\bigg|_{\mathrm{S}} = \frac{3}{16\pi}F_S\sin^2\theta_L \tag{17}$$

As both S- and P-wave are complex amplitudes, the addition of both results interference terms of S- and P-wave decay rate, which are parametrized:

$$\begin{aligned}\frac{1}{(\Gamma+\bar{\Gamma})}\frac{\mathrm{d}(\Gamma+\bar{\Gamma})}{\mathrm{dcos}\theta_L\,\mathrm{dcos}\theta_K\,\mathrm{d}\phi}\bigg|_{\mathrm{PS}} = \frac{3}{16\pi}\Big[&S_{S1}\sin^2\theta_L\cos\theta_K\\ &+S_{S2}\sin 2\theta_L\sin\theta_K\cos\phi && + S_{S3}\sin\theta_L\sin\theta_K\cos\phi\\ &+S_{S4}\sin\theta_L\sin\theta_K\sin\phi && + S_{S5}\sin 2\theta_L\sin\theta_K\sin\phi\Big]\end{aligned} \tag{18}$$

3.3.3 The resulting P- and S-wave differential angular decay rate

Both components (P-wave and S-wave plus their interference terms) are summed up to the total differential decay rate. By definition, the P-wave part is scaled by $(1 - F_S)$. The resulting formula is given in Eq. (19)

$$
\begin{aligned}
&\frac{1}{(\Gamma+\bar{\Gamma})}\left.\frac{\mathrm{d}(\Gamma+\bar{\Gamma})}{\mathrm{dcos}\theta_L\,\mathrm{dcos}\theta_K\,\mathrm{d}\phi}\right|_{\mathrm{S+P+PS}} = \\
&(1-F_S)\frac{9}{32\pi}\Big[\tfrac{3}{4}(1-F_L)\sin^2\theta_K + F_L\cos^2\theta_K \\
&\quad +\tfrac{1}{4}(1-F_L)\sin^2\theta_K\cos 2\theta_L - F_L\cos^2\theta_K\cos 2\theta_L \\
&\quad +S_3\sin^2\theta_K\sin^2\theta_L\cos 2\phi + S_4\sin 2\theta_K\sin 2\theta_L\cos\phi \\
&\quad +S_5\sin 2\theta_K\sin\theta_L\cos\phi + \tfrac{3}{4}A_{FB}\sin^2\theta_K\cos\theta_L \\
&\quad +S_7\sin 2\theta_K\sin\theta_L\sin\phi + S_8\sin 2\theta_K\sin 2\theta_L\sin\phi \\
&\quad +S_9\sin^2\theta_K\sin^2\theta_L\sin 2\phi\Big] \\
&+\frac{3}{16\pi}\Big[F_S\sin^2\theta_L + S_{S1}\sin^2\theta_L\cos\theta_K \\
&\quad +S_{S2}\sin 2\theta_L\sin\theta_K\cos\phi + S_{S3}\sin\theta_L\sin\theta_K\cos\phi \\
&\quad +S_{S4}\sin\theta_L\sin\theta_K\sin\phi + S_{S5}\sin 2\theta_L\sin\theta_K\sin\phi\Big].
\end{aligned}
\tag{19}
$$

3.3.4 ... of the angular background component

The background component in the three decay angles is parametrized using Chebyshev polynomials T_i of up to second order in $\cos\theta_L$ and $\cos\theta_K$. In ϕ no significant shapes in the background distributions were seen in the upper- and lower-mass sidebands of the B^+ peak, as shown in Fig. 29 for the combined Run I and Run II background in the reference channel. We therefore only use a constant distribution in ϕ. The background events originate from randomly combined tracks which allows the assumption that the angular background probability factorizes in the three decay angles. This assumption was tested on weighted background events, which show little to no correlation between all three angular distributions for all q^2 bins. The tables of all correlations are given in the appendix, Appendix A.11.

Also, the background component modelling will be treated as nuisance parameters in the final fit, as they will not be published.

Hence, the differential decay rate of background events is given by:

$$
\left.\frac{\mathrm{d}(\Gamma+\bar{\Gamma})}{\mathrm{dcos}\theta_L\,\mathrm{dcos}\theta_K\,\mathrm{d}\phi}\right|_{\mathrm{BKG}} = \left(\sum_{i=0}^{2} c_i^{\cos\theta_L} T_i(\cos\theta_L)\right) \times \left(\sum_{j=0}^{2(4)} c_j^{\cos\theta_K} T_j(\cos\theta_K)\right) \times \left(c_0^{\phi} T_0(\phi)\right) \tag{20}
$$

with the Chebyshev polynomials, $T_0 = 1$, $T_1 = x$, $T_2 = 2x^2 - 1$, $T_3 = 4x^3 - 3x$ and $T_4 = 8x^4 - 8x^2 + 1$. The maximum order in $\cos\theta_K$ in the rare channel was found to be sufficiently described using up to second order polynomials, while the larger statistics of the reference channel require up to order 4. All fits to background distributions in eight q^2 bin of the signal channel can be found in the appendix, Appendix A.10. The coefficients

c_i^x of the individual polynomials are left floating in the fit. In the fit, this distribution has to be normalized to become a probability density function. This normalization is done by the three dimensional integral over the three decay angles

$$\mathcal{N}_{\mathrm{BKG}}(\cos\theta_L, \cos\theta_K, \phi) = \int_{-1}^{+1}\int_{-1}^{+1}\int_{-\pi}^{+\pi} \frac{\mathrm{d}(\Gamma+\bar{\Gamma})}{\mathrm{dcos}\theta_L\,\mathrm{dcos}\theta_K\,\mathrm{d}\phi}\bigg|_{\mathrm{BKG}} \mathrm{d}\phi\,\mathrm{dcos}\theta_K\,\mathrm{dcos}\theta_L \quad (21)$$

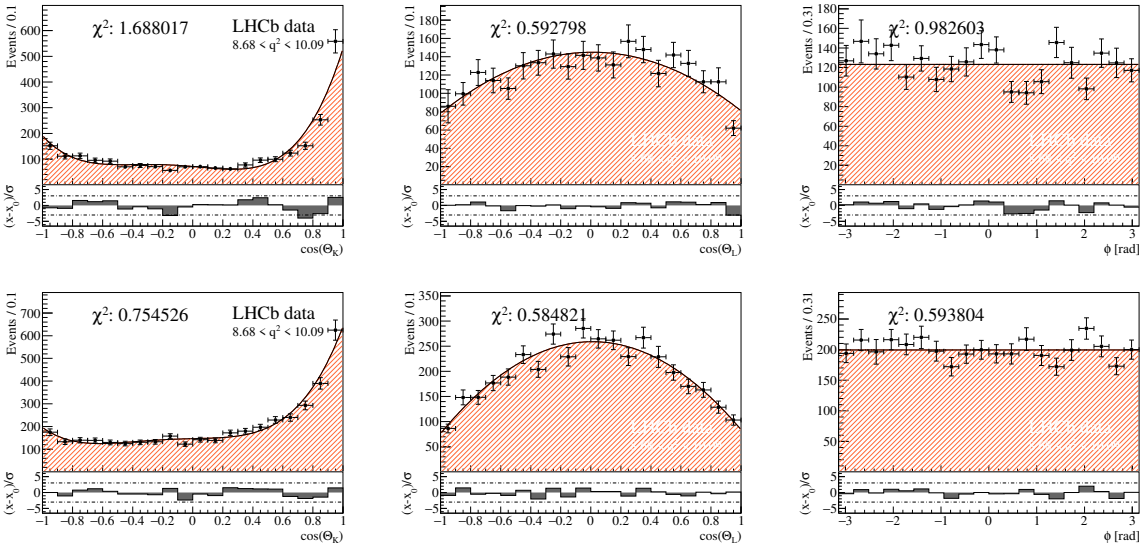

Figure 29: Angular distributions of background candidates from the reference channel. Combination of the full data-set. Top and bottom row show low and high mass side-band events, respectively. This means events more than 50 MeV/c^2 below (above) the B^+ mass for low (high) mass side-band. The background is described by polynomials of up to order 0 (ϕ), 2 ($\cos\theta_L$) and 4 ($\cos\theta_K$).

3.3.5 ... of the $m_{K\pi}$ background component

In addition to the angular background, the background in the $m_{K\pi}$ dimension is investigated and parametrized by a linear polynomial. The linear description is shown in Fig. 30.

3.3.6 $P_x^{(\prime)}$ angular basis

The S_x observables from Section 3.3 can also be expressed in the so called $P_x^{(\prime)}$ basis. From the theoretical point of view, this basis is advantageous, as form factor contributions cancel out on first order. Hence, the theoretical prediction for angular observables, $P_x^{(\prime)}$, has a smaller uncertainty. [29]
Therefore, the following angular observables are used in addition to the nominal angular observables, S_x. For the angular observables in the $P_x^{(\prime)}$ basis separated fits are performed and the observables are directly determined by the fitter. The parameters are defined following the previous LHCb convention [25]:

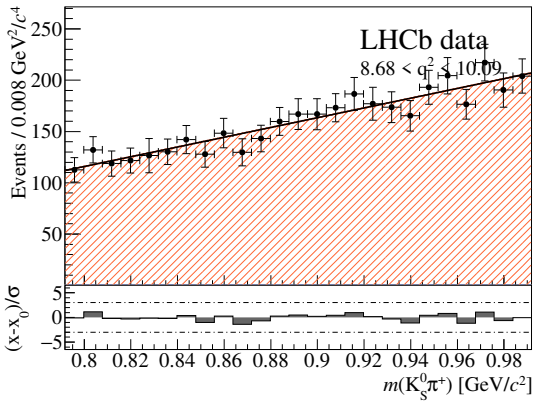

Figure 30: Background distributions of the upper mass side-band of the reference channel. Combination of the full data-set. The background is well described by a linear polynomial.

$$
\begin{aligned}
P_1 =& 2\frac{S_3}{1-F_L} \\
P_2 =& \frac{1}{2}\frac{S_{6s}}{1-F_L} \\
P_3 =& -\frac{S_9}{1-F_L} \\
P_4' =& \frac{S_4}{\sqrt{F_L\,(1-F_L)}} \\
P_5' =& \frac{S_5}{\sqrt{F_L\,(1-F_L)}} \\
P_6' =& \frac{S_7}{\sqrt{F_L\,(1-F_L)}} \\
P_8' =& \frac{S_8}{\sqrt{F_L\,(1-F_L)}}
\end{aligned}
\tag{22}
$$

3.4 Angular acceptance

The angular decay rate of $B^+ \to K^{*+}\mu^+\mu^-$ introduced in Section 3.3 can only be correctly measured, if the non-flat angular acceptance in the distributions of all angles ($\cos\theta_L$, $\cos\theta_K$ and ϕ, see Section 3.2) and q^2 of signal events is corrected for. The non-flat angular acceptance in the 4D space of the angles and q^2 is the accumulated result of the forward geometry of the LHCb detector, the trigger, stripping line cuts and the event selection shown in Section 2. A potential non-flat acceptance in m($K\ \pi$) has been investigated and was not observed and hence this dimension is not further included in any studies concerning acceptance effects. Plots of the flat acceptance in the m($K\ \pi$) dimension are show in the appendix, Appendix A.5.

For the previously mentioned four dimensions the angular acceptance has to be equalized before extracting the angular observables from our data sample. In the following, the determination of the angular acceptance from phase-space MC events and the

implementation of the acceptance correction into the fitter framework is explained in detail.

3.4.1 Phase-space MC events

For the angular acceptance correction, we again follow the method of Ref. [25] and use the same tools that have been developed for that analysis. A dedicated set of simulated MC events is generated for all six years with a pure phase-space (PHSP) coupling between the decay daughters and their mothers. This – by construction – generates flat distribution at generator level of the simulated events in all of the three angular distributions, $\cos\theta_L$, $\cos\theta_K$ and ϕ. Furthermore, to produce similar statistics of simulated events in all q^2 bins, the option `FLATQ2` is used for the generation. Since the option does not generate a fully flat distribution, the q^2 distribution of the PHSP MC events is corrected prior to the parametrization, explained in the next paragraph (Section 3.4.2). Also, the PHSP MC events are corrected for discrepancies between signal data and PHSP MC using the same weights as for signal channel MC, as introduced in Section 2.7.4. These MC-data weights are essential for the use of MC events for the correction of acceptance effects in data. Discrepancy between MC and data events would bias the results of the angular observables, which has been confirmed by tests on toy events.
By knowing that the initial distribution of the simulated PHSP MC sample is flat, we can determine the angular acceptance in the four dimensions of $\cos\theta_L$, $\cos\theta_K$, ϕ and q^2. The acceptance observed in the PHSP MC is parametrized and applied to the actual fit data by means of weights, as explained in the following sections.

3.4.2 Parametrization of the angular acceptance

The key to a working acceptance correction using simulated PHSP MC events is flatness of all four generated distributions, $\cos\theta_L$, $\cos\theta_K$, ϕ and q^2. Since the generated distribution in q^2 is not entirely flat, especially towards the boundaries at low and high q^2, the PHSP MC events are itself weighted to account for this non-flatness at generation. Due to the finite width of the K^{*+} the weights are rising towards large q^2, as the effect of non-zero width of the K^{*+} is not correct for in the `FLATQ2` option. The one dimensional weights are obtained from one million locally generated PHSP events with no selection or acceptance cuts. The resulting weight distribution is shown in Fig. 31.

By weighting in q^2, all four dimensions are flat at generation. Legendere polynomials, $P_{l,m,n,o}$, in 4D are chosen to parametrize the angular acceptance. Here, we do not assume factorization of the four dimensions by using the full parametrization in 4D space:

$$\epsilon(\cos\theta_L, \cos\theta_K, \phi, q^2) = \sum_{l,m,n,o} c_{lmno} \times P_l(q^2) \times P_m(\cos\theta_L) \times P_n(\cos\theta_K) \times P_o(\phi). \quad (23)$$

The maximum order of Legendre polynomials included in this parametrization was chosen such, that the complexity of the acceptance is described sufficiently while preventing over-parametrization of statistical fluctuations in the PHSP MC sample. The parametrization is forced to be symmetric in ϕ, which is motivated by the definition of ϕ being the angle between the decay planes. Reversal of the magnetic field during the data acquisition and the fact that we integrate over the charge conjugated process removes

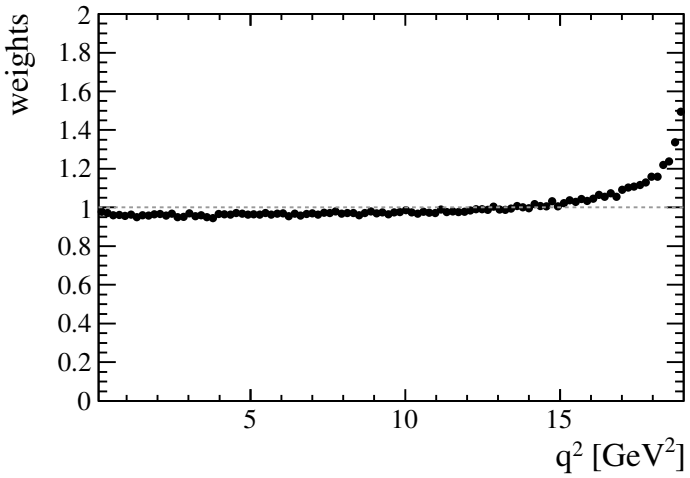

Figure 31: The distribution of PHSP MC weights. The weights correct the non-flat distribution of the simulated events at generation in the q^2 dimension. The rising structure towards high q^2 is a result of the non-zero width of K^{*+}, which is not corrected for in the `FLATQ2` option.

any sources of potential asymmetry in acceptance of ϕ. The symmetry is confirmed by the goodness of the parametrization and the fit results of the reference channel (see Section 4.4.7). For a potential symmetry in $\cos\theta_L$, given the two symmetric particles μ^+ and μ^-, we will have a systematic check in Section 6.2. After the coefficients c_{lmno} are determined from the PHSP MC using a moments analysis, the Legendre polynomial parametrization is converted into multidimensional polynomials of the form

$$\epsilon(\cos\theta_L, \cos\theta_K, \phi, q^2) = \sum_{h,i,j,k} c_{hijk} \times \left(q^2\right)^h \times (\cos\theta_L)^i \times (\cos\theta_K)^j \times (\phi)^k \,. \tag{24}$$

The maximum orders necessary to describe the angular acceptance sufficiently was found to be 4 for $\cos\theta_L$, 5 in $\cos\theta_K$, 6 in ϕ and 7 in q^2. They are obtained by scanning through the maximum order in each dimension with a visual quality check on the one dimensional projections as a first step. The final decision on the exact maximum order is subsequently made by using the χ^2 goodness of the parametrization.
The angular acceptance correction is done individually in six sub-sets: split into every two years (2011+12, 2015+16 and 2017+18) as well as split by `DD` tracks and `LL` tracks. In each of these six sub-sets, the angular acceptance correction is normalized by the 4D integral over the full phase-space to match the integral of an flat acceptance equal to one. The resulting projections of the four-dimensional acceptance parametrization are shown in Figs. 32 to 34 for Run I and Figs. 35 to 40 for Run II for all eight bins of q^2. In addition, Figs. 41 to 43 show the angular acceptance integrated over the full q^2 range, as well as the acceptance in q^2 itself.

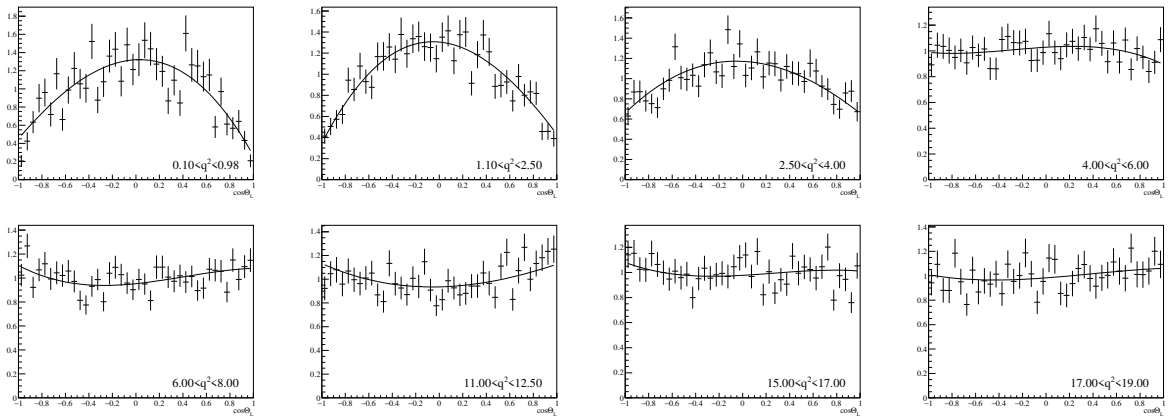

Figure 32: One dimensional projections of the angular acceptance in the dimension of $\cos\theta_L$ in eight bins of q^2. The data points are events from phase-space MC of Run I and the solid curve the parametrization of multi-dimensional polynomials.

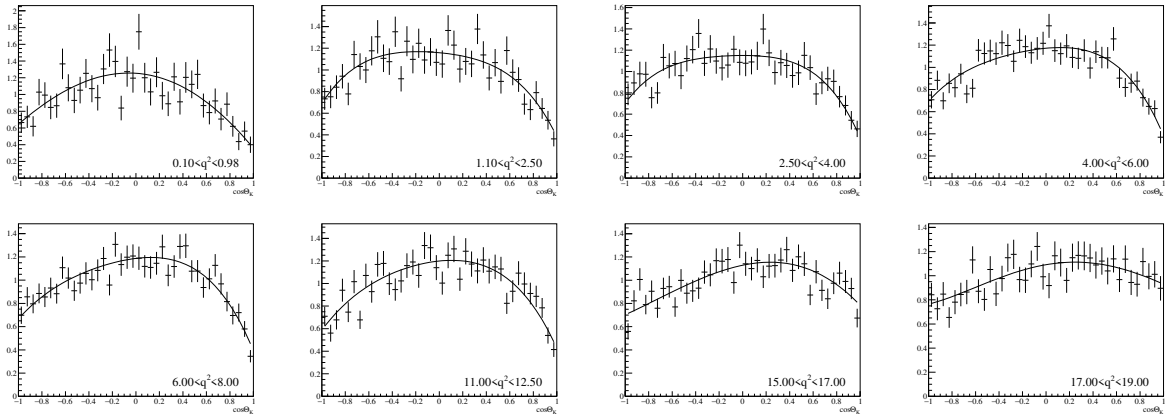

Figure 33: One dimensional projections of the angular acceptance in the dimension of $\cos\theta_K$ in eight bins of q^2. The data points are events from phase-space MC of Run I and the solid curve the parametrization of multi-dimensional polynomials.

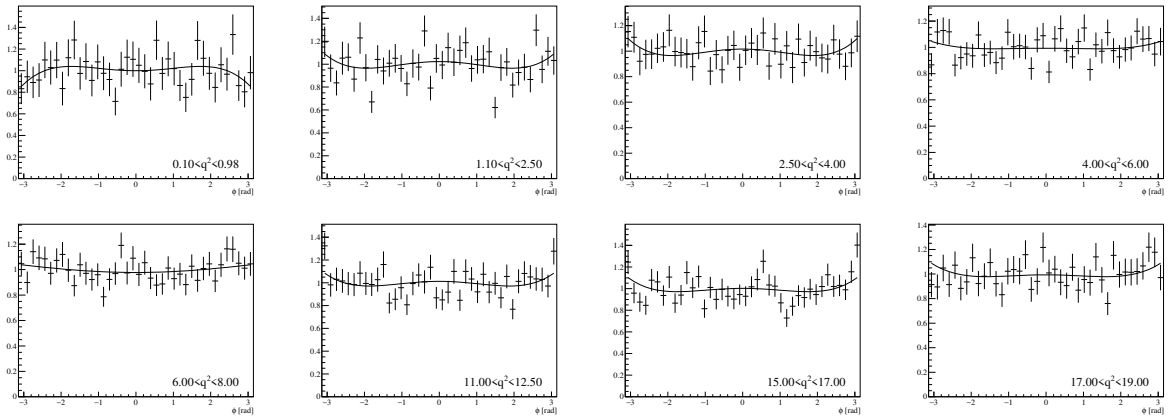

Figure 34: One dimensional projections of the angular acceptance in the dimension of ϕ in eight bins of q^2. The data points are events from phase-space MC of Run I and the solid curve the parametrization of multi-dimensional polynomials.

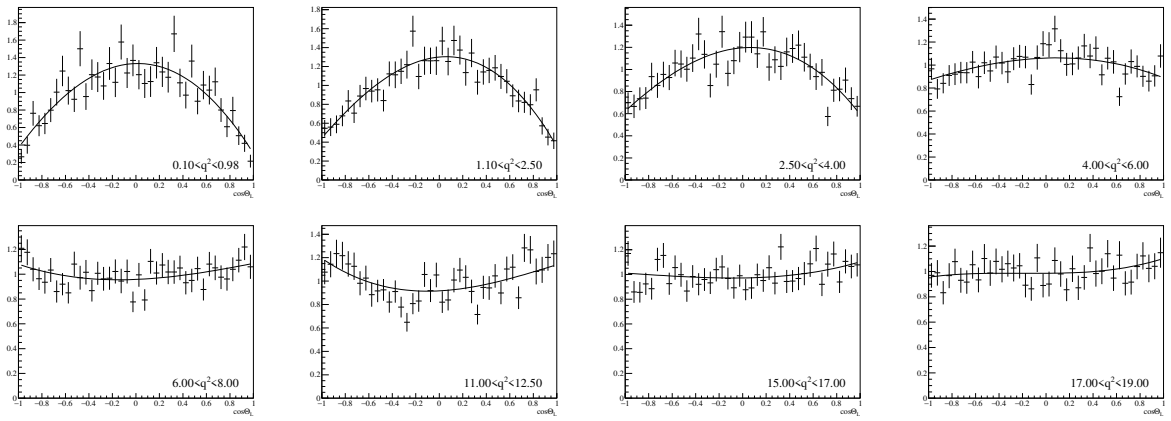

Figure 35: One dimensional projections of the angular acceptance in the dimension of $\cos\theta_L$ in eight bins of q^2. The data points are events from phase-space MC of the first half of Run II (2015+16) and the solid curve the parametrization of multi-dimensional polynomials.

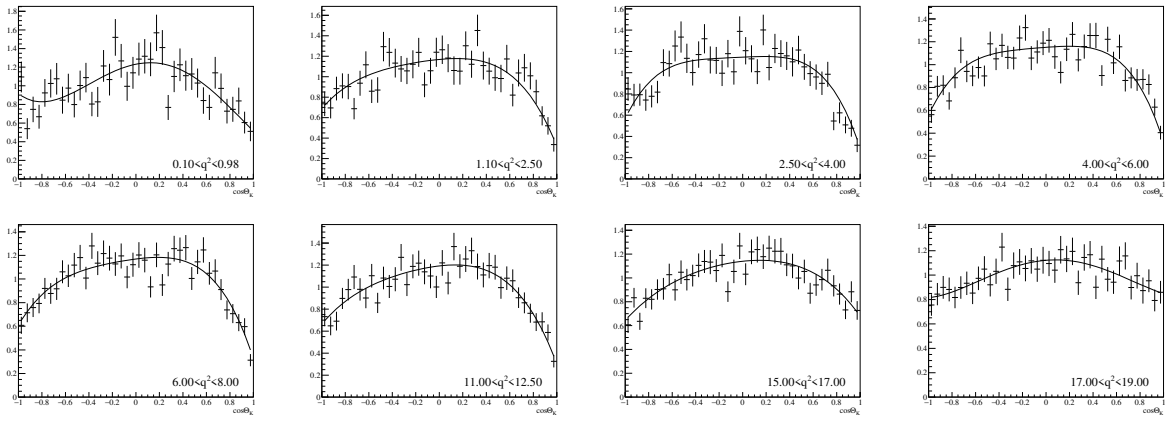

Figure 36: One dimensional projections of the angular acceptance in the dimension of $\cos\theta_K$ in eight bins of q^2. The data points are events from phase-space MC of the first half of Run II (2015+16) and the solid curve the parametrization of multi-dimensional polynomials.

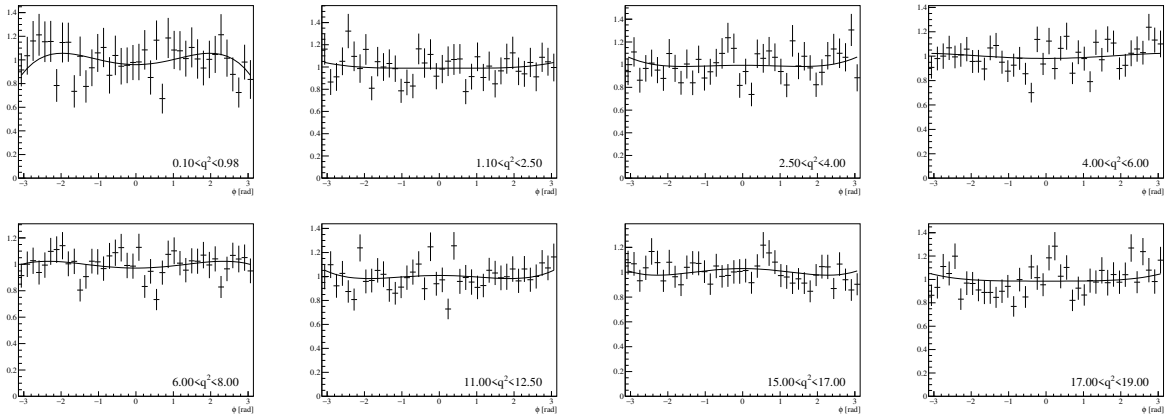

Figure 37: One dimensional projections of the angular acceptance in the dimension of ϕ in eight bins of q^2. The data points are events from phase-space MC of the first half of Run II (2015+16) and the solid curve the parametrization of multi-dimensional polynomials.

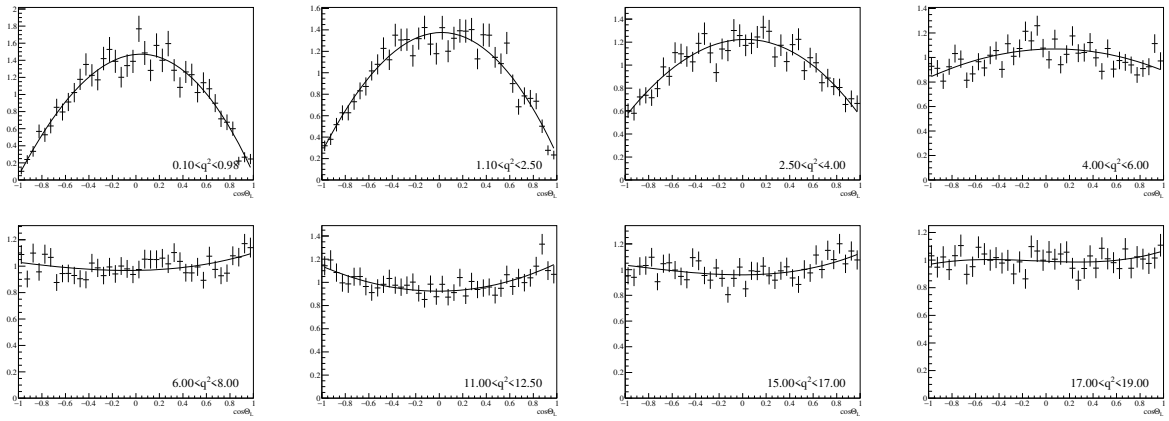

Figure 38: One dimensional projections of the angular acceptance in the dimension of $\cos\theta_L$ in eight bins of q^2. The data points are events from phase-space MC of the second half of Run II (2017+18) and the solid curve the parametrization of multi-dimensional polynomials.

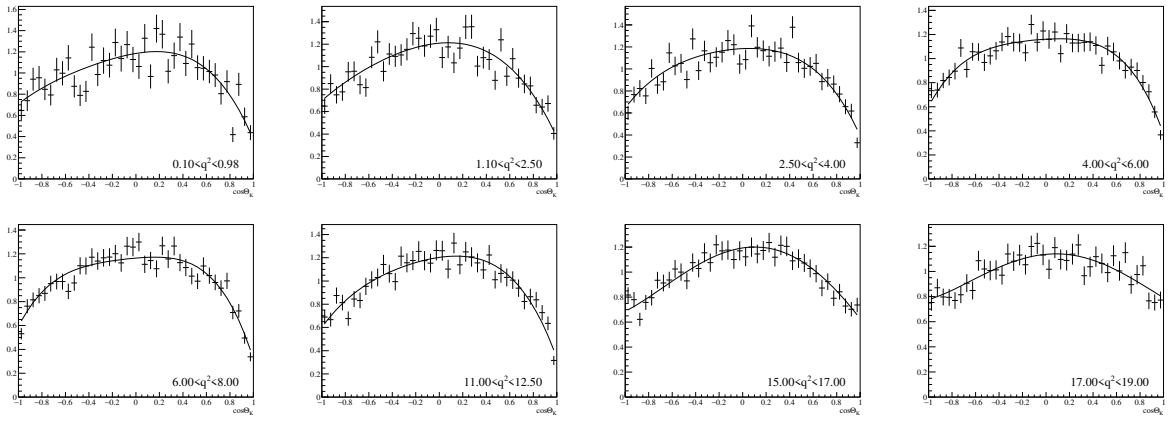

Figure 39: One dimensional projections of the angular acceptance in the dimension of $\cos\theta_K$ in eight bins of q^2. The data points are events from phase-space MC of the second half of Run II (2017+18) and the solid curve the parametrization of multi-dimensional polynomials.

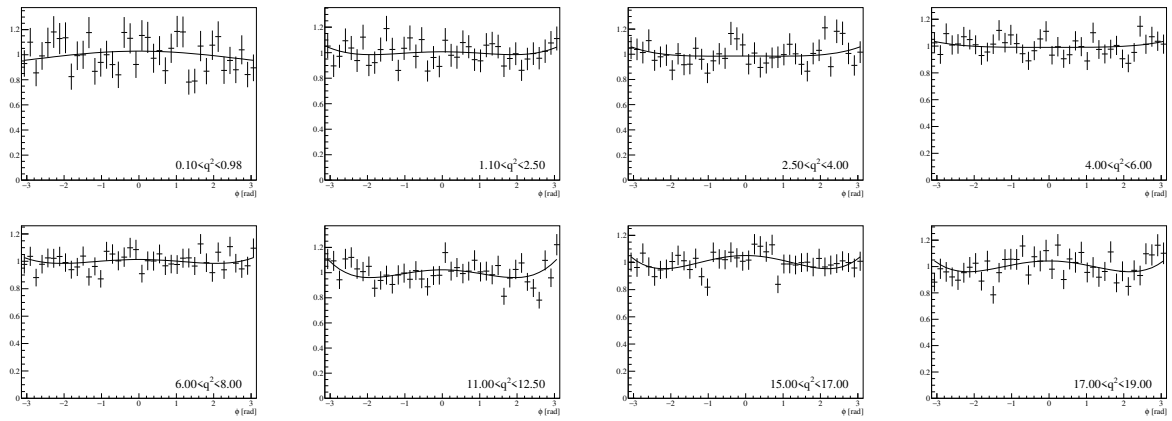

Figure 40: One dimensional projections of the angular acceptance in the dimension of ϕ in eight bins of q^2. The data points are events from phase-space MC of the second half of Run II (2017+18) and the solid curve the parametrization of multi-dimensional polynomials.

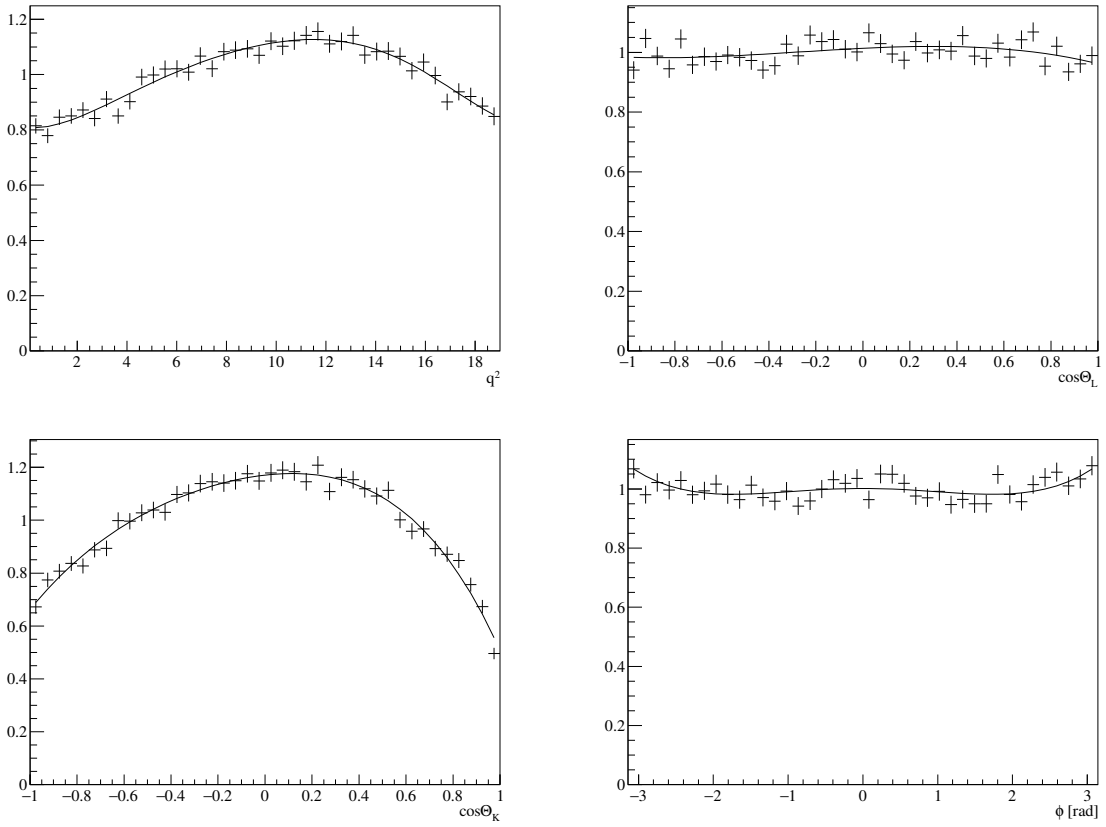

Figure 41: One dimensional projections of the angular acceptance in all four dimensions over the full q^2 range. The data points are events from phase-space MC of Run I and the solid curve the parametrization of multi-dimensional polynomials.

3.4.3 Weighting of events

Differently from the B^0 analysis of Run I [25], the acceptance correction is not built into the fit PDF, but weights are assigned to each event according to the determined acceptance. This method was chosen, as the built-in acceptance correction has shown non-negligible biases in toy studies for the validation of angular folding (see Section 3.5). In addition to avoiding biases, the per-event-weighting has the advantage of not being binned in q^2, as each event gets the weight assigned according to the exact q^2 value of this event, other than an average value per q^2 bin. This individual weight is a function of q^2, $\cos\theta_L$, $\cos\theta_K$ and ϕ and is calculated directly from the inverse of the efficiency of each event:

$$w(\cos\theta_L, \cos\theta_K, \phi, q^2) = \frac{1}{\epsilon(\cos\theta_L, \cos\theta_K, \phi, q^2)} \tag{25}$$

The exact implementation of the weights is discussed in Section 4.3.3.

3.5 Angular folding

The angular decay rate is explained in Section 3.3 in details. From Eq. (13) we directly get the number of free parameters required to fit the angular distributions of $B^+ \to K^{*+}\mu^+\mu^-$,

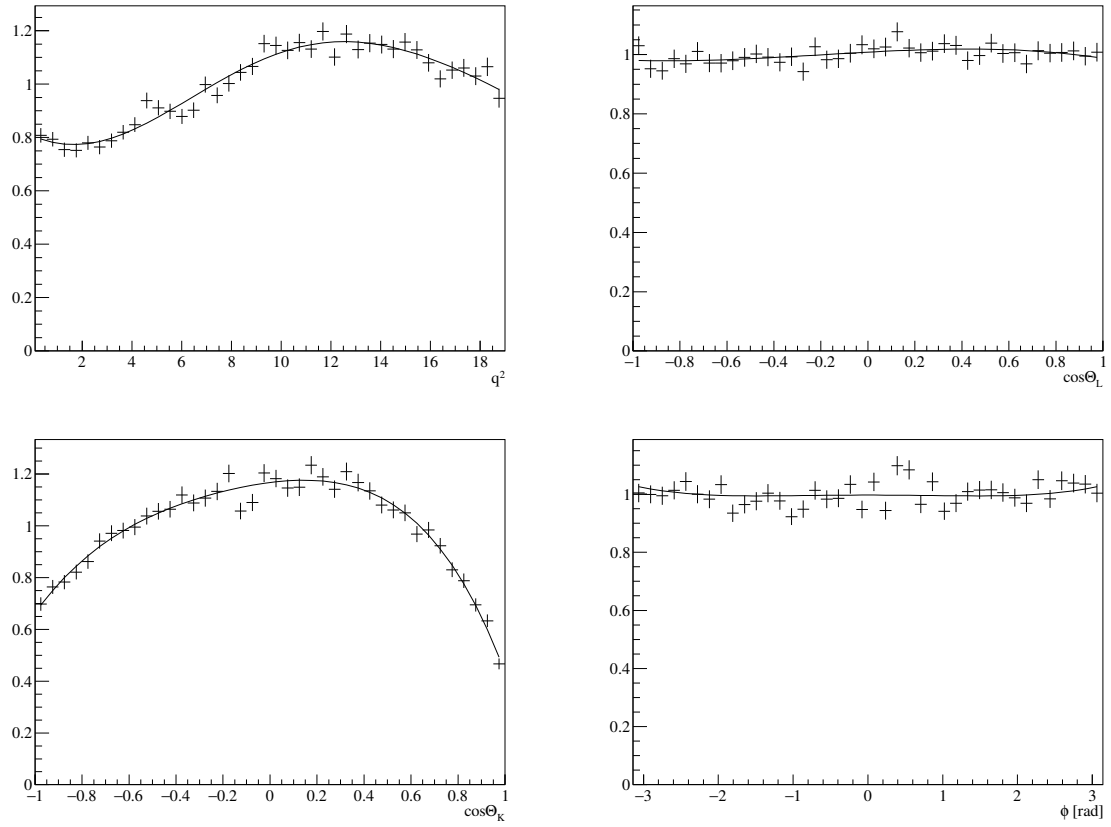

Figure 42: One dimensional projections of the angular acceptance in all four dimensions over the full q^2 range. The data points are events from phase-space MC of the first half of Run II (2015+16) and the solid curve the parametrization of multi-dimensional polynomials.

which is eight. In addition, there are free parameters from the parametrization of the mass peaks (m_{B^+} and $m_{K^{*+}}$), the S-wave contribution as well as background in all dimensions. As has been shown in Section 2.9, the signal yield for the complete data sample of Run I and Run II is only a few hundred events. The distribution of events among the eight q^2 bins (see Section 3.1) decreases the statistics per fit even further. Due to these low event numbers, and the large number of free parameters of the angular decay rate, we are going to make use of technical trick called *angular folding* to reduce the number of parameters in the fit and, hence, stabilize the fit and remove biases in the results.

With dedicated angular folding definitions we reduce the number of angular observables in each fit down to three or four, as most angular moments cancel out due to the folding of angles. With a set of five foldings we can still extract all eight angular observables. The definition of how the three angles are folded is taken from Ref. [30] and is shown in Eq. (26):

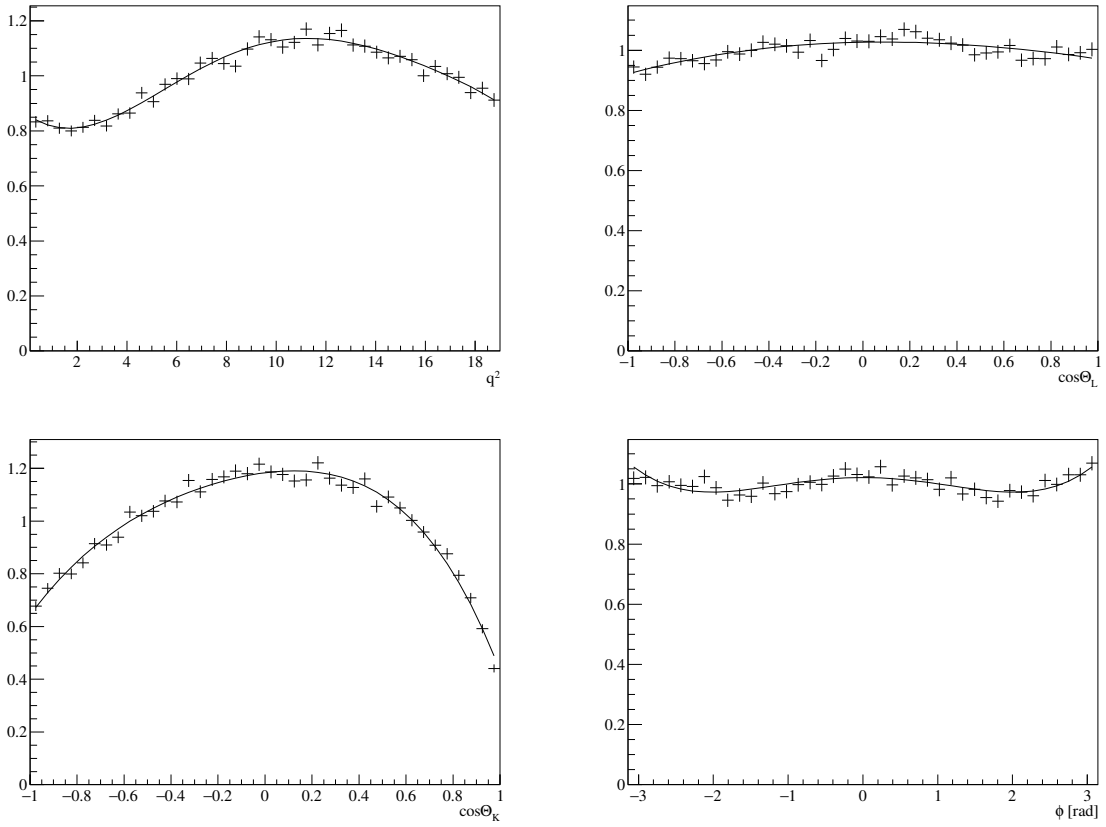

Figure 43: One dimensional projections of the angular acceptance in all four dimensions over the full q^2 range. The data points are events from phase-space MC of the second half of Run II (2017+18) and the solid curve the parametrization of multi-dimensional polynomials.

$$
\begin{aligned}
&\textbf{folding 0:} \\
&\qquad \phi \;\to\; \phi + \pi \qquad \text{for } \phi < 0 \\
&\textbf{folding 1:} \\
&\qquad \phi \;\to\; -\phi \qquad \text{for } \phi < 0 \\
&\qquad \phi \;\to \pi - \phi \qquad \text{for } \cos\theta_L < 0 \\
&\qquad \cos\theta_L \;\to\; -\cos\theta_L \qquad \text{for } \cos\theta_L < 0 \\
&\textbf{folding 2:} \\
&\qquad \phi \;\to\; -\phi \qquad \text{for } \phi < 0 \\
&\qquad \cos\theta_L \;\to\; -\cos\theta_L \qquad \text{for } \cos\theta_L < 0 \\
&\textbf{folding 3:} \\
&\qquad \cos\theta_L \;\to\; -\cos\theta_L \qquad \text{for } \cos\theta_L < 0 \\
&\qquad \phi \;\to\; \pi - \phi \qquad \text{for } \phi > \frac{\pi}{2} \\
&\qquad \phi \;\to\; -\pi - \phi \qquad \text{for } \phi < -\frac{\pi}{2} \\
&\textbf{folding 4:} \\
&\qquad \cos\theta_K \;\to\; -\cos\theta_K \qquad \text{for } \cos\theta_L < 0 \\
&\qquad \cos\theta_L \;\to\; -\cos\theta_L \qquad \text{for } \cos\theta_L < 0 \\
&\qquad \phi \;\to\; \pi - \phi \qquad \text{for } \phi > \frac{\pi}{2} \\
&\qquad \phi \;\to\; -\pi - \phi \qquad \text{for } \phi < -\frac{\pi}{2}
\end{aligned}
\tag{26}
$$

Table 16: Summary of the angular folding techniques and which P-wave angular moments each folding is sensitive to. The '✓' symbol indicates that the folding is sensitive to the angular observable.

observable	moment	0	1	2	3	4
S_{1s}	$\cos^2\theta_K$	✓	✓	✓	✓	✓
S_3	$\sin^2\theta_K \sin^2\theta_L \cos 2\phi$	✓	✓	✓	✓	✓
S_4	$\sin 2\theta_K \sin 2\theta_L \cos\phi$		✓			
S_5	$\sin 2\theta_K \sin\theta_L \cos\phi$			✓		
S_{6s}	$\sin^2\theta_K \cos\theta_L$	✓				
S_7	$\sin 2\theta_K \sin\theta_L \sin\phi$				✓	
S_8	$\sin 2\theta_K \sin 2\theta_L \sin\phi$					✓
S_9	$\sin^2\theta_K \sin^2\theta_L \sin 2\phi$	✓				

Please note, that folding 4 indeed is folding $\cos\theta_K$ in dependence of $\cos\theta_L$. The costs at which this advantage comes along, is that we can not extract the full correlation matrix of all angular observables, but only the correlations between angular observables which are fitted by the same folding[4]. Which angular observables are extracted together in the same folding is shown in Table 16.

3.5.1 Angular moment cancellations

Which folding technique is sensitive to which observables is summaries in Table 16. Fitting all five different foldings gives access to all eight angular observables. Some components of the S-wave contribution cancel out under folding as well, which is summarized in Table 17. And last, some Chebyshev polynomials of the angular background description cancel out under the angular folding. For $\cos\theta_L$ the odd order Chebyshev polynomials cancel out for foldings 1 – 4. In $\cos\theta_K$, only for folding 4 all odd orders cancel out and in ϕ, odd order polynomials cancel out for folding 1 + 2.

The angular ranges change size due to the angular folding. For all foldings, the folded angular ranges are shown in Table 18, together with the reduction factor of the angular phase-space.

[4]As discussed later in Section 4.9, the full correlation matrix will be determined using the BOOTSTRAPPING [31] method.

Table 17: Cancellation and sensitivity of the S-wave angular moments for all foldings. The '✓' symbol indicates that the folding is sensitive to the S-wave component.

observable	moment	0	1	2	3	4
F_S	$\sin^2\theta_L$	✓	✓	✓	✓	✓
S_{S1}	$\sin^2\theta_L\cos\theta_K$	✓	✓	✓	✓	
S_{S2}	$\sin 2\theta_L\sin\theta_K\cos\phi$		✓			
S_{S3}	$\sin\theta_L\sin\theta_K\cos\phi$			✓		
S_{S4}	$\sin\theta_L\sin\theta_K\sin\phi$				✓	✓
S_{S5}	$\sin 2\theta_L\sin\theta_K\sin\phi$					

Table 18: The size of the angular phase space decreases due to angular folding. The size, reduction factor and ranges for the angular dimensions for all foldings is shown.

folding	0	1	2	3	4
$\cos\theta_L$	[-1,+1]	[0,+1]	[0,+1]	[0,+1]	[0,+1]
$\cos\theta_K$	[-1,+1]	[-1,+1]	[-1,+1]	[-1,+1]	[-1,+1]
ϕ	[0,π]	[0,π]	[0,π]	$[-\frac{\pi}{2},\frac{\pi}{2}]$	$[-\frac{\pi}{2},\frac{\pi}{2}]$
factor	2	4	4	4	4

4 Angular fitter

4.1 Introduction to the fitter framework

This analysis uses the FCNCFITTER, which was developed by LHCb colleagues for the angular analysis of $B^0 \to K^{*0}\mu^+\mu^-$ for Run I [25] and was since used for different angular analyses, such as again $B^0 \to K^{*0}\mu^+\mu^-$ (Run I + 2016 [7]) or $B_s^0 \to \phi\mu^+\mu^-$ [32]. It is a C++ based framework to run a Maximum Likelihood fit using the TMINUIT minimization class of the ROOT framework. The FCNCFITTER is dedicated to angular analyses of decays of a pseudo-scalar meson to a vector meson with two opposite-charged leptons. In Section 3.3.3 the angular decay rate of these so called *b-to-sll* transitions was introduced, which will be directly transformed into a probability density function (PDF) for the Maximum Likelihood fit.
All details on the implementation of weighting of single events to compensate the angular acceptance (Section 3.4) together with angular folding (Section 3.5) are presented.
The fit can be performed in up to five dimensions,

- the invariant mass of the B^+, $m_{K\pi\mu^+\mu^-}$,
- the invariant mass of the K^{*+}, $m_{K\pi}$ and
- three decay angles, $\cos\theta_L$, $\cos\theta_K$ and ϕ,

which can be included individually. An arbitrary number of sub-sets can be fitted simultaneously, with individual configurations, own acceptance corrections and different parameter values. Of course, some parameters are possible to be shared between the different sub-sets, hence the term *simultaneous*.

In addition to the final fits of the signal channel, dedicated fits to pure background samples, fewer dimensional fits to extract F_S, fits to MC events to obtain signal peak shapes, fits to the resonant channel to validate the fitter setup and fits to toy event samples are executed. All these fits will be explained in details in the following sections.

Since the FCNCFITTER was used and validated before for other analyses, the validation and tests of the fitter in following sections will focus on new implementations and the decay specific tools. First, all new implementations, which mainly concern the angular folding techniques are validated with toy events, shown in Section 4.4.1 for large statistic samples. Toy studies with realistic signal yield estimations shown in Section 4.4.2 then validate the functionality of the FCNCFITTER for the use in this very angular analysis. A fit to the reference channel $B^+ \to J/\psi\, K^{*+}$ is used to test the fitter at large statistics, with a simultaneous fit, angular folding and verify the functionality of the angular acceptance correction. Here the advantage is, that the results of the reference channel can be compared to published results of different experiments, as presented in Section 4.4.7.
Comparing the results of a fit to signal channel MC events after the selection and a fit to the same events at generator level[5] further verifies the angular folding and angular acceptance correction in Section 4.4.4. The configuration used for the final fit is discussed

[5]The term *generator level* refers to events that are not selected at all and did not experience any cuts but to be in the acceptance of the LHCb detector.

in Section 4.5. As a cross-check of the results from the fitter, a moment analysis [33] is performed and introduced in Section 4.7.

4.2 Fitter strategy

The strategy to extract the angular observables from the rare channel foresees two individual fits:

- 2D fit in $m_{K\pi\mu^+\mu^-}$ and $m_{K\pi}$ to extract F_S
- 4D fit in $m_{K\pi\mu^+\mu^-}$, $\cos\theta_L$, $\cos\theta_K$ and ϕ to extract the angular observables

For both fits, the $m_{K\pi\mu^+\mu^-}$ dimension is used to determine the signal and background fraction.
Given the limited statistics and the weak sensitivity to F_S, its value cannot be determined in the nominal q^2 binning scheme. Furthermore, the 2D fit has shown similar sensitivity on the S-wave fraction as a full 5D fit, as shown in Fig. 158 which is taken from Ref. [34]. The idea is to perform a 2D fit to extract F_S and use this value as a Gaussian constraint in the 4D. The dedicated toy event studies in Section 4.4.6 show that this strategy does not bias the uncertainty on the observables we want to measure.

The binning scheme for the 2D fit consists of three bins: below (1.1-8.0 GeV^2/c^4), in between (11.0-12.5 GeV^2/c^4) and above (15.0-19.0 GeV^2/c^4) the $c\bar{c}$ resonance regions. According to Ref. [25], the S-wave fraction has approximately the same q^2 dependence as the longitudinal polarization fraction, F_L. Therefore, the q^2 dependence of F_L is obtained using the flav.io [35] package and was observed to be reasonable flat in the larger bins used. The resulting F_L curve obtained from flav.io is shown in the appendix (Appendix A.8). The very low q^2 region below 1.0 GeV^2/c^4 is excluded from the fit as F_L is about 50% smaller than in the region between 1.1-8.0 GeV^2/c^4. An estimation on F_S for the lowest q^2 bin is therefore extrapolated using the q^2 dependence of F_L. All other q^2 bins receive only a minor correction of F_S according to the F_L trend. The exact values obtained from the flav.io package are given in the appendix, Appendix A.8.
The precision of this S-wave fraction determination is addressed in a systematic study in Section 5.4 by varying the value for F_S within its uncertainty from the 2D mass fits.

4.3 Fit PDF

The probability density function (PDF) for the fitter is constructed by adding and multiplying individual (sub-)PDF. The total PDF consists of a signal and background component, which are added in relation using the signal fraction, $\mathrm{f_{sig}}$.

$$PDF(m,\vec{\Omega}) = \mathrm{f_{sig}} \cdot PDF_{\mathrm{sig}}(m,\vec{\Omega}) + (1-\mathrm{f_{sig}}) \cdot PDF_{\mathrm{bkg}}(m,\vec{\Omega}). \tag{27}$$

Both, the signal and background PDF consist of sub-PDF: for (up to two) mass dimensions and the angular basis, $\vec{\Omega}$.
For the first fit (2D) in two mass dimensions ($m_{K\pi\mu^+\mu^-}$ and $m_{K\pi}$), no angular PDF is included. In the final fit (4D), the mass dimension of the B meson ($m_{K\pi\mu^+\mu^-}$) is fitted together with the PDF of the three decay angles. Here, the Gaussian constraint on F_S from the 2D fit is included.

4.3.1 2D mass fit

The sole purpose of this 2D fit is to constrain the S-wave fraction, F_S, which will be used in the 4D later on. In the following, a detailed description of both PDF is discussed, including the introduction of the second mass dimension ($m_{K\pi}$) into the angular PDF.

- **Invariant mass of the B^+:** $m_{K\pi\mu^+\mu^-}$

The signal component of the invariant mass of the B^+ is modelled by a two tailed Crystal Ball [15] function.
A single exponential function is used for the background model for `LL` tracks or `DD` tracks events.
These methods were previously applied in the event selection and are described in detail in Section 2.5. The main contribution from a fit to the mass dimension of the B^+ is to determine the signal fraction, $\mathrm{f_{sig}}$. The fit range is $5150 - 6000\,\mathrm{MeV}/c^2$, which cuts away any partial reconstructed background below $5150\,\mathrm{MeV}/c^2$. An upper invariant mass cut at $6000\,\mathrm{MeV}/c^2$ is a good compromise of having enough statistics for the background while removing any potential non-combinatorial background at higher invariant masses.

- **Invariant mass of the K^{*+}:** $m_{K\pi}$

Fitting the invariant mass of the K^{*+} improves the constraint of the S-wave fraction, F_S, as it was shown in [25]. Only events within a window of $100\,\mathrm{MeV}/c^2$ above and below the K^{*+} mass peak are selected and fitted. A larger mass window in $m_{K\pi}$ would improve the sensitivity on the S-wave fraction, F_S. On the other side, the larger $m_{K\pi}$ mass range significantly increases the absolute value of F_S, as the S-wave is rather flat in the mass range around the K^{*+} mass, while the P-wave is peaking with a width of roughly $50\,\mathrm{MeV}/c^2$. Consequently, the sensitivity of the P-wave observables in the 4D angular fit decreases, as the S-wave events are non-distinguishable background that has to be fitted. This effect outweighs the advantage of the improved sensitivity on F_S. Therefore, the $m_{K\pi}$ mass window was chosen as small as possible to reduce the impact of S-wave events in the final fit, while still covering the majority of the full width of the K^{*+} mass peak.
The composition of the PDF in this dimension and the explanation in the following paragraph is taken from Section 6.2.12 of [25]. The two signal components are modelled by a Breit-Wigner function and a LASS parametrization [36] for P-wave and S-wave, respectively.
The Breit-Wigner formula is given by

$$\begin{aligned}\mathcal{A}_{\mathrm{P}}(m_{K\pi}) =& \sqrt{kp} \times B'_{L_B}(k, k_0, d) \left(\frac{k}{m_{B^+}}\right)^{L_B} \times B'_{L_{K^{*+}}}(p, p_0, d) \left(\frac{p}{m_{K^{*+}}}\right)^{L_{K^{*+}}} \\ & \times \frac{1}{{m_{K^{*+}}}^2 - {m_{K\pi}}^2 - i m_{K^{*+}} \Gamma(m_{K\pi})},\end{aligned} \tag{28}$$

with the momentum k (p) of the K^{*+} (K^0_{S}) in the rest-frame of B^+ (K^{*+}) and k_0 (p_0) the corresponding quantities at the K^{*+} resonance peak. The phase-space factor, $\sqrt{kp}$, origins from the three-body phase space integrated over helicity angle, θ_K, and the Jacobian of the transformation to $m_{K\pi}$. Further, the radial angular momenta L_B and $L_{K^{*+}}$ of the form $L = S, P, D, ...$ and not to be mixed up with the angular momenta of the

final state particles in the decay. And finally, the Blatt-Weisskopf function B_{L_x}, following the definition from Ref. [37]:

$$\begin{aligned} B'_0\left(p, p_0, d\right) =& 1 \\ B'_1\left(p, p_0, d\right) =& \sqrt{\frac{1+\left(p_0 d\right)^2}{1+\left(p\ d\right)^2}} \end{aligned} \tag{29}$$

with the size of the decaying particle fixed to $d = 1.6\,\mathrm{GeV}^{-1}$ [38]. This value for d (also notated as R in some literature) was previously up to discussion: In the recent LHCb analysis of $B^+ \to J/\psi\,\rho^+$ [39], d was left to float in the fit, resulting in approximately $1.64\,\mathrm{GeV}^{-1}$. In a Z(4430) analysis [37] (in Section 9.2) the parameter d was thoroughly investigated and evaluated, indicating that the fit model favours values close to zero when the parameter is left to float. For this analysis a fit to the reference channel in which d was left floating resulting in 2.5 ± 0.2, . At fit to the rare channel to extract d is not possible due to low statistics. Hence, the choice of the small value of $d = 1.6\,\mathrm{GeV}^{-1}$ (equal to 0.3 fm) seems the a reasonable conclusion to be consistent with previous analyses, and which also showed to not impact the measurement of the S-wave fraction, F_S, with respect to the value obtained in the reference channel.

Using the angular momenta of the P-wave, $L_B = 0$ and $L_{K^{*+}} = 1$, the P-wave fit PDF simplifies to:

$$\mathcal{A}_{\mathrm{P}}(m_{K\pi}) = \sqrt{kp} \times \sqrt{\frac{1+\left(p_0 d\right)^2}{1+\left(p\ d\right)^2}} \times \frac{p}{m_{K^{*+}}} \times \frac{1}{{m_{K^{*+}}}^2 - {m_{K\pi}}^2 - i m_{K^{*+}} \Gamma(m_{K\pi})}. \tag{30}$$

The S-wave component of the $m_{K\pi}$ is modelled using the LASS parametrization

$$\begin{aligned} \mathcal{A}_{\mathrm{S}}(m_{K\pi}) =& \sqrt{kp} \times B'_{L_B}(k, k_0, d) \left(\frac{k}{m_{B^+}}\right)^{L_B} \times B'_{L_{K^{*+}}}(p, p_0, d) \left(\frac{p}{m_{K^{*+}}}\right)^{L_{K^{*+}}} \\ & \times \left(\frac{1}{\cot\delta_B - i} + e^{2i\delta_B} \frac{1}{\cot\delta_R - i}\right), \end{aligned} \tag{31}$$

with $\cot\delta_B = \frac{1}{ap} + \frac{1}{2} rp$ and $\cot\delta_R = \frac{{m_{K^{*+}}}^2 - {m_{K\pi}}^2}{m_{K^{*+}} \Gamma(m_{K\pi})}$. The values $a = 1.95$ and $r = 1.78$ are fixed to the same values as in Ref. [25]. For each q^2 bin, the central value of the q^2 bin is chosen for the calculating Γ in the Breit-Wigner model. Again, simplifying the general form of the parametrization by the angular momenta involved in the S-wave decay, $L_B = 1$ and $L_{K^{*+}} = 0$, the fit PDF is given by

$$\mathcal{A}_{\mathrm{S}}(m_{K\pi}) = \sqrt{kp} \times \sqrt{\frac{1+\left(k_0 d\right)^2}{1+\left(k\ d\right)^2}} \times \frac{k}{m_{B^+}} \times \left(\frac{1}{\cot\delta_B - i} + e^{2i\delta_B} \frac{1}{\cot\delta_R - i}\right), \tag{32}$$

The P- and S-wave contributions are added using the S-wave fraction, F_S, via

$$\left.\frac{\mathrm{d}\Gamma}{\mathrm{d}m_{K\pi}}\right|_{\mathrm{S+P}} = (1 - F_S) \left|\mathcal{A}'_{\mathrm{P}}(m_{K\pi})\right|^2 + F_S \left|\mathcal{A}'_{\mathrm{S}}(m_{K\pi})\right|^2, \tag{33}$$

with $\mathcal{A}'_{\mathrm{S(P)}}(m_{K\pi})$, the normalized decay amplitudes of S- and P-wave. The background component in the $K^0_{\mathrm{S}}\pi^+$ mass dimension is described by a linear curve, as demonstrated on events – selected from the side-band of $m_{K\pi\mu^+\mu^-}$ – in Section 3.3.5.

- **Combining the PDF for both mass dimensions**

With the details given for both mass dimensions, the signal PDF consist of the product of a two tailed Crystal Ball function in the $m_{K\pi\mu^+\mu^-}$ dimension times the more complicated function in the $m_{K\pi}$ dimension, the sum of P- and S-wave, as shown in Eq. (33).
The background PDF is the product of an exponential background in $m_{K\pi\mu^+\mu^-}$ and the linear polynomial in the $m_{K\pi}$ mass dimension.
From the $m_{K\pi}$ mass dimension the S-wave fraction, F_S is extracted.

4.3.2 4D angular fit

The actual fit to extract the angular observable takes four dimensions into account: $m_{K\pi\mu^+\mu^-}$, $\cos\theta_L$, $\cos\theta_K$ and ϕ. In addition, the extracted S-wave fraction, F_S, is Gaussian constrained to the values obtained from the 2D mass fit (Section 4.3.1).
Both, the signal PDF and the background PDF, are the product of PDF in the $m_{K\pi\mu^+\mu^-}$ dimension and the PDF in the angular dimensions.

- **Invariant mass of the B^+: $m_{K\pi\mu^+\mu^-}$**

The mass dimension PDF for $m_{K\pi\mu^+\mu^-}$ is identical to the description mentioned in the previous paragraph and defined already in Section 2.5. As mentioned, the signal PDF is the two-tailed Crystal Ball and an exponential curve as background PDF. In the final fit of the rare channel data, the only free parameters in the mass dimension are the exponential slope for the combinatorial background description and the mean position of the mass peak. The shape of the mass peak is fixed to values obtained from MC in each q^2 bin, with the width of the peak being scaled accordingly to width ratio of data events and MC in the reference channel. The values of this width scaling are determined individually for each of the four sub-sets: 1.18 (1.15) for `DD` tracks and 1.06 (1.12) for `LL` tracks in Run I (Run II). Scales larger 1 refer to a larger width in data compared to MC.

- **Angular dimensions: $\vec{\Omega}$**

According to the introduction in Section 3.3, the PDF corresponds to the normalized differential decay rate. The full formula of the normalized differential decay rate is given in Eq. (19).
The angular background PDF consists of the Chebyshev polynomials, as introduced in Section 3.3.4.

4.3.3 Minimization strategy

As mentioned before, the FCNCFITTER uses the built-in minimization tool of ROOT: TMINUIT. From the PDF, a likelihood, $\mathcal{L}_e$, for each event, e, is calculated from the PDF

$$\mathcal{L}_e = PDF(m_e, \vec{\Omega}_e | S_i, \lambda_{nuis}), \tag{34}$$

with the angular observables, S_i, as well as other (free) parameters in the PDF, λ_{nuis}. The later are background, S-wave or mass parameters, which are not of interest for the physics results of this angular analysis and which will not be published. The likelihoods of all events are added up to the the total likelihood, containing all angular observables

and free nuisance parameters. And the total likelihood is maximized by minimizing the negative logarithm of the very same:

$$-\log \mathcal{L} = \sum_e \log PDF(m_e, \vec{\Omega}_e | S_i, \lambda_{nuis}) \tag{35}$$

The statistical uncertainty on the angular observables (and nuisance parameters) is determined using either the HESSE or MINOS method. HESSE uses the second derivative matrix, which results in a symmetric uncertainty, while MINOS scans the likelihood and uses the condition $-2\Delta \log \mathcal{L} = 1$ for the uncertainty, potentially creating asymmetric uncertainties. The four sub-sets (see Section 2.1) are fitted simultaneously, with all angular observables of both P- and S-wave being shared between the PDF. Other parameters, such as background components or the B meson mass peak are left independent for every fit.

4.4 Fitter validation and testing

The correct and un-biased functionality of the FCNCFITTER has to be tested. This is done before extracting the angular observables via the final fit to the signal channel events. This validation is done using different event samples: toy events, MC events and data of the reference channel $B^+ \to J/\psi K^{*+}$.
In the next Section 4.4.1 toy event studies using large event samples for the fit are performed. By estimating the signal yield from the reference channel and interpolating the background pollution from the mass-side-bands, we get an estimation of the number of events in the final fit. This estimation is used in the second series of toy event studies (Section 4.4.2) to verify the fitter is able to fit the estimated number of events without biasing the angular observables.
After the fitter itself was validated with toy event studies, we proceed to fitting actual data. First a fit to simulated signal events in Section 4.4.4 to validate the functionality of the angular acceptance correction is performed. Again, the different folding techniques are compared and the correct implementation is tested. All tests with signal channel MC events are done in the identical q^2 bins as the final fit.
Lastly, we fit the reference channel $B^+ \to J/\psi K^{*+}$ in Section 4.4.7. This is the first fit to actual data recorded by the LHCb experiment. The sample consists of more than 0.1M events and serves as a cross-check of the functionality and stability of the fitter. Of course, angular acceptance correction, angular folding as well as S-wave contribution is included in these fits.
With all those tests unbiased results are assured.

4.4.1 Acceptance correction and folding validation with large statistic toy events

The FCNCFITTER required some new implementations and changes for being used in this angular analysis. To verify and test all new features and changes, test fits with a large sample of generated toy events was used. Usually the word *large* refers to 10000 events, which are distributed over the eight q^2 bins, if not stated otherwise. For the toy studies, usually some 100 fits are performed on randomly generated toy event samples. With this method, we can spot biases, which have been introduced to the fitter, as well as

incorrect statistical uncertainties determined by the fit.
Every set of randomly generated events is fitted and the resulting parameter values are saved. For the analysis of these toy event studies, the deviation of the resulting fit parameters from the generated value is calculated and divided by the statistical uncertainty from the fit:

$$pull = \frac{x - x_0}{\sigma} \tag{36}$$

If both, the mean position and the width are correct, the pull distributions are Gaussian shaped with centre at zero and width equal to one. An example of a single pull distribution for one parameter in one q^2 bin is given on the right side of Fig. 44.
Plots to simplify and summarize all resulting pull distributions in a single overview are introduced in Fig. 44. From the pull distributions of every parameter and for every q^2 bin, the mean position and the width of a Gaussian fit including their uncertainties are extracted. Those two values are plotted by two markers. The color of the marker indicates the absolute deviation of the value from the expected values[6].
The overview histograms of the results from these toy studies are shown in Figs. 45 to 47. All numbers for the mean position and the width of the pull distributions for all foldings and parameters are listed in the appendix, Appendix A.12. The large statistic studies are found in Appendix A.12.1. In total, 3000 fits of 3000 independent toy event samples are performed for each q^2 bin and for each folding or not-folding. This number of fits results in an uncertainty on the mean position and the width of the pull distribution of about 0.018, which is confirmed by the values given in the tables of Appendix A.12.
For all foldings and for the full angular fit we do not observe any biases or incorrect widths for studies with 10000 toy events.
The width of the S-wave fraction, F_S, is out of scope and not plotted in the summary histograms. Due to the Gaussian constraint on F_S from the 2D fit, as explained in Sections 4.3.1 and 4.3.2, the width of the distribution is much smaller as 1, which is expected. It is however demonstrated that the Gaussian constraint on F_S does not introduce any bias to other observables.

[6]Expected values are: 0 for the mean position and 1 for the width/sigma.

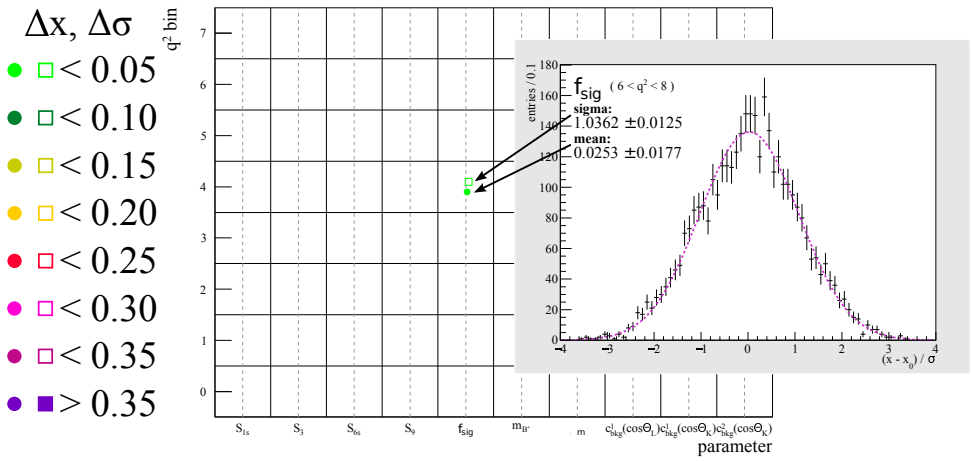

Figure 44: A sketch to illustrate the creation of the summary plots for all toy event studies. From each pull distribution the mean and width are exported to the summary histogram. Full circles show the mean position and hollow squares indicate the width of the pull distribution. The dashed line indicates the theoretical values of a perfect distribution. The color code of the markers illustrates the absolute deviation from those theoretical values in steps of 0.05.

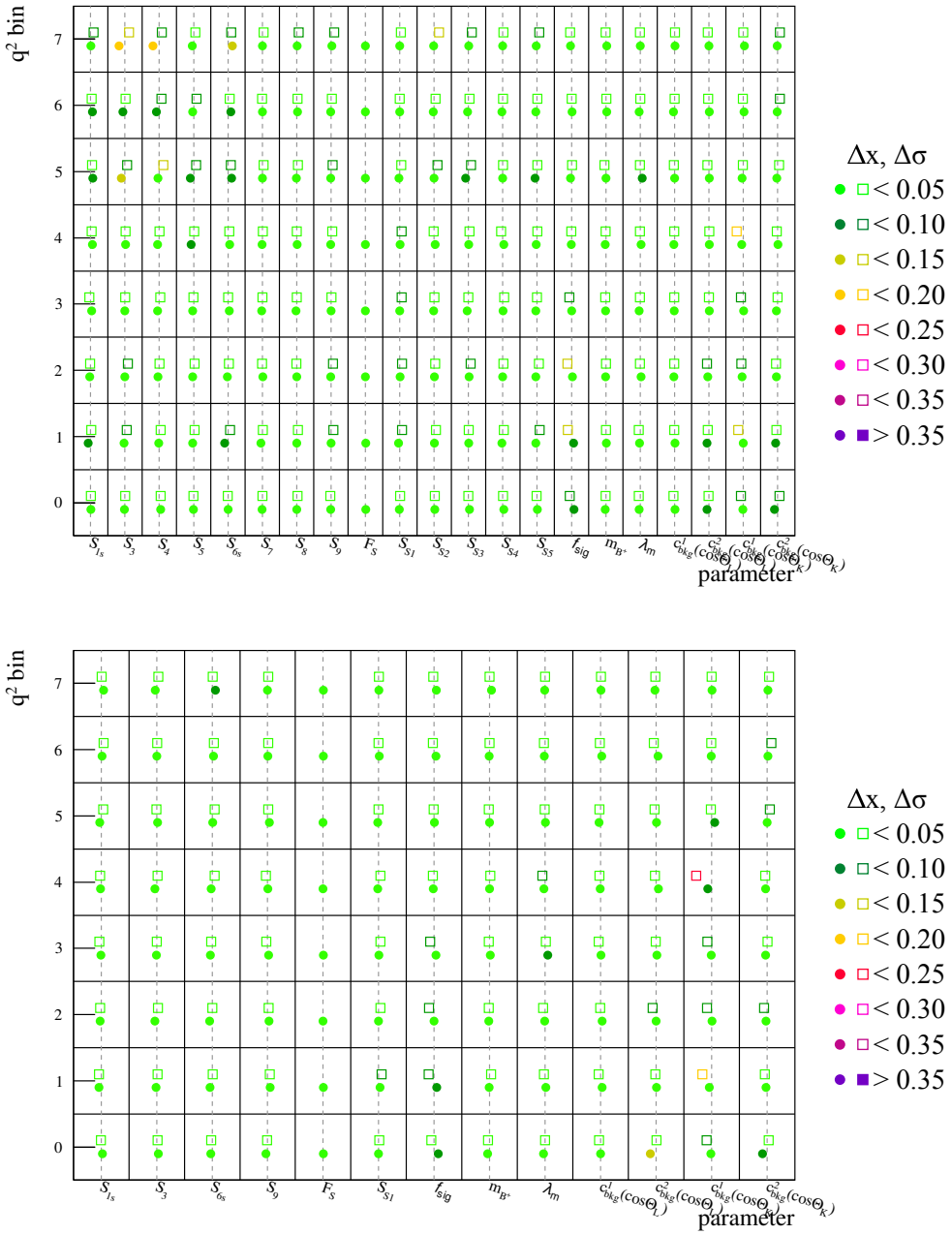

Figure 45: Toy event studies with no angular folding (top) and folding 0 (bottom) using 10000 toy events per fit. Summary of the pull distributions for all free parameters in all q^2 bins. Each cell contains two markers, the hollow squares indicate the width of the pull distribution from toy studies, while the filled circles show the mean position of the pull distribution. The dashed line in each cell indicates the designated positions 0 (1) for the mean (width). See Fig. 44 for explanations on the color code and how these summary histograms are filled.

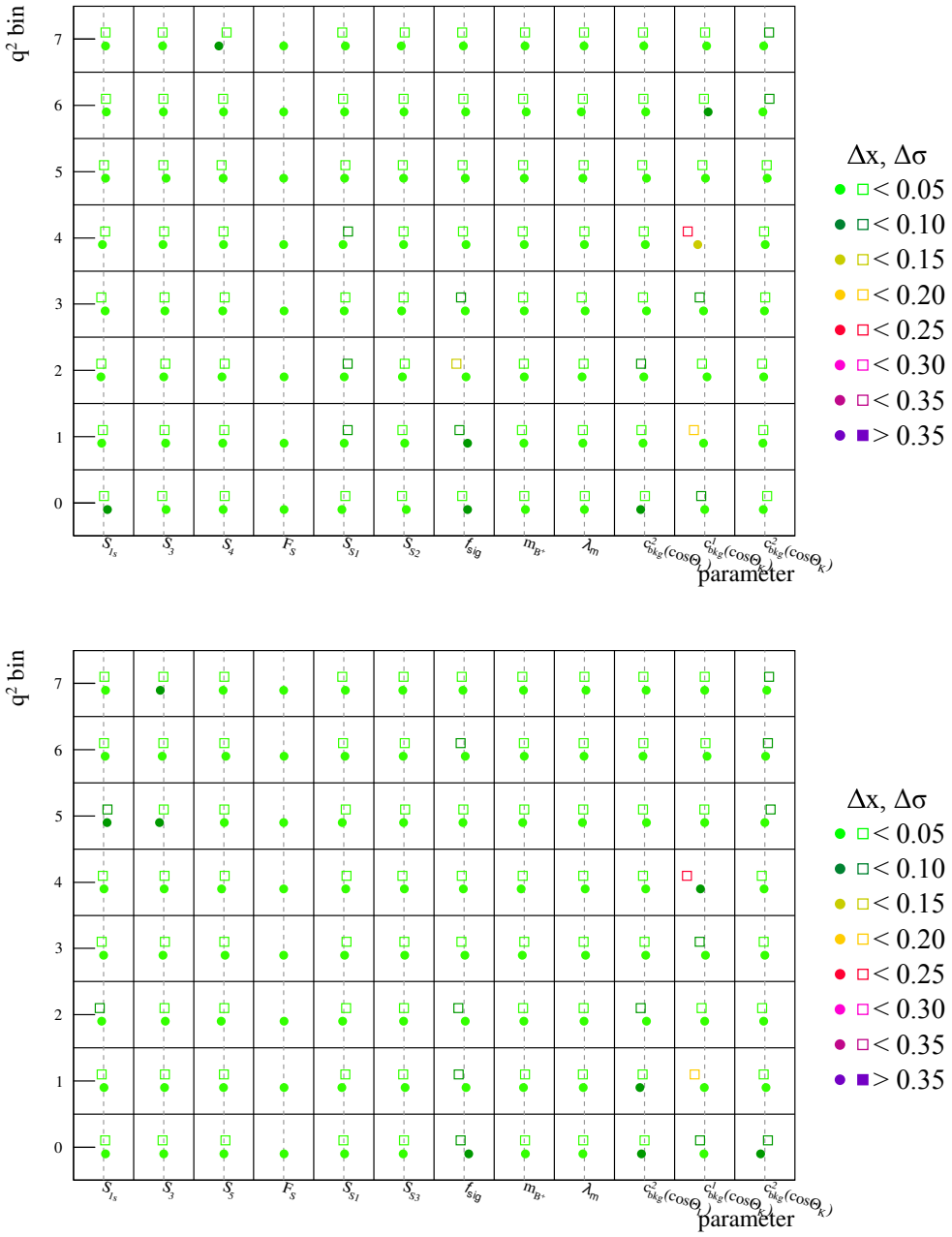

Figure 46: Toy event studies for angular folding 1 (top) and 2 (bottom) using 10000 toy events per fit. Summary of the pull distributions for all free parameters in all q^2 bins. Each cell contains two markers, the hollow squares indicate the width of the pull distribution from toy studies, while the filled circles show the mean position of the pull distribution. The dashed line in each cell indicates the designated positions 0 (1) for the mean (width). See Fig. 44 for explanations on the color code and how these summary histograms are filled.

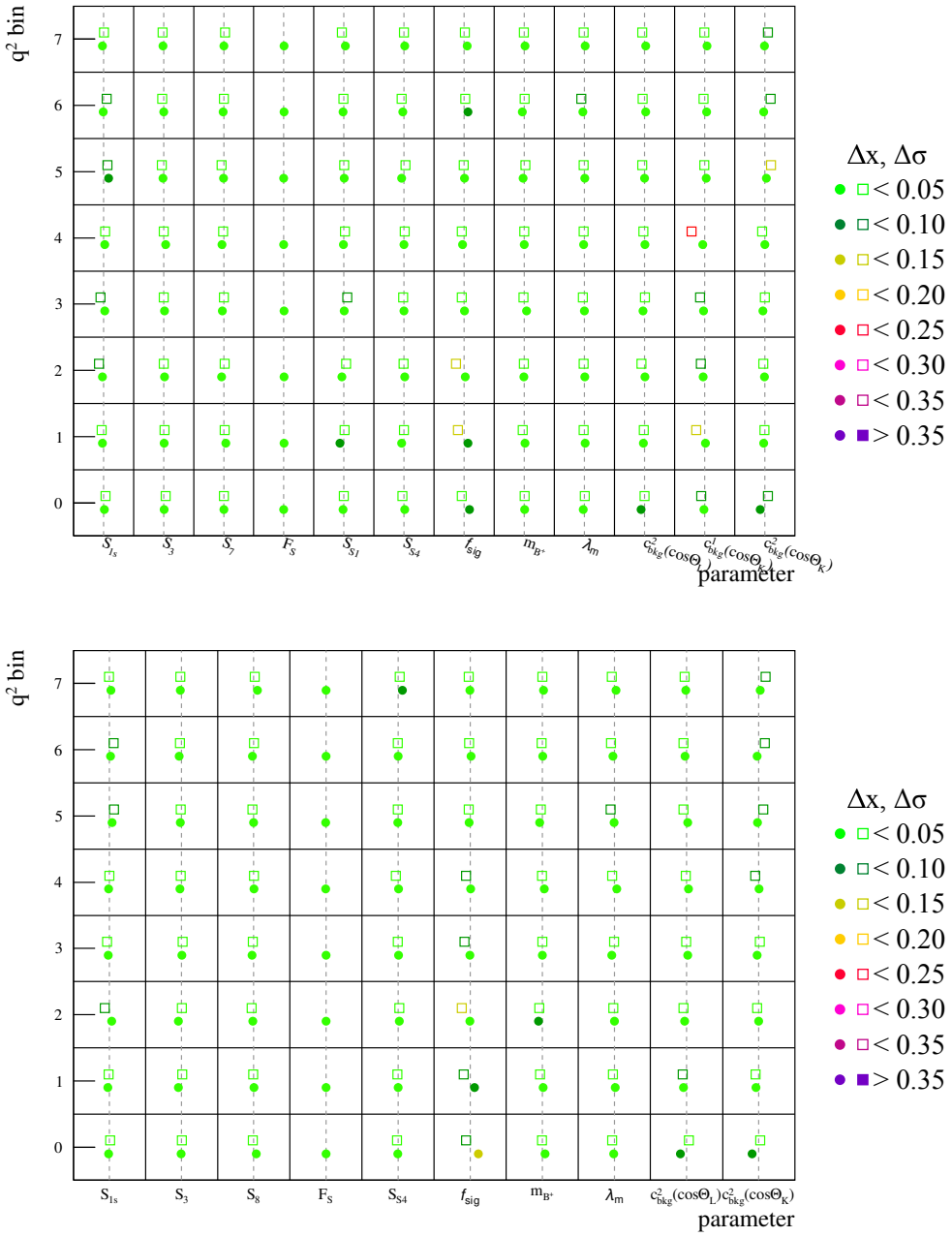

Figure 47: Toy event studies for angular folding 3 (top) and 4 (bottom) using 10000 toy events per fit. Summary of the pull distributions for all free parameters in all q^2 bins. Each cell contains two markers, the hollow squares indicate the width of the pull distribution from toy studies, while the filled circles show the mean position of the pull distribution. The dashed line in each cell indicates the designated positions 0 (1) for the mean (width). See Fig. 44 for explanations on the color code and how these summary histograms are filled.

Table 19: Number of estimated signal and background events for the complete data-set of the rare signal channel in Run I + II. Signal event yield is scaled from the reference channel by the corresponding branching ratios, while the background event yield is interpolated from the mass-sidebands and is integrated over the full mass range (5150 MeV/c^2– 6000 MeV/c^2).

bin	q^2 (GeV^2)	S	B
0	[0.10-0.98]	101	131
	ϕ		
1	[1.10-2.50]	61	206
2	[2.50-4.00]	62	279
3	[4.00-6.00]	96	358
4	[6.00-8.00]	125	358
	J/ψ	*108k*	
5	[11.00-12.50]	124	247
	ψ(2s)		
6	[15.00-17.00]	129	158
7	[17.00-19.00]	69	93
	total	**767**	1830

4.4.2 Acceptance correction and folding validation with realistic statistic toy events

To demonstrate the FCNCFITTER is suitable and returns unbiased results in this analysis, toy event studies with statistics equivalent to expectations in the final fit on data events are performed. The number of signal channel events is estimated from the yield in the reference channel, as presented in Section 2.9. Using the world average for the branching ratios of the two decays and taking into account the branching ratio of $J/\psi \to \mu^+\mu^-$, we get a first order estimation of the signal event yield for the rare signal channel. The distribution of signal events among the eight q^2 bins is taken from the normalized distribution of simulated signal channel MC events, since this information cannot be determined from the J/ψ resonant channel alone. Signal channel MC is generated with distributions accordingly to Ref. [40].

For the background yield estimation the upper and lower mass-sideband of m_{B^+} are fitted and interpolated to get the number of background events. The stated numbers are integrated over the full mass window, from 5150 MeV/c^2 to 6000 MeV/c^2. A summary of all estimated numbers, which will be used for the following toy studies, are presented in Table 19.

In total, 3000 fits of 3000 independent toy event samples are performed for each q^2 bin. The resulting pull distributions are summarized in Figs. 48 to 50. Note that the results from the full angular fit in the top plot in Fig. 48 clearly shows large biases and under(over-)coverage of the uncertainty. This is directly visible by the orange, red and purple markers. Hence, no full angular fit is performed on the rare channel, but only angular folding fits are used.

With a focus on the angular observables, S_i, no significant biases or incorrect uncertainties can be seen for all five foldings and in all eight q^2 bins. This confirms the hypothesis,

which was already mentioned in Section 3.5, that angular folding is needed due to low number of data events. For the foldings, and of course also for full angular, some biases and incorrect widths are observed for some S-wave parameters as well as for the angular background parameters. The background parameter $c^1_{bkg}(\cos\theta_K)$ is highlighted in yellow and red quite often, which is (as evaluations of the pull distributions show) due to the limited range of the parameter in these toy studies, as it is also shown in Fig. 52. The range was therefore increase for further studies and fits to solve this issue, which is also visible in the right plot of Fig. 52.

However, since those are only nuisance parameters and do not impact the angular observables, some small deviations from the norm are acceptable.

All numbers for the mean position and the width of the pull distributions for all foldings and parameters are found in the appendix, Appendix A.12. The studies using the estimated event numbers are found in Appendix A.12.2.

Please note, that the toy studies in this section are only representing a simplified version of the fit. In Section 4.4.6, the exact same fit configuration as on data is used for toy event studies. The remaining biases from these studies are being assigned as a systematic uncertainty, which is presented in Section 5.12.

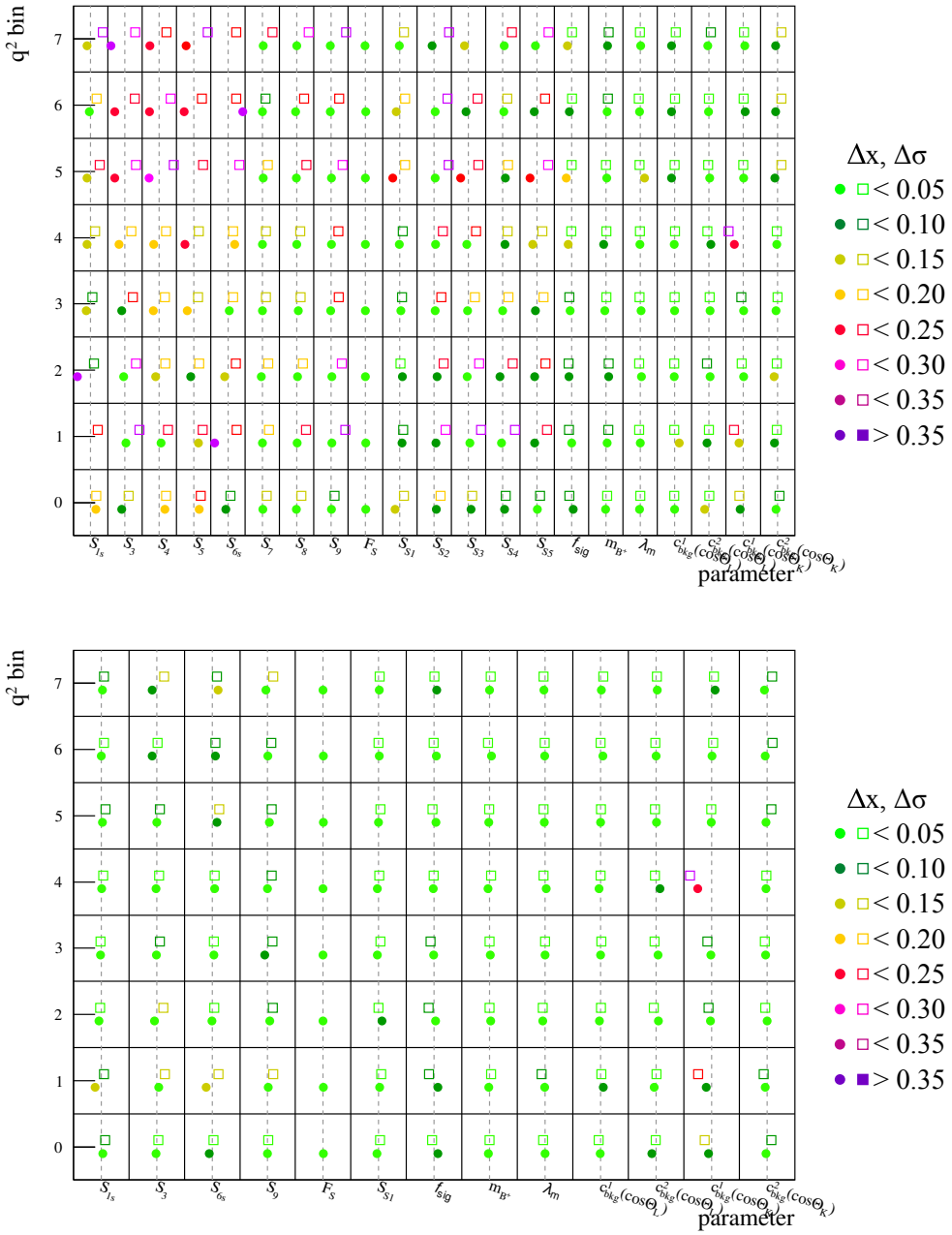

Figure 48: Toy event studies with no angular folding (top) and folding 0 (bottom) using 2597 (see Table 19) toy events per fit. The top plot clearly shows, that a full angular fit does not work on the expected number of signal events. Hence, angular folding is applied. The summary of the pull distributions for all free parameters in all q^2 bins. Each cell contains two markers, the hollow squares indicate the width of the pull distribution from toy studies, while the filled circles show the mean position of the pull distribution. The dashed line in each cell indicates the designated positions 0 (1) for the mean (width). See Fig. 44 for explanations on the color code and how these summary histograms are filled.

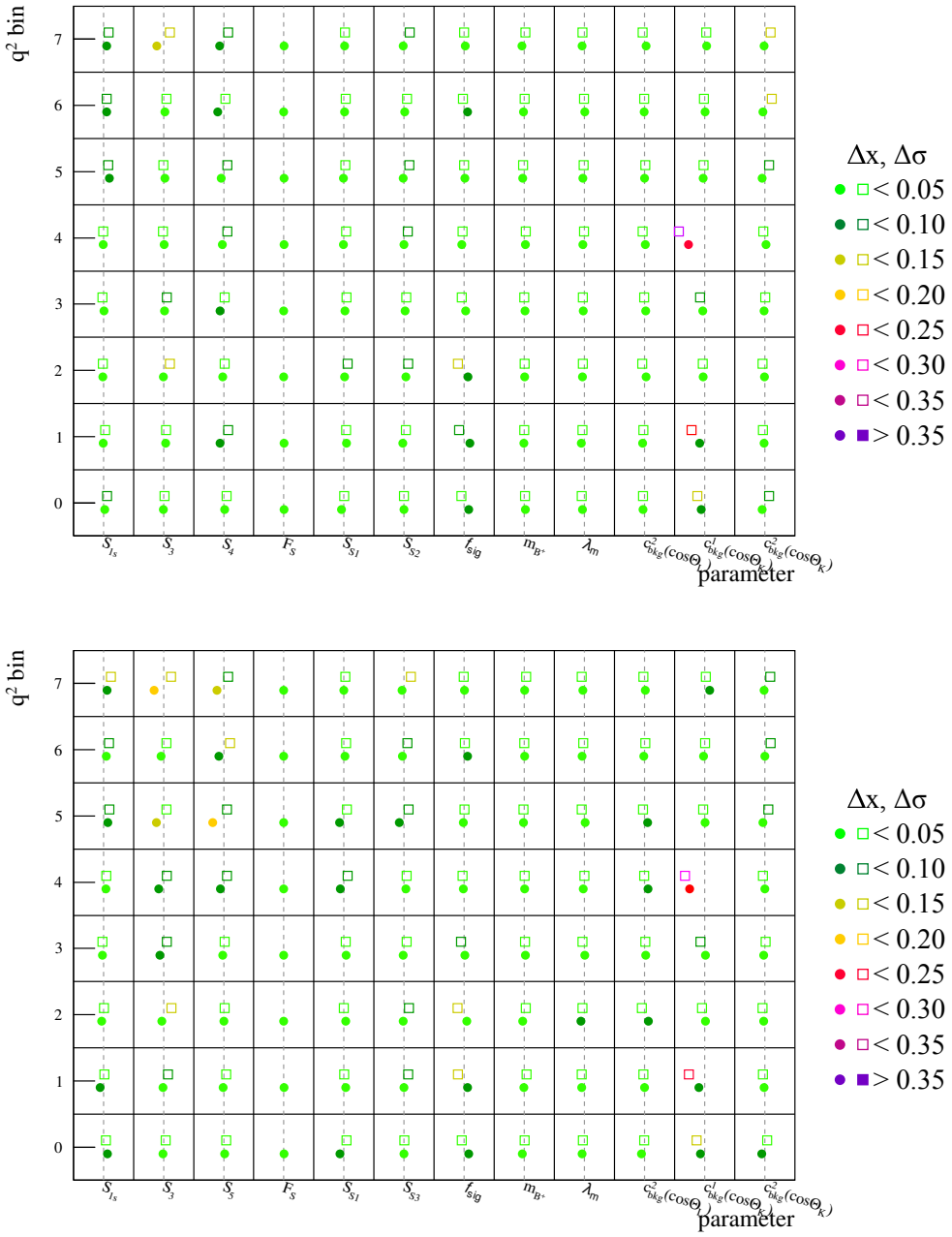

Figure 49: Toy event studies for angular folding 1 (top) and 2 (bottom) using 2597 (see Table 19) toy events per fit. Summary of the pull distributions for all free parameters in all q^2 bins. Each cell contains two markers, the hollow squares indicate the width of the pull distribution from toy studies, while the filled circles show the mean position of the pull distribution. The dashed line in each cell indicates the designated positions 0 (1) for the mean (width). See Fig. 44 for explanations on the color code and how these summary histograms are filled.

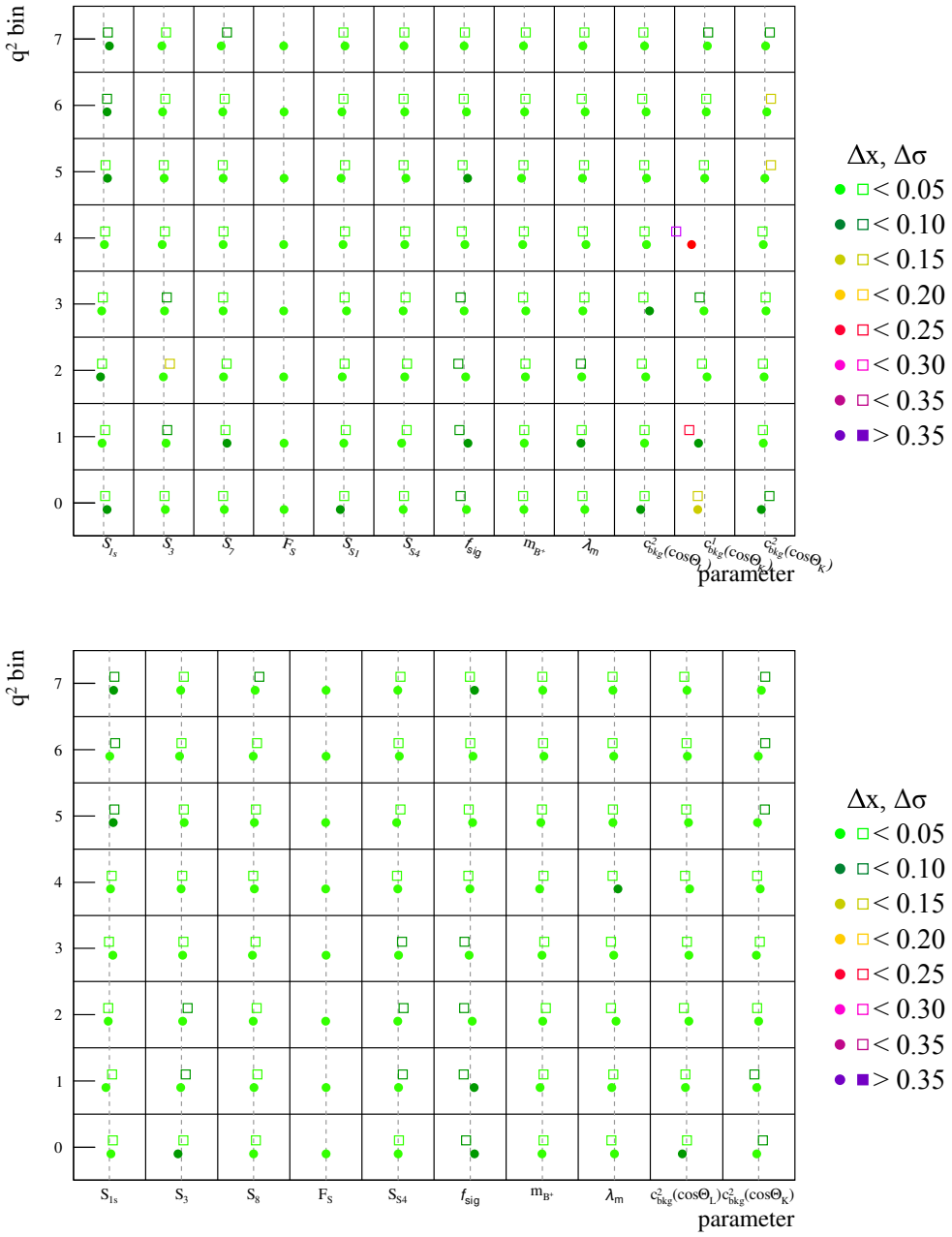

Figure 50: Toy event studies for angular folding 3 (top) and 4 (bottom) using 2597 (see Table 19) toy events per fit. Summary of the pull distributions for all free parameters in all q^2 bins. Each cell contains two markers, the hollow squares indicate the width of the pull distribution from toy studies, while the filled circles show the mean position of the pull distribution. The dashed line in each cell indicates the designated positions 0 (1) for the mean (width). See Fig. 44 for explanations on the color code and how these summary histograms are filled.

4.4.3 Correlations in two dimensional evaluation and of toy studies

The baseline evaluation of toy event studies determines the width and mean position of a one dimensional pull distributions, which is described by a Gaussian bell shape, as discussed before. In addition one can check correlations between two fit parameters by using 2D pull distributions. Since the amount of histograms scales with the square of the number of free parameter, the plots are not included in this document, but the results from this studies are described qualitatively in the following.

In general the two dimensional pull distributions show no features that deviate from the nominal 2D Gaussian bell shape with no correlation between the two variables. The largest correlation are found between S_{6s} and linear background parameter in $\cos\theta_K$, $c^1_{bkg}(\cos\theta_K)$, which is expected as they are linear combinations of one another. This correlation was found to be as high as 20% for some q^2 bins. Some further correlation between S_{1s} and S_{6s} or the linear background parameter in $\cos\theta_L$, $c^1_{bkg}(\cos\theta_L)$ show some correlations of up to about 10%. All in all these correlations are found to be at an expectable level and with only minor boundary effects visible in the distributions of parameters close to their limits, this 2D pull study verifies the functionality of the fitter. Some selected correlations for the previously mentioned observables and background parameters can be seen in Fig. 51. The red and pink points in the toy event studies for the background parameter $c^1_{bkg}(\cos\theta_K)$ in q^2 bin 4 have been plotted in a two dimensional way to clearly see the boundary effect causing this bias in Fig. 52. The limits have been removed afterwards to get rid of this bias effect.

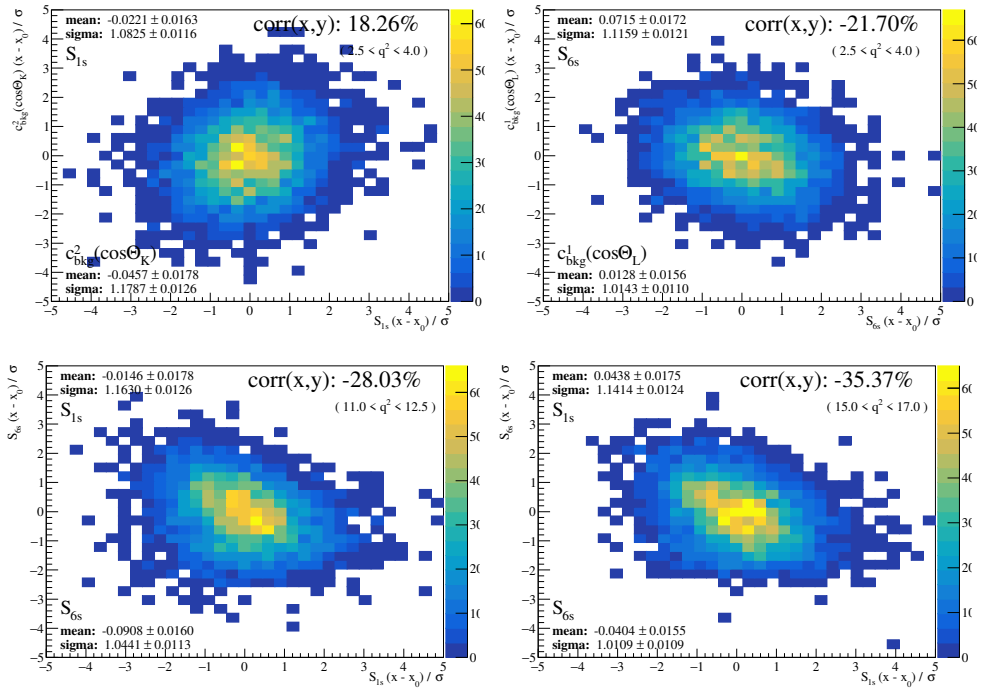

Figure 51: Some correlation plots between selected parameters which show a significant correlation of larger 0.2. Not all q^2 bins see the same level of correlations for all parameter combinations, hence only one q^2 bin per parameter combination (i.e. S_{1s} versus S_{6s}) is given. No other angular observables see correlations of larger 0.2.

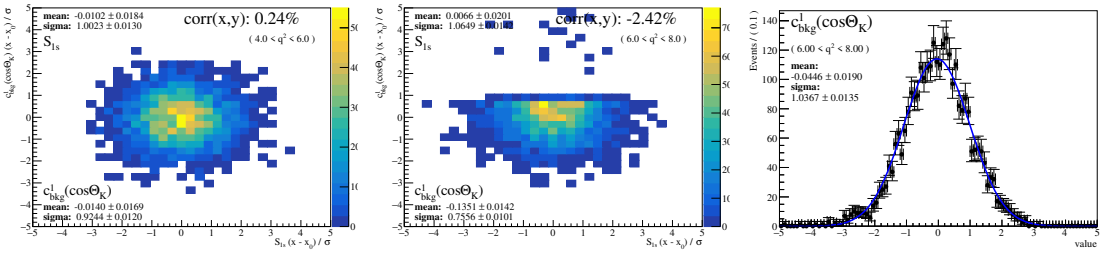

Figure 52: Two dimensional visualisations of the observed bias for $c^1_{bkg}(\cos\theta_K)$ in q^2 bin 4 (plus bin 3 for comparison of a nominal distribution), as it can be seen in Figs. 48 to 50. The parameter limit has been increased ever since to prevent the parameter to run into boundaries. The one dimensional plot on the right shows that this works flawless.

4.4.4 Fit to signal channel MC events

Officially simulated events of the signal channel were selected identically to data events. The sample is used for tests of the FCNCFITTER, the angular acceptance correction and angular folding. Those tests are executed in the same eight q^2 bins (Table 15) as the final fit on data events and will be performed to check for any q^2 dependent effects. The fit is done simultaneously with the same four sub-sets like the final fit (`DD` tracks & `LL` tracks and Run I & Run II) with the angular observables shared between the PDF.
In addition, the generated values of the angular observables are extracted from a specially generated sample of events. The tag *generator level* defines, that the events were generated from the DECfile directly (EVTGEN standalone, *i.e.* without detector acceptance) and did not undergo any selection at all. Hence, no acceptance correction is applied to the fit of generator level MC events, when determining the angular observables. In addition this fit simplifies further, as no S-wave pollution is present and no mass fit is required for signal background separation ($m_{K\pi\mu^+\mu^-}$) or to Gaussian constrain the S-wave fraction ($m_{K\pi}$). As the B^+ is decayed using the form-factor model BTOSLLBALL [40] in the DECfile, the extraction of the angular observables using the FCNCFITTER was the most practical method.
The results are presented in Fig. 53 and show a perfect agreement between the full angular fit and all five folding techniques. This statement is valid for all eight q^2 bins. In addition, the agreement with the results obtained from generator level MC is perfect in almost all q^2 bins and for all angular observables. Few parameters show deviations larger than their uncertainties in one or two q^2 bins. However, those deviations are significantly smaller than the statistical precision we expect in the final fit and are therefore no longer investigated.

4.4.5 Toy event studies of 2D mass fit

The first fit in the two mass dimension has been tested for potential biases and over- or undercoverage of the statistical uncertainties. Especially, potential biases in the extraction of F_S are of interest. For this, the toy events are generated using the full 5D description including non-zero values for the S- and P-wave interference terms.
Latter might introduce a bias to the results of the 2D fit, as the 2D fit is not sensitive to the interference. In Fig. 54 the results from these toy studies is shown, with only minor deviations from the nominal values in the decay width of the K^{*+}, $\Gamma(K^{*+})$. This

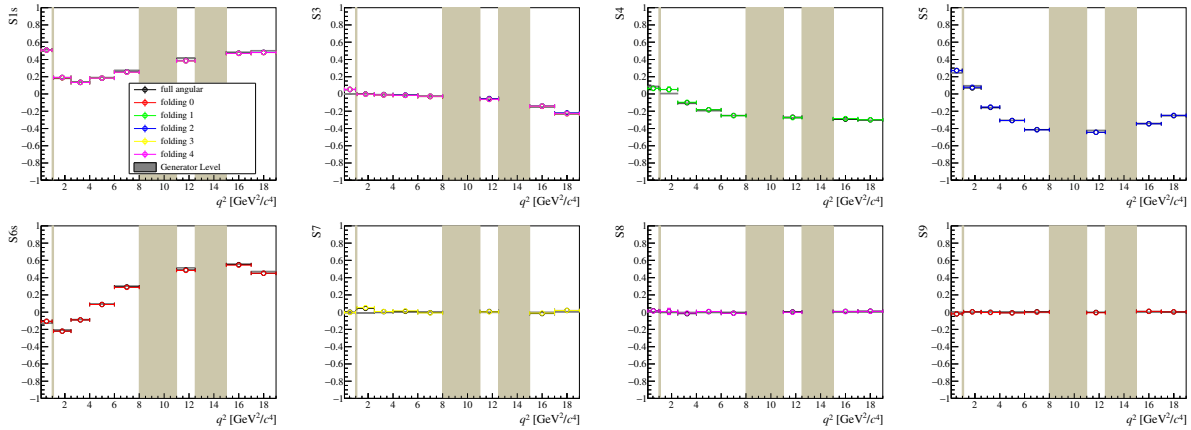

Figure 53: Comparison of six different fits to simulated signal channel events. The first fit in black markers does not use any angular folding, and is therefore present for all eight angular observables. The coloured markers show the results from angular folding 0–5. In addition, the simulated events at generator level were fitted without any angular acceptance correction and without angular folding. Those results are shown in the gray boxes. The perfect agreement between all techniques validates the functionality of the folding techniques as well as the angular acceptance correction.

however is of now concern this fit, which solely addresses the extraction of F_S from the two dimensional fit.

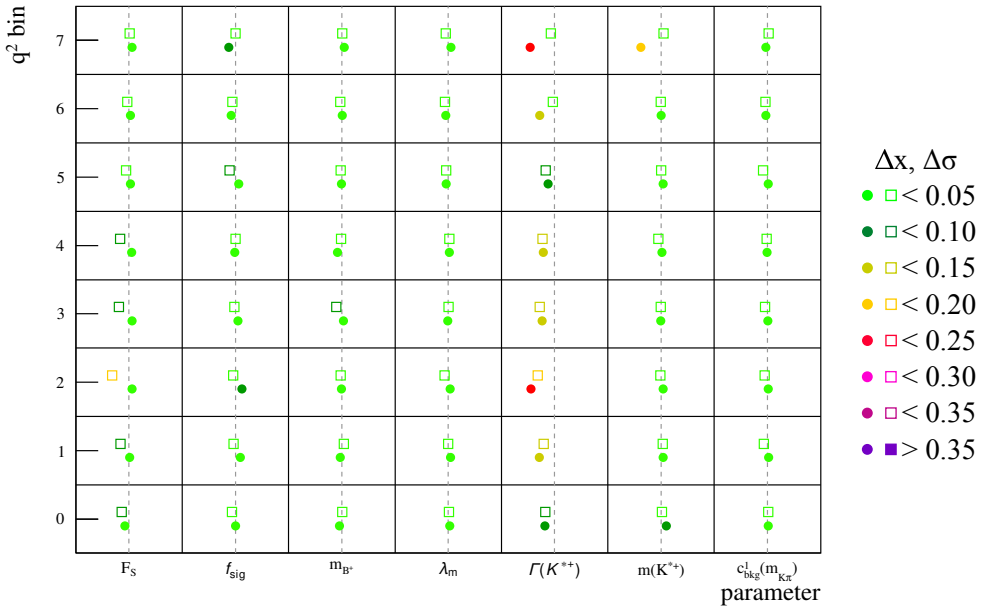

Figure 54: The pull results from a toy event study using a binned fit in 2D. Full circles indicate the mean position and hollow squared the width of the pull distribution. For mean (width) the dashed line indicates the position of the nominal value, 0 (1). The color scheme represents the deviations from these nominal values in steps of 0.05 and the scheme is explained in details in Fig. 44.

4.4.6 Validation of the final fit configuration: 2D + 4D toy event studies

In this paragraph the complete and final fit configuration, as in all details described in Section 4.5, is tested on toy events. This includes the 2D mass fit in larger q^2 bins together with the scaling of F_S from these larger bins to the nominal eight q^2 bins. Using this input, the consecutive fit in four dimensions is performed. The estimated event numbers as previously mentioned in Table 19 are used for this study.

Tables 20 and 21 show the mean and width values for the pull distributions using Standard Model prediction as values for the toy studies. The coverage for all parameters and q^2 bins is good, as the widths are almost completely within 0.1 away from 1.0 and only few widths just shy of this limit. In addition to the angular observables, the signal and S-wave fraction are given to show the behaviour when neglecting the correlation between both parameters from the 2D mass fit. The correlations from the 2D mass fit in the larger q^2 bins are given Appendix A.17.

Tables 22 and 23 repeats the same study for theoretical predictions with a New Physics contribution that has the Wilson coefficient $\mathcal{C}_9 = -1.0$.

The pull distributions of toy studies with start values equal to the SM and to $\mathcal{C}_9 = -1.0$ both show small biases, sometimes exceeding the 0.1 deviation from the nominal value. However, as it is shown in the following, a systematic is assigned to the bias of toy studies with final fit result values, which appears to be clearly dominating.

For this test, the results from the final fit are copied to the toy event generator[7] and used for another full toy event study. These results are given in Tables 24 and 25. The coverage of these toy studies with final fit results is good for all but one case (S_{6s} in q^2 bin 5. As a conservative approach, all observables in all q^2 bins will get a Feldman-Cousins scan to obtain the uncertainties, see Section 4.6.

The biases observed for the toy event studies with SM values (Table 20) are assigned to a systematic uncertainty associated with the unknown S-wave fraction, F_S, in Section 5.4. The biases observed in the toy event studies with final fit values (Table 24) are assigned as a systematic uncertainty in Section 5.12, which is clearly dominated by the sizes of the biases in the toy studies with final fit results.

The same toy studies with P basis angular observables are performed and the results are given in Appendix A.14. And the corresponding systematic uncertainty is given in Tables 133 and 140 in Appendix A.21.

[7] This copying of result values is done internally and does not require any unblinding of the results. All values are either saved in files or directly copied within the functions.

Table 20: Mean values of the pull distribution from toy event studies using the SM values for the generation of toy events. The results are obtained using the 2D+4D fit method as described in Section 4.2 with angular folding. Values for S_{1s} and S_3 are obtained from folding 4.

q^2 bin	0	1	2	3
S_{1s}	-0.2526 ± 0.0341	-0.0453 ± 0.0332	0.0665 ± 0.0314	0.0806 ± 0.0296
S_3	-0.0092 ± 0.0325	-0.0164 ± 0.0326	-0.0131 ± 0.0315	0.0564 ± 0.0320
S_4	-0.0310 ± 0.0319	-0.0597 ± 0.0338	-0.0505 ± 0.0327	-0.1015 ± 0.0333
S_5	-0.0318 ± 0.0336	-0.0306 ± 0.0312	-0.0113 ± 0.0308	0.1407 ± 0.0316
S_{6s}	-0.0047 ± 0.0311	0.0212 ± 0.0335	0.0400 ± 0.0320	-0.0531 ± 0.0325
S_7	-0.0293 ± 0.0318	-0.0616 ± 0.0321	0.0619 ± 0.0315	0.0133 ± 0.0324
S_8	-0.0136 ± 0.0350	0.0300 ± 0.0325	-0.0353 ± 0.0324	0.0354 ± 0.0334
S_9	-0.0199 ± 0.0301	0.0019 ± 0.0320	0.0103 ± 0.0320	0.0125 ± 0.0328
F_S	-0.0442 ± 0.0313	-0.1211 ± 0.0315	-0.1834 ± 0.0299	-0.2068 ± 0.0308
f_{sig}	0.1210 ± 0.0329	-0.0265 ± 0.0350	-0.0976 ± 0.0355	-0.0773 ± 0.0334
q^2 bin	4	5	6	7
S_{1s}	0.0663 ± 0.0299	0.1296 ± 0.0325	0.0047 ± 0.0347	0.0148 ± 0.0340
S_3	0.0645 ± 0.0329	0.0835 ± 0.0317	0.0559 ± 0.0330	0.0984 ± 0.0324
S_4	-0.0107 ± 0.0330	0.0509 ± 0.0323	0.0253 ± 0.0337	-0.0156 ± 0.0337
S_5	0.1247 ± 0.0315	0.1679 ± 0.0309	0.0977 ± 0.0317	-0.0519 ± 0.0360
S_{6s}	-0.0420 ± 0.0340	-0.1051 ± 0.0338	-0.0979 ± 0.0340	-0.0752 ± 0.0344
S_7	-0.0476 ± 0.0304	-0.0327 ± 0.0322	-0.0618 ± 0.0328	-0.0271 ± 0.0345
S_8	-0.0369 ± 0.0341	-0.0212 ± 0.0320	0.0563 ± 0.0317	0.0073 ± 0.0345
S_9	-0.0444 ± 0.0316	-0.0844 ± 0.0328	0.0243 ± 0.0347	0.0308 ± 0.0348
F_S	-0.1930 ± 0.0305	-0.2543 ± 0.0327	-0.2910 ± 0.0335	-0.3261 ± 0.0332
f_{sig}	-0.0820 ± 0.0324	0.0342 ± 0.0324	0.0486 ± 0.0343	0.0065 ± 0.0341

Table 21: The widths of pull distribution from toy event studies using the SM values for the generation of toy events. The results are obtained using the 2D+4D fit method as described in Section 4.2 with angular folding. Values for S_{1s} and S_3 are obtained from folding 4.

q^2 bin	0	1	2	3
S_{1s}	1.0773 ± 0.0241	1.0459 ± 0.0235	0.9858 ± 0.0222	0.9370 ± 0.0210
S_3	1.0290 ± 0.0230	1.0255 ± 0.0230	0.9862 ± 0.0223	1.0116 ± 0.0226
S_4	1.0089 ± 0.0226	1.0494 ± 0.0239	1.0152 ± 0.0232	1.0524 ± 0.0236
S_5	1.0629 ± 0.0238	0.9809 ± 0.0221	0.9643 ± 0.0218	0.9985 ± 0.0224
S_{6s}	0.9825 ± 0.0220	1.0053 ± 0.0237	0.9783 ± 0.0226	1.0243 ± 0.0230
S_7	1.0061 ± 0.0225	0.9984 ± 0.0227	0.9890 ± 0.0223	1.0245 ± 0.0229
S_8	1.1074 ± 0.0248	1.0137 ± 0.0230	1.0077 ± 0.0229	1.0555 ± 0.0236
S_9	0.9505 ± 0.0213	0.9980 ± 0.0227	0.9984 ± 0.0226	1.0359 ± 0.0232
F_S	0.9888 ± 0.0221	0.9943 ± 0.0223	0.9440 ± 0.0211	0.9738 ± 0.0218
f_{sig}	1.0419 ± 0.0233	1.0889 ± 0.0247	1.1012 ± 0.0251	1.0540 ± 0.0236
q^2 bin	4	5	6	7
S_{1s}	0.9454 ± 0.0211	1.0288 ± 0.0230	1.0983 ± 0.0246	1.0757 ± 0.0241
S_3	1.0419 ± 0.0233	1.0023 ± 0.0224	1.0425 ± 0.0233	1.0232 ± 0.0229
S_4	1.0423 ± 0.0233	1.0215 ± 0.0229	1.0654 ± 0.0238	1.0597 ± 0.0238
S_5	0.9950 ± 0.0223	0.9744 ± 0.0219	1.0027 ± 0.0224	1.1353 ± 0.0255
S_{6s}	1.0746 ± 0.0241	1.0577 ± 0.0239	1.0713 ± 0.0241	1.0703 ± 0.0243
S_7	0.9611 ± 0.0215	1.0190 ± 0.0228	1.0383 ± 0.0232	1.0896 ± 0.0244
S_8	1.0790 ± 0.0241	1.0128 ± 0.0227	1.0028 ± 0.0224	1.0900 ± 0.0244
S_9	0.9986 ± 0.0223	1.0352 ± 0.0232	1.0967 ± 0.0245	1.1009 ± 0.0247
F_S	0.9649 ± 0.0216	1.0333 ± 0.0231	1.0601 ± 0.0237	1.0511 ± 0.0235
f_{sig}	1.0236 ± 0.0229	1.0241 ± 0.0229	1.0832 ± 0.0242	1.0775 ± 0.0241

Table 22: Mean values of the pull distribution from toy event studies using theoretically predicted values for a new physics scenario of a Wilson coefficient $C_9 = -1$ for the generation of toy events. The results are obtained using the 2D+4D fit method as described in Section 4.2 with angular folding. Values for S_{1s} and S_3 are obtained from folding 4.

q^2 bin	0	1	2	3
S_{1s}	-0.1969 ± 0.0316	-0.0932 ± 0.0330	0.1080 ± 0.0312	0.0931 ± 0.0306
S_3	-0.0671 ± 0.0311	0.0098 ± 0.0314	0.0015 ± 0.0308	-0.0104 ± 0.0325
S_4	-0.0736 ± 0.0350	-0.0338 ± 0.0329	0.0042 ± 0.0338	-0.0375 ± 0.0323
S_5	0.0077 ± 0.0326	-0.0115 ± 0.0307	-0.0137 ± 0.0308	0.0427 ± 0.0306
S_{6s}	-0.0013 ± 0.0318	0.0931 ± 0.0341	0.0138 ± 0.0339	0.0125 ± 0.0328
S_7	-0.0237 ± 0.0325	-0.0283 ± 0.0311	-0.0075 ± 0.0313	0.0723 ± 0.0307
S_8	0.0488 ± 0.0340	0.0725 ± 0.0339	0.0206 ± 0.0330	-0.0037 ± 0.0325
S_9	0.0002 ± 0.0308	0.0004 ± 0.0321	0.0180 ± 0.0321	-0.0008 ± 0.0317
q^2 bin	4	5	6	7
S_{1s}	0.0995 ± 0.0304	0.0852 ± 0.0346	0.0058 ± 0.0331	0.0381 ± 0.0354
S_3	-0.0101 ± 0.0319	0.0734 ± 0.0310	0.1412 ± 0.0310	0.0661 ± 0.0320
S_4	-0.0343 ± 0.0347	0.0343 ± 0.0327	0.0111 ± 0.0343	-0.0303 ± 0.0350
S_5	0.0495 ± 0.0320	0.1433 ± 0.0316	0.0922 ± 0.0340	0.0199 ± 0.0349
S_{6s}	0.0041 ± 0.0323	-0.1097 ± 0.0347	-0.1405 ± 0.0335	-0.0286 ± 0.0338
S_7	0.0514 ± 0.0324	0.0005 ± 0.0322	0.0037 ± 0.0318	0.0227 ± 0.0333
S_8	-0.0189 ± 0.0322	-0.0090 ± 0.0314	0.0404 ± 0.0331	0.0227 ± 0.0340
S_9	0.0074 ± 0.0324	-0.0751 ± 0.0308	0.0121 ± 0.0329	0.0187 ± 0.0340

Table 23: The widths of pull distribution from toy event studies using theoretically predicted values for a new physics scenario of a Wilson coefficient $C_9 = -1$ for the generation of toy events. The results are obtained using the 2D+4D fit method as described in Section 4.2 with angular folding. Values for S_{1s} and S_3 are obtained from folding 4.

q^2 bin	0	1	2	3
S_{1s}	0.9991 ± 0.0224	1.0367 ± 0.0233	0.9820 ± 0.0221	0.9667 ± 0.0216
S_3	0.9809 ± 0.0220	0.9850 ± 0.0222	0.9676 ± 0.0218	1.0263 ± 0.0230
S_4	1.1053 ± 0.0247	1.0244 ± 0.0233	1.0418 ± 0.0239	1.0201 ± 0.0228
S_5	1.0293 ± 0.0230	0.9634 ± 0.0217	0.9718 ± 0.0218	0.9661 ± 0.0216
S_{6s}	1.0037 ± 0.0225	1.0248 ± 0.0241	1.0409 ± 0.0240	1.0364 ± 0.0232
S_7	1.0265 ± 0.0230	0.9714 ± 0.0220	0.9824 ± 0.0221	0.9695 ± 0.0217
S_8	1.0745 ± 0.0241	1.0558 ± 0.0240	1.0328 ± 0.0233	1.0279 ± 0.0230
S_9	0.9733 ± 0.0218	1.0053 ± 0.0227	0.9997 ± 0.0227	1.0009 ± 0.0224
q^2 bin	4	5	6	7
S_{1s}	0.9605 ± 0.0215	1.0939 ± 0.0245	1.0471 ± 0.0234	1.1182 ± 0.0250
S_3	1.0082 ± 0.0225	0.9809 ± 0.0219	0.9793 ± 0.0219	1.0109 ± 0.0226
S_4	1.0978 ± 0.0246	1.0335 ± 0.0232	1.0835 ± 0.0242	1.0989 ± 0.0248
S_5	1.0123 ± 0.0226	0.9987 ± 0.0224	1.0756 ± 0.0241	1.1009 ± 0.0247
S_{6s}	1.0227 ± 0.0229	1.0964 ± 0.0246	1.0571 ± 0.0237	1.0633 ± 0.0239
S_7	1.0242 ± 0.0229	1.0172 ± 0.0227	1.0051 ± 0.0225	1.0536 ± 0.0236
S_8	1.0176 ± 0.0228	0.9936 ± 0.0222	1.0462 ± 0.0234	1.0762 ± 0.0241
S_9	1.0240 ± 0.0229	0.9734 ± 0.0218	1.0403 ± 0.0233	1.0745 ± 0.0241

Table 24: Mean values of the pull distribution from toy event studies using the final fit values for the generation of toy events. The results are obtained using the 2D+4D fit method as described in Section 4.2 with angular folding. Values for S_{1s} and S_3 are obtained from folding 4.

q^2 bin	0	1	2	3
S_{1s}	-0.2125 ± 0.0332	-0.0720 ± 0.0340	0.0146 ± 0.0353	0.0856 ± 0.0311
S_3	-0.0469 ± 0.0305	-0.0674 ± 0.0327	-0.0206 ± 0.0306	0.0471 ± 0.0313
S_4	-0.0254 ± 0.0338	-0.0648 ± 0.0324	0.1719 ± 0.0335	0.3203 ± 0.0341
S_5	-0.0366 ± 0.0331	-0.1048 ± 0.0295	0.1189 ± 0.0315	0.0431 ± 0.0314
S_{6s}	-0.0041 ± 0.0315	0.0895 ± 0.0328	-0.0138 ± 0.0321	0.0335 ± 0.0328
S_7	0.0457 ± 0.0324	0.0151 ± 0.0321	0.0371 ± 0.0312	0.0097 ± 0.0309
S_8	0.0125 ± 0.0346	0.0665 ± 0.0347	0.0619 ± 0.0324	0.0221 ± 0.0324
S_9	0.0128 ± 0.0329	-0.0068 ± 0.0321	-0.0823 ± 0.0315	0.0958 ± 0.0326
q^2 bin	4	5	6	7
S_{1s}	0.0488 ± 0.0347	0.1083 ± 0.0341	0.1390 ± 0.0338	0.0931 ± 0.0362
S_3	0.0818 ± 0.0321	0.0179 ± 0.0311	0.2036 ± 0.0328	-0.0200 ± 0.0321
S_4	-0.0314 ± 0.0353	0.0753 ± 0.0321	-0.0160 ± 0.0332	-0.0076 ± 0.0349
S_5	0.0104 ± 0.0315	0.1352 ± 0.0300	-0.0859 ± 0.0331	0.0298 ± 0.0346
S_{6s}	0.0598 ± 0.0323	-0.7443 ± 0.0411	-0.1608 ± 0.0352	-0.0075 ± 0.0341
S_7	0.1089 ± 0.0322	0.0215 ± 0.0297	0.0576 ± 0.0319	0.0139 ± 0.0334
S_8	0.0580 ± 0.0320	-0.0082 ± 0.0315	0.0150 ± 0.0313	0.0377 ± 0.0340
S_9	-0.0134 ± 0.0326	-0.2308 ± 0.0350	-0.1203 ± 0.0340	-0.0038 ± 0.0347

Table 25: The widths of pull distribution from toy event studies using the final fit values for the generation of toy events. The results are obtained using the 2D+4D fit method as described in Section 4.2 with angular folding. Values for S_{1s} and S_3 are obtained from folding 4.

q^2 bin	0	1	2	3
S_{1s}	1.0497 ± 0.0235	1.0754 ± 0.0241	1.0957 ± 0.0249	0.9837 ± 0.0220
S_3	0.9632 ± 0.0215	1.0163 ± 0.0231	0.9648 ± 0.0216	0.9909 ± 0.0222
S_4	1.0691 ± 0.0239	0.9786 ± 0.0229	0.9914 ± 0.0237	1.0435 ± 0.0241
S_5	1.0448 ± 0.0234	0.9051 ± 0.0209	0.9691 ± 0.0223	0.9925 ± 0.0222
S_{6s}	0.9967 ± 0.0223	0.9969 ± 0.0232	1.0029 ± 0.0227	1.0380 ± 0.0232
S_7	1.0234 ± 0.0229	1.0010 ± 0.0227	0.9737 ± 0.0221	0.9769 ± 0.0219
S_8	1.0924 ± 0.0245	1.0842 ± 0.0245	1.0129 ± 0.0229	1.0258 ± 0.0229
S_9	1.0388 ± 0.0233	1.0060 ± 0.0227	0.9810 ± 0.0223	1.0303 ± 0.0230
q^2 bin	4	5	6	7
S_{1s}	1.0983 ± 0.0246	1.0775 ± 0.0241	1.0686 ± 0.0239	1.1457 ± 0.0257
S_3	1.0143 ± 0.0227	0.9832 ± 0.0220	1.0375 ± 0.0232	1.0152 ± 0.0227
S_4	1.1149 ± 0.0250	1.0152 ± 0.0227	1.0493 ± 0.0235	1.0999 ± 0.0247
S_5	0.9966 ± 0.0223	0.9440 ± 0.0212	1.0452 ± 0.0234	1.0869 ± 0.0245
S_{6s}	1.0216 ± 0.0228	1.2451 ± 0.0294	1.1095 ± 0.0249	1.0770 ± 0.0241
S_7	1.0167 ± 0.0227	0.9402 ± 0.0210	1.0082 ± 0.0225	1.0561 ± 0.0236
S_8	1.0130 ± 0.0227	0.9956 ± 0.0223	0.9907 ± 0.0222	1.0744 ± 0.0241
S_9	1.0323 ± 0.0231	1.1056 ± 0.0248	1.0753 ± 0.0241	1.0968 ± 0.0246

4.4.7 Fit to $J/\psi K^{*+}$ channel with full statistic

The event yield of the reference channel $B^+ \to J/\psi K^{*+}$ for the complete data-set of Run I + II is approximately 108 thousand events. Using those events in the same four sub-sets (see Section 2.1), we again validate the angular folding, the angular acceptance correction, the S-wave contribution and the fitter itself. The only part not covered by the reference channel is any q^2 dependence in the fit PDF, which was addressed in Section 4.4.4 when validating the fitter on signal channel MC events.
The fit to the reference channel is performes in the q^2 region of the J/ψ: 8.68 – 10.09 GeV^2/c^2 (see Table 15). The tiny fraction of non-resonant $\mu^+\mu^-$ events (our actual signal channel) in this q^2 range cannot be separated from the resonant decay, but is negligible compared to the huge number of resonant decays, and is therefore not further considered. A total of six fits are performed, one without any angular folding and afterwards one fit for each angular folding technique (0 – 5), which are introduced in Section 3.5. The fit projections are shown for the full angular fit (no angular folding) as well as for all five folding techniques. For each of these six sets, the projections of the four sub-samples are shown in Figs. 55 to 65 and the summed up fit projections of the complete dataset of Run I + II in Figs. 56 to 66.

All results of the angular observables from the six fits to the $J/\psi K^{*+}$ sample are presented in Table 26. We see a very consistent picture, as all results from the five foldings agree with the full angular fit. The correlation matrices from these fits are given in the appendix in Appendix A.18.
Furthermore, the results from these fits are compared with the results published by Belle [41], BaBar [42] and LHCb [43].

For this, the decay amplitudes ($A_\perp$ and $A_\parallel$) published by Belle [41], BaBar [42] and LHCb [43] together with their corresponding complex phases are converted to the angular observables S_i for the comparison. The conversion was used before and is explained in the analysis note of the B^0 decay [25] in Equation 13 in Section 6.1.2. The comparison between all results is shown in Table 27 and in Table 28, the difference all previous measurement results to our fit is given in standard deviations. As the LHCb measurement was performed on a data sample purely consisting of B^0 decays, in contrast to the BaBar result, which uses B^0 and B^+ decays, the results have to be compared with caution. The Belle measurement yields to the only available results exclusively determined from our reference channel. The uncertainties of the converted angular observables are determined from toy events. For this, 100000 altered sets of decay amplitudes are generated using the covariance matrix of the decay amplitudes and converting all sets into angular observables. The width of the resulting distribution for every angular observable is its propagated uncertainty. Since the publications of BaBar and Belle do not include a correlation matrix, the correlation matrix from the LHCb document (Table VI in Ref. [43]) is used for the uncertainty propagation of all three $J/\psi K^{*+}$ results. With this in mind, all results are in fair agreement and show no significant differences between the four measurements are observed. Hence, these test fits further confirm the correct functionality of the FCNCfitter. With this, in the next sections the configuration of the fitter for the final data fit on the rare channel is discussed.

Table 26: Results of the fit to the reference channel for the full angular fit as well as for all five foldings. The different results agree within their uncertainties for all observables. The full correlation matrices for the full angular fit and for all foldings are given in Appendix A.18.

$[8.68, 10.09]$ GeV^2/c^2	folding					
	non	0	1	2	3	4
S_{1s}	0.321 ± 0.004	0.321 ± 0.005	0.321 ± 0.004	0.321 ± 0.005	0.321 ± 0.005	0.321 ± 0.002
S_3	-0.002 ± 0.007	-0.003 ± 0.007	-0.002 ± 0.007	-0.003 ± 0.007	-0.003 ± 0.007	-0.004 ± 0.003
S_4	-0.246 ± 0.008	-	-0.246 ± 0.008	-	-	-
S_5	-0.003 ± 0.008	-	-	-0.002 ± 0.008	-	-
S_{6s}	-0.003 ± 0.006	-0.004 ± 0.006	-	-	-	-
S_7	-0.001 ± 0.008	-	-	-	-0.002 ± 0.008	-
S_8	-0.063 ± 0.008	-	-	-	-	-0.061 ± 0.004
S_9	-0.084 ± 0.007	-0.084 ± 0.007	-	-	-	-
F_S	0.055 ± 0.013	0.055 ± 0.013	0.055 ± 0.013	0.055 ± 0.013	0.055 ± 0.013	0.055 ± 0.005
S_{S1}	-0.193 ± 0.014	-0.195 ± 0.014	-0.193 ± 0.014	-0.195 ± 0.014	-0.195 ± 0.014	-
S_{S2}	0.024 ± 0.009	-	0.024 ± 0.008	-	-	-
S_{S3}	-0.001 ± 0.008	-	-	0.001 ± 0.008	-	-
S_{S4}	-0.004 ± 0.008	-	-	-	-0.003 ± 0.008	-0.002 ± 0.004
S_{S5}	-0.074 ± 0.009	-	-	-	-	-

Table 27: Comparison of the results of our full angular fit to the reference channel data of $B^+ \to J/\psi K^{*+}$ to published results from BaBar [42], Belle [41] and LHCb [43]. In the publications, the results are given in polarization amplitudes, which have been converted into the angular observable basis, S_i, to be comparable to the results of the FCNCFITTER. The uncertainties of the angular observables are determined from the spread of 100000 randomly generated toys. All results are in fair agreement.

	our fit	Belle (B^+)	BaBar ($B^+ + B^0$)	LHCb (B^0)
S_{1s}	0.321 ± 0.004	0.297 ± 0.011	0.333 ± 0.007	0.321 ± 0.006
S_3	-0.002 ± 0.007	-0.018 ± 0.017	0.011 ± 0.011	-0.013 ± 0.010
S_4	-0.246 ± 0.008	-0.255 ± 0.010	-0.237 ± 0.007	-0.250 ± 0.006
S_5	-0.003 ± 0.008	0	0	0
S_{6s}	-0.003 ± 0.006	0	0	0
S_7	-0.001 ± 0.008	0	0	0
S_8	-0.063 ± 0.008	-0.037 ± 0.018	-0.058 ± 0.015	-0.048 ± 0.007
S_9	-0.084 ± 0.007	-0.041 ± 0.016	-0.095 ± 0.014	-0.084 ± 0.006

Table 28: The standard deviations of all three literature measurements from the previous table (Table 27) to our fit result. The standard deviation is determined by the absolute difference of both results divided by their quadratically added uncertainties. No deviation exceeds 3 standard deviations.

	Belle (B^+)	BaBar ($B^+ + B^0$)	LHCb (B^0)
S_{1s}	2.05	1.49	0.00
S_3	0.87	1.00	0.90
S_4	0.70	0.85	0.40
S_5	0.38	0.38	0.38
S_{6s}	0.50	0.50	0.50
S_7	0.12	0.12	0.12
S_8	1.32	0.29	1.41
S_9	2.46	0.70	0.00

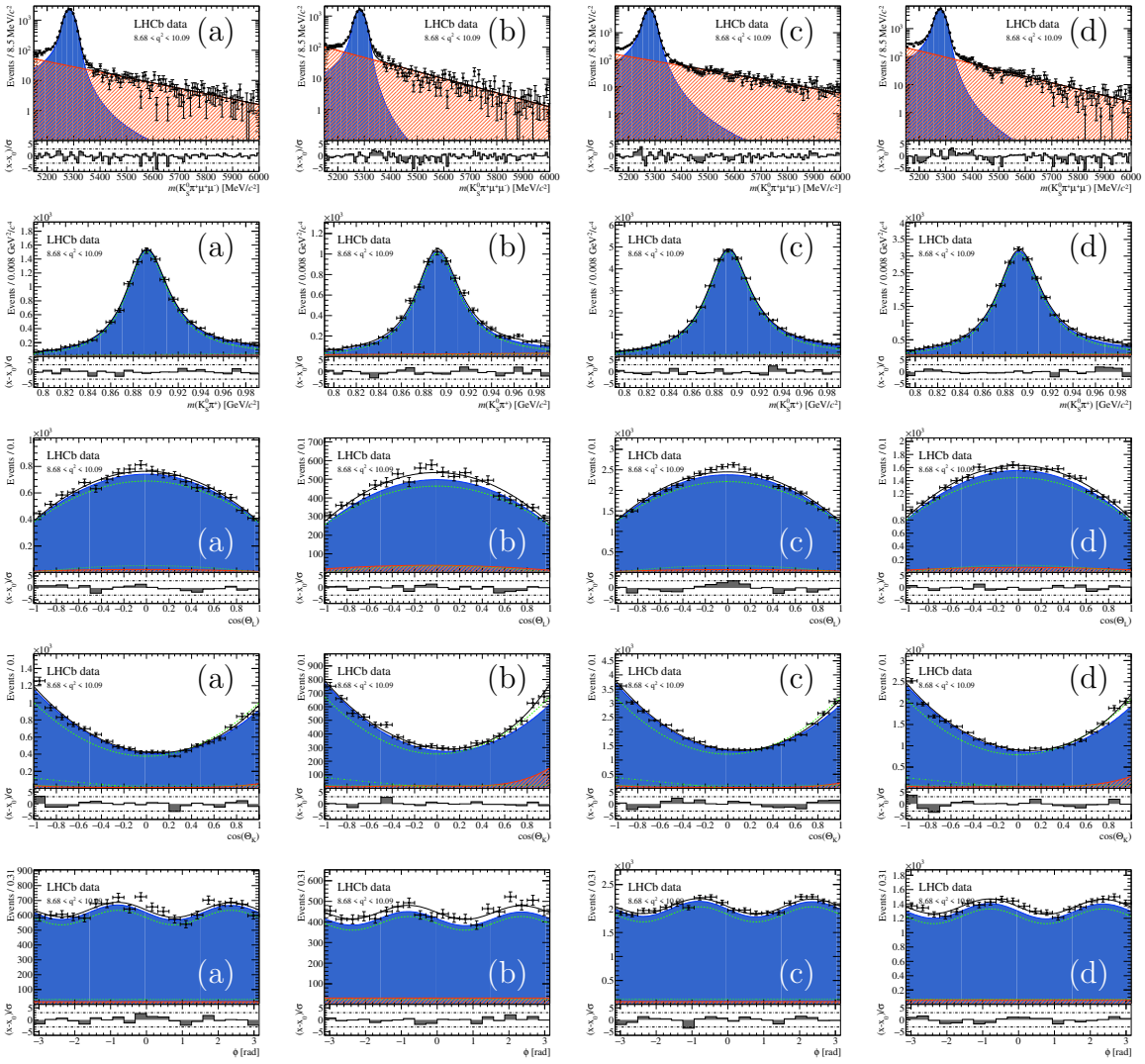

Figure 55: Projection of the simultaneous 5D fit to the full data-set of $B^+ \to J/\psi K^{*+}$ events. All events are weighted according to the acceptance correction function. No angular folding is applied. The sub-sets are Run I (a) + (b) and Run II (c) + (d) with DD tracks and LL tracks events, respectively. Note that the m_{B^+} distributions in the first row are plotted semi-logarithmically, while all following histograms experienced a cut in m_{B^+} to show only events with maximum $50\,\mathrm{MeV}/c^2$ deviation from the peak centre.

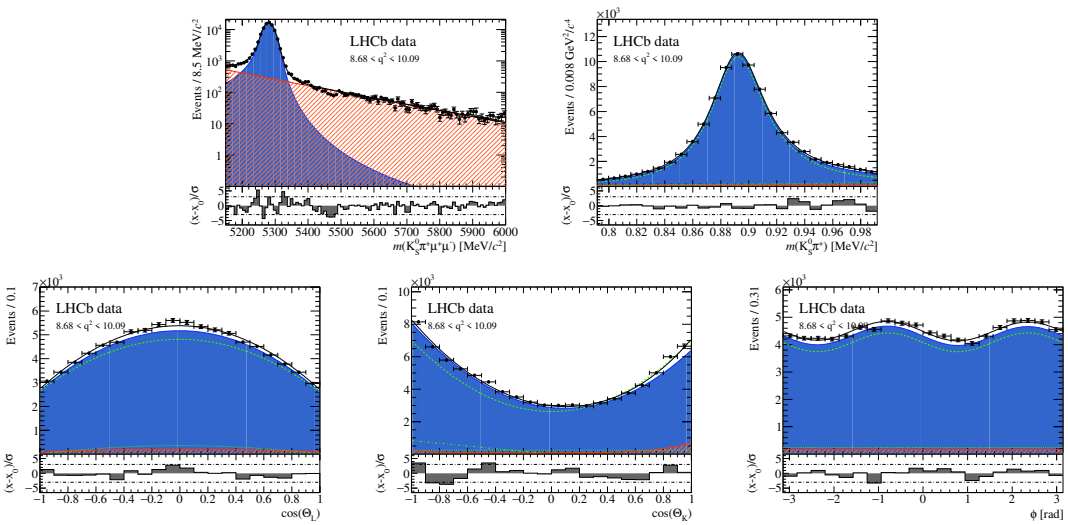

Figure 56: The individual sub-sets of the simultaneous fit to $B^+ \to J/\psi K^{*+}$ events as shown in Fig. 55 are added up into one histogram. All events are weighted according to the acceptance correction function. The fit does not include any angular folding. Note that the m_{B^+} distribution is plotted semi-logarithmically, while all following histograms experienced a cut in m_{B^+} to show only events with maximum $50\,\mathrm{MeV}/c^2$ deviation from the peak centre.

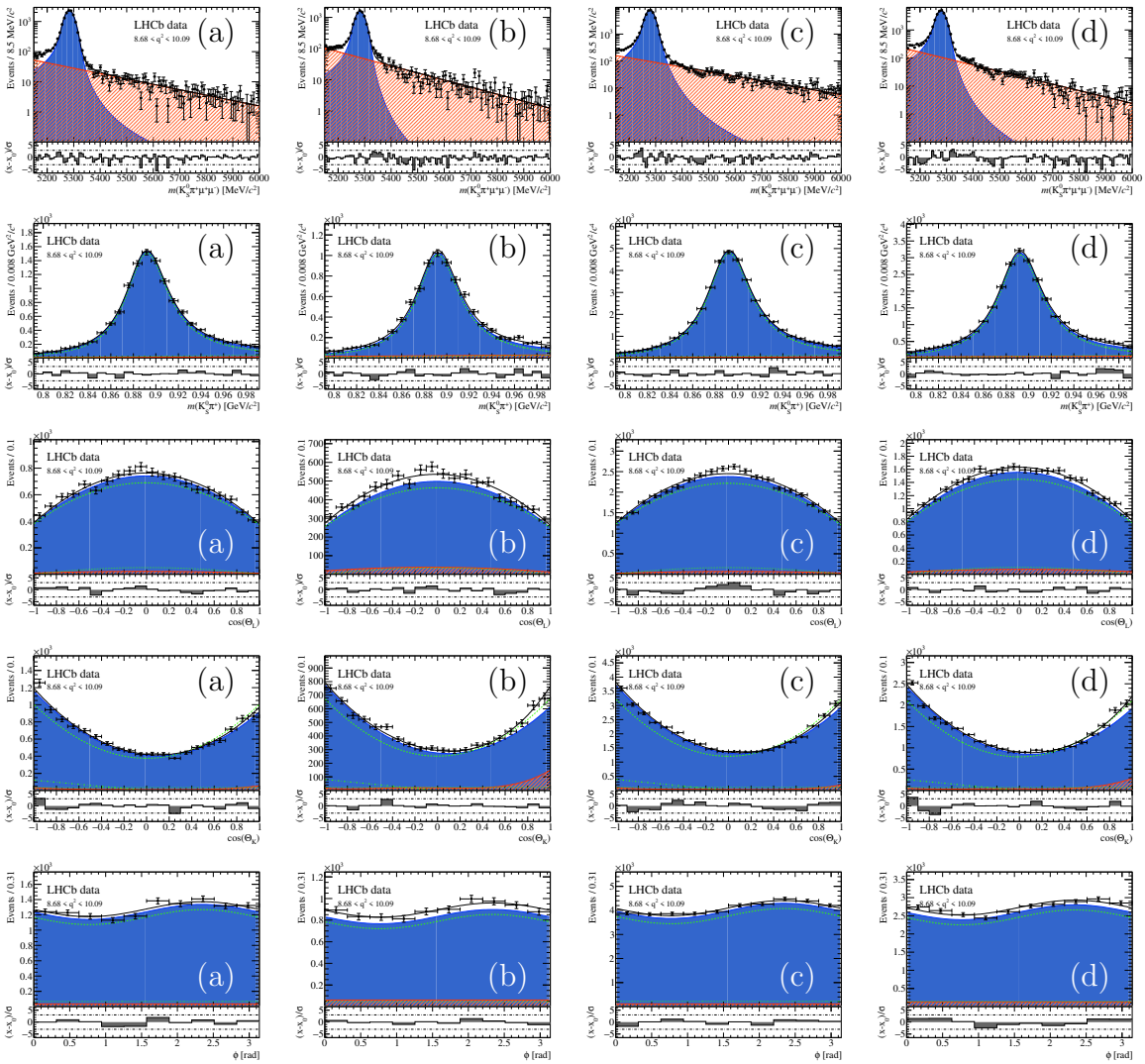

Figure 57: Angular folding 0 - Projection of the simultaneous 5D fit to the full data-set of $B^+ \to J/\psi K^{*+}$ events. All events are weighted according to the acceptance correction function. The sub-sets are Run I (a) + (b) and Run II (c) + (d) with DD tracks and LL tracks events, respectively. Note that the m_{B^+} distributions in the first row are plotted semi-logarithmically, while all following histograms experienced a cut in m_{B^+} to show only events with maximum $50\,\mathrm{MeV}/c^2$ deviation from the peak centre.

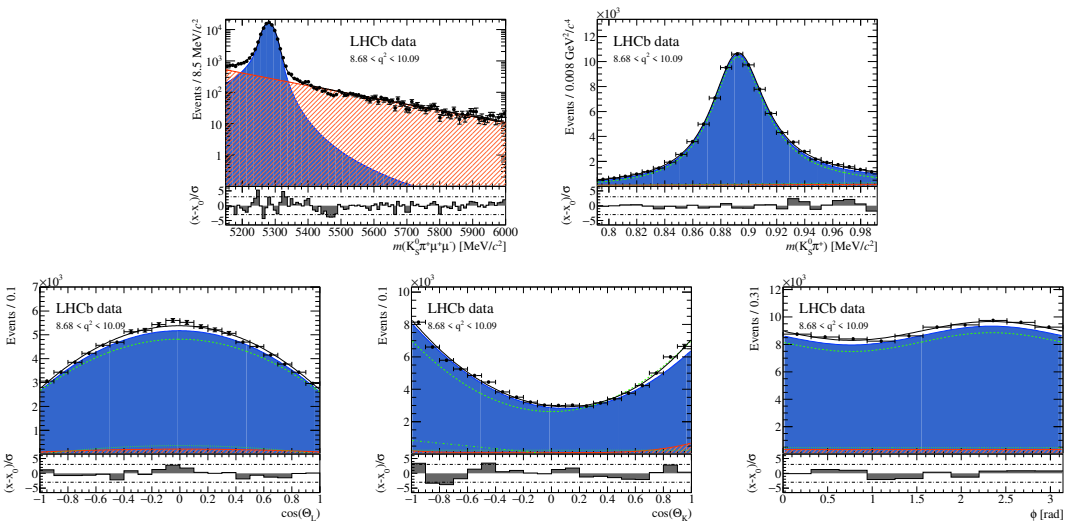

Figure 58: Angular folding 0 - The individual sub-sets of the simultaneous fit to $B^+ \to J/\psi\, K^{*+}$ events as shown in Fig. 57 are added up into one histogram. All events are weighted according to the acceptance correction function. Note that the m_{B^+} distribution is plotted semi-logarithmically, while all following histograms experienced a cut in m_{B^+} to show only events with maximum $50\,\mathrm{MeV}/c^2$ deviation from the peak centre.

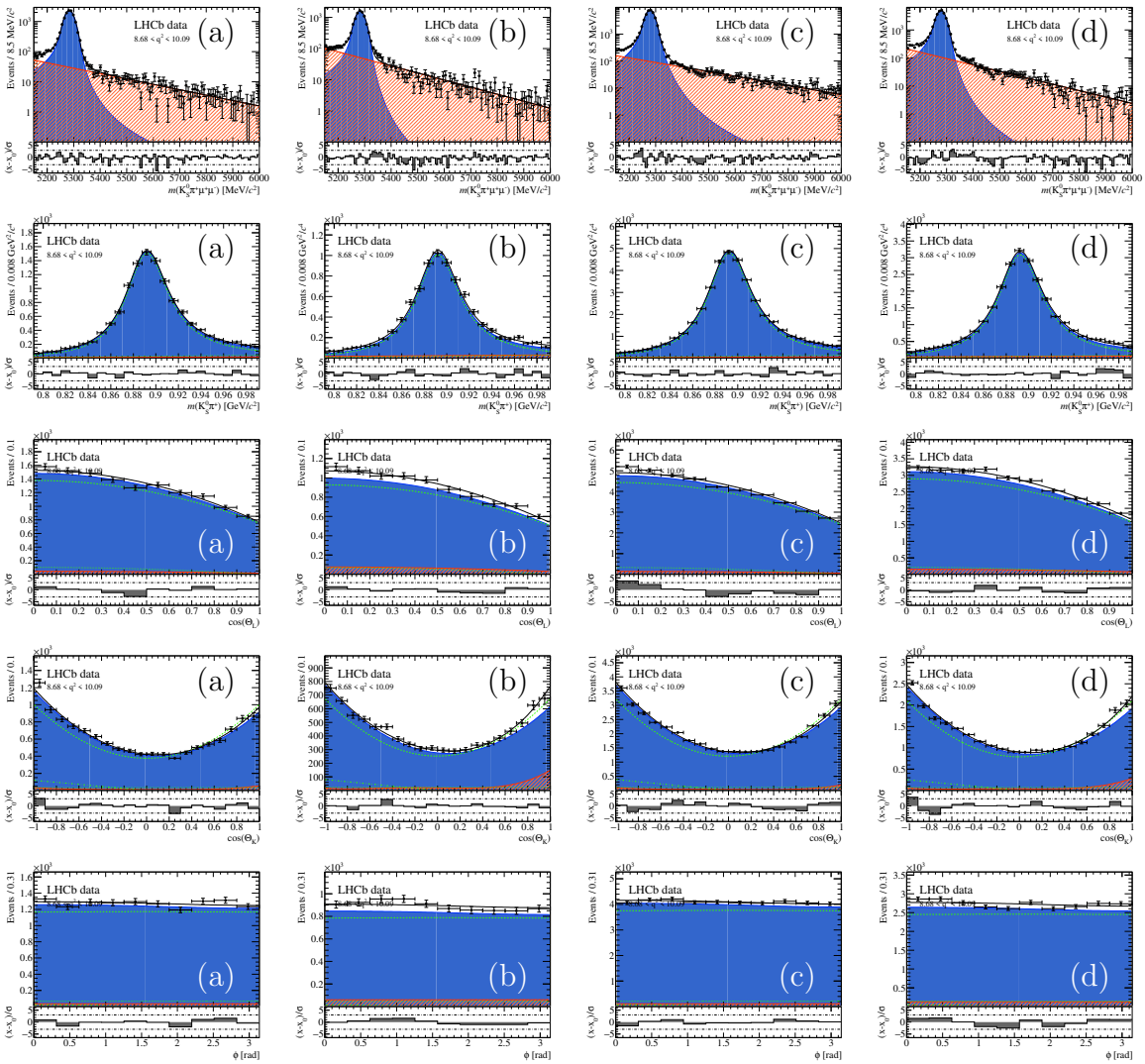

Figure 59: Angular folding 1 - Projection of the simultaneous 5D fit to the full data-set of $B^+ \to J/\psi K^{*+}$ events. All events are weighted according to the acceptance correction function. The sub-sets are Run I (a) + (b) and Run II (c) + (d) with DD tracks and LL tracks events, respectively. Note that the m_{B^+} distributions in the first row are plotted semi-logarithmically, while all following histograms experienced a cut in m_{B^+} to show only events with maximum $50\,\mathrm{MeV}/c^2$ deviation from the peak centre.

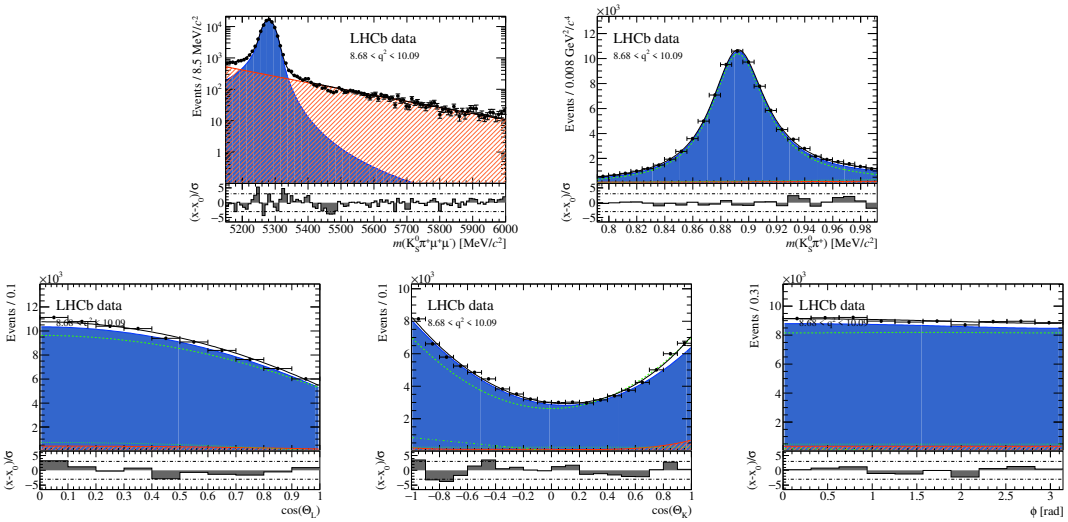

Figure 60: Angular folding 1 - The individual sub-sets of the simultaneous fit to $B^+ \to J/\psi\, K^{*+}$ events as shown in Fig. 59 are added up into one histogram. All events are weighted according to the acceptance correction function. Note that the m_{B^+} distribution is plotted semi-logarithmically, while all following histograms experienced a cut in m_{B^+} to show only events with maximum $50\,\mathrm{MeV}/c^2$ deviation from the peak centre.

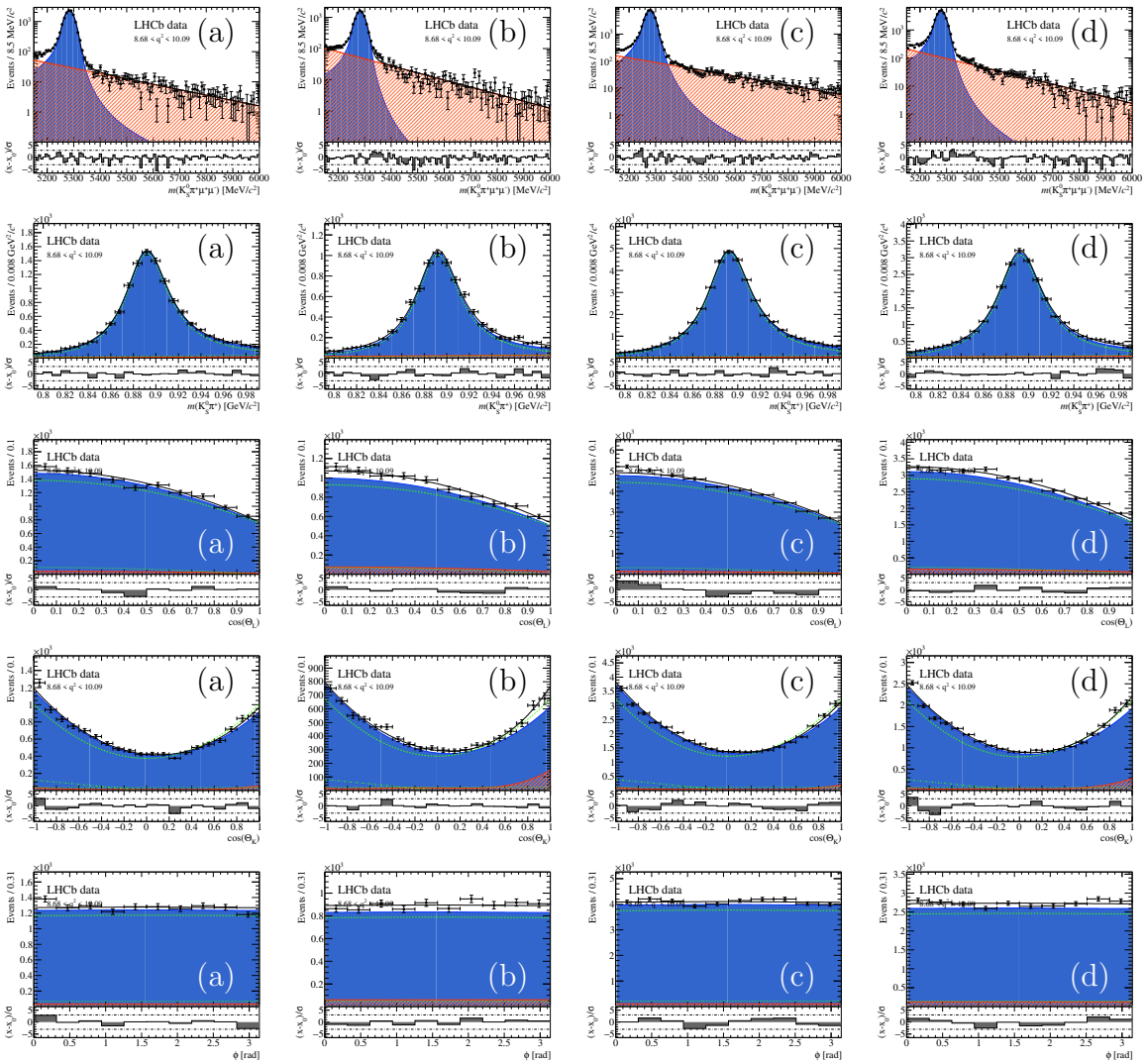

Figure 61: Angular folding 2 - Projection of the simultaneous 5D fit to the full data-set of $B^+ \to J/\psi K^{*+}$ events. All events are weighted according to the acceptance correction function. The sub-sets are Run I (a) + (b) and Run II (c) + (d) with DD tracks and LL tracks events, respectively. Note that the m_{B^+} distributions in the first row are plotted semi-logarithmically, while all following histograms experienced a cut in m_{B^+} to show only events with maximum 50 MeV/c^2 deviation from the peak centre.

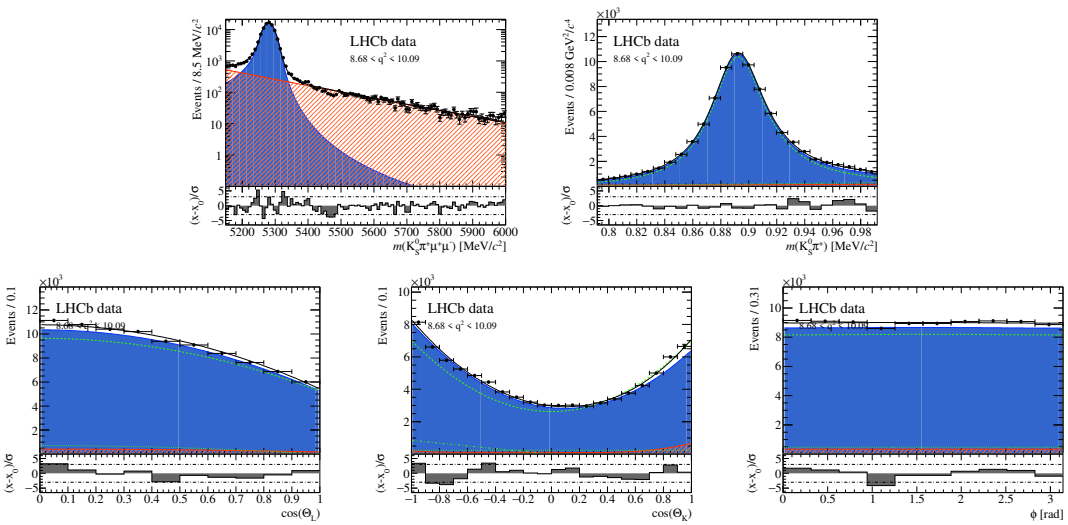

Figure 62: Angular folding 2 - The individual sub-sets of the simultaneous fit to $B^+ \to J/\psi\, K^{*+}$ events as shown in Fig. 61 are added up into one histogram. All events are weighted according to the acceptance correction function. Note that the m_{B^+} distribution is plotted semi-logarithmically, while all following histograms experienced a cut in m_{B^+} to show only events with maximum $50\,\mathrm{MeV}/c^2$ deviation from the peak centre.

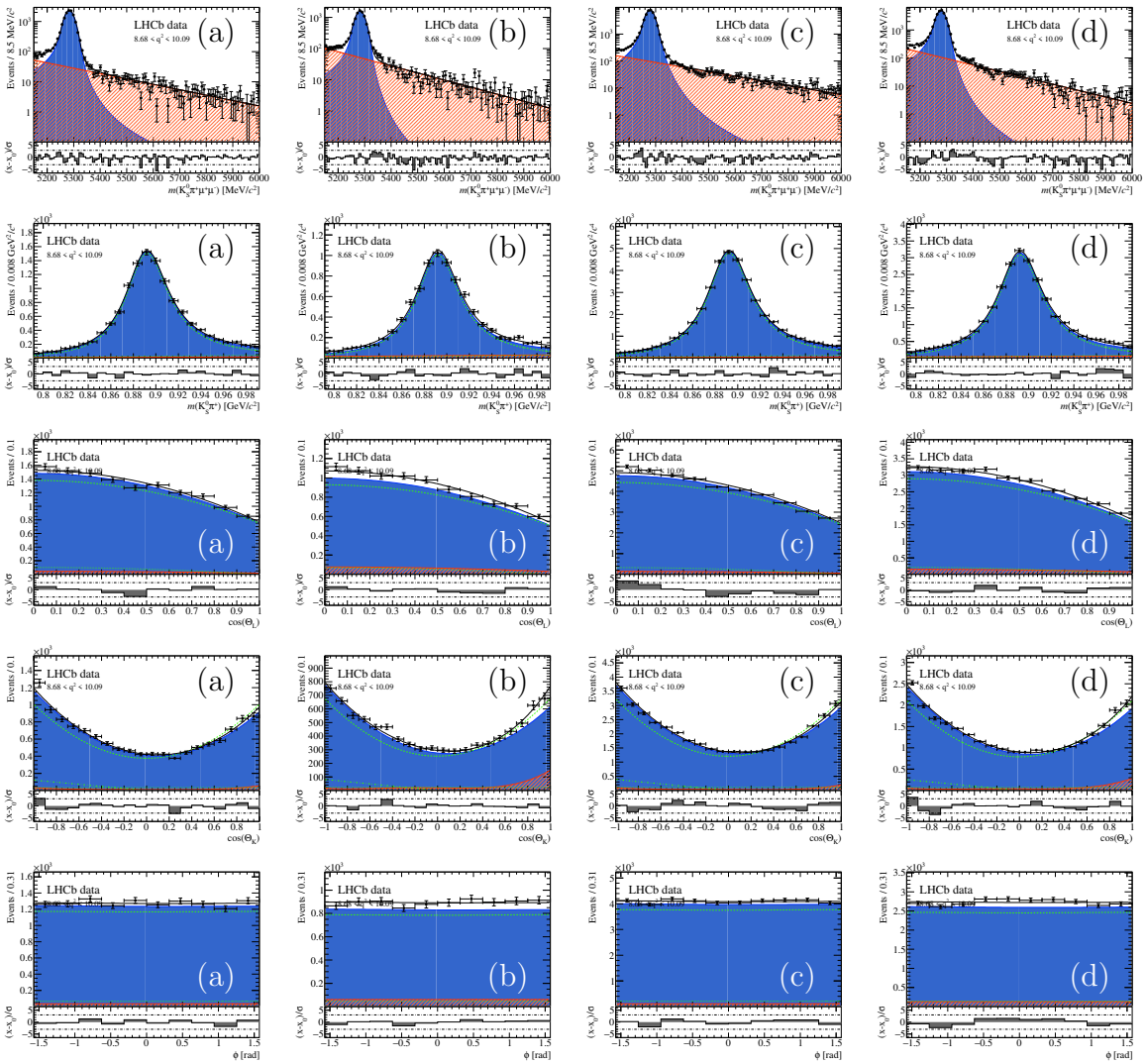

Figure 63: Angular folding 3 - Projection of the simultaneous 5D fit to the full data-set of $B^+ \to J/\psi K^{*+}$ events. All events are weighted according to the acceptance correction function. The sub-sets are Run I (a) + (b) and Run II (c) + (d) with DD tracks and LL tracks events, respectively. Note that the m_{B^+} distributions in the first row are plotted semi-logarithmically, while all following histograms experienced a cut in m_{B^+} to show only events with maximum 50 MeV/c^2 deviation from the peak centre.

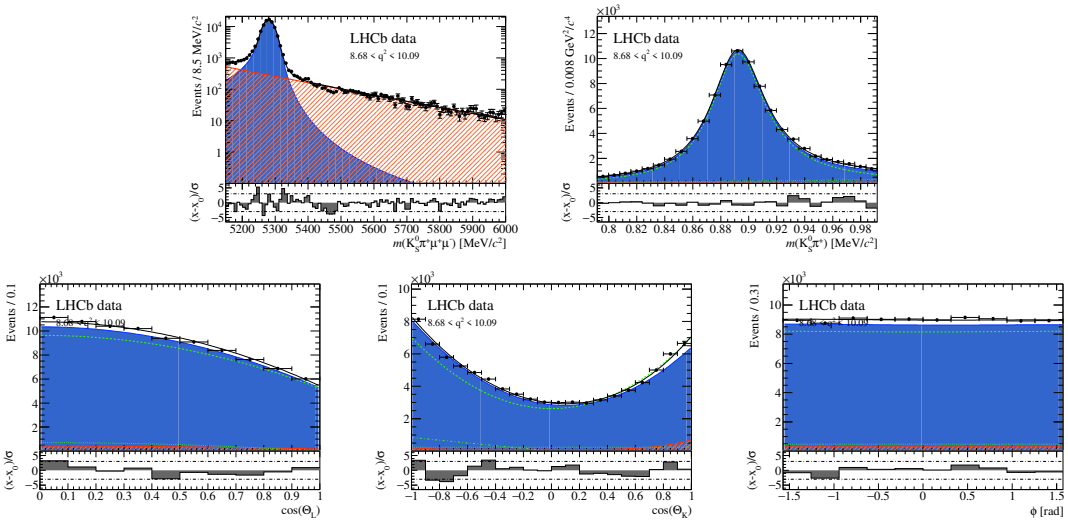

Figure 64: Angular folding 3 - The individual sub-sets of the simultaneous fit to $B^+ \to J/\psi\, K^{*+}$ events as shown in Fig. 63 are added up into one histogram. All events are weighted according to the acceptance correction function. Note that the m_{B^+} distribution is plotted semi-logarithmically, while all following histograms experienced a cut in m_{B^+} to show only events with maximum $50\,\mathrm{MeV}/c^2$ deviation from the peak centre.

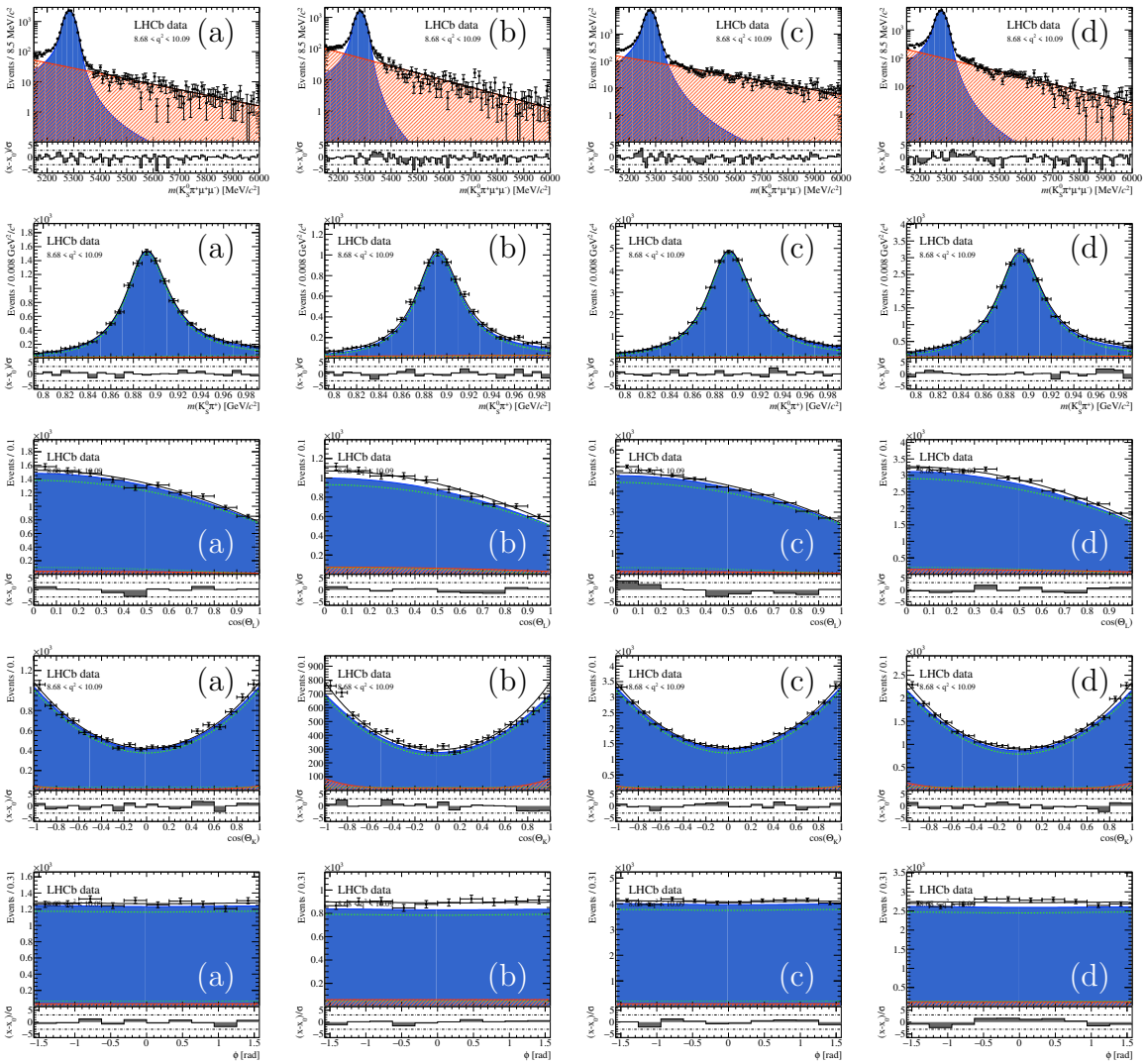

Figure 65: Angular folding 4 - Projection of the simultaneous 5D fit to the full data-set of $B^+ \to J/\psi K^{*+}$ events. All events are weighted according to the acceptance correction function. The sub-sets are Run I (a) + (b) and Run II (c) + (d) with DD tracks and LL tracks events, respectively. Note that the m_{B^+} distributions in the first row are plotted semi-logarithmically, while all following histograms experienced a cut in m_{B^+} to show only events with maximum 50 MeV/c^2 deviation from the peak centre.

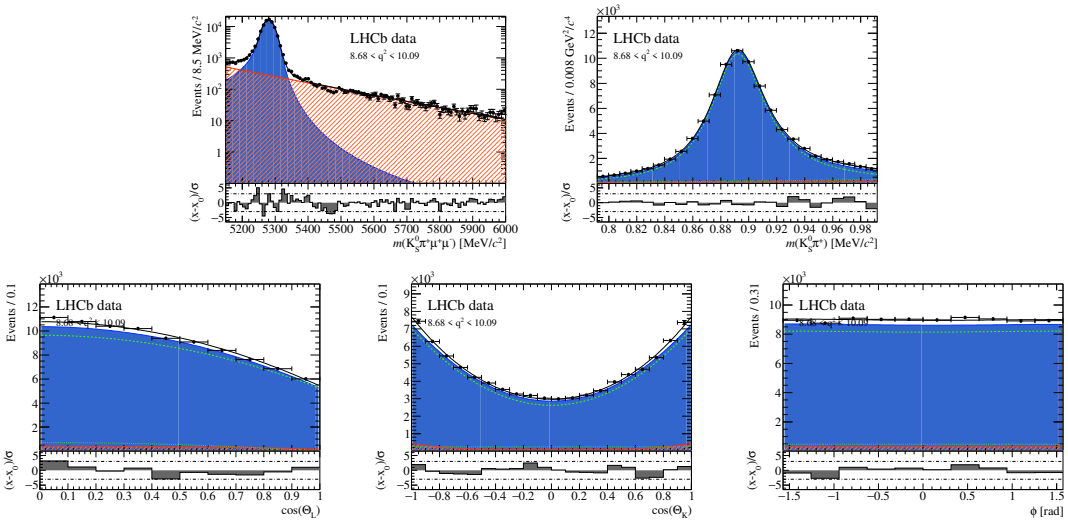

Figure 66: Angular folding 4 - The individual sub-sets of the simultaneous fit to $B^+ \to J/\psi\, K^{*+}$ events as shown in Fig. 65 are added up into one histogram. All events are weighted according to the acceptance correction function. Note that the m_{B^+} distribution is plotted semi-logarithmically, while all following histograms experienced a cut in m_{B^+} to show only events with maximum $50\,\mathrm{MeV}/c^2$ deviation from the peak centre.

4.4.8 Fits to $J/\psi\, K^{*+}$ channel using signal channel statistics

In addition to the fits of the complete data-set of the reference channel, the reference channel was fitted with a statistic as low as expected for the rare signal channel. For this, the estimated statistics of the second q^2 bin (see Table 19) have been randomly selected from the full data-set of the reference channel. Please note, that the number of events is equal to fits of the rare channel in the second q^2 bin, but the signal fraction is much larger in the J/ψ channel (approximately 0.8-0.9) compared to the rare channel (about 0.5 in this q^2 bin). This means, that the performed fits in the J/ψ channel have a larger absolute number of signal events. However, since this is hard to correct precisely and the q^2 bin with the lowest occupancy in the signal channel was taken as reference, this strategy is good enough as a further cross-check.

In total 1000 fits were performed for each folding and the results have been evaluated. Table 29 shows the results obtained from taking the average of all fit results. The given uncertainty is equal to the spread of the result distribution. Both values are obtained from an unbinned likelihood fit to the result distribution, similar to what is used for the toy study evaluations.

The obtained results are in very good agreement with the results from the full data-set fit, as presented in the previous paragraph, Section 4.4.7.

Table 29: Comparison of the results from the reference channel between the average of 1000 fits of low statistics (as expected for the signal channel) and from the full data-set of the reference channel, as already presented in Table 26. For both cases, the results are obtained from the five different foldings. The results are in very good agreement to each other.

$[8.68, 10.09]\,\mathrm{GeV}^2/c^2$	full data-set	low statistic (average)
S_{1s}	0.321 ± 0.002	0.316 ± 0.047
S_3	-0.002 ± 0.004	-0.001 ± 0.067
S_4	-0.246 ± 0.004	-0.256 ± 0.095
S_5	-0.003 ± 0.004	-0.008 ± 0.078
S_{6s}	-0.003 ± 0.003	-0.006 ± 0.062
S_7	-0.001 ± 0.004	-0.005 ± 0.085
S_8	-0.063 ± 0.004	-0.060 ± 0.086
S_9	-0.084 ± 0.004	-0.085 ± 0.070

4.5 Fitter configuration for the final fit

As mentioned before, the FCNCFITTER is highly flexible and may be configured in various different ways. In this section, all relevant configuration steps are collected and give an overview of how the fitter is configured for the final fit on signal data events.
The four sub-sets (see Section 2.1) are fitted simultaneously with all angular observables (P-wave and S-wave) shared between the four sets. All further fit parameters are independent for each sub-set. Each sub-set uses a different angular acceptance correction function, which is extracted from the corresponding sub-set of PHSP MC events.
In total there are 40 individual final fits, one fit for each q^2 bin, as they are shown in Table 15 and for each of the five folding techniques. The statistical uncertainty is determined using the HESSE method and a scan in the likelihood profile is used to confirm the correct determination of the statistical uncertainties. If the two methods do not show coherent results, further techniques like Feldman-Cousin (see Section 4.6) have to be considered.

4.5.1 Configuration of the S-wave component

The toy studies with estimated event yield statistics indicate that the S-wave fraction, F_S, has to be Gaussian constrained. Toy studies with a floating F_S show biases in the mean values for some angular observables. Therefore, F_S will be Gaussian constrained to the value (together with its uncertainties) obtained from a 2D fit to the invariant masses of the B and K^{*+} meson. This fit is as well used for the method of moments, which will be introduced in Section 4.7.

4.5.2 Results for S_{1s} and S_3 from different folding techniques

Using five different angular foldings, as introduced in Section 3.5, yields five different results for the angular observables S_{1s} and S_3. All other angular observables are only determined by a single folding technique, as shown in Table 16.

For S_{1s} and S_3, the mean value obtained by the fit using folding 4 will be chosen for the final results. Toy studies have revealed, that folding 4 shows the least biases in the final fit configuration, which is consistent with having the lowest number of free parameters in the fit (folding 4 is the only folding in all three angles, see Eq. (26)). Tests to the reference channel show no significant deviations between the five foldings for these two observables, but a systematic uncertainty will be applied if necessary. The details about an additional uncertainty on S_{1s} and S_3 due to the different foldings will be discussed in the studies on the systematic uncertainties.

4.6 Feldman-Cousin scans

For both sets of angular observables, Feldman-Cousins [44] scans are used to determine the statistical uncertainty. Albeit the angular observables of the S basis showing only small deviations from the nominal width of the pull distribution up to values between 0.1 and 0.2 as shown in Tables 21, 23 and 25, the effort of running Feldman-Cousins scans is only a question of computing resources once correctly implemented. Latter is given, as the Feldman-Cousins scans are obviously required for the observables in the P basis, as

the poor coverage for different variables in Appendix A.14 is showing.
Hence, each parameter (15 S and P observables without F_L) are scanned in eight q^2 bins. Around all resulting values of the S (P) observable, a range from ± 0.5 (± 1.0) is scanned in steps of 0.01. At each step, 500 toy samples are generated with the investigated parameter fixed to the value at the corresponding step. Each toy sample is fitted twice: once with the parameter fixed and once with the parameter floating. Also the data sample is fitted with the parameter value fixed according to each step. The fraction of toy samples with a $\Delta \log \mathcal{L}_{j,s}$ smaller than the $\Delta \log \mathcal{L}_s^{data}$ in data is obtained at each step and the trends are plotted. The index s indicates the step in the scan and index j runs over the toy samples. The likelihood ratios are determined

$$\Delta \log \mathcal{L} = \log \mathcal{L}_{fixed} - \log \mathcal{L}_{floated} \tag{37}$$

The likelihood from the fit with the parameter floating is of course not dependent on the steps, is equal to the initial fit to data and only run once. All other likelihoods are obtained individually at each step. From these scans, the 68.3% confidence level intervals (1σ) are extracted and used as the statistical uncertainty. The results are shown in Section 7.3.

4.7 Method of moments

The Method of Moments [45] is a tool to extract the angular observables from the signal events without using a fit. However, any results from this method are not foreseen to be attached to the paper, but act as an internal cross-check or validation for the likelihood fit.

The P-wave angular moments of $b \to s\ell^+\ell^-$ decays are orthogonal by definition[8]. As

[8]The angular terms f_{1s},f_{1c},f_{2s} and f_{2c} are correlated as described in Eq. (15) and will be treated accordingly in the Method of Moments.

introduced in Eq. (14), the angular moments from the angular decay rate are

$$
\begin{aligned}
f_{1s}(\cos\theta_L, \cos\theta_K, \phi) &= \sin^2\theta_K \\
f_{1c}(\cos\theta_L, \cos\theta_K, \phi) &= \cos^2\theta_K \\
f_{2s}(\cos\theta_L, \cos\theta_K, \phi) &= \sin^2\theta_K \cos 2\theta_L \\
f_{2c}(\cos\theta_L, \cos\theta_K, \phi) &= \cos^2\theta_K \cos 2\theta_L \\
f_{3}(\cos\theta_L, \cos\theta_K, \phi) &= \sin^2\theta_K \sin^2\theta_L \cos 2\phi \\
f_{4}(\cos\theta_L, \cos\theta_K, \phi) &= \sin 2\theta_K \sin 2\theta_L \cos\phi \\
f_{5}(\cos\theta_L, \cos\theta_K, \phi) &= \sin 2\theta_K \sin\theta_L \cos\phi \\
f_{6s}(\cos\theta_L, \cos\theta_K, \phi) &= \sin^2\theta_K \cos\theta_L \\
f_{6c}(\cos\theta_L, \cos\theta_K, \phi) &= \cos^2\theta_K \cos\theta_L \\
f_{7}(\cos\theta_L, \cos\theta_K, \phi) &= \sin 2\theta_K \sin\theta_L \sin\phi \\
f_{8}(\cos\theta_L, \cos\theta_K, \phi) &= \sin 2\theta_K \sin 2\theta_L \sin\phi \\
f_{9}(\cos\theta_L, \cos\theta_K, \phi) &= \sin^2\theta_K \sin^2\theta_L \sin 2\phi \\
f_{FS}(\cos\theta_L, \cos\theta_K, \phi) &= \sin^2\theta_L \\
f_{S1}(\cos\theta_L, \cos\theta_K, \phi) &= \sin^2\theta_L \cos\theta_K \\
f_{S2}(\cos\theta_L, \cos\theta_K, \phi) &= \sin 2\theta_L \sin\theta_K \cos\phi \\
f_{S3}(\cos\theta_L, \cos\theta_K, \phi) &= \sin\theta_L \sin\theta_K \cos\phi \\
f_{S4}(\cos\theta_L, \cos\theta_K, \phi) &= \sin\theta_L \sin\theta_K \sin\phi \\
f_{S5}(\cos\theta_L, \cos\theta_K, \phi) &= \sin 2\theta_L \sin\theta_K \sin\phi
\end{aligned}
\tag{38}
$$

The angular dimensions can be expressed by the vectorial notation $\vec{\Omega} = (\cos\theta_L, \cos\theta_K, \phi)$. By integrating these angular moments for each q^2 bin, one can determined the expectation value M_i for each P-wave angular moment f_i

$$
M_i = \int \frac{\mathrm{d}^3\Gamma(\vec{\Omega})}{\mathrm{d}\vec{\Omega}} \cdot f_i(\vec{\Omega})\mathrm{d}\vec{\Omega} = \int \frac{9}{32\pi} \sum_j S_j f_j(\vec{\Omega}) \cdot f_i(\vec{\Omega})\mathrm{d}\vec{\Omega}, \tag{39}
$$

providing a relation between the expectation value M_i and the angular observables S_i. For all orthogonal moments, the angular observable, f_i, is directly related to the expectation, M_i. However, the correlations of f_{1s},f_{1c},f_{2s} and f_{2c} as presented in Eq. (15) have to be considered and are included in the conversion of expectation values to angular observables. Furthermore, f_{6s} and f_{6c} require a 2D linear equation system, with only very minor contributions from f_{6c}. For completeness, the f_{6c} term is included. These resulting

relations – solved for the angular observables S_i – are

$$\begin{aligned}
S_{1s} &= \frac{15}{8}\left(M_{1s} - \frac{2}{3}\right) \\
S_3 &= \frac{25}{8}M_3 \\
S_4 &= \frac{25}{8}M_4 \\
S_5 &= \frac{5}{2}M_5 \\
S_{6s} &= 3M_{6c} - 2M_{6s} \\
S_7 &= \frac{5}{2}M_7 \\
S_8 &= \frac{25}{8}M_8 \\
S_9 &= \frac{25}{8}M_9
\end{aligned} \tag{40}$$

To determine the angular observables from data using the Method of Moments, the expectation values M_i are calculated from the *sWeighted* data-set by summing over all events, e,

$$M_i = \frac{1}{\sum_{e=1}^{N}\omega_e}\sum_{e=1}^{N}\omega_e f_i(\vec{\Omega}_e) \tag{41}$$

with, ω_e, the product of the angular acceptance correction weight and the *sWeights* for each event e and N, the total number of events. The uncertainties on all M_i are estimated by the weighted variance

$$\delta M_i = \frac{1}{\sum_{e=1}^{N}\omega_e}\sqrt{\sum_{e=1}^{N}\omega_e^2\left(M_i - f_i(\vec{\Omega})\right)^2} \tag{42}$$

The *sWeights* are obtained from a 2D fit in the $m_{K\pi\mu^+\mu^-}$ and $m_{K\pi}$ dimensions, as explained in Section 4.3.1. In addition, the S-wave fraction F_S is taken from the 2D mass fit and is used to scale the P-wave expectation values M_i before the conversion to the angular observables S_i.

For the Method of Moments, the full data-set is evaluated without any splitting by Runs or by K^0_S track types, but the full set is used at once. The acceptance correction weights for each event however are assigned according to the sub-sets as described in Section 3.4.

With the validation of the Method of Moment on signal channel MC events and the reference channel data in the following two paragraphs, it is shown that this alternative approach of extracting the angular observables is a suitable tool to cross-check the maximum likelihood fit. The comparison of the Method of Moments results using data from the rare signal channel will be presented and discussed in Appendix A.23.

4.7.1 Results from signal channel MC events

To validate the method and compare the Method of Moments with the likelihood fit, the signal channel MC data-set is evaluated using a pure signal sample without S-wave pollution. Therefore, no 2D fit prior to the Method of Moments is required and the Method of Moments can be applied directly after assigning the acceptance correction weights.

In Tables 113 and 114 (in the appendix) as well as in Fig. 67, the Method of Moments is compared to the likelihood fit from Section 4.4.4 and are found to be in very good agreement throughout all q^2 bins and for all angular observables.

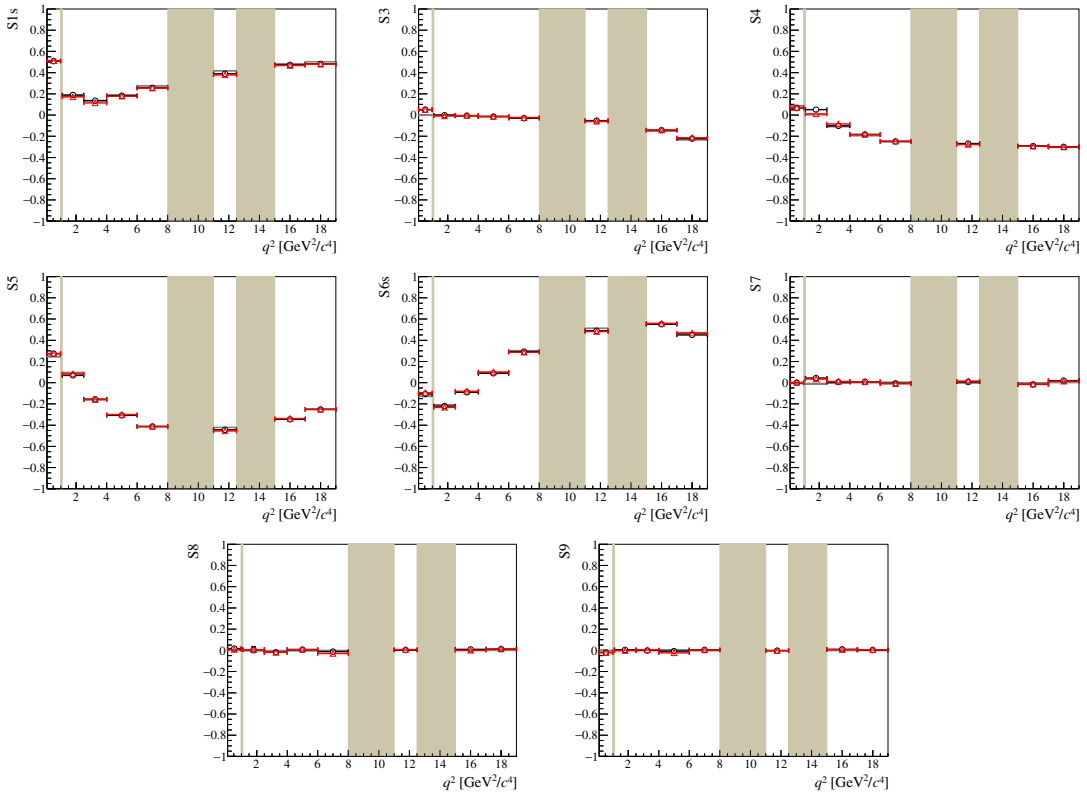

Figure 67: The Method of Moments (red) is compared to the likelihood fit (black) from Section 4.4.4. In addition, the generator level results are shown in dashed grey. Throughout all q^2 bins, the two methods are in very good agreement.

4.7.2 Toy event studies for Method of moments

The functionality of the method of moments is verified using toy event samples with the same statistics as expected for the final fit. These are the same event numbers as used for the toy studies of the likelihood fit (see Section 2.6). In Tables 30 and 31 the width and the mean positions of the angular observables are summarized for toy event studies with starting values compatible with SM predictions. Small biases are observed and the uncertainty of F_L is clearly over-estimated, as the width of the pull distribution is smaller than one. Therefore, the statistical uncertainty of F_L from the Method of moments is scaled by the widths in row one of Table 30 for the final Method of moments on the rare signal channel. The same is true for the identical toy event studies with toys generated

from predictions of NP contributions of $\mathcal{C}_9 = -1.0$. Note that some widths are slightly smaller than one, but are not corrected for, as the differences are not exceeding 0.1. The narrow width of F_L is only present for low statistics and in the presence of an S-wave contribution. Larger samples, such as the application of the Method of moments to MC or J/ψ are therefore not affected.

Table 30: The widths of the pull distribution obtained from toy event studies with Method of moments. The event statistics used for this are the same as previously used for the likelihood fit and as given in Section 2.6. All observables but F_L are showing good agreement with the expected width equal to one. The overestimation of the uncertainty of F_L is correct for in later use.

q^2 bin	0	1	2	3
F_L	0.3618 ± 0.0083	0.4098 ± 0.0110	0.4421 ± 0.0119	0.5212 ± 0.0131
S_3	1.0117 ± 0.0227	0.9676 ± 0.0222	0.9113 ± 0.0211	0.9583 ± 0.0219
S_4	1.0043 ± 0.0225	1.0061 ± 0.0233	0.9451 ± 0.0222	0.9606 ± 0.0220
S_5	0.9955 ± 0.0223	0.9360 ± 0.0217	0.9344 ± 0.0218	0.9628 ± 0.0221
A_{FB}	1.0544 ± 0.0236	1.0193 ± 0.0234	1.0170 ± 0.0235	0.9658 ± 0.0219
S_7	1.0262 ± 0.0230	0.9442 ± 0.0217	0.9461 ± 0.0220	0.9320 ± 0.0213
S_8	1.0520 ± 0.0236	1.0121 ± 0.0234	0.9779 ± 0.0229	0.9625 ± 0.0221
S_9	0.9914 ± 0.0222	0.9252 ± 0.0212	0.9348 ± 0.0217	0.9479 ± 0.0216
q^2 bin	4	5	6	7
F_L	0.5675 ± 0.0132	0.5221 ± 0.0118	0.5953 ± 0.0134	0.4280 ± 0.0098
S_3	0.9652 ± 0.0217	0.9627 ± 0.0215	0.9885 ± 0.0221	0.9885 ± 0.0222
S_4	0.9661 ± 0.0217	0.9453 ± 0.0212	0.9812 ± 0.0219	1.0066 ± 0.0226
S_5	0.9949 ± 0.0224	0.9550 ± 0.0214	0.9927 ± 0.0222	0.9890 ± 0.0221
A_{FB}	1.0020 ± 0.0225	0.9162 ± 0.0205	0.9678 ± 0.0216	0.9743 ± 0.0218
S_7	0.9933 ± 0.0223	0.9268 ± 0.0207	0.9935 ± 0.0222	1.0518 ± 0.0236
S_8	0.9866 ± 0.0222	0.9543 ± 0.0213	0.9689 ± 0.0217	0.9976 ± 0.0223
S_9	0.9844 ± 0.0221	0.9249 ± 0.0207	1.0024 ± 0.0224	0.9949 ± 0.0223

4.7.3 Results from reference channel events

In the reference channel, S-wave and background events are present and, hence, the 2D mass fit is needed to constrain the S-wave fraction F_S and to determine the *sWeights*. The reference channel consists of a single q^2 bin of which the results are given in Table 34 in comparison with results from the likelihood fit in Section 4.4.7. All angular observables are in good agreement between the two methods. Largest deviation was found in the S-wave parameter S_{S1}, which is not of interest for the analysis results. Both projections from the 2D fit can be seen in Fig. 68.

4.7.4 Fit to signal channel data

Due to the limited statistics of the signal channel, the *sWeights* for the method of moments will be extracted from a mass fit to the full data-set without splitting the data up into

Table 31: The mean position of the pull distribution obtained from toy event studies with the Method of moments. The event statistics used for this are the same as previously used for the likelihood fit and as given in Section 2.6.

q^2 bin	0	1	2	3
F_L	0.0615 ± 0.0118	-0.1261 ± 0.0155	-0.1411 ± 0.0168	-0.1842 ± 0.0186
S_3	-0.0552 ± 0.0321	-0.0050 ± 0.0313	-0.0321 ± 0.0299	0.0396 ± 0.0310
S_4	0.0256 ± 0.0318	-0.0322 ± 0.0329	0.0506 ± 0.0313	0.0573 ± 0.0311
S_5	0.0240 ± 0.0315	-0.0231 ± 0.0306	0.0408 ± 0.0309	0.0861 ± 0.0312
A_{FB}	0.0234 ± 0.0334	0.1192 ± 0.0331	0.0148 ± 0.0332	-0.0322 ± 0.0310
S_7	0.0092 ± 0.0325	0.0396 ± 0.0307	0.0182 ± 0.0312	0.0237 ± 0.0301
S_8	-0.0178 ± 0.0333	0.0149 ± 0.0331	0.0511 ± 0.0324	0.0589 ± 0.0312
S_9	0.0343 ± 0.0314	-0.0234 ± 0.0300	0.0048 ± 0.0306	-0.0722 ± 0.0305
q^2 bin	4	5	6	7
F_L	-0.1316 ± 0.0187	0.0594 ± 0.0167	0.0562 ± 0.0190	0.1155 ± 0.0139
S_3	-0.0047 ± 0.0307	-0.0142 ± 0.0305	0.0878 ± 0.0313	0.0977 ± 0.0313
S_4	0.0105 ± 0.0307	0.0061 ± 0.0299	0.0863 ± 0.0310	0.1524 ± 0.0319
S_5	0.0858 ± 0.0317	0.0654 ± 0.0303	0.0904 ± 0.0314	0.0418 ± 0.0313
A_{FB}	-0.0782 ± 0.0318	-0.0459 ± 0.0290	-0.0451 ± 0.0306	-0.0399 ± 0.0309
S_7	0.0822 ± 0.0316	0.0123 ± 0.0293	0.0736 ± 0.0314	-0.0011 ± 0.0333
S_8	0.0572 ± 0.0313	0.0065 ± 0.0302	-0.0367 ± 0.0306	0.0032 ± 0.0316
S_9	0.0105 ± 0.0313	-0.0633 ± 0.0293	0.0162 ± 0.0317	0.0264 ± 0.0315

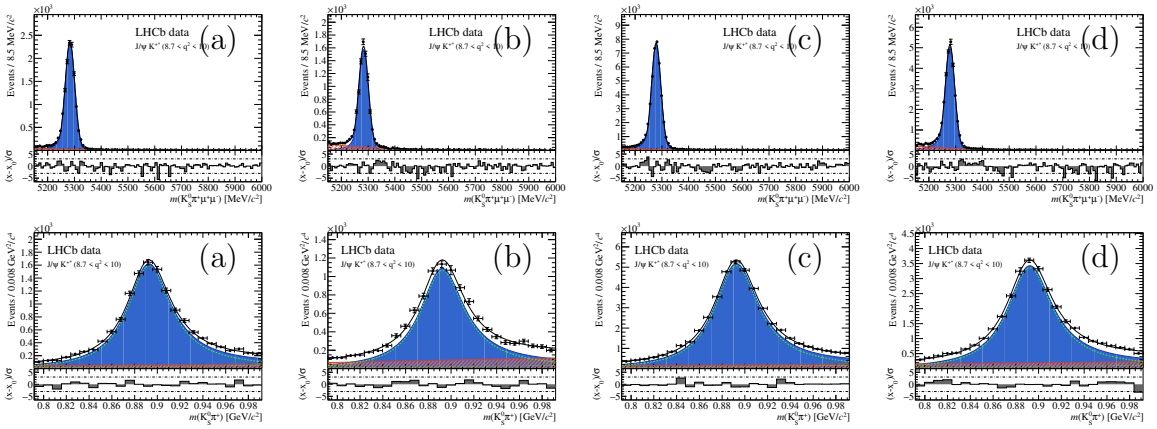

Figure 68: The two dimensional fit in the invariant mass of the B meson and the K^{*+} meson are shown for the reference channel. The data is split into Run I, (a) and (b), and Run II, (c) and (d), for DD tracks and LL tracks events, respectively.

Run I and Run II or DD tracks and LL tracks. The results from these fits are used in the pre-unblinding cross-checks in Section 7.1 to compare to the results from the likelihood fit. For completeness, the numerical values of the results from the method of moments are given in Appendix A.23.

Table 32: Toy study evaluation of the method of moments using generated values equal to a Wilson coefficient $\mathcal{C}_9 = -1.0$. The widths of the pull distribution obtained from toy event studies to verify the non-existence of bias in the Method of moments. The event statistics used for this are the same as previously used for the likelihood fit and as given in Section 2.6. All observables but F_L are showing good agreement with the expected width equal to one. The overestimation of the uncertainty of F_L is correct for in later use.

q^2 bin	0	1	2	3
F_L	0.3641 ± 0.0085	0.4762 ± 0.0123	0.3314 ± 0.0085	0.3996 ± 0.0100
S_3	1.0011 ± 0.0224	0.9313 ± 0.0214	0.9026 ± 0.0210	0.9514 ± 0.0219
S_4	1.0262 ± 0.0230	0.9807 ± 0.0227	0.9568 ± 0.0227	0.9510 ± 0.0220
S_5	1.0299 ± 0.0231	0.9867 ± 0.0227	0.9641 ± 0.0226	0.9486 ± 0.0218
A_{FB}	1.0378 ± 0.0233	1.0300 ± 0.0236	1.0073 ± 0.0232	0.9389 ± 0.0214
S_7	0.9836 ± 0.0220	0.9944 ± 0.0228	0.9516 ± 0.0223	0.9437 ± 0.0217
S_8	1.0035 ± 0.0225	0.9672 ± 0.0224	0.9681 ± 0.0227	0.9532 ± 0.0220
S_9	1.0008 ± 0.0224	0.9426 ± 0.0216	0.9230 ± 0.0214	0.9529 ± 0.0219
q^2 bin	4	5	6	7
F_L	0.5514 ± 0.0127	0.5742 ± 0.0130	0.6426 ± 0.0144	0.3955 ± 0.0090
S_3	0.9914 ± 0.0222	0.9760 ± 0.0218	0.9858 ± 0.0221	1.0017 ± 0.0224
S_4	0.9932 ± 0.0223	0.9351 ± 0.0210	1.0210 ± 0.0229	1.0138 ± 0.0227
S_5	0.9805 ± 0.0220	0.9611 ± 0.0215	0.9741 ± 0.0218	0.9929 ± 0.0222
A_{FB}	1.0066 ± 0.0226	0.9486 ± 0.0212	0.9868 ± 0.0221	0.9868 ± 0.0221
S_7	0.9851 ± 0.0221	0.9374 ± 0.0210	1.0053 ± 0.0225	1.0144 ± 0.0227
S_8	0.9843 ± 0.0221	0.9460 ± 0.0212	1.0172 ± 0.0228	1.0500 ± 0.0235
S_9	0.9689 ± 0.0217	0.9937 ± 0.0222	0.9601 ± 0.0215	1.0326 ± 0.0231

Table 33: Toy study evaluation of the method of moments using generated values equal to a Wilson coefficient $\mathcal{C}_9 = -1.0$. The mean position of the pull distribution obtained from toy event studies to verify the non-existence of bias in the Method of moments. The event statistics used for this are the same as previously used for the likelihood fit and as given in Section 2.6. The biases of F_L will be correct together with the widths, as mentioned in the previous table.

q^2 bin	0	1	2	3
F_L	0.0903 ± 0.0120	-0.1314 ± 0.0174	-0.1009 ± 0.0120	-0.1023 ± 0.0142
S_3	-0.0118 ± 0.0317	-0.1012 ± 0.0302	0.0142 ± 0.0297	0.0020 ± 0.0309
S_4	0.0412 ± 0.0325	0.0157 ± 0.0322	0.0822 ± 0.0321	0.0010 ± 0.0311
S_5	-0.0034 ± 0.0326	-0.0020 ± 0.0321	0.0636 ± 0.0320	0.0574 ± 0.0309
A_{FB}	0.0146 ± 0.0329	0.0249 ± 0.0334	0.0306 ± 0.0328	-0.0512 ± 0.0303
S_7	0.0335 ± 0.0312	0.0201 ± 0.0323	0.0282 ± 0.0315	-0.0297 ± 0.0307
S_8	-0.0287 ± 0.0318	0.0641 ± 0.0317	0.0450 ± 0.0321	-0.0008 ± 0.0312
S_9	-0.0212 ± 0.0317	-0.0126 ± 0.0306	0.0364 ± 0.0303	-0.0338 ± 0.0310
q^2 bin	4	5	6	7
F_L	-0.0997 ± 0.0179	0.0998 ± 0.0183	0.1182 ± 0.0204	0.0881 ± 0.0128
S_3	0.0221 ± 0.0314	-0.0180 ± 0.0309	0.0277 ± 0.0312	0.0968 ± 0.0317
S_4	0.0139 ± 0.0315	0.0302 ± 0.0296	0.1098 ± 0.0323	0.1373 ± 0.0321
S_5	-0.0033 ± 0.0311	0.0021 ± 0.0304	0.1024 ± 0.0308	0.0336 ± 0.0314
A_{FB}	-0.0278 ± 0.0319	-0.0491 ± 0.0300	-0.0527 ± 0.0312	-0.0478 ± 0.0312
S_7	0.0559 ± 0.0312	-0.0028 ± 0.0297	0.0492 ± 0.0318	0.0210 ± 0.0321
S_8	-0.0078 ± 0.0312	-0.0263 ± 0.0299	0.0208 ± 0.0322	-0.0398 ± 0.0332
S_9	-0.0268 ± 0.0307	0.0077 ± 0.0315	-0.0469 ± 0.0304	-0.0153 ± 0.0327

Table 34: Comparison of Method of Moments and the likelihood fit for all eight angular observables in the reference channel.

$[8.68, 10.09]$	fit	MoM
S_{1s}	0.313 ± 0.002	0.308 ± 0.002
S_3	-0.004 ± 0.003	-0.005 ± 0.003
S_4	-0.246 ± 0.004	-0.240 ± 0.005
S_5	-0.003 ± 0.004	0.002 ± 0.004
S_{6s}	-0.003 ± 0.003	-0.003 ± 0.003
S_7	-0.001 ± 0.004	0.000 ± 0.004
S_8	-0.062 ± 0.004	-0.058 ± 0.004
S_9	-0.083 ± 0.004	-0.083 ± 0.004
F_S	0.053 ± 0.006	0.057 ± 0.011
S_{S1}	-0.161 ± 0.006	-0.119 ± 0.008
S_{S2}	0.022 ± 0.004	0.016 ± 0.004
S_{S3}	-0.001 ± 0.004	-0.006 ± 0.004
S_{S4}	-0.005 ± 0.004	0.001 ± 0.004
S_{S5}	-0.073 ± 0.005	-0.070 ± 0.004

4.8 Discussion on the nominal method

The nominal method for the extraction of the angular observables is investigated by using studies on generated toy event samples. The results from these fits (or method of moment) are used as an input to perform a global fit using the flav.io [35] framework to determine the sensitivity on the Wilson coefficient $\mathcal{C}_9$. The Method of Moments profits from having a full correlation matrix of all angular observables. It should be noted that in the Method of Moments (see Tables 35 and 36) and in the fit to the reference channel (see Table 116) only small correlations of up to about 0.2 are observed.
For the likelihood fit, the different foldings do not give a full correlation matrix but the statistical precision of the fit is greater than for the Method of Moments. The evaluation of the toy study results on the Wilson coefficient $\mathcal{C}_9$ compares two different results from the likelihod fit. One is the combined results from all foldings, with the correlation matrix filled up with zeros if no correlation was determined from the fit. The other scenario uses only information from folding 2, which is sensitive to S_{1s} and S_5, which are most sensitive to $\mathcal{C}_9$. The resulting likelihood distributions for $\mathcal{C}_9$ are shown in Fig. 69.

The single folding with results only for S_{1s}, S_3 and S_5 clearly shows the least sensitivity on $\mathcal{C}_9$, followed by the Method of Moments. The combination of results from five folded likelihood fits performs best. However, the result assumes a full correlation matrix, even if many correlations are set to zero by the lack of knowledge. This assumption is including not known information.
To solve this, we will derive the correlation matrix between different foldings using the BOOTSTRAPPING [31] on the signal data. The full strategy is shown in the following paragraph, Section 4.9.

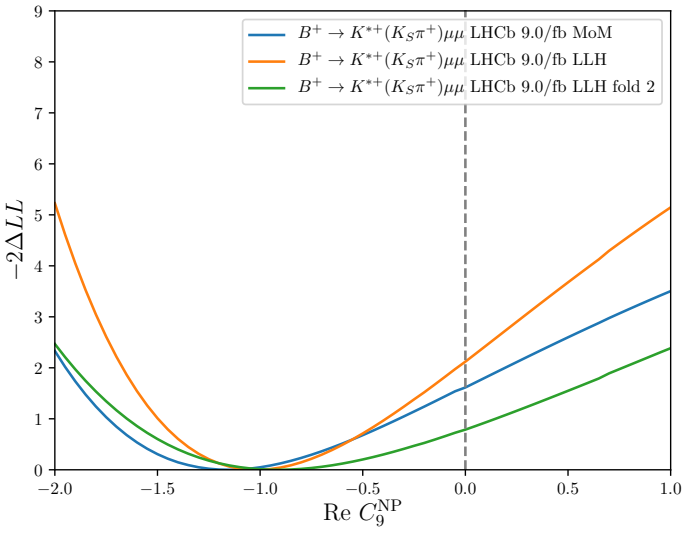

Figure 69: Sensitivity study on the Wilson coefficient $\mathcal{C}_9$ for three different methods: Method of moments, a likelihood fit with only folding 2 and a likelihood fit with all five foldings. The toy events are generated with theoretical values determined for a Wilson coefficient $\mathcal{C}_9 = -1.0$. See text for more details.

Table 35: The averaged correlation matrices for q^2 bins 1-4 from toy event studies using 1000 generated toy samples. The statistics are using the event estimation for the rare channel in the final fit configuration, as previously shown in Table 19.

bin 0	F_L	S_3	S_4	S_5	A_{FB}	S_7	S_8	S_9
F_L	1.000	−0.001	−0.004	−0.014	−0.016	−0.000	−0.001	−0.001
S_3		1.000	0.036	0.115	0.007	−0.002	0.003	0.003
S_4			1.000	−0.071	0.043	−0.004	−0.000	0.002
S_5				1.000	0.032	0.001	−0.004	−0.004
A_{FB}					1.000	0.001	−0.001	0.007
S_7						1.000	−0.075	0.109
S_8							1.000	0.032
S_9								1.000

bin 1	F_L	S_3	S_4	S_5	A_{FB}	S_7	S_8	S_9
F_L	1.000	0.001	0.003	−0.001	−0.010	−0.002	0.000	−0.002
S_3		1.000	−0.008	0.022	0.003	0.000	0.000	0.004
S_4			1.000	−0.038	0.001	−0.003	−0.018	0.004
S_5				1.000	−0.004	−0.016	−0.002	−0.004
A_{FB}					1.000	0.004	0.007	0.004
S_7						1.000	−0.034	0.017
S_8							1.000	0.008
S_9								1.000

bin 2	F_L	S_3	S_4	S_5	A_{FB}	S_7	S_8	S_9
F_L	1.000	−0.001	−0.002	0.000	−0.007	0.003	0.002	−0.001
S_3		1.000	−0.013	−0.038	0.001	−0.002	0.001	−0.009
S_4			1.000	0.000	−0.006	0.004	−0.001	0.014
S_5				1.000	0.000	−0.008	0.004	0.001
A_{FB}					1.000	−0.001	0.004	−0.007
S_7						1.000	−0.009	−0.034
S_8							1.000	0.000
S_9								1.000

bin 3	F_L	S_3	S_4	S_5	A_{FB}	S_7	S_8	S_9
F_L	1.000	0.001	−0.005	0.006	0.014	0.001	−0.002	0.000
S_3		1.000	−0.028	−0.065	0.008	0.010	−0.002	−0.004
S_4			1.000	0.032	−0.051	−0.005	−0.001	0.000
S_5				1.000	−0.035	−0.006	0.001	0.001
A_{FB}					1.000	0.002	0.002	−0.004
S_7						1.000	0.020	−0.079
S_8							1.000	−0.017
S_9								1.000

4.9 Correlation matrix from bootstrapping

The direct extraction of the full correlation matrix from the likelihood fitter is sacrificed in favour of fit stability due to angular folding, as explained in Section 3.5. However,

Table 36: The averaged correlation matrices for q^2 bins 5-8 from toy event studies using 1000 generated toy samples. The statistics are using the event estimation for the rare channel in the final fit configuration, as previously shown in Table 19.

bin 4	F_L	S_3	S_4	S_5	A_{FB}	S_7	S_8	S_9
F_L	1.000	−0.001	−0.028	0.001	0.100	0.002	−0.001	0.000
S_3		1.000	−0.039	−0.119	0.006	−0.010	−0.003	0.003
S_4			1.000	0.083	−0.089	−0.001	0.002	0.001
S_5				1.000	−0.060	−0.006	−0.002	0.004
A_{FB}					1.000	−0.002	0.002	0.004
S_7						1.000	0.072	−0.131
S_8							1.000	−0.041
S_9								1.000

bin 5	F_L	S_3	S_4	S_5	A_{FB}	S_7	S_8	S_9
F_L	1.000	−0.015	−0.022	−0.001	0.157	−0.000	0.002	−0.001
S_3		1.000	−0.046	−0.121	−0.036	0.006	−0.002	0.002
S_4			1.000	0.240	−0.186	−0.002	−0.001	0.002
S_5				1.000	−0.212	−0.008	−0.001	0.005
A_{FB}					1.000	−0.001	0.001	−0.007
S_7						1.000	0.156	−0.153
S_8							1.000	−0.059
S_9								1.000

bin 6	F_L	S_3	S_4	S_5	A_{FB}	S_7	S_8	S_9
F_L	1.000	−0.045	0.018	0.014	0.169	0.001	0.001	−0.001
S_3		1.000	−0.078	−0.125	−0.014	−0.000	0.003	−0.000
S_4			1.000	0.237	−0.112	−0.005	0.000	−0.002
S_5				1.000	−0.104	0.001	−0.005	0.002
A_{FB}					1.000	0.001	−0.002	−0.002
S_7						1.000	0.209	−0.141
S_8							1.000	−0.084
S_9								1.000

bin 7	F_L	S_3	S_4	S_5	A_{FB}	S_7	S_8	S_9
F_L	1.000	−0.028	0.013	0.015	0.071	0.001	−0.000	0.003
S_3		1.000	−0.107	−0.112	0.017	0.003	0.002	0.004
S_4			1.000	0.187	−0.040	0.002	−0.005	0.001
S_5				1.000	−0.049	0.000	0.000	0.006
A_{FB}					1.000	−0.001	0.000	−0.002
S_7						1.000	0.161	−0.101
S_8							1.000	−0.088
S_9								1.000

studies on the sensitivity of the global fit to the results of this analysis revealed a great improvement of the usage of the full parameter set with a full correlation matrix over the use of only a single folding, see Fig. 69.

This full correlation matrix is extracted using BOOTSTRAPPING [31] on signal data events. For this, 3000 sets of randomly chosen events are each fitted by all five foldings. The size of these randomized samples is also randomly altered by a Poissonial probability with a mean equal to the genuine size. From these, the correlation for each pair of two parameters is determined from the 3000 results. The precision of the correlation factor scales with $\frac{1}{\sqrt{N}}$, which is about 0.018 for 3000 samples. In the following paragraph, Section 4.9.1, this method is validated on toy events. The resulting correlation matrices of for the signal data are later given with the fit results in Section 7.2.

4.9.1 Validation of bootstrapping method

The technique to extract the correlation matrix via the BOOTSTRAPPING method is validated using some large statistic toy samples. One q^2 bin is filled with four times 2000 toy events. Then first one nominal fit with full angular configuration is performed to obtain the reference correlation matrix, which the BOOTSTRAPPING method is compared to. Afterwards, each toy sample is fitted with all five foldings for 667 bootstrapped samples. For seven samples, with five fits for 667 bootstrappings, this adds up to $7 \times 5 \times 667 = 23345$ fits with each a statistic of about 8000 toy events. This huge number is the reason for limited statistics in both the number of samples and number of bootstrappings per sample. From the bootstrapping results, the correlation for each off-diagonal cell[9] are determined by using the $n = 667$ results for both variables. The correlations are calculated using the formula

$$corr_{xy} = \frac{n \sum_i x_i y_i - \sum_i x_i \sum_i y_i}{\sqrt{n \sum_i x_i^2 - \left(\sum_i x_i\right)^2} \sqrt{n \sum_i y_i^2 - \left(\sum_i y_i\right)^2}} \tag{43}$$

for the two variables x and y. The resulting correlation matrices are all listed in Appendix A.19. All off-diagonal cells from all seven pairs of correlation matrices are compared between the correlation matrix from the full angular fit and the BOOTSTRAPPING method. The mean value as shown in Fig. 70 is fairly compatible with zero, as would be expected. Even though the small bias has an almost three sigma significance, the absolute value of only 0.015 is small compared to the precision required for the signal channel. The width of about 0.067 is in good agreement with the expected value for the spread of the correlation values. This expectation is based on the observed spread of correlations equal to $\frac{1}{sqrt(N)}$, which can be observed on simple toy experiments with random numbers. For this validation, the corresponding $N_{1,2}$ for the uncertainties on the correlation matrices are $N_1 = 8000$ for the full angular likelihood fit and $N_2 = 667$ for the BOOTSTRAPPING method. For the presented study, the numbers result in an expected width of $\sigma_{diff} = \sqrt{\sigma_1^2 + \sigma_2^2} = \sqrt{\frac{1}{8000} + \frac{1}{667}} \approx 0.040$. Given that this is a theoretical limit for the precision, the observed width of 0.067 in Fig. 70 is in good agreement and satisfies the precision needed for the correlation matrix extraction.
The method is therefore validated for extracting the correlation of the final fit from different foldings.

[9] The diagonals have been evaluated in the beginning to verify that the results are equal to one, but later are skipped to save computing resources.

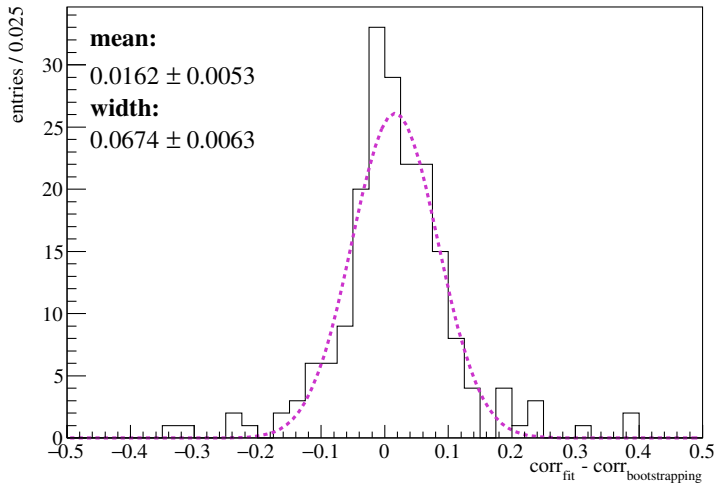

Figure 70: Absolute differences of correlation values of each cell (top right triangle only and without diagonal elements) of the correlation matrices obtained from the full angular fit and from the BOOTSTRAPPING method. Seven toy samples with each 8000 toy events are evaluated. The mean and width values are obtained from a binned fit using a Gaussian bell shape. The agreement between both methods is good enough for the expected precision and therefore validates the usage of the BOOTSTRAPPING method for the extraction of the correlation matrix. See text for more details.

5 Study of systematic uncertainties

In addition to the statistical uncertainty on the determined values for all angular observables, the following list of systematic effects is investigated and their uncertainty is quantified.
The first parts investigate systematic effects of the angular acceptance correction and the PHSP MC which the acceptance correction weights are obtained from. The MC-data re-weighting of PHSP MC events is investigated. In addition, the uncertainty of finite statistics of the PHSP MC samples is quantified by using the bootstrapping method. The uncertainty due to the parametrization of the 4D acceptance correction using Legendre polynomials is evaluated by increasing the maximum order of these polynomials by 2 in each of the four dimensions.
The S-wave fraction, F_S, is varied within the uncertainty of the 2D mass fit and the systematic effect on the angular observables is determined.
All systematic effects are summarized and added up quadratically to a final systematic uncertainty on each observable in each q^2 bin. The final systematic uncertainties are given in Section 5.13.

5.1 Re-weighting of PHSP MC

To match the kinematic distributions of simulated events and recorded data, all MC events are re-weighted as described in Section 2.7.4. In order to understand the impact of this reweighting on the angular observables, a systematic study was performed and a systematic uncertainty is assigned. This systematic uncertainty is taken from 200 fits with different acceptance correction configurations. In each configurations the weights for every underlying PHSP MC event has been varied within the weight's uncertainty. The width of the result distributions for all angular observables in all eight q^2 bins is assigned as the systematic uncertainty. All fits are performed on toy event samples of large statistics (four times 2000 events) to remove any statistical effects on the differences and extract the pure effect of the PHSP MC reweighting. The resulting values are summarized in Table 37.

Table 37: The width of the resulting distributions for all parameters due to fluctuating the PHSP MC weights for the angular acceptance correction parametrization is assigned as a systematic uncertainty of this PHSP MC reweighting.

q^2 bin	0	1	2	3	4	5	6	7
S_{1s}	0.0134	0.0021	0.0011	0.0023	0.0007	0.0010	0.0009	0.0012
S_3	0.0023	0.0015	0.0011	0.0009	0.0009	0.0012	0.0015	0.0023
S_4	0.0062	0.0029	0.0022	0.0058	0.0013	0.0015	0.0017	0.0021
S_5	0.0191	0.0025	0.0019	0.0030	0.0015	0.0018	0.0016	0.0024
S_{6s}	0.0097	0.0020	0.0011	0.0012	0.0009	0.0012	0.0013	0.0013
S_7	0.0015	0.0005	0.0007	0.0014	0.0003	0.0003	0.0003	0.0003
S_8	0.0376	0.0009	0.0009	0.0018	0.0008	0.0005	0.0007	0.0007
S_9	0.0378	0.0003	0.0003	0.0004	0.0002	0.0002	0.0002	0.0002

5.2 Bootstrapping of PHSP MC

The finite statistics of the PHSP MC sample are introducing a possible systematic effect on the result of the angular observables as the parametrization of the acceptance correction uses a moment analysis for the 4D polynomials. Due to the finite statistics, the parametrization may describe statistical fluctuations inside the 4D space of the PHSP MC.

To evaluate the effect of the statistical power, the BOOTSTRAPPING [31] method is used. Sets of identical statistics as the original PHSP MC samples but with the events resampled randomly are used to generate randomly fluctuated acceptance corrections.[10] For each generated acceptance correction, a fit to an identical toy event sample (which is generated using the nominal acceptance correction) is performed in all eight q^2 bins and the angular observables are saved. 200 iterations of this strategy generate a Gaussian-like distribution for each angular observable and in each q^2 bin. The width of these distributions is taken as the systematic uncertainty associated to the PHSP MC statistics and all values are given in Table 38.

Table 38: The statistical power of the PHSP MC sample is determined using the BOOTSTRAPPING method. 500 random subsets with equal size to the original PHSP MC set are taken, acceptance correction determined for each and the width of the signal parameter distribution is equal to the systematic uncertainty.

q^2 bin	0	1	2	3	4	5	6	7
S_{1s}	0.0166	0.0166	0.0068	0.0079	0.0065	0.0082	0.0067	0.0125
S_3	0.0194	0.0065	0.0056	0.0048	0.0049	0.0054	0.0078	0.0150
S_4	0.0334	0.0184	0.0142	0.0139	0.0084	0.0087	0.0109	0.0155
S_5	0.0282	0.0165	0.0125	0.0128	0.0080	0.0080	0.0088	0.0180
S_{6s}	0.0348	0.0143	0.0066	0.0078	0.0073	0.0104	0.0080	0.0146
S_7	0.0117	0.0069	0.0051	0.0051	0.0027	0.0044	0.0031	0.0102
S_8	0.0183	0.0128	0.0066	0.0088	0.0033	0.0075	0.0063	0.0169
S_9	0.0377	0.0025	0.0012	0.0011	0.0010	0.0009	0.0010	0.0033

5.3 Parametrization of angular acceptance

The PHSP MC is parametrized as described in Section 3.4 and uses four dimensional polynomials with a finite maximal order. This maximum order has been thoroughly studied and optimized as described. Since a description with one or two more orders does not improve the residuals in the projections nor improves the determined χ^2 of the parametrization, a systematic is assigned to this part.

To assign a systematic uncertainty to this cut-off in the polynomial approximation of the distributions, all orders in the four dimensions have been increased by two more orders. Fitting each of the 200 toy event samples with the two different sets of angular

[10] The BOOTSTRAPPING method would actually also require fluctuations of the total number of events selected. This is thought to be a negligible second order effect and would require a more complicated technical implementation. Hence the number of events is kept identical to the original PHSP MC sample.

acceptance corrections, a systematic uncertainty is determined from the mean position of the distribution of resulting differences for every angular observable. These numbers are given in Table 39.

Table 39: The absolute value of the difference in the mean values of all signal parameters between a fit with acceptance correction using the nominal order of polynomials and one fit of where the acceptance is parametrized by two additional orders per dimension. The absolute value of the difference is considered as an estimation of the systematic uncertainty for the PHSP MC parametrization.

q^2 bin	0	1	2	3	4	5	6	7
S_{1s}	0.0250	0.0189	0.0370	0.0127	0.0036	0.0033	0.0065	0.0122
S_3	0.0093	0.0216	0.0056	0.0003	0.0140	0.0114	0.0139	0.0283
S_4	0.0124	0.0223	0.0004	0.0137	0.0000	0.0179	0.0063	0.0522
S_5	0.0166	0.0415	0.0091	0.0195	0.0108	0.0195	0.0214	0.0317
S_{6s}	0.0020	0.0420	0.0165	0.0006	0.0056	0.0032	0.0004	0.0141
S_7	0.0043	0.0185	0.0217	0.0103	0.0028	0.0104	0.0131	0.0055
S_8	0.0166	0.0301	0.0129	0.0200	0.0156	0.0079	0.0057	0.0143
S_9	0.0101	0.0026	0.0069	0.0112	0.0028	0.0045	0.0066	0.0112

5.4 S-wave parameter constraints

The final fit configuration toy studies (see Section 4.4.6) show a bias in the mean position of the pull distribution (see Table 20). This bias was diagnosed to origin from the fact that the constraint on F_S from the 2D mass fits is not strong enough. In the investigations leading to this conclusion, the constraint on F_S was artificially strengthened (similar to the toy studies in Section 4.4.2) and it was found that at an Gaussian constraint on F_S of 0.01 or better, the bias is removed from the pull distributions. Therefore, this bias is assigned as a systematic uncertainty of the S-wave parameter. In Table 40 the resulting systematics are shown.

5.5 Signal peak mass model

To evaluate a potential systematic effect due to the usage of a double-sided Crystal Ball function as the model for the signal peak in the mass dimension of the mother B meson, a toy study is performed. In this study the events are generated using the nominal signal peak model, the double-sided Crystal Ball function. The distributions of 200 independent sets of toy events is then fitted using a single Gaussian bell curve with the same width as the Crystal Ball function. As for the systematics studies before, the distribution of $x - x_0$ is plotted for every angular observable and in each of the eight q^2 bins. From these distributions, the shift of the mean position is obtained using a Gaussian fit model and is assigned as the systematic uncertainty. All values are summarized in the following Table 41.

Table 40: Due to the large uncertainty on the Gaussian constraint of F_S, the toy study results of the final fit configuration with SM values show a bias, as shown in Table 20. The bias disappears when a stronger Gaussian constraint is applied for F_S. Here, the resulting values are not given relative to the statistical uncertainty as in Table 20, but the absolute values of the shift are given. These values are assigned as a systematic uncertainty.

q^2 bin	0	1	2	3	4	5	6	7
S_{1s}	0.0230	0.0317	0.0291	0.0009	0.0031	0.0053	0.0008	0.0003
S_3	0.0001	0.0006	0.0001	0.0080	0.0080	0.0065	0.0030	0.0141
S_4	0.0046	0.0123	0.0211	0.0138	0.0040	0.0037	0.0003	0.0132
S_5	0.0019	0.0051	0.0102	0.0136	0.0097	0.0069	0.0058	0.0188
S_{6s}	0.0020	0.0212	0.0011	0.0057	0.0005	0.0010	0.0037	0.0063
S_7	0.0032	0.0007	0.0177	0.0029	0.0070	0.0074	0.0083	0.0063
S_8	0.0041	0.0071	0.0146	0.0104	0.0054	0.0041	0.0076	0.0008
S_9	0.0029	0.0009	0.0041	0.0012	0.0070	0.0111	0.0026	0.0081

Table 41: The toy events are generated with the nominal double-sided Crystal Ball model for the B meson signal peak. Then these events are fitted with a single Gaussian bell shape and the mean value of the $x - x_0$ distributions is assigned as the systematic uncertainty for the mass model.

q^2 bin	0	1	2	3	4	5	6	7
S_{1s}	0.0007	0.0005	0.0010	0.0013	0.0021	0.0022	0.0005	0.0015
S_3	0.0013	0.0019	0.0035	0.0001	0.0000	0.0033	0.0035	0.0048
S_4	0.0033	0.0020	0.0003	0.0027	0.0086	0.0068	0.0077	0.0038
S_5	0.0009	0.0086	0.0007	0.0064	0.0030	0.0082	0.0074	0.0049
S_{6s}	0.0063	0.0023	0.0042	0.0018	0.0036	0.0000	0.0050	0.0065
S_7	0.0009	0.0019	0.0020	0.0027	0.0094	0.0009	0.0014	0.0038
S_8	0.0014	0.0012	0.0003	0.0007	0.0039	0.0011	0.0002	0.0004
S_9	0.0018	0.0002	0.0004	0.0037	0.0008	0.0002	0.0010	0.0023

5.6 Veto against peaking background

In Section 2.4, the veto cut against peaking background from $B^0 \to K^0_S \mu^+ \mu^-$ plus a random π^+ is explained. As the cut around the B^0 mass also removes combinatorial background, as it can be seen by a undershoot in the residual at around 5500 MeV/c^2 in Figs. 5 and 6, the effect of this removal is investigated in a dedicated toy study. For this, a negative gaussian shape at 5500 MeV with width of 30 MeV/c^2 and a relative normalization to the exponential of 2% is added to the exponential model of the background at toy event generation. This negative shape imitates the removal of combinatorial background at this masses and generates a hole in the exponential distribution. The values of the Gaussian are obtained from reference distributions in Figs. 5 and 6 and averaged. Applying this artificial cut into the generated background spectrum results in the systematic uncertainties given

in Table 42.

Table 42: By removing a Gaussian shaped hole from the upper mass side-band during the generation of toy events, the veto against $B^0 \to K^0_S \mu^+ \mu^-$ plus a random π^+ decays are simulated. In the fit, only the nominal background model is applied. The mean value of the difference between a nominal fit and the modified fit are assigned as the systematic uncertainty.

q^2 bin	0	1	2	3	4	5	6	7
S_{1s}	0.0004	0.0020	0.0036	0.0003	0.0009	0.0016	0.0021	0.0004
S_3	0.0000	0.0058	0.0045	0.0004	0.0044	0.0003	0.0002	0.0044
S_4	0.0002	0.0061	0.0013	0.0023	0.0016	0.0022	0.0008	0.0057
S_5	0.0002	0.0048	0.0010	0.0028	0.0009	0.0018	0.0018	0.0000
S_{6s}	0.0040	0.0076	0.0013	0.0016	0.0042	0.0009	0.0037	0.0003
S_7	0.0008	0.0047	0.0077	0.0046	0.0075	0.0010	0.0057	0.0016
S_8	0.0056	0.0075	0.0036	0.0003	0.0012	0.0050	0.0077	0.0001
S_9	0.0076	0.0014	0.0042	0.0046	0.0017	0.0016	0.0031	0.0049

5.7 Angular backround model

The polynomial parametrization of angular background is cut-off at orders 2 for $\cos\theta_K$ and $\cos\theta_L$. In the ϕ dimension it is a flat distribution (order 0). This orders were found by examining the mass sidebands, as explained in Section 3.3.4. To cover a potential under-coverage of the actual angular background components, toy studies are generated with an additional order of size 0.1 These generated events are then fitted with the nominal angular background model and the results are compared to the nominal toy event fits. The mean of the shift of these results is assigned as a systematic uncertainty. The values are given in Table 43.

5.8 Angular resolution

The finite angular resolution is determined in Appendix A.6. To propagate the resolution to the final results of the angular observables, a toy event study with 2000 toy events per sub-set and per q^2 bin is performed. For 200 times, the same set of toy events is used and all angular values ($\cos\theta_K$, $\cos\theta_L$ and ϕ) for each event in this set is varied randomly within the angular resolution. From the distribution of these 200 fit results, the width is obtained for each angular observable and in each q^2 bin. This width is assigned as the systematic uncertainty of the angular resolution and all values are shown in Table 44. The effect is very small compared to the statistical uncertainties and as well to other systematic effects.

5.9 Study of systematic effects on S_{1s} and S_3 due to angular folding

Since S_{1s} and S_3 are accessible in all five angular foldings, as it is shown in Table 16, a systematic tests has been performed to investigate potential biases by the choice of

Table 43: The angular background model is increased by an additional polynomial order compared to the nominal orders ($\cos\theta_K$: 2, $\cos\theta_L$: 2 and ϕ : 0) with an amplitude of 0.1 for the new order. The events are then fitted with the nominal background model and the difference to fit to a nominal background sample are compared. The mean differences are assigned as the systematic uncertainty.

q^2 bin	0	1	2	3	4	5	6	7
S_{1s}	0.0016	0.0001	0.0008	0.0003	0.0026	0.0003	0.0013	0.0023
S_3	0.0041	0.0063	0.0054	0.0037	0.0043	0.0005	0.0012	0.0064
S_4	0.0015	0.0065	0.0027	0.0023	0.0041	0.0015	0.0016	0.0031
S_5	0.0030	0.0055	0.0020	0.0014	0.0047	0.0017	0.0045	0.0014
S_{6s}	0.0033	0.0015	0.0044	0.0012	0.0045	0.0031	0.0026	0.0023
S_7	0.0034	0.0035	0.0033	0.0044	0.0041	0.0006	0.0028	0.0007
S_8	0.0031	0.0015	0.0035	0.0002	0.0063	0.0061	0.0051	0.0022
S_9	0.0089	0.0143	0.0182	0.0166	0.0154	0.0134	0.0108	0.0100

Table 44: Results of the systematic effects of the angular resolutions on the angular observables. The angular resolutions have been determined using the TRUE information on MC, which is presented in Appendix A.6. For this study, the generated angles of all toy events have been repeatedly varied within their resolution. The width of the result distribution from all fits is given in this table and assigned as an systematic uncertainty.

q^2 bin	0	1	2	3	4	5	6	7
S_{1s}	0.0007	0.0011	0.0005	0.0004	0.0005	0.0004	0.0002	0.0003
S_3	0.0007	0.0004	0.0004	0.0005	0.0004	0.0004	0.0003	0.0004
S_4	0.0015	0.0015	0.0009	0.0008	0.0007	0.0006	0.0007	0.0006
S_5	0.0013	0.0009	0.0006	0.0007	0.0005	0.0005	0.0004	0.0006
S_{6s}	0.0028	0.0013	0.0006	0.0006	0.0004	0.0006	0.0003	0.0004
S_7	0.0014	0.0011	0.0007	0.0007	0.0005	0.0005	0.0004	0.0004
S_8	0.0029	0.0020	0.0011	0.0008	0.0006	0.0005	0.0005	0.0005
S_9	0.0005	0.0005	0.0006	0.0005	0.0005	0.0004	0.0003	0.0004

using the results from folding 0 for these two observables. Toy events studies are run to investigate potential biases in the different foldings. Every toy sample is fitted with all five foldings, which is repeated on 3000 sets of toy events. The For this effect, only very small biases have been observed, as can be seen in Table 45. The systematic uncertainty is accordingly assigned for the choice of picking folding 0 as reference for S_{1s} and S_3.

5.10 L0Muon efficiency disagreement in Monte Carlo and data

The obvious difference in L0Muon efficiency in data and MC events, as determined and explained in Section 2.7.6, was used to determined a potential systematic effect of this difference on the angular observable. Using the ratio of data and MC efficiencies from

Table 45: The root mean square of the mean values from five different foldings for each angular observable and in each q^2 bin is determined. The mean values are determined from 3000 fits to randomly generated toy event samples.

q^2 bin	0	1	2	3
S_{1s}	0.0018 ± 0.0005	-0.0020 ± 0.0013	-0.0023 ± 0.0004	0.0015 ± 0.0007
S_3	-0.0010 ± 0.0010	0.0013 ± 0.0012	-0.0004 ± 0.0018	0.0000 ± 0.0022
q^2 bin	4	5	6	7
S_{1s}	0.0028 ± 0.0004	0.0045 ± 0.0008	0.0023 ± 0.0005	0.0025 ± 0.0013
S_3	-0.0025 ± 0.0013	-0.0007 ± 0.0031	-0.0012 ± 0.0018	-0.0081 ± 0.0043

Fig. 13 (blue graphs), the PHSP MC events are weighted prior to the parametrization of the angular acceptance correction. With these resampled PHSP MC sets, an alternative set of angular acceptance correction coefficients is determined. Using toy events studies with 2000 events per bin and per sub-set, and 200 fits per bin, the mean values for each angular observable and in each q^2 bin are determined. For no systematic effect, the mean value should be (compatible with) zero. The results of this systematic study reveal a very small systematic effect, with the numbers presented in Table 46 and these values will be assigned as a systematic uncertainty. Within three sigma, all values are compatible with zero.

Table 46: The differences in the L0Muon trigger line efficiency (see Fig. 13) is used for an alternative determination of the angular acceptance correction coefficients. Toy studies are performed by generating events with the nominal acceptance and fitted with the alternative acceptance correction. This table presents the observed absolute values of the bias in the result distribution, which is assigned as a systematic uncertainty to the L0Muon trigger efficiency difference in data and MC events.

q^2 bin	0	1	2	3	4	5	6	7
S_{1s}	0.0024	0.0026	0.0014	0.0003	0.0003	0.0012	0.0004	0.0011
S_3	0.0022	0.0010	0.0022	0.0000	0.0005	0.0041	0.0001	0.0012
S_4	0.0022	0.0051	0.0019	0.0025	0.0033	0.0036	0.0010	0.0043
S_5	0.0028	0.0004	0.0008	0.0038	0.0023	0.0014	0.0006	0.0001
S_{6s}	0.0058	0.0009	0.0025	0.0001	0.0018	0.0016	0.0005	0.0002
S_7	0.0003	0.0018	0.0005	0.0024	0.0078	0.0031	0.0047	0.0036
S_8	0.0037	0.0056	0.0034	0.0055	0.0026	0.0007	0.0022	0.0016
S_9	0.0004	0.0006	0.0012	0.0021	0.0007	0.0005	0.0009	0.0028

5.11 Discrepancy in $K^0_{\rm S}$ $p_{\rm T}$ between data and MC

The comparison of resonant J/ψ data and resonant J/ψ MC show a mostly great agreement between *sWeighted* data and re-weighted MC events. A observed discrepancy in the $p_{\rm T}$

spectrum of K^0_S and K^{*+} in the DD tracks sample was observed, as it is shown in Figs. 138, 142 and 146.

Table 47: The non-flat ratio between MC and data DD tracks events in K^0_S p_T are used to weight the PHSP MC events prior to the determination of the angular acceptance correction coefficients. With the alternative coefficients, as well as with the nominal coefficients, toy events have been fitted repeatedly. The shift in the mean position of the difference distribution is assigned as an systematic uncertainty. Compared to other systematic effects, the size of this uncertainty is small.

q^2 bin	0	1	2	3	4	5	6	7
S_{1s}	0.0002	0.0025	0.0018	0.0009	0.0036	0.0023	0.0042	0.0026
S_3	0.0010	0.0080	0.0049	0.0052	0.0033	0.0043	0.0029	0.0013
S_4	0.0045	0.0031	0.0049	0.0025	0.0011	0.0032	0.0004	0.0068
S_5	0.0003	0.0009	0.0006	0.0014	0.0008	0.0018	0.0023	0.0035
S_{6s}	0.0014	0.0004	0.0018	0.0029	0.0016	0.0042	0.0018	0.0040
S_7	0.0011	0.0028	0.0044	0.0015	0.0021	0.0014	0.0030	0.0002
S_8	0.0041	0.0027	0.0000	0.0024	0.0006	0.0005	0.0004	0.0018
S_9	0.0001	0.0023	0.0036	0.0038	0.0030	0.0019	0.0008	0.0001

5.12 General bias of the likelihood fit

The toy event studies reveal some biases for different parameters and in different q^2 bins. As the bias is not identical for different start values, the biases from different toy event configurations are added up quadratically to form a single systematic uncertainty. The systematic uncertainty is clearly dominated by values of the toy studies using final fit on data events. The mean and width for all pull distributions of these studies are given in Tables 24 and 25, with a significant bias of the mean position visible for some parameters in different q^2 bins. The coverage of the pull distributions however is good (except the one case of S_{6s}, which will use Feldman-Cousins to obtain the uncertainty) and though the bias is assigned as a systematic uncertainty. Results of these systematic uncertainties are given in Table 48.

5.13 Summary of systematic uncertainties

The final systematic uncertainties assigned to the results are given in Table 49. In this table, all previously measured systematic uncertainties are added up quadratically for each parameter and in each q^2 bin. The total systematic uncertainty is dominated by the systematic effects of the angular acceptance correction and the bias of the toy studies with final fit values as start values. However, the total systematic uncertainty is small in comparison to the expected statistical uncertainty for each angular observable and in each q^2 bin.

Table 48: The observed bias in toy studies with values equal to the final fit results are assigned as a general systematic uncertainty to the unknown bias of the likelihood fit.

q^2 bin	0	1	2	3	4	5	6	7
S_{1s}	0.0194	0.0261	0.0020	0.0014	0.0018	0.0040	0.0084	0.0069
S_3	0.0064	0.0065	0.0078	0.0025	0.0088	0.0027	0.0189	0.0042
S_4	0.0057	0.0084	0.0268	0.0416	0.0083	0.0042	0.0026	0.0104
S_5	0.0043	0.0121	0.0105	0.0045	0.0011	0.0008	0.0128	0.0048
S_{6s}	0.0032	0.0091	0.0039	0.0010	0.0059	0.0666	0.0085	0.0001
S_7	0.0051	0.0117	0.0035	0.0006	0.0119	0.0029	0.0039	0.0039
S_8	0.0015	0.0213	0.0143	0.0020	0.0078	0.0007	0.0019	0.0066
S_9	0.0081	0.0021	0.0039	0.0083	0.0046	0.0183	0.0091	0.0034

Table 49: The final quadratic summation of systematic uncertainties. These values are assigned to the results in addition to the statistical uncertainties. All results can be found in Section 7.

q^2 bin	0	1	2	3	4	5	6	7
S_{1s}	0.0447	0.0485	0.0478	0.0154	0.0098	0.0119	0.0137	0.0195
S_3	0.0232	0.0265	0.0152	0.0127	0.0205	0.0175	0.0257	0.0378
S_4	0.0375	0.0345	0.0376	0.0486	0.0162	0.0225	0.0152	0.0581
S_5	0.0384	0.0480	0.0215	0.0287	0.0179	0.0240	0.0286	0.0419
S_{6s}	0.0379	0.0507	0.0196	0.0106	0.0133	0.0677	0.0141	0.0228
S_7	0.0145	0.0240	0.0302	0.0141	0.0208	0.0143	0.0184	0.0148
S_8	0.0461	0.0410	0.0258	0.0251	0.0202	0.0142	0.0150	0.0233
S_9	0.0562	0.0152	0.0211	0.0230	0.0182	0.0258	0.0162	0.0188

5.14 Systematics for $P^{(\prime)}$ observables

All previous systematic studies have been repeated using the $P^{(\prime)}$ angular basis. The resulting total systematic uncertainties are given in Table 50, whereas all individual results are shown in the appendix in Appendix A.21.

5.15 Systematics of S- and $P^{(\prime)}$ observables in two larger q^2 bins

In addition to the nominal q^2 binning scheme as defined in Table 15, two extra large bins are fitted as well. The systematics for both observable bases have been evaluated in the very same way as before and the resulting values are presented in the combined table for both observable bases in Table 51.

Table 50: The final quadratic summation of systematic uncertainties for angular observables in the $P^{(\prime)}$ basis. The individual systematic uncertainties are listed in tables in the appendix (Appendix A.21). These values will be assigned to the results in addition to the statistical uncertainty. All results can be found in Section 7.

q^2 bin	0	1	2	3	4	5	6	7
F_L	0.0642	0.0340	0.0444	0.0309	0.0176	0.0299	0.0204	0.0371
P_1	0.1063	0.3167	0.2232	0.2909	0.1026	0.0861	0.0710	0.0932
P_2	0.0330	0.1515	0.1132	0.0628	0.0545	0.0436	0.0263	0.0439
P_3	0.0472	0.1801	0.2039	0.1499	0.0565	0.0455	0.0167	0.0174
P'_4	0.1187	0.1126	0.1413	0.0916	0.0628	0.0744	0.0750	0.1320
P'_5	0.1217	0.1036	0.0917	0.0856	0.0647	0.0549	0.0615	0.1275
P'_6	0.0622	0.0818	0.0539	0.0467	0.0264	0.0254	0.0218	0.0379
P'_8	0.0922	0.0499	0.0709	0.0511	0.0200	0.0388	0.0449	0.0729

Table 51: The final quadratic summation of systematic uncertainties for angular observables in the S- and $P^{(\prime)}$ basis in the two larger q^2 bins. The individual systematic uncertainties are listed in tables in the appendix (Appendix A.22). These values will be assigned to the results in addition to the statistical uncertainty. All results can be found in Section 7.

q^2 bin	[1.1-6.0]	[15.0-19.0]	q^2 bin	[1.1-6.0]	[15.0-19.0]
S_{1s}	0.0189	0.0207	F_L	0.0263	0.0219
S_3	0.0094	0.0292	P_1	0.0760	0.0664
S_4	0.0271	0.0577	P_2	0.0453	0.0352
S_5	0.0209	0.0247	P_3	0.0446	0.0331
S_{6s}	0.0320	0.0522	P'_4	0.0665	0.1047
S_7	0.0135	0.0110	P'_5	0.0427	0.0479
S_8	0.0242	0.0124	P'_6	0.0374	0.0312
S_9	0.0137	0.0211	P'_8	0.0618	0.0266

6 Further systematic checks

In addition to the systematic studies in Section 5, which resulted in assigning a systematic uncertainty to the final result values, further checks on systematic effects have been performed. These tests might have used toy events or were cross-checks of different kinds.

6.1 Potential mix-up of primary π^+ and π^+ from K^0_S

A potential mix-up of the π^+ originating from the K^{*+} (primary π^+) with the π^+ from the K^0_S (secondary π^+) was investigated for the LL tracks sample. In the DD tracks sample, the large flight distance of the K^0_S prevents a potential mix-up.
For the LL tracks sample, the invariant mass of the primary π^+ and the π^- from the K^0_S was determined for all events with a K^0_S flight distance of 10mm or less. The cut on the K^0_S flight distance was motivated by the fact, that primary and secondary π^+ would need a (close to) common vertex of origin to be mixed up. In the invariant mass spectrum of the full DD tracks data-set (2011–2018), a yield of around 29 ± 5 mix-up events could be observed using a gaussian fit plus some polynomial background to fit the region around the K^0_S mass. With a total number of more than 75000 events, this results in a sub-per-mill effect and is considered negligible.

6.2 Forcing a symmetric angular acceptance in $\cos\theta_L$

Due to the symmetry in the di-muon system, the angular acceptance correction parametrization could be argued to be symmetric in the $\cos\theta_L$ dimension. Investigations on whether this statement is justified resulted in the systematic study by repeating toy event fits with the nominal acceptance correction (allowing for even and odd polynomials in the parametrization of $\cos\theta_L$) and a fit with a forced symmetry in the acceptance correction. Each toy event sample is generated using the nominal acceptance correction and is afterwards fitted twice; once with the nominal acceptance correction and once with a symmetric acceptance correction in $\cos\theta_L$. The difference of each each angular observable is filled into histograms for every q^2 bin. In Table 52 the mean position of this difference is shown, representing the effect of the forced symmetry in the acceptance of $\cos\theta_L$. The result shows significant biases, especially in the observable S_4.
These results are not assigned as an systematic uncertainty, but show a potential bias due to symmetric acceptance corrections. This is confirmed by observing a significant bias in the results of the reference channel, when using a symmetric acceptance correction. The value of $S_4 = -0.266 \pm 0.005$ differs significantly from the literature values in Table 27. All other results from this fit can be seen in Table 129 in the Appendix A.20.

6.3 Angular background

The angular background is described using Chebyshev polynomials, as extensively described in Section 3.3.4. From the lower and upper mass-sideband, the background description is interpolated into the signal region underneath the B^+ mass peak and hence the two sidebands should agree in their angular distributions to justify the negligence of a mass-dependent description of the angular background polynomials.
To verify this statement, the lower and upper mass-sideband of the rare channel background

Table 52: The absolute value of the difference in the mean values of all signal parameters between a fit with acceptance correction using the assumption that $\cos\theta_L$ should have a symmetric acceptance effect and one fit of where the acceptance may contain non-symmetric terms in $\cos\theta_L$. These values are not assigned as a systematic uncertainty.

q^2 bin	0	1	2	3	4	5	6	7
S_{1s}	0.0017	0.0005	0.0007	0.0042	0.0008	0.0033	0.0003	0.0002
S_3	0.0004	0.0009	0.0028	0.0029	0.0005	0.0019	0.0007	0.0051
S_4	0.0169	0.0304	0.0424	0.0360	0.0275	0.0191	0.0164	0.0410
S_5	0.0019	0.0030	0.0052	0.0020	0.0070	0.0057	0.0013	0.0085
S_{6s}	0.0074	0.0047	0.0020	0.0112	0.0077	0.0041	0.0016	0.0019
S_7	0.0035	0.0004	0.0031	0.0037	0.0048	0.0035	0.0015	0.0021
S_8	0.0067	0.0000	0.0060	0.0004	0.0020	0.0044	0.0011	0.0030
S_9	0.0006	0.0023	0.0017	0.0013	0.0023	0.0022	0.0015	0.0002

samples have been parametrized individually as well as in a combined way. For this, the data-set is not split into Run I and Run II nor in `DD` tracks and `LL` tracks due to the very limited statistics. In most bins, the total amount of background events is just about 100 for the full data-set.

The results for the four angular background coefficients (2 in $\cos\theta_L$ and 2 in $\cos\theta_K$) are presented in Table 53. Even though some parameters swap signs between upper and lower mass-sideband, the large uncertainty on these values still provides a fair agreement for all parameters. Hence, the chosen parametrization is justified and no systematic uncertainty will be assigned to this.

6.4 Upper limit of B meson mass window

A potentially larger mass window for the B^+ mass of up to 7000 MeV/c^2 was investigated using toy event studies. The nominal window up to 6000 MeV/c^2 is used as a reference point. The results of evaluating the sensitivity from 1000 toy events are given in Tables 54 and 55. Throughout all bins and parameters, no benefit from the increased mass window is visible, as the values agree for the full tables. Hence, the upper limit of the B^+ mass window is set to 6000 MeV/c^2.

Table 53: The angular background coefficients from fits to pure background samples in the rare channel. The data-set is only split into lower and upper mass-sideband (or the combined set of both sidebands). The coefficients have significant uncertainties and are in fair agreement for all q^2 bins.

$c^1_{bkg}(\cos\theta_L)$	low	high	combined
$[0.10, 0.98]$	-0.433 ± 0.384	-0.262 ± 0.219	-0.303 ± 0.190
$[1.10, 2.50]$	-0.001 ± 0.316	0.090 ± 0.222	0.067 ± 0.183
$[2.50, 4.00]$	0.332 ± 0.255	0.080 ± 0.167	0.163 ± 0.142
$[4.00, 6.00]$	0.136 ± 0.245	0.140 ± 0.186	0.139 ± 0.155
$[6.00, 8.00]$	-0.248 ± 0.212	0.197 ± 0.167	0.050 ± 0.135
$[11.00, 12.50]$	0.353 ± 0.235	-0.206 ± 0.205	0.010 ± 0.158
$[15.00, 17.00]$	0.540 ± 0.307	0.184 ± 0.206	0.288 ± 0.170
$[17.00, 19.00]$	-0.149 ± 0.426	0.137 ± 0.217	0.078 ± 0.194
$c^2_{bkg}(\cos\theta_L)$	low	high	combined
$[0.10, 0.98]$	0.678 ± 0.223	0.582 ± 0.150	0.609 ± 0.125
$[1.10, 2.50]$	0.592 ± 0.224	0.542 ± 0.158	0.555 ± 0.131
$[2.50, 4.00]$	0.898 ± 0.084	0.544 ± 0.107	0.663 ± 0.080
$[4.00, 6.00]$	0.408 ± 0.216	0.519 ± 0.121	0.498 ± 0.106
$[6.00, 8.00]$	0.309 ± 0.205	0.407 ± 0.136	0.387 ± 0.113
$[11.00, 12.50]$	-0.080 ± 0.285	-0.209 ± 0.204	-0.151 ± 0.167
$[15.00, 17.00]$	0.147 ± 0.309	-0.009 ± 0.195	0.030 ± 0.168
$[17.00, 19.00]$	-0.007 ± 0.439	0.022 ± 0.225	0.012 ± 0.202
$c^1_{bkg}(\cos\theta_K)$	low	high	combined
$[0.10, 0.98]$	1.000 ± 0.000	0.774 ± 0.233	0.882 ± 0.207
$[1.10, 2.50]$	0.371 ± 0.335	0.997 ± 1.154	0.853 ± 0.200
$[2.50, 4.00]$	0.901 ± 0.457	0.801 ± 0.159	0.831 ± 0.153
$[4.00, 6.00]$	0.512 ± 0.260	0.791 ± 0.190	0.727 ± 0.158
$[6.00, 8.00]$	0.902 ± 0.263	0.992 ± 0.619	0.961 ± 0.231
$[11.00, 12.50]$	0.681 ± 0.296	0.566 ± 0.200	0.620 ± 0.170
$[15.00, 17.00]$	0.405 ± 0.366	0.240 ± 0.228	0.351 ± 0.196
$[17.00, 19.00]$	0.341 ± 0.420	0.243 ± 0.231	0.271 ± 0.201
$c^2_{bkg}(\cos\theta_K)$	low	high	combined
$[0.10, 0.98]$	0.342 ± 0.310	0.312 ± 0.148	0.322 ± 0.127
$[1.10, 2.50]$	0.398 ± 0.247	0.622 ± 0.268	0.588 ± 0.093
$[2.50, 4.00]$	0.507 ± 0.218	0.493 ± 0.097	0.503 ± 0.085
$[4.00, 6.00]$	0.240 ± 0.226	0.565 ± 0.099	0.509 ± 0.092
$[6.00, 8.00]$	0.517 ± 0.162	0.508 ± 0.112	0.506 ± 0.085
$[11.00, 12.50]$	0.290 ± 0.167	0.549 ± 0.139	0.434 ± 0.107
$[15.00, 17.00]$	0.316 ± 0.274	-0.303 ± 0.211	-0.102 ± 0.171
$[17.00, 19.00]$	0.280 ± 0.330	0.185 ± 0.174	0.207 ± 0.153

Table 54: Sensitivity study on the angular observables with an upper B^+ mass window at $6000\,\mathrm{MeV}/c^2$ using 1000 toy event samples. Comparison with results of Table 55 are shown no difference, more details in the text.

q^2 bin	0	1	2	3	4	5	6	7
S_{1s}	0.0801	0.1746	0.1697	0.0925	0.0769	0.0737	0.0626	0.0848
S_3	0.1253	0.2226	0.2231	0.1545	0.1187	0.1253	0.1138	0.1725
S_4	0.1800	0.2986	0.2849	0.1940	0.1586	0.1530	0.1311	0.1934
S_5	0.1436	0.2412	0.2476	0.1737	0.1405	0.1421	0.1160	0.1765
S_{6s}	0.1792	0.2737	0.2594	0.1525	0.1224	0.1228	0.1089	0.1642
S_7	0.1315	0.2406	0.2401	0.1779	0.1497	0.1338	0.1234	0.1730
S_8	0.1787	0.2908	0.2807	0.1845	0.1523	0.1429	0.1331	0.1830
S_9	0.1194	0.2449	0.2217	0.1498	0.1295	0.1273	0.1162	0.1754

Table 55: Sensitivity study on the angular observables with an upper B^+ mass window at $7000\,\mathrm{MeV}/c^2$ using 1000 toy event samples. Comparison with results of Table 54 are shown no difference, more details in the text.

q^2 bin	0	1	2	3	4	5	6	7
S_{1s}	0.0814	0.1650	0.1659	0.0926	0.0748	0.0738	0.0613	0.0847
S_3	0.1219	0.2084	0.2229	0.1479	0.1225	0.1205	0.1119	0.1681
S_4	0.1812	0.3095	0.2817	0.1968	0.1562	0.1463	0.1379	0.1962
S_5	0.1435	0.2403	0.2349	0.1712	0.1406	0.1419	0.1222	0.1798
S_{6s}	0.1776	0.2739	0.2604	0.1492	0.1257	0.1244	0.1122	0.1618
S_7	0.1365	0.2393	0.2419	0.1757	0.1436	0.1368	0.1182	0.1860
S_8	0.1690	0.2990	0.2801	0.1936	0.1431	0.1366	0.1361	0.1872
S_9	0.1205	0.2284	0.2275	0.1584	0.1249	0.1231	0.1081	0.1796

7 Results

After selection and fitting, the resulting values of the angular analysis of $B^+ \to K^{*+}\mu^+\mu^-$ with $K^{*+} \to K^0_S\pi^+$ are presented in the following sections. Not only the likelihood fit with S_x and $P_x^{(\prime)}$ angular observables, but also the method of moments results are listed. Prior to unblinding of the final results of the angular observables, different cross-checks are performed.

7.1 Pre-unblinding cross-checks

In agreement with the review referees and as introduced in Section 1.2, the following cross-checks between different sub-sets (methods) of the full dataset are performed. Each step is communicated with the referees and possible measured are discussed.
The cross-checks are performed in the following order for both sets of angular observables:

1) Method of moments compared to Likelihood fit (only S observables)

2) Polarity comparison: magnet down versus magnet up sub-samples

3) Run I compared to Run II

4) `DD` tracks compared to `LL` tracks sub-sets

From all converged fits to the two sub-samples (methods), the deviations between all parameters in all q^2 bins are calculated as follows

$$\chi^2 = \frac{S_{x,a} - S_{x,b}}{\sqrt{\sigma_a^2 + \sigma_b^2}} \tag{44}$$

with the two sub-set indices a and b. A maximum of $N = 64$ deviations can be obtained per test, mean 8 parameter in 8 q^2 bins.
The deviations are added up to a total χ^2

$$\chi^2_{tot} = \sum_{i=0}^{N} \chi^2_i \tag{45}$$

and a p-value is determined for a hypothesis test using a test statistic distribution of χ^2, that is obtained from toy event fits. The null hypothesis, meaning that the two sub-samples (methods) agree, is rejected for p-values below 0.05. For p-values below 0.05, the alternative hypothesis (the two sub-samples (methods) do not agree) is accepted.
If the null hypothesis is false the following investigations will be performed:

1) Consider the reference channel for the same cross-check

2) Repeat the comparison using the method of moments[11]

3) Further toy studies might help to find the source of the dis-agreement

[11] In the case of likelihood fit versus method of moments comparison, the cross-check can be repeated in different sub-samples, like in magnet down or magnet up. This however might need a different q^2 binning scheme to guarantee the fit convergence.

7.1.1 Toy studies with halved event statistics

During the attempts to demonstrate - using toy studies with statistics half of the expected event numbers - that a fit to the sub-sample gives reasonable result, we had to discard the ideas of comparing sub-samples of the already very limited statistics. The fits to sub-samples are not suitable for pre-unblinding comparisons, as Tables 56 and 57 show the mean positions and widths of the pull distributions. Especially the uncertainties are significantly over-covering in many cases. In addition, the percentage of non-converged fits on toy samples with half statistics is above 50% for q^2 bins with lowest occupancy, mainly bin 2 and 3.
The pre-unblinding strategy is therefore adjusted to only compare the two methods - likelihood fit and methods of moments - in the granularity of eight q^2 bins. Magnet polarity comparisons, `DD` tracks and `LL` tracks comparisons and Run I versus Run II comparisons are evaluated on the two larger q^2 bins.

Table 56: Mean position of the pull distribution of toy event studies with statistics equal to half the estimated event yields. The mean positions (together with the widths in Table 57) of the pull distributions show, that the splitting of the dataset to compare both half for a pre-unblinding study does not work.

q^2 bin	0	1	2	3
S_{1s}	-0.1015 ± 0.1248	-0.1592 ± 0.1193	0.2102 ± 0.1137	0.0171 ± 0.0936
S_3	-0.0961 ± 0.1137	0.1464 ± 0.1161	0.0758 ± 0.1086	-0.0900 ± 0.1098
S_4	-0.0660 ± 0.1204	-0.0284 ± 0.0947	-0.1227 ± 0.0911	-0.1787 ± 0.0878
S_5	0.1423 ± 0.1031	-0.0391 ± 0.1034	0.1812 ± 0.0939	-0.0044 ± 0.1018
S_{6s}	0.1718 ± 0.1117	0.1651 ± 0.1387	0.3546 ± 0.1063	0.0412 ± 0.1023
S_7	-0.0856 ± 0.1074	0.1220 ± 0.0995	-0.0076 ± 0.0968	0.0426 ± 0.1063
S_8	0.0292 ± 0.1023	0.1531 ± 0.1158	-0.0605 ± 0.1036	0.2404 ± 0.0965
S_9	0.0246 ± 0.1043	0.0256 ± 0.1188	0.0511 ± 0.1144	-0.0979 ± 0.0970
q^2 bin	4	5	6	7
S_{1s}	0.0131 ± 0.0961	0.1301 ± 0.1104	-0.0106 ± 0.1154	0.0062 ± 0.1221
S_3	-0.0619 ± 0.1006	0.1468 ± 0.1105	0.0891 ± 0.1001	0.3917 ± 0.1178
S_4	-0.0492 ± 0.1121	-0.2044 ± 0.0928	0.0333 ± 0.1026	0.2598 ± 0.1124
S_5	0.1368 ± 0.0986	0.2994 ± 0.1189	-0.0700 ± 0.1060	-0.1016 ± 0.1221
S_{6s}	-0.0919 ± 0.1021	-0.0809 ± 0.1048	-0.2532 ± 0.1081	-0.1012 ± 0.1085
S_7	0.0805 ± 0.0866	0.1056 ± 0.0983	0.0342 ± 0.0940	-0.0490 ± 0.1006
S_8	-0.0874 ± 0.1102	0.1409 ± 0.0979	0.0346 ± 0.1115	-0.1065 ± 0.1104
S_9	0.0467 ± 0.0900	-0.1864 ± 0.1054	-0.0507 ± 0.1143	0.1282 ± 0.1284

Table 57: Width of the pull distribution of toy event studies with statistics equal to half the estimated event yields. The widths (together with the mean positions in Table 56) of the pull distributions show, that the splitting of the dataset to compare both half for a pre-unblinding study does not work.

q^2 bin	0	1	2	3
S_{1s}	1.1968 ± 0.0884	1.1000 ± 0.0844	1.0730 ± 0.0805	0.8928 ± 0.0662
S_3	1.0845 ± 0.0804	1.0449 ± 0.0821	0.9659 ± 0.0768	1.0241 ± 0.0776
S_4	1.2161 ± 0.0854	0.8685 ± 0.0670	0.8198 ± 0.0644	0.8645 ± 0.0621
S_5	1.0360 ± 0.0729	0.9812 ± 0.0731	0.8911 ± 0.0664	1.0230 ± 0.0719
S_{6s}	1.1170 ± 0.0790	1.0293 ± 0.0981	0.9271 ± 0.0752	0.9968 ± 0.0723
S_7	1.0846 ± 0.0760	0.9332 ± 0.0703	0.9282 ± 0.0684	1.0627 ± 0.0751
S_8	0.9762 ± 0.0723	0.9967 ± 0.0819	0.9213 ± 0.0733	0.9005 ± 0.0683
S_9	1.0585 ± 0.0738	1.0221 ± 0.0840	1.0730 ± 0.0809	0.9697 ± 0.0686
q^2 bin	4	5	6	7
S_{1s}	0.9170 ± 0.0680	1.0595 ± 0.0781	1.1071 ± 0.0817	1.1582 ± 0.0864
S_3	0.9598 ± 0.0711	1.0601 ± 0.0782	0.9599 ± 0.0708	1.0985 ± 0.0833
S_4	1.1324 ± 0.0793	0.9420 ± 0.0656	1.0317 ± 0.0726	1.0900 ± 0.0795
S_5	0.9861 ± 0.0697	1.1828 ± 0.0843	1.0761 ± 0.0750	1.1588 ± 0.0865
S_{6s}	1.0164 ± 0.0722	1.0373 ± 0.0741	1.0977 ± 0.0765	1.0121 ± 0.0767
S_7	0.8834 ± 0.0612	1.0076 ± 0.0695	0.9637 ± 0.0665	1.0162 ± 0.0711
S_8	1.0456 ± 0.0779	0.9389 ± 0.0692	1.0696 ± 0.0788	1.0238 ± 0.0781
S_9	0.9184 ± 0.0637	1.0800 ± 0.0746	1.1709 ± 0.0809	1.2834 ± 0.0913

7.1.2 Likelihood fit versus method of moments

The actual results from the likelihood fit are compared to the results from the method of moments. Both methods use the same full dataset of the signal decay and are therefore correlated. The test statistics for the statistical evaluation of the discrepancy between method of moments and the likelihood fit are given in Fig. 71. The comparison between data and the toy event test statistic will be done using χ^2_{tot}, even though we see a slightly lower number of degrees of freedom in the toy test statistics, with an average of about 60 (compared to the 63 in data). The slightly lower numbers in the number of degrees of freedom is the result of few toy event fits not properly converging with a correct fit status from the HESSE error calculations.
Taking χ^2_{tot} however is seen as the more conservative approach as compared to the usage of the reduced $\chi^2_{tot}/d.o.f.$.

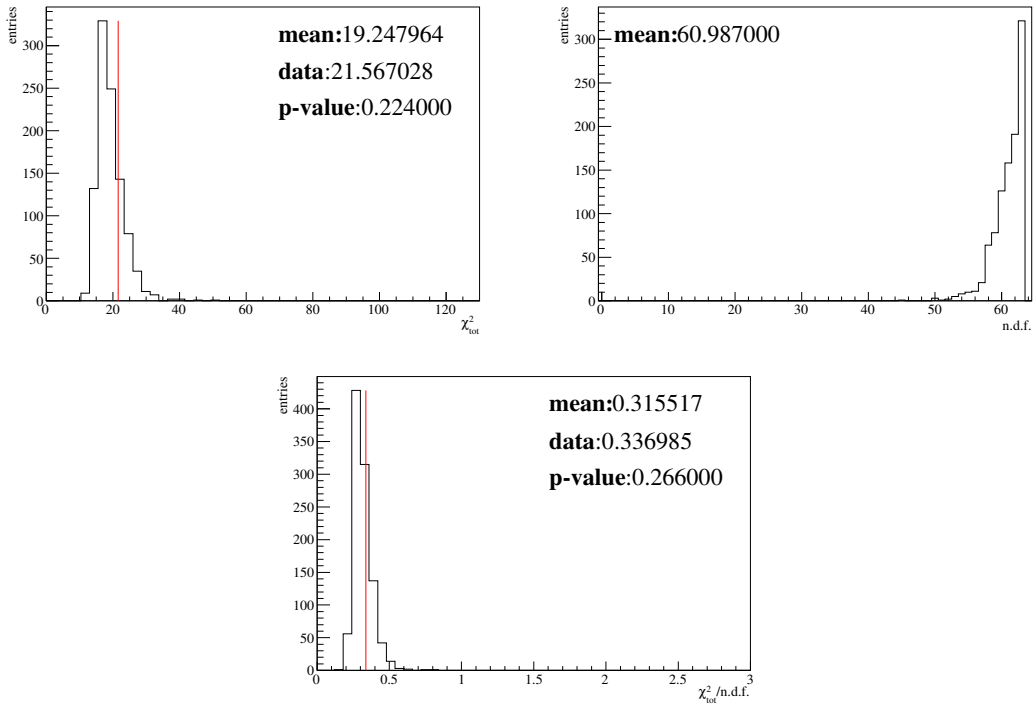

Figure 71: Distribution of the χ^2_{tot} (as defined in Eq. (44)) for 1000 toy event samples. The degree of freedoms may slightly vary, if individual fits did not converge. Using the value for χ^2_{tot} obtained in data, the p-value is determined by the fraction of toy results with a larger χ^2_{tot} than in data. Details in the text.

7.1.3 Magnet down versus up

For this cross-check, Run I and Run II are fitted individually in two large q^2 bins. Other than before, all four PDFs are fitted simultaneously. Again, toy event studies are used to determine the total χ^2 distribution for two datasets with agreeing underlying distributions. The total χ^2 along with the number of degrees of freedom, which represents the number of successfully converged fits, and the reduced total χ^2 are shown in Fig. 73.

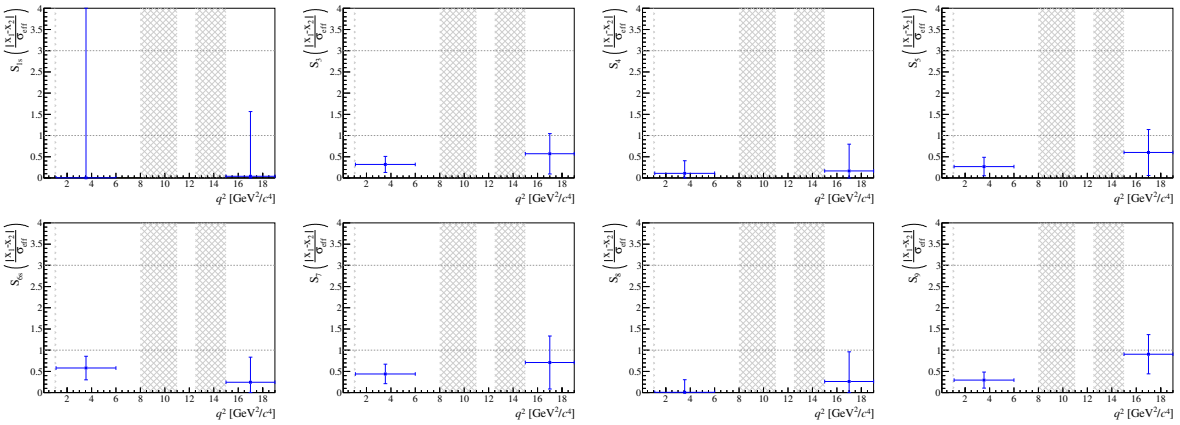

Figure 72: Deviations (as defined in Eq. (44)) for all eight angular observables in the S-basis between results from dataset split up by the magnet polarity into magnet down and magnet up. These deviations are statistically evaluated in Fig. 73.

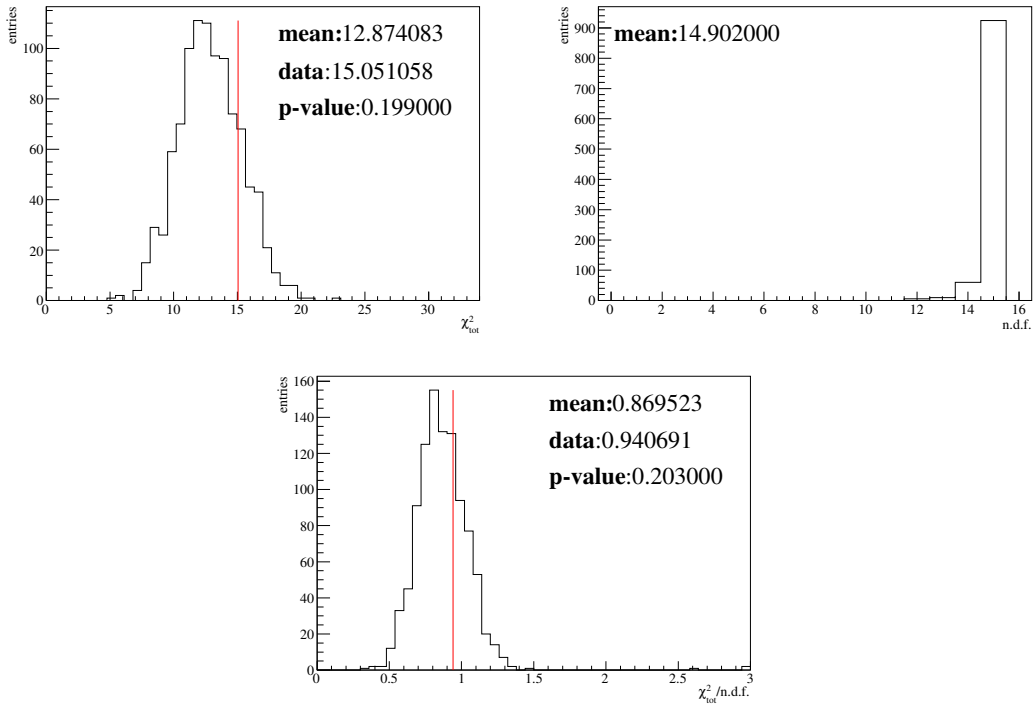

Figure 73: Distribution of the χ^2_{tot} (as defined in Eq. (44)) for 1000 toy event samples of the two magnet polarities for the S angular observables. The degree of freedoms may slightly vary, if individual fits did not converge. Using the value for χ^2_{tot} obtained in data, the p-value is determined by the fraction of toy results with a larger χ^2_{tot} than seen in the data fit.

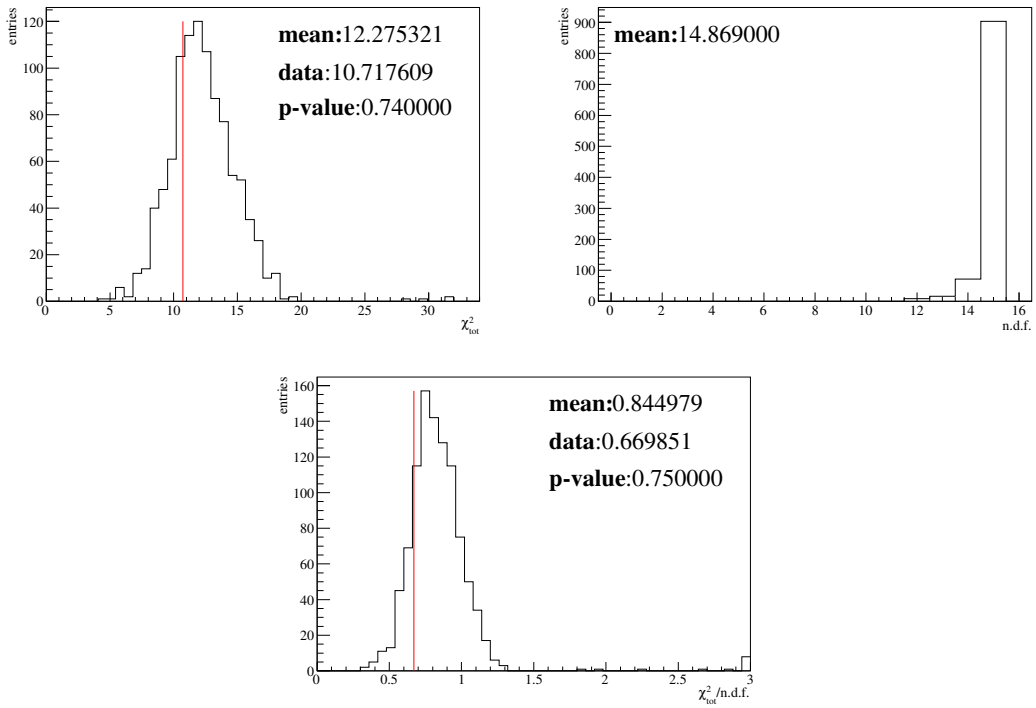

Figure 74: Distribution of the χ^2_{tot} (as defined in Eq. (44)) for 1000 toy event samples of the two magnet polarities for the P' angular observables. The degree of freedoms may slightly vary, if individual fits did not converge. Using the value for χ^2_{tot} obtained in data, the p-value is determined by the fraction of toy results with a larger χ^2_{tot} than seen in the data fit.

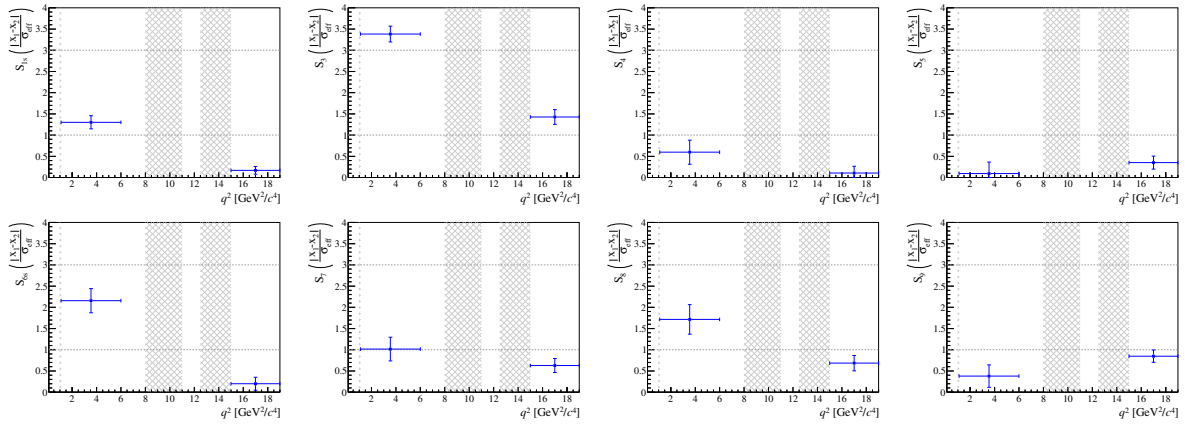

Figure 75: Deviations (as defined in Eq. (44)) for all eight angular observables in the S-basis between results from dataset split up by the magnet polarity into magnet down and magnet up. These deviations are statistically evaluated in Fig. 73.

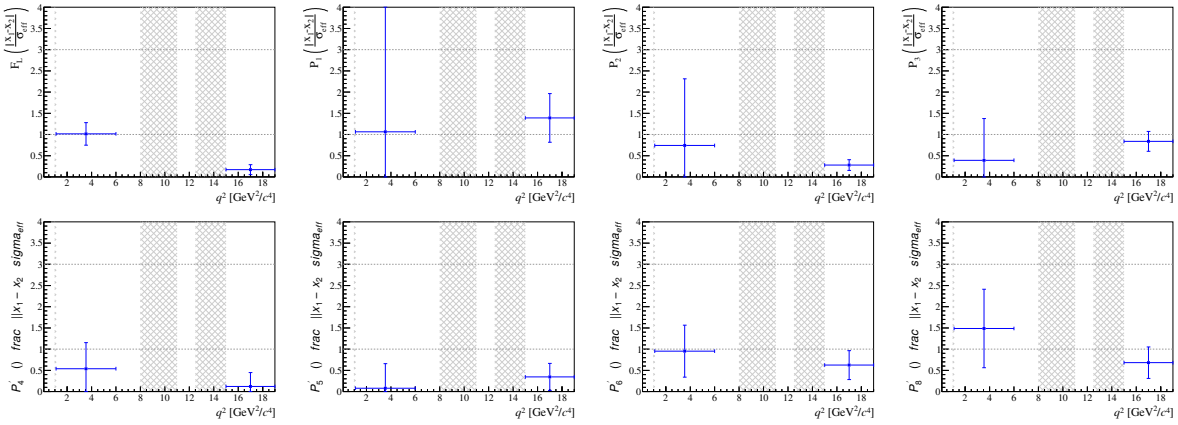

Figure 76: Deviations (as defined in Eq. (44)) for all eight angular observables in the P'-basis between results from dataset split up by the magnet polarity into magnet down and magnet up. These deviations are statistically evaluated in Fig. 74.

7.1.4 Run I versus Run II

For this cross-check, Run I and Run II are fitted individually in two large q^2 bins. Only two PDFs are fitted simultaneously (DD tracks and LL tracks), which also reduces the number of free parameters in the fit. Again, toy event studies are used to determine the total χ^2 distribution for two datasets with agreeing underlying distributions. The total χ^2 along with the number of degrees of freedom, which represents the number of successfully converged fits, and the reduced total χ^2 are shown in Fig. 77.

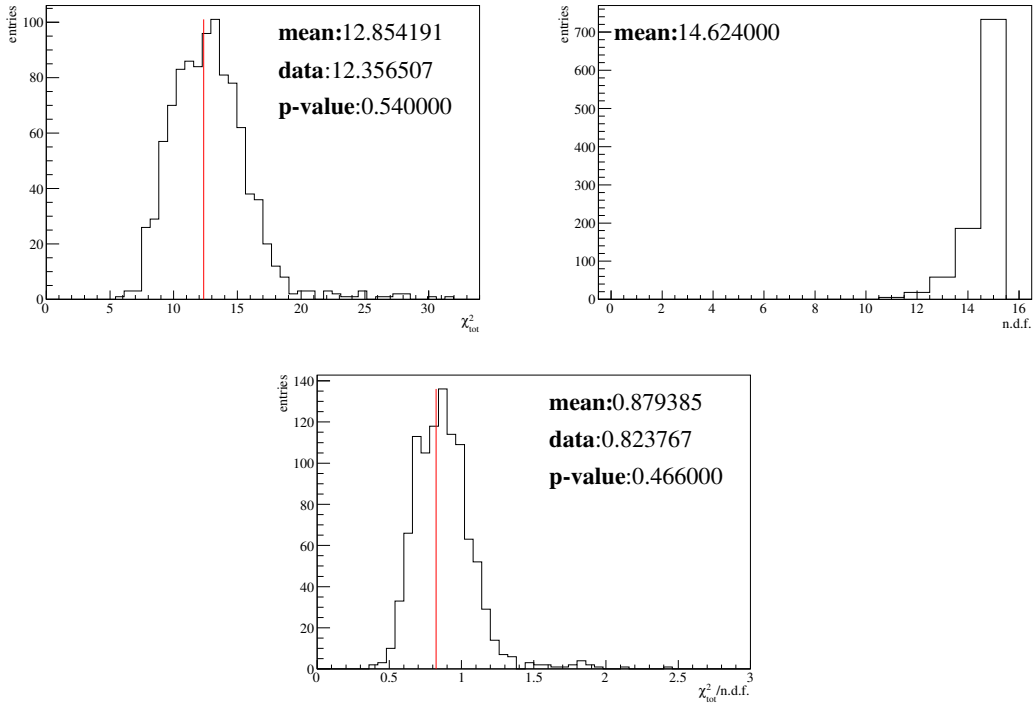

Figure 77: Distribution of the χ^2_{tot} (as defined in Eq. (44)) for 1000 toy event samples of Run I versus Run II comparisons for the S angular observables. The degree of freedoms may slightly vary, if individual fits did not converge. Using the value for χ^2_{tot} obtained in data, the p-value is determined by the fraction of toy results with a larger χ^2_{tot} than seen in the data fit.

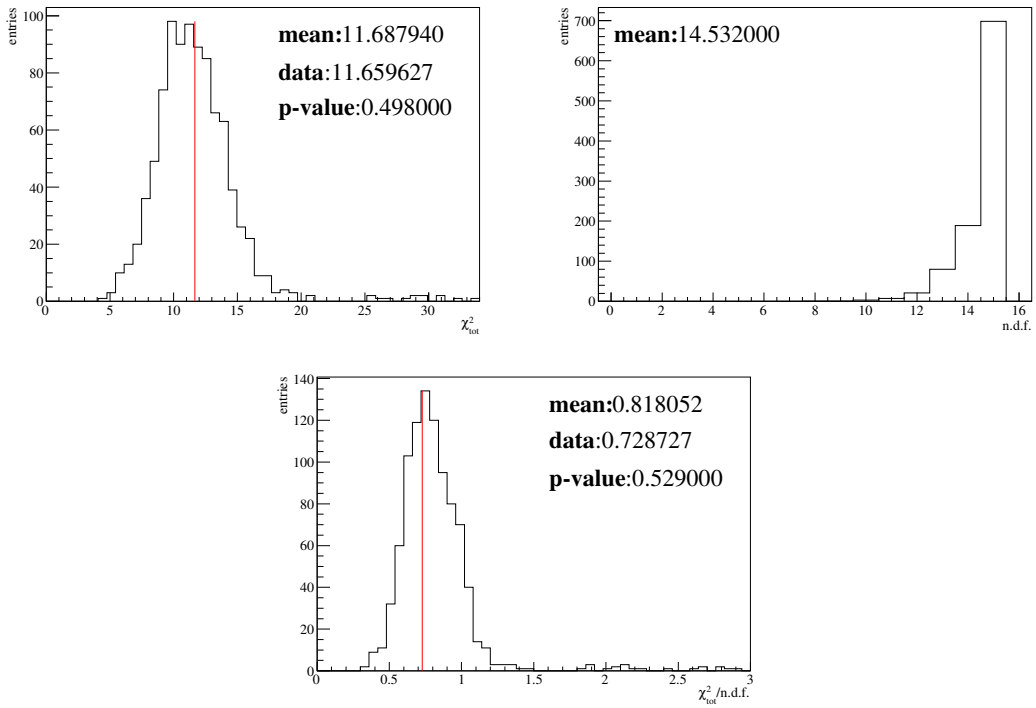

Figure 78: Distribution of the χ^2_{tot} (as defined in Eq. (44)) for 1000 toy event samples of Run I versus Run II comparisons P' angular observables. The degree of freedoms may slightly vary, if individual fits did not converge. Using the value for χ^2_{tot} obtained in data, the p-value is determined by the fraction of toy results with a larger χ^2_{tot} than seen in the data fit.

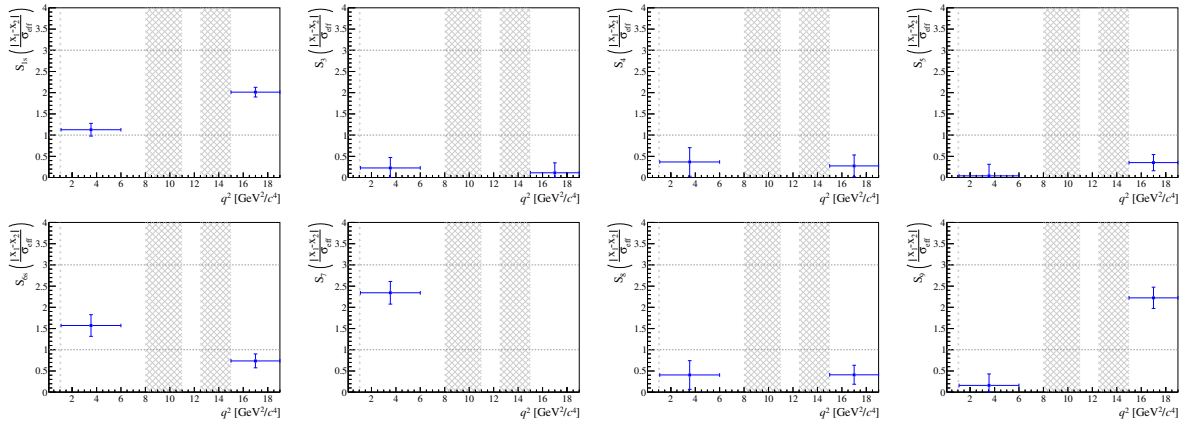

Figure 79: Deviations (as defined in Eq. (44)) for all eight angular observables in the S-basis between results from the Run I dataset and from the Run II dataset. These deviations are statistically evaluated in Fig. 77.

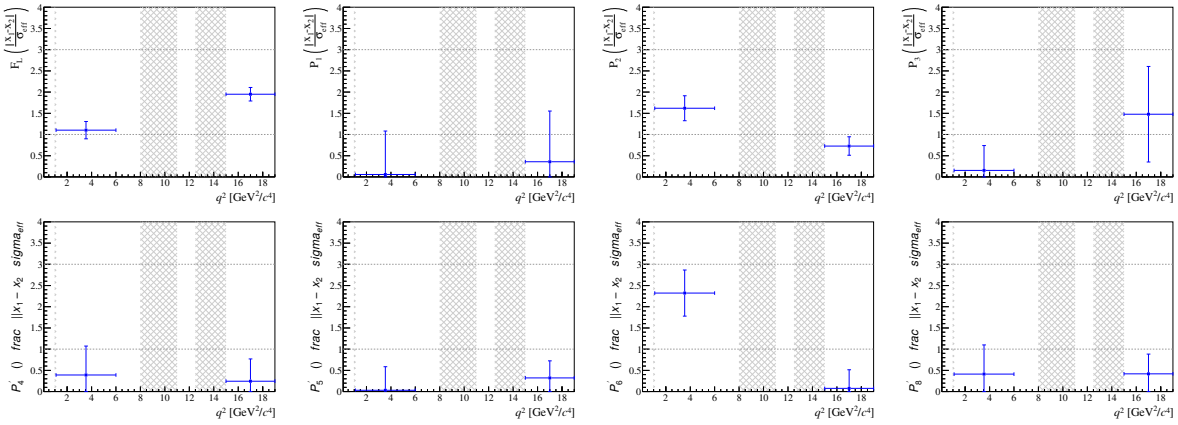

Figure 80: Deviations (as defined in Eq. (44)) for all eight angular observables in the P'-basis between results from the Run I dataset and from the Run II dataset. These deviations are statistically evaluated in Fig. 78.

7.1.5 DD tracks versus LL tracks

For this cross-check, DD tracks and LL tracks are fitted individually in two large q^2 bins. Only two PDFs are fitted simultaneously (Run I and Run II), which also reduces the number of free parameters in the fit. As before, toy event studies are used to determine the total χ^2 distribution for two datasets with agreeing underlying distributions. The total χ^2 along with the number of degrees of freedom, which represents the number of successfully converged fits, and the reduced total χ^2 are shown in Fig. 81.

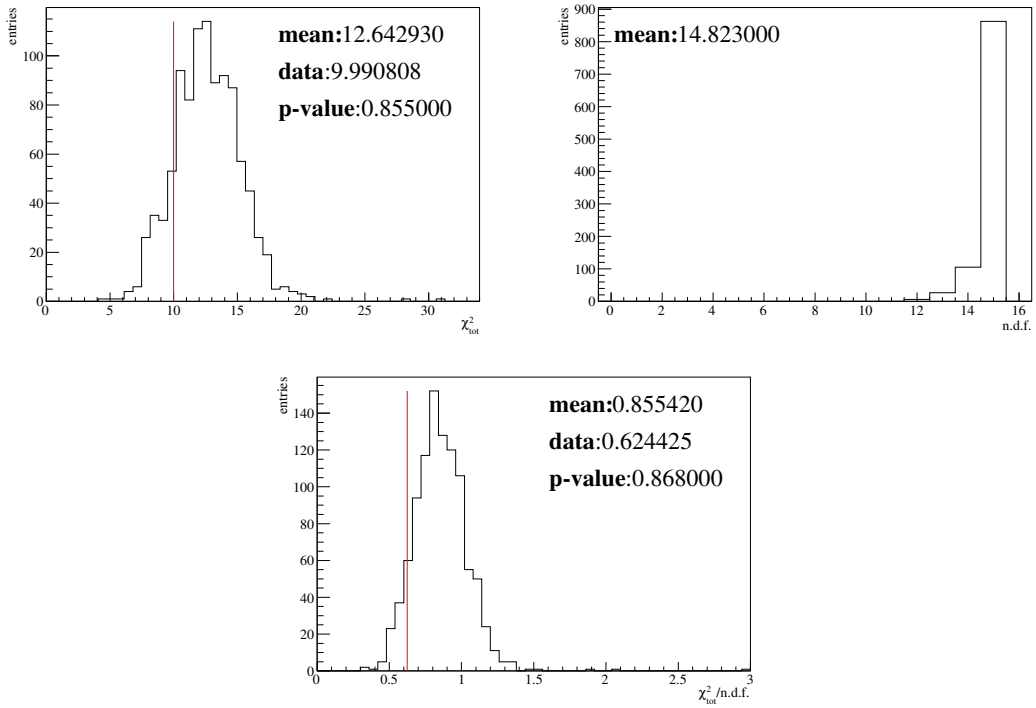

Figure 81: Distribution of the χ^2_{tot} (as defined in Eq. (44)) for 1000 toy event samples of DD tracks versus LL tracks comparisons for the S angular observables. The degree of freedoms may slightly vary, if individual fits did not converge. Using the value for χ^2_{tot} obtained in data, the p-value is determined by the fraction of toy results with a larger χ^2_{tot} than seen in the data fit.

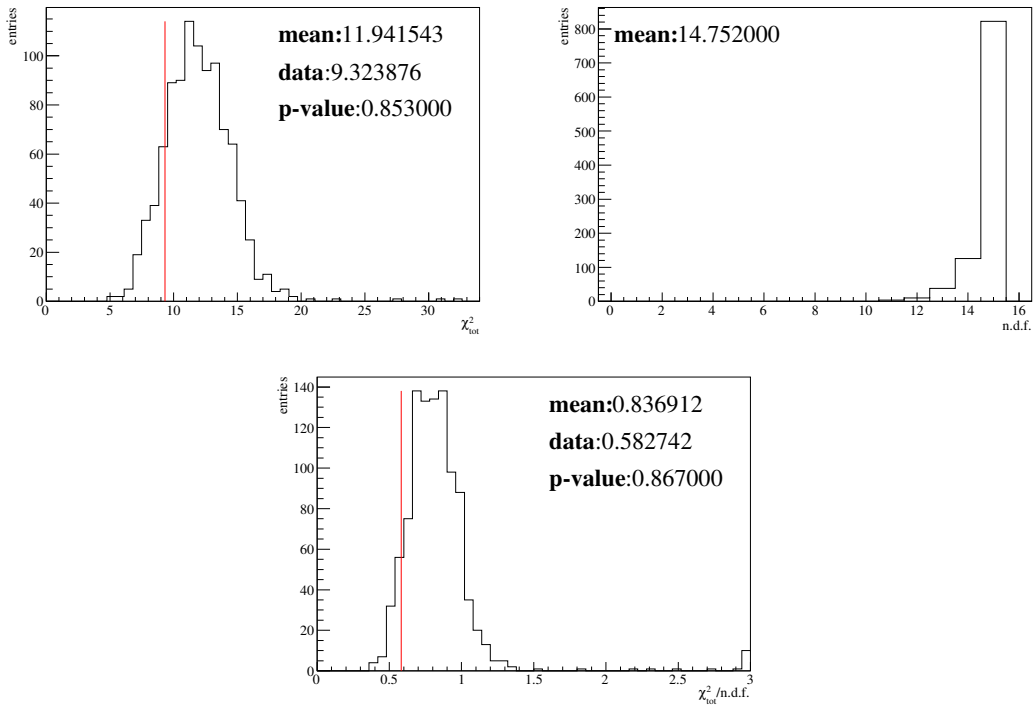

Figure 82: Distribution of the χ^2_{tot} (as defined in Eq. (44)) for 1000 toy event samples of DD tracks versus LL tracks comparisons for the P' angular observables. The degree of freedoms may slightly vary, if individual fits did not converge. Using the value for χ^2_{tot} obtained in data, the p-value is determined by the fraction of toy results with a larger χ^2_{tot} than seen in the data fit.

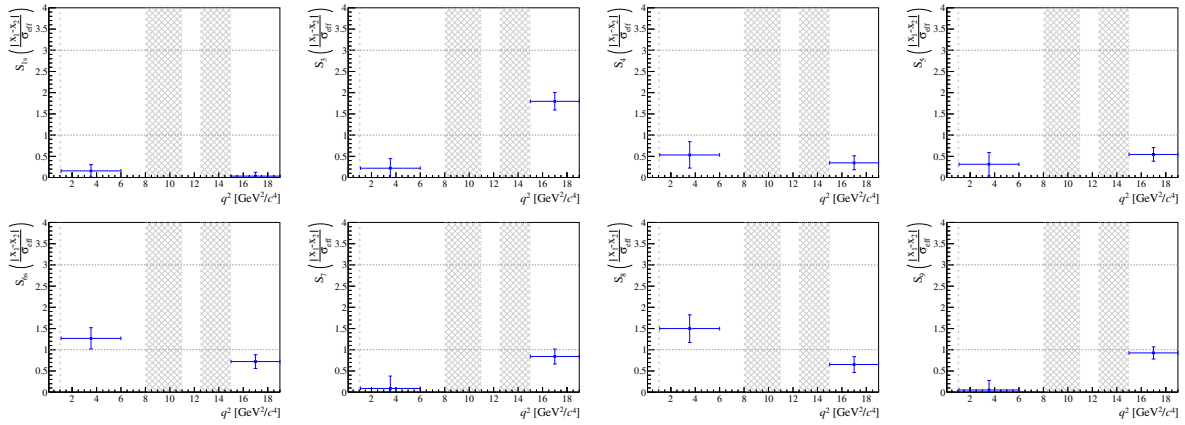

Figure 83: Deviations (as defined in Eq. (44)) for all eight angular observables in the S-basis between results from the DD tracks dataset and from the LL tracks dataset. These deviations are statistically evaluated in Fig. 81.

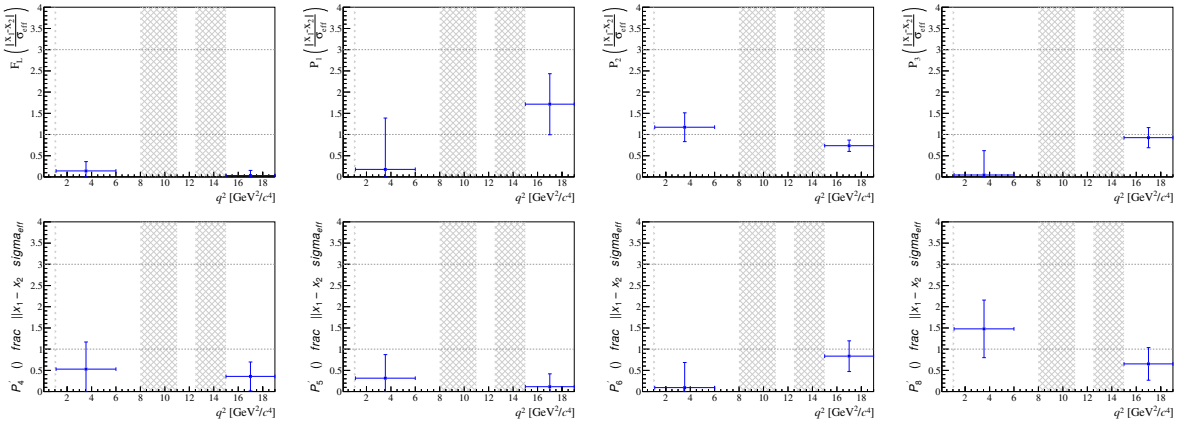

Figure 84: Deviations (as defined in Eq. (44)) for all eight angular observables in the P'-basis between results from the DD tracks dataset and from the LL tracks dataset. These deviations are statistically evaluated in Fig. 82.

7.1.6 Comparisons of the reference channel

All four previously mentioned cross-checks have been performed on the reference channel. The main difference is that no toy event samples are consulted to generate test statistics for the comparison, due to the large statistics of more than 100.000 signal candidates. The large statistic justify the assumption that the differences follow a χ^2 distribution, and hence the p-value can directly be calculated from the χ^2_{tot} and the number of degree of freedom. In Fig. 85, the deviations between every two sub-samples for all eight q^2 bins are shown, together with the resulting p-values. All cross-checks show a p-value larger 0.05, confirming the hypothesis that every two sub-samples have the same underlying distributions.

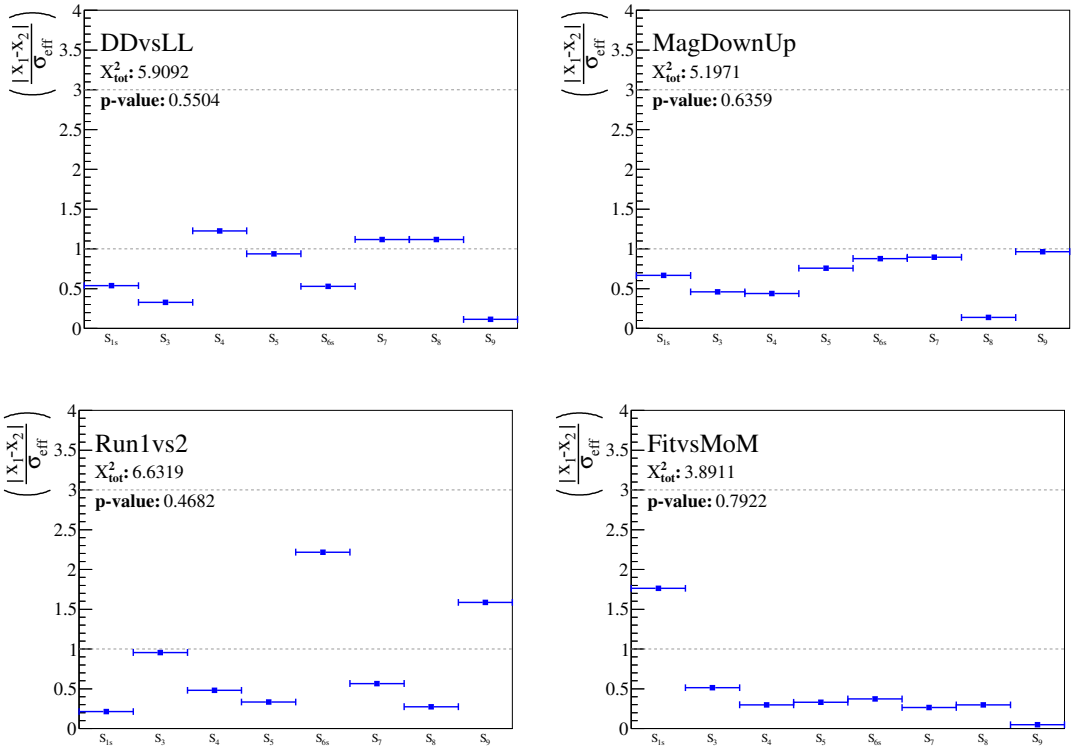

Figure 85: Summary plots for the deviations in terms of sigma (as defined in Eq. (44)) between resulting angular observables from two sub-sets (or extraction methods) using fits to the reference channel data-set. No significant differences are observed and the resulting p-values are above the previously defined threshold for agreement of 0.05.

7.1.7 Summary

The pre-unblinding cross-checks between different sub-samples shows a consistent and good agreement for all performed tests. In the comparisons between DD/LL, magnet down/up and Run 1/2 for both sets of angular observables as well as the method of moments with the likelihood fit for the S observables, all determined p-values are significantly above the set threshold for agreement of 0.05.
The cross-checks are therefore considered a success.

7.1.8 Mass fits and signal yield

After the blinded result comparison of different sub-samples or different analysis method have been performed, the fit projection in the mass-dimension of the B^+ are unblinded. The projection of the fit are checked for consistency with the underlying event distributions. All fit projections of the 2D fit in the dimension of the invariant mass of the B^+ are shown in Fig. 86. The four sub-sets (Run I and Run II with DD tracks and LL tracks) are added together into one plot to achieve a proper statistics for each q^2 bin and limit the number of plots in this section. The 2D fit uses the option of extended likelihood, in which the signal fraction, f_{sig}, is defined by the ratio of the number of signal candidates, n_{sig}, over the sum of signal and background candidates, $n_{sig} + n_{bkg}$. In addition to the standard PDF, the sum n_{sig} of n_{bkg} is constrained by a Poissonian PDF to the total number of events in the fit. From this method, one gets a reliable number of signal and background events with their corresponding uncertainties.
Table 58 shows the extracted numbers of signal events from all q^2 bins. Compared to the estimated numbers of signal events in Table 19, the total number of events in Table 58 is in good agreement. The number of events in the lowest occupancy bins between 1.1 and 4.0 is lower than expected from the MC extrapolation. The individuals yields per Run dataset and in each q^2 bin are fluctuating and show no sign of a systematic inefficiency in the selection for the low occupancy q^2 region. Additional toy event studies are used to verify that these fluctuations have not impact on the results of the analysis. The observed background numbers are slightly lower than expected from the estimation in Table 19, but the difference of about 10% is acceptable.

Table 58: Combined yield of signal candidates from the final fit for all eight q^2 bins and for the full dataset of combined Run I + II and DD tracks plus LL tracks. Both, signal and background event numbers, are given over the integrated mass range of the B meson, from 5150 MeV/c^2 to 6000 MeV/c^2.

bin	q^2 (GeV$^2/c^4$)	signal events	background events
1	[0.1, 0.98]	101.6 ± 12.4	186.1 ± 15.4
2	[1.1, 2.5]	49.0 ± 9.9	219.2 ± 16.5
3	[2.5, 4.0]	42.2 ± 9.7	274.9 ± 18.1
4	[4.0, 6.0]	108.8 ± 13.4	286.9 ± 19.0
5	[6.0, 8.0]	104.6 ± 13.9	297.7 ± 19.7
6	[11.0, 12.5]	110.6 ± 12.9	170.8 ± 15.0
7	[15.0, 17.0]	144.2 ± 13.4	108.7 ± 12.0
8	[17.0, 19.0]	75.7 ± 9.8	106.0 ± 11.2
	total	736.7 ± 34.1	1650.35 ± 45.6

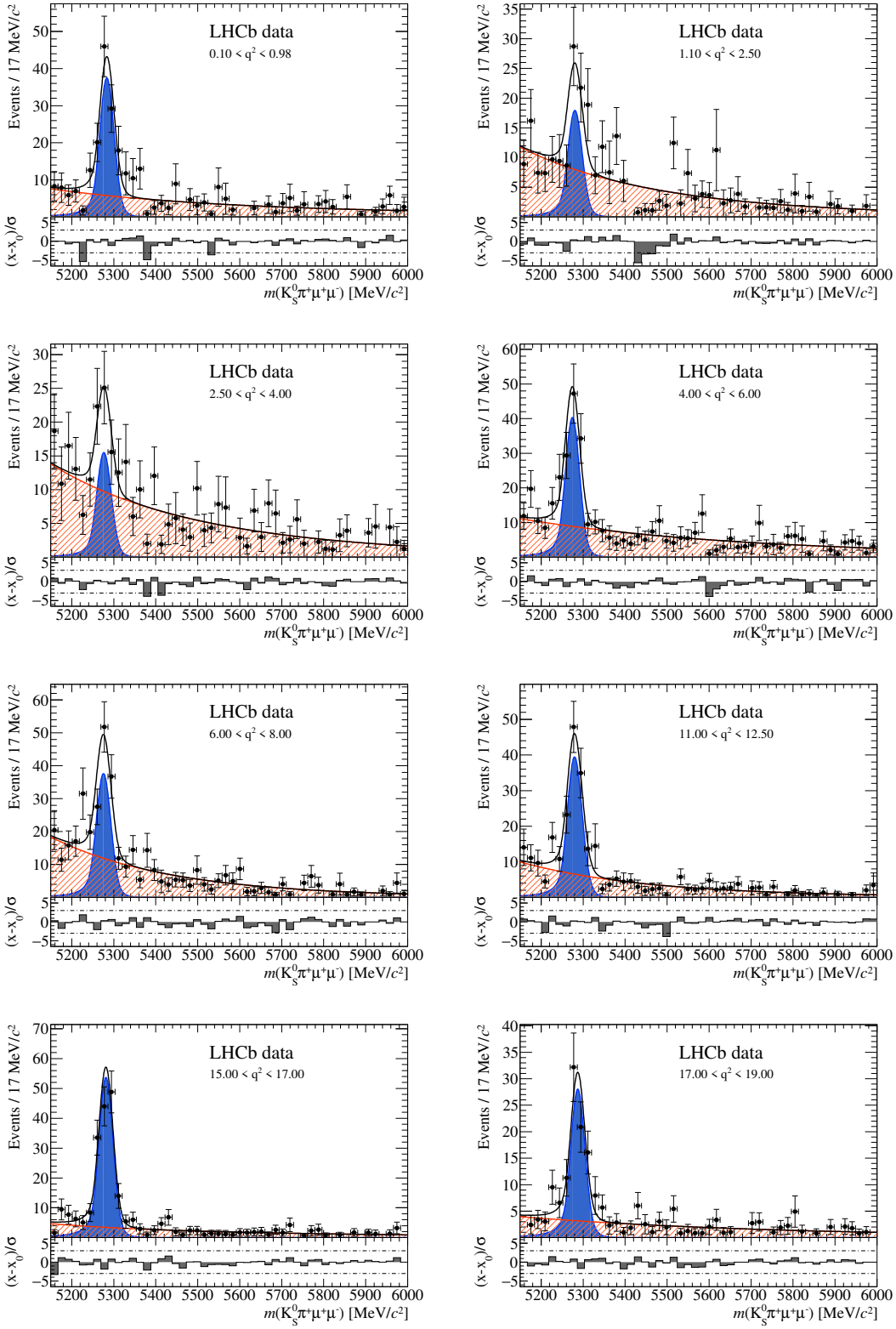

Figure 86: All mass projection of the eight q^2 bins. Shown here are the fit results in the B^+ mass dimension from the 2D fits (which is using an extended likelihood to extract the number of signal and background events). All fit projections look fine. In addition, the projections are identical to the fits from all five foldings. The number of signal candidates are listed in Table 58.

7.2 Results from likelihood fit

In the following, the resulting values from the likelihood fits to the data events are presented for both, the S_x observables in Section 7.2.2 and the $P_x^{(\prime)}$ angular observables in Section 7.2.3. Along with the values, the statistical uncertainties from the Feldman-Cousins scans (see Sections 4.6 and 7.3) and the systematic uncertainties (see Sections 5.13 and 5.14) are stated. In addition, the correlation between all angular parameters (see Section 4.9) of the same basis are shown in the corresponding tables. However, first all fit projections of the angular 4D fit are given in Section 7.2.1. For these projections, the four sub-sets are combined into one projections, in which both the event distributions as well as the fit PDF are added up.

7.2.1 Fit projections of the 4D angular fit

In the following, the fit projections of the invariant mass of the B meson and the three angles, $\cos\theta_K$, $\cos\theta_L$ and ϕ are given for all angular foldings 0 – 4 in Figs. 87 to 91 for the nominal eight q^2 bins. Also, the fit projections of the two larger bins are given in

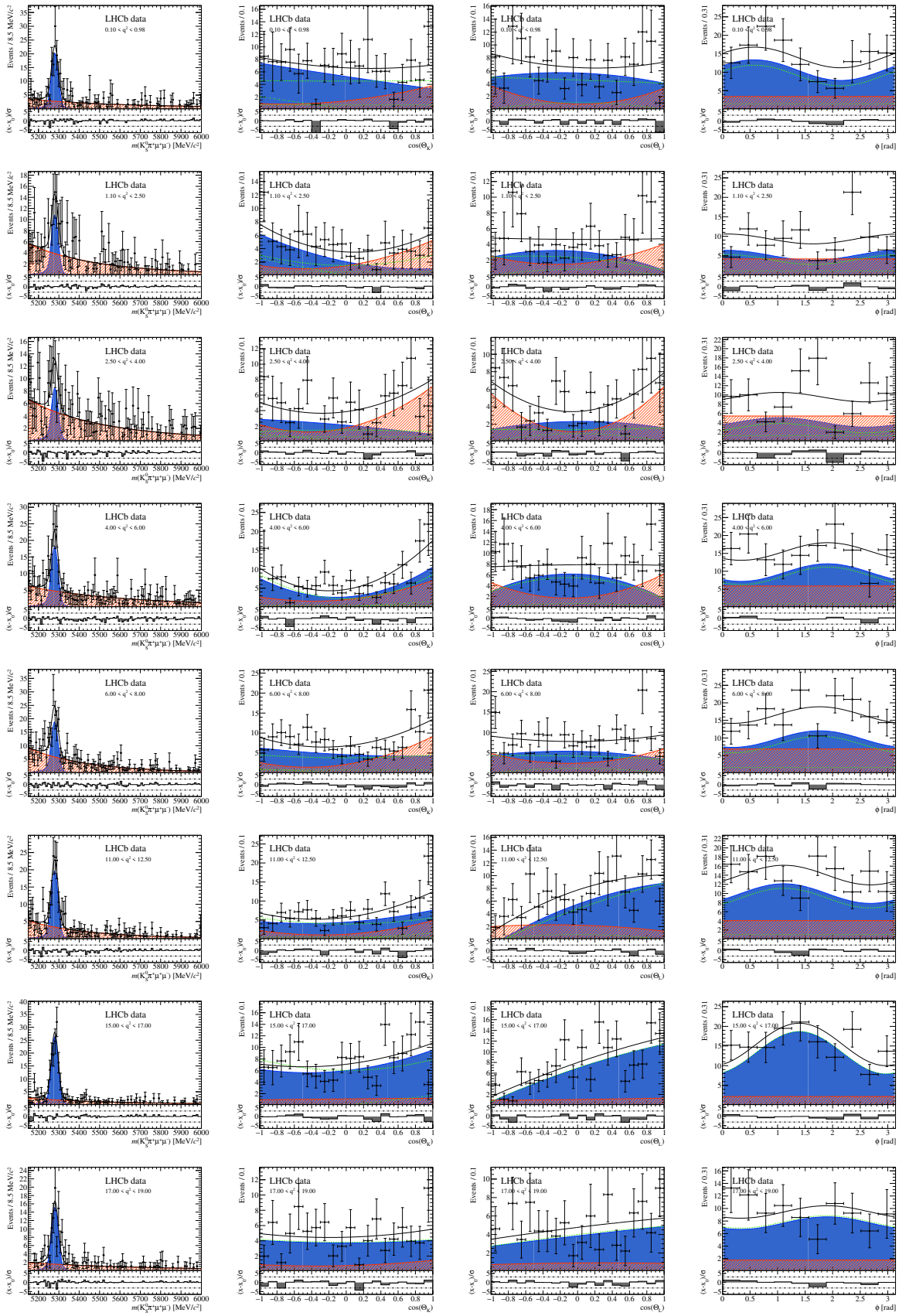

Figure 87: Fit projections using the angular folding 0 in all eight nominal q^2 bins in the four dimensions of the angular fit, m_{B^+} (left), $\cos\theta_K$ (central left), $\cos\theta_L$ (central right) and ϕ (right). The eight rows show the eight q^2 bins. The formerly splitted data-set is recombined for the projections. Signal PDF are shown in blue with background PDF in orange. The total PDF is given by the solid black line. Weighted events are shown in black markers. The angular distributions show only events (and the corresponding PDF) within the signal region of $\pm 50\,\mathrm{MeV}/c^2$ around the measured peak of the B meson mass. Agreement between fit PDF and the underlying event distribution is given by pulls underneath the main histogram.

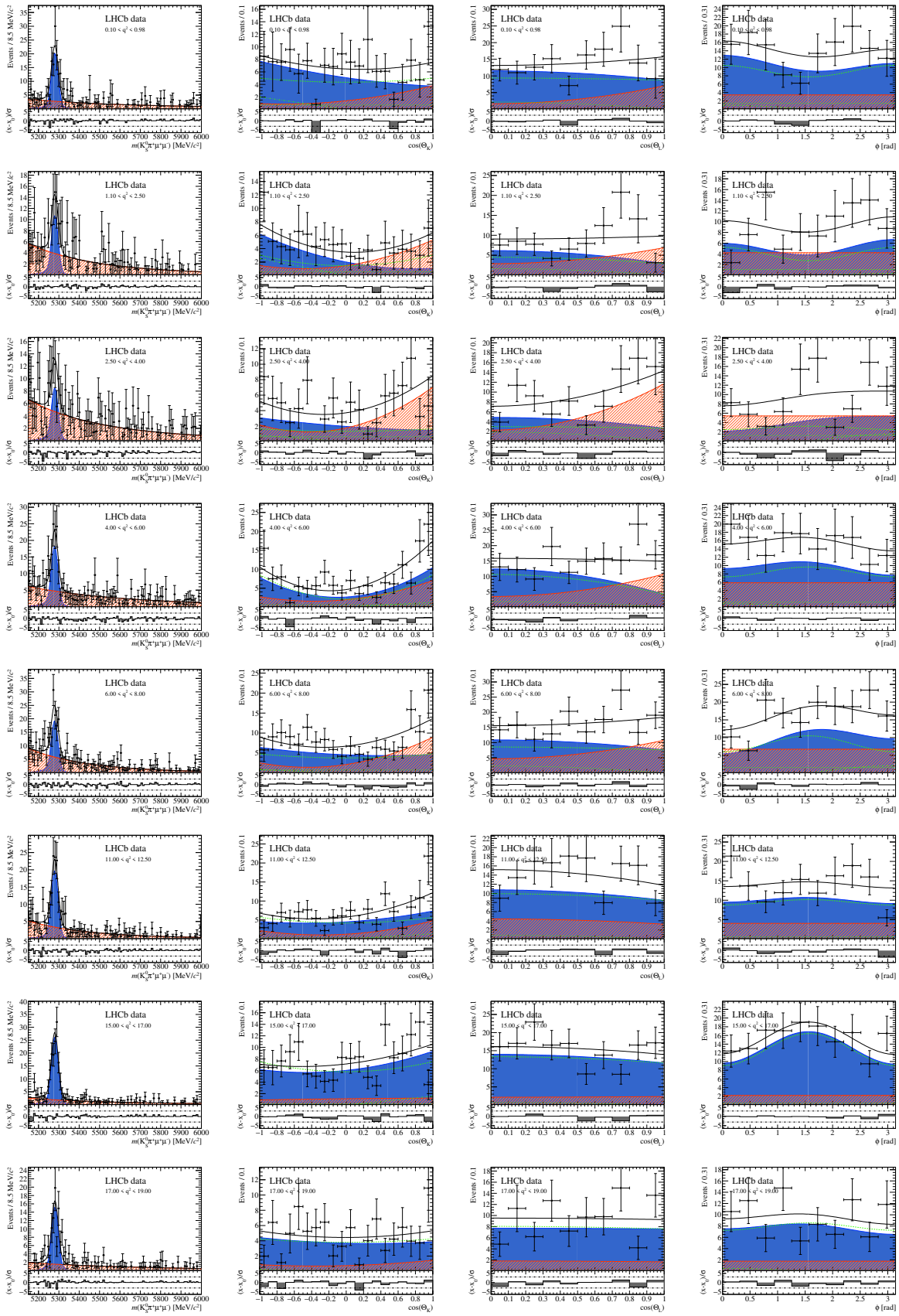

Figure 88: Fit projections using the angular folding 1 in all eight nominal q^2 bins in the four dimensions of the angular fit, m_{B^+} (left), $\cos\theta_K$ (central left), $\cos\theta_L$ (central right) and ϕ (right). The eight rows show the eight q^2 bins. The formerly splitted data-set is recombined for the projections. Signal PDF are shown in blue with background PDF in orange. The total PDF is given by the solid black line. Weighted events are shown in black markers. The angular distributions show only events (and the corresponding PDF) within the signal region of $\pm 50\,\mathrm{MeV}/c^2$ around the measured peak of the B meson mass. Agreement between fit PDF and the underlying event distribution is given by pulls underneath the main histogram.

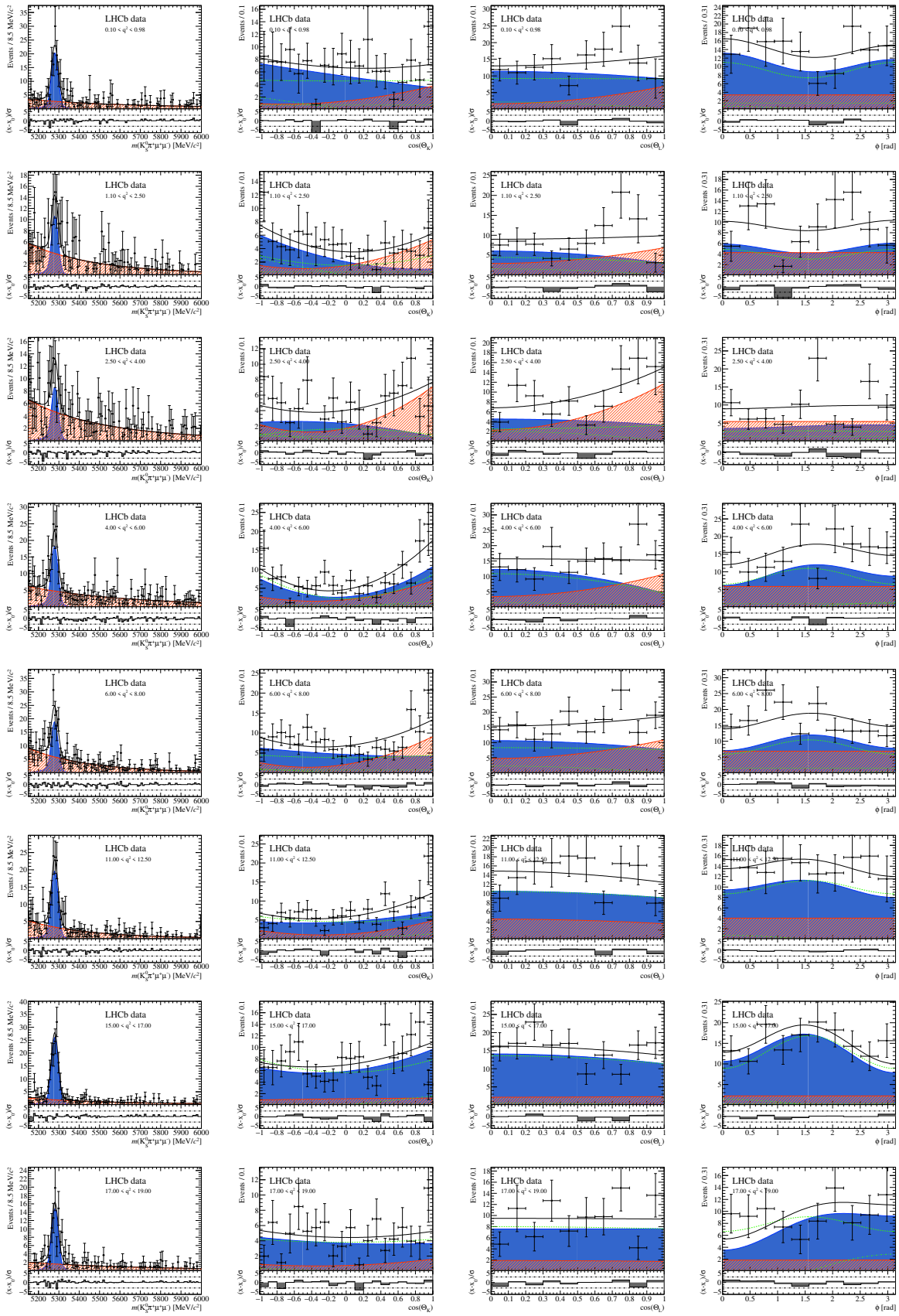

Figure 89: Fit projections using the angular folding 2 in all eight nominal q^2 bins in the four dimensions of the angular fit, m_{B^+} (left), $\cos\theta_K$ (central left), $\cos\theta_L$ (central right) and ϕ (right). The eight rows show the eight q^2 bins. The formerly splitted data-set is recombined for the projections. Signal PDF are shown in blue with background PDF in orange. The total PDF is given by the solid black line. Weighted events are shown in black markers. The angular distributions show only events (and the corresponding PDF) within the signal region of $\pm 50\,\mathrm{MeV}/c^2$ around the measured peak of the B meson mass. Agreement between fit PDF and the underlying event distribution is given by pulls underneath the main histogram.

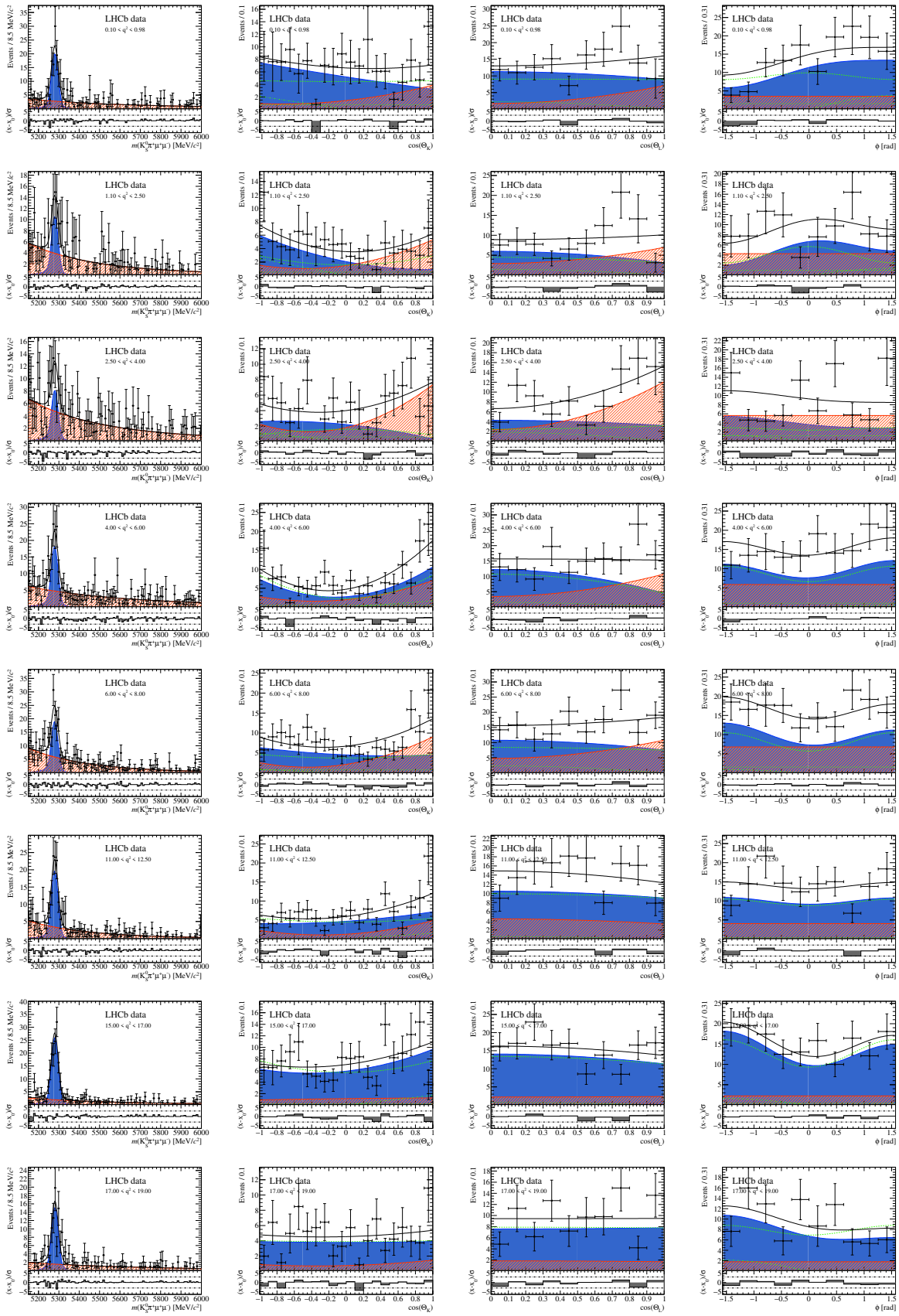

Figure 90: Fit projections using the angular folding 3 in all eight nominal q^2 bins in the four dimensions of the angular fit, m_{B^+} (left), $\cos\theta_K$ (central left), $\cos\theta_L$ (central right) and ϕ (right). The eight rows show the eight q^2 bins. The formerly splitted data-set is recombined for the projections. Signal PDF are shown in blue with background PDF in orange. The total PDF is given by the solid black line. Weighted events are shown in black markers. The angular distributions show only events (and the corresponding PDF) within the signal region of $\pm 50\,\mathrm{MeV}/c^2$ around the measured peak of the B meson mass. Agreement between fit PDF and the underlying event distribution is given by pulls underneath the main histogram.

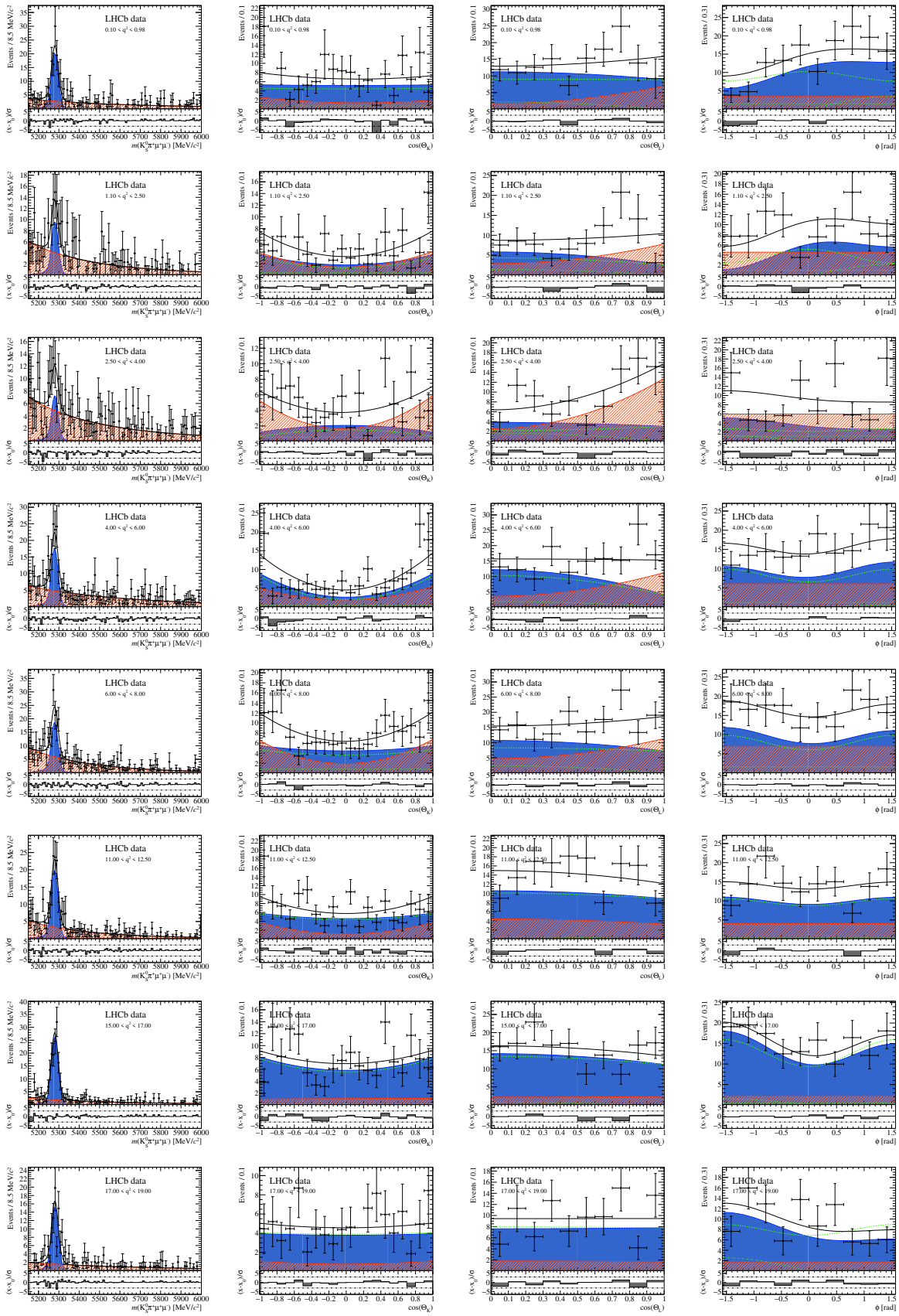

Figure 91: Fit projections using the angular folding 4 in all eight nominal q^2 bins in the four dimensions of the angular fit, m_{B^+} (left), $\cos\theta_K$ (central left), $\cos\theta_L$ (central right) and ϕ (right). The eight rows show the eight q^2 bins. The formerly splitted data-set is recombined for the projections. Signal PDF are shown in blue with background PDF in orange. The total PDF is given by the solid black line. Weighted events are shown in black markers. The angular distributions show only events (and the corresponding PDF) within the signal region of $\pm 50\,\mathrm{MeV}/c^2$ around the measured peak of the B meson mass. Agreement between fit PDF and the underlying event distribution is given by pulls underneath the main histogram.

7.2.2 S_x angular observables

The fits including angular folding techniques to the signal channel data have returned the following values for the angular observables, S_x. In addition to the statistical uncertainty from the Feldman-Cousins scans (see Section 7.3), the systematic uncertainty from Section 5.13 are added to the values. The resulting profiles from the Feldman-Cousins scans for the S_x observables are shown in Figs. 94 to 101 in Section 7.3.
The numeric tables with final results and their statistical and systematic uncertainties are given in Table 59 for all eight plus two extra q^2 bins. The results from the nominal eight q^2 bins are plotted as a function of q^2 for all eight angular observables in Fig. 92. The Feldman-Cousins profile scans revealed a global minimum in the fit of folding 3 in the q^2 region between 1.1–2.5 GeV^2/c^4, which consequently resulted in changing the central value of the result for S_7 in this bin to the new best fit value.
All eight plus two correlation matrices obtained by the bootstrapping (see Section 4.9) of data event samples are given in Tables 60 to 67 and Tables 68 and 69. The correlation matrices obtained by the bootstrapping method are statistically compared to the results from the folded fits. This cross-check is only executable for correlations between observables which are fitted within the same folding. The results show no sign of a bias between the two methods, and the statistical precision is quantified with 11%, which is slightly higher than estimated in Section 4.9. This finding however does not impact the final results of the analysis, as the precision of the correlation matrix is only a qualitative information given in the paper.

Remark on usage of F_L and A_FB: Even though the observables S_{1s} and S_{6s} are measured and investigated throughout the analysis, the results in the paper are given for F_L and A_FB, which are directly correlated to former observables, as defined in Section 3.3.1. This is done to be consistent with previous analyses. Numerical values of the results and their visualisations in figures in the paper are converted from S_{1s} to F_L and from S_{6s} to A_FB. In this document the tabular values for S_{1s} and S_{6s} are given and only the visual presentation of the results in Fig. 92 are converted to F_L and A_FB.

Table 59: Result values of the S_x basis angular observables for all eight nominal and the two larger q^2 bins, the numerically labelled bins are the nominal bins as defined in Table 15 plus the two extra bins. The first uncertainty is of statistical nature coming from the Feldman-Cousins scans and the second is the combined uncertainty from the systematic studies. The values and uncertainties for the nominal eight q^2 bins are plotted in Fig. 92 along with the theoretical predictions.

q^2 [GeV$^2/c^4$]	S_{1s}	S_3	S_4	S_5
$[0.1, 0.98]$	$0.494^{+0.075}_{-0.077} \pm 0.045$	$0.144^{+0.151}_{-0.144} \pm 0.023$	$-0.041^{+0.170}_{-0.161} \pm 0.037$	$0.240^{+0.117}_{-0.148} \pm 0.038$
$[1.1, 2.5]$	$0.345^{+0.134}_{-0.155} \pm 0.048$	$0.368^{+0.972}_{-0.406} \pm 0.027$	$0.288^{+0.342}_{-0.274} \pm 0.034$	$0.440^{+0.377}_{-0.319} \pm 0.048$
$[2.5, 4.0]$	$0.619^{+0.241}_{-0.173} \pm 0.048$	$-0.121^{+0.664}_{-0.389} \pm 0.015$	$-0.392^{+0.476}_{-0.453} \pm 0.038$	$-0.351^{+0.409}_{-0.314} \pm 0.022$
$[4.0, 6.0]$	$0.246^{+0.104}_{-0.087} \pm 0.015$	$-0.204^{+0.157}_{-0.193} \pm 0.013$	$-0.373^{+0.201}_{-0.125} \pm 0.049$	$-0.117^{+0.144}_{-0.186} \pm 0.029$
$[6.0, 8.0]$	$0.457^{+0.155}_{-0.147} \pm 0.010$	$-0.238^{+0.181}_{-0.171} \pm 0.021$	$-0.209^{+0.200}_{-0.183} \pm 0.016$	$-0.070^{+0.159}_{-0.196} \pm 0.018$
$[11.0, 12.5]$	$0.458^{+0.130}_{-0.177} \pm 0.012$	$-0.098^{+0.127}_{-0.127} \pm 0.017$	$-0.307^{+0.142}_{-0.165} \pm 0.023$	$-0.429^{+0.137}_{-0.163} \pm 0.024$
$[15.0, 17.0]$	$0.441^{+0.106}_{-0.158} \pm 0.014$	$-0.259^{+0.122}_{-0.106} \pm 0.026$	$-0.155^{+0.104}_{-0.114} \pm 0.015$	$-0.069^{+0.095}_{-0.100} \pm 0.029$
$[17.0, 19.0]$	$0.493^{+0.079}_{-0.093} \pm 0.019$	$-0.133^{+0.197}_{-0.167} \pm 0.038$	$-0.273^{+0.137}_{-0.154} \pm 0.058$	$-0.318^{+0.158}_{-0.338} \pm 0.042$
$[1.1, 6.0]$	$0.307^{+0.065}_{-0.071} \pm 0.019$	$-0.103^{+0.109}_{-0.108} \pm 0.009$	$-0.200^{+0.126}_{-0.137} \pm 0.027$	$-0.036^{+0.120}_{-0.122} \pm 0.021$
$[15.0, 19.0]$	$0.453^{+0.082}_{-0.098} \pm 0.021$	$-0.212^{+0.095}_{-0.085} \pm 0.029$	$-0.191^{+0.100}_{-0.132} \pm 0.058$	$-0.118^{+0.075}_{-0.073} \pm 0.025$
q^2 [GeV$^2/c^4$]	S_{6s}	S_7	S_8	S_9
$[0.1, 0.98]$	$-0.067^{+0.154}_{-0.163} \pm 0.038$	$-0.008^{+0.188}_{-0.172} \pm 0.015$	$0.215^{+0.215}_{-0.198} \pm 0.046$	$0.279^{+0.146}_{-0.123} \pm 0.056$
$[1.1, 2.5]$	$-0.275^{+0.256}_{-0.302} \pm 0.051$	$0.145^{+0.325}_{-0.720} \pm 0.024$	$0.057^{+0.397}_{-0.370} \pm 0.041$	$0.045^{+0.368}_{-0.301} \pm 0.015$
$[2.5, 4.0]$	$0.037^{+0.374}_{-0.343} \pm 0.020$	$-0.152^{+0.489}_{-0.691} \pm 0.030$	$0.043^{+0.746}_{-0.578} \pm 0.026$	$0.315^{+0.389}_{-0.356} \pm 0.021$
$[4.0, 6.0]$	$-0.101^{+0.124}_{-0.128} \pm 0.011$	$-0.043^{+0.183}_{-0.202} \pm 0.014$	$-0.072^{+0.206}_{-0.223} \pm 0.025$	$-0.176^{+0.222}_{-0.328} \pm 0.023$
$[6.0, 8.0]$	$-0.072^{+0.152}_{-0.164} \pm 0.013$	$-0.360^{+0.185}_{-0.154} \pm 0.021$	$-0.189^{+0.181}_{-0.155} \pm 0.020$	$-0.108^{+0.210}_{-0.197} \pm 0.018$
$[11.0, 12.5]$	$0.723^{+0.276}_{-0.234} \pm 0.068$	$-0.054^{+0.138}_{-0.143} \pm 0.014$	$0.064^{+0.140}_{-0.139} \pm 0.014$	$0.189^{+0.236}_{-0.187} \pm 0.026$
$[15.0, 17.0]$	$0.539^{+0.055}_{-0.125} \pm 0.014$	$-0.236^{+0.107}_{-0.110} \pm 0.018$	$-0.170^{+0.119}_{-0.108} \pm 0.015$	$0.140^{+0.122}_{-0.093} \pm 0.016$
$[17.0, 19.0]$	$0.182^{+0.163}_{-0.100} \pm 0.023$	$0.057^{+0.162}_{-0.155} \pm 0.015$	$0.171^{+0.178}_{-0.159} \pm 0.023$	$-0.077^{+0.153}_{-0.146} \pm 0.019$
$[1.1, 6.0]$	$-0.109^{+0.095}_{-0.102} \pm 0.032$	$-0.101^{+0.111}_{-0.129} \pm 0.014$	$0.016^{+0.130}_{-0.141} \pm 0.024$	$-0.048^{+0.108}_{-0.117} \pm 0.014$
$[15.0, 19.0]$	$0.410^{+0.075}_{-0.076} \pm 0.052$	$-0.139^{+0.075}_{-0.085} \pm 0.011$	$-0.055^{+0.087}_{-0.092} \pm 0.012$	$0.041^{+0.080}_{-0.062} \pm 0.021$

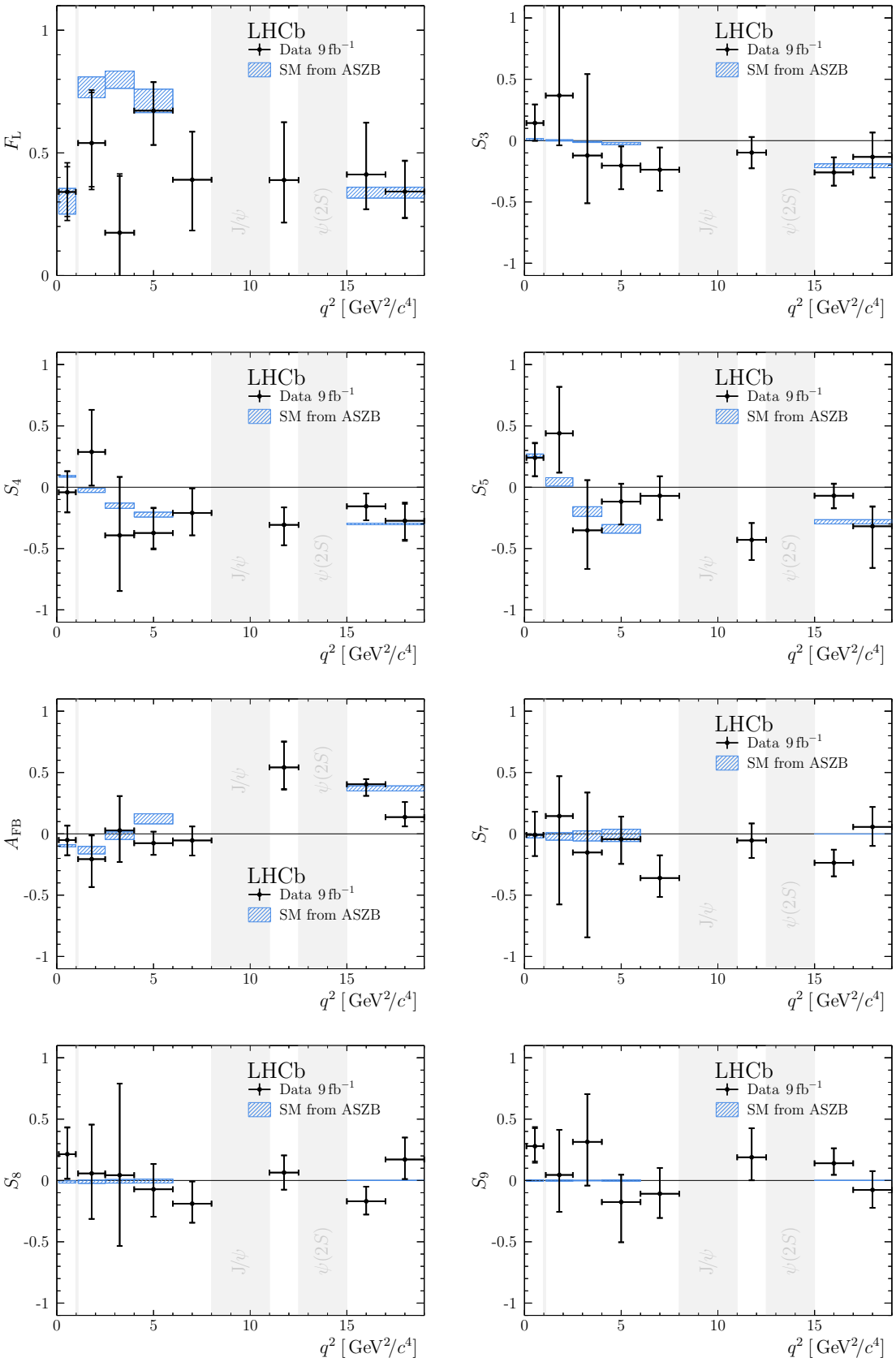

Figure 92: The final results for the S_x basis angular observables in the nominal eight q^2 bins in comparison with the predictions from FLAV.IO [35] in blue. The numerical values are given in Table 59.

Table 60: Correlation matrix for all eight angular observables in the S_x basis for the q^2 bin 0.1-0.98 GeV^2/c^4. The matrix is determined from 3000 pseudo-experiment samples generated by applying the bootstrapping method to data events, as explained in details in Section 4.9.

bin 0	S_{1s}	S_3	S_4	S_5	S_{6s}	S_7	S_8	S_9
S_{1s}	1.000	−0.043	0.010	−0.029	−0.045	−0.125	0.005	0.113
S_3		1.000	−0.025	0.117	−0.015	0.018	0.059	0.025
S_4			1.000	−0.270	−0.091	−0.253	0.236	−0.061
S_5				1.000	0.103	0.216	−0.177	0.060
S_{6s}					1.000	0.186	−0.273	−0.064
S_7						1.000	−0.349	0.220
S_8							1.000	−0.082
S_9								1.000

Table 61: Correlation matrix for all eight angular observables in the S_x basis for the q^2 bin 1.1-2.5 GeV^2/c^4. The matrix is determined from 3000 pseudo-experiment samples generated by applying the bootstrapping method to data events, as explained in details in Section 4.9.

bin 1	S_{1s}	S_3	S_4	S_5	S_{6s}	S_7	S_8	S_9
S_{1s}	1.000	−0.165	0.047	−0.107	−0.115	−0.040	0.102	0.028
S_3		1.000	0.056	0.093	−0.025	0.135	−0.013	−0.115
S_4			1.000	−0.018	0.172	0.050	0.325	0.089
S_5				1.000	0.196	0.221	−0.058	0.039
S_{6s}					1.000	0.203	0.114	0.116
S_7						1.000	0.062	0.162
S_8							1.000	0.215
S_9								1.000

Table 62: Correlation matrix for all eight angular observables in the S_x basis for the q^2 bin 2.5-4.0 GeV^2/c^4. The matrix is determined from 3000 pseudo-experiment samples generated by applying the bootstrapping method to data events, as explained in details in Section 4.9.

bin 2	S_{1s}	S_3	S_4	S_5	S_{6s}	S_7	S_8	S_9
S_{1s}	1.000	−0.019	0.007	−0.061	0.081	0.017	0.074	−0.038
S_3		1.000	0.020	−0.057	−0.013	−0.027	0.072	0.016
S_4			1.000	0.000	−0.061	0.098	−0.048	−0.005
S_5				1.000	0.009	−0.070	0.004	−0.110
S_{6s}					1.000	0.052	0.056	−0.161
S_7						1.000	0.262	−0.142
S_8							1.000	−0.086
S_9								1.000

Table 63: Correlation matrix for all eight angular observables in the S_x basis for the q^2 bin 4.0-6.0 GeV^2/c^4. The matrix is determined from 3000 pseudo-experiment samples generated by applying the bootstrapping method to data events, as explained in details in Section 4.9.

bin 3	S_{1s}	S_3	S_4	S_5	S_{6s}	S_7	S_8	S_9
S_{1s}	1.000	−0.201	0.091	0.091	−0.073	−0.008	−0.155	0.034
S_3		1.000	−0.076	−0.100	0.026	0.109	0.174	0.031
S_4			1.000	−0.081	−0.152	0.072	−0.035	0.048
S_5				1.000	−0.173	−0.017	0.092	−0.024
S_{6s}					1.000	−0.041	−0.027	−0.011
S_7						1.000	0.089	0.088
S_8							1.000	−0.081
S_9								1.000

Table 64: Correlation matrix for all eight angular observables in the S_x basis for the q^2 bin 6.0-8.0 GeV^2/c^4. The matrix is determined from 3000 pseudo-experiment samples generated by applying the bootstrapping method to data events, as explained in details in Section 4.9.

bin 4	S_{1s}	S_3	S_4	S_5	S_{6s}	S_7	S_8	S_9
S_{1s}	1.000	−0.263	0.014	−0.068	−0.011	0.043	−0.062	−0.054
S_3		1.000	0.013	−0.035	−0.053	0.083	−0.043	−0.004
S_4			1.000	0.352	0.022	−0.054	−0.028	−0.101
S_5				1.000	0.022	−0.106	−0.071	−0.166
S_{6s}					1.000	−0.048	−0.192	−0.134
S_7						1.000	−0.102	−0.055
S_8							1.000	0.035
S_9								1.000

Table 65: Correlation matrix for all eight angular observables in the S_x basis for the q^2 bin 11.0-12.5 GeV^2/c^4. The matrix is determined from 3000 pseudo-experiment samples generated by applying the bootstrapping method to data events, as explained in details in Section 4.9.

bin 5	S_{1s}	S_3	S_4	S_5	S_{6s}	S_7	S_8	S_9
S_{1s}	1.000	−0.092	−0.033	−0.092	0.444	0.091	0.133	0.076
S_3		1.000	−0.079	−0.134	−0.076	−0.043	−0.042	−0.188
S_4			1.000	0.078	0.055	−0.047	−0.090	0.119
S_5				1.000	−0.297	0.053	−0.037	−0.100
S_{6s}					1.000	0.097	0.106	0.151
S_7						1.000	0.054	−0.067
S_8							1.000	−0.066
S_9								1.000

Table 66: Correlation matrix for all eight angular observables in the S_x basis for the q^2 bin 15.0-17.0 GeV^2/c^4. The matrix is determined from 3000 pseudo-experiment samples generated by applying the bootstrapping method to data events, as explained in details in Section 4.9.

bin 6	S_{1s}	S_3	S_4	S_5	S_{6s}	S_7	S_8	S_9
S_{1s}	1.000	−0.195	−0.039	−0.069	0.283	0.058	0.131	0.071
S_3		1.000	−0.093	−0.057	0.036	0.013	−0.062	0.010
S_4			1.000	0.269	0.072	0.098	0.064	0.143
S_5				1.000	−0.153	0.092	−0.061	−0.134
S_{6s}					1.000	0.074	−0.022	0.161
S_7						1.000	0.231	0.024
S_8							1.000	0.003
S_9								1.000

Table 67: Correlation matrix for all eight angular observables in the S_x basis for the q^2 bin 17.0-19.0 GeV^2/c^4. The matrix is determined from 3000 pseudo-experiment samples generated by applying the bootstrapping method to data events, as explained in details in Section 4.9.

bin 7	S_{1s}	S_3	S_4	S_5	S_{6s}	S_7	S_8	S_9
S_{1s}	1.000	0.100	0.020	0.098	0.099	−0.066	0.098	0.013
S_3		1.000	−0.076	0.061	0.088	0.013	0.075	−0.022
S_4			1.000	−0.058	−0.070	0.001	0.058	0.038
S_5				1.000	−0.194	−0.026	0.090	0.022
S_{6s}					1.000	0.168	0.014	−0.073
S_7						1.000	−0.168	0.103
S_8							1.000	−0.194
S_9								1.000

Table 68: Correlation matrix for all eight angular observables in the S_x basis for the q^2 bin 1.1-6.0 GeV^2/c^4. The matrix is determined from 3000 pseudo-experiment samples generated by applying the bootstrapping method to data events, as explained in details in Section 4.9.

bin 0	S_{1s}	S_3	S_4	S_5	S_{6s}	S_7	S_8	S_9
S_{1s}	1.000	−0.170	0.001	0.018	−0.007	−0.041	−0.084	−0.057
S_3		1.000	−0.010	−0.024	−0.017	0.040	−0.034	−0.051
S_4			1.000	−0.030	0.056	−0.019	0.192	−0.013
S_5				1.000	0.008	0.143	0.044	0.043
S_{6s}					1.000	−0.047	0.041	0.054
S_7						1.000	0.166	−0.016
S_8							1.000	−0.014
S_9								1.000

Table 69: Correlation matrix for all eight angular observables in the S_x basis for the q^2 bin 15.0-19.0 GeV^2/c^4. The matrix is determined from 3000 pseudo-experiment samples generated by applying the bootstrapping method to data events, as explained in details in Section 4.9.

bin 1	S_{1s}	S_3	S_4	S_5	S_{6s}	S_7	S_8	S_9
S_{1s}	1.000	−0.130	0.046	0.019	0.172	0.025	−0.034	0.046
S_3		1.000	−0.073	−0.004	−0.016	0.122	0.100	−0.050
S_4			1.000	0.046	−0.139	0.065	0.049	−0.021
S_5				1.000	0.049	−0.069	0.067	−0.055
S_{6s}					1.000	−0.102	−0.030	0.104
S_7						1.000	0.150	−0.009
S_8							1.000	−0.089
S_9								1.000

7.2.3 $P_x^{(\prime)}$ angular observables

The fits including angular folding techniques to the signal channel data have returned the following values for the angular observables, $P_x^{(\prime)}$. In addition to the statistical uncertainty from the Feldman-Cousins scans (see Section 7.3), the systematic uncertainty from Section 5.14 are added to the values.

The resulting profiles from the Feldman-Cousins scans for the $P_x^{(\prime)}$ observables are shown in Figs. 104 to 110 in Section 7.3 and for F_L in Fig. 103. The numeric tables with final results and their statistical and systematic uncertainties are given in Table 70 for all eight plus two extra q^2 bins. The results from the nominal eight q^2 bins are plotted as a function of q^2 for all eight angular observables in Fig. 93. All eight plus two correlation matrices obtained by the bootstrapping (see Section 4.9) of data event samples are given in Tables 71 to 78 and Tables 79 and 80.

Table 70: Result values of the $P_x^{(\prime)}$ basis angular observables for all eight nominal and the two larger q^2 bins, the numerically labelled bins are the nominal bins as defined in Table 15 plus the two larger bins. The first uncertainty is of statistical nature coming from the Feldman-Cousins scans and the second is the combined uncertainty from the systematic studies. The values and uncertainties for the nominal eight q^2 bins are plotted in Fig. 93 along with the theoretical predictions.

q^2 bin	F_L	P_1	P_2	P_3
$[0.1, 0.98]$	$0.341^{+0.103}_{-0.101} \pm 0.064$	$0.435^{+0.381}_{-0.397} \pm 0.106$	$-0.051^{+0.122}_{-0.123} \pm 0.033$	$-0.421^{+0.201}_{-0.213} \pm 0.047$
$[1.1, 2.5]$	$0.540^{+0.181}_{-0.188} \pm 0.034$	$1.600^{+4.915}_{-1.746} \pm 0.317$	$-0.277^{+0.243}_{-0.418} \pm 0.151$	$-0.091^{+0.701}_{-0.990} \pm 0.180$
$[2.5, 4.0]$	$0.175^{+0.239}_{-0.141} \pm 0.044$	$-0.294^{+1.426}_{-1.036} \pm 0.223$	$0.026^{+0.255}_{-0.253} \pm 0.113$	$-0.448^{+0.504}_{-0.621} \pm 0.204$
$[4.0, 6.0]$	$0.672^{+0.108}_{-0.140} \pm 0.031$	$-1.245^{+0.991}_{-1.171} \pm 0.291$	$-0.148^{+0.189}_{-0.203} \pm 0.063$	$0.515^{+0.821}_{-0.619} \pm 0.150$
$[6.0, 8.0]$	$0.390^{+0.197}_{-0.207} \pm 0.018$	$-0.780^{+0.614}_{-0.695} \pm 0.103$	$-0.057^{+0.116}_{-0.130} \pm 0.055$	$0.172^{+0.333}_{-0.307} \pm 0.056$
$[11.0, 12.5]$	$0.389^{+0.229}_{-0.160} \pm 0.030$	$-0.319^{+0.441}_{-0.517} \pm 0.086$	$0.617^{+0.551}_{-0.145} \pm 0.044$	$-0.323^{+0.294}_{-0.654} \pm 0.045$
$[15.0, 17.0]$	$0.412^{+0.176}_{-0.136} \pm 0.020$	$-0.882^{+0.413}_{-0.671} \pm 0.071$	$0.446^{+0.034}_{-0.072} \pm 0.026$	$-0.232^{+0.164}_{-0.201} \pm 0.017$
$[17.0, 19.0]$	$0.342^{+0.107}_{-0.119} \pm 0.037$	$-0.404^{+0.585}_{-0.567} \pm 0.093$	$0.141^{+0.096}_{-0.100} \pm 0.044$	$0.119^{+0.210}_{-0.212} \pm 0.017$
$[1.1, 6.0]$	$0.590^{+0.095}_{-0.096} \pm 0.026$	$-0.505^{+0.560}_{-0.541} \pm 0.076$	$-0.133^{+0.125}_{-0.132} \pm 0.045$	$0.117^{+0.274}_{-0.284} \pm 0.045$
$[15.0, 19.0]$	$0.396^{+0.125}_{-0.110} \pm 0.022$	$-0.702^{+0.353}_{-0.434} \pm 0.066$	$0.336^{+0.092}_{-0.066} \pm 0.035$	$-0.068^{+0.116}_{-0.126} \pm 0.033$
q^2 bin	P_4'	P_5'	P_6'	P_8'
$[0.1, 0.98]$	$-0.086^{+0.356}_{-0.353} \pm 0.119$	$0.507^{+0.301}_{-0.284} \pm 0.122$	$-0.017^{+0.396}_{-0.345} \pm 0.062$	$0.453^{+0.495}_{-0.391} \pm 0.092$
$[1.1, 2.5]$	$0.576^{+0.621}_{-0.564} \pm 0.113$	$0.879^{+0.701}_{-0.714} \pm 0.104$	$0.255^{+1.216}_{-1.317} \pm 0.082$	$0.116^{+0.750}_{-0.761} \pm 0.050$
$[2.5, 4.0]$	$-0.808^{+1.087}_{-0.842} \pm 0.141$	$-0.867^{+1.005}_{-1.683} \pm 0.092$	$-0.370^{+1.590}_{-3.905} \pm 0.054$	$0.115^{+7.892}_{-4.953} \pm 0.071$
$[4.0, 6.0]$	$-0.795^{+0.474}_{-0.275} \pm 0.092$	$-0.246^{+0.321}_{-0.401} \pm 0.086$	$-0.090^{+0.402}_{-0.413} \pm 0.047$	$-0.153^{+0.437}_{-0.482} \pm 0.051$
$[6.0, 8.0]$	$-0.430^{+0.412}_{-0.455} \pm 0.063$	$-0.145^{+0.403}_{-0.413} \pm 0.065$	$-0.741^{+0.288}_{-0.401} \pm 0.026$	$-0.387^{+0.296}_{-0.393} \pm 0.020$
$[11.0, 12.5]$	$-0.626^{+0.301}_{-0.342} \pm 0.074$	$-0.878^{+0.282}_{-0.336} \pm 0.055$	$-0.111^{+0.284}_{-0.291} \pm 0.025$	$0.132^{+0.292}_{-0.303} \pm 0.039$
$[15.0, 17.0]$	$-0.317^{+0.225}_{-0.218} \pm 0.075$	$-0.141^{+0.212}_{-0.203} \pm 0.061$	$-0.481^{+0.207}_{-0.205} \pm 0.022$	$-0.345^{+0.225}_{-0.224} \pm 0.045$
$[17.0, 19.0]$	$-0.570^{+0.291}_{-0.358} \pm 0.132$	$-0.665^{+0.364}_{-0.801} \pm 0.127$	$0.120^{+0.335}_{-0.328} \pm 0.038$	$0.361^{+0.367}_{-0.329} \pm 0.073$
$[1.1, 6.0]$	$-0.408^{+0.282}_{-0.281} \pm 0.067$	$-0.073^{+0.248}_{-0.251} \pm 0.043$	$-0.206^{+0.234}_{-0.234} \pm 0.037$	$0.032^{+0.265}_{-0.276} \pm 0.062$
$[15.0, 19.0]$	$-0.393^{+0.175}_{-0.211} \pm 0.105$	$-0.241^{+0.158}_{-0.160} \pm 0.048$	$-0.285^{+0.190}_{-0.142} \pm 0.031$	$-0.113^{+0.195}_{-0.179} \pm 0.027$

Table 71: Correlation matrix for all eight angular observables in the $P_x^{(\prime)}$ basis for the q^2 bin 0.1-0.98 GeV^2/c^4. The matrix is determined from 3000 pseudo-experiment samples generated by applying the bootstrapping method to data events, as explained in details in Section 4.9.

bin 0	F_L	P_1	P_2	P_3	P_4'	P_5'	P_6'	P_8'
F_L	1.000	−0.141	0.023	−0.182	−0.027	0.002	0.123	−0.006
P_1		1.000	−0.002	−0.011	−0.027	0.167	0.009	0.027
P_2			1.000	0.024	−0.076	0.090	0.188	−0.238
P_3				1.000	0.055	−0.032	−0.206	0.040
P_4'					1.000	−0.216	−0.232	0.151
P_5'						1.000	0.184	−0.183
P_6'							1.000	−0.251
P_8'								1.000

Table 72: Correlation matrix for all eight angular observables in the $P_x^{(\prime)}$ basis for the q^2 bin 1.1-2.5 GeV^2/c^4. The matrix is determined from 3000 pseudo-experiment samples generated by applying the bootstrapping method to data events, as explained in details in Section 4.9.

bin 1	F_L	P_1	P_2	P_3	P_4'	P_5'	P_6'	P_8'
F_L	1.000	0.032	0.020	−0.008	−0.061	−0.008	0.047	−0.078
P_1		1.000	−0.054	−0.014	0.061	−0.089	−0.033	0.037
P_2			1.000	−0.053	0.151	0.118	0.103	0.127
P_3				1.000	−0.076	−0.073	−0.018	−0.127
P_4'					1.000	0.025	−0.007	0.219
P_5'						1.000	0.093	−0.079
P_6'							1.000	−0.011
P_8'								1.000

Table 73: Correlation matrix for all eight angular observables in the $P_x^{(\prime)}$ basis for the q^2 bin 2.5-4.0 GeV^2/c^4. The matrix is determined from 3000 pseudo-experiment samples generated by applying the bootstrapping method to data events, as explained in details in Section 4.9.

bin 2	F_L	P_1	P_2	P_3	P_4'	P_5'	P_6'	P_8'
F_L	1.000	0.004	0.001	0.022	−0.019	−0.034	−0.064	−0.030
P_1		1.000	0.003	0.041	0.041	0.000	−0.039	−0.061
P_2			1.000	0.069	−0.009	0.042	0.036	−0.034
P_3				1.000	−0.035	0.019	0.061	−0.015
P_4'					1.000	0.072	0.060	0.081
P_5'						1.000	−0.016	−0.086
P_6'							1.000	0.209
P_8'								1.000

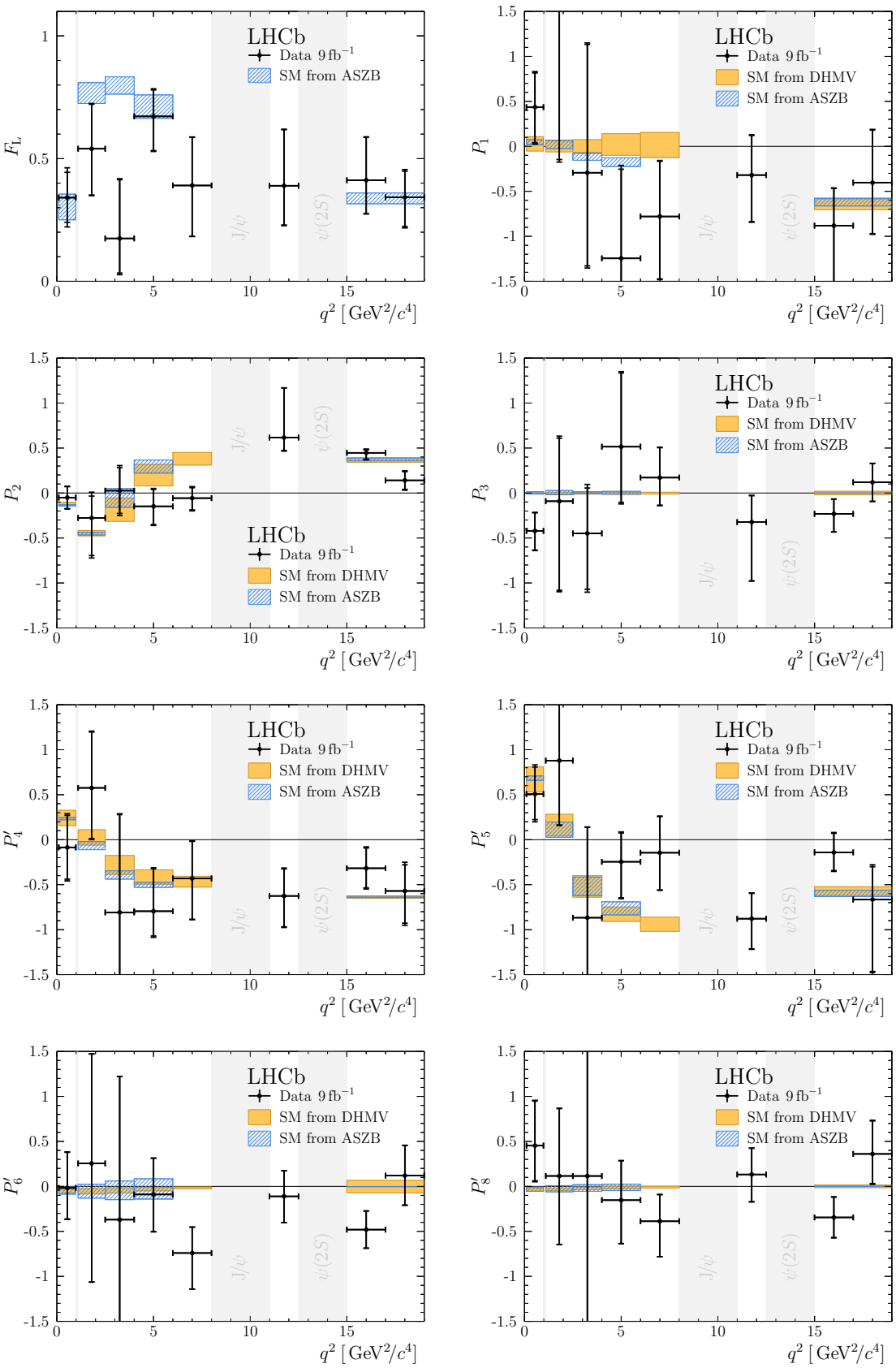

Figure 93: The final results for the $P_x^{(\prime)}$ basis angular observables in the nominal eight q^2 bins in comparison with the predictions from FLAV.IO [35] in blue and from Ref. [46] in orange. The numerical values are given in Table 70.

Table 74: Correlation matrix for all eight angular observables in the $P_x^{(\prime)}$ basis for the q^2 bin 4.0-6.0 GeV^2/c^4. The matrix is determined from 3000 pseudo-experiment samples generated by applying the bootstrapping method to data events, as explained in details in Section 4.9.

bin 3	F_L	P_1	P_2	P_3	P_4'	P_5'	P_6'	P_8'
F_L	1.000	0.157	−0.096	0.019	−0.023	−0.084	0.019	0.080
P_1		1.000	−0.032	0.022	−0.076	0.026	0.026	0.081
P_2			1.000	0.042	−0.124	−0.137	−0.034	−0.053
P_3				1.000	−0.023	−0.016	−0.047	0.091
P_4'					1.000	−0.108	−0.014	−0.098
P_5'						1.000	−0.045	0.068
P_6'							1.000	0.054
P_8'								1.000

Table 75: Correlation matrix for all eight angular observables in the $P_x^{(\prime)}$ basis for the q^2 bin 6.0-8.0 GeV^2/c^4. The matrix is determined from 3000 pseudo-experiment samples generated by applying the bootstrapping method to data events, as explained in details in Section 4.9.

bin 4	F_L	P_1	P_2	P_3	P_4'	P_5'	P_6'	P_8'
F_L	1.000	0.111	−0.097	0.014	−0.033	0.051	−0.049	−0.001
P_1		1.000	−0.036	0.011	0.013	−0.023	0.015	−0.063
P_2			1.000	0.117	−0.010	0.016	−0.046	−0.172
P_3				1.000	0.037	0.124	0.001	−0.041
P_4'					1.000	0.251	−0.033	−0.011
P_5'						1.000	−0.083	−0.059
P_6'							1.000	−0.050
P_8'								1.000

Table 76: Correlation matrix for all eight angular observables in the $P_x^{(\prime)}$ basis for the q^2 bin 11.0-12.5 GeV^2/c^4. The matrix is determined from 3000 pseudo-experiment samples generated by applying the bootstrapping method to data events, as explained in details in Section 4.9.

bin 5	F_L	P_1	P_2	P_3	P_4'	P_5'	P_6'	P_8'
F_L	1.000	−0.052	0.347	−0.093	0.001	0.039	−0.060	−0.138
P_1		1.000	−0.048	0.170	−0.086	−0.140	−0.035	−0.025
P_2			1.000	−0.155	0.118	−0.139	−0.004	0.073
P_3				1.000	−0.091	0.060	0.070	0.092
P_4'					1.000	0.043	−0.028	−0.099
P_5'						1.000	0.051	−0.010
P_6'							1.000	0.064
P_8'								1.000

Table 77: Correlation matrix for all eight angular observables in the $P_x^{(\prime)}$ basis for the q^2 bin 15.0-17.0 GeV^2/c^4. The matrix is determined from 3000 pseudo-experiment samples generated by applying the bootstrapping method to data events, as explained in details in Section 4.9.

bin 6	F_L	P_1	P_2	P_3	P_4'	P_5'	P_6'	P_8'
F_L	1.000	0.074	0.150	−0.091	0.084	0.094	0.003	−0.095
P_1		1.000	0.011	−0.050	0.000	−0.010	−0.002	−0.057
P_2			1.000	−0.226	0.096	−0.058	0.066	−0.031
P_3				1.000	−0.147	0.103	−0.028	0.019
P_4'					1.000	0.274	0.094	0.051
P_5'						1.000	0.095	−0.069
P_6'							1.000	0.209
P_8'								1.000

Table 78: Correlation matrix for all eight angular observables in the $P_x^{(\prime)}$ basis for the q^2 bin 17.0-19.0 GeV^2/c^4. The matrix is determined from 3000 pseudo-experiment samples generated by applying the bootstrapping method to data events, as explained in details in Section 4.9.

bin 7	F_L	P_1	P_2	P_3	P_4'	P_5'	P_6'	P_8'
F_L	1.000	−0.101	0.095	0.074	0.016	−0.104	0.061	−0.080
P_1		1.000	0.063	0.043	−0.103	0.019	−0.015	0.065
P_2			1.000	0.075	−0.070	−0.163	0.130	−0.004
P_3				1.000	−0.083	0.028	−0.076	0.174
P_4'					1.000	−0.081	−0.033	0.049
P_5'						1.000	0.003	0.079
P_6'							1.000	−0.118
P_8'								1.000

Table 79: Correlation matrix for all eight angular observables in the $P_x^{(\prime)}$ basis for the q^2 bin 1.1-6.0 GeV^2/c^4. The matrix is determined from 3000 pseudo-experiment samples generated by applying the bootstrapping method to data events, as explained in details in Section 4.9.

bin 0	F_L	P_1	P_2	P_3	P_4'	P_5'	P_6'	P_8'
F_L	1.000	0.111	−0.194	0.013	−0.014	−0.022	0.016	0.079
P_1		1.000	−0.046	0.073	0.010	−0.010	0.001	−0.038
P_2			1.000	−0.063	0.040	0.004	−0.050	0.012
P_3				1.000	0.015	−0.039	0.013	0.009
P_4'					1.000	−0.033	−0.019	0.175
P_5'						1.000	0.140	0.043
P_6'							1.000	0.171
P_8'								1.000

Table 80: Correlation matrix for all eight angular observables in the $P_x^{(\prime)}$ basis for the q^2 bin 15.0-19.0 GeV^2/c^4. The matrix is determined from 3000 pseudo-experiment samples generated by applying the bootstrapping method to data events, as explained in details in Section 4.9.

bin 1	F_L	P_1	P_2	P_3	P_4'	P_5'	P_6'	P_8'
F_L	1.000	−0.003	0.029	−0.012	0.004	0.006	0.027	0.051
P_1		1.000	0.009	0.039	−0.065	0.035	0.029	0.085
P_2			1.000	−0.065	−0.128	−0.002	−0.124	−0.029
P_3				1.000	0.026	0.042	0.022	0.079
P_4'					1.000	−0.001	0.122	0.037
P_5'						1.000	−0.090	0.073
P_6'							1.000	0.167
P_8'								1.000

7.3 Feldman-Cousins scan results

From the scans with toy event samples at steps around the mean value, the confidence level for each parameter at each q^2 bin is obtained. The procedure is explained in details in Section 4.6. In the following, the projections of these scans to the S_x observables are given in Figs. 94 to 101 for the nominal eight q^2 bins and in Fig. 102 for the two extra large bins. Identically the scans for the $P_x^{(\prime)}$ observables are shown in Figs. 104 to 110 and Fig. 111 for the eight and two large q^2 bins, respectively.

The result from the nominal likelihood fit is indicated by the black triangular marker in the profile scans. All scans of all observables and q^2 bins show very good agreement between the minimum of the Feldman-Cousins (FC) scans, except for S_7 (P_6') in q^2 bin 1.1–2.5 GeV^2/c^4. The nominal fit got stuck in the local minimum. Reconstructing the procedure of the FC scans, the fit can be brought to converge into the global minimum by fitting once, changing S_7 (P_6') to the value of the minimum and repeating the fit with these new start values for all floating fit parameters. Hence, the newly found minimum is quoted in the results and is treated as the central value for these parameters in the mentioned q^2 bin.

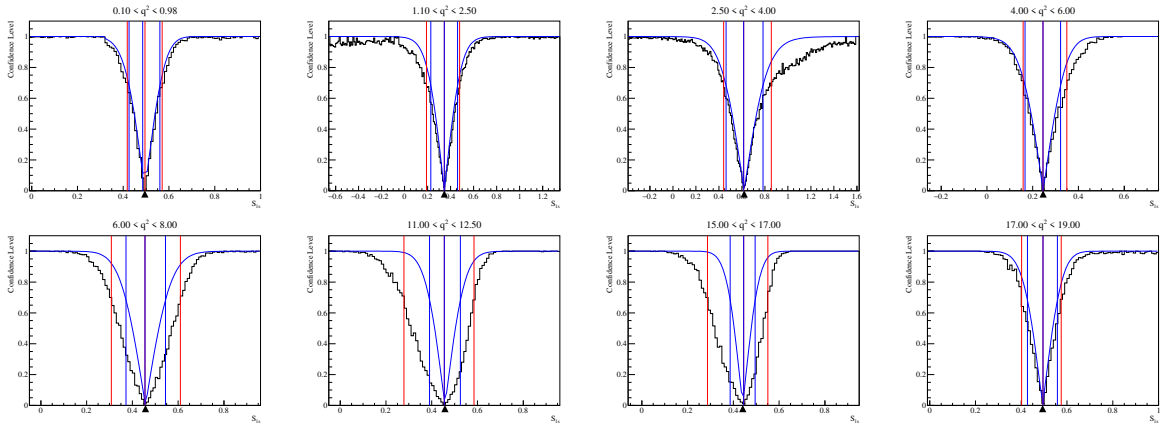

Figure 94: Resulting profiles of the Feldman-Cousins scan performed on parameter S_{1s} in all eight q^2 bins. The results from the toy event studies at each step are given by the black histogram, plus the red vertical lines indicating the positions of the maximum likelihood position and the $\pm 1\sigma$ values. In addition, the likelihood profile is shown in blue. The black triangular marker notates the value obtained in the actual fit to the data.

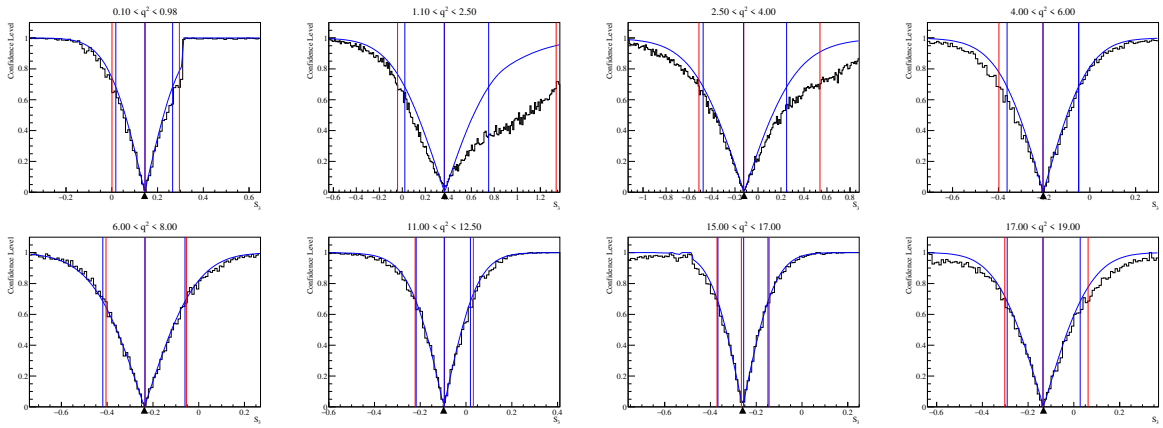

Figure 95: Resulting profiles of the Feldman-Cousins scan performed on parameter S_3 in all eight q^2 bins. The results from the toy event studies at each step are given by the black histogram, plus the red vertical lines indicating the positions of the maximum likelihood position and the $\pm 1\sigma$ values. In addition, the likelihood profile is shown in blue. The black triangular marker notates the value obtained in the actual fit to the data.

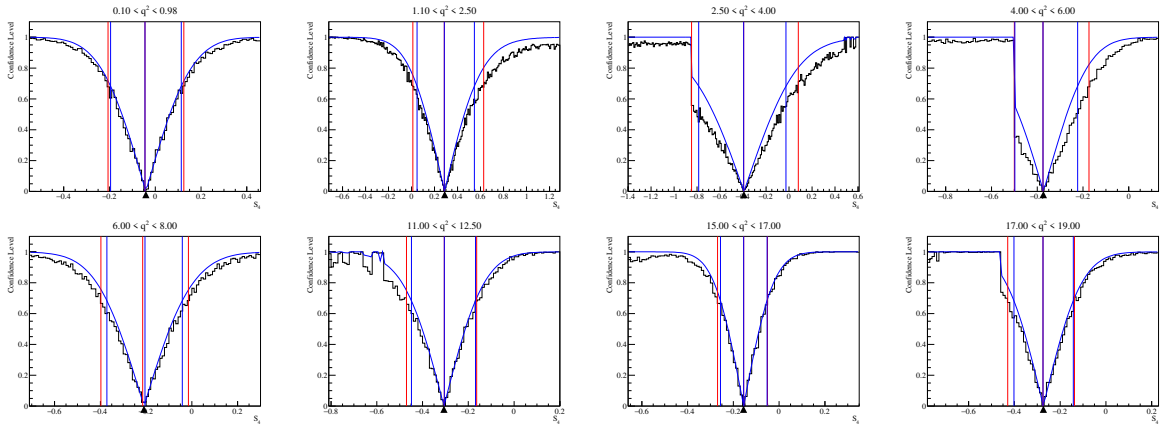

Figure 96: Resulting profiles of the Feldman-Cousins scan performed on parameter S_4 in all eight q^2 bins. The results from the toy event studies at each step are given by the black histogram, plus the red vertical lines indicating the positions of the maximum likelihood position and the $\pm 1\sigma$ values. In addition, the likelihood profile is shown in blue. The black triangular marker notates the value obtained in the actual fit to the data.

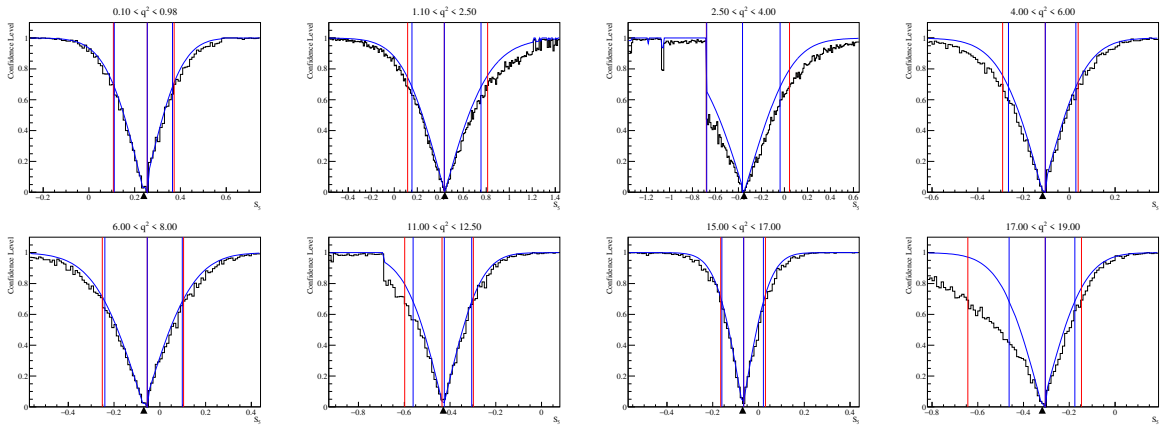

Figure 97: Resulting profiles of the Feldman-Cousins scan performed on parameter S_5 in all eight q^2 bins. The results from the toy event studies at each step are given by the black histogram, plus the red vertical lines indicating the positions of the maximum likelihood position and the $\pm 1\sigma$ values. In addition, the likelihood profile is shown in blue. The black triangular marker notates the value obtained in the actual fit to the data.

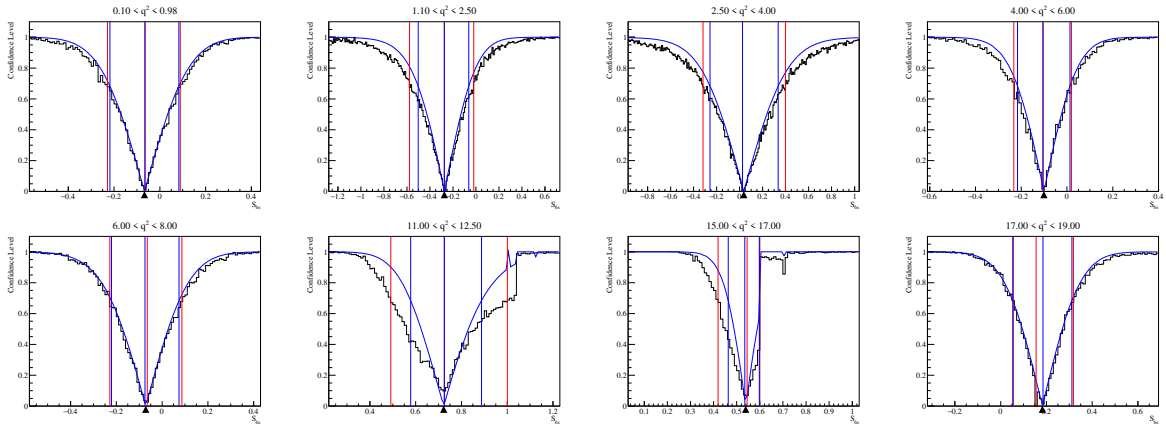

Figure 98: Resulting profiles of the Feldman-Cousins scan performed on parameter S_{6s} in all eight q^2 bins. The results from the toy event studies at each step are given by the black histogram, plus the red vertical lines indicating the positions of the maximum likelihood position and the $\pm 1\sigma$ values. In addition, the likelihood profile is shown in blue. The black triangular marker notates the value obtained in the actual fit to the data.

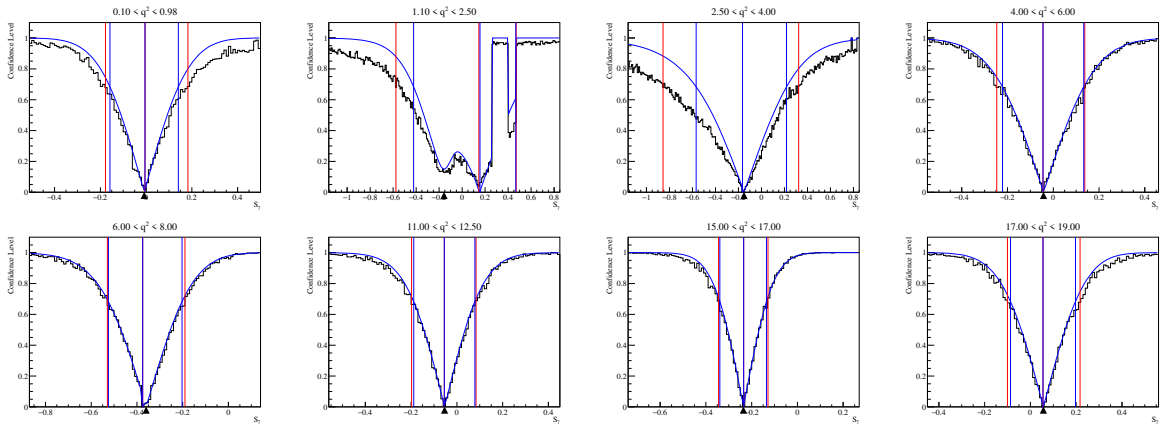

Figure 99: Resulting profiles of the Feldman-Cousins scan performed on parameter S_7 in all eight q^2 bins. The results from the toy event studies at each step are given by the black histogram, plus the red vertical lines indicating the positions of the maximum likelihood position and the $\pm 1\sigma$ values. In addition, the likelihood profile is shown in blue. The black triangular marker notates the value obtained in the actual fit to the data.

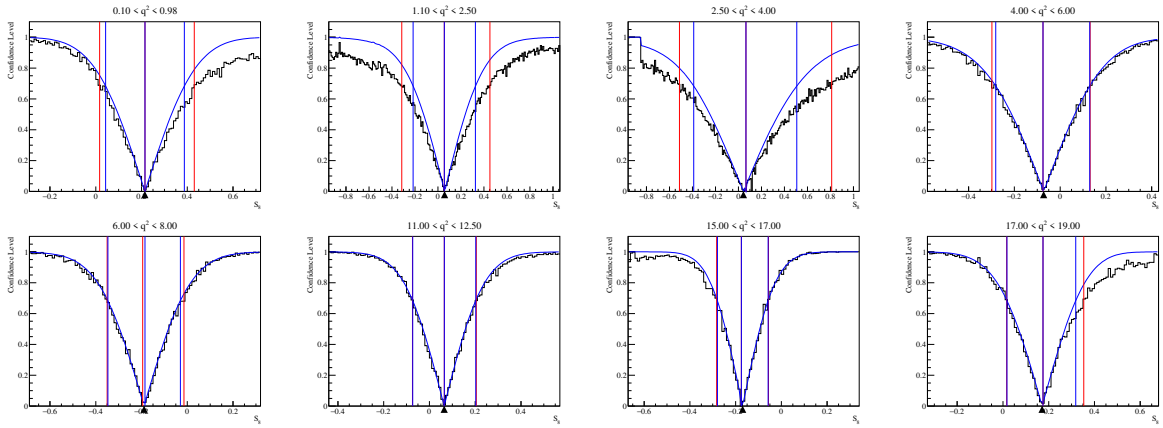

Figure 100: Resulting profiles of the Feldman-Cousins scan performed on parameter S_8 in all eight q^2 bins. The results from the toy event studies at each step are given by the black histogram, plus the red vertical lines indicating the positions of the maximum likelihood position and the $\pm 1\sigma$ values. In addition, the likelihood profile is shown in blue. The black triangular marker notates the value obtained in the actual fit to the data.

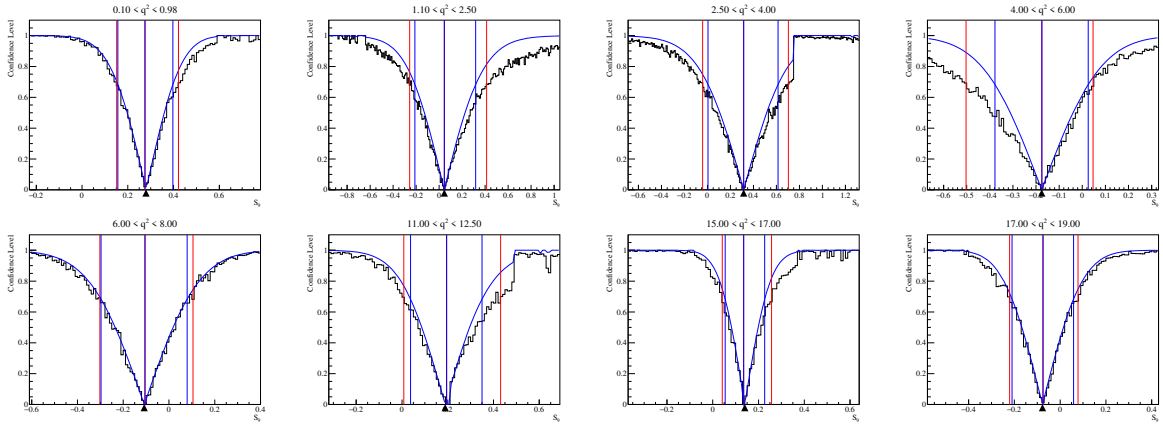

Figure 101: Resulting profiles of the Feldman-Cousins scan performed on parameter S_9 in all eight q^2 bins. The results from the toy event studies at each step are given by the black histogram, plus the red vertical lines indicating the positions of the maximum likelihood position and the $\pm 1\sigma$ values. In addition, the likelihood profile is shown in blue. The black triangular marker notates the value obtained in the actual fit to the data.

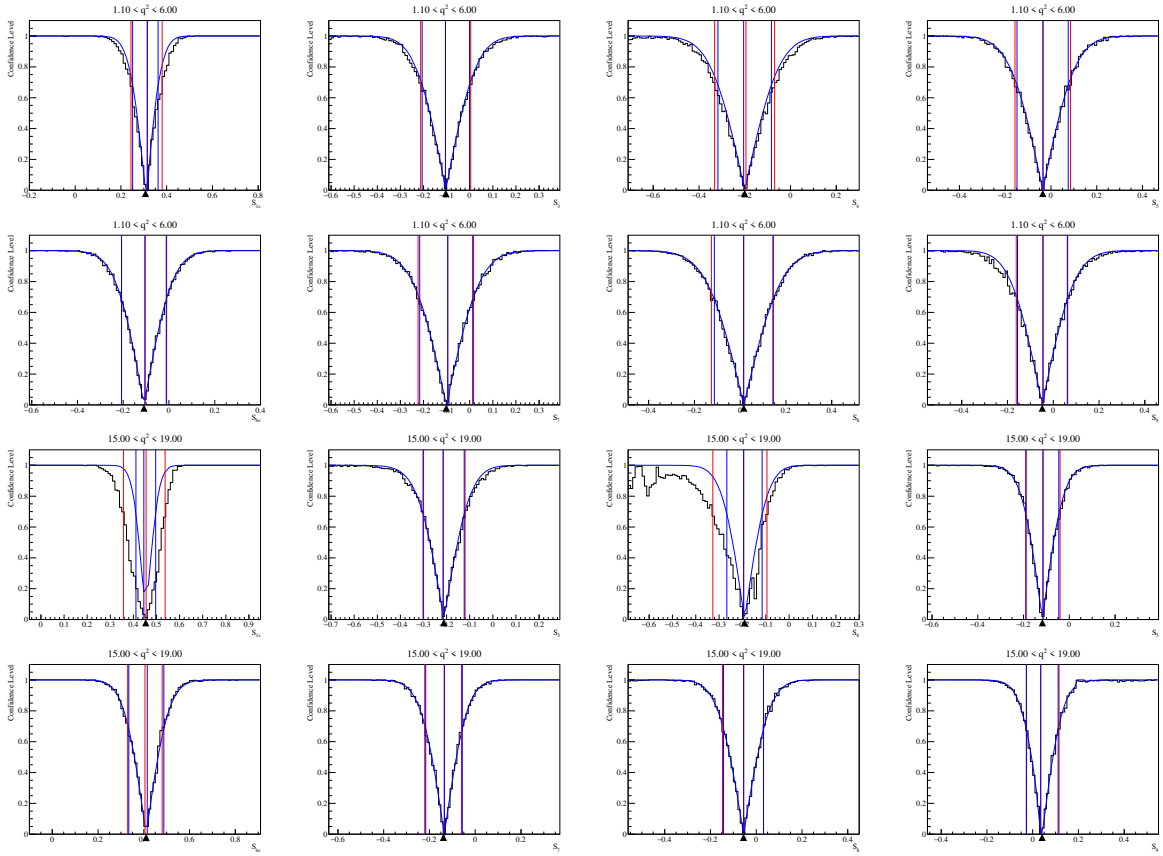

Figure 102: Resulting profiles of the Feldman-Cousins scan performed on all eight S_x observables in the two larger q^2 bins. The first two rows show the eight observables for the bin [1.1-6.0] GeV^2/c^4 and two bottom rows show the observables in the bin [15.0-19.0] GeV^2/c^4. The results from the toy event studies at each step are given by the black histogram, plus the red vertical lines indicating the positions of the maximum likelihood position and the $\pm 1\sigma$ values. In addition, the likelihood profile is shown in blue. The black triangular marker notates the value obtained in the actual fit to the data.

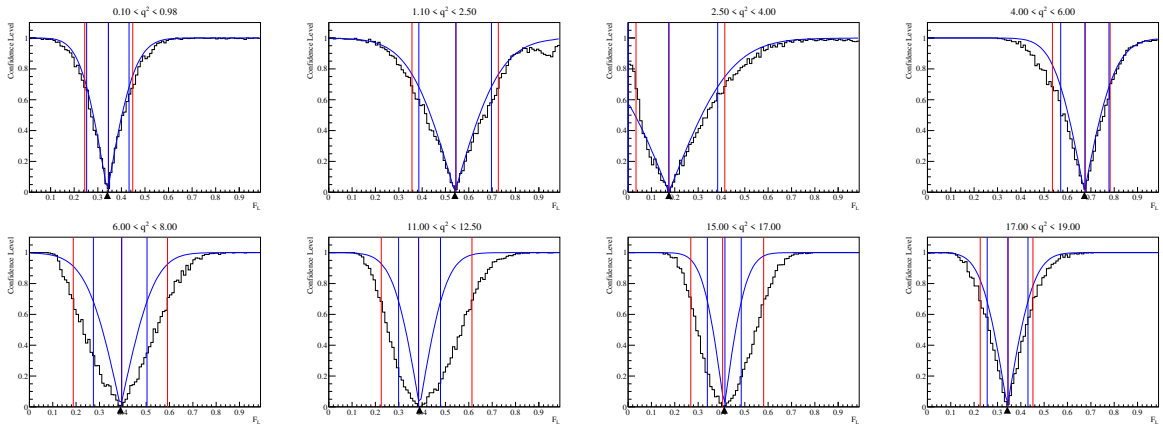

Figure 103: Resulting profiles of the Feldman-Cousins scan performed on parameter F_L in all eight q^2 bins. The results from the toy event studies at each step are given by the black histogram, plus the red vertical lines indicating the positions of the maximum likelihood position and the $\pm 1\sigma$ values. In addition, the likelihood profile is shown in blue. The black triangular marker notates the value obtained in the actual fit to the data.

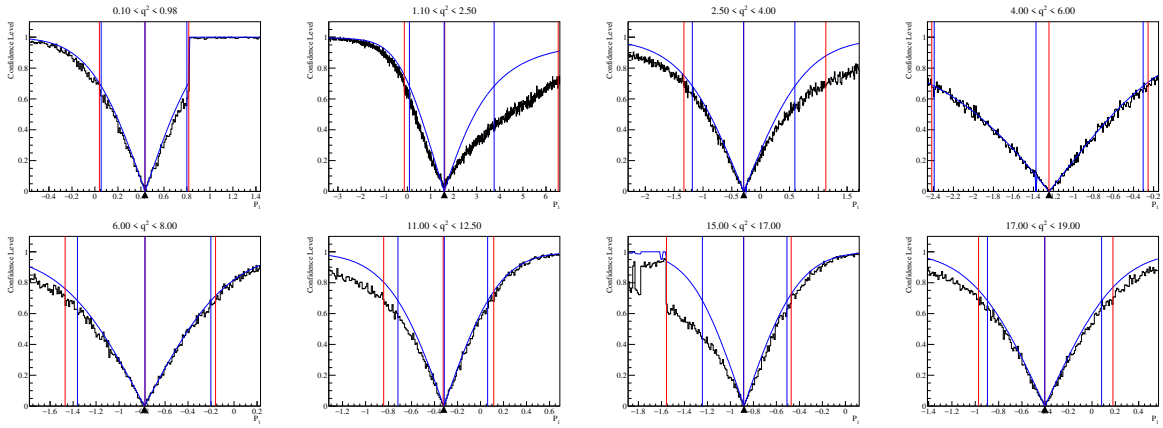

Figure 104: Resulting profiles of the Feldman-Cousins scan performed on parameter P_1 in all eight q^2 bins. The results from the toy event studies at each step are given by the black histogram, plus the red vertical lines indicating the positions of the maximum likelihood position and the $\pm 1\sigma$ values. In addition, the likelihood profile is shown in blue. The black triangular marker notates the value obtained in the actual fit to the data.

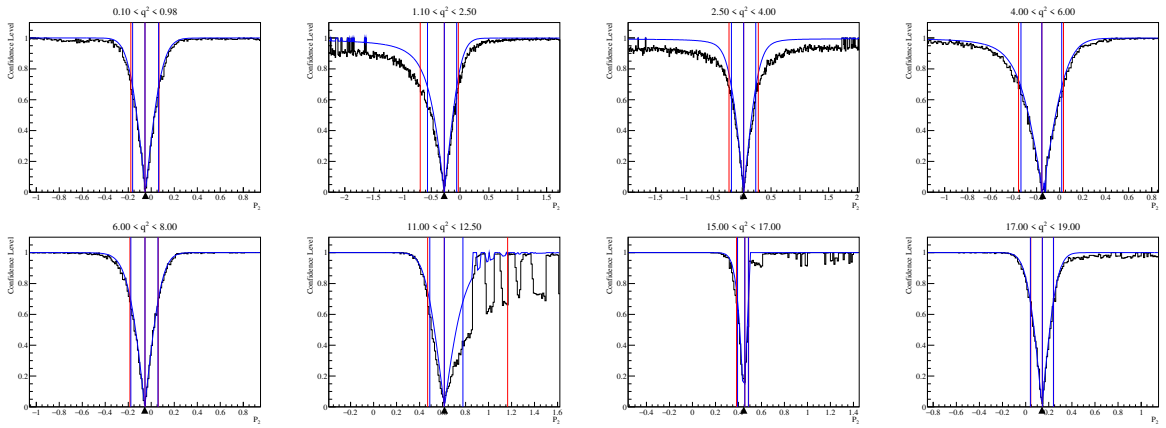

Figure 105: Resulting profiles of the Feldman-Cousins scan performed on parameter P_2 in all eight q^2 bins. The results from the toy event studies at each step are given by the black histogram, plus the red vertical lines indicating the positions of the maximum likelihood position and the $\pm 1\sigma$ values. In addition, the likelihood profile is shown in blue. The black triangular marker notates the value obtained in the actual fit to the data.

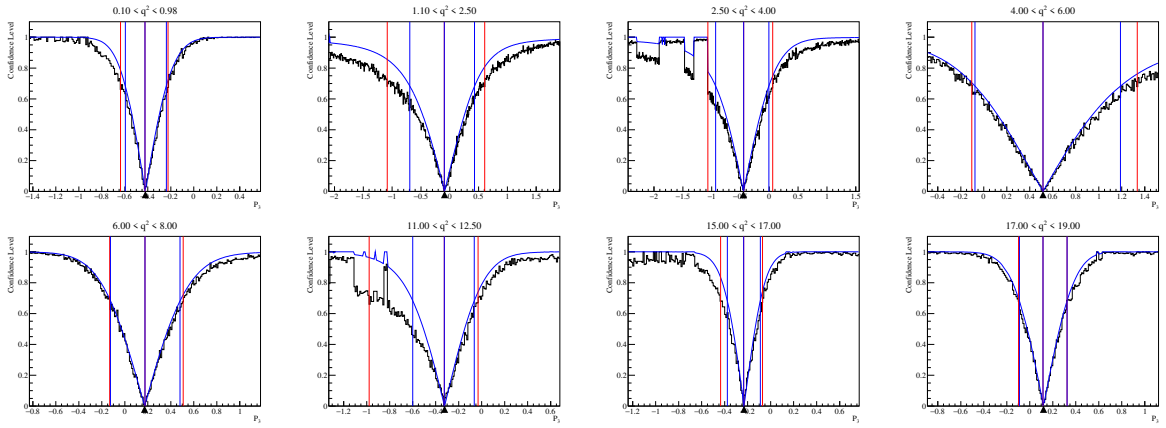

Figure 106: Resulting profiles of the Feldman-Cousins scan performed on parameter P_3 in all eight q^2 bins. The results from the toy event studies at each step are given by the black histogram, plus the red vertical lines indicating the positions of the maximum likelihood position and the $\pm 1\sigma$ values. In addition, the likelihood profile is shown in blue. The black triangular marker notates the value obtained in the actual fit to the data.

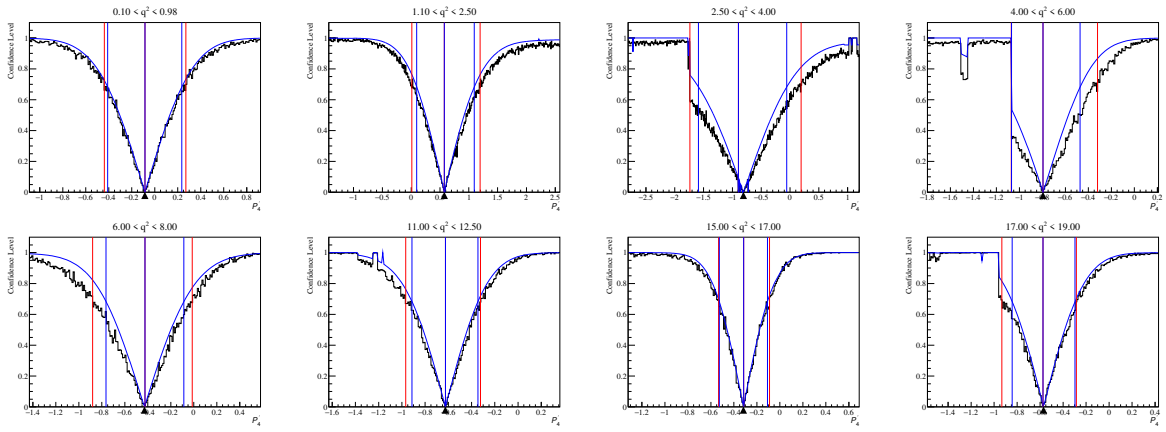

Figure 107: Resulting profiles of the Feldman-Cousins scan performed on parameter P_4 in all eight q^2 bins. The results from the toy event studies at each step are given by the black histogram, plus the red vertical lines indicating the positions of the maximum likelihood position and the $\pm 1\sigma$ values. In addition, the likelihood profile is shown in blue. The black triangular marker notates the value obtained in the actual fit to the data.

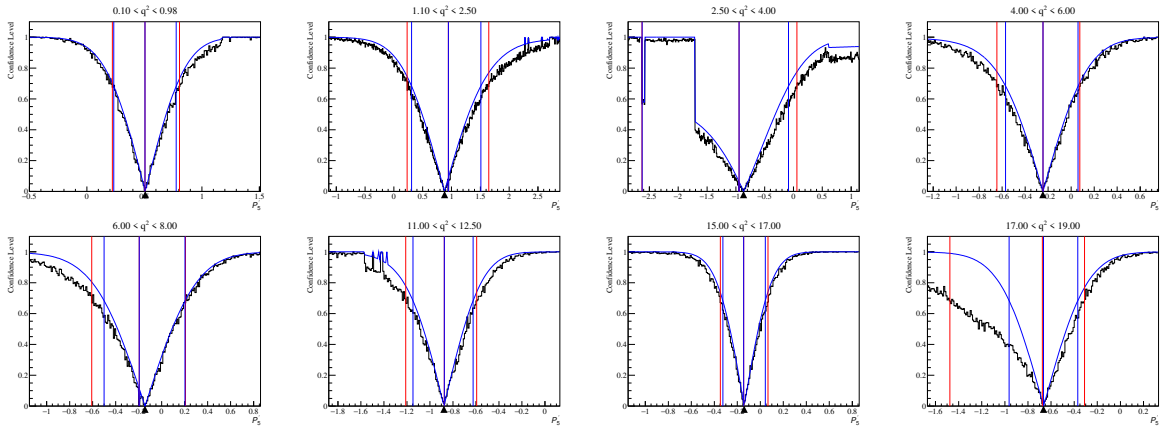

Figure 108: Resulting profiles of the Feldman-Cousins scan performed on parameter P_5 in all eight q^2 bins. The results from the toy event studies at each step are given by the black histogram, plus the red vertical lines indicating the positions of the maximum likelihood position and the $\pm 1\sigma$ values. In addition, the likelihood profile is shown in blue. The black triangular marker notates the value obtained in the actual fit to the data.

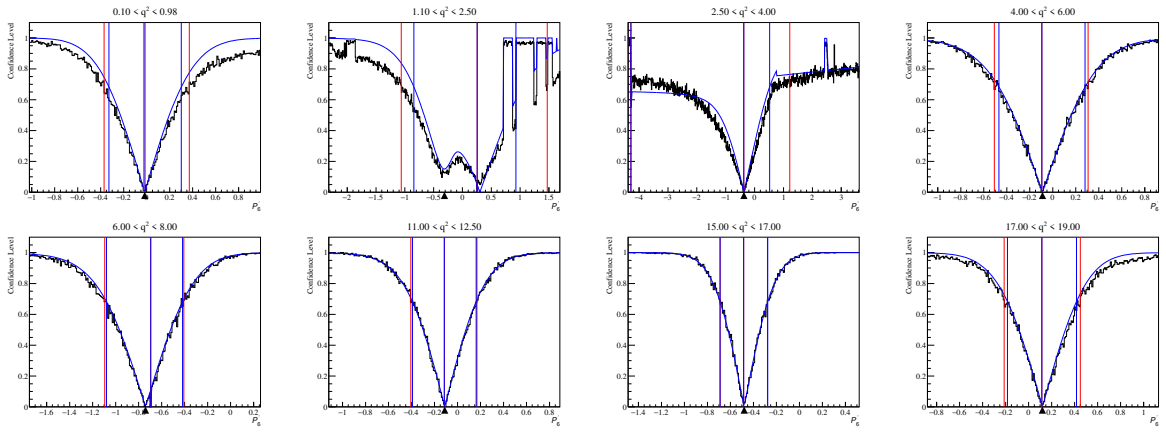

Figure 109: Resulting profiles of the Feldman-Cousins scan performed on parameter P_6 in all eight q^2 bins. The results from the toy event studies at each step are given by the black histogram, plus the red vertical lines indicating the positions of the maximum likelihood position and the $\pm 1\sigma$ values. In addition, the likelihood profile is shown in blue. The black triangular marker notates the value obtained in the actual fit to the data.

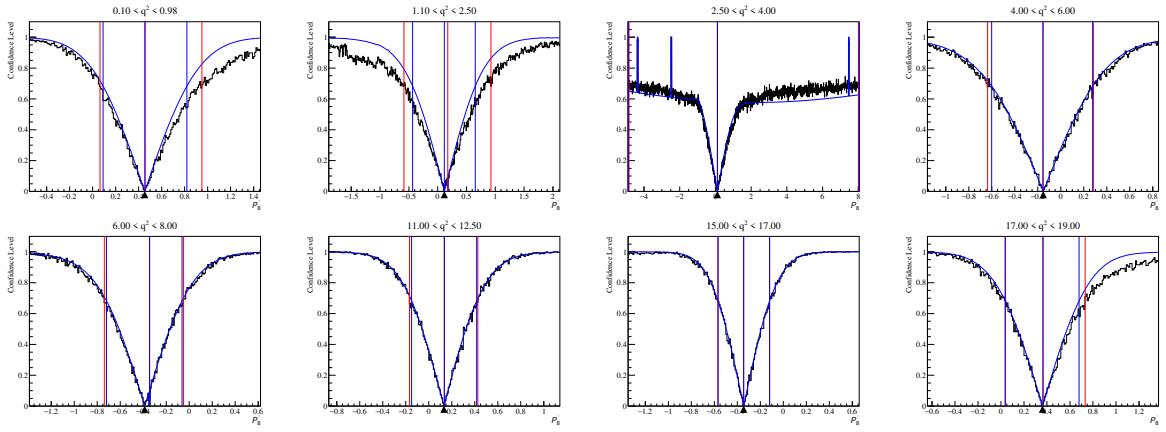

Figure 110: Resulting profiles of the Feldman-Cousins scan performed on parameter P_8 in all eight q^2 bins. The results from the toy event studies at each step are given by the black histogram, plus the red vertical lines indicating the positions of the maximum likelihood position and the $\pm 1\sigma$ values. In addition, the likelihood profile is shown in blue. The black triangular marker notates the value obtained in the actual fit to the data.

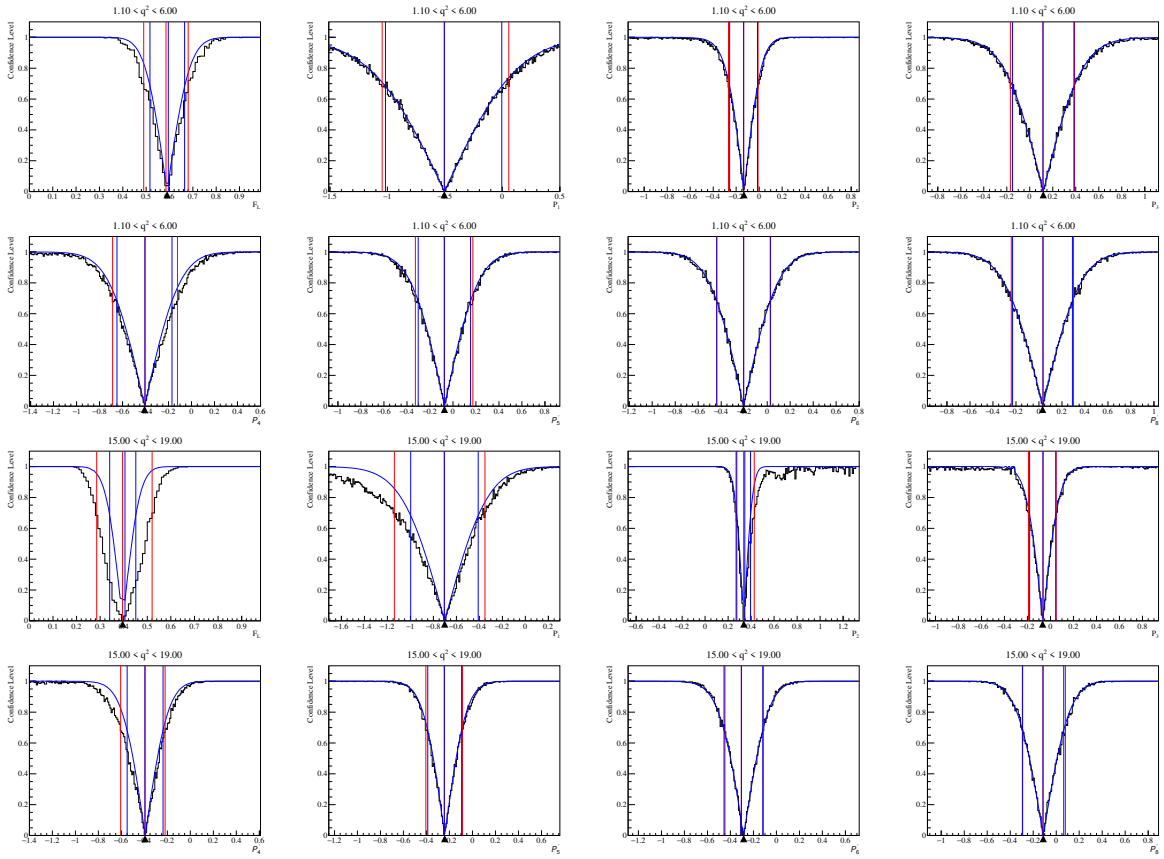

Figure 111: Resulting profiles of the Feldman-Cousins scan performed on all eight $P_x^{(\prime)}$ observables in the two larger q^2 bins. The first two rows show the eight observables for the bin [1.1-6.0] GeV^2/c^4 and two bottom rows show the observables in the bin [15.0-19.0] GeV^2/c^4. The results from the toy event studies at each step are given by the black histogram, plus the red vertical lines indicating the positions of the maximum likelihood position and the $\pm 1\sigma$ values. In addition, the likelihood profile is shown in blue. The black triangular marker notates the value obtained in the actual fit to the data.

A Appendices

A.1 Trigger configuration

The HLT configuration is saved in a Trigger Configuration Key (TCK). A complete list of used TCK in the complete data-set from 2011 to 2018 is given in Tables 81 and 82 for Run I and Run II, respectively.

Table 81: All TCK used for the data acquisition for all years Run I and for both magnet polarities (up and down). The total and relative number of events recorded in this HLT configuration.

data-set	TCK	events	fraction [%]
2011 down	360032	2536	0.50
	480032	1497	0.29
	4a0033	2080	0.41
	5a0032	24475	4.82
	5b0032	47	0.01
	6d0032	86781	17.08
	700034	950	0.19
	710035	868	0.17
	730035	54310	10.69
	760037	167538	32.98
	790038	166959	32.86
2011 up	5a0032	25557	7.36
	5b0032	1262	0.36
	5d0033	1241	0.36
	730035	107650	31.02
	740036	3318	0.96
	760037	86990	25.06
	790037	28324	8.16
	790038	92731	26.72
2012 down	7e003a	59	0.01
	7f0040	205	0.02
	860040	3990	0.44
	8c0040	55255	6.05
	8e0040	506	0.06
	94003d	90147	9.87
	95003d	1010	0.11
	97003d	140235	15.35
	990042	176819	19.35
	990044	101568	11.12
	a30044	135808	14.86
	a30046	9160	1.00
	a90046	57298	6.27
	ab0046	49213	5.39
	ac0046	92431	10.12
	ad0046	27	0.00
2012 up	94003d	167149	15.98
	95003d	123	0.01
	97003d	123996	11.85
	990042	382918	36.61
	990043	2481	0.24
	990044	30438	2.91
	9a0042	14	0.00
	9f0045	27356	2.62
	a10044	25692	2.46
	a10045	78053	7.46
	a20044	1430	0.14
	a30044	176031	16.83
	a30046	21075	2.01
	ac0046	9240	0.88
	ad0046	50	0.00

Table 82: All TCK used for the data acquisition for Run II and for both magnet polarities (up and down). The total and relative number of events recorded in this HLT configuration.

data-set	TCK	events	fraction [%]
2015 down	10600a2	132582	50.33
	10600a3	99710	37.85
	10600a6	82	0.03
	10600a7	2021	0.77
	10700a1	10688	4.06
	10800a2	18331	6.96
2015 up	10800a2	76056	39.75
	11400a8	115294	60.25
2016 down	11291600	8610	0.71
	11291603	54137	4.46
	11291604	38846	3.20
	11291605	118218	9.74
	11371609	93173	7.68
	1137160e	33973	2.80
	11381609	10121	0.83
	1138160e	47072	3.88
	1138160f	809285	66.69
2016 up	11321609	159801	13.83
	11341609	179726	15.55
	11351609	32569	2.82
	11361609	593831	51.38
	11381611	64709	5.60
	11381612	125226	10.83
2017 down	11541707	118639	10.09
	115417a7	638	0.05
	11561707	297539	25.32
	11611707	161553	13.75
	11611708	203675	17.33
	11611709	393266	33.46
2017 up	114e1702	4202	0.38
	114e1703	2391	0.22
	11501703	31274	2.84
	11501704	36176	3.28
	11501705	161821	14.68
	11501706	33023	3.00
	11561707	113734	10.32
	11601707	142334	12.91
	11601708	146844	13.32
	11611709	430635	39.06
2018 down	11741801	112116	8.69
	11751801	365265	28.30
	11771801	19934	1.54
	117a18a2	687151	53.24
	117a18a4	106303	8.24
2018 up	11671801	5755	0.47
	11711801	6736	0.55
	11731801	125663	10.18
	11741801	215701	17.47
	11771801	234149	18.97
	117718a1	597	0.05
	117a18a2	378874	30.69
	117a18a4	267084	21.63

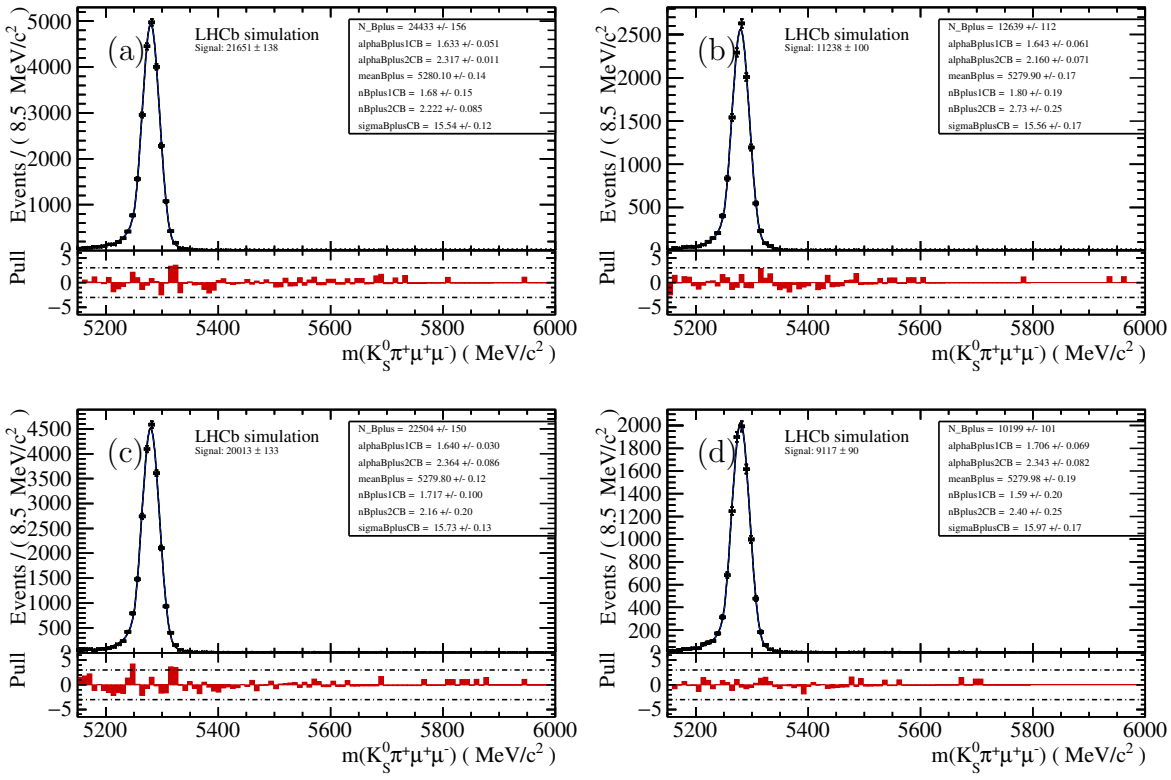

Figure 112: B^+ mass distribution of J/ψ MC events from 2011 DD (a) and LL (b) track events and 2012 DD (c) and LL (d) track events. These data samples consist entirely of $\mu^+\mu^-$ decays coming from a J/ψ. In consistency with the data selection, the invariant mass squared of the $\mu^+\mu^-$ is cut, $8.68\,\text{GeV}^2/c^4 < q^2 < 10.09\,\text{GeV}^2/c^4$. The B^+ mass peak is modelled by a two tailed Crystal Ball (one tail to low mass region and one towards high mass region).

A.2 Monte Carlo mass shape fits

To fix certain parameters of the Crystal Ball function in the fits to pre-selected data, a fit to the corresponding sample in MC is performed. Equal to the fit projections of data in Figs. 5 and 6 in Section 2.5, the mass fits of MC events for Run I and Run II are shown in Figs. 112 and 113.

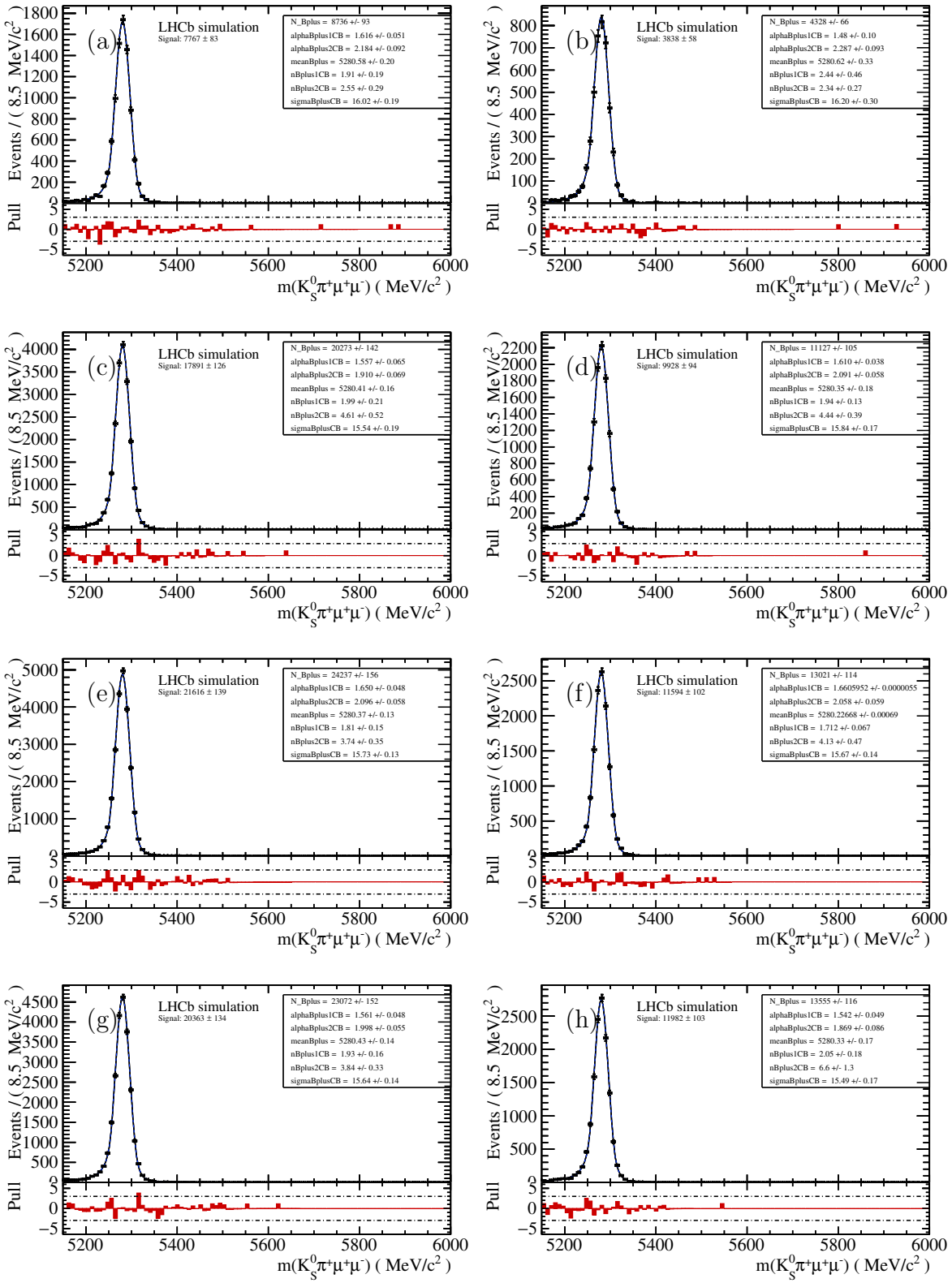

Figure 113: B^+ mass shape of signal MC events from 2015 DD (a) and LL (b), 2016 DD (c) and LL (d), 2017 DD (e) and LL (f) and 2018 DD (g) and LL (h) track events. These signal channel MC events do not have a q^2 cut applied. The B^+ mass peak is modelled by a two tailed Crystal Ball (one tail to low mass region and one towards high mass region).

A.3 Data-Monte Carlo comparison

Data events are *sWeighted* and simulated MC events are re-weighted to these data events. To check the agreement between both, the distributions of both are shown in direct comparison and their normalized ratio is created. All variables of interest for all six years are presented. The following pages present the comparison of data events from the full q^2 range (mostly resonant J/ψ events) with signal channel MC events for the years 2011 DD tracks and LL tracks in Figs. 114 to 117, 2012 DD tracks and LL tracks in Figs. 118 to 121, 2015 DD tracks and LL tracks in Figs. 122 to 125, 2016 DD tracks and LL tracks in Figs. 126 to 129, 2017 DD tracks and LL tracks in Figs. 130 to 133, and 2018 DD tracks and LL tracks in Figs. 134 to 137.

In addition, the comparison between resonant data events and resonant channel MC events is presented for 2011 DD tracks and LL tracks in Figs. 138 to 141, 2012 DD tracks and LL tracks in Figs. 142 to 144 and 149 and 2016 DD tracks and LL tracks in Figs. 144, 146, 147 and 149.

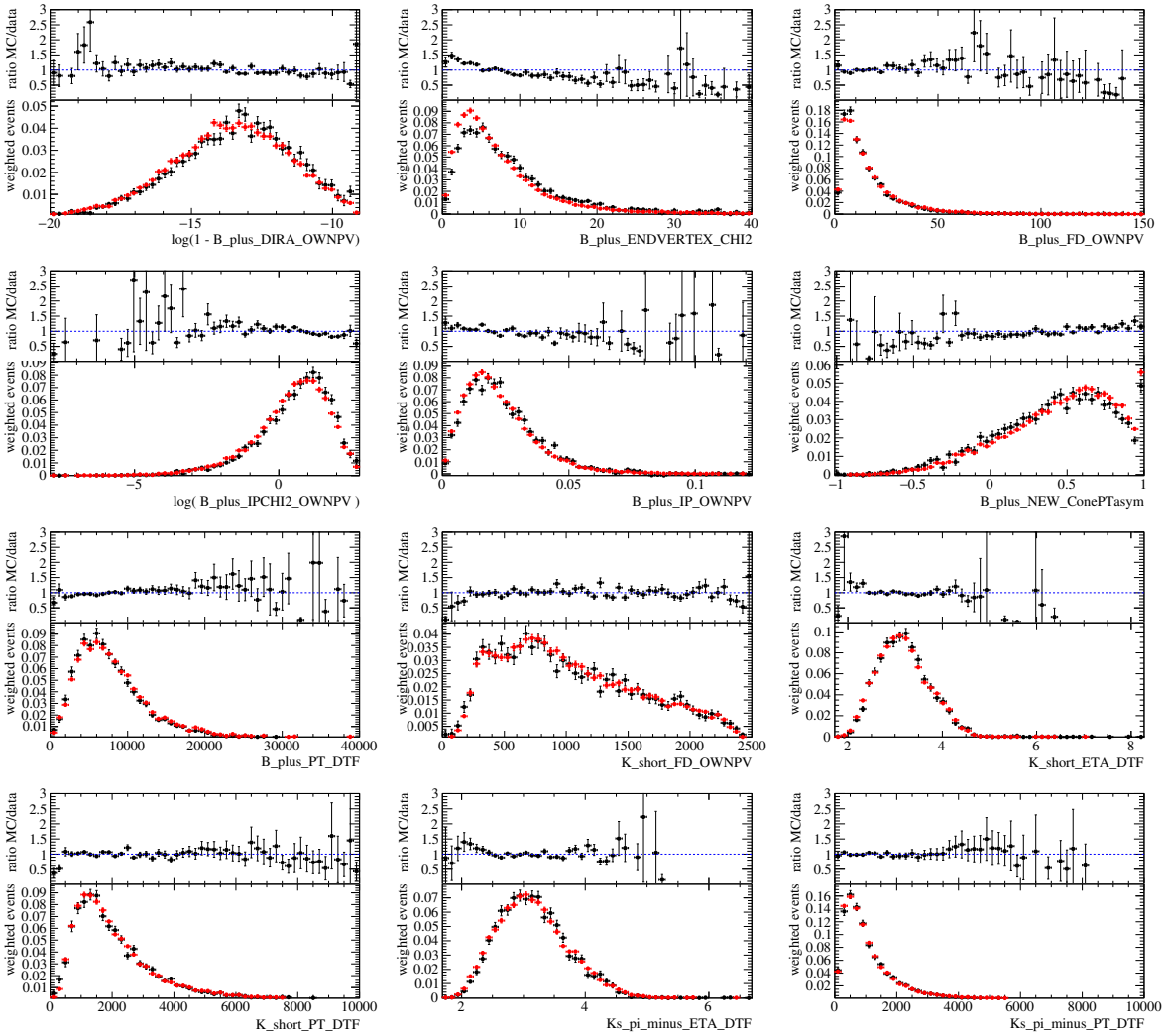

Figure 114: Comparison (1/2) of variables between *sWeighted* data (black) and 2 × 1D re-weighted simulated events (red). The samples are 2011 with DD tracks only.

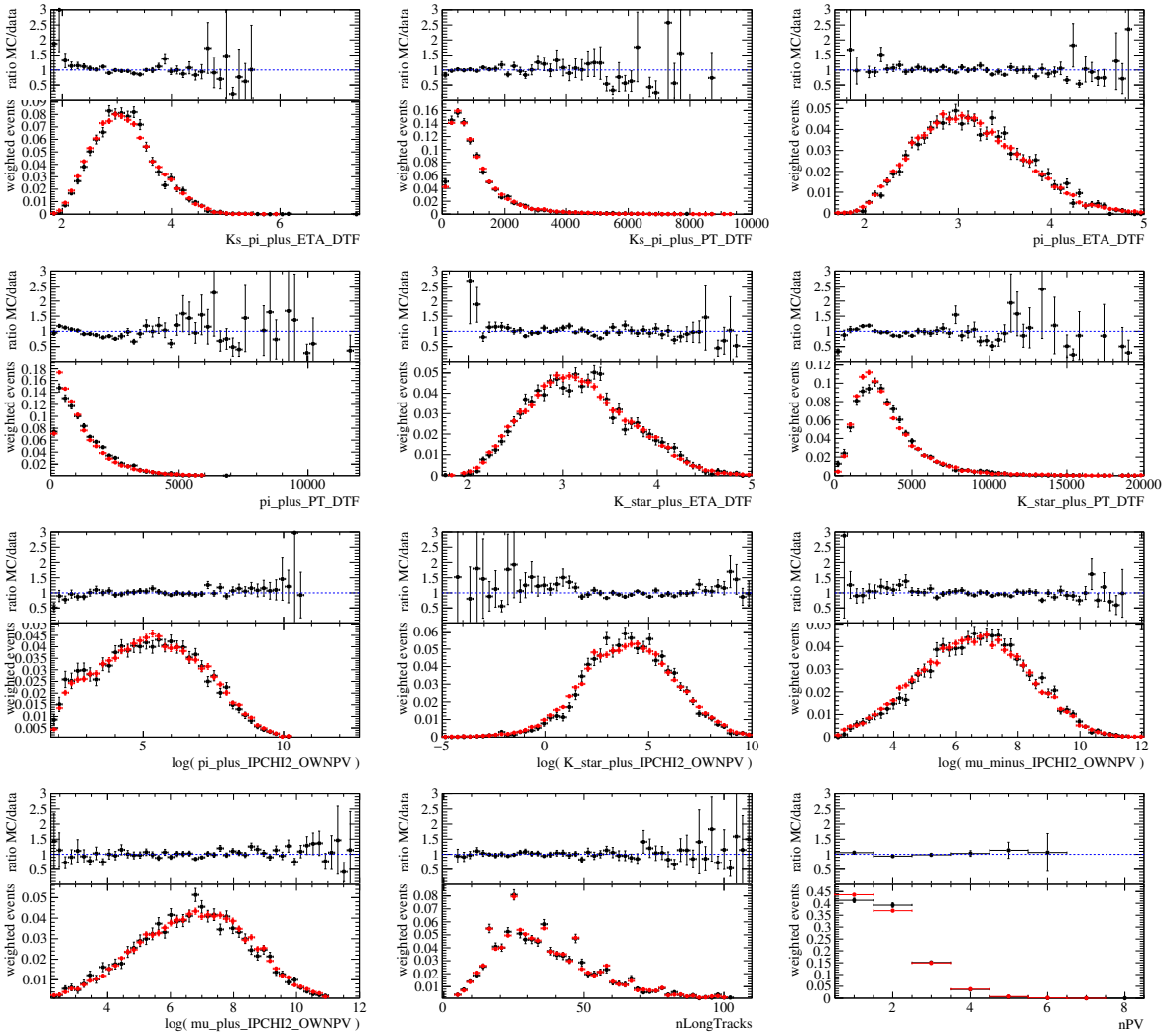

Figure 115: Comparison (2/2) of variables between *sWeighted* data (black) and 2 × 1D reweighted simulated events (red). The samples are 2011 with DD tracks only.

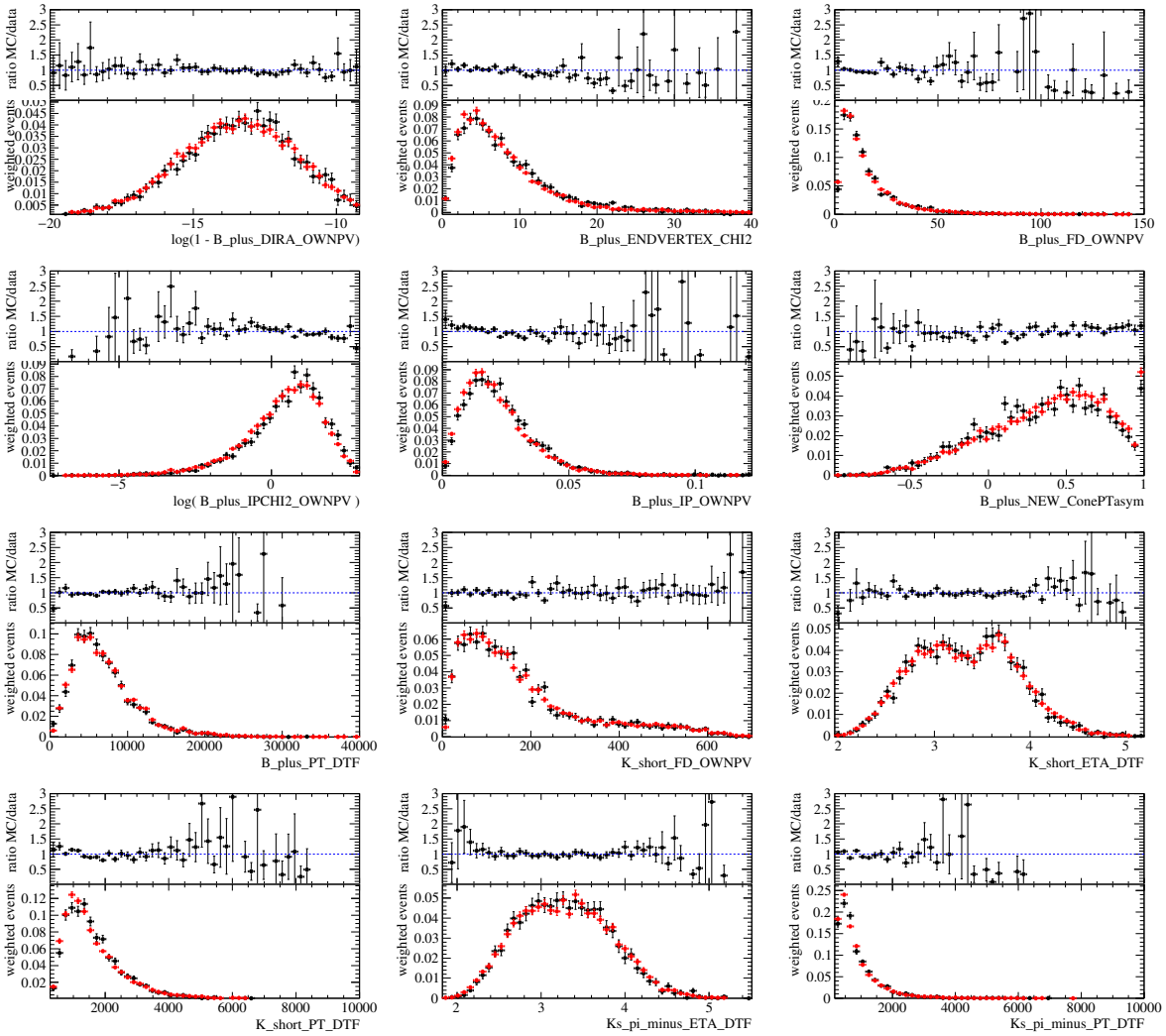

Figure 116: Comparison (1/2) of variables between *sWeighted* data (black) and 2 × 1D reweighted simulated events (red). The samples are 2011 with LL tracks only.

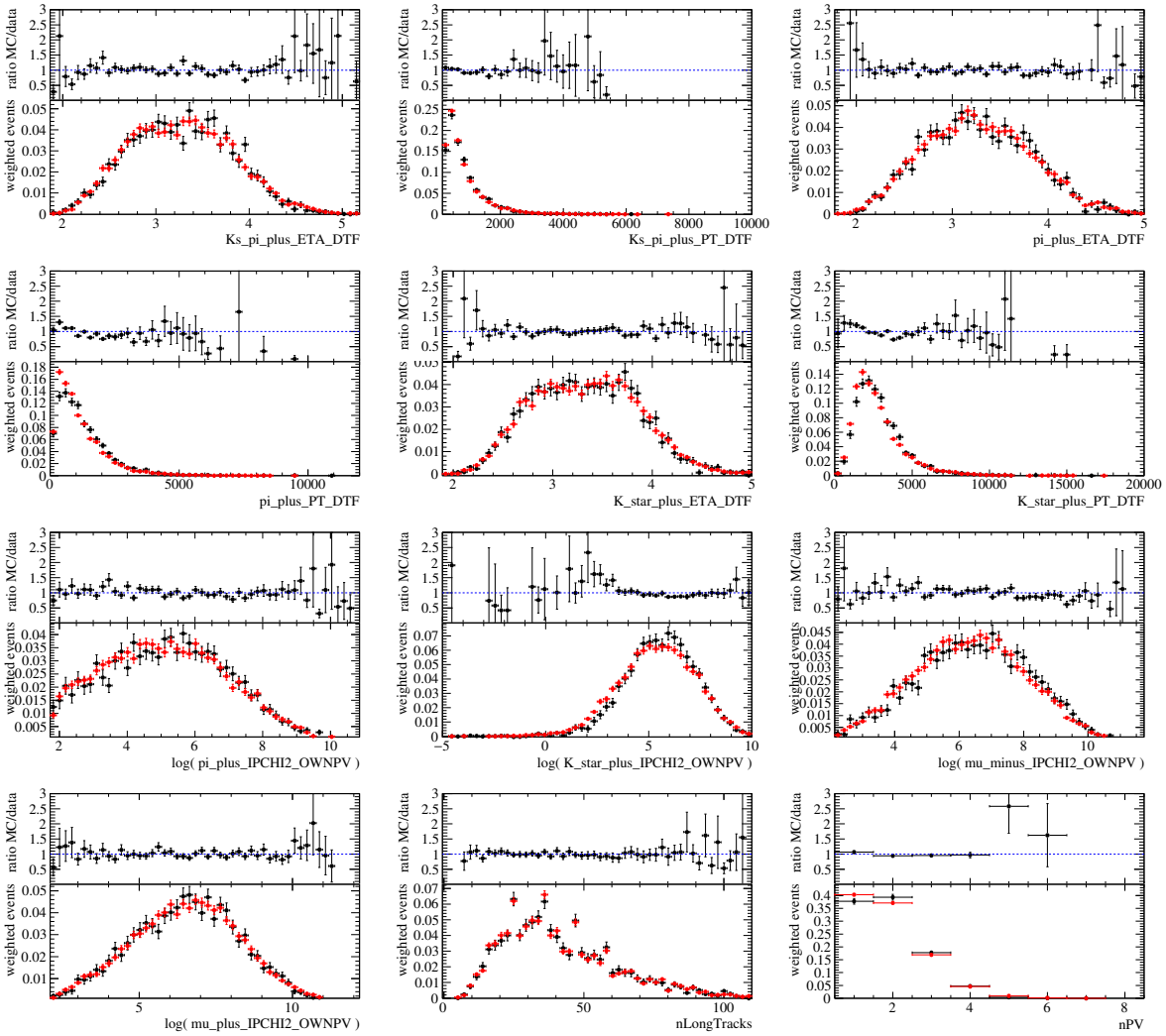

Figure 117: Comparison (2/2) of variables between *sWeighted* data (black) and 2 × 1D reweighted simulated events (red). The samples are 2011 with LL tracks only.

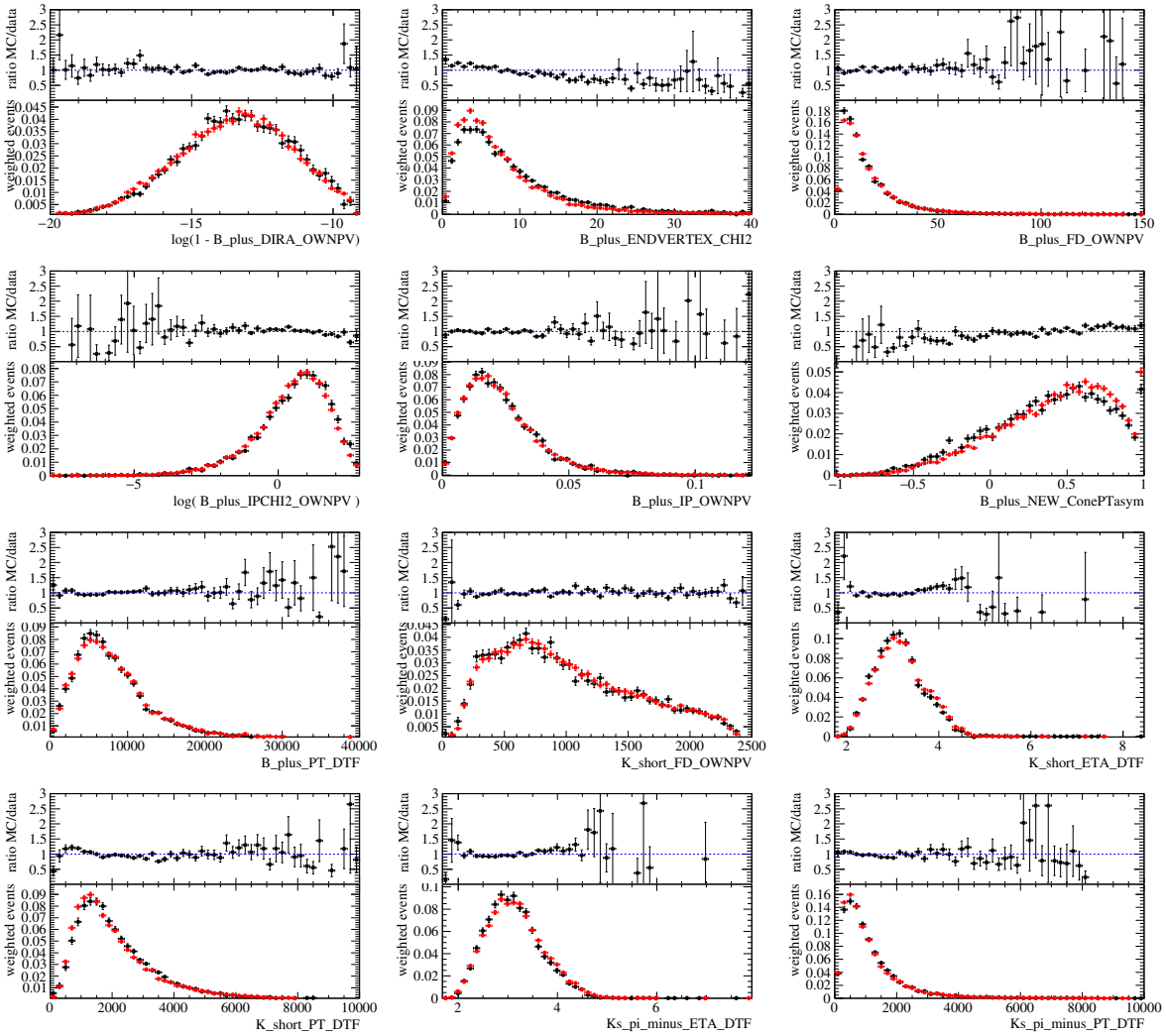

Figure 118: Comparison (1/2) of variables between *sWeighted* data (black) and 2 × 1D reweighted simulated events (red). The samples are 2012 with DD tracks only.

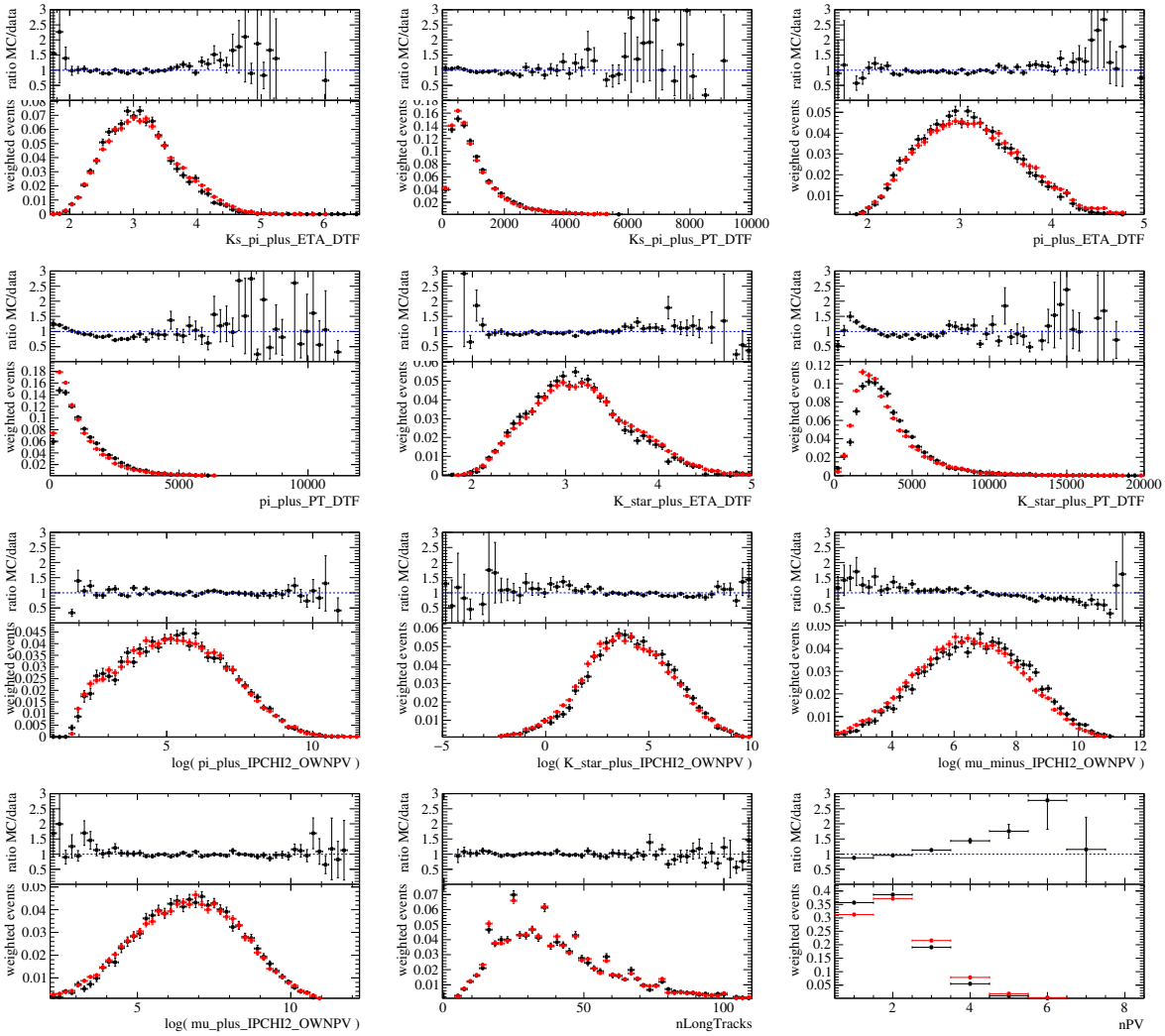

Figure 119: Comparison (2/2) of variables between *sWeighted* data (black) and 2 × 1D reweighted simulated events (red). The samples are 2012 with DD tracks only.

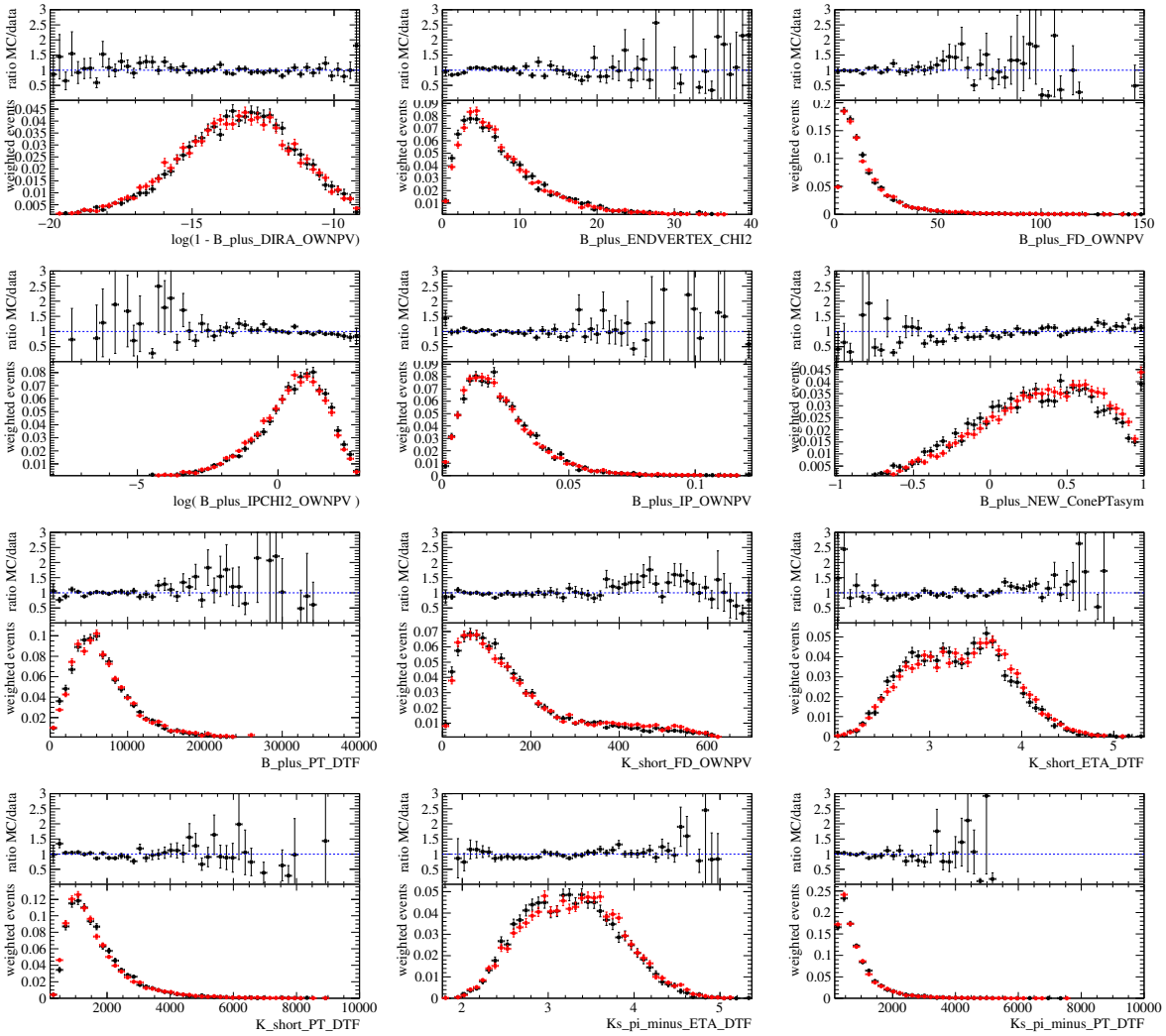

Figure 120: Comparison (1/2) of variables between *sWeighted* data (black) and 2 × 1D reweighted simulated events (red). The samples are 2012 with LL tracks only.

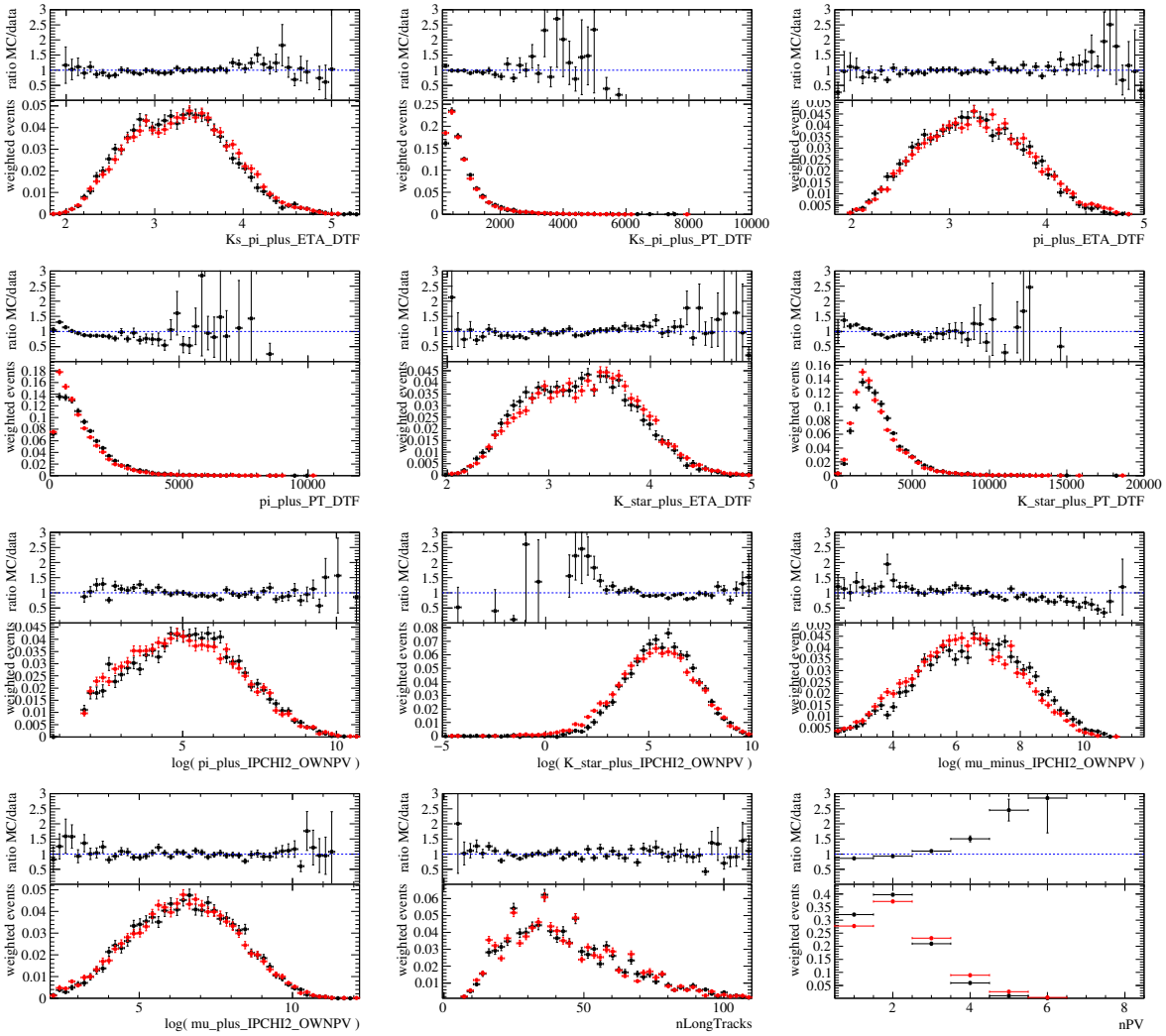

Figure 121: Comparison (2/2) of variables between *sWeighted* data (black) and 2 × 1D reweighted simulated events (red). The samples are 2012 with LL tracks only.

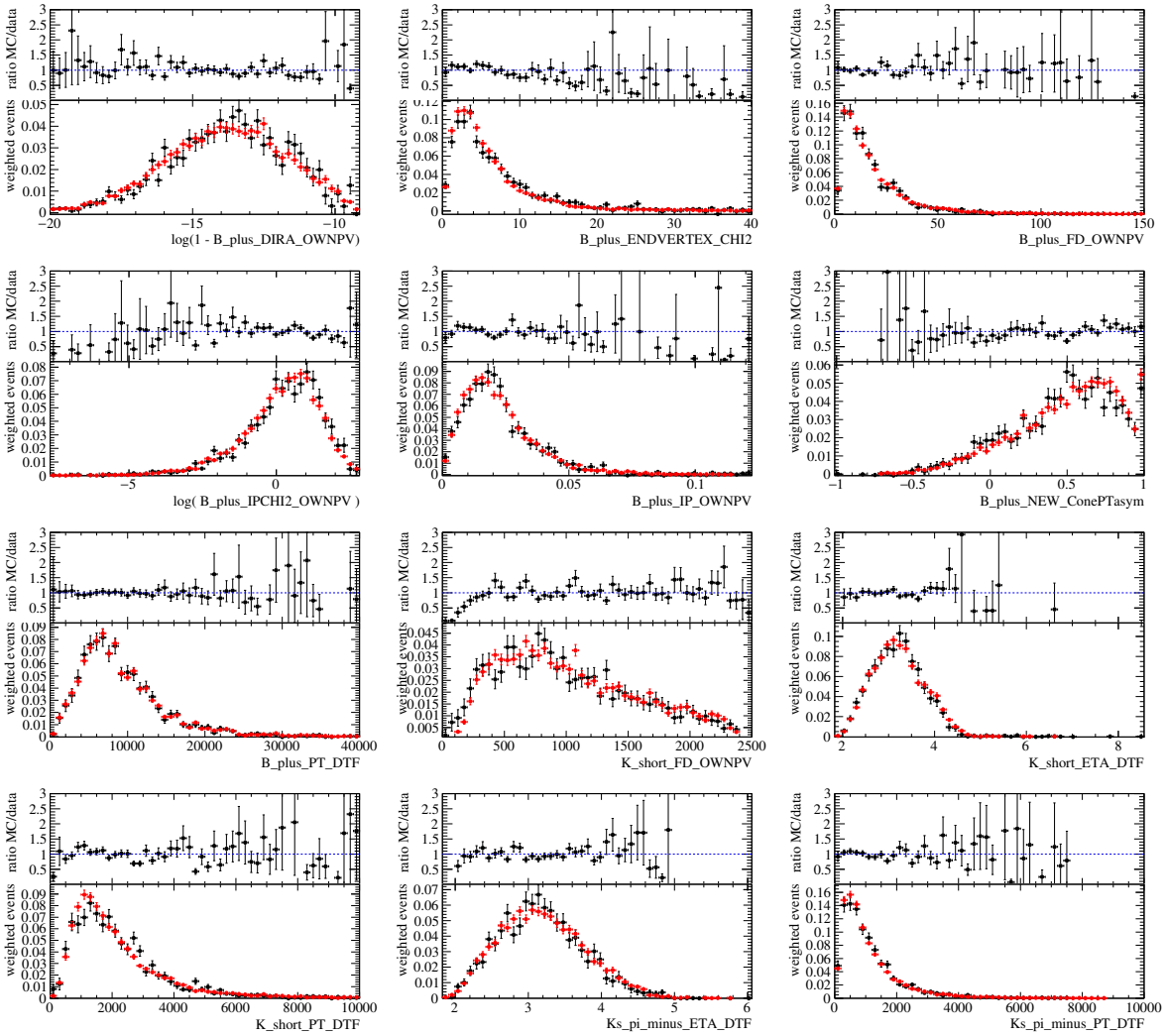

Figure 122: Comparison (1/2) of variables between *sWeighted* data (black) and 2 × 1D reweighted simulated events (red). The samples are 2015 with DD tracks only.

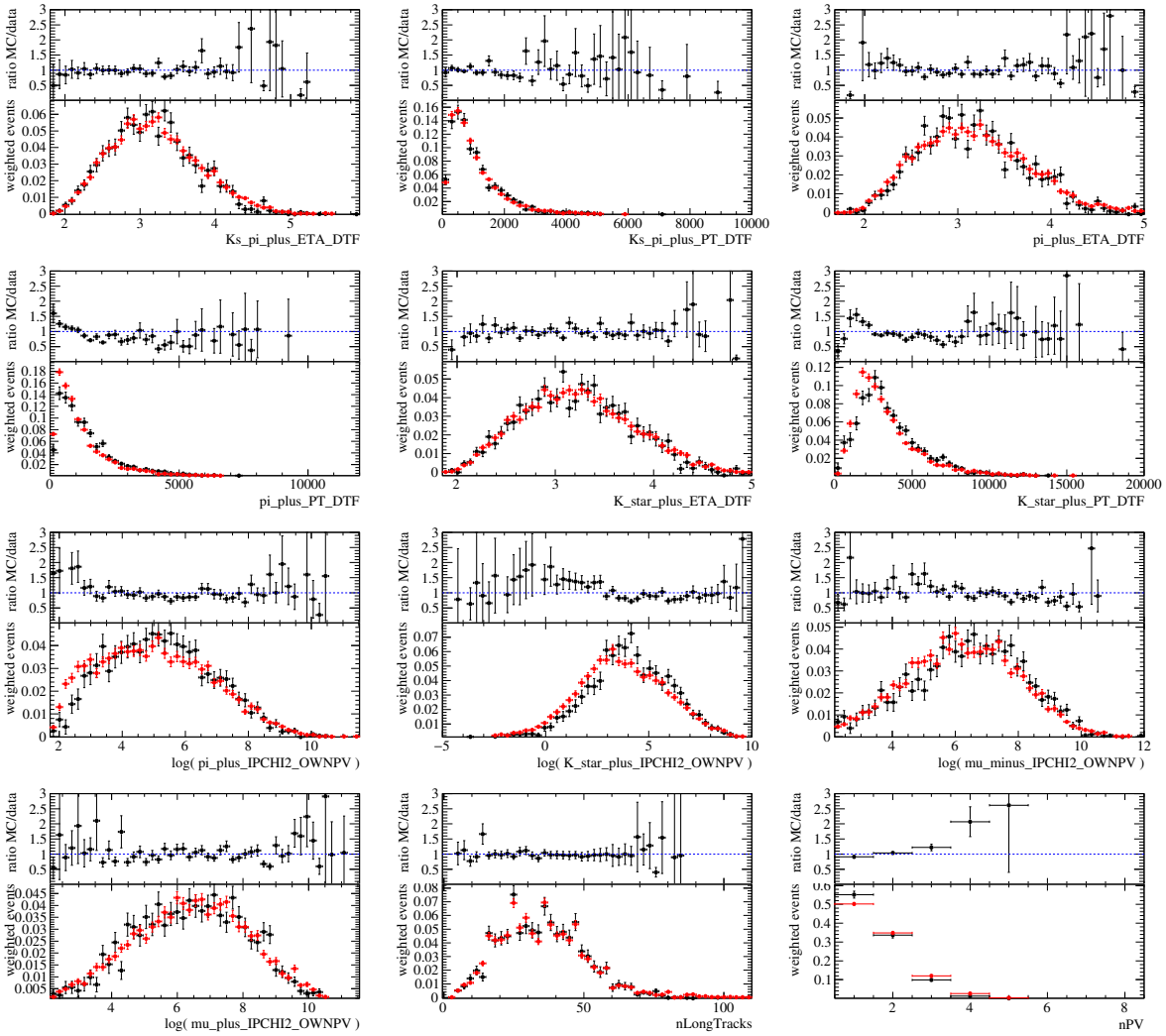

Figure 123: Comparison (2/2) of variables between *sWeighted* data (black) and 2 × 1D reweighted simulated events (red). The samples are 2015 with DD tracks only.

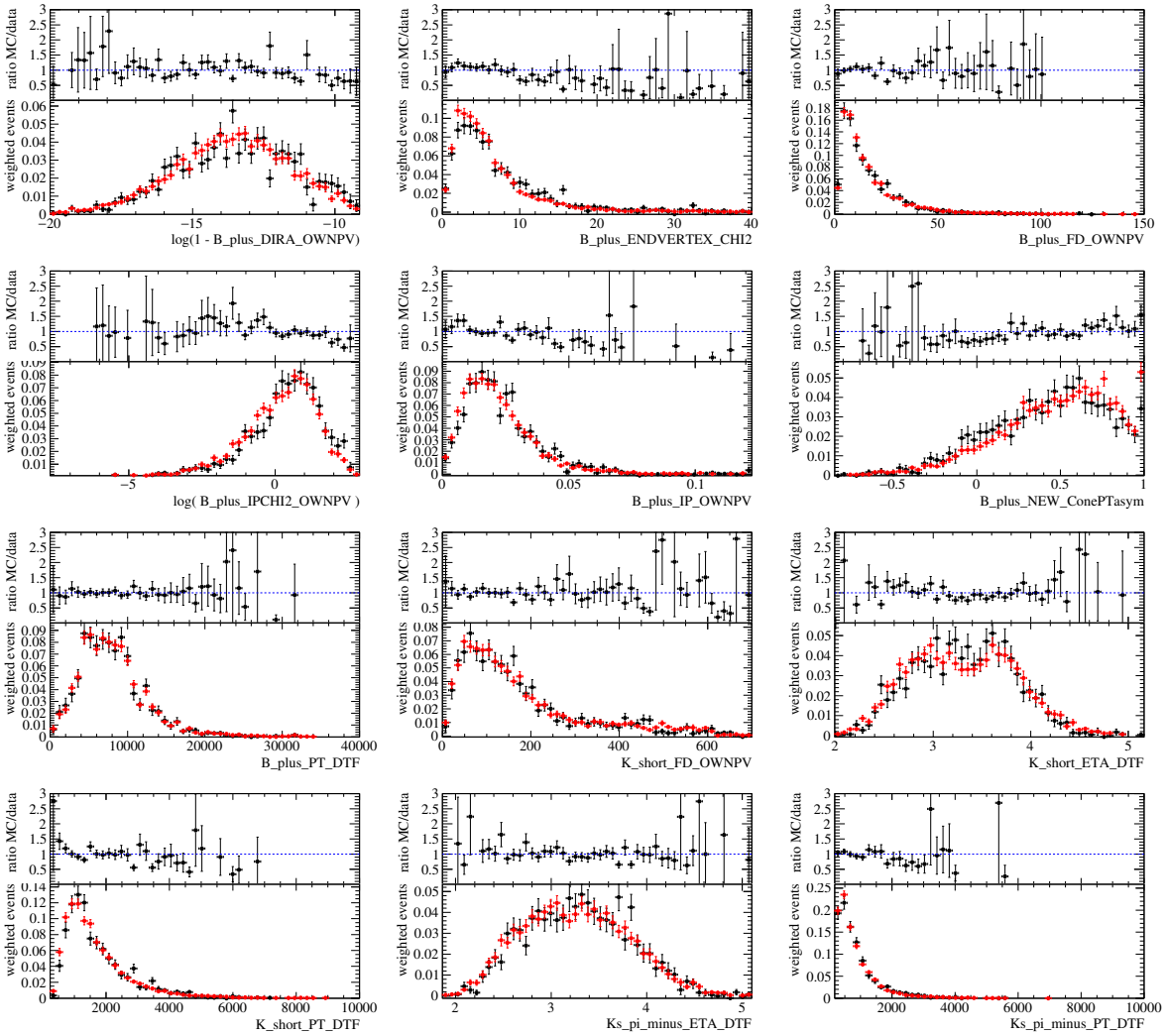

Figure 124: Comparison (1/2) of variables between *sWeighted* data (black) and 2 × 1D reweighted simulated events (red). The samples are 2015 with LL tracks only.

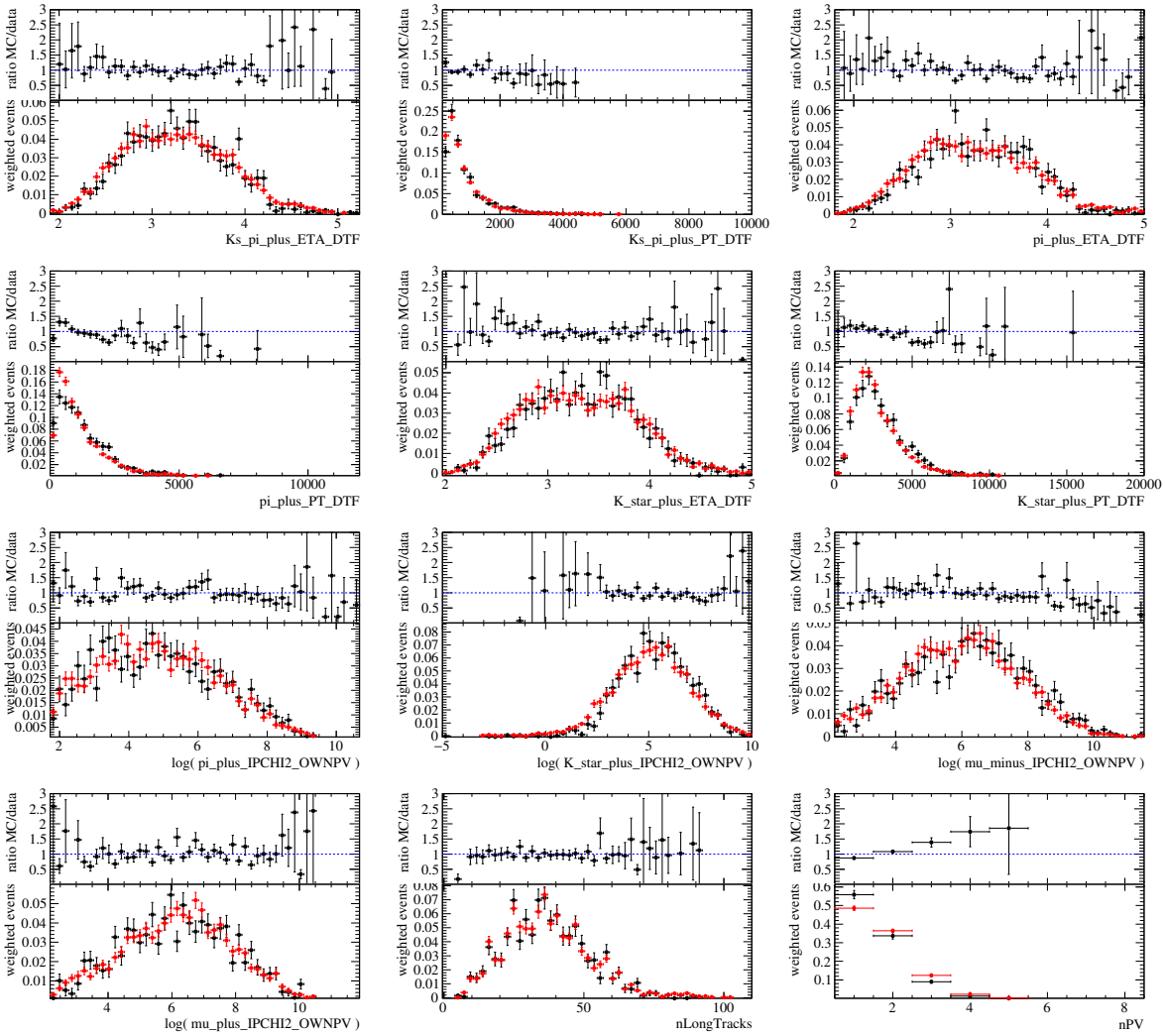

Figure 125: Comparison (2/2) of variables between *sWeighted* data (black) and 2 × 1D reweighted simulated events (red). The samples are 2015 with LL tracks only.

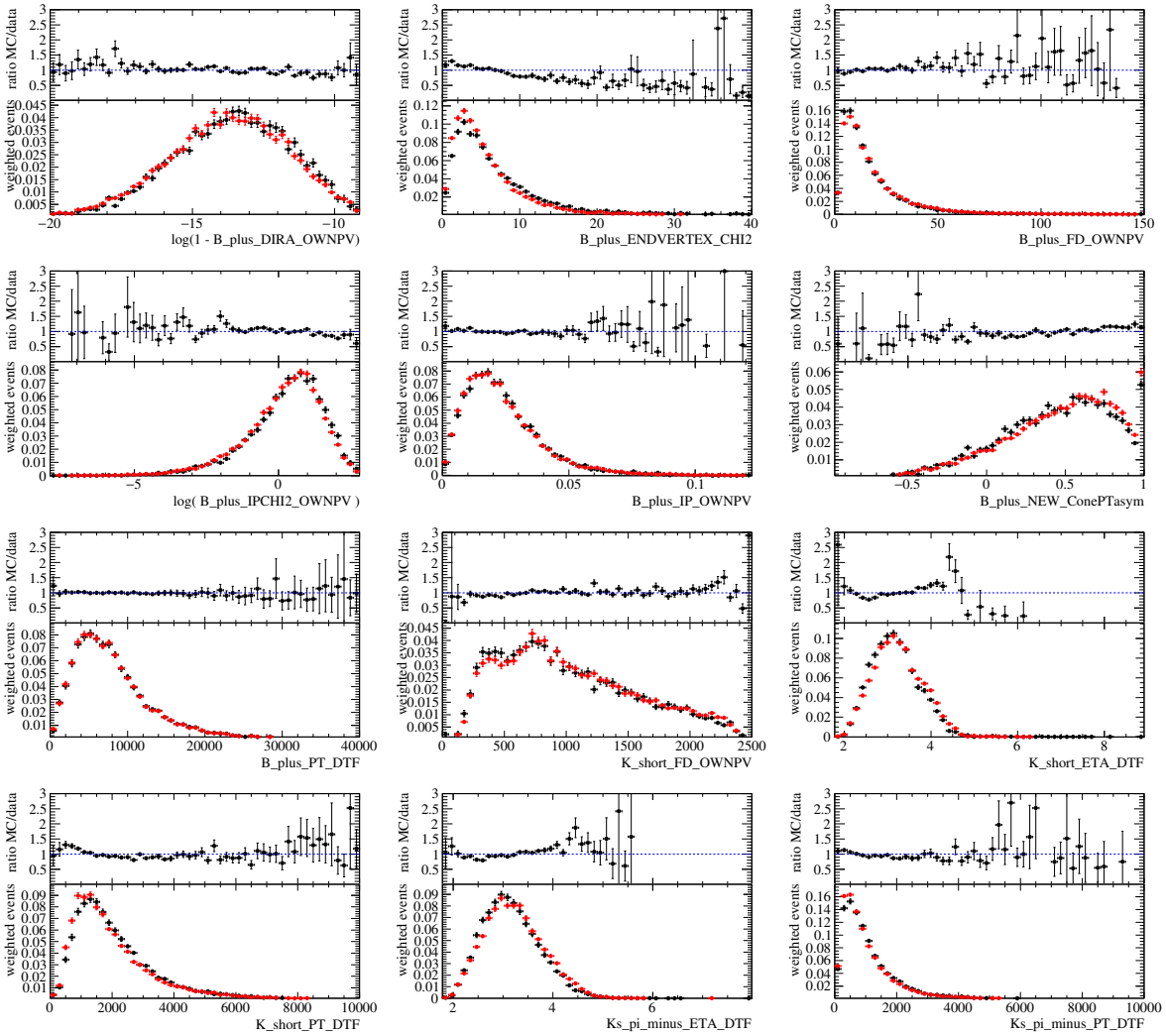

Figure 126: Comparison (1/2) of variables between *sWeighted* data (black) and 2 × 1D reweighted simulated events (red). The samples are 2016 with DD tracks only.

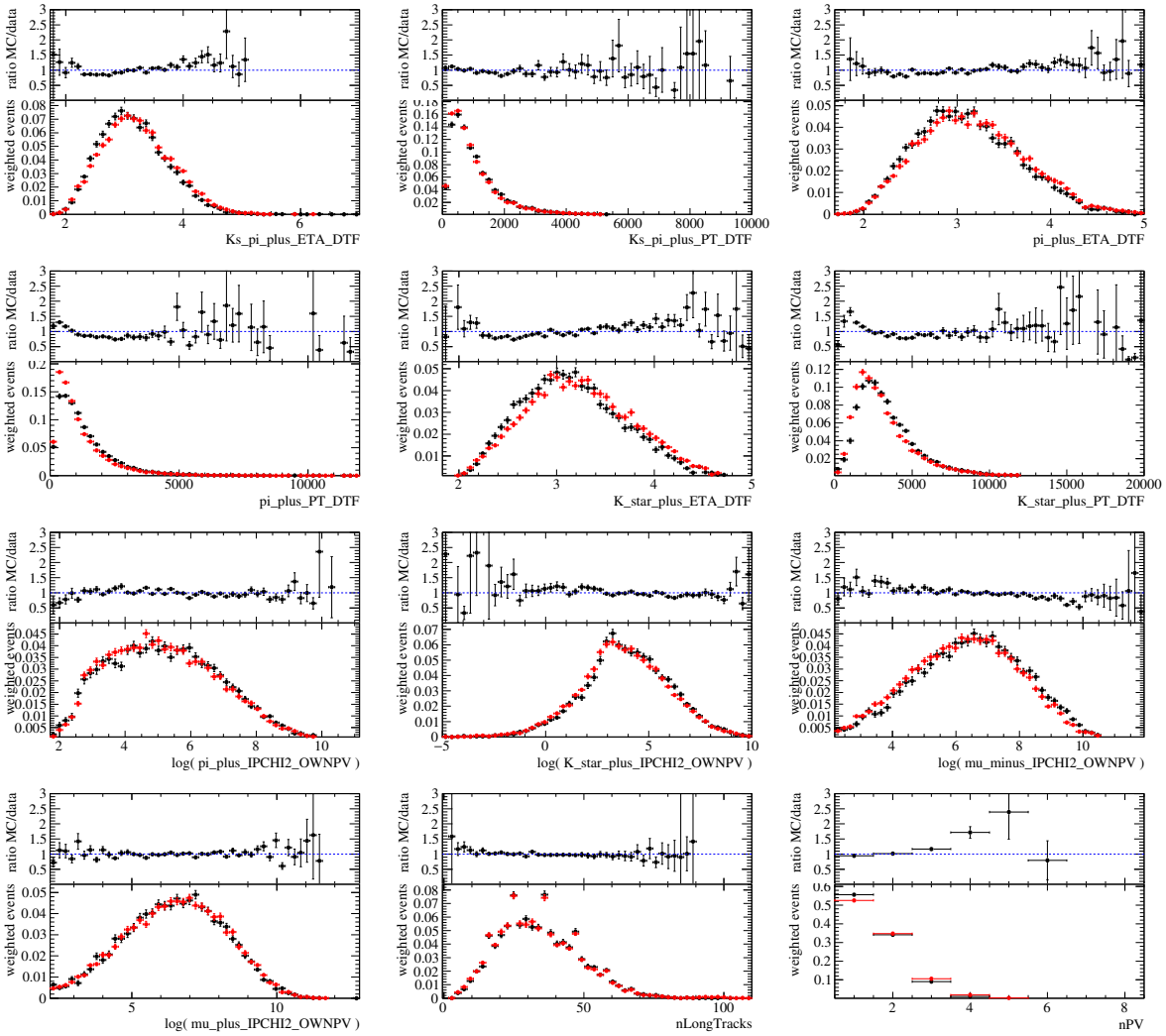

Figure 127: Comparison (2/2) of variables between *sWeighted* data (black) and 2 × 1D reweighted simulated events (red). The samples are 2016 with DD tracks only.

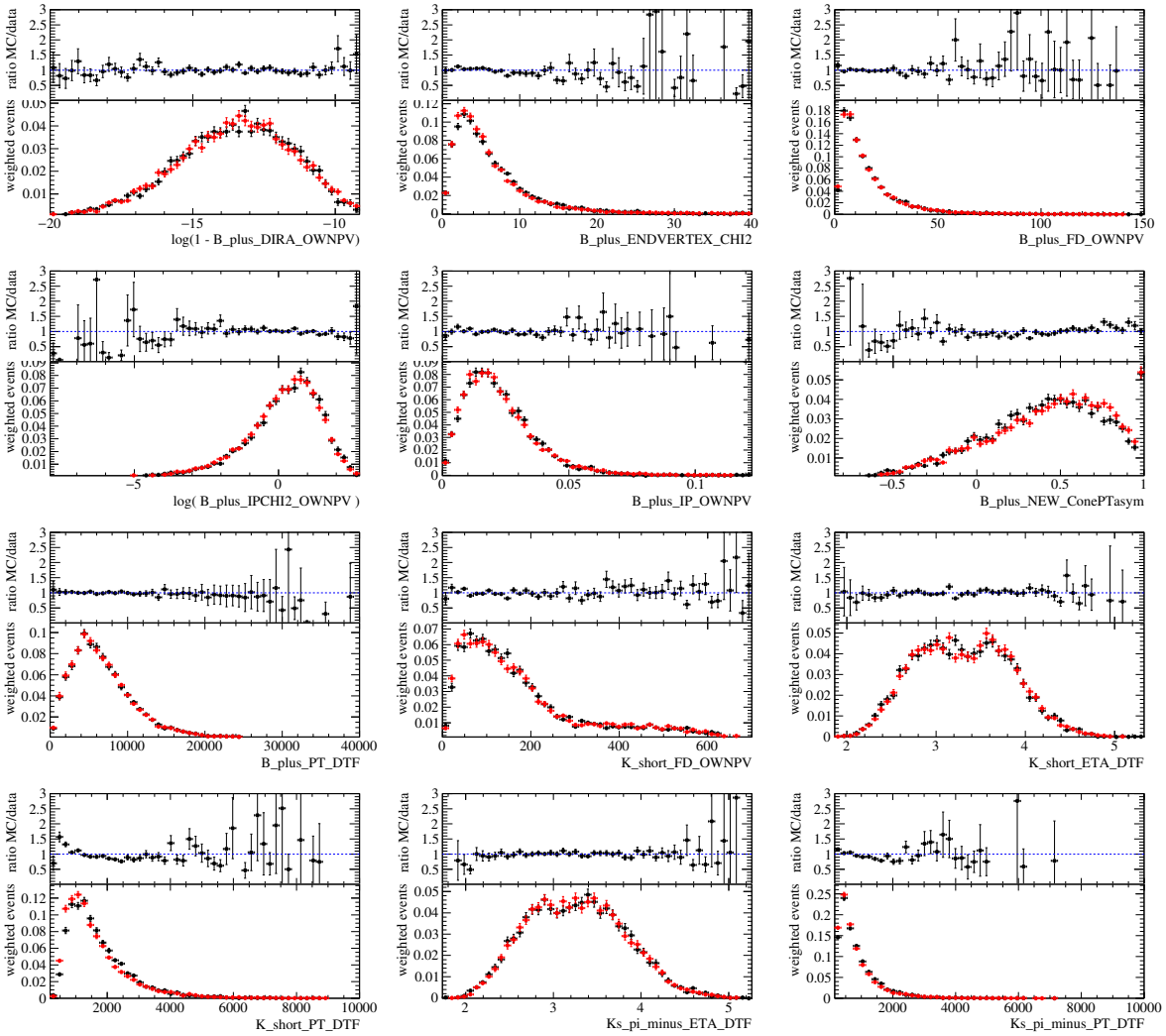

Figure 128: Comparison (1/2) of variables between *sWeighted* data (black) and 2 × 1D reweighted simulated events (red). The samples are 2016 with LL tracks only.

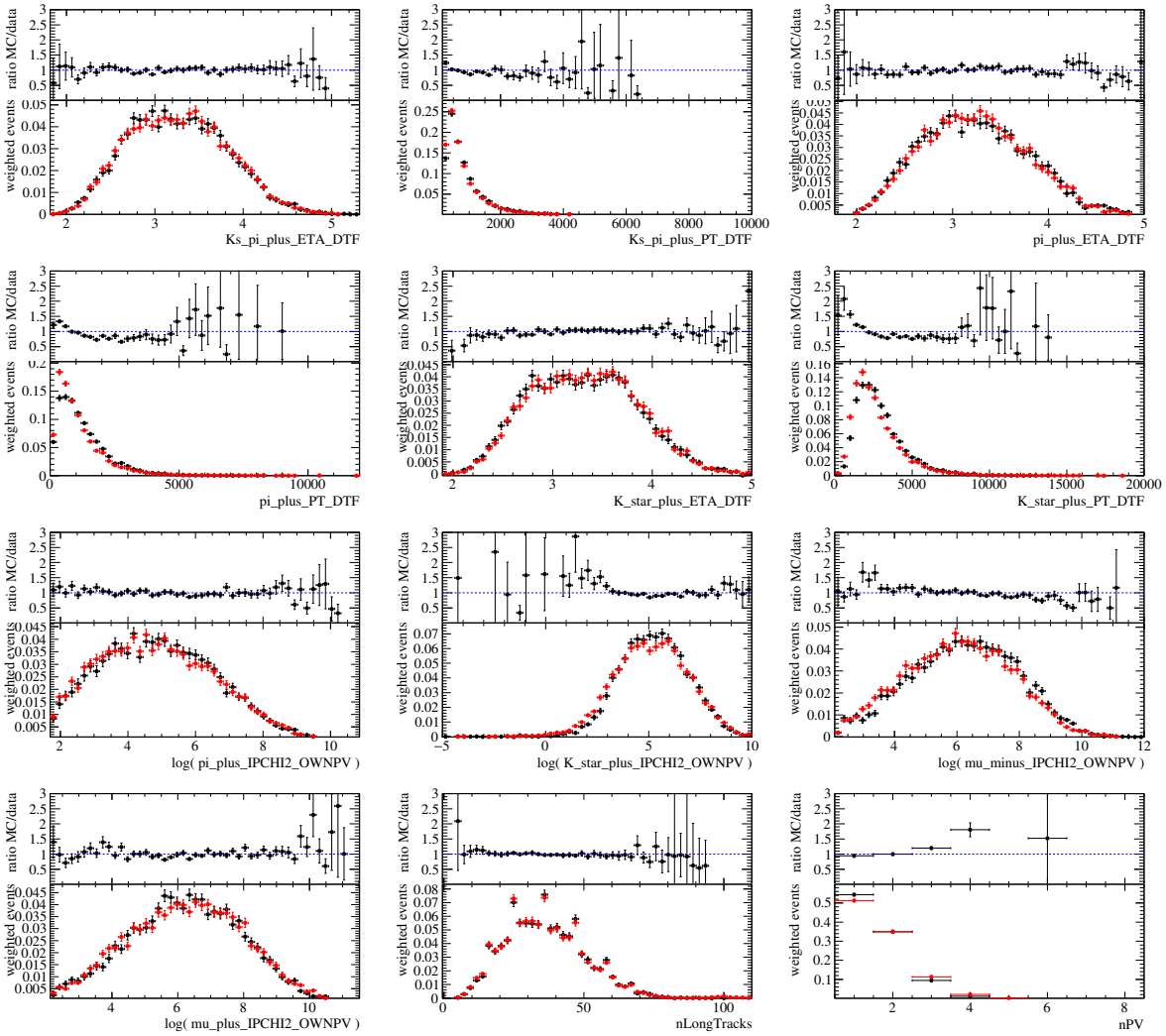

Figure 129: Comparison (2/2) of variables between *sWeighted* data (black) and 2 × 1D reweighted simulated events (red). The samples are 2016 with LL tracks only.

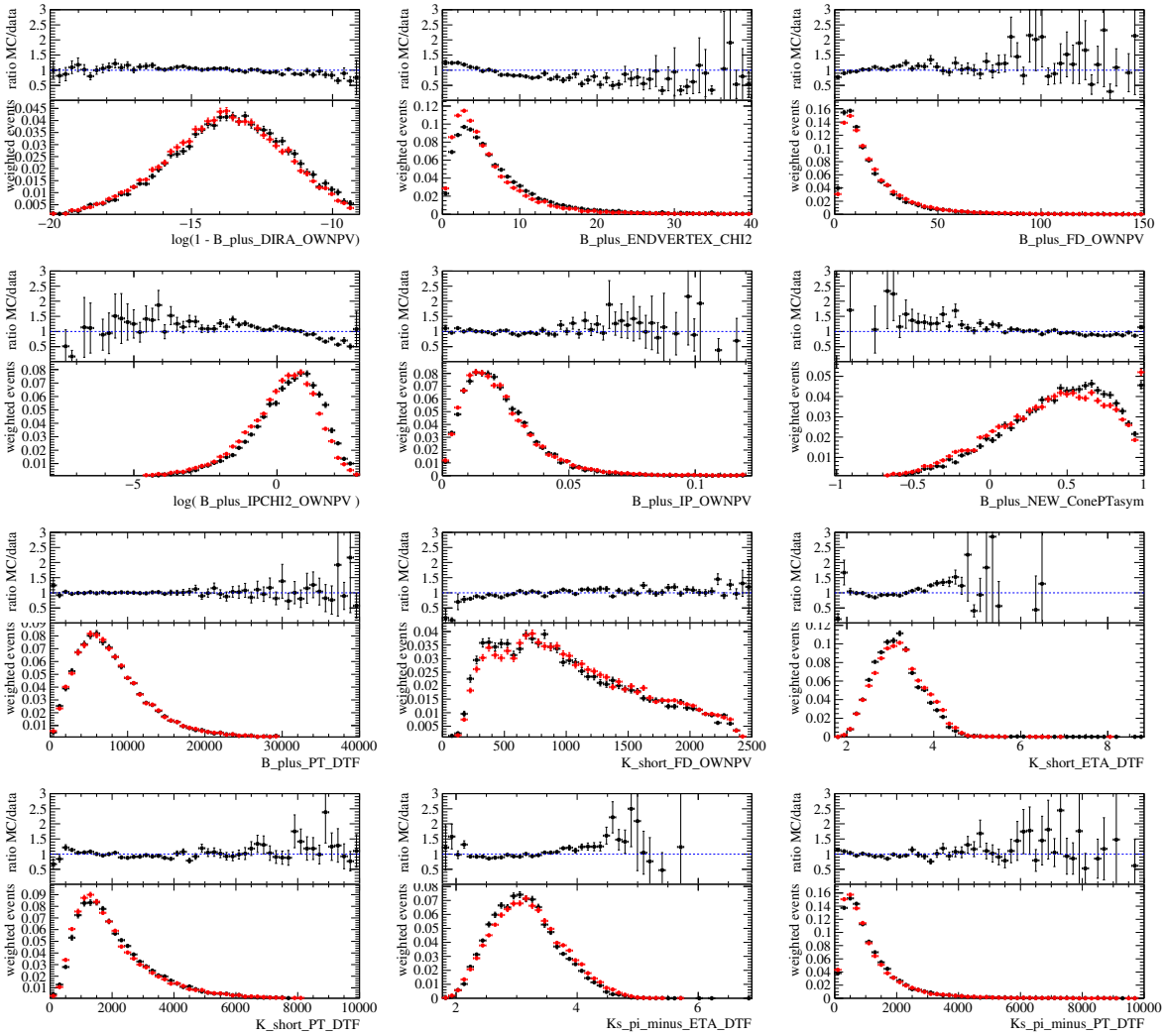

Figure 130: Comparison (1/2) of variables between *sWeighted* data (black) and 2 × 1D reweighted simulated events (red). The samples are 2017 with DD tracks only.

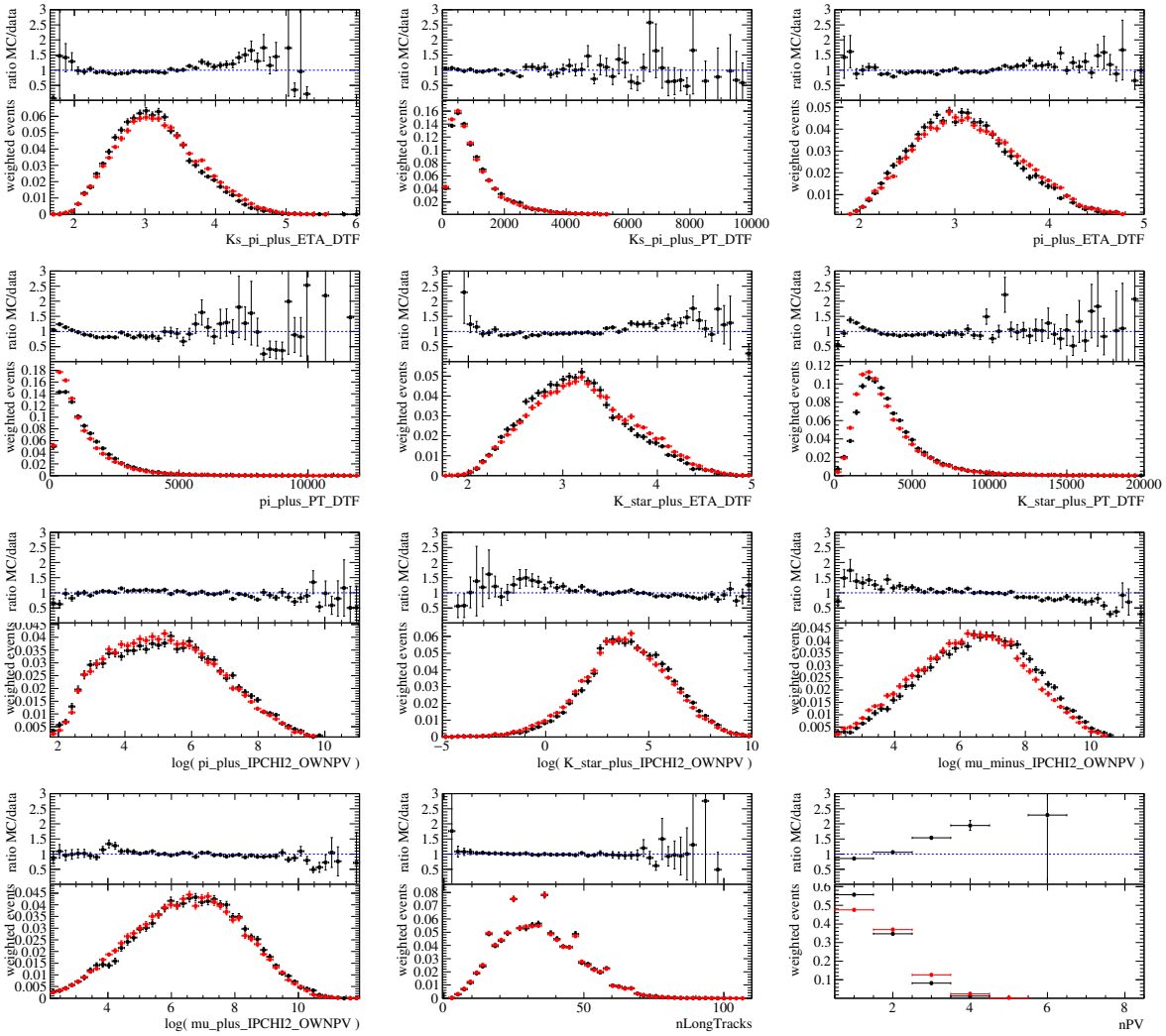

Figure 131: Comparison (2/2) of variables between *sWeighted* data (black) and 2 × 1D reweighted simulated events (red). The samples are 2017 with DD tracks only.

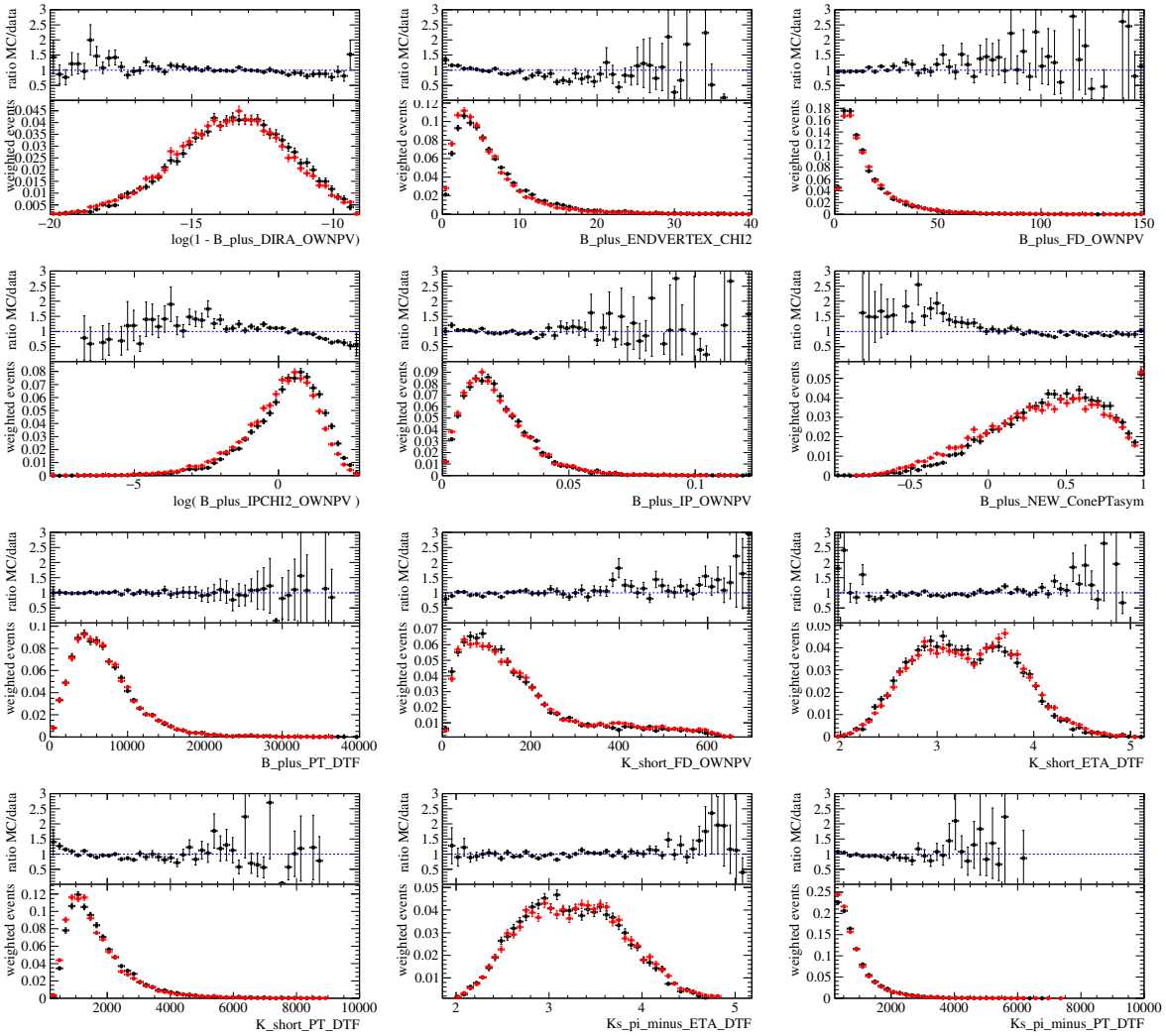

Figure 132: Comparison (1/2) of variables between *sWeighted* data (black) and 2 × 1D reweighted simulated events (red). The samples are 2017 with LL tracks only.

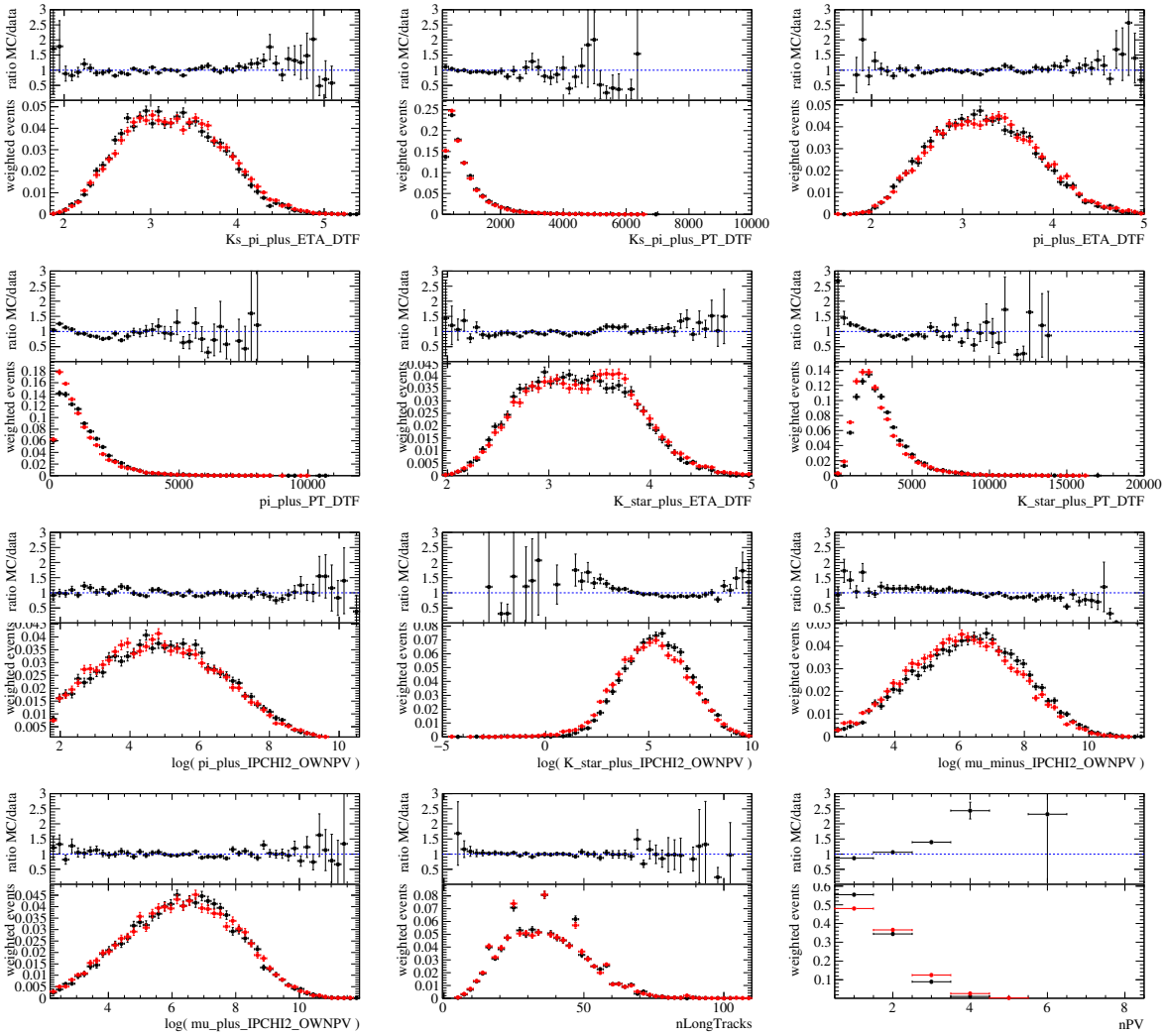

Figure 133: Comparison (2/2) of variables between *sWeighted* data (black) and 2 × 1D reweighted simulated events (red). The samples are 2017 with LL tracks only.

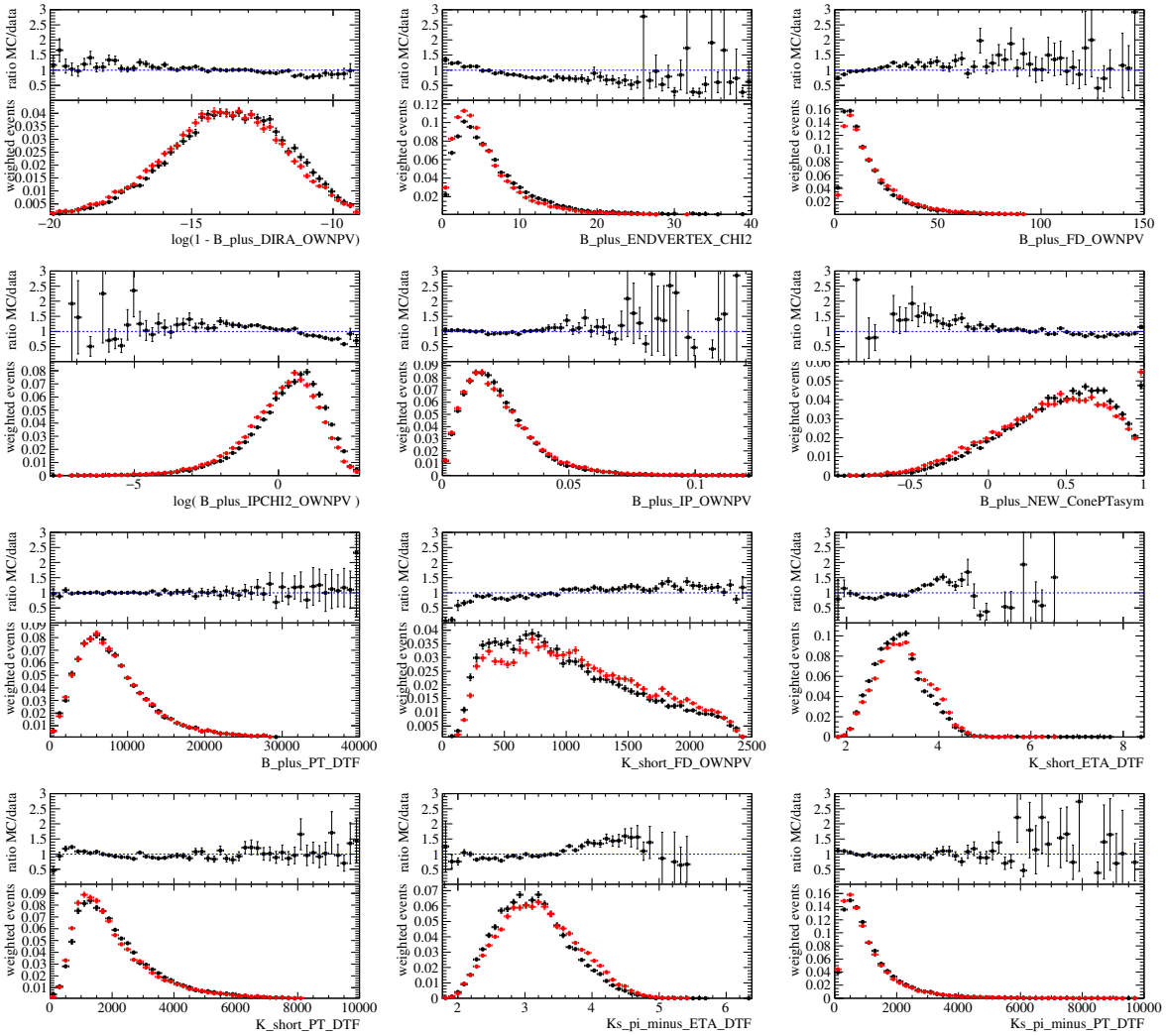

Figure 134: Comparison (1/2) of variables between *sWeighted* data (black) and 2 × 1D reweighted simulated events (red). The samples are 2018 with DD tracks only.

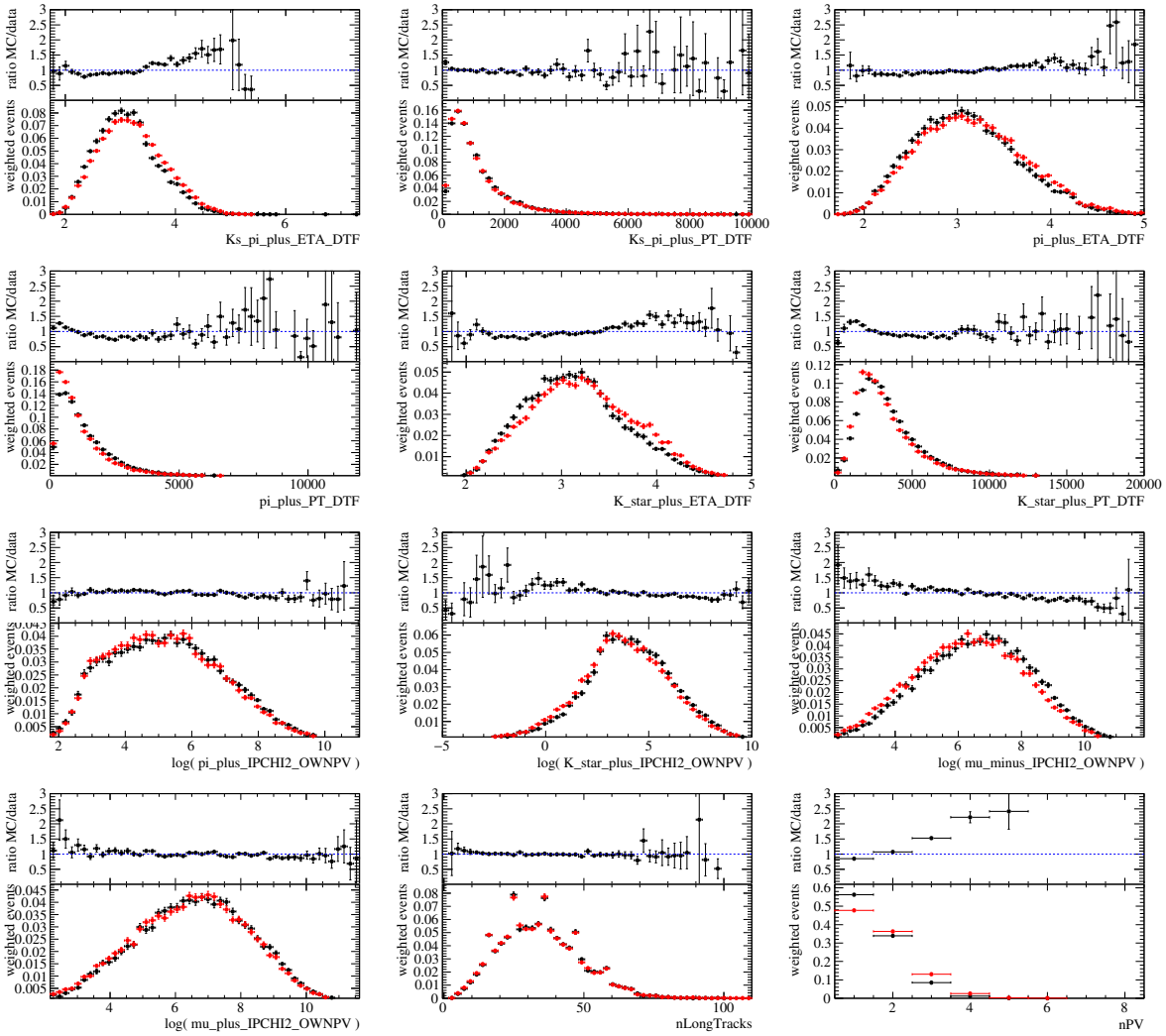

Figure 135: Comparison (2/2) of variables between *sWeighted* data (black) and 2 × 1D reweighted simulated events (red). The samples are 2018 with DD tracks only.

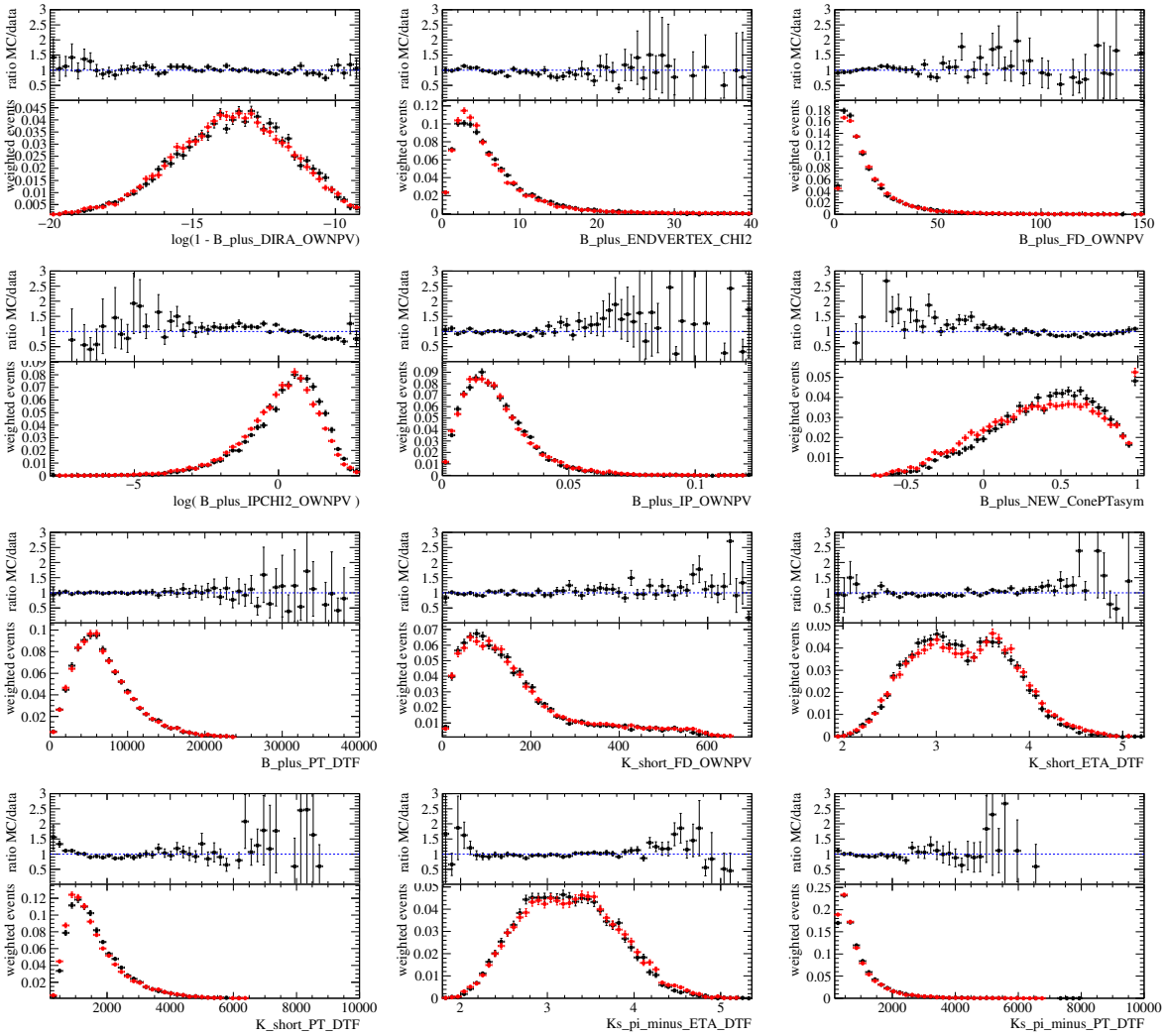

Figure 136: Comparison (1/2) of variables between *sWeighted* data (black) and 2 × 1D reweighted simulated events (red). The samples are 2018 with LL tracks only.

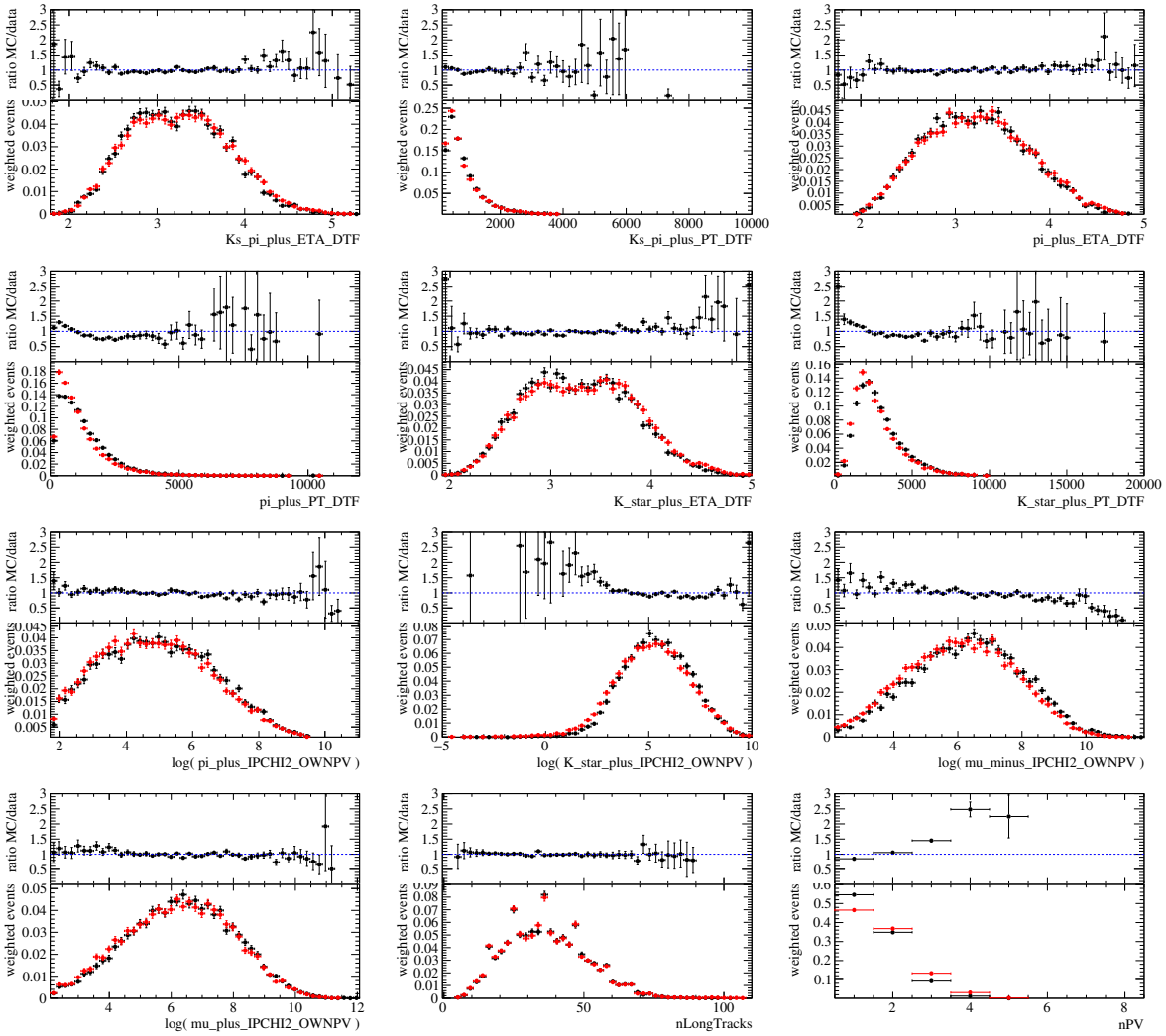

Figure 137: Comparison (2/2) of variables between *sWeighted* data (black) and 2 × 1D reweighted simulated events (red). The samples are 2018 with LL tracks only.

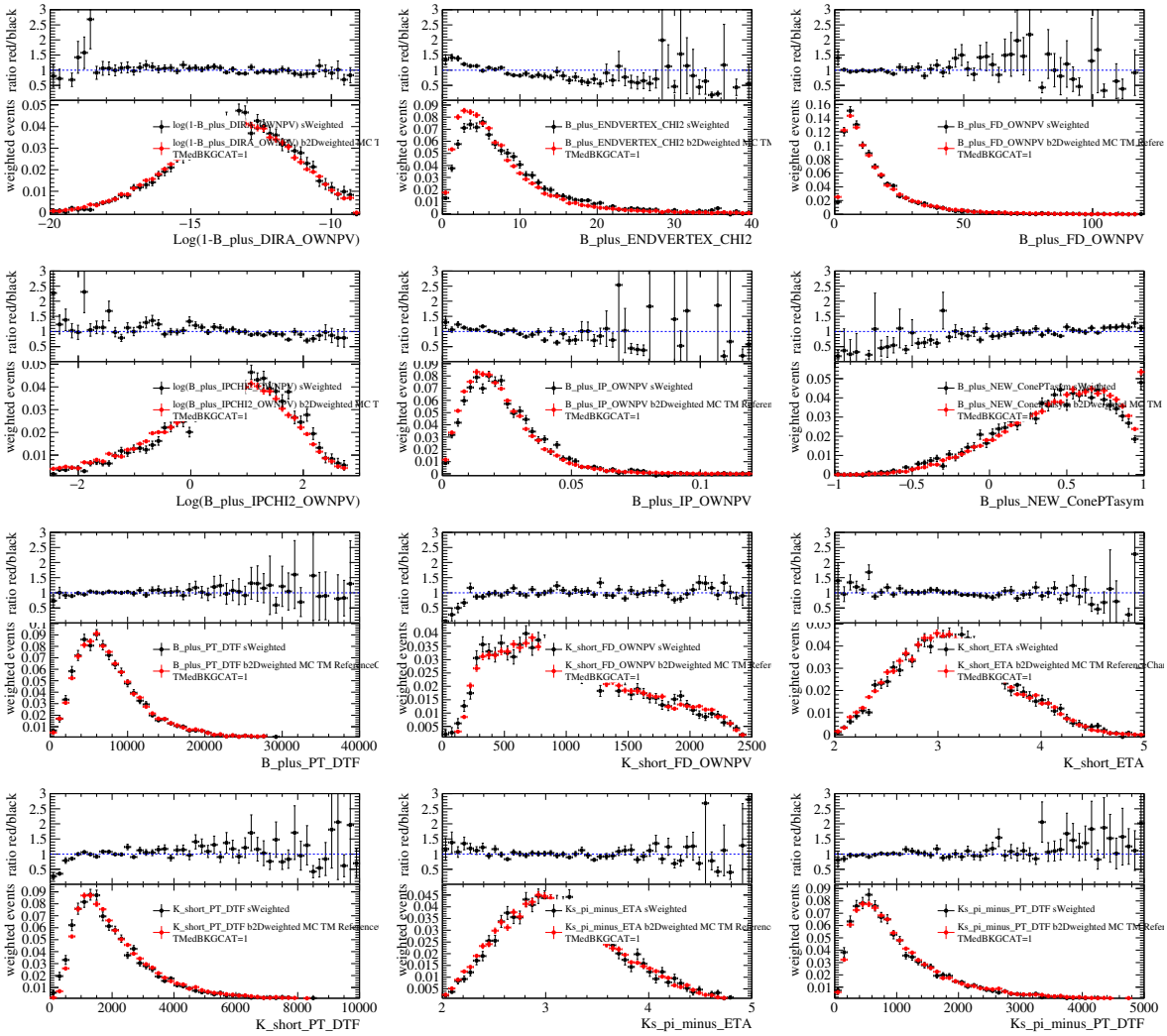

Figure 138: Comparison (1/2) of variables between *sWeighted J/ψ* data (black) and 2 × 1D re-weighted simulated J/ψ events (red). The samples are 2011 with DD tracks only.

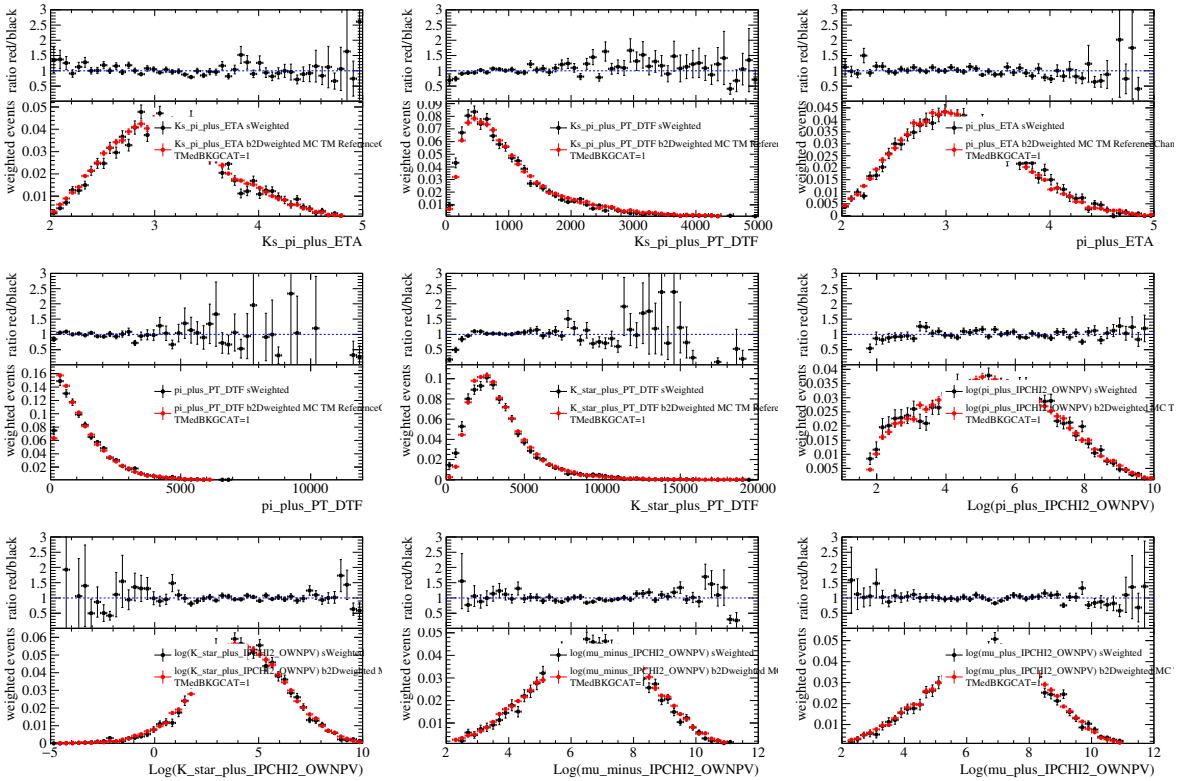

Figure 139: Comparison (2/2) of variables between *sWeighted J/ψ* data (black) and 2 × 1D re-weighted simulated J/ψ events (red). The samples are 2011 with DD tracks only.

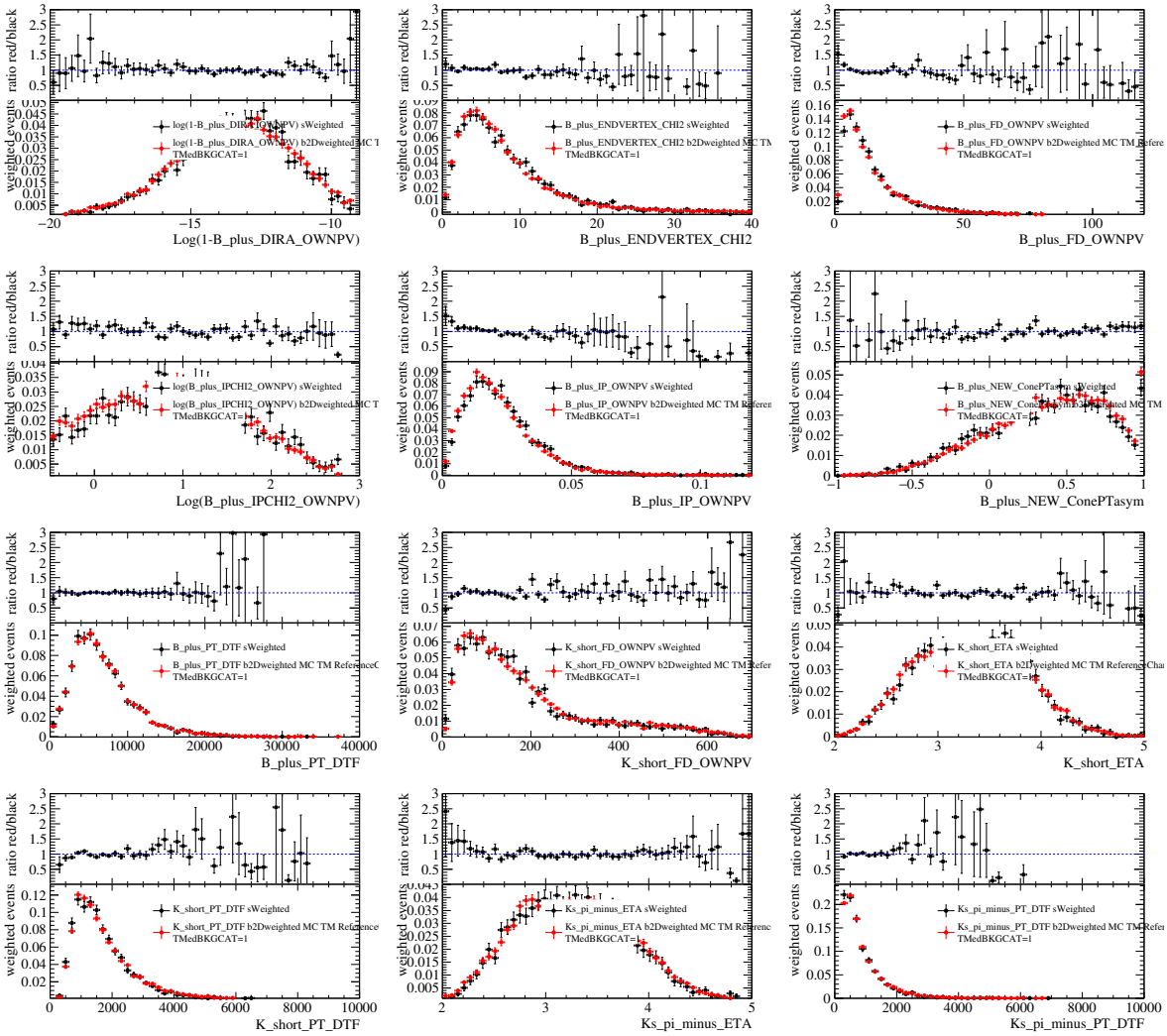

Figure 140: Comparison (1/2) of variables between *sWeighted* J/ψ data (black) and 2×1D re-weighted simulated J/ψ events (red). The samples are 2011 with LL tracks only.

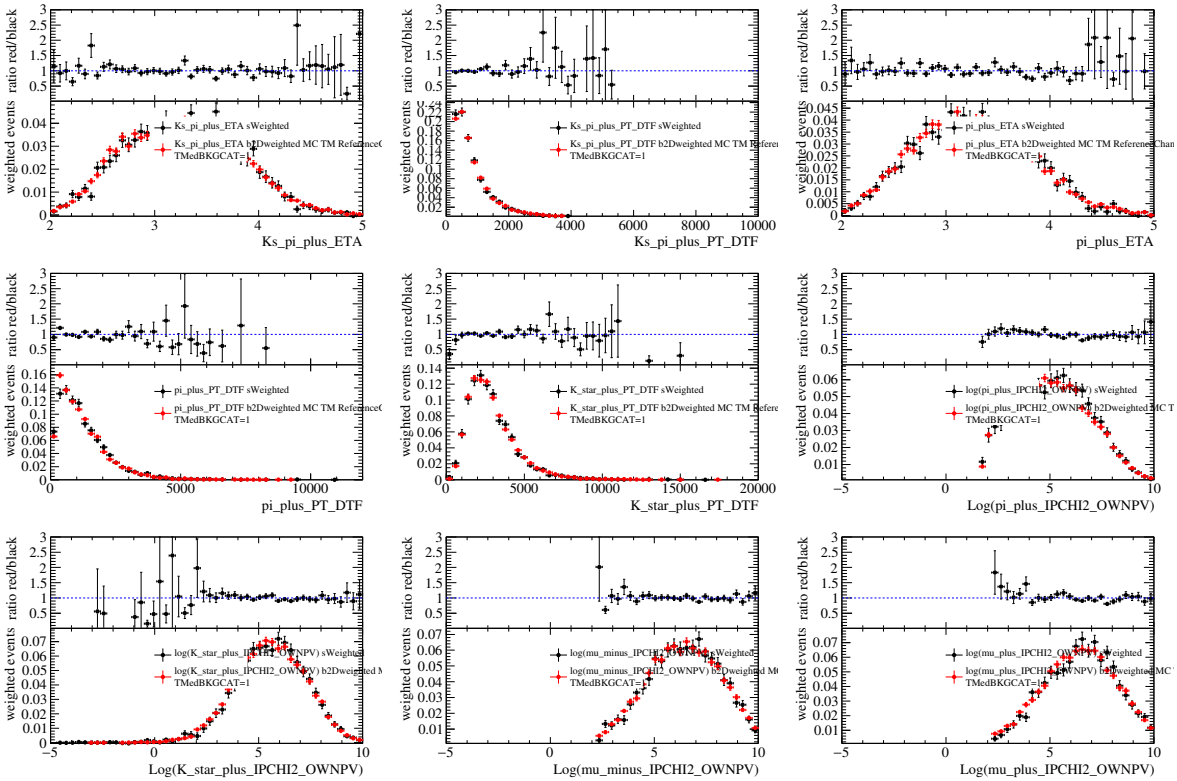

Figure 141: Comparison (2/2) of variables between *sWeighted J/ψ* data (black) and 2 × 1D re-weighted simulated *J/ψ* events (red). The samples are 2011 with LL tracks only.

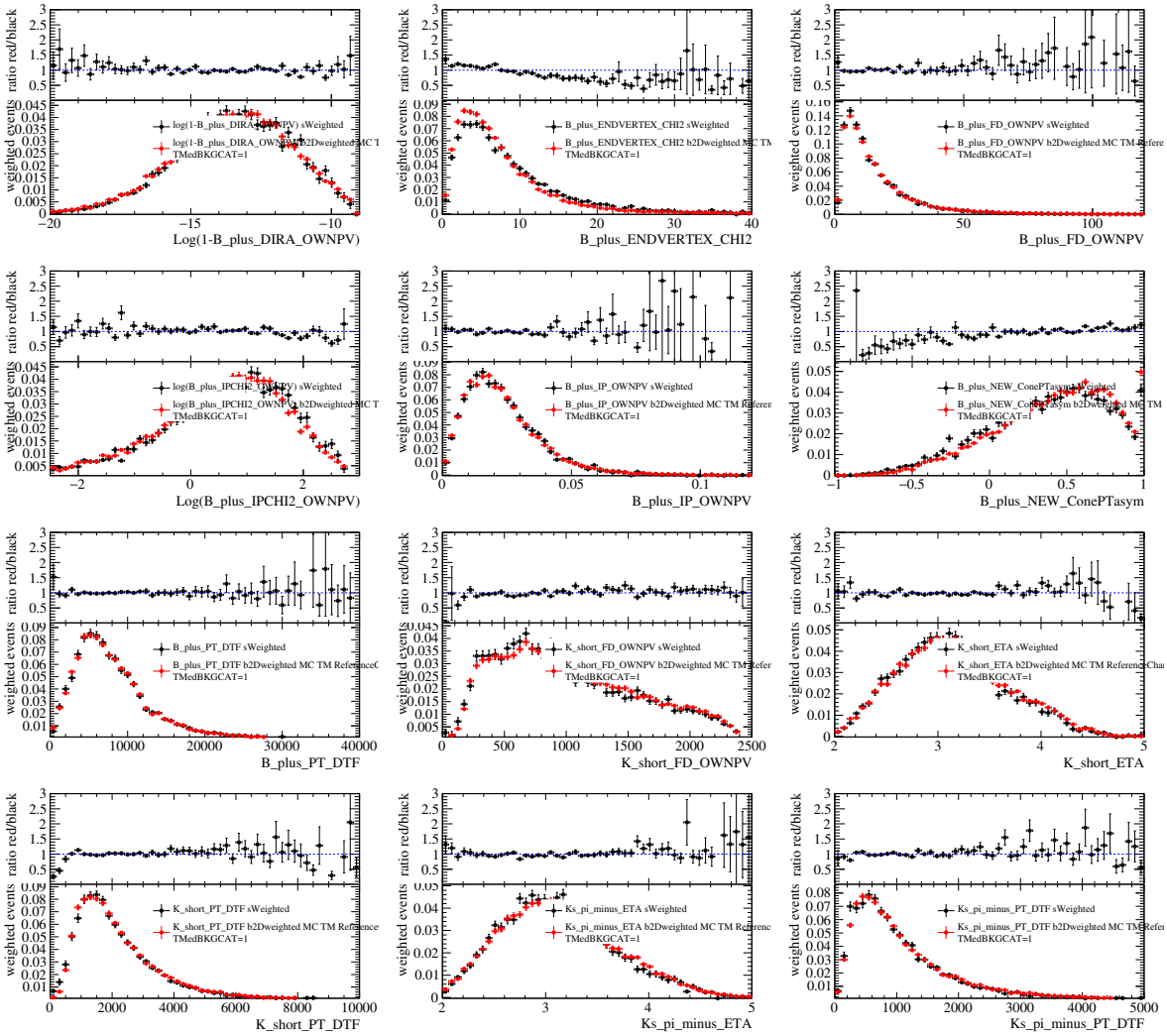

Figure 142: Comparison (1/2) of variables between *sWeighted* J/ψ data (black) and 2 $\times$ 1D re-weighted simulated J/ψ events (red). The samples are 2012 with DD tracks only.

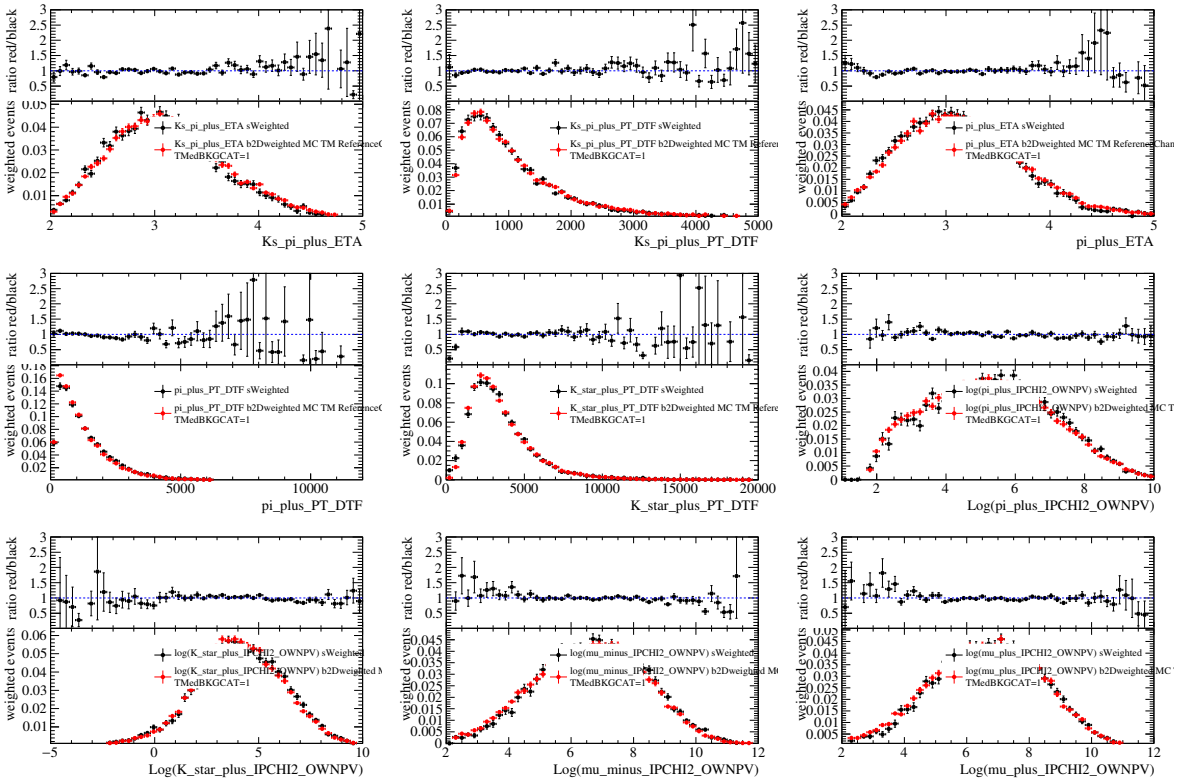

Figure 143: Comparison (2/2) of variables between *sWeighted J/ψ* data (black) and 2 × 1D re-weighted simulated *J/ψ* events (red). The samples are 2012 with DD tracks only.

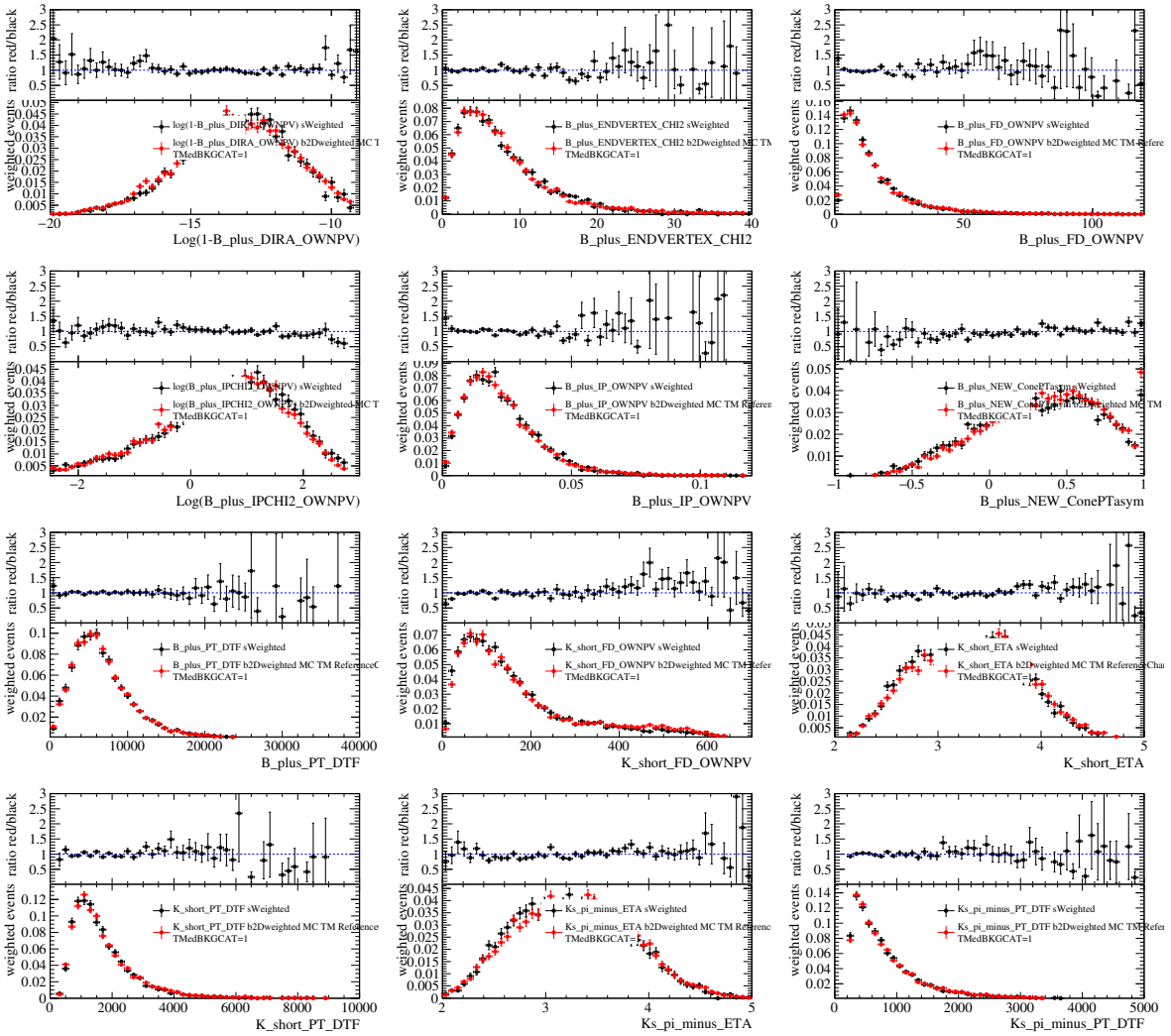

Figure 144: Comparison (1/2) of variables between *sWeighted* J/ψ data (black) and 2 $\times$ 1D re-weighted simulated J/ψ events (red). The samples are 2012 with LL tracks only.

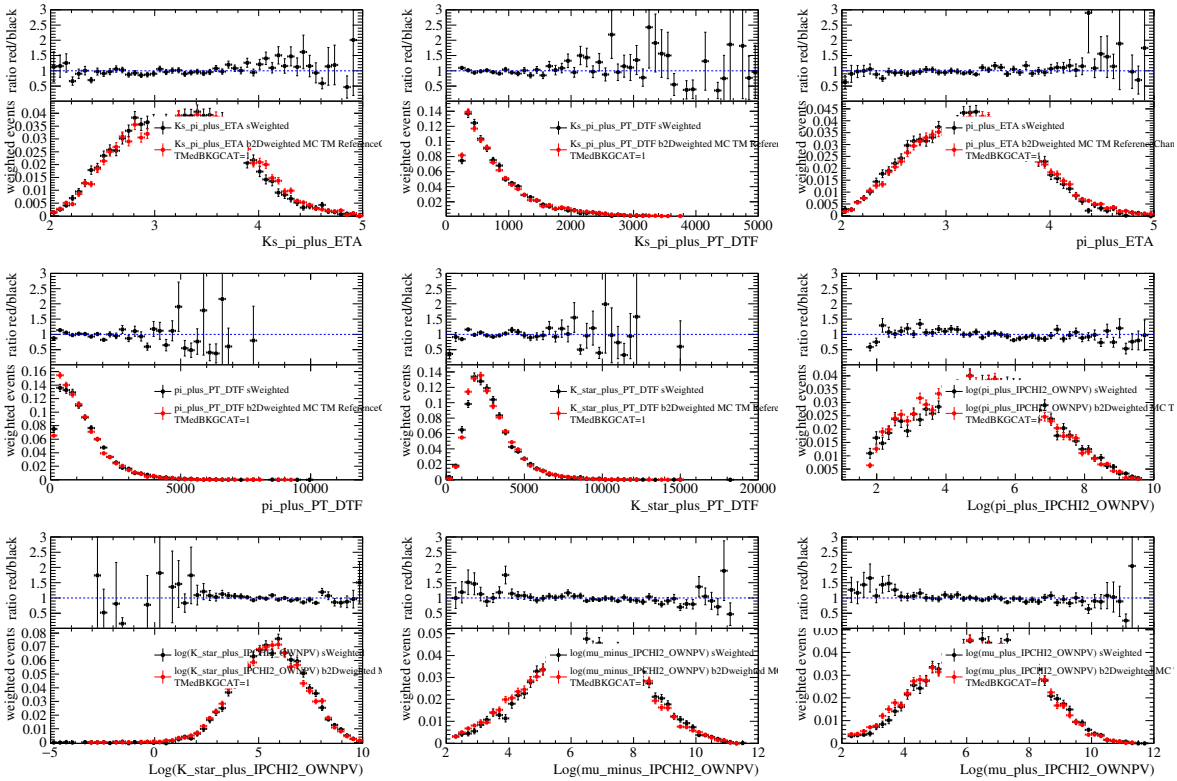

Figure 145: Comparison (2/2) of variables between *sWeighted J/ψ* data (black) and 2 × 1D re-weighted simulated *J/ψ* events (red). The samples are 2012 with LL tracks only.

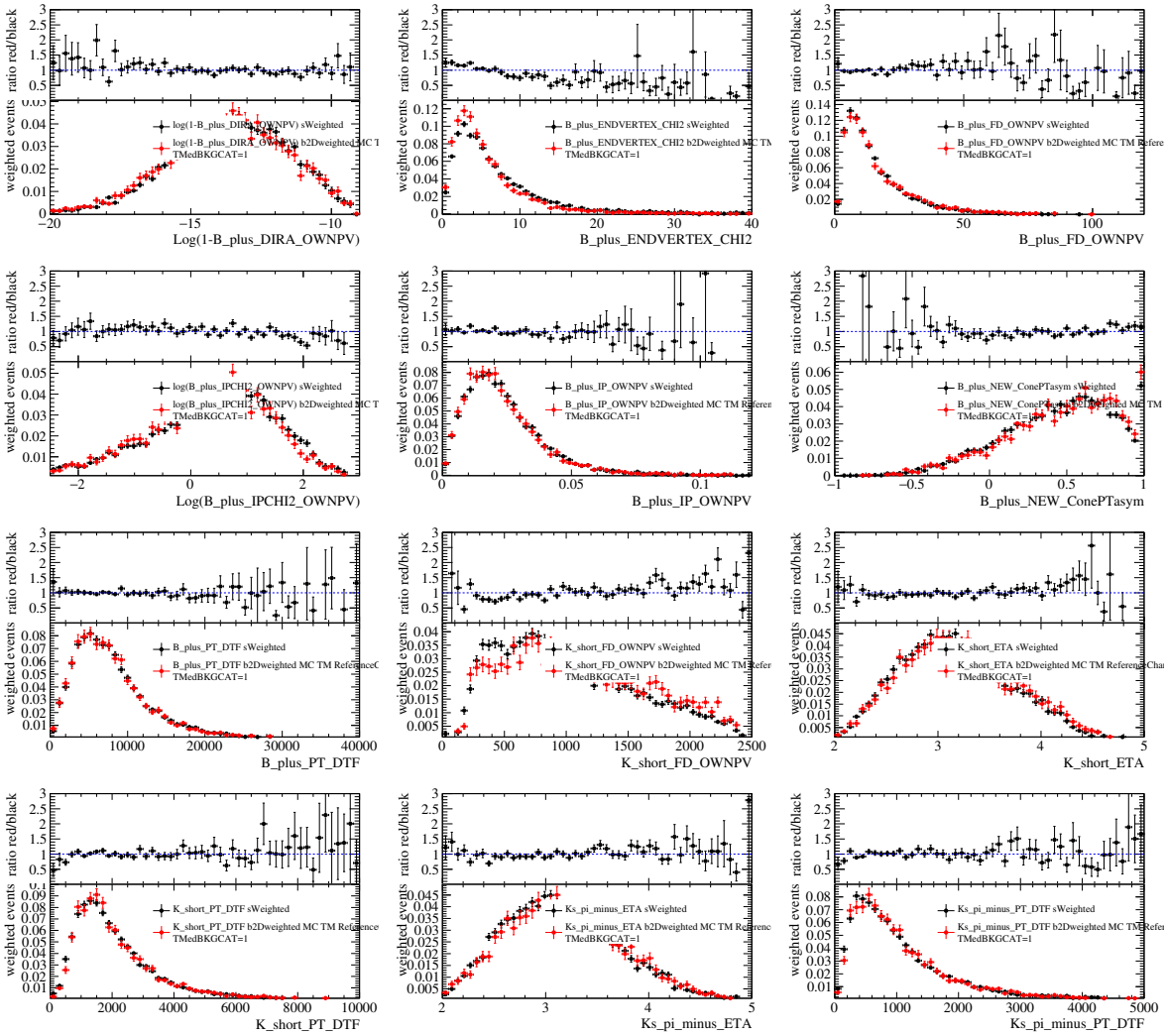

Figure 146: Comparison (1/2) of variables between *sWeighted* J/ψ data (black) and 2 $\times$ 1D re-weighted simulated J/ψ events (red). The samples are 2016 with DD tracks only.

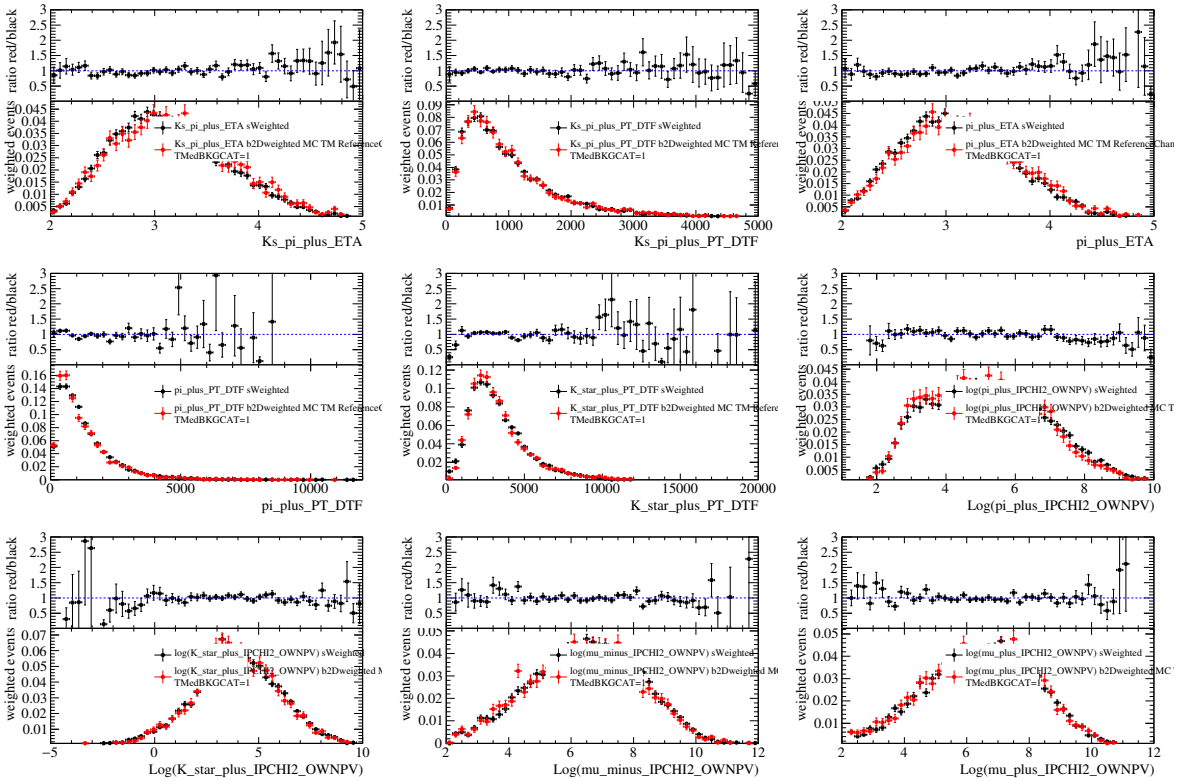

Figure 147: Comparison (2/2) of variables between *sWeighted J/ψ* data (black) and 2 × 1D re-weighted simulated *J/ψ* events (red). The samples are 2016 with DD tracks only.

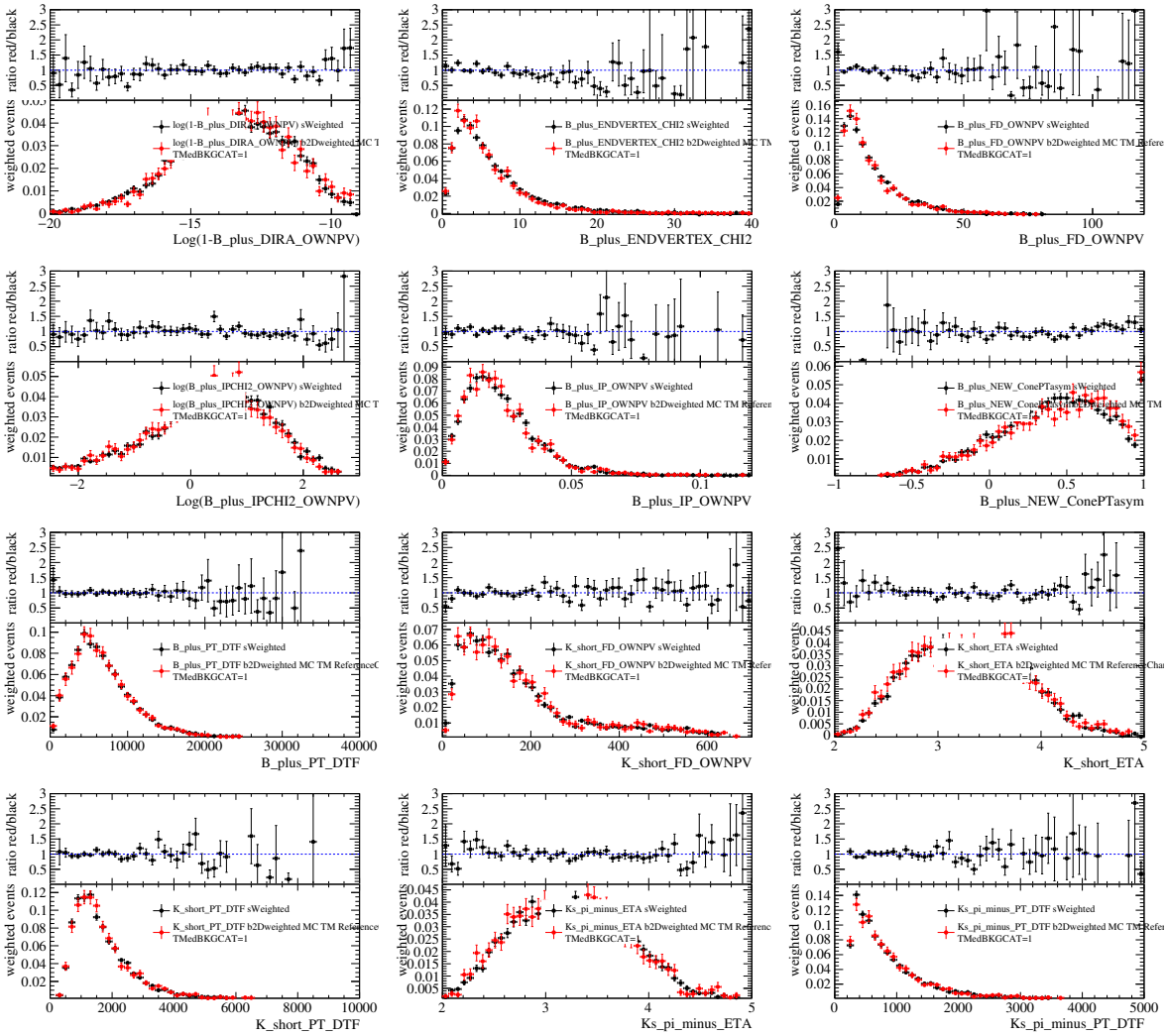

Figure 148: Comparison (1/2) of variables between *sWeighted* J/ψ data (black) and 2 $\times$ 1D re-weighted simulated J/ψ events (red). The samples are 2016 with LL tracks only.

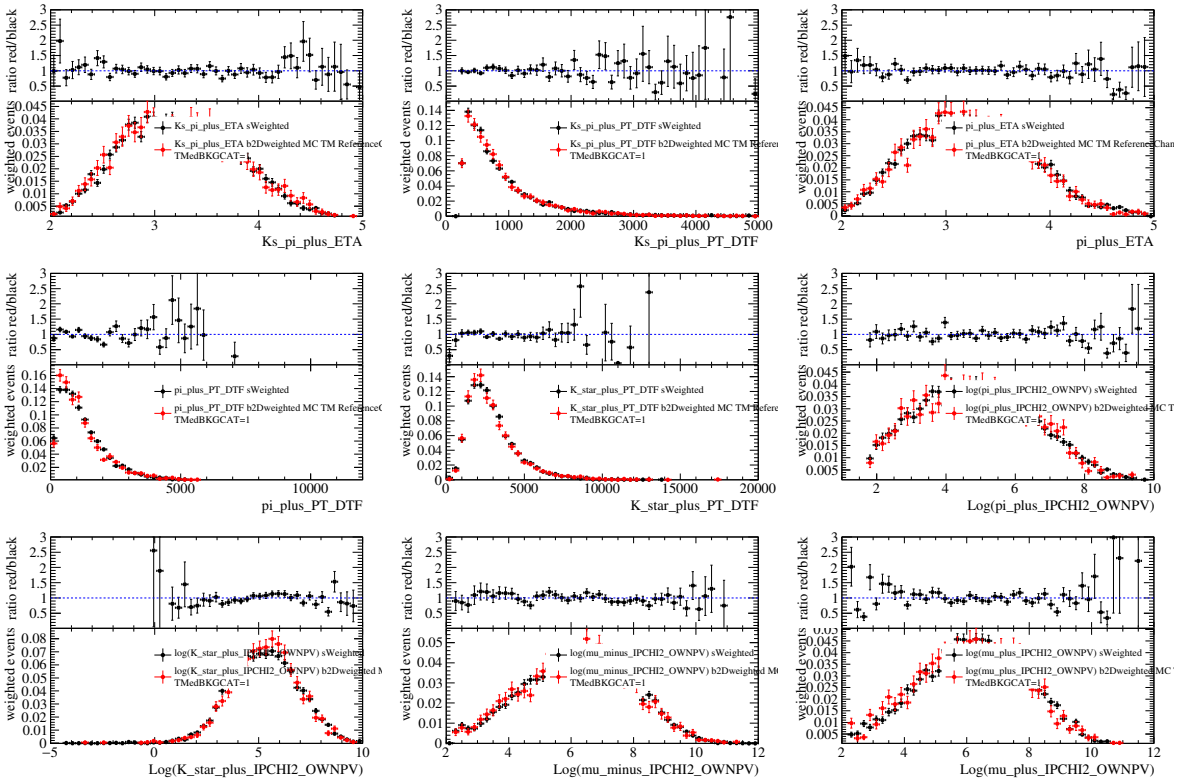

Figure 149: Comparison (2/2) of variables between *sWeighted J/ψ* data (black) and 2 × 1D re-weighted simulated *J/ψ* events (red). The samples are 2016 with LL tracks only.

A.4 Angular efficiency of the peaking background veto

The effect of the veto against peaking background from $B^0 \to K^0_S \mu^+ \mu^-$ plus a random π^+ on the angular distributions of the upper mass side-band was investigated. In $\cos\theta_L$ and ϕ, no significant changes in the angular distribution have been observed. Fig. 150 shows the distributions before and after the veto, as well as their difference. In Fig. 151, the ratio of the distributions before and after the veto are given. The vetoed background events peaking towards $\cos\theta_K = 1$ is very plausible for the background coming from decays of $B^0 \to K^0_S \mu^+ \mu^-$ plus a random π^+. The reconstructed momenta of the K^{*+} from these events is clearly dominated by the K^0_S. And since θ_K is the angle between the flight directions of the K^{*+} and the K^0_S, values of $\cos\theta_K$ close to one are expected.
As the distributions do not suffer from generated spikes or peak by the veto, and as the agreement between lower and upper mass side-band was demonstrated in Section 3.3.4, no systematic uncertainty applied to this veto.

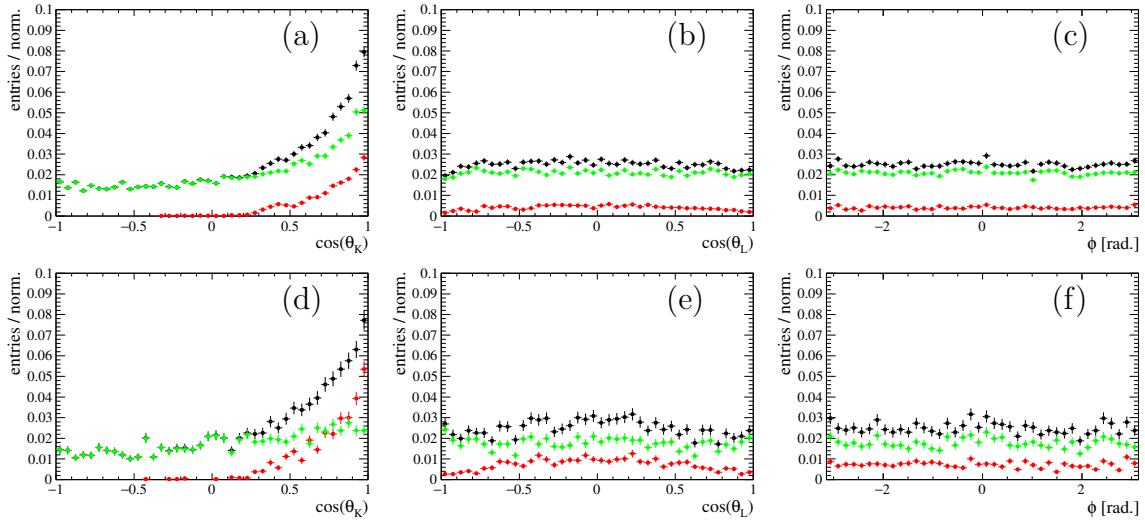

Figure 150: The efficiency of the veto against $B^0 \to K^0_S \mu^+ \mu^-$ in the angular distributions is investigated. The data is from 2017 with magnet polarity *up*, a reconstructed $m(B^+) > 5350\,\text{MeV}/c^2$ and for DD tracks in the top row (a)-(c) and LL tracks in the lower row (d)-(f). In black all events passing the pre-selection are shown, in green the events that pass the veto and in red the vetoed events. For $\cos\theta_L$ in (b) and (e) as well as ϕ in (c) and (f), no significant effect on the angular distributions is observed. For $\cos\theta_K$ in (a) and (d), the veto cuts away the peaking structure towards $\cos\theta_K = 1.0$, which is expected. The remaining distributions are not distorted.

A.5 Selection efficiency in the m($K\pi^+$) dimension

The acceptance correction is done in four dimensions (q^2 and the three decay angles), where the m($K\pi^+$) dimension is not considered. This requires and flat acceptance in this dimension and hence was tested using the PHSP MC tuples. In analogy to q^2, the m($K\pi^+$) dimension is tested in the invariant mass squared of the system, p^2. In Figs. 152 to 154, the distribution of before (black) and after (red) selection are shown as a function of p^2, together with the ratio of both distributions. We observe no signs of any acceptance effects.

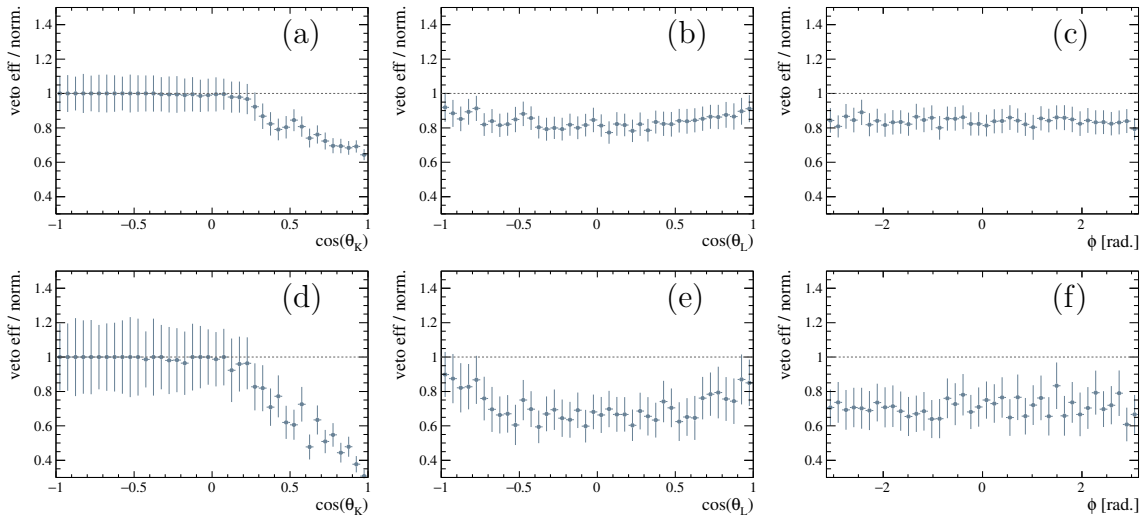

Figure 151: The efficiency of the veto against $B^0 \to K^0_S \mu^+ \mu^-$. The data is from 2017 with magnet polarity *up*, a reconstructed $m(B^+) > 5350\,\text{MeV}/c^2$ and for `DD` tracks in the top row (a)-(c) and `LL` tracks in the lower row (d)-(f). The efficiency corresponds to the ratio of the green and black curves in Fig. 150.

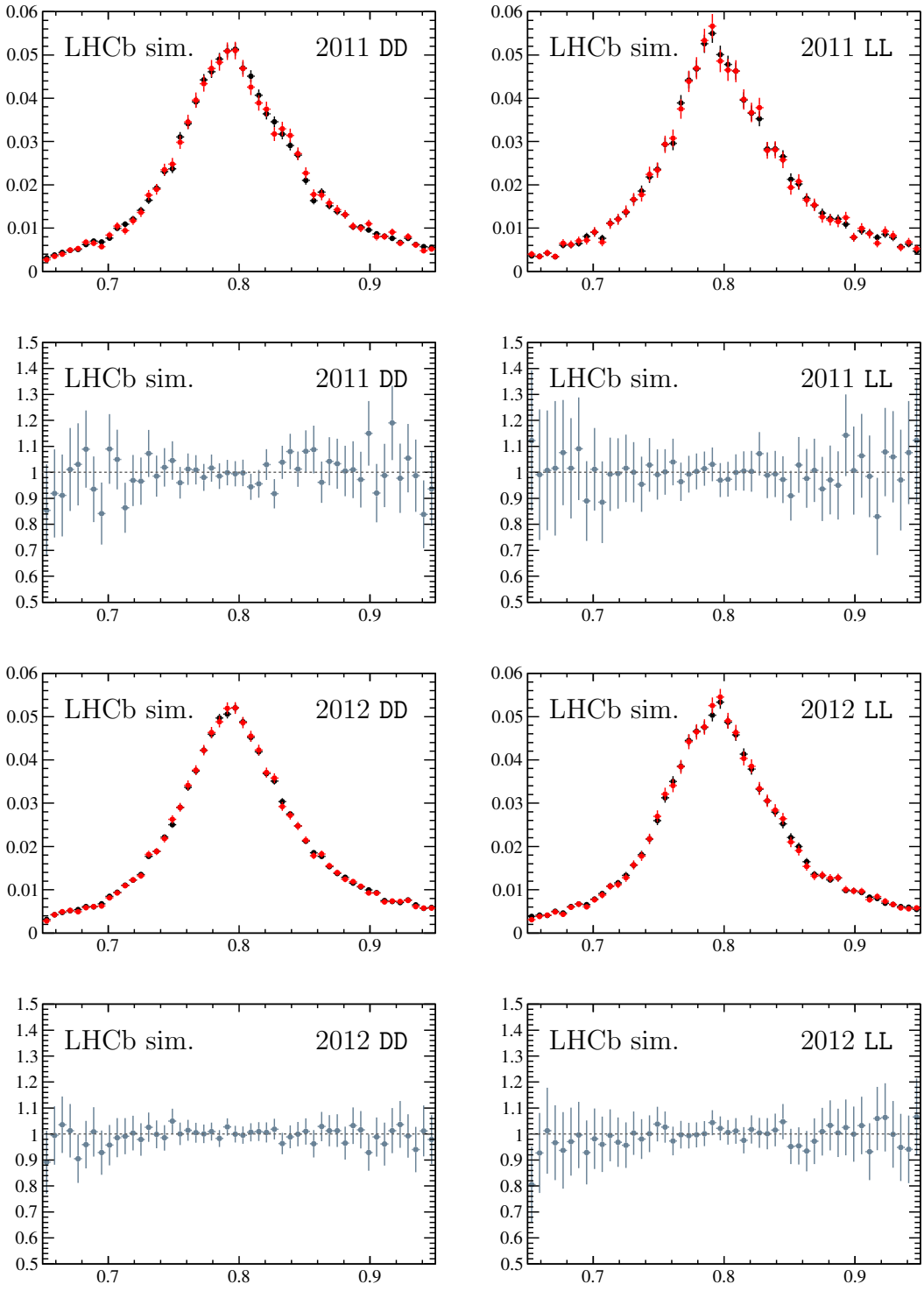

Figure 152: Run I: The comparison of the p^2 distribution before (black) and after (red) the full selection using PHSP MC events. Both, the distributions and the ratios show no sign of a non-flat acceptance effect.

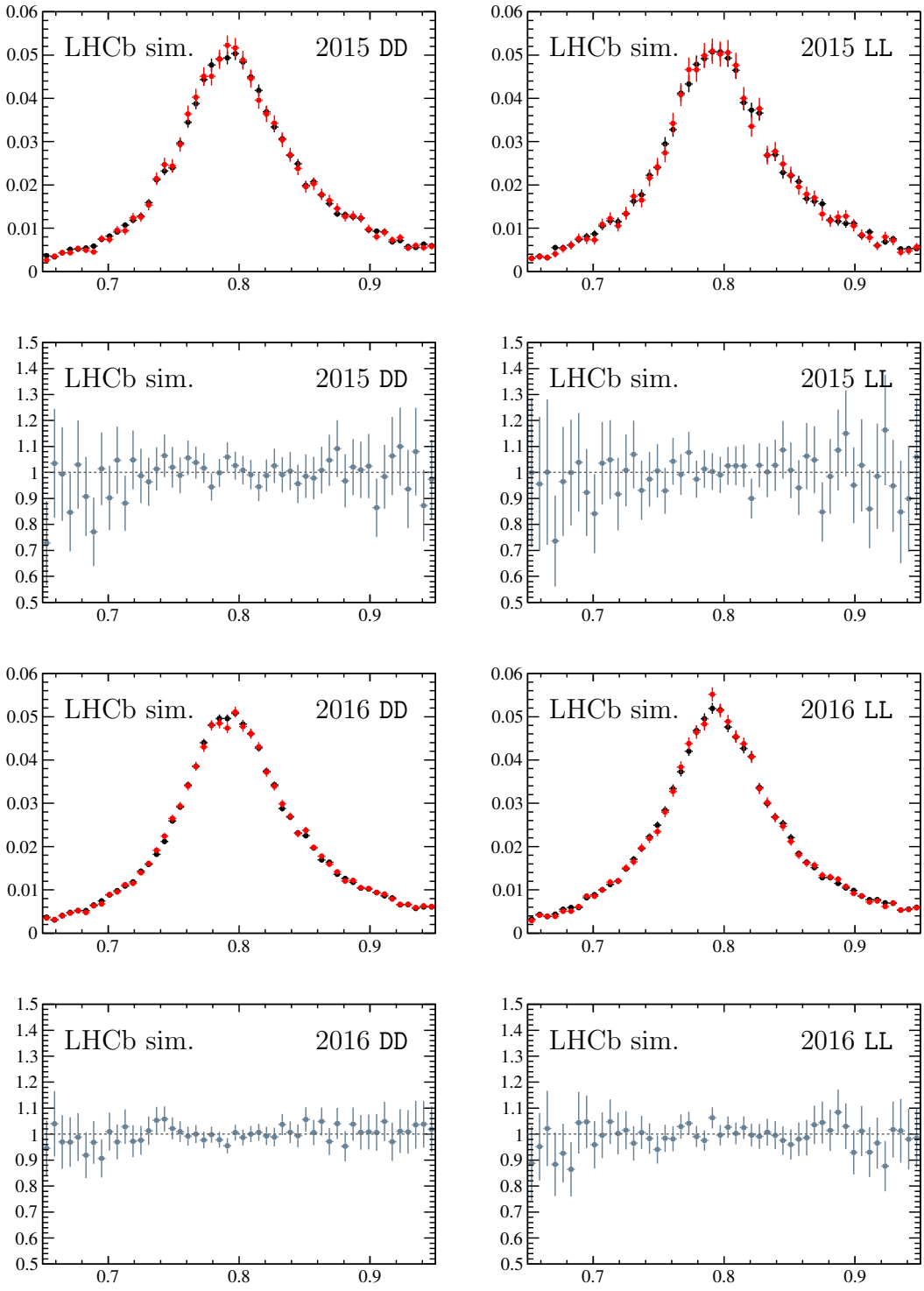

Figure 153: 2015+16: The comparison of the p^2 distribution before (black) and after (red) the full selection using PHSP MC events. Both, the distributions and the ratios show no sign of a non-flat acceptance effect.

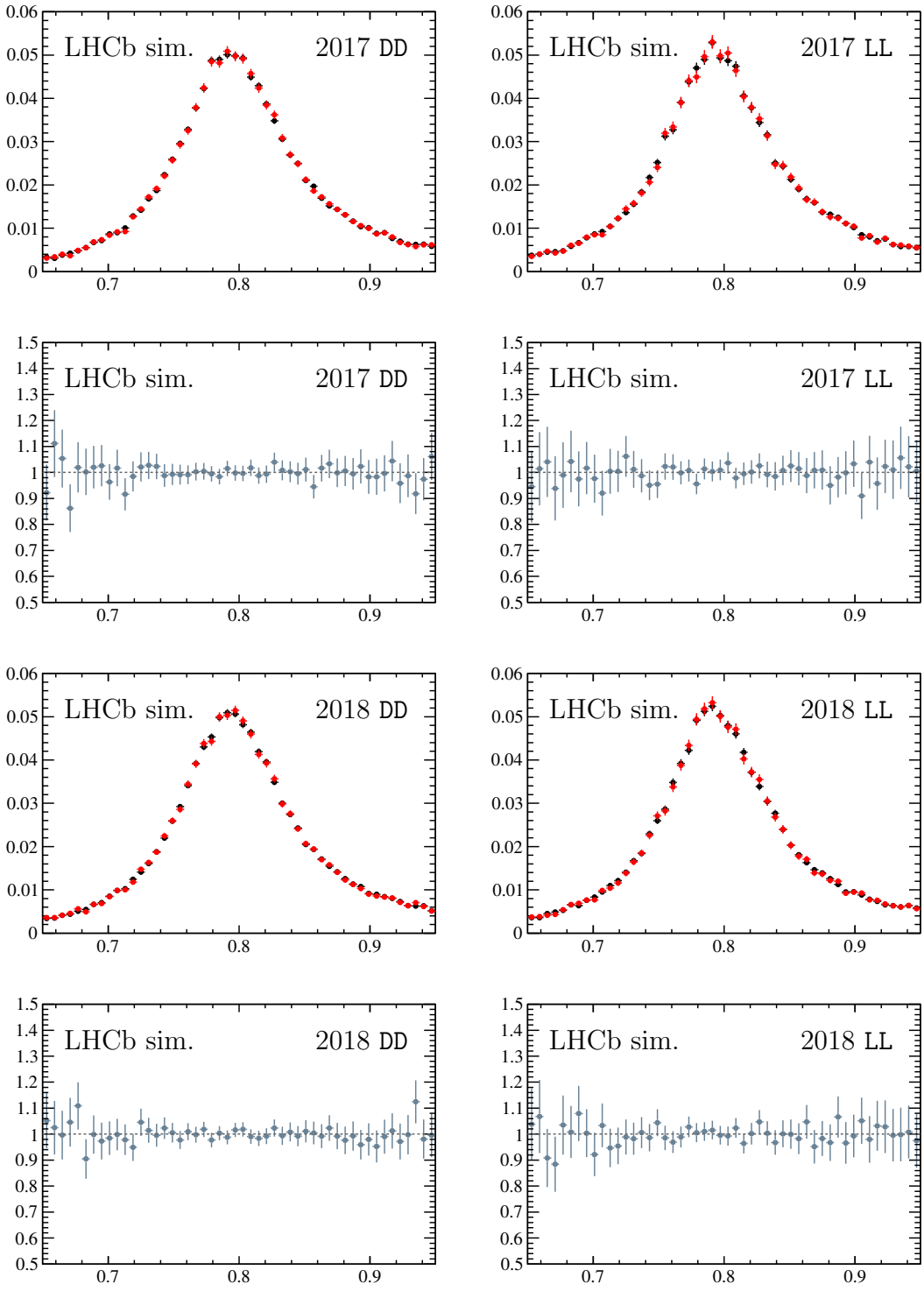

Figure 154: 2017+18: The comparison of the p^2 distribution before (black) and after (red) the full selection using PHSP MC events. Both, the distributions and the ratios show no sign of a non-flat acceptance effect.

A.6 Angular resolution

In the following Figs. 155 to 157 the angular resolutions are shown. The distributions are determined from MC events for all six years and are calculated from the difference of the reconstructed angle and the true angle. For the true angle, the true momentum information of the MC events are used.
The resolution is obtained by a fit using the sum of two Gaussian distributions and by calculating the effective width from the relative fraction and the two individual width:

$$\sigma_{eff} = \sqrt{f \cdot \sigma_1^2 + (1 - f) \cdot \sigma_2^2}, \tag{46}$$

the relative fraction, f, and individual widths $\sigma_{1,2}$ of the two Gaussian bell functions.
In LL tracks tracks, the resolution is found to be a slightly better, especially for the Run I data-set. However, the difference between DD tracks and LL tracks samples is low enough to not be considered in the simultaneous fit, given the low event statistics of the fit and the absolute values of the angular resolutions.

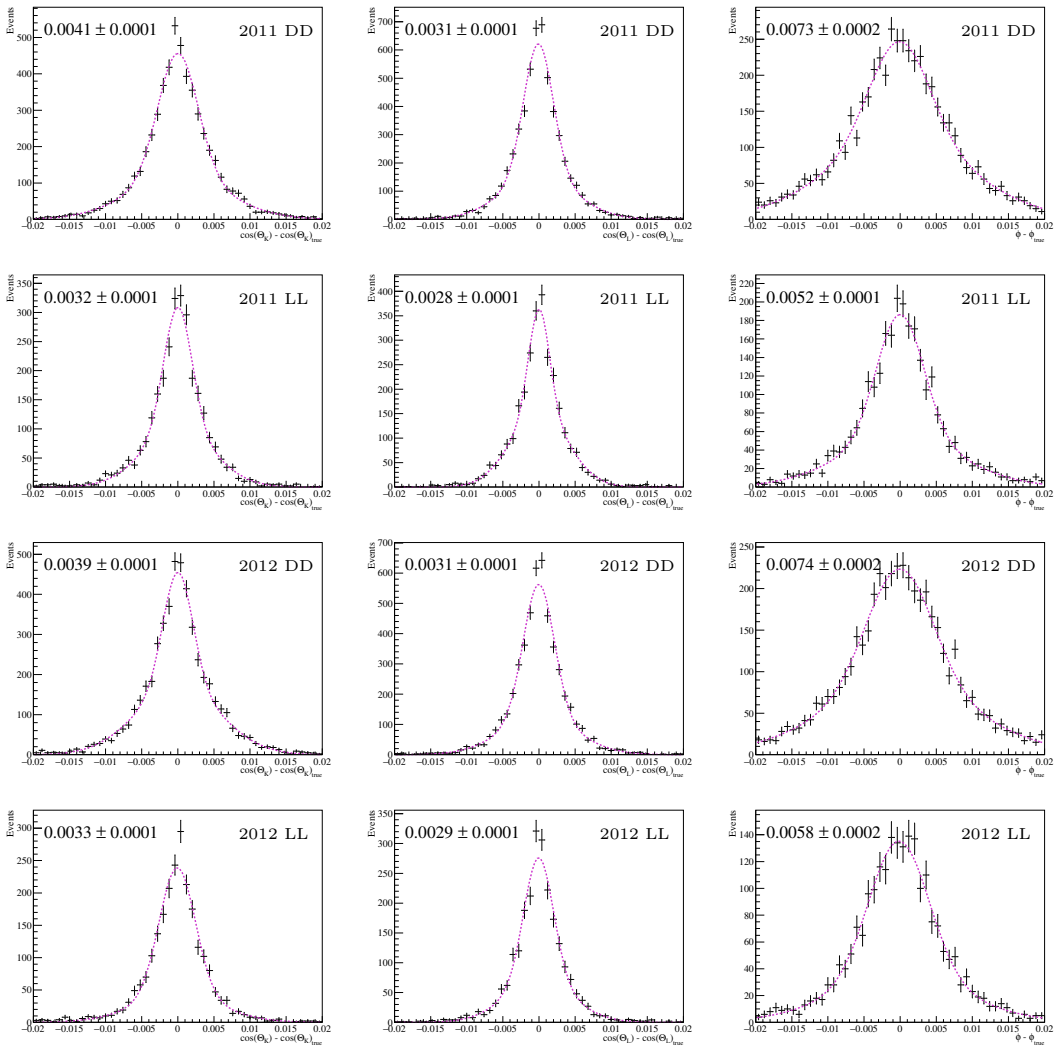

Figure 155: The angular resolution for all three angles, $\cos\theta_K$ (left column), $\cos\theta_L$ (central column) and ϕ (right column) for both years of Run I. The data-set is split in DD tracks and LL tracks events by every other row. For all distribution, the effective width (see text) of a double-gaussian fit is stated in the plot. The LL tracks samples are found to have a slightly better resolution.

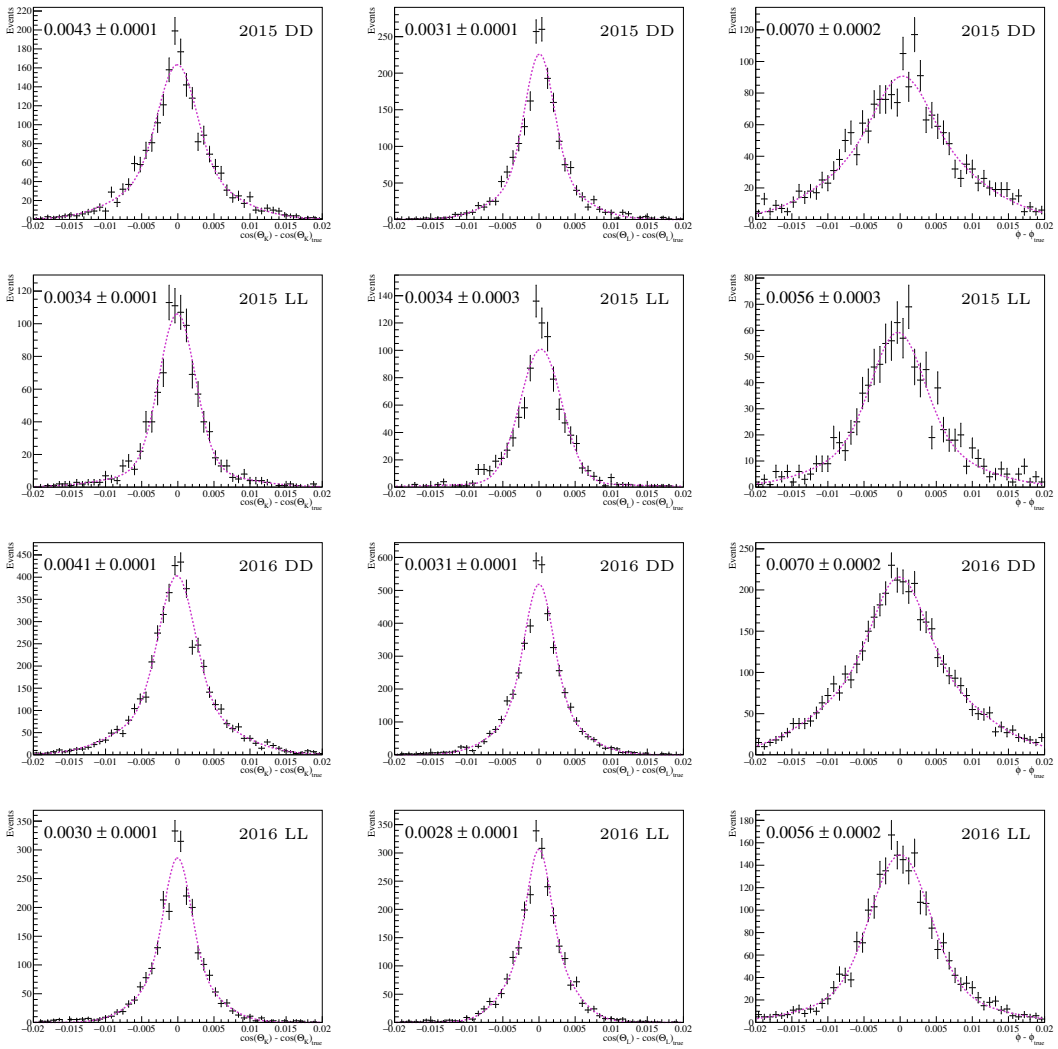

Figure 156: The angular resolution for all three angles, $\cos\theta_K$ (left column), $\cos\theta_L$ (central column) and ϕ (right column) for the first two years of Run II, 2015 & 2016. The data-set is split in DD tracks and LL tracks events by every other row. For all distribution, the effective width (see text) of a double-gaussian fit is stated in the plot. The LL tracks samples are found to have a very slightly better resolution.

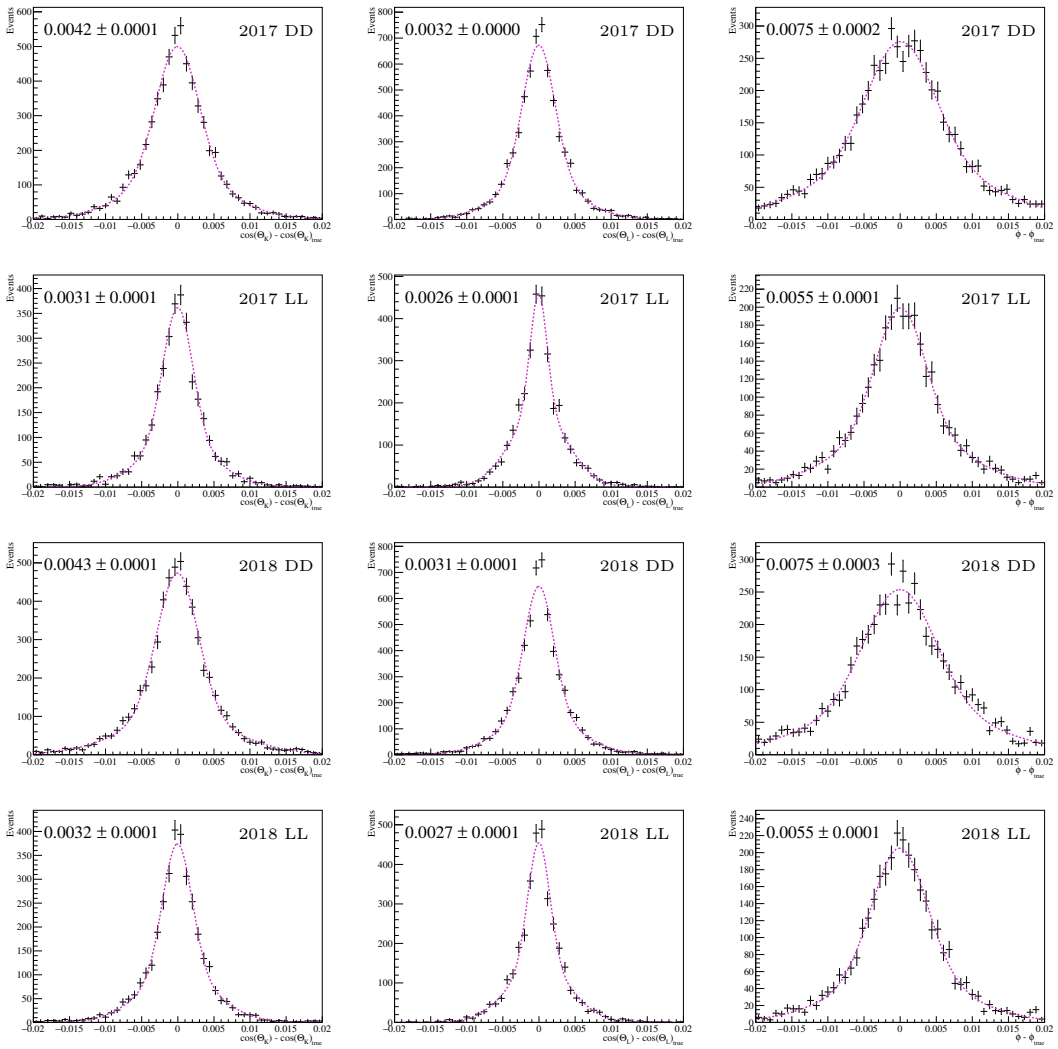

Figure 157: The angular resolution for all three angles, $\cos\theta_K$ (left column), $\cos\theta_L$ (central column) and ϕ (right column) for the first two years of Run II, 2017 & 2018. The data-set is split in DD tracks and LL tracks events by every other row. For all distribution, the effective width (see text) of a double-gaussian fit is stated in the plot. The LL tracks samples are found to have a very slightly better resolution.

A.7 Sensitivity on F_S by differently dimensional fits

The sensitivity on the S-wave fraction, F_S was studied in details in Section 8.5 of Ref. [34]. In Fig. 158, the results of these sensitivity studies are given. The results show, that the sensitivity on F_S comes mainly from the K^{*+} mass dimension, as the 2D fit shows similar sensitivity as the full 5D fit.

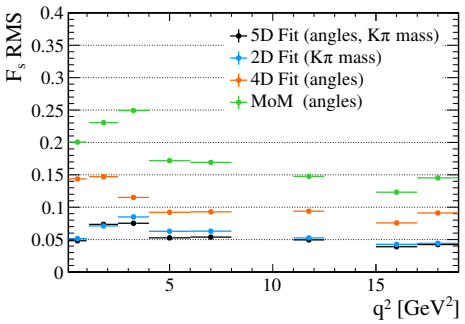

Figure 158: Sensitivity study on F_S by Ref. [34]. 2D fit (in blue) shows a similar sensitivity as the full 5D fit (black).

A.8 Scaling of F_S using the F_L q^2 dependence

Due to low statistics, F_S can only be determined in large q^2 bins. In order to obtain the values for the nominal q^2 bins (see Table 15), one exploits the fact that the q^2 dependence of F_L and F_S is the approximately the same (as shown later). The F_S value in each nominal bin is therefore obtained by scaling the F_S value in the large bin by the ratio of the value of F_L in the nominal and the large bin. In the following, in Table 83 the ratio of F_L between the larger binning scheme and the nominal, finer binning scheme are given. The values are obtained from the flav.io package [35] and the resulting scaling factors for F_S are given. All absolute values for the two q^2 binning schemes are shown in Fig. 159, which is made from the results of the flav.io package.

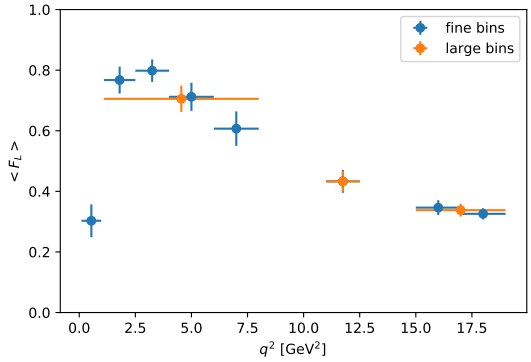

Figure 159: Trend of the longitudinal polarization fraction F_L in different q^2 binnings. The values are determined by the flav.io package [35].

The method was tested on previous results of F_S measured in the neutral B meson decay [47]. For this, the values of the finer (eight) q^2 bins were averaged and the scaled

Table 83: Ratio of F_L between larger and nominal q^2 bins, which are used to scale F_S in the 4D fit. Values obtained using the flav.io package [35] and are shown in Fig. 159.

larger binning	nominal binning	ratio
scaled from next bin	[0.1, 0.98]	0.430
[1.1, 8.0]	[1.1, 2.5]	1.088
	[2.5, 4.0]	1.132
	[4.0, 6.0]	1.009
	[6.0, 8.0]	0.860
[11.0, 12.5]	[11.0, 12.5]	1.0
[15.0, 19.0]	[15.0, 17.0]	1.025
	[17.0, 19.0]	0.964

accordingly to the F_L distribution in Table 83. The results are in good agreement with the original measurement and peaks in the F_S distribution are smoothed out. See Fig. 160 for the overlay of the original measurement and the representation after applying the F_L scaling.

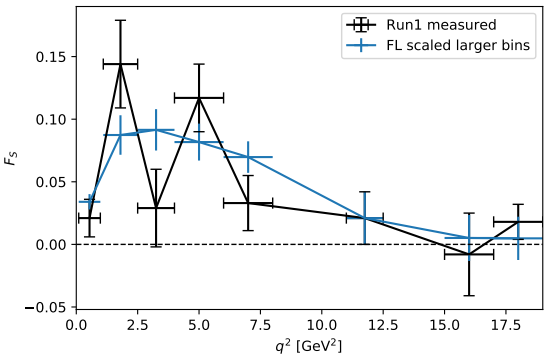

Figure 160: Test application of the F_L scaling strategy on the results published in Ref. [47]. For the scaling, the F_L ratios from Table 83 are applied after the F_S values were averaged to the larger q^2 bins, as described in the table and text. The scaled values are a good representation of the underlying distribution.

A.9 Background in ϕ in bins of $\cos\theta_L$ and $\cos\theta_K$

In addition to the background distribution of the reference channel in Fig. 29, the flatness of the ϕ distribution is verified in different regions of $\cos\theta_L$ and $\cos\theta_K$. Fig. 161 shows the ϕ background distributions in each four bins (of width 0.5) in $\cos\theta_L$ and in $\cos\theta_K$. The ϕ background distribution in the four quadrants of the $\cos\theta_L$-$\cos\theta_K$ plane are shown in Fig. 162. All bins show a very good agreement with the assumption of a flat background distribution in ϕ.

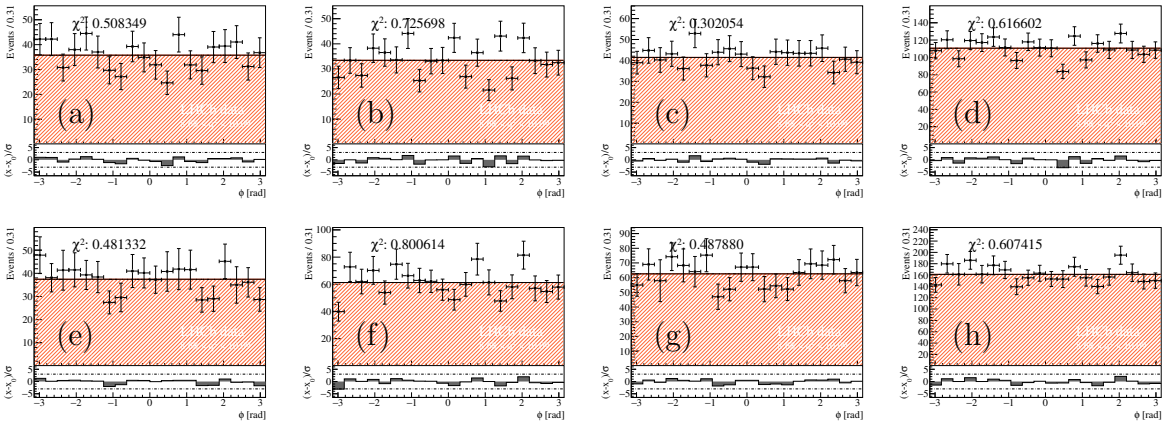

Figure 161: Distribution of background events in the ϕ dimension for events of the reference channel. Top (bottom) row shows the background in bins of $\cos\theta_K$ ($\cos\theta_L$). Each histogram shows a $\cos\theta_K$ ($\cos\theta_L$) bin of size 0.5; starting of range [-1.0, -0.5] for $\cos\theta_K$ in (a) to [0.5, 1.0] for $\cos\theta_L$ in (h). All bins show a flat background distribution for ϕ.

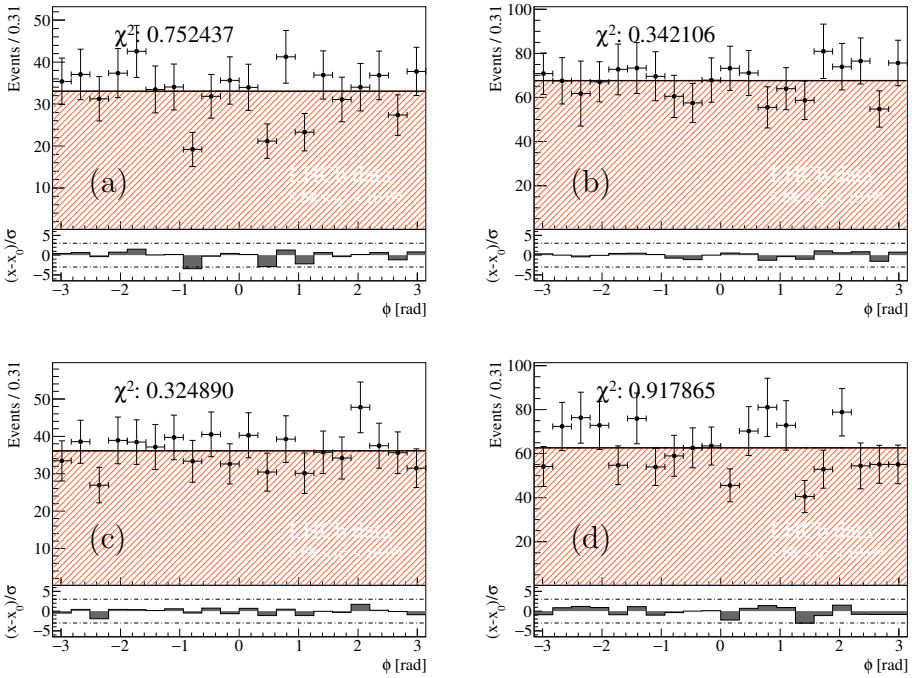

Figure 162: Distribution of background events in the ϕ dimension for events of the reference channel. The events are binned in the four regions of the $\cos\theta_K$-$\cos\theta_L$ plane. The four quadrants of the plane are given with the four histograms being aligned as if they form the plane: $\cos\theta_K$ on the x-axis and $\cos\theta_L$ on the y-axis, i.e. (b) is for both $\cos\theta_K$ and $\cos\theta_L$ positive and (d) for positive $\cos\theta_K$ but negative $\cos\theta_L$. All bins show a flat background distribution for ϕ.

A.10 Angular background distributions of signal channel

By removing the mass window around in the B^+ peak ($\pm$ 50 MeV/c^2), a pure background sample is generated. The combined data-set of Run I + II (including both, DD tracks and LL tracks) is fitted for each q^2 bin to obtain the angular background description, which

will be fixed in the final fit. Figs. 163 and 164 show all three angles $\cos\theta_K$, $\cos\theta_L$ and ϕ. The maximum order of Chebyshev polynomials (see subSection 3.2 is: 0 (ϕ) and 2 ($\cos\theta_K$ and $\cos\theta_L$).

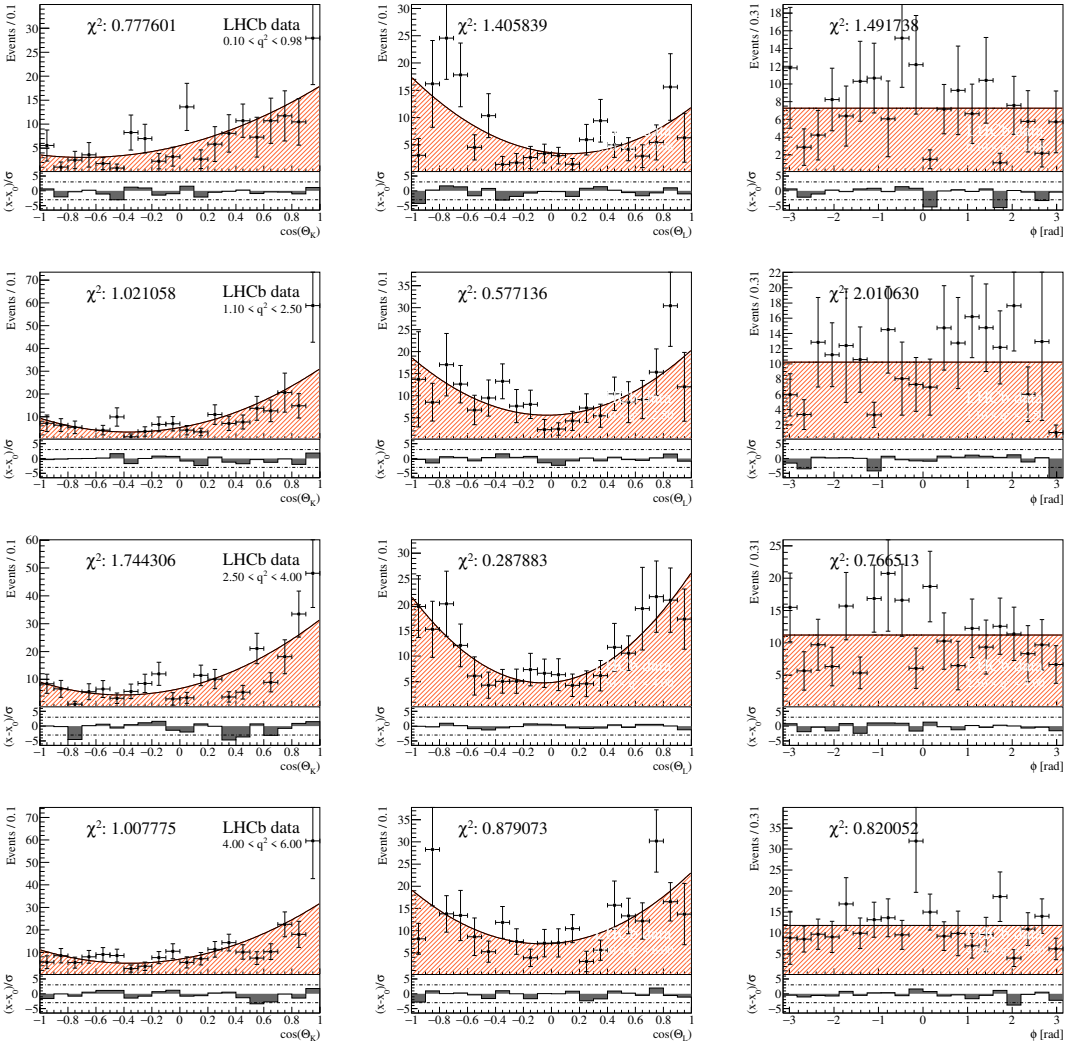

Figure 163: The pure background distributions of the signal channel for q^2 bin 0 – 3. Each row contains the three projections of one q^2 bin, with the left, central and right column showing the angles $\cos\theta_K$, $\cos\theta_L$ and ϕ, respectively. The maximum order of polynomials is 0 (ϕ) and 2 ($\cos\theta_K$ and $\cos\theta_L$).

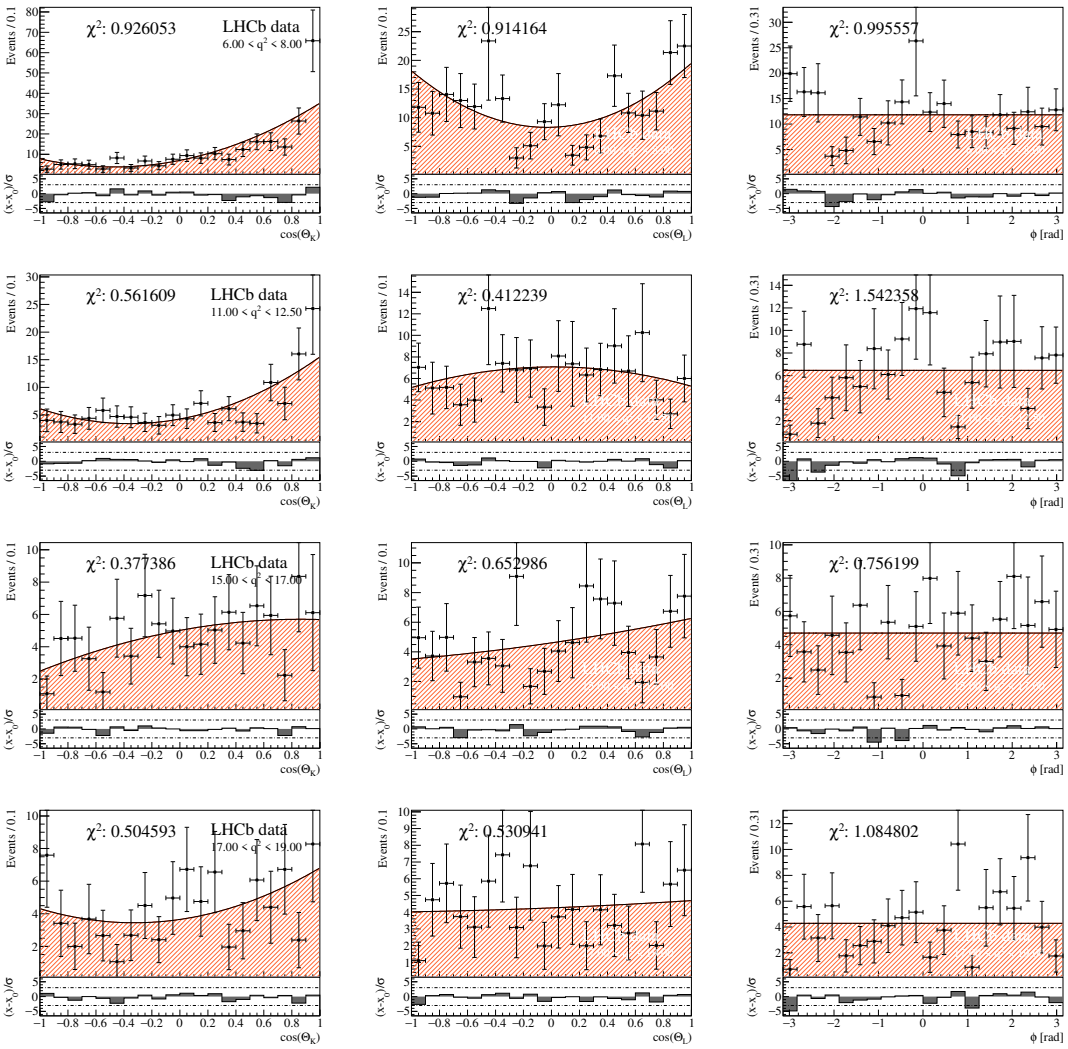

Figure 164: The pure background distributions of the signal channel for q^2 bin 4 – 7. Each row contains the three projections of one q^2 bin, with the left, central and right column showing the angles $\cos\theta_K$, $\cos\theta_L$ and ϕ, respectively. The maximum order of polynomials is 0 (ϕ) and 2 ($\cos\theta_K$ and $\cos\theta_L$).

Table 84: The correlation between the angular dimensions for the full data-set of background events in all eight q^2 bins. Background events are selected to have $m_{K\pi\mu^+\mu^-}$ at least $50\,\mathrm{MeV}/c^2$ away from the B^+ PDG value. The observed correlation is small and in most cases negligible, as expected. Hence a factorizable description of the background PDF is justified.

[0.10, 0.98]	$\cos\theta_L$	$\cos\theta_K$	ϕ
$\cos\theta_L$	1.00	-0.019	-0.116
$\cos\theta_K$		1.00	0.012
ϕ			1.00

[1.10, 2.50]	$\cos\theta_L$	$\cos\theta_K$	ϕ
$\cos\theta_L$	1.00	0.055	-0.004
$\cos\theta_K$		1.00	-0.065
ϕ			1.00

[2.50, 4.00]	$\cos\theta_L$	$\cos\theta_K$	ϕ
$\cos\theta_L$	1.00	-0.009	-0.093
$\cos\theta_K$		1.00	-0.061
ϕ			1.00

[4.00, 6.00]	$\cos\theta_L$	$\cos\theta_K$	ϕ
$\cos\theta_L$	1.00	-0.094	-0.013
$\cos\theta_K$		1.00	0.135
ϕ			1.00

[6.00, 8.00]	$\cos\theta_L$	$\cos\theta_K$	ϕ
$\cos\theta_L$	1.00	-0.067	0.059
$\cos\theta_K$		1.00	-0.046
ϕ			1.00

[11.0, 12.50]	$\cos\theta_L$	$\cos\theta_K$	ϕ
$\cos\theta_L$	1.00	-0.040	-0.002
$\cos\theta_K$		1.00	0.086
ϕ			1.00

[15.0, 17.0]	$\cos\theta_L$	$\cos\theta_K$	ϕ
$\cos\theta_L$	1.00	0.026	0.042
$\cos\theta_K$		1.00	0.012
ϕ			1.00

[17.0, 19.0]	$\cos\theta_L$	$\cos\theta_K$	ϕ
$\cos\theta_L$	1.00	0.080	0.027
$\cos\theta_K$		1.00	0.115
ϕ			1.00

Table 85: The correlation between the angular dimensions for the full data-set of background events in the reference channel. Background events are selected to have $m_{K\pi\mu^+\mu^-}$ at least $50\,\mathrm{MeV}/c^2$ away from the B^+ PDG value. The observed correlation is negligible, as expected. Hence a factorizable description of the background PDF is justified.

[8.68, 10.09]	$\cos\theta_L$	$\cos\theta_K$	ϕ
$\cos\theta_L$	1.00	0.011	-0.009
$\cos\theta_K$		1.00	0.004
ϕ			1.00

A.11 Correlation of angular background distributions

The events used in the following are weighted accordingly to the angular acceptance correction. For all eight q^2 bins plus the reference channel q^2 bin, the correlation between angular dimensions was determined. In Tables 84 and 85 the correlation between angular dimensions are given for the eight bins of the signal channel and the single bin of the reference channel, respectively.

A.12 Toy study result tables

In addition to the quick and easy to read summary plots from subSections 4.4.1 and 4.4.2, all values for the mean position of the pull distribution, the width of the pull distribution and the sensitivity from the toy studies are given in the following pages. For the large (realistic) statistic toy studies, the tables for the full angular fits and for all five foldings are presented in Appendix A.12.1 (Appendix A.12.2).

A.12.1 Large statistic toy study result tables

Table 86: Results from the toy event studies with 10000 events. No angular folding is used. All eight q^2 bins are shown.

[0.10, 0.98]	pull mean	pull width	sensitivity
S_{1s}	0.010 ± 0.019	1.005 ± 0.015	0.034 ± 0.000
S_3	-0.021 ± 0.019	1.007 ± 0.013	0.055 ± 0.001
S_4	0.043 ± 0.020	1.040 ± 0.017	0.079 ± 0.001
S_5	-0.001 ± 0.019	0.995 ± 0.014	0.059 ± 0.001
S_{6s}	0.008 ± 0.019	0.995 ± 0.014	0.075 ± 0.001
S_7	-0.008 ± 0.019	0.999 ± 0.014	0.061 ± 0.001
S_8	-0.003 ± 0.019	1.024 ± 0.015	0.077 ± 0.001
S_9	-0.011 ± 0.019	0.982 ± 0.014	0.054 ± 0.001
F_S	0.006 ± 0.004	0.054 ± 0.018	0.000 ± 0.000
S_{S1}	-0.010 ± 0.019	1.013 ± 0.015	0.096 ± 0.001
S_{S2}	0.020 ± 0.019	1.023 ± 0.015	0.090 ± 0.001
S_{S3}	0.026 ± 0.019	0.996 ± 0.014	0.068 ± 0.001
S_{S4}	0.032 ± 0.019	1.007 ± 0.013	0.068 ± 0.001
S_{S5}	0.002 ± 0.019	0.989 ± 0.014	0.090 ± 0.001
$f_{\rm sig}$	0.077 ± 0.018	0.949 ± 0.013	0.023 ± 0.000
m_{B^+}	-0.013 ± 0.018	0.988 ± 0.014	1.159 ± 0.015
$\lambda_{\rm m}$	-0.026 ± 0.018	0.955 ± 0.013	0.000 ± 0.000
$c^1_{bkg}(\cos\theta_L)$	0.008 ± 0.018	0.973 ± 0.013	0.095 ± 0.001
$c^2_{bkg}(\cos\theta_L)$	-0.059 ± 0.018	0.990 ± 0.014	0.066 ± 0.001
$c^1_{bkg}(\cos\theta_K)$	-0.007 ± 0.017	0.937 ± 0.013	0.092 ± 0.001
$c^2_{bkg}(\cos\theta_K)$	-0.085 ± 0.020	1.057 ± 0.014	0.079 ± 0.001

[1.10, 2.50]	pull mean	pull width	sensitivity
S_{1s}	-0.068 ± 0.019	1.014 ± 0.014	0.046 ± 0.001
S_3	-0.032 ± 0.020	1.052 ± 0.016	0.064 ± 0.001
S_4	-0.013 ± 0.019	1.034 ± 0.015	0.104 ± 0.001
S_5	-0.029 ± 0.019	1.027 ± 0.014	0.084 ± 0.001
S_{6s}	-0.099 ± 0.020	1.056 ± 0.015	0.081 ± 0.001
S_7	-0.042 ± 0.019	1.010 ± 0.013	0.085 ± 0.001
S_8	0.005 ± 0.019	1.031 ± 0.014	0.104 ± 0.001
S_9	0.004 ± 0.020	1.067 ± 0.015	0.065 ± 0.001
F_S	0.008 ± 0.005	0.054 ± 0.017	0.000 ± 0.000
S_{S1}	-0.033 ± 0.020	1.068 ± 0.015	0.151 ± 0.002
S_{S2}	0.007 ± 0.020	1.050 ± 0.014	0.104 ± 0.001
S_{S3}	0.003 ± 0.019	1.009 ± 0.013	0.078 ± 0.001
S_{S4}	-0.032 ± 0.019	1.029 ± 0.014	0.078 ± 0.001
S_{S5}	-0.038 ± 0.020	1.069 ± 0.014	0.105 ± 0.001
$f_{\rm sig}$	0.064 ± 0.017	0.890 ± 0.012	0.018 ± 0.000
m_{B^+}	0.012 ± 0.019	1.009 ± 0.013	1.583 ± 0.020
$\lambda_{\rm m}$	-0.021 ± 0.018	0.963 ± 0.013	0.000 ± 0.000
$c^1_{bkg}(\cos\theta_L)$	0.018 ± 0.018	0.989 ± 0.013	0.071 ± 0.001
$c^2_{bkg}(\cos\theta_L)$	-0.054 ± 0.018	0.970 ± 0.013	0.048 ± 0.001
$c^1_{bkg}(\cos\theta_K)$	-0.003 ± 0.016	0.855 ± 0.012	0.058 ± 0.001
$c^2_{bkg}(\cos\theta_K)$	-0.056 ± 0.018	0.963 ± 0.014	0.041 ± 0.001

[2.50, 4.00]	pull mean	pull width	sensitivity
S_{1s}	-0.028 ± 0.018	0.980 ± 0.013	0.046 ± 0.001
S_3	-0.009 ± 0.020	1.084 ± 0.016	0.071 ± 0.001
S_4	-0.039 ± 0.019	1.006 ± 0.014	0.104 ± 0.001
S_5	-0.024 ± 0.019	1.024 ± 0.014	0.089 ± 0.001
S_{6s}	-0.021 ± 0.019	1.027 ± 0.014	0.076 ± 0.001
S_7	0.009 ± 0.018	0.996 ± 0.014	0.089 ± 0.001
S_8	0.007 ± 0.018	0.992 ± 0.013	0.104 ± 0.001
S_9	-0.015 ± 0.020	1.058 ± 0.015	0.070 ± 0.001
F_S	0.002 ± 0.002	0.055 ± 0.019	0.000 ± 0.000
S_{S1}	0.009 ± 0.021	1.064 ± 0.016	0.159 ± 0.002
S_{S2}	0.010 ± 0.019	1.026 ± 0.014	0.102 ± 0.001
S_{S3}	0.020 ± 0.020	1.062 ± 0.015	0.082 ± 0.001
S_{S4}	-0.002 ± 0.019	1.018 ± 0.014	0.082 ± 0.001
S_{S5}	-0.039 ± 0.020	1.048 ± 0.015	0.104 ± 0.001
$f_{\rm sig}$	0.023 ± 0.017	0.884 ± 0.012	0.015 ± 0.000
m_{B^+}	-0.007 ± 0.019	0.999 ± 0.014	1.790 ± 0.023
$\lambda_{\rm m}$	0.025 ± 0.019	0.995 ± 0.014	0.000 ± 0.000
$c^1_{bkg}(\cos\theta_L)$	-0.015 ± 0.019	0.993 ± 0.014	0.055 ± 0.001
$c^2_{bkg}(\cos\theta_L)$	-0.032 ± 0.018	0.949 ± 0.013	0.034 ± 0.000
$c^1_{bkg}(\cos\theta_K)$	-0.034 ± 0.018	0.949 ± 0.013	0.054 ± 0.001
$c^2_{bkg}(\cos\theta_K)$	-0.034 ± 0.018	0.959 ± 0.015	0.037 ± 0.000

[4.00, 6.00]	pull mean	pull width	sensitivity
S_{1s}	0.029 ± 0.018	0.964 ± 0.013	0.036 ± 0.000
S_3	-0.009 ± 0.019	1.008 ± 0.014	0.058 ± 0.001
S_4	-0.046 ± 0.019	1.028 ± 0.014	0.080 ± 0.001
S_5	-0.027 ± 0.019	0.997 ± 0.014	0.071 ± 0.001
S_{6s}	0.033 ± 0.019	1.003 ± 0.013	0.057 ± 0.001
S_7	-0.022 ± 0.019	1.006 ± 0.014	0.074 ± 0.001
S_8	-0.020 ± 0.019	1.005 ± 0.014	0.080 ± 0.001
S_9	-0.004 ± 0.019	1.018 ± 0.014	0.059 ± 0.001
F_S	0.000 ± 0.001	0.056 ± 0.020	0.000 ± 0.000
S_{S1}	0.004 ± 0.020	1.054 ± 0.015	0.135 ± 0.002
S_{S2}	-0.017 ± 0.019	1.014 ± 0.013	0.079 ± 0.001
S_{S3}	-0.034 ± 0.019	1.001 ± 0.014	0.068 ± 0.001
S_{S4}	0.011 ± 0.019	1.037 ± 0.015	0.072 ± 0.001
S_{S5}	-0.036 ± 0.019	0.997 ± 0.014	0.080 ± 0.001
$f_{\rm sig}$	0.006 ± 0.017	0.933 ± 0.012	0.014 ± 0.000
m_{B^+}	-0.006 ± 0.018	0.977 ± 0.014	1.439 ± 0.019
$\lambda_{\rm m}$	-0.036 ± 0.018	0.991 ± 0.013	0.000 ± 0.000
$c^1_{bkg}(\cos\theta_L)$	-0.011 ± 0.018	0.985 ± 0.013	0.051 ± 0.001
$c^2_{bkg}(\cos\theta_L)$	0.013 ± 0.019	1.005 ± 0.013	0.041 ± 0.001
$c^1_{bkg}(\cos\theta_K)$	0.009 ± 0.017	0.935 ± 0.013	0.045 ± 0.001
$c^2_{bkg}(\cos\theta_K)$	-0.036 ± 0.019	1.000 ± 0.014	0.034 ± 0.000

[6.00, 8.00]	pull mean	pull width	sensitivity
S_{1s}	0.049 ± 0.019	1.035 ± 0.015	0.031 ± 0.000
S_3	0.023 ± 0.019	1.017 ± 0.014	0.050 ± 0.001
S_4	-0.045 ± 0.019	1.005 ± 0.014	0.061 ± 0.001
S_5	-0.070 ± 0.019	1.011 ± 0.014	0.058 ± 0.001
S_{6s}	0.046 ± 0.019	1.038 ± 0.015	0.048 ± 0.001
S_7	-0.012 ± 0.019	1.018 ± 0.014	0.063 ± 0.001
S_8	0.010 ± 0.019	1.000 ± 0.014	0.065 ± 0.001
S_9	-0.016 ± 0.019	1.034 ± 0.014	0.050 ± 0.001
F_S	-0.000 ± 0.001	0.056 ± 0.020	0.000 ± 0.000
S_{S1}	0.013 ± 0.020	1.050 ± 0.014	0.111 ± 0.001
S_{S2}	0.032 ± 0.018	0.991 ± 0.013	0.064 ± 0.001
S_{S3}	0.004 ± 0.019	1.028 ± 0.015	0.060 ± 0.001
S_{S4}	0.024 ± 0.018	0.951 ± 0.013	0.059 ± 0.001
S_{S5}	-0.028 ± 0.019	1.007 ± 0.013	0.067 ± 0.001
$f_{\rm sig}$	-0.007 ± 0.018	0.993 ± 0.014	0.014 ± 0.000
m_{B^+}	-0.019 ± 0.019	0.991 ± 0.014	1.110 ± 0.014
$\lambda_{\rm m}$	0.022 ± 0.019	0.997 ± 0.013	0.000 ± 0.000
$c^1_{bkg}(\cos\theta_L)$	-0.019 ± 0.018	0.986 ± 0.014	0.052 ± 0.001
$c^2_{bkg}(\cos\theta_L)$	0.015 ± 0.019	1.014 ± 0.014	0.043 ± 0.001
$c^1_{bkg}(\cos\theta_K)$	-0.042 ± 0.016	0.810 ± 0.013	0.039 ± 0.001
$c^2_{bkg}(\cos\theta_K)$	0.008 ± 0.018	0.978 ± 0.013	0.029 ± 0.000

[11.00, 12.50]	pull mean	pull width	sensitivity
S_{1s}	0.065 ± 0.020	1.041 ± 0.014	0.031 ± 0.000
S_3	-0.106 ± 0.020	1.059 ± 0.015	0.053 ± 0.001
S_4	-0.039 ± 0.021	1.114 ± 0.016	0.060 ± 0.001
S_5	-0.098 ± 0.021	1.077 ± 0.016	0.056 ± 0.001
S_{6s}	0.100 ± 0.021	1.084 ± 0.014	0.047 ± 0.001
S_7	0.005 ± 0.019	1.032 ± 0.014	0.061 ± 0.001
S_8	-0.007 ± 0.019	1.030 ± 0.015	0.060 ± 0.001
S_9	-0.005 ± 0.020	1.050 ± 0.016	0.053 ± 0.001
F_S	-0.000 ± 0.001	0.056 ± 0.020	0.000 ± 0.000
S_{S1}	-0.021 ± 0.019	1.047 ± 0.015	0.098 ± 0.001
S_{S2}	-0.002 ± 0.021	1.099 ± 0.016	0.067 ± 0.001
S_{S3}	-0.085 ± 0.020	1.074 ± 0.016	0.064 ± 0.001
S_{S4}	-0.003 ± 0.019	1.005 ± 0.014	0.065 ± 0.001
S_{S5}	-0.058 ± 0.019	1.010 ± 0.014	0.068 ± 0.001
$f_{\rm sig}$	-0.034 ± 0.019	1.014 ± 0.013	0.017 ± 0.000
m_{B^+}	0.009 ± 0.018	0.962 ± 0.013	1.047 ± 0.014
$\lambda_{\rm m}$	0.054 ± 0.019	0.991 ± 0.014	0.001 ± 0.000
$c^1_{bkg}(\cos\theta_L)$	0.002 ± 0.018	0.979 ± 0.014	0.062 ± 0.001
$c^2_{bkg}(\cos\theta_L)$	0.008 ± 0.018	0.951 ± 0.013	0.056 ± 0.001
$c^1_{bkg}(\cos\theta_K)$	-0.037 ± 0.018	0.993 ± 0.013	0.064 ± 0.001
$c^2_{bkg}(\cos\theta_K)$	-0.028 ± 0.019	1.047 ± 0.015	0.050 ± 0.001

[15.00, 17.00]	pull mean	pull width	sensitivity
S_{1s}	0.056 ± 0.019	1.034 ± 0.014	0.029 ± 0.000
S_3	-0.056 ± 0.019	1.022 ± 0.014	0.054 ± 0.001
S_4	-0.086 ± 0.020	1.059 ± 0.015	0.056 ± 0.001
S_5	-0.024 ± 0.020	1.081 ± 0.016	0.055 ± 0.001
S_{6s}	0.086 ± 0.020	1.048 ± 0.015	0.049 ± 0.001
S_7	0.008 ± 0.018	0.986 ± 0.014	0.059 ± 0.001
S_8	0.020 ± 0.019	1.024 ± 0.014	0.061 ± 0.001
S_9	-0.006 ± 0.019	1.024 ± 0.014	0.054 ± 0.001
F_S	0.002 ± 0.002	0.055 ± 0.019	0.000 ± 0.000
S_{S1}	-0.006 ± 0.019	1.000 ± 0.014	0.090 ± 0.001
S_{S2}	-0.025 ± 0.019	1.046 ± 0.014	0.066 ± 0.001
S_{S3}	-0.026 ± 0.019	1.025 ± 0.014	0.062 ± 0.001
S_{S4}	-0.029 ± 0.019	1.011 ± 0.014	0.071 ± 0.001
S_{S5}	-0.044 ± 0.019	1.008 ± 0.014	0.073 ± 0.001
$f_{\rm sig}$	0.018 ± 0.019	1.000 ± 0.013	0.020 ± 0.000
m_{B^+}	0.027 ± 0.019	1.020 ± 0.014	1.238 ± 0.016
$\lambda_{\rm m}$	-0.029 ± 0.019	1.000 ± 0.013	0.000 ± 0.000
$c^1_{bkg}(\cos\theta_L)$	-0.035 ± 0.019	1.002 ± 0.013	0.081 ± 0.001
$c^2_{bkg}(\cos\theta_L)$	0.008 ± 0.018	0.982 ± 0.014	0.084 ± 0.001
$c^1_{bkg}(\cos\theta_K)$	0.021 ± 0.018	0.988 ± 0.013	0.083 ± 0.001
$c^2_{bkg}(\cos\theta_K)$	-0.016 ± 0.020	1.062 ± 0.015	0.072 ± 0.001

[17.00, 19.00]	pull mean	pull width	sensitivity
S_{1s}	0.013 ± 0.020	1.085 ± 0.015	0.043 ± 0.001
S_3	-0.171 ± 0.022	1.119 ± 0.017	0.088 ± 0.001
S_4	-0.186 ± 0.020	1.078 ± 0.015	0.088 ± 0.001
S_5	-0.037 ± 0.019	1.045 ± 0.014	0.078 ± 0.001
S_{6s}	0.125 ± 0.021	1.092 ± 0.015	0.078 ± 0.001
S_7	0.002 ± 0.019	1.039 ± 0.015	0.087 ± 0.001
S_8	0.013 ± 0.020	1.058 ± 0.015	0.092 ± 0.001
S_9	0.020 ± 0.020	1.086 ± 0.015	0.084 ± 0.001
F_S	0.000 ± 0.001	0.056 ± 0.020	0.000 ± 0.000
S_{S1}	0.000 ± 0.019	1.029 ± 0.014	0.126 ± 0.002
S_{S2}	-0.014 ± 0.021	1.140 ± 0.016	0.111 ± 0.001
S_{S3}	0.006 ± 0.020	1.096 ± 0.016	0.095 ± 0.001
S_{S4}	-0.008 ± 0.019	1.021 ± 0.014	0.106 ± 0.001
S_{S5}	-0.025 ± 0.020	1.061 ± 0.015	0.116 ± 0.001
$f_{\rm sig}$	-0.032 ± 0.018	0.958 ± 0.012	0.026 ± 0.000
m_{B^+}	0.031 ± 0.018	0.989 ± 0.014	1.767 ± 0.023
$\lambda_{\rm m}$	0.002 ± 0.019	0.996 ± 0.014	0.000 ± 0.000
$c^1_{bkg}(\cos\theta_L)$	0.009 ± 0.019	1.012 ± 0.015	0.096 ± 0.001
$c^2_{bkg}(\cos\theta_L)$	-0.000 ± 0.018	0.968 ± 0.013	0.099 ± 0.001
$c^1_{bkg}(\cos\theta_K)$	0.037 ± 0.019	0.995 ± 0.014	0.107 ± 0.001
$c^2_{bkg}(\cos\theta_K)$	-0.010 ± 0.020	1.064 ± 0.015	0.101 ± 0.001

Table 87: Results from the toy event studies with 10000 events. Angular folding 0 is used. All eight q^2 bins are shown.

[0.10, 0.98]	pull mean	pull width	sensitivity
S_{1s}	0.020 ± 0.019	0.992 ± 0.014	0.035 ± 0.000
S_3	0.027 ± 0.019	1.015 ± 0.015	0.056 ± 0.001
S_{6s}	-0.027 ± 0.018	0.980 ± 0.014	0.074 ± 0.001
S_9	-0.029 ± 0.018	0.992 ± 0.013	0.055 ± 0.001
F_S	0.002 ± 0.002	0.055 ± 0.019	0.000 ± 0.000
S_{S1}	-0.002 ± 0.019	1.014 ± 0.014	0.098 ± 0.001
$f_{\rm sig}$	0.072 ± 0.018	0.950 ± 0.014	0.022 ± 0.000
m_{B^+}	-0.033 ± 0.018	0.970 ± 0.014	1.130 ± 0.015
$\lambda_{\rm m}$	-0.029 ± 0.019	0.999 ± 0.014	0.000 ± 0.000
$c^1_{bkg}(\cos\theta_L)$	-0.002 ± 0.018	0.969 ± 0.013	0.096 ± 0.001
$c^2_{bkg}(\cos\theta_L)$	-0.107 ± 0.019	1.010 ± 0.014	0.068 ± 0.001
$c^1_{bkg}(\cos\theta_K)$	-0.014 ± 0.017	0.914 ± 0.013	0.091 ± 0.001
$c^2_{bkg}(\cos\theta_K)$	-0.083 ± 0.019	1.030 ± 0.014	0.079 ± 0.001

[1.10, 2.50]	pull mean	pull width	sensitivity
S_{1s}	-0.037 ± 0.018	0.963 ± 0.013	0.043 ± 0.001
S_3	-0.014 ± 0.019	1.015 ± 0.015	0.059 ± 0.001
S_{6s}	-0.041 ± 0.019	1.012 ± 0.014	0.075 ± 0.001
S_9	0.043 ± 0.019	1.037 ± 0.014	0.061 ± 0.001
F_S	0.005 ± 0.004	0.055 ± 0.019	0.000 ± 0.000
S_{S1}	0.028 ± 0.020	1.051 ± 0.015	0.148 ± 0.002
$f_{\rm sig}$	0.050 ± 0.017	0.903 ± 0.012	0.018 ± 0.000
m_{B^+}	-0.009 ± 0.019	1.024 ± 0.014	1.592 ± 0.021
$\lambda_{\rm m}$	0.014 ± 0.019	0.977 ± 0.013	0.000 ± 0.000
$c^1_{bkg}(\cos\theta_L)$	0.030 ± 0.018	0.966 ± 0.013	0.071 ± 0.001
$c^2_{bkg}(\cos\theta_L)$	0.006 ± 0.018	0.984 ± 0.013	0.048 ± 0.001
$c^1_{bkg}(\cos\theta_K)$	-0.041 ± 0.016	0.836 ± 0.011	0.058 ± 0.001
$c^2_{bkg}(\cos\theta_K)$	-0.020 ± 0.018	0.962 ± 0.013	0.041 ± 0.001

[2.50, 4.00]	pull mean	pull width	sensitivity
S_{1s}	-0.018 ± 0.018	0.981 ± 0.013	0.046 ± 0.001
S_3	-0.030 ± 0.019	1.021 ± 0.015	0.064 ± 0.001
S_{6s}	-0.045 ± 0.019	1.006 ± 0.014	0.073 ± 0.001
S_9	0.027 ± 0.019	1.021 ± 0.014	0.064 ± 0.001
F_S	-0.000 ± 0.001	0.056 ± 0.020	0.000 ± 0.000
S_{S1}	0.001 ± 0.020	1.030 ± 0.015	0.157 ± 0.002
$f_{\rm sig}$	0.001 ± 0.017	0.906 ± 0.013	0.015 ± 0.000
m_{B^+}	-0.017 ± 0.018	0.988 ± 0.013	1.775 ± 0.023
$\lambda_{\rm m}$	-0.006 ± 0.018	0.964 ± 0.012	0.000 ± 0.000
$c^1_{bkg}(\cos\theta_L)$	0.031 ± 0.019	0.991 ± 0.013	0.055 ± 0.001
$c^2_{bkg}(\cos\theta_L)$	0.002 ± 0.018	0.936 ± 0.013	0.034 ± 0.000
$c^1_{bkg}(\cos\theta_K)$	0.011 ± 0.017	0.919 ± 0.012	0.052 ± 0.001
$c^2_{bkg}(\cos\theta_K)$	-0.016 ± 0.018	0.948 ± 0.013	0.036 ± 0.000

[4.00, 6.00]	pull mean	pull width	sensitivity
S_{1s}	-0.004 ± 0.018	0.969 ± 0.013	0.037 ± 0.000
S_3	-0.002 ± 0.019	1.006 ± 0.015	0.057 ± 0.001
S_{6s}	-0.030 ± 0.018	0.985 ± 0.014	0.056 ± 0.001
S_9	0.019 ± 0.018	0.979 ± 0.014	0.056 ± 0.001
F_S	0.001 ± 0.001	0.055 ± 0.020	0.000 ± 0.000
S_{S1}	0.006 ± 0.019	1.033 ± 0.014	0.133 ± 0.002
$f_{\rm sig}$	0.034 ± 0.017	0.928 ± 0.013	0.014 ± 0.000
m_{B^+}	0.016 ± 0.018	0.986 ± 0.014	1.456 ± 0.019
$\lambda_{\rm m}$	0.050 ± 0.019	1.017 ± 0.014	0.000 ± 0.000
$c^1_{bkg}(\cos\theta_L)$	0.008 ± 0.018	0.966 ± 0.013	0.050 ± 0.001
$c^2_{bkg}(\cos\theta_L)$	0.014 ± 0.019	0.996 ± 0.014	0.040 ± 0.001
$c^1_{bkg}(\cos\theta_K)$	-0.007 ± 0.017	0.927 ± 0.013	0.045 ± 0.001
$c^2_{bkg}(\cos\theta_K)$	-0.023 ± 0.019	1.010 ± 0.014	0.034 ± 0.000

[6.00, 8.00]	pull mean	pull width	sensitivity
S_{1s}	-0.011 ± 0.018	0.980 ± 0.013	0.031 ± 0.000
S_3	-0.030 ± 0.019	1.018 ± 0.014	0.051 ± 0.001
S_{6s}	-0.020 ± 0.019	1.043 ± 0.015	0.048 ± 0.001
S_9	0.006 ± 0.018	0.968 ± 0.013	0.049 ± 0.001
F_S	0.001 ± 0.001	0.055 ± 0.020	0.000 ± 0.000
S_{S1}	-0.019 ± 0.019	1.036 ± 0.015	0.114 ± 0.001
$f_{\rm sig}$	-0.019 ± 0.018	0.977 ± 0.014	0.014 ± 0.000
m_{B^+}	0.001 ± 0.019	1.016 ± 0.014	1.170 ± 0.015
$\lambda_{\rm m}$	-0.023 ± 0.018	0.950 ± 0.013	0.000 ± 0.000
$c^1_{bkg}(\cos\theta_L)$	-0.006 ± 0.018	0.978 ± 0.013	0.051 ± 0.001
$c^2_{bkg}(\cos\theta_L)$	0.045 ± 0.018	0.983 ± 0.014	0.043 ± 0.001
$c^1_{bkg}(\cos\theta_K)$	-0.067 ± 0.016	0.722 ± 0.011	0.039 ± 0.001
$c^2_{bkg}(\cos\theta_K)$	-0.024 ± 0.018	0.969 ± 0.012	0.029 ± 0.000

[11.00, 12.50]	pull mean	pull width	sensitivity
S_{1s}	-0.023 ± 0.019	1.037 ± 0.014	0.031 ± 0.000
S_3	0.017 ± 0.019	0.998 ± 0.014	0.049 ± 0.001
S_{6s}	0.008 ± 0.020	1.047 ± 0.014	0.046 ± 0.001
S_9	0.031 ± 0.019	1.013 ± 0.015	0.051 ± 0.001
F_S	-0.001 ± 0.001	0.055 ± 0.020	0.000 ± 0.000
S_{S1}	-0.014 ± 0.019	0.996 ± 0.014	0.098 ± 0.001
$f_{\rm sig}$	0.008 ± 0.018	0.988 ± 0.013	0.017 ± 0.000
m_{B^+}	0.001 ± 0.018	0.989 ± 0.015	1.053 ± 0.014
$\lambda_{\rm m}$	0.007 ± 0.019	0.994 ± 0.014	0.001 ± 0.000
$c^1_{bkg}(\cos\theta_L)$	-0.028 ± 0.018	0.981 ± 0.014	0.061 ± 0.001
$c^2_{bkg}(\cos\theta_L)$	0.008 ± 0.018	0.974 ± 0.013	0.057 ± 0.001
$c^1_{bkg}(\cos\theta_K)$	0.059 ± 0.018	0.985 ± 0.014	0.064 ± 0.001
$c^2_{bkg}(\cos\theta_K)$	0.000 ± 0.020	1.052 ± 0.015	0.051 ± 0.001

[15.00, 17.00]	pull mean	pull width	sensitivity
S_{1s}	0.017 ± 0.019	1.041 ± 0.015	0.030 ± 0.000
S_3	-0.001 ± 0.019	1.011 ± 0.014	0.054 ± 0.001
S_{6s}	0.025 ± 0.019	1.032 ± 0.014	0.049 ± 0.001
S_9	0.001 ± 0.019	1.009 ± 0.014	0.054 ± 0.001
F_S	0.001 ± 0.001	0.055 ± 0.020	0.000 ± 0.000
S_{S1}	0.012 ± 0.019	0.997 ± 0.014	0.093 ± 0.001
$f_{\rm sig}$	0.032 ± 0.018	0.978 ± 0.013	0.019 ± 0.000
m_{B^+}	-0.005 ± 0.019	0.996 ± 0.014	1.238 ± 0.016
$\lambda_{\rm m}$	-0.013 ± 0.018	0.982 ± 0.013	0.000 ± 0.000
$c^1_{bkg}(\cos\theta_L)$	0.020 ± 0.018	0.985 ± 0.013	0.080 ± 0.001
$c^2_{bkg}(\cos\theta_L)$	0.035 ± 0.018	0.961 ± 0.013	0.081 ± 0.001
$c^1_{bkg}(\cos\theta_K)$	-0.005 ± 0.019	0.995 ± 0.013	0.084 ± 0.001
$c^2_{bkg}(\cos\theta_K)$	0.014 ± 0.020	1.080 ± 0.016	0.074 ± 0.001

[17.00, 19.00]	pull mean	pull width	sensitivity
S_{1s}	0.044 ± 0.019	1.011 ± 0.013	0.041 ± 0.001
S_3	-0.024 ± 0.020	1.033 ± 0.016	0.078 ± 0.001
S_{6s}	0.062 ± 0.019	1.007 ± 0.014	0.072 ± 0.001
S_9	-0.003 ± 0.019	1.009 ± 0.014	0.079 ± 0.001
F_S	0.002 ± 0.002	0.055 ± 0.020	0.000 ± 0.000
S_{S1}	0.005 ± 0.019	1.007 ± 0.014	0.130 ± 0.002
$f_{\rm sig}$	0.039 ± 0.018	0.986 ± 0.013	0.027 ± 0.000
m_{B^+}	0.032 ± 0.019	0.996 ± 0.014	1.766 ± 0.023
$\lambda_{\rm m}$	-0.006 ± 0.019	0.996 ± 0.013	0.000 ± 0.000
$c^1_{bkg}(\cos\theta_L)$	0.009 ± 0.019	1.005 ± 0.015	0.096 ± 0.001
$c^2_{bkg}(\cos\theta_L)$	-0.023 ± 0.018	0.985 ± 0.013	0.102 ± 0.001
$c^1_{bkg}(\cos\theta_K)$	0.007 ± 0.019	1.002 ± 0.015	0.108 ± 0.001
$c^2_{bkg}(\cos\theta_K)$	0.018 ± 0.019	1.034 ± 0.014	0.100 ± 0.001

Table 88: Results from the toy event studies with 10000 events. Angular folding 1 is used. All eight q^2 bins are shown.

[0.10, 0.98]	pull mean	pull width	sensitivity
S_{1s}	0.063 ± 0.019	1.011 ± 0.013	0.036 ± 0.000
S_3	0.041 ± 0.018	0.974 ± 0.014	0.056 ± 0.001
S_4	-0.012 ± 0.019	1.014 ± 0.014	0.079 ± 0.001
F_S	0.001 ± 0.001	0.055 ± 0.020	0.000 ± 0.000
S_{S1}	-0.036 ± 0.019	1.026 ± 0.014	0.099 ± 0.001
S_{S2}	0.039 ± 0.018	0.968 ± 0.013	0.089 ± 0.001
$f_{\rm sig}$	0.054 ± 0.018	0.965 ± 0.013	0.023 ± 0.000
m_{B^+}	0.017 ± 0.019	0.999 ± 0.013	1.170 ± 0.015
$\lambda_{\rm m}$	-0.000 ± 0.019	1.008 ± 0.014	0.000 ± 0.000
$c^2_{bkg}(\cos\theta_L)$	-0.061 ± 0.019	1.004 ± 0.014	0.068 ± 0.001
$c^1_{bkg}(\cos\theta_K)$	-0.002 ± 0.018	0.943 ± 0.013	0.093 ± 0.001
$c^2_{bkg}(\cos\theta_K)$	-0.026 ± 0.020	1.040 ± 0.014	0.077 ± 0.001

[1.10, 2.50]	pull mean	pull width	sensitivity
S_{1s}	-0.028 ± 0.018	0.989 ± 0.013	0.044 ± 0.001
S_3	0.033 ± 0.019	1.017 ± 0.014	0.061 ± 0.001
S_4	-0.018 ± 0.019	1.011 ± 0.014	0.101 ± 0.001
F_S	0.001 ± 0.001	0.055 ± 0.020	0.000 ± 0.000
S_{S1}	0.006 ± 0.020	1.060 ± 0.015	0.150 ± 0.002
S_{S2}	0.010 ± 0.018	0.976 ± 0.014	0.096 ± 0.001
$f_{\rm sig}$	0.057 ± 0.017	0.925 ± 0.012	0.018 ± 0.000
m_{B^+}	-0.006 ± 0.018	0.963 ± 0.013	1.544 ± 0.020
$\lambda_{\rm m}$	-0.025 ± 0.018	0.975 ± 0.014	0.000 ± 0.000
$c^2_{bkg}(\cos\theta_L)$	-0.027 ± 0.018	0.952 ± 0.013	0.047 ± 0.001
$c^1_{bkg}(\cos\theta_K)$	-0.018 ± 0.016	0.820 ± 0.011	0.057 ± 0.001
$c^2_{bkg}(\cos\theta_K)$	-0.033 ± 0.019	0.978 ± 0.014	0.042 ± 0.001

[2.50, 4.00]	pull mean	pull width	sensitivity
S_{1s}	-0.044 ± 0.018	0.961 ± 0.013	0.045 ± 0.001
S_3	0.004 ± 0.019	1.030 ± 0.015	0.063 ± 0.001
S_4	-0.032 ± 0.019	1.018 ± 0.014	0.105 ± 0.001
F_S	0.001 ± 0.001	0.055 ± 0.020	0.000 ± 0.000
S_{S1}	0.005 ± 0.020	1.062 ± 0.015	0.158 ± 0.002
S_{S2}	-0.028 ± 0.019	1.008 ± 0.014	0.099 ± 0.001
$f_{\rm sig}$	0.034 ± 0.016	0.869 ± 0.012	0.015 ± 0.000
m_{B^+}	-0.002 ± 0.019	0.996 ± 0.013	1.796 ± 0.023
$\lambda_{\rm m}$	-0.035 ± 0.018	0.990 ± 0.013	0.000 ± 0.000
$c^2_{bkg}(\cos\theta_L)$	-0.009 ± 0.018	0.942 ± 0.013	0.034 ± 0.000
$c^1_{bkg}(\cos\theta_K)$	0.037 ± 0.018	0.955 ± 0.013	0.053 ± 0.001
$c^2_{bkg}(\cos\theta_K)$	-0.018 ± 0.018	0.958 ± 0.013	0.036 ± 0.000

[4.00, 6.00]	pull mean	pull width	sensitivity
S_{1s}	0.026 ± 0.018	0.966 ± 0.013	0.036 ± 0.000
S_3	0.022 ± 0.019	1.016 ± 0.014	0.058 ± 0.001
S_4	-0.019 ± 0.019	1.019 ± 0.015	0.081 ± 0.001
F_S	0.003 ± 0.002	0.055 ± 0.019	0.000 ± 0.000
S_{S1}	0.003 ± 0.019	1.027 ± 0.014	0.134 ± 0.002
S_{S2}	-0.042 ± 0.018	0.989 ± 0.013	0.080 ± 0.001
$f_{\rm sig}$	0.018 ± 0.018	0.947 ± 0.013	0.014 ± 0.000
m_{B^+}	-0.003 ± 0.018	0.981 ± 0.013	1.458 ± 0.019
$\lambda_{\rm m}$	0.015 ± 0.018	0.953 ± 0.013	0.000 ± 0.000
$c^2_{bkg}(\cos\theta_L)$	0.034 ± 0.018	0.977 ± 0.013	0.040 ± 0.001
$c^1_{bkg}(\cos\theta_K)$	-0.015 ± 0.017	0.917 ± 0.013	0.045 ± 0.001
$c^2_{bkg}(\cos\theta_K)$	-0.004 ± 0.019	1.006 ± 0.013	0.034 ± 0.000

[6.00, 8.00]	pull mean	pull width	sensitivity
S_{1s}	-0.020 ± 0.019	1.025 ± 0.014	0.032 ± 0.000
S_3	-0.014 ± 0.019	1.010 ± 0.015	0.052 ± 0.001
S_4	-0.006 ± 0.019	0.996 ± 0.014	0.064 ± 0.001
F_S	-0.002 ± 0.002	0.055 ± 0.019	0.000 ± 0.000
S_{S1}	-0.013 ± 0.020	1.068 ± 0.014	0.117 ± 0.002
S_{S2}	-0.005 ± 0.018	0.993 ± 0.013	0.068 ± 0.001
$f_{\rm sig}$	0.029 ± 0.018	0.978 ± 0.014	0.014 ± 0.000
m_{B^+}	0.002 ± 0.018	0.975 ± 0.013	1.130 ± 0.015
$\lambda_{\rm m}$	0.003 ± 0.019	0.997 ± 0.014	0.000 ± 0.000
$c^2_{bkg}(\cos\theta_L)$	0.012 ± 0.018	0.986 ± 0.014	0.042 ± 0.001
$c^1_{bkg}(\cos\theta_K)$	-0.111 ± 0.016	0.720 ± 0.011	0.039 ± 0.001
$c^2_{bkg}(\cos\theta_K)$	0.007 ± 0.018	0.986 ± 0.013	0.030 ± 0.000

[11.00, 12.50]	pull mean	pull width	sensitivity
S_{1s}	0.031 ± 0.019	1.010 ± 0.014	0.031 ± 0.000
S_3	0.043 ± 0.019	0.996 ± 0.014	0.054 ± 0.001
S_4	-0.010 ± 0.018	0.967 ± 0.013	0.059 ± 0.001
F_S	-0.000 ± 0.001	0.056 ± 0.020	0.000 ± 0.000
S_{S1}	0.013 ± 0.019	1.025 ± 0.015	0.100 ± 0.001
S_{S2}	-0.010 ± 0.018	0.979 ± 0.013	0.068 ± 0.001
$f_{\rm sig}$	0.017 ± 0.018	0.976 ± 0.013	0.017 ± 0.000
m_{B^+}	-0.003 ± 0.018	0.979 ± 0.013	1.063 ± 0.014
$\lambda_{\rm m}$	-0.023 ± 0.018	0.987 ± 0.014	0.001 ± 0.000
$c^2_{bkg}(\cos\theta_L)$	0.031 ± 0.018	0.963 ± 0.014	0.057 ± 0.001
$c^1_{bkg}(\cos\theta_K)$	0.016 ± 0.018	0.966 ± 0.013	0.063 ± 0.001
$c^2_{bkg}(\cos\theta_K)$	0.039 ± 0.020	1.031 ± 0.014	0.051 ± 0.001

[15.00, 17.00]	pull mean	pull width	sensitivity
S_{1s}	0.049 ± 0.019	1.043 ± 0.014	0.031 ± 0.000
S_3	-0.001 ± 0.019	0.995 ± 0.014	0.057 ± 0.001
S_4	-0.006 ± 0.019	0.988 ± 0.015	0.057 ± 0.001
F_S	-0.001 ± 0.001	0.055 ± 0.020	0.000 ± 0.000
S_{S1}	0.008 ± 0.018	0.982 ± 0.013	0.093 ± 0.001
S_{S2}	-0.003 ± 0.018	0.991 ± 0.014	0.071 ± 0.001
$f_{\rm sig}$	0.027 ± 0.018	0.985 ± 0.014	0.020 ± 0.000
m_{B^+}	0.028 ± 0.018	0.980 ± 0.013	1.239 ± 0.016
$\lambda_{\rm m}$	-0.049 ± 0.018	0.973 ± 0.013	0.000 ± 0.000
$c^2_{bkg}(\cos\theta_L)$	0.020 ± 0.018	0.983 ± 0.013	0.084 ± 0.001
$c^1_{bkg}(\cos\theta_K)$	0.058 ± 0.018	0.989 ± 0.013	0.083 ± 0.001
$c^2_{bkg}(\cos\theta_K)$	-0.027 ± 0.020	1.080 ± 0.015	0.074 ± 0.001

[17.00, 19.00]	pull mean	pull width	sensitivity
S_{1s}	0.035 ± 0.019	1.031 ± 0.015	0.042 ± 0.001
S_3	-0.020 ± 0.018	0.986 ± 0.014	0.079 ± 0.001
S_4	-0.077 ± 0.020	1.046 ± 0.015	0.083 ± 0.001
F_S	-0.000 ± 0.001	0.056 ± 0.020	0.000 ± 0.000
S_{S1}	0.026 ± 0.018	0.975 ± 0.013	0.127 ± 0.002
S_{S2}	-0.044 ± 0.019	1.013 ± 0.014	0.105 ± 0.001
$f_{\rm sig}$	-0.013 ± 0.018	0.967 ± 0.013	0.026 ± 0.000
m_{B^+}	0.010 ± 0.019	1.010 ± 0.014	1.790 ± 0.023
$\lambda_{\rm m}$	-0.006 ± 0.018	0.991 ± 0.013	0.000 ± 0.000
$c^2_{bkg}(\cos\theta_L)$	-0.011 ± 0.018	0.973 ± 0.013	0.104 ± 0.001
$c^1_{bkg}(\cos\theta_K)$	0.031 ± 0.019	1.005 ± 0.014	0.109 ± 0.001
$c^2_{bkg}(\cos\theta_K)$	-0.018 ± 0.020	1.073 ± 0.015	0.102 ± 0.001

Table 89: Results from the toy event studies with 10000 events. Angular folding 2 is used. All eight q^2 bins are shown.

[0.10, 0.98]	pull mean	pull width	sensitivity
S_{1s}	0.032 ± 0.019	1.029 ± 0.015	0.035 ± 0.000
S_3	0.000 ± 0.018	0.981 ± 0.014	0.055 ± 0.001
S_5	0.000 ± 0.019	1.026 ± 0.014	0.062 ± 0.001
F_S	0.003 ± 0.003	0.055 ± 0.019	0.000 ± 0.000
S_{S1}	0.010 ± 0.019	0.993 ± 0.014	0.095 ± 0.001
S_{S3}	-0.012 ± 0.019	0.997 ± 0.013	0.068 ± 0.001
$f_{\rm sig}$	0.076 ± 0.018	0.939 ± 0.013	0.023 ± 0.000
m_{B^+}	0.016 ± 0.019	1.011 ± 0.014	1.161 ± 0.015
$\lambda_{\rm m}$	-0.023 ± 0.018	0.980 ± 0.013	0.000 ± 0.000
$c^2_{bkg}(\cos\theta_L)$	-0.053 ± 0.019	0.999 ± 0.013	0.068 ± 0.001
$c^1_{bkg}(\cos\theta_K)$	-0.014 ± 0.017	0.924 ± 0.012	0.091 ± 0.001
$c^2_{bkg}(\cos\theta_K)$	-0.069 ± 0.020	1.055 ± 0.015	0.080 ± 0.001

[1.10, 2.50]	pull mean	pull width	sensitivity
S_{1s}	0.010 ± 0.018	0.968 ± 0.013	0.044 ± 0.001
S_3	0.017 ± 0.019	1.021 ± 0.014	0.061 ± 0.001
S_5	-0.001 ± 0.019	1.004 ± 0.014	0.083 ± 0.001
F_S	0.002 ± 0.002	0.055 ± 0.019	0.000 ± 0.000
S_{S1}	-0.032 ± 0.019	1.021 ± 0.015	0.149 ± 0.002
S_{S3}	0.016 ± 0.018	0.986 ± 0.014	0.074 ± 0.001
$f_{\rm sig}$	0.030 ± 0.017	0.908 ± 0.012	0.018 ± 0.000
m_{B^+}	-0.011 ± 0.019	1.013 ± 0.014	1.609 ± 0.021
$\lambda_{\rm m}$	-0.022 ± 0.018	0.977 ± 0.013	0.000 ± 0.000
$c^2_{bkg}(\cos\theta_L)$	-0.077 ± 0.018	0.967 ± 0.013	0.048 ± 0.001
$c^1_{bkg}(\cos\theta_K)$	-0.007 ± 0.016	0.838 ± 0.011	0.057 ± 0.001
$c^2_{bkg}(\cos\theta_K)$	0.023 ± 0.019	0.980 ± 0.013	0.042 ± 0.001

[2.50, 4.00]	pull mean	pull width	sensitivity
S_{1s}	-0.030 ± 0.018	0.939 ± 0.014	0.044 ± 0.001
S_3	0.027 ± 0.019	1.015 ± 0.015	0.064 ± 0.001
S_5	-0.040 ± 0.019	1.008 ± 0.014	0.087 ± 0.001
F_S	0.001 ± 0.001	0.055 ± 0.020	0.000 ± 0.000
S_{S1}	-0.021 ± 0.019	1.034 ± 0.015	0.156 ± 0.002
S_{S3}	-0.005 ± 0.019	0.997 ± 0.014	0.078 ± 0.001
$f_{\rm sig}$	0.018 ± 0.017	0.901 ± 0.013	0.015 ± 0.000
m_{B^+}	-0.008 ± 0.018	0.984 ± 0.014	1.772 ± 0.023
$\lambda_{\rm m}$	-0.005 ± 0.019	0.986 ± 0.013	0.000 ± 0.000
$c^2_{bkg}(\cos\theta_L)$	0.035 ± 0.017	0.936 ± 0.013	0.033 ± 0.000
$c^1_{bkg}(\cos\theta_K)$	0.003 ± 0.018	0.951 ± 0.013	0.053 ± 0.001
$c^2_{bkg}(\cos\theta_K)$	-0.015 ± 0.018	0.956 ± 0.013	0.036 ± 0.000

[4.00, 6.00]	pull mean	pull width	sensitivity
S_{1s}	0.001 ± 0.018	0.969 ± 0.014	0.036 ± 0.000
S_3	-0.010 ± 0.019	1.020 ± 0.015	0.058 ± 0.001
S_5	0.023 ± 0.019	1.008 ± 0.014	0.072 ± 0.001
F_S	-0.000 ± 0.001	0.056 ± 0.020	0.000 ± 0.000
S_{S1}	0.010 ± 0.019	1.042 ± 0.015	0.132 ± 0.002
S_{S3}	0.012 ± 0.019	1.006 ± 0.014	0.068 ± 0.001
$f_{\rm sig}$	0.013 ± 0.018	0.953 ± 0.014	0.014 ± 0.000
m_{B^+}	-0.030 ± 0.019	0.999 ± 0.013	1.455 ± 0.019
$\lambda_{\rm m}$	0.018 ± 0.018	0.987 ± 0.013	0.000 ± 0.000
$c^2_{bkg}(\cos\theta_L)$	0.018 ± 0.019	1.003 ± 0.014	0.040 ± 0.001
$c^1_{bkg}(\cos\theta_K)$	0.016 ± 0.017	0.918 ± 0.012	0.045 ± 0.001
$c^2_{bkg}(\cos\theta_K)$	0.000 ± 0.018	0.985 ± 0.013	0.033 ± 0.000

[6.00, 8.00]	pull mean	pull width	sensitivity
S_{1s}	0.006 ± 0.018	0.992 ± 0.013	0.031 ± 0.000
S_3	0.010 ± 0.019	1.014 ± 0.014	0.051 ± 0.001
S_5	-0.037 ± 0.019	1.017 ± 0.014	0.059 ± 0.001
F_S	0.000 ± 0.001	0.056 ± 0.020	0.000 ± 0.000
S_{S1}	0.028 ± 0.019	1.044 ± 0.014	0.112 ± 0.001
S_{S3}	0.005 ± 0.018	0.974 ± 0.013	0.058 ± 0.001
$f_{\rm sig}$	-0.013 ± 0.018	0.963 ± 0.014	0.014 ± 0.000
m_{B^+}	-0.049 ± 0.018	0.973 ± 0.013	1.123 ± 0.014
$\lambda_{\rm m}$	0.011 ± 0.018	0.983 ± 0.013	0.000 ± 0.000
$c^2_{bkg}(\cos\theta_L)$	0.023 ± 0.018	0.974 ± 0.013	0.042 ± 0.001
$c^1_{bkg}(\cos\theta_K)$	-0.068 ± 0.016	0.709 ± 0.010	0.039 ± 0.001
$c^2_{bkg}(\cos\theta_K)$	-0.008 ± 0.018	0.951 ± 0.013	0.029 ± 0.000

[11.00, 12.50]	pull mean	pull width	sensitivity
S_{1s}	0.057 ± 0.020	1.065 ± 0.014	0.032 ± 0.000
S_3	-0.065 ± 0.019	1.002 ± 0.014	0.054 ± 0.001
S_5	0.006 ± 0.019	1.008 ± 0.013	0.054 ± 0.001
F_S	0.000 ± 0.001	0.056 ± 0.020	0.000 ± 0.000
S_{S1}	-0.028 ± 0.019	1.031 ± 0.014	0.098 ± 0.001
S_{S3}	-0.010 ± 0.019	1.019 ± 0.013	0.062 ± 0.001
$f_{\rm sig}$	-0.023 ± 0.019	0.989 ± 0.013	0.017 ± 0.000
m_{B^+}	-0.028 ± 0.019	0.998 ± 0.014	1.065 ± 0.014
$\lambda_{\rm m}$	-0.032 ± 0.018	0.980 ± 0.013	0.001 ± 0.000
$c^2_{bkg}(\cos\theta_L)$	0.033 ± 0.018	0.973 ± 0.014	0.056 ± 0.001
$c^1_{bkg}(\cos\theta_K)$	0.003 ± 0.019	0.992 ± 0.014	0.064 ± 0.001
$c^2_{bkg}(\cos\theta_K)$	0.000 ± 0.021	1.095 ± 0.015	0.052 ± 0.001

[15.00, 17.00]	pull mean	pull width	sensitivity
S_{1s}	0.030 ± 0.019	1.011 ± 0.013	0.030 ± 0.000
S_3	-0.025 ± 0.019	0.996 ± 0.014	0.057 ± 0.001
S_5	0.036 ± 0.019	1.012 ± 0.014	0.054 ± 0.001
F_S	0.000 ± 0.001	0.056 ± 0.020	0.000 ± 0.000
S_{S1}	0.020 ± 0.018	0.983 ± 0.013	0.093 ± 0.001
S_{S3}	-0.011 ± 0.019	1.010 ± 0.014	0.062 ± 0.001
$f_{\rm sig}$	0.015 ± 0.017	0.939 ± 0.013	0.019 ± 0.000
m_{B^+}	-0.001 ± 0.018	0.994 ± 0.014	1.265 ± 0.016
$\lambda_{\rm m}$	-0.003 ± 0.018	0.987 ± 0.013	0.000 ± 0.000
$c^2_{bkg}(\cos\theta_L)$	-0.025 ± 0.019	0.983 ± 0.014	0.085 ± 0.001
$c^1_{bkg}(\cos\theta_K)$	0.037 ± 0.019	1.013 ± 0.014	0.085 ± 0.001
$c^2_{bkg}(\cos\theta_K)$	0.012 ± 0.020	1.052 ± 0.014	0.073 ± 0.001

[17.00, 19.00]	pull mean	pull width	sensitivity
S_{1s}	0.033 ± 0.019	1.012 ± 0.014	0.042 ± 0.001
S_3	-0.056 ± 0.019	0.999 ± 0.013	0.083 ± 0.001
S_5	-0.011 ± 0.019	1.012 ± 0.015	0.076 ± 0.001
F_S	-0.000 ± 0.001	0.056 ± 0.020	0.000 ± 0.000
S_{S1}	0.024 ± 0.018	0.972 ± 0.014	0.125 ± 0.002
S_{S3}	-0.021 ± 0.018	0.990 ± 0.014	0.087 ± 0.001
$f_{\rm sig}$	-0.021 ± 0.018	0.960 ± 0.013	0.026 ± 0.000
m_{B^+}	-0.012 ± 0.018	0.969 ± 0.013	1.716 ± 0.022
$\lambda_{\rm m}$	0.027 ± 0.019	0.997 ± 0.014	0.000 ± 0.000
$c^2_{bkg}(\cos\theta_L)$	0.028 ± 0.018	0.981 ± 0.013	0.105 ± 0.001
$c^1_{bkg}(\cos\theta_K)$	0.003 ± 0.019	0.999 ± 0.014	0.107 ± 0.001
$c^2_{bkg}(\cos\theta_K)$	0.034 ± 0.020	1.074 ± 0.016	0.101 ± 0.001

Table 90: Results from the toy event studies with 10000 events. Angular folding 3 is used. All eight q^2 bins are shown.

[0.10, 0.98]	pull mean	pull width	sensitivity
S_{1s}	0.018 ± 0.019	1.033 ± 0.016	0.036 ± 0.000
S_3	0.010 ± 0.019	1.032 ± 0.014	0.058 ± 0.001
S_7	0.006 ± 0.019	1.002 ± 0.013	0.061 ± 0.001
F_S	-0.000 ± 0.001	0.056 ± 0.020	0.000 ± 0.000
S_{S1}	-0.013 ± 0.019	0.995 ± 0.013	0.097 ± 0.001
S_{S4}	0.008 ± 0.018	0.974 ± 0.013	0.068 ± 0.001
$f_{\rm sig}$	0.089 ± 0.018	0.961 ± 0.013	0.023 ± 0.000
m_{B^+}	0.009 ± 0.019	1.009 ± 0.014	1.166 ± 0.015
$\lambda_{\rm m}$	-0.022 ± 0.019	1.005 ± 0.014	0.000 ± 0.000
$c^2_{bkg}(\cos\theta_L)$	-0.055 ± 0.019	0.998 ± 0.015	0.067 ± 0.001
$c^1_{bkg}(\cos\theta_K)$	-0.010 ± 0.018	0.942 ± 0.014	0.092 ± 0.001
$c^2_{bkg}(\cos\theta_K)$	-0.077 ± 0.020	1.053 ± 0.015	0.079 ± 0.001

[1.10, 2.50]	pull mean	pull width	sensitivity
S_{1s}	-0.016 ± 0.018	0.970 ± 0.014	0.044 ± 0.001
S_3	0.012 ± 0.019	1.013 ± 0.014	0.061 ± 0.001
S_7	0.034 ± 0.019	1.014 ± 0.014	0.084 ± 0.001
F_S	0.002 ± 0.002	0.055 ± 0.019	0.000 ± 0.000
S_{S1}	-0.068 ± 0.020	1.012 ± 0.014	0.147 ± 0.002
S_{S4}	-0.043 ± 0.019	0.999 ± 0.014	0.076 ± 0.001
$f_{\rm sig}$	0.063 ± 0.017	0.895 ± 0.012	0.017 ± 0.000
m_{B^+}	0.013 ± 0.018	0.975 ± 0.013	1.564 ± 0.020
$\lambda_{\rm m}$	0.016 ± 0.018	0.989 ± 0.013	0.000 ± 0.000
$c^2_{bkg}(\cos\theta_L)$	-0.018 ± 0.019	0.990 ± 0.014	0.049 ± 0.001
$c^1_{bkg}(\cos\theta_K)$	0.017 ± 0.016	0.858 ± 0.012	0.058 ± 0.001
$c^2_{bkg}(\cos\theta_K)$	-0.019 ± 0.019	0.995 ± 0.014	0.042 ± 0.001

[2.50, 4.00]	pull mean	pull width	sensitivity
S_{1s}	-0.020 ± 0.017	0.922 ± 0.013	0.043 ± 0.001
S_3	0.013 ± 0.019	1.003 ± 0.015	0.063 ± 0.001
S_7	-0.032 ± 0.019	1.018 ± 0.014	0.090 ± 0.001
F_S	0.001 ± 0.001	0.055 ± 0.020	0.000 ± 0.000
S_{S1}	-0.037 ± 0.019	1.039 ± 0.015	0.157 ± 0.002
S_{S4}	0.011 ± 0.018	0.994 ± 0.014	0.078 ± 0.001
$f_{\rm sig}$	0.016 ± 0.016	0.862 ± 0.011	0.014 ± 0.000
m_{B^+}	-0.010 ± 0.019	0.996 ± 0.013	1.800 ± 0.023
$\lambda_{\rm m}$	0.006 ± 0.019	0.989 ± 0.013	0.000 ± 0.000
$c^2_{bkg}(\cos\theta_L)$	0.004 ± 0.018	0.952 ± 0.013	0.034 ± 0.000
$c^1_{bkg}(\cos\theta_K)$	-0.027 ± 0.017	0.940 ± 0.012	0.053 ± 0.001
$c^2_{bkg}(\cos\theta_K)$	-0.003 ± 0.018	0.975 ± 0.013	0.037 ± 0.000

[4.00, 6.00]	pull mean	pull width	sensitivity
S_{1s}	0.018 ± 0.018	0.950 ± 0.013	0.036 ± 0.000
S_3	0.012 ± 0.019	1.000 ± 0.014	0.057 ± 0.001
S_7	-0.022 ± 0.019	1.001 ± 0.014	0.074 ± 0.001
F_S	0.000 ± 0.001	0.056 ± 0.020	0.000 ± 0.000
S_{S1}	0.002 ± 0.020	1.054 ± 0.015	0.136 ± 0.002
S_{S4}	-0.005 ± 0.018	0.987 ± 0.014	0.070 ± 0.001
$f_{\rm sig}$	0.009 ± 0.018	0.962 ± 0.013	0.014 ± 0.000
m_{B^+}	0.037 ± 0.018	0.984 ± 0.014	1.451 ± 0.019
$\lambda_{\rm m}$	-0.002 ± 0.018	0.976 ± 0.013	0.000 ± 0.000
$c^2_{bkg}(\cos\theta_L)$	-0.023 ± 0.019	1.010 ± 0.014	0.041 ± 0.001
$c^1_{bkg}(\cos\theta_K)$	-0.020 ± 0.017	0.922 ± 0.013	0.045 ± 0.001
$c^2_{bkg}(\cos\theta_K)$	-0.033 ± 0.019	1.005 ± 0.014	0.034 ± 0.000

[6.00, 8.00]	pull mean	pull width	sensitivity
S_{1s}	0.020 ± 0.019	1.028 ± 0.014	0.033 ± 0.000
S_3	0.035 ± 0.019	1.000 ± 0.014	0.052 ± 0.001
S_7	-0.026 ± 0.018	0.993 ± 0.013	0.063 ± 0.001
F_S	-0.002 ± 0.002	0.055 ± 0.019	0.000 ± 0.000
S_{S1}	-0.009 ± 0.019	1.018 ± 0.013	0.115 ± 0.001
S_{S4}	-0.005 ± 0.019	1.010 ± 0.014	0.063 ± 0.001
$f_{\rm sig}$	-0.027 ± 0.018	0.958 ± 0.013	0.014 ± 0.000
m_{B^+}	0.001 ± 0.019	1.000 ± 0.015	1.154 ± 0.015
$\lambda_{\rm m}$	-0.014 ± 0.018	0.986 ± 0.013	0.000 ± 0.000
$c^2_{bkg}(\cos\theta_L)$	0.004 ± 0.018	0.982 ± 0.014	0.043 ± 0.001
$c^1_{bkg}(\cos\theta_K)$	-0.033 ± 0.016	0.783 ± 0.012	0.040 ± 0.001
$c^2_{bkg}(\cos\theta_K)$	0.002 ± 0.018	0.955 ± 0.013	0.029 ± 0.000

[11.00, 12.50]	pull mean	pull width	sensitivity
S_{1s}	0.088 ± 0.020	1.064 ± 0.014	0.033 ± 0.000
S_3	-0.008 ± 0.018	0.970 ± 0.012	0.054 ± 0.001
S_7	-0.002 ± 0.018	0.963 ± 0.014	0.059 ± 0.001
F_S	0.000 ± 0.001	0.056 ± 0.020	0.000 ± 0.000
S_{S1}	0.001 ± 0.019	1.007 ± 0.014	0.102 ± 0.001
S_{S4}	-0.041 ± 0.019	1.021 ± 0.014	0.069 ± 0.001
$f_{\rm sig}$	0.004 ± 0.018	0.994 ± 0.014	0.017 ± 0.000
m_{B^+}	-0.017 ± 0.019	1.017 ± 0.015	1.063 ± 0.014
$\lambda_{\rm m}$	0.009 ± 0.019	0.986 ± 0.013	0.001 ± 0.000
$c^2_{bkg}(\cos\theta_L)$	0.004 ± 0.018	0.964 ± 0.013	0.057 ± 0.001
$c^1_{bkg}(\cos\theta_K)$	0.027 ± 0.019	0.993 ± 0.014	0.064 ± 0.001
$c^2_{bkg}(\cos\theta_K)$	0.027 ± 0.021	1.101 ± 0.015	0.052 ± 0.001

[15.00, 17.00]	pull mean	pull width	sensitivity
S_{1s}	-0.005 ± 0.020	1.056 ± 0.014	0.032 ± 0.000
S_3	0.002 ± 0.018	0.978 ± 0.013	0.057 ± 0.001
S_7	-0.008 ± 0.019	1.001 ± 0.014	0.062 ± 0.001
F_S	0.001 ± 0.001	0.055 ± 0.020	0.000 ± 0.000
S_{S1}	-0.016 ± 0.019	0.993 ± 0.014	0.096 ± 0.001
S_{S4}	-0.021 ± 0.018	0.960 ± 0.013	0.072 ± 0.001
$f_{\rm sig}$	0.064 ± 0.019	1.016 ± 0.015	0.020 ± 0.000
m_{B^+}	-0.030 ± 0.019	1.004 ± 0.014	1.265 ± 0.016
$\lambda_{\rm m}$	-0.023 ± 0.018	0.948 ± 0.013	0.000 ± 0.000
$c^2_{bkg}(\cos\theta_L)$	0.019 ± 0.018	0.971 ± 0.013	0.084 ± 0.001
$c^1_{bkg}(\cos\theta_K)$	0.036 ± 0.018	0.982 ± 0.014	0.082 ± 0.001
$c^2_{bkg}(\cos\theta_K)$	-0.018 ± 0.021	1.096 ± 0.015	0.075 ± 0.001

[17.00, 19.00]	pull mean	pull width	sensitivity
S_{1s}	-0.016 ± 0.019	1.009 ± 0.013	0.043 ± 0.001
S_3	-0.007 ± 0.018	0.982 ± 0.014	0.080 ± 0.001
S_7	0.006 ± 0.019	1.024 ± 0.015	0.087 ± 0.001
F_S	0.002 ± 0.002	0.055 ± 0.019	0.000 ± 0.000
S_{S1}	0.022 ± 0.018	0.965 ± 0.013	0.125 ± 0.002
S_{S4}	0.013 ± 0.019	0.997 ± 0.014	0.103 ± 0.001
$f_{\rm sig}$	0.047 ± 0.019	1.014 ± 0.015	0.027 ± 0.000
m_{B^+}	0.011 ± 0.019	0.996 ± 0.014	1.768 ± 0.023
$\lambda_{\rm m}$	0.015 ± 0.018	0.988 ± 0.014	0.000 ± 0.000
$c^2_{bkg}(\cos\theta_L)$	0.017 ± 0.018	0.963 ± 0.013	0.102 ± 0.001
$c^1_{bkg}(\cos\theta_K)$	0.038 ± 0.019	0.995 ± 0.013	0.108 ± 0.001
$c^2_{bkg}(\cos\theta_K)$	-0.003 ± 0.020	1.054 ± 0.014	0.102 ± 0.001

Table 91: Results from the toy event studies with 10000 events. Angular folding 4 is used. All eight q^2 bins are shown.

[0.10, 0.98]	pull mean	pull width	sensitivity
S_{1s}	-0.011 ± 0.019	1.008 ± 0.013	0.035 ± 0.000
S_3	-0.010 ± 0.019	1.006 ± 0.014	0.057 ± 0.001
S_8	0.034 ± 0.018	0.987 ± 0.014	0.077 ± 0.001
F_S	-0.000 ± 0.001	0.056 ± 0.020	0.000 ± 0.000
S_{S4}	-0.005 ± 0.018	0.985 ± 0.014	0.067 ± 0.001
$f_{\rm sig}$	0.111 ± 0.018	0.942 ± 0.012	0.023 ± 0.000
m_{B^+}	0.036 ± 0.019	0.997 ± 0.014	1.172 ± 0.015
$\lambda_{\rm m}$	-0.013 ± 0.018	0.967 ± 0.013	0.000 ± 0.000
$c^2_{bkg}(\cos\theta_L)$	-0.085 ± 0.019	1.031 ± 0.015	0.069 ± 0.001
$c^2_{bkg}(\cos\theta_K)$	-0.092 ± 0.019	1.023 ± 0.013	0.082 ± 0.001

[1.10, 2.50]	pull mean	pull width	sensitivity
S_{1s}	-0.022 ± 0.018	0.985 ± 0.014	0.045 ± 0.001
S_3	-0.046 ± 0.019	1.007 ± 0.014	0.061 ± 0.001
S_8	0.004 ± 0.019	0.994 ± 0.013	0.104 ± 0.001
F_S	0.001 ± 0.001	0.055 ± 0.020	0.000 ± 0.000
S_{S4}	-0.001 ± 0.019	0.993 ± 0.015	0.074 ± 0.001
$f_{\rm sig}$	0.060 ± 0.017	0.909 ± 0.012	0.018 ± 0.000
m_{B^+}	0.009 ± 0.018	0.967 ± 0.013	1.618 ± 0.021
$\lambda_{\rm m}$	0.010 ± 0.018	0.978 ± 0.013	0.000 ± 0.000
$c^2_{bkg}(\cos\theta_L)$	-0.044 ± 0.018	0.949 ± 0.012	0.047 ± 0.001
$c^2_{bkg}(\cos\theta_K)$	-0.038 ± 0.018	0.959 ± 0.015	0.046 ± 0.001

[2.50, 4.00]	pull mean	pull width	sensitivity
S_{1s}	0.028 ± 0.017	0.933 ± 0.013	0.044 ± 0.001
S_3	-0.043 ± 0.019	1.001 ± 0.014	0.064 ± 0.001
S_8	-0.015 ± 0.018	0.971 ± 0.013	0.103 ± 0.001
F_S	0.003 ± 0.002	0.055 ± 0.019	0.000 ± 0.000
S_{S4}	0.017 ± 0.019	1.020 ± 0.014	0.081 ± 0.001
$f_{\rm sig}$	-0.005 ± 0.016	0.884 ± 0.012	0.015 ± 0.000
m_{B^+}	-0.055 ± 0.018	0.956 ± 0.013	1.765 ± 0.023
$\lambda_{\rm m}$	0.002 ± 0.018	0.983 ± 0.014	0.000 ± 0.000
$c^2_{bkg}(\cos\theta_L)$	-0.029 ± 0.018	0.956 ± 0.013	0.034 ± 0.000
$c^2_{bkg}(\cos\theta_K)$	-0.003 ± 0.018	0.976 ± 0.014	0.038 ± 0.000

[4.00, 6.00]	pull mean	pull width	sensitivity
S_{1s}	-0.020 ± 0.018	0.964 ± 0.013	0.037 ± 0.000
S_3	0.001 ± 0.019	1.012 ± 0.015	0.058 ± 0.001
S_8	-0.025 ± 0.018	0.987 ± 0.014	0.082 ± 0.001
F_S	0.001 ± 0.001	0.055 ± 0.020	0.000 ± 0.000
S_{S4}	0.009 ± 0.019	0.995 ± 0.014	0.069 ± 0.001
$f_{\rm sig}$	-0.003 ± 0.017	0.922 ± 0.013	0.014 ± 0.000
m_{B^+}	0.002 ± 0.019	1.003 ± 0.014	1.533 ± 0.020
$\lambda_{\rm m}$	-0.036 ± 0.018	0.993 ± 0.013	0.000 ± 0.000
$c^2_{bkg}(\cos\theta_L)$	0.018 ± 0.019	0.997 ± 0.014	0.040 ± 0.001
$c^2_{bkg}(\cos\theta_K)$	-0.021 ± 0.019	1.017 ± 0.015	0.036 ± 0.000

[6.00, 8.00]	pull mean	pull width	sensitivity
S_{1s}	-0.015 ± 0.019	0.999 ± 0.013	0.032 ± 0.000
S_3	-0.025 ± 0.018	0.986 ± 0.013	0.052 ± 0.001
S_8	0.000 ± 0.019	1.001 ± 0.013	0.069 ± 0.001
F_S	-0.000 ± 0.001	0.056 ± 0.020	0.000 ± 0.000
S_{S4}	0.008 ± 0.018	0.971 ± 0.013	0.062 ± 0.001
$f_{\rm sig}$	0.008 ± 0.018	0.945 ± 0.014	0.014 ± 0.000
m_{B^+}	0.028 ± 0.019	0.997 ± 0.014	1.197 ± 0.015
$\lambda_{\rm m}$	0.033 ± 0.018	0.970 ± 0.014	0.000 ± 0.000
$c^2_{bkg}(\cos\theta_L)$	0.025 ± 0.018	0.989 ± 0.013	0.043 ± 0.001
$c^2_{bkg}(\cos\theta_K)$	0.007 ± 0.018	0.950 ± 0.013	0.033 ± 0.000

[11.00, 12.50]	pull mean	pull width	sensitivity
S_{1s}	0.038 ± 0.020	1.062 ± 0.015	0.033 ± 0.000
S_3	-0.020 ± 0.018	0.987 ± 0.014	0.054 ± 0.001
S_8	-0.003 ± 0.018	0.980 ± 0.014	0.065 ± 0.001
F_S	-0.002 ± 0.002	0.055 ± 0.019	0.000 ± 0.000
S_{S4}	-0.003 ± 0.019	0.994 ± 0.013	0.068 ± 0.001
$f_{\rm sig}$	-0.017 ± 0.018	0.980 ± 0.013	0.017 ± 0.000
m_{B^+}	-0.035 ± 0.018	0.980 ± 0.013	1.076 ± 0.014
$\lambda_{\rm m}$	-0.008 ± 0.018	0.946 ± 0.013	0.001 ± 0.000
$c^2_{bkg}(\cos\theta_L)$	0.018 ± 0.018	0.957 ± 0.014	0.056 ± 0.001
$c^2_{bkg}(\cos\theta_K)$	-0.017 ± 0.020	1.061 ± 0.015	0.052 ± 0.001

[15.00, 17.00]	pull mean	pull width	sensitivity
S_{1s}	0.013 ± 0.020	1.055 ± 0.015	0.032 ± 0.000
S_3	-0.033 ± 0.018	0.974 ± 0.014	0.057 ± 0.001
S_8	-0.017 ± 0.019	1.002 ± 0.014	0.066 ± 0.001
F_S	0.000 ± 0.001	0.056 ± 0.020	0.000 ± 0.000
S_{S4}	-0.000 ± 0.018	0.995 ± 0.013	0.072 ± 0.001
$f_{\rm sig}$	0.010 ± 0.018	0.988 ± 0.014	0.020 ± 0.000
m_{B^+}	0.008 ± 0.018	0.988 ± 0.014	1.264 ± 0.016
$\lambda_{\rm m}$	-0.020 ± 0.018	0.953 ± 0.013	0.000 ± 0.000
$c^2_{bkg}(\cos\theta_L)$	-0.020 ± 0.018	0.958 ± 0.013	0.083 ± 0.001
$c^2_{bkg}(\cos\theta_K)$	-0.023 ± 0.020	1.087 ± 0.015	0.075 ± 0.001

[17.00, 19.00]	pull mean	pull width	sensitivity
S_{1s}	0.020 ± 0.019	0.995 ± 0.014	0.042 ± 0.001
S_3	-0.019 ± 0.019	0.982 ± 0.014	0.081 ± 0.001
S_8	0.048 ± 0.019	1.016 ± 0.014	0.093 ± 0.001
F_S	0.002 ± 0.002	0.055 ± 0.019	0.000 ± 0.000
S_{S4}	0.063 ± 0.019	1.023 ± 0.014	0.106 ± 0.001
$f_{\rm sig}$	-0.003 ± 0.018	0.978 ± 0.014	0.027 ± 0.000
m_{B^+}	0.016 ± 0.019	1.001 ± 0.013	1.784 ± 0.023
$\lambda_{\rm m}$	0.024 ± 0.018	0.962 ± 0.012	0.000 ± 0.000
$c^2_{bkg}(\cos\theta_L)$	-0.011 ± 0.018	0.972 ± 0.013	0.104 ± 0.001
$c^2_{bkg}(\cos\theta_K)$	0.023 ± 0.020	1.094 ± 0.015	0.104 ± 0.001

A.12.2 Estimated statistic toy study result tables

For each q^2 bin 3000 fits have been performed, using toy events equal to the estimations from Table 19. Table 92 shows biased parameters for all q^2 bins with a shifted mean position greater 0.1, 0.2 and even more. This result demonstrates the necessity to use angular folding (see Section 3.5). The following Tables 93 to 97 show unbiased results from the same event statistics.

Table 92: Results from the toy event studies with number of events equal to estimations in Table 19. No angular folding is used. All eight q^2 bins are shown.

[0.10, 0.98]	pull mean	pull width	sensitivity
S_{1s}	0.157 ± 0.022	1.167 ± 0.017	0.081 ± 0.001
S_3	-0.092 ± 0.021	1.106 ± 0.016	0.127 ± 0.002
S_4	0.165 ± 0.022	1.192 ± 0.016	0.201 ± 0.003
S_5	0.157 ± 0.023	1.204 ± 0.018	0.153 ± 0.002
S_{6s}	-0.063 ± 0.020	1.074 ± 0.016	0.165 ± 0.002
S_7	0.009 ± 0.021	1.130 ± 0.016	0.139 ± 0.002
S_8	-0.010 ± 0.021	1.136 ± 0.016	0.184 ± 0.002
S_9	0.015 ± 0.021	1.099 ± 0.016	0.125 ± 0.002
F_S	0.012 ± 0.007	0.052 ± 0.016	0.000 ± 0.000
S_{S1}	-0.131 ± 0.022	1.124 ± 0.017	0.219 ± 0.003
S_{S2}	0.070 ± 0.023	1.185 ± 0.018	0.221 ± 0.003
S_{S3}	0.075 ± 0.021	1.110 ± 0.016	0.156 ± 0.002
S_{S4}	0.051 ± 0.020	1.083 ± 0.015	0.150 ± 0.002
S_{S5}	0.006 ± 0.020	1.088 ± 0.015	0.202 ± 0.003
$f_{\rm sig}$	0.053 ± 0.018	0.938 ± 0.013	0.044 ± 0.001
m_{B^+}	-0.005 ± 0.019	1.039 ± 0.014	2.388 ± 0.031
$\lambda_{\rm m}$	-0.019 ± 0.019	0.999 ± 0.014	0.001 ± 0.000
$c^1_{bkg}(\cos\theta_L)$	0.003 ± 0.018	0.985 ± 0.013	0.190 ± 0.002
$c^2_{bkg}(\cos\theta_L)$	-0.126 ± 0.019	1.012 ± 0.014	0.139 ± 0.002
$c^1_{bkg}(\cos\theta_K)$	-0.092 ± 0.018	0.885 ± 0.011	0.183 ± 0.002
$c^2_{bkg}(\cos\theta_K)$	-0.046 ± 0.020	1.051 ± 0.015	0.156 ± 0.002

[1.10, 2.50]	pull mean	pull width	sensitivity
S_{1s}	-0.515 ± 0.025	1.215 ± 0.020	0.153 ± 0.002
S_3	0.028 ± 0.028	1.422 ± 0.022	0.242 ± 0.003
S_4	0.045 ± 0.025	1.252 ± 0.019	0.302 ± 0.004
S_5	0.143 ± 0.025	1.257 ± 0.018	0.241 ± 0.003
S_{6s}	-0.393 ± 0.026	1.246 ± 0.019	0.284 ± 0.004
S_7	0.003 ± 0.023	1.198 ± 0.018	0.232 ± 0.003
S_8	0.012 ± 0.025	1.267 ± 0.019	0.308 ± 0.004
S_9	0.018 ± 0.028	1.416 ± 0.022	0.246 ± 0.003
F_S	0.009 ± 0.006	0.053 ± 0.018	0.000 ± 0.000
S_{S1}	0.071 ± 0.022	1.096 ± 0.016	0.330 ± 0.004
S_{S2}	0.051 ± 0.027	1.335 ± 0.019	0.361 ± 0.005
S_{S3}	0.039 ± 0.027	1.370 ± 0.020	0.278 ± 0.004
S_{S4}	-0.036 ± 0.027	1.352 ± 0.021	0.281 ± 0.004
S_{S5}	-0.068 ± 0.026	1.287 ± 0.018	0.358 ± 0.005
$f_{\rm sig}$	0.005 ± 0.018	0.921 ± 0.014	0.036 ± 0.000
m_{B^+}	0.039 ± 0.021	1.067 ± 0.016	3.306 ± 0.045
$\lambda_{\rm m}$	-0.001 ± 0.019	0.968 ± 0.013	0.001 ± 0.000
$c^1_{bkg}(\cos\theta_L)$	0.131 ± 0.019	0.986 ± 0.014	0.140 ± 0.002
$c^2_{bkg}(\cos\theta_L)$	-0.052 ± 0.020	0.999 ± 0.015	0.096 ± 0.001
$c^1_{bkg}(\cos\theta_K)$	-0.120 ± 0.018	0.735 ± 0.012	0.115 ± 0.002
$c^2_{bkg}(\cos\theta_K)$	-0.094 ± 0.019	0.973 ± 0.014	0.086 ± 0.001

[2.50, 4.00]	pull mean	pull width	sensitivity
S_{1s}	-0.388 ± 0.021	1.095 ± 0.015	0.147 ± 0.002
S_3	-0.042 ± 0.026	1.318 ± 0.019	0.263 ± 0.004
S_4	-0.101 ± 0.023	1.179 ± 0.017	0.297 ± 0.004
S_5	-0.085 ± 0.023	1.160 ± 0.016	0.244 ± 0.003
S_{6s}	-0.101 ± 0.024	1.227 ± 0.017	0.252 ± 0.003
S_7	-0.028 ± 0.023	1.174 ± 0.017	0.245 ± 0.003
S_8	0.028 ± 0.023	1.185 ± 0.017	0.298 ± 0.004
S_9	0.025 ± 0.026	1.316 ± 0.018	0.261 ± 0.003
F_S	-0.006 ± 0.004	0.054 ± 0.019	0.000 ± 0.000
S_{S1}	0.074 ± 0.021	1.018 ± 0.016	0.351 ± 0.005
S_{S2}	0.083 ± 0.025	1.278 ± 0.018	0.348 ± 0.005
S_{S3}	-0.036 ± 0.026	1.315 ± 0.020	0.288 ± 0.004
S_{S4}	-0.085 ± 0.025	1.288 ± 0.020	0.290 ± 0.004
S_{S5}	-0.073 ± 0.025	1.238 ± 0.017	0.346 ± 0.005
$f_{\rm sig}$	-0.073 ± 0.018	0.918 ± 0.013	0.030 ± 0.000
m_{B^+}	0.078 ± 0.021	1.080 ± 0.015	3.723 ± 0.050
$\lambda_{\rm m}$	0.034 ± 0.019	0.974 ± 0.014	0.001 ± 0.000
$c^1_{bkg}(\cos\theta_L)$	-0.004 ± 0.019	0.992 ± 0.014	0.108 ± 0.001
$c^2_{bkg}(\cos\theta_L)$	0.034 ± 0.019	0.949 ± 0.014	0.067 ± 0.001
$c^1_{bkg}(\cos\theta_K)$	0.012 ± 0.018	0.957 ± 0.013	0.106 ± 0.001
$c^2_{bkg}(\cos\theta_K)$	-0.101 ± 0.019	0.980 ± 0.014	0.074 ± 0.001

[4.00, 6.00]	pull mean	pull width	sensitivity
S_{1s}	-0.127 ± 0.020	1.055 ± 0.015	0.087 ± 0.001
S_3	-0.093 ± 0.023	1.235 ± 0.017	0.169 ± 0.002
S_4	-0.179 ± 0.022	1.165 ± 0.017	0.200 ± 0.003
S_5	-0.192 ± 0.021	1.129 ± 0.016	0.175 ± 0.002
S_{6s}	0.040 ± 0.022	1.152 ± 0.017	0.145 ± 0.002
S_7	0.006 ± 0.021	1.105 ± 0.014	0.171 ± 0.002
S_8	0.043 ± 0.021	1.112 ± 0.016	0.191 ± 0.002
S_9	-0.007 ± 0.023	1.222 ± 0.017	0.169 ± 0.002
F_S	-0.003 ± 0.002	0.055 ± 0.019	0.000 ± 0.000
S_{S1}	0.032 ± 0.020	1.065 ± 0.015	0.275 ± 0.004
S_{S2}	0.035 ± 0.023	1.215 ± 0.017	0.226 ± 0.003
S_{S3}	-0.027 ± 0.022	1.187 ± 0.017	0.188 ± 0.002
S_{S4}	-0.005 ± 0.022	1.163 ± 0.017	0.187 ± 0.002
S_{S5}	-0.052 ± 0.022	1.183 ± 0.016	0.216 ± 0.003
$f_{\rm sig}$	-0.039 ± 0.018	0.936 ± 0.013	0.028 ± 0.000
m_{B^+}	-0.026 ± 0.019	1.018 ± 0.015	2.923 ± 0.038
$\lambda_{\rm m}$	0.024 ± 0.019	0.983 ± 0.014	0.000 ± 0.000
$c^1_{bkg}(\cos\theta_L)$	-0.001 ± 0.019	0.998 ± 0.014	0.101 ± 0.001
$c^2_{bkg}(\cos\theta_L)$	0.030 ± 0.019	1.021 ± 0.014	0.080 ± 0.001
$c^1_{bkg}(\cos\theta_K)$	0.010 ± 0.018	0.945 ± 0.013	0.090 ± 0.001
$c^2_{bkg}(\cos\theta_K)$	-0.048 ± 0.019	1.003 ± 0.014	0.067 ± 0.001

[6.00, 8.00]	pull mean	pull width	sensitivity
S_{1s}	-0.107 ± 0.022	1.129 ± 0.016	0.074 ± 0.001
S_3	-0.170 ± 0.022	1.185 ± 0.017	0.142 ± 0.002
S_4	-0.167 ± 0.023	1.200 ± 0.018	0.164 ± 0.002
S_5	-0.257 ± 0.022	1.150 ± 0.016	0.147 ± 0.002
S_{6s}	0.196 ± 0.022	1.154 ± 0.017	0.119 ± 0.002
S_7	0.002 ± 0.021	1.103 ± 0.015	0.141 ± 0.002
S_8	0.006 ± 0.021	1.108 ± 0.016	0.157 ± 0.002
S_9	0.008 ± 0.023	1.210 ± 0.017	0.143 ± 0.002
F_S	-0.003 ± 0.003	0.055 ± 0.019	0.000 ± 0.000
S_{S1}	-0.014 ± 0.020	1.084 ± 0.015	0.238 ± 0.003
S_{S2}	0.043 ± 0.024	1.257 ± 0.019	0.184 ± 0.002
S_{S3}	-0.049 ± 0.023	1.219 ± 0.018	0.160 ± 0.002
S_{S4}	0.063 ± 0.021	1.137 ± 0.015	0.153 ± 0.002
S_{S5}	-0.131 ± 0.022	1.148 ± 0.017	0.176 ± 0.002
$f_{\rm sig}$	-0.101 ± 0.018	0.989 ± 0.013	0.028 ± 0.000
m_{B^+}	-0.062 ± 0.019	1.014 ± 0.014	2.276 ± 0.029
$\lambda_{\rm m}$	-0.013 ± 0.019	0.997 ± 0.013	0.000 ± 0.000
$c^1_{bkg}(\cos\theta_L)$	-0.004 ± 0.019	1.015 ± 0.014	0.103 ± 0.001
$c^2_{bkg}(\cos\theta_L)$	0.057 ± 0.018	0.955 ± 0.012	0.082 ± 0.001
$c^1_{bkg}(\cos\theta_K)$	-0.258 ± 0.017	0.576 ± 0.011	0.072 ± 0.001
$c^2_{bkg}(\cos\theta_K)$	-0.028 ± 0.018	0.977 ± 0.013	0.058 ± 0.001

[11.00, 12.50]	pull mean	pull width	sensitivity
S_{1s}	-0.107 ± 0.024	1.269 ± 0.019	0.083 ± 0.001
S_3	-0.293 ± 0.026	1.326 ± 0.021	0.166 ± 0.002
S_4	-0.301 ± 0.028	1.424 ± 0.022	0.195 ± 0.003
S_5	-0.523 ± 0.025	1.274 ± 0.019	0.168 ± 0.002
S_{6s}	0.584 ± 0.027	1.334 ± 0.019	0.156 ± 0.002
S_7	0.031 ± 0.022	1.160 ± 0.017	0.153 ± 0.002
S_8	-0.015 ± 0.024	1.286 ± 0.020	0.187 ± 0.002
S_9	0.008 ± 0.025	1.336 ± 0.020	0.159 ± 0.002
F_S	0.003 ± 0.003	0.055 ± 0.019	0.000 ± 0.000
S_{S1}	-0.204 ± 0.022	1.152 ± 0.018	0.234 ± 0.003
S_{S2}	0.027 ± 0.027	1.427 ± 0.022	0.231 ± 0.003
S_{S3}	-0.222 ± 0.025	1.294 ± 0.020	0.185 ± 0.002
S_{S4}	0.077 ± 0.022	1.158 ± 0.017	0.169 ± 0.002
S_{S5}	-0.205 ± 0.026	1.319 ± 0.020	0.223 ± 0.003
$f_{\rm sig}$	-0.157 ± 0.019	1.002 ± 0.014	0.034 ± 0.000
m_{B^+}	0.026 ± 0.019	1.007 ± 0.014	2.099 ± 0.027
$\lambda_{\rm m}$	0.121 ± 0.019	0.975 ± 0.014	0.001 ± 0.000
$c^1_{bkg}(\cos\theta_L)$	-0.089 ± 0.019	1.003 ± 0.015	0.123 ± 0.002
$c^2_{bkg}(\cos\theta_L)$	0.027 ± 0.019	0.975 ± 0.014	0.113 ± 0.001
$c^1_{bkg}(\cos\theta_K)$	0.016 ± 0.019	1.001 ± 0.013	0.127 ± 0.002
$c^2_{bkg}(\cos\theta_K)$	-0.084 ± 0.021	1.108 ± 0.015	0.107 ± 0.001

[15.00, 17.00]	pull mean	pull width	sensitivity
S_{1s}	-0.041 ± 0.022	1.181 ± 0.017	0.073 ± 0.001
S_3	-0.293 ± 0.025	1.288 ± 0.020	0.156 ± 0.002
S_4	-0.287 ± 0.026	1.332 ± 0.019	0.180 ± 0.002
S_5	-0.276 ± 0.025	1.245 ± 0.018	0.153 ± 0.002
S_{6s}	0.428 ± 0.024	1.244 ± 0.018	0.143 ± 0.002
S_7	0.002 ± 0.020	1.092 ± 0.015	0.140 ± 0.002
S_8	-0.029 ± 0.023	1.213 ± 0.017	0.166 ± 0.002
S_9	-0.019 ± 0.023	1.236 ± 0.017	0.149 ± 0.002
F_S	0.005 ± 0.004	0.055 ± 0.018	0.000 ± 0.000
S_{S1}	-0.104 ± 0.022	1.158 ± 0.016	0.220 ± 0.003
S_{S2}	0.036 ± 0.026	1.386 ± 0.022	0.220 ± 0.003
S_{S3}	-0.073 ± 0.024	1.269 ± 0.020	0.174 ± 0.002
S_{S4}	0.033 ± 0.021	1.127 ± 0.016	0.168 ± 0.002
S_{S5}	-0.078 ± 0.023	1.227 ± 0.018	0.203 ± 0.003
$f_{\rm sig}$	-0.060 ± 0.019	1.011 ± 0.014	0.039 ± 0.001
m_{B^+}	0.038 ± 0.020	1.058 ± 0.015	2.588 ± 0.034
$\lambda_{\rm m}$	-0.021 ± 0.018	0.963 ± 0.013	0.001 ± 0.000
$c^1_{bkg}(\cos\theta_L)$	-0.090 ± 0.019	1.012 ± 0.015	0.160 ± 0.002
$c^2_{bkg}(\cos\theta_L)$	-0.010 ± 0.019	1.000 ± 0.014	0.167 ± 0.002
$c^1_{bkg}(\cos\theta_K)$	0.054 ± 0.019	1.015 ± 0.014	0.167 ± 0.002
$c^2_{bkg}(\cos\theta_K)$	-0.060 ± 0.021	1.116 ± 0.016	0.149 ± 0.002

[17.00, 19.00]	pull mean	pull width	sensitivity
S_{1s}	-0.107 ± 0.026	1.355 ± 0.022	0.138 ± 0.002
S_3	-0.407 ± 0.026	1.303 ± 0.018	0.302 ± 0.004
S_4	-0.275 ± 0.027	1.203 ± 0.018	0.324 ± 0.004
S_5	-0.215 ± 0.028	1.413 ± 0.022	0.296 ± 0.004
S_{6s}	0.514 ± 0.026	1.240 ± 0.018	0.239 ± 0.003
S_7	0.021 ± 0.025	1.298 ± 0.020	0.270 ± 0.004
S_8	0.003 ± 0.026	1.345 ± 0.020	0.316 ± 0.004
S_9	-0.020 ± 0.028	1.434 ± 0.022	0.293 ± 0.004
F_S	-0.009 ± 0.006	0.053 ± 0.017	0.000 ± 0.000
S_{S1}	-0.016 ± 0.023	1.124 ± 0.016	0.362 ± 0.005
S_{S2}	-0.057 ± 0.029	1.432 ± 0.021	0.404 ± 0.005
S_{S3}	-0.121 ± 0.030	1.488 ± 0.023	0.345 ± 0.005
S_{S4}	0.041 ± 0.024	1.263 ± 0.019	0.308 ± 0.004
S_{S5}	-0.047 ± 0.027	1.330 ± 0.019	0.380 ± 0.005
$f_{\rm sig}$	-0.118 ± 0.019	1.012 ± 0.015	0.053 ± 0.001
m_{B^+}	0.052 ± 0.021	1.081 ± 0.015	3.684 ± 0.049
$\lambda_{\rm m}$	0.017 ± 0.019	0.994 ± 0.014	0.001 ± 0.000
$c^1_{bkg}(\cos\theta_L)$	-0.083 ± 0.020	1.035 ± 0.014	0.200 ± 0.003
$c^2_{bkg}(\cos\theta_L)$	-0.027 ± 0.021	1.055 ± 0.016	0.234 ± 0.003
$c^1_{bkg}(\cos\theta_K)$	0.048 ± 0.020	1.026 ± 0.015	0.216 ± 0.003
$c^2_{bkg}(\cos\theta_K)$	-0.057 ± 0.022	1.112 ± 0.017	0.210 ± 0.003

Table 93: Results from the toy event studies with number of events equal to estimations in Table 19. Angular folding 0 is used. All eight q^2 bins are shown.

[0.10, 0.98]	pull mean	pull width	sensitivity
S_{1s}	0.031 ± 0.020	1.071 ± 0.016	0.072 ± 0.001
S_3	-0.010 ± 0.019	1.028 ± 0.015	0.111 ± 0.001
S_{6s}	-0.051 ± 0.019	1.022 ± 0.015	0.151 ± 0.002
S_9	-0.002 ± 0.019	1.011 ± 0.015	0.110 ± 0.001
F_S	0.005 ± 0.003	0.055 ± 0.019	0.000 ± 0.000
S_{S1}	-0.027 ± 0.019	1.028 ± 0.014	0.193 ± 0.003
$f_{\rm sig}$	0.067 ± 0.018	0.964 ± 0.014	0.044 ± 0.001
m_{B^+}	-0.022 ± 0.019	0.997 ± 0.014	2.270 ± 0.029
$\lambda_{\rm m}$	-0.002 ± 0.019	0.968 ± 0.013	0.001 ± 0.000
$c^1_{bkg}(\cos\theta_L)$	-0.009 ± 0.018	0.964 ± 0.013	0.184 ± 0.002
$c^2_{bkg}(\cos\theta_L)$	-0.076 ± 0.019	0.997 ± 0.013	0.137 ± 0.002
$c^1_{bkg}(\cos\theta_K)$	-0.053 ± 0.018	0.877 ± 0.012	0.185 ± 0.002
$c^2_{bkg}(\cos\theta_K)$	-0.022 ± 0.020	1.078 ± 0.015	0.159 ± 0.002

[1.10, 2.50]	pull mean	pull width	sensitivity
S_{1s}	-0.112 ± 0.020	1.053 ± 0.016	0.103 ± 0.001
S_3	0.037 ± 0.022	1.149 ± 0.018	0.154 ± 0.002
S_{6s}	-0.109 ± 0.021	1.114 ± 0.015	0.189 ± 0.002
S_9	0.010 ± 0.021	1.104 ± 0.015	0.155 ± 0.002
F_S	0.006 ± 0.004	0.054 ± 0.018	0.000 ± 0.000
S_{S1}	0.021 ± 0.020	1.048 ± 0.015	0.293 ± 0.004
$f_{\rm sig}$	0.065 ± 0.017	0.908 ± 0.012	0.035 ± 0.000
m_{B^+}	-0.014 ± 0.019	1.028 ± 0.014	3.162 ± 0.041
$\lambda_{\rm m}$	-0.009 ± 0.018	0.940 ± 0.013	0.001 ± 0.000
$c^1_{bkg}(\cos\theta_L)$	0.050 ± 0.019	1.017 ± 0.014	0.143 ± 0.002
$c^2_{bkg}(\cos\theta_L)$	-0.036 ± 0.019	1.009 ± 0.015	0.098 ± 0.001
$c^1_{bkg}(\cos\theta_K)$	-0.098 ± 0.019	0.757 ± 0.012	0.115 ± 0.001
$c^2_{bkg}(\cos\theta_K)$	-0.030 ± 0.018	0.941 ± 0.013	0.081 ± 0.001

[2.50, 4.00]	pull mean	pull width	sensitivity
S_{1s}	-0.039 ± 0.018	0.983 ± 0.014	0.100 ± 0.001
S_3	-0.041 ± 0.021	1.122 ± 0.016	0.170 ± 0.002
S_{6s}	-0.001 ± 0.019	1.040 ± 0.013	0.166 ± 0.002
S_9	0.036 ± 0.021	1.093 ± 0.016	0.168 ± 0.002
F_S	-0.001 ± 0.001	0.055 ± 0.020	0.000 ± 0.000
S_{S1}	0.058 ± 0.020	0.997 ± 0.015	0.312 ± 0.004
$f_{\rm sig}$	0.024 ± 0.017	0.904 ± 0.012	0.029 ± 0.000
m_{B^+}	0.018 ± 0.019	1.001 ± 0.013	3.480 ± 0.046
$\lambda_{\rm m}$	-0.043 ± 0.018	0.957 ± 0.014	0.001 ± 0.000
$c^1_{bkg}(\cos\theta_L)$	-0.023 ± 0.019	1.005 ± 0.015	0.110 ± 0.001
$c^2_{bkg}(\cos\theta_L)$	0.042 ± 0.019	0.959 ± 0.014	0.068 ± 0.001
$c^1_{bkg}(\cos\theta_K)$	-0.020 ± 0.018	0.948 ± 0.013	0.105 ± 0.001
$c^2_{bkg}(\cos\theta_K)$	0.005 ± 0.018	0.968 ± 0.013	0.071 ± 0.001

[4.00, 6.00]	pull mean	pull width	sensitivity
S_{1s}	-0.014 ± 0.018	0.988 ± 0.014	0.074 ± 0.001
S_3	-0.007 ± 0.020	1.060 ± 0.015	0.127 ± 0.002
S_{6s}	0.033 ± 0.019	1.030 ± 0.014	0.117 ± 0.002
S_9	-0.054 ± 0.020	1.087 ± 0.016	0.128 ± 0.002
F_S	-0.000 ± 0.001	0.056 ± 0.020	0.000 ± 0.000
S_{S1}	-0.020 ± 0.020	1.032 ± 0.015	0.266 ± 0.003
$f_{\rm sig}$	-0.007 ± 0.018	0.934 ± 0.013	0.027 ± 0.000
m_{B^+}	0.012 ± 0.019	0.997 ± 0.014	2.898 ± 0.038
$\lambda_{\rm m}$	0.001 ± 0.019	0.999 ± 0.014	0.000 ± 0.000
$c^1_{bkg}(\cos\theta_L)$	0.000 ± 0.019	1.017 ± 0.014	0.103 ± 0.001
$c^2_{bkg}(\cos\theta_L)$	0.037 ± 0.018	0.975 ± 0.013	0.078 ± 0.001
$c^1_{bkg}(\cos\theta_K)$	-0.010 ± 0.017	0.922 ± 0.013	0.088 ± 0.001
$c^2_{bkg}(\cos\theta_K)$	-0.027 ± 0.018	0.962 ± 0.013	0.065 ± 0.001

[6.00, 8.00]	pull mean	pull width	sensitivity
S_{1s}	0.011 ± 0.019	1.035 ± 0.015	0.065 ± 0.001
S_3	-0.010 ± 0.019	1.042 ± 0.016	0.108 ± 0.001
S_{6s}	0.047 ± 0.019	1.045 ± 0.015	0.101 ± 0.001
S_9	-0.006 ± 0.020	1.075 ± 0.015	0.110 ± 0.001
F_S	0.000 ± 0.001	0.056 ± 0.020	0.000 ± 0.000
S_{S1}	-0.022 ± 0.019	1.010 ± 0.014	0.223 ± 0.003
$f_{\rm sig}$	-0.015 ± 0.019	0.994 ± 0.015	0.028 ± 0.000
m_{B^+}	-0.029 ± 0.019	1.028 ± 0.014	2.312 ± 0.030
$\lambda_{\rm m}$	0.017 ± 0.018	0.973 ± 0.013	0.000 ± 0.000
$c^1_{bkg}(\cos\theta_L)$	-0.024 ± 0.019	0.998 ± 0.013	0.101 ± 0.001
$c^2_{bkg}(\cos\theta_L)$	0.073 ± 0.019	0.979 ± 0.014	0.084 ± 0.001
$c^1_{bkg}(\cos\theta_K)$	-0.251 ± 0.017	0.613 ± 0.013	0.073 ± 0.001
$c^2_{bkg}(\cos\theta_K)$	-0.017 ± 0.019	0.992 ± 0.013	0.060 ± 0.001

[11.00, 12.50]	pull mean	pull width	sensitivity
S_{1s}	0.022 ± 0.020	1.079 ± 0.015	0.065 ± 0.001
S_3	0.003 ± 0.020	1.059 ± 0.015	0.110 ± 0.001
S_{6s}	0.087 ± 0.022	1.125 ± 0.017	0.106 ± 0.001
S_9	0.031 ± 0.020	1.076 ± 0.016	0.110 ± 0.001
F_S	0.003 ± 0.002	0.055 ± 0.019	0.000 ± 0.000
S_{S1}	-0.003 ± 0.019	1.033 ± 0.014	0.196 ± 0.003
$f_{\rm sig}$	0.034 ± 0.018	0.969 ± 0.013	0.032 ± 0.000
m_{B^+}	-0.013 ± 0.018	0.989 ± 0.013	2.076 ± 0.027
$\lambda_{\rm m}$	-0.013 ± 0.019	0.971 ± 0.014	0.001 ± 0.000
$c^1_{bkg}(\cos\theta_L)$	0.003 ± 0.019	1.007 ± 0.014	0.122 ± 0.002
$c^2_{bkg}(\cos\theta_L)$	0.007 ± 0.019	0.981 ± 0.014	0.113 ± 0.001
$c^1_{bkg}(\cos\theta_K)$	-0.008 ± 0.019	0.993 ± 0.013	0.128 ± 0.002
$c^2_{bkg}(\cos\theta_K)$	-0.020 ± 0.020	1.082 ± 0.015	0.105 ± 0.001

[15.00, 17.00]	pull mean	pull width	sensitivity
S_{1s}	0.004 ± 0.020	1.050 ± 0.015	0.061 ± 0.001
S_3	-0.078 ± 0.019	1.017 ± 0.014	0.111 ± 0.001
S_{6s}	0.057 ± 0.020	1.057 ± 0.015	0.105 ± 0.001
S_9	0.005 ± 0.020	1.068 ± 0.015	0.115 ± 0.001
F_S	0.002 ± 0.002	0.055 ± 0.019	0.000 ± 0.000
S_{S1}	0.012 ± 0.019	0.999 ± 0.014	0.184 ± 0.002
$f_{\rm sig}$	0.038 ± 0.018	0.993 ± 0.013	0.039 ± 0.001
m_{B^+}	0.030 ± 0.018	0.970 ± 0.013	2.396 ± 0.031
$\lambda_{\rm m}$	-0.006 ± 0.019	0.991 ± 0.013	0.001 ± 0.000
$c^1_{bkg}(\cos\theta_L)$	0.039 ± 0.019	0.998 ± 0.013	0.162 ± 0.002
$c^2_{bkg}(\cos\theta_L)$	0.002 ± 0.019	0.990 ± 0.014	0.166 ± 0.002
$c^1_{bkg}(\cos\theta_K)$	0.012 ± 0.019	1.033 ± 0.014	0.169 ± 0.002
$c^2_{bkg}(\cos\theta_K)$	-0.034 ± 0.020	1.098 ± 0.016	0.150 ± 0.002

[17.00, 19.00]	pull mean	pull width	sensitivity
S_{1s}	0.026 ± 0.021	1.052 ± 0.014	0.091 ± 0.001
S_3	-0.078 ± 0.021	1.135 ± 0.018	0.195 ± 0.003
S_{6s}	0.104 ± 0.021	1.086 ± 0.016	0.171 ± 0.002
S_9	-0.034 ± 0.020	1.100 ± 0.016	0.183 ± 0.002
F_S	-0.002 ± 0.002	0.055 ± 0.020	0.000 ± 0.000
S_{S1}	0.009 ± 0.019	1.019 ± 0.014	0.264 ± 0.003
$f_{\rm sig}$	0.050 ± 0.019	1.004 ± 0.014	0.053 ± 0.001
m_{B^+}	0.002 ± 0.019	1.017 ± 0.014	3.475 ± 0.045
$\lambda_{\rm m}$	-0.018 ± 0.018	0.975 ± 0.013	0.001 ± 0.000
$c^1_{bkg}(\cos\theta_L)$	0.016 ± 0.020	1.047 ± 0.016	0.202 ± 0.003
$c^2_{bkg}(\cos\theta_L)$	0.023 ± 0.020	1.018 ± 0.014	0.226 ± 0.003
$c^1_{bkg}(\cos\theta_K)$	0.063 ± 0.019	1.042 ± 0.015	0.216 ± 0.003
$c^2_{bkg}(\cos\theta_K)$	-0.043 ± 0.020	1.091 ± 0.016	0.207 ± 0.003

Table 94: Results from the toy event studies with number of events equal to estimations in Table 19. Angular folding 1 is used. All eight q^2 bins are shown.

[0.10, 0.98]	pull mean	pull width	sensitivity
S_{1s}	0.019 ± 0.020	1.061 ± 0.016	0.072 ± 0.001
S_3	-0.006 ± 0.019	1.012 ± 0.014	0.111 ± 0.001
S_4	0.016 ± 0.020	1.048 ± 0.015	0.162 ± 0.002
F_S	0.004 ± 0.003	0.055 ± 0.019	0.000 ± 0.000
S_{S1}	-0.038 ± 0.019	1.006 ± 0.014	0.191 ± 0.002
S_{S2}	0.001 ± 0.019	0.998 ± 0.014	0.178 ± 0.002
$f_{\rm sig}$	0.076 ± 0.018	0.952 ± 0.013	0.044 ± 0.001
m_{B^+}	0.021 ± 0.019	1.015 ± 0.014	2.308 ± 0.030
$\lambda_{\rm m}$	-0.031 ± 0.018	0.958 ± 0.014	0.001 ± 0.000
$c^2_{bkg}(\cos\theta_L)$	-0.028 ± 0.018	0.972 ± 0.013	0.137 ± 0.002
$c^1_{bkg}(\cos\theta_K)$	-0.056 ± 0.018	0.881 ± 0.011	0.182 ± 0.002
$c^2_{bkg}(\cos\theta_K)$	-0.046 ± 0.021	1.075 ± 0.016	0.157 ± 0.002

[1.10, 2.50]	pull mean	pull width	sensitivity
S_{1s}	-0.007 ± 0.020	1.026 ± 0.016	0.093 ± 0.001
S_3	0.034 ± 0.020	1.041 ± 0.016	0.137 ± 0.002
S_4	-0.060 ± 0.020	1.075 ± 0.016	0.218 ± 0.003
F_S	0.004 ± 0.003	0.055 ± 0.019	0.000 ± 0.000
S_{S1}	0.044 ± 0.020	1.034 ± 0.015	0.292 ± 0.004
S_{S2}	-0.019 ± 0.020	1.033 ± 0.014	0.218 ± 0.003
$f_{\rm sig}$	0.098 ± 0.017	0.916 ± 0.013	0.035 ± 0.000
m_{B^+}	-0.004 ± 0.019	0.998 ± 0.014	3.133 ± 0.041
$\lambda_{\rm m}$	-0.049 ± 0.018	0.966 ± 0.014	0.001 ± 0.000
$c^2_{bkg}(\cos\theta_L)$	-0.030 ± 0.019	0.984 ± 0.013	0.096 ± 0.001
$c^1_{bkg}(\cos\theta_K)$	-0.079 ± 0.016	0.784 ± 0.012	0.112 ± 0.001
$c^2_{bkg}(\cos\theta_K)$	-0.011 ± 0.018	0.968 ± 0.014	0.082 ± 0.001

[2.50, 4.00]	pull mean	pull width	sensitivity
S_{1s}	-0.009 ± 0.019	0.987 ± 0.013	0.099 ± 0.001
S_3	-0.006 ± 0.021	1.105 ± 0.017	0.163 ± 0.002
S_4	-0.018 ± 0.019	1.018 ± 0.014	0.226 ± 0.003
F_S	-0.000 ± 0.001	0.056 ± 0.020	0.000 ± 0.000
S_{S1}	0.009 ± 0.020	1.061 ± 0.015	0.316 ± 0.004
S_{S2}	0.032 ± 0.020	1.068 ± 0.015	0.229 ± 0.003
$f_{\rm sig}$	0.063 ± 0.017	0.899 ± 0.012	0.029 ± 0.000
m_{B^+}	0.008 ± 0.019	1.008 ± 0.014	3.458 ± 0.045
$\lambda_{\rm m}$	-0.030 ± 0.019	0.976 ± 0.013	0.001 ± 0.000
$c^2_{bkg}(\cos\theta_L)$	0.025 ± 0.018	0.960 ± 0.014	0.069 ± 0.001
$c^1_{bkg}(\cos\theta_K)$	-0.024 ± 0.018	0.970 ± 0.013	0.108 ± 0.001
$c^2_{bkg}(\cos\theta_K)$	-0.005 ± 0.018	0.965 ± 0.014	0.072 ± 0.001

[4.00, 6.00]	pull mean	pull width	sensitivity
S_{1s}	0.008 ± 0.018	0.982 ± 0.014	0.075 ± 0.001
S_3	0.018 ± 0.020	1.053 ± 0.015	0.125 ± 0.002
S_4	-0.062 ± 0.019	1.016 ± 0.014	0.165 ± 0.002
F_S	0.000 ± 0.001	0.056 ± 0.020	0.000 ± 0.000
S_{S1}	0.017 ± 0.020	1.041 ± 0.016	0.264 ± 0.003
S_{S2}	0.019 ± 0.019	1.035 ± 0.015	0.170 ± 0.002
$f_{\rm sig}$	0.025 ± 0.018	0.963 ± 0.014	0.028 ± 0.000
m_{B^+}	0.015 ± 0.019	1.001 ± 0.013	2.854 ± 0.037
$\lambda_{\rm m}$	-0.016 ± 0.018	0.975 ± 0.014	0.000 ± 0.000
$c^2_{bkg}(\cos\theta_L)$	0.020 ± 0.019	0.996 ± 0.015	0.080 ± 0.001
$c^1_{bkg}(\cos\theta_K)$	-0.028 ± 0.017	0.927 ± 0.012	0.090 ± 0.001
$c^2_{bkg}(\cos\theta_K)$	-0.013 ± 0.019	1.008 ± 0.015	0.068 ± 0.001

[6.00, 8.00]	pull mean	pull width	sensitivity
S_{1s}	-0.003 ± 0.019	0.994 ± 0.014	0.063 ± 0.001
S_3	0.007 ± 0.018	0.988 ± 0.014	0.104 ± 0.001
S_4	-0.022 ± 0.020	1.058 ± 0.016	0.140 ± 0.002
F_S	0.000 ± 0.001	0.056 ± 0.020	0.000 ± 0.000
S_{S1}	-0.009 ± 0.020	1.035 ± 0.015	0.228 ± 0.003
S_{S2}	0.001 ± 0.020	1.065 ± 0.015	0.144 ± 0.002
$f_{\rm sig}$	-0.036 ± 0.018	0.971 ± 0.013	0.028 ± 0.000
m_{B^+}	0.016 ± 0.019	1.022 ± 0.014	2.292 ± 0.030
$\lambda_{\rm m}$	-0.027 ± 0.018	0.992 ± 0.013	0.000 ± 0.000
$c^2_{bkg}(\cos\theta_L)$	0.011 ± 0.018	0.970 ± 0.013	0.082 ± 0.001
$c^1_{bkg}(\cos\theta_K)$	-0.266 ± 0.018	0.570 ± 0.011	0.073 ± 0.001
$c^2_{bkg}(\cos\theta_K)$	0.018 ± 0.018	0.978 ± 0.013	0.059 ± 0.001

[11.00, 12.50]	pull mean	pull width	sensitivity
S_{1s}	0.096 ± 0.020	1.077 ± 0.016	0.065 ± 0.001
S_3	0.022 ± 0.019	0.997 ± 0.014	0.108 ± 0.001
S_4	-0.044 ± 0.020	1.058 ± 0.015	0.131 ± 0.002
F_S	0.001 ± 0.001	0.055 ± 0.020	0.000 ± 0.000
S_{S1}	-0.006 ± 0.020	1.025 ± 0.015	0.199 ± 0.003
S_{S2}	-0.012 ± 0.020	1.089 ± 0.015	0.150 ± 0.002
$f_{\rm sig}$	0.010 ± 0.019	1.000 ± 0.014	0.033 ± 0.000
m_{B^+}	-0.029 ± 0.018	0.977 ± 0.014	2.093 ± 0.027
$\lambda_{\rm m}$	-0.025 ± 0.019	0.985 ± 0.014	0.001 ± 0.000
$c^2_{bkg}(\cos\theta_L)$	-0.000 ± 0.019	1.014 ± 0.014	0.115 ± 0.001
$c^1_{bkg}(\cos\theta_K)$	-0.027 ± 0.018	0.982 ± 0.013	0.125 ± 0.002
$c^2_{bkg}(\cos\theta_K)$	-0.042 ± 0.020	1.070 ± 0.015	0.103 ± 0.001

[15.00, 17.00]	pull mean	pull width	sensitivity
S_{1s}	0.056 ± 0.019	1.051 ± 0.014	0.061 ± 0.001
S_3	0.019 ± 0.020	1.047 ± 0.015	0.117 ± 0.002
S_4	-0.099 ± 0.020	1.031 ± 0.015	0.129 ± 0.002
F_S	0.000 ± 0.001	0.056 ± 0.020	0.000 ± 0.000
S_{S1}	0.009 ± 0.019	1.030 ± 0.014	0.192 ± 0.002
S_{S2}	0.008 ± 0.020	1.048 ± 0.015	0.149 ± 0.002
$f_{\rm sig}$	0.060 ± 0.019	0.980 ± 0.014	0.039 ± 0.001
m_{B^+}	-0.015 ± 0.019	1.003 ± 0.014	2.495 ± 0.032
$\lambda_{\rm m}$	0.009 ± 0.019	0.995 ± 0.014	0.001 ± 0.000
$c^2_{bkg}(\cos\theta_L)$	-0.005 ± 0.019	0.996 ± 0.014	0.167 ± 0.002
$c^1_{bkg}(\cos\theta_K)$	0.005 ± 0.019	0.991 ± 0.014	0.164 ± 0.002
$c^2_{bkg}(\cos\theta_K)$	-0.033 ± 0.021	1.118 ± 0.016	0.152 ± 0.002

[17.00, 19.00]	pull mean	pull width	sensitivity
S_{1s}	0.054 ± 0.021	1.087 ± 0.016	0.089 ± 0.001
S_3	-0.113 ± 0.021	1.106 ± 0.017	0.185 ± 0.002
S_4	-0.067 ± 0.021	1.072 ± 0.015	0.202 ± 0.003
F_S	0.001 ± 0.001	0.055 ± 0.020	0.000 ± 0.000
S_{S1}	0.008 ± 0.019	1.019 ± 0.015	0.269 ± 0.003
S_{S2}	-0.015 ± 0.020	1.097 ± 0.016	0.236 ± 0.003
$f_{\rm sig}$	0.020 ± 0.019	0.997 ± 0.014	0.053 ± 0.001
m_{B^+}	-0.038 ± 0.019	1.016 ± 0.014	3.478 ± 0.045
$\lambda_{\rm m}$	-0.038 ± 0.018	0.970 ± 0.013	0.001 ± 0.000
$c^2_{bkg}(\cos\theta_L)$	0.024 ± 0.019	0.967 ± 0.015	0.205 ± 0.003
$c^1_{bkg}(\cos\theta_K)$	0.035 ± 0.020	1.025 ± 0.015	0.220 ± 0.003
$c^2_{bkg}(\cos\theta_K)$	-0.011 ± 0.021	1.100 ± 0.016	0.211 ± 0.003

Table 95: Results from the toy event studies with number of events equal to estimations in Table 19. Angular folding 2 is used. All eight q^2 bins are shown.

[0.10, 0.98]	pull mean	pull width	sensitivity
S_{1s}	0.064 ± 0.021	1.043 ± 0.015	0.073 ± 0.001
S_3	-0.013 ± 0.019	1.032 ± 0.015	0.115 ± 0.001
S_5	0.014 ± 0.019	1.039 ± 0.014	0.123 ± 0.002
F_S	0.005 ± 0.003	0.055 ± 0.019	0.000 ± 0.000
S_{S1}	-0.064 ± 0.020	1.045 ± 0.014	0.197 ± 0.003
S_{S3}	0.001 ± 0.019	1.004 ± 0.014	0.137 ± 0.002
$f_{\rm sig}$	0.076 ± 0.018	0.958 ± 0.013	0.045 ± 0.001
m_{B^+}	-0.033 ± 0.019	1.005 ± 0.014	2.276 ± 0.029
$\lambda_{\rm m}$	-0.041 ± 0.018	0.973 ± 0.013	0.001 ± 0.000
$c^2_{bkg}(\cos\theta_L)$	-0.047 ± 0.019	0.997 ± 0.014	0.136 ± 0.002
$c^1_{bkg}(\cos\theta_K)$	-0.066 ± 0.018	0.867 ± 0.012	0.186 ± 0.002
$c^2_{bkg}(\cos\theta_K)$	-0.051 ± 0.020	1.039 ± 0.014	0.158 ± 0.002

[1.10, 2.50]	pull mean	pull width	sensitivity
S_{1s}	-0.053 ± 0.020	1.014 ± 0.016	0.093 ± 0.001
S_3	-0.012 ± 0.020	1.073 ± 0.016	0.149 ± 0.002
S_5	-0.008 ± 0.020	1.043 ± 0.015	0.173 ± 0.002
F_S	0.002 ± 0.002	0.055 ± 0.020	0.000 ± 0.000
S_{S1}	0.032 ± 0.019	1.001 ± 0.013	0.285 ± 0.004
S_{S3}	-0.001 ± 0.020	1.070 ± 0.016	0.172 ± 0.002
$f_{\rm sig}$	0.057 ± 0.017	0.895 ± 0.013	0.034 ± 0.000
m_{B^+}	-0.007 ± 0.020	1.039 ± 0.015	3.171 ± 0.041
$\lambda_{\rm m}$	-0.042 ± 0.019	0.956 ± 0.014	0.001 ± 0.000
$c^2_{bkg}(\cos\theta_L)$	0.004 ± 0.019	0.985 ± 0.014	0.094 ± 0.001
$c^1_{bkg}(\cos\theta_K)$	-0.094 ± 0.017	0.739 ± 0.011	0.113 ± 0.001
$c^2_{bkg}(\cos\theta_K)$	-0.008 ± 0.019	0.970 ± 0.014	0.084 ± 0.001

[2.50, 4.00]	pull mean	pull width	sensitivity
S_{1s}	-0.031 ± 0.019	1.008 ± 0.015	0.099 ± 0.001
S_3	-0.028 ± 0.021	1.132 ± 0.016	0.171 ± 0.002
S_5	0.004 ± 0.019	1.017 ± 0.014	0.183 ± 0.002
F_S	-0.004 ± 0.003	0.055 ± 0.019	0.000 ± 0.000
S_{S1}	0.031 ± 0.020	0.999 ± 0.015	0.305 ± 0.004
S_{S3}	-0.014 ± 0.020	1.081 ± 0.015	0.189 ± 0.002
$f_{\rm sig}$	0.047 ± 0.017	0.888 ± 0.012	0.029 ± 0.000
m_{B^+}	-0.026 ± 0.019	1.024 ± 0.016	3.490 ± 0.046
$\lambda_{\rm m}$	-0.056 ± 0.018	0.970 ± 0.013	0.001 ± 0.000
$c^2_{bkg}(\cos\theta_L)$	0.066 ± 0.018	0.958 ± 0.013	0.068 ± 0.001
$c^1_{bkg}(\cos\theta_K)$	0.016 ± 0.018	0.957 ± 0.014	0.107 ± 0.001
$c^2_{bkg}(\cos\theta_K)$	-0.018 ± 0.018	0.965 ± 0.014	0.072 ± 0.001

[4.00, 6.00]	pull mean	pull width	sensitivity
S_{1s}	-0.016 ± 0.018	0.985 ± 0.014	0.074 ± 0.001
S_3	-0.061 ± 0.020	1.054 ± 0.015	0.128 ± 0.002
S_5	-0.018 ± 0.019	1.018 ± 0.013	0.147 ± 0.002
F_S	-0.001 ± 0.001	0.055 ± 0.020	0.000 ± 0.000
S_{S1}	0.034 ± 0.019	1.028 ± 0.015	0.259 ± 0.003
S_{S3}	-0.013 ± 0.020	1.044 ± 0.015	0.149 ± 0.002
$f_{\rm sig}$	0.011 ± 0.018	0.949 ± 0.013	0.028 ± 0.000
m_{B^+}	0.021 ± 0.019	1.009 ± 0.014	2.904 ± 0.038
$\lambda_{\rm m}$	0.007 ± 0.018	0.967 ± 0.013	0.000 ± 0.000
$c^2_{bkg}(\cos\theta_L)$	0.023 ± 0.019	1.015 ± 0.015	0.081 ± 0.001
$c^1_{bkg}(\cos\theta_K)$	0.012 ± 0.017	0.931 ± 0.013	0.090 ± 0.001
$c^2_{bkg}(\cos\theta_K)$	-0.020 ± 0.020	1.014 ± 0.013	0.069 ± 0.001

[6.00, 8.00]	pull mean	pull width	sensitivity
S_{1s}	0.039 ± 0.020	1.049 ± 0.015	0.064 ± 0.001
S_3	-0.078 ± 0.020	1.056 ± 0.015	0.111 ± 0.001
S_5	-0.056 ± 0.021	1.054 ± 0.016	0.124 ± 0.002
F_S	-0.003 ± 0.002	0.055 ± 0.019	0.000 ± 0.000
S_{S1}	-0.061 ± 0.020	1.063 ± 0.015	0.225 ± 0.003
S_{S3}	0.033 ± 0.019	1.042 ± 0.014	0.126 ± 0.002
$f_{\rm sig}$	-0.013 ± 0.018	0.971 ± 0.013	0.028 ± 0.000
m_{B^+}	0.006 ± 0.019	1.006 ± 0.014	2.253 ± 0.029
$\lambda_{\rm m}$	-0.017 ± 0.019	1.000 ± 0.014	0.000 ± 0.000
$c^2_{bkg}(\cos\theta_L)$	0.060 ± 0.019	0.992 ± 0.013	0.083 ± 0.001
$c^1_{bkg}(\cos\theta_K)$	-0.248 ± 0.017	0.675 ± 0.014	0.075 ± 0.001
$c^2_{bkg}(\cos\theta_K)$	0.001 ± 0.018	0.971 ± 0.013	0.058 ± 0.001

[11.00, 12.50]	pull mean	pull width	sensitivity
S_{1s}	0.073 ± 0.021	1.099 ± 0.016	0.066 ± 0.001
S_3	-0.117 ± 0.019	1.046 ± 0.015	0.118 ± 0.002
S_5	-0.183 ± 0.021	1.053 ± 0.015	0.120 ± 0.002
F_S	-0.002 ± 0.002	0.055 ± 0.019	0.000 ± 0.000
S_{S1}	-0.071 ± 0.020	1.048 ± 0.014	0.205 ± 0.003
S_{S3}	-0.076 ± 0.020	1.077 ± 0.015	0.134 ± 0.002
$f_{\rm sig}$	-0.011 ± 0.019	1.006 ± 0.014	0.033 ± 0.000
m_{B^+}	-0.011 ± 0.018	0.985 ± 0.013	2.092 ± 0.027
$\lambda_{\rm m}$	0.014 ± 0.018	0.957 ± 0.013	0.001 ± 0.000
$c^2_{bkg}(\cos\theta_L)$	0.052 ± 0.018	0.975 ± 0.013	0.113 ± 0.001
$c^1_{bkg}(\cos\theta_K)$	0.011 ± 0.018	0.975 ± 0.014	0.123 ± 0.002
$c^2_{bkg}(\cos\theta_K)$	-0.030 ± 0.020	1.062 ± 0.015	0.101 ± 0.001

[15.00, 17.00]	pull mean	pull width	sensitivity
S_{1s}	0.047 ± 0.020	1.090 ± 0.015	0.064 ± 0.001
S_3	-0.043 ± 0.020	1.050 ± 0.014	0.124 ± 0.002
S_5	-0.083 ± 0.021	1.105 ± 0.017	0.121 ± 0.002
F_S	-0.000 ± 0.001	0.056 ± 0.020	0.000 ± 0.000
S_{S1}	0.015 ± 0.019	1.039 ± 0.014	0.195 ± 0.003
S_{S3}	-0.026 ± 0.020	1.058 ± 0.014	0.133 ± 0.002
$f_{\rm sig}$	0.060 ± 0.019	1.010 ± 0.013	0.039 ± 0.001
m_{B^+}	0.009 ± 0.019	0.999 ± 0.013	2.462 ± 0.032
$\lambda_{\rm m}$	-0.037 ± 0.019	0.984 ± 0.014	0.001 ± 0.000
$c^2_{bkg}(\cos\theta_L)$	-0.011 ± 0.019	1.015 ± 0.015	0.168 ± 0.002
$c^1_{bkg}(\cos\theta_K)$	-0.016 ± 0.019	1.007 ± 0.014	0.167 ± 0.002
$c^2_{bkg}(\cos\theta_K)$	-0.000 ± 0.021	1.097 ± 0.015	0.148 ± 0.002

[17.00, 19.00]	pull mean	pull width	sensitivity
S_{1s}	0.060 ± 0.022	1.127 ± 0.017	0.092 ± 0.001
S_3	-0.157 ± 0.022	1.123 ± 0.016	0.205 ± 0.003
S_5	-0.115 ± 0.021	1.074 ± 0.015	0.181 ± 0.002
F_S	-0.004 ± 0.003	0.055 ± 0.019	0.000 ± 0.000
S_{S1}	-0.005 ± 0.020	1.023 ± 0.015	0.275 ± 0.004
S_{S3}	-0.032 ± 0.021	1.116 ± 0.017	0.212 ± 0.003
$f_{\rm sig}$	0.005 ± 0.019	0.992 ± 0.015	0.053 ± 0.001
m_{B^+}	0.004 ± 0.019	1.031 ± 0.014	3.543 ± 0.046
$\lambda_{\rm m}$	-0.026 ± 0.018	0.958 ± 0.014	0.001 ± 0.000
$c^2_{bkg}(\cos\theta_L)$	0.014 ± 0.019	0.985 ± 0.015	0.207 ± 0.003
$c^1_{bkg}(\cos\theta_K)$	0.082 ± 0.019	1.022 ± 0.015	0.216 ± 0.003
$c^2_{bkg}(\cos\theta_K)$	-0.010 ± 0.021	1.093 ± 0.016	0.210 ± 0.003

Table 96: Results from the toy event studies with number of events equal to estimations in Table 19. Angular folding 3 is used. All eight q^2 bins are shown.

[0.10, 0.98]	pull mean	pull width	sensitivity
S_{1s}	0.058 ± 0.019	1.029 ± 0.014	0.072 ± 0.001
S_3	0.025 ± 0.019	1.018 ± 0.014	0.111 ± 0.001
S_7	0.010 ± 0.018	0.988 ± 0.013	0.120 ± 0.002
F_S	0.005 ± 0.004	0.055 ± 0.019	0.000 ± 0.000
S_{S1}	-0.062 ± 0.019	1.007 ± 0.015	0.195 ± 0.003
S_{S4}	-0.014 ± 0.019	0.999 ± 0.014	0.134 ± 0.002
$f_{\rm sig}$	0.040 ± 0.018	0.943 ± 0.014	0.043 ± 0.001
m_{B^+}	-0.008 ± 0.018	0.980 ± 0.014	2.286 ± 0.030
$\lambda_{\rm m}$	0.006 ± 0.018	0.969 ± 0.013	0.001 ± 0.000
$c^2_{bkg}(\cos\theta_L)$	-0.064 ± 0.019	0.999 ± 0.013	0.136 ± 0.002
$c^1_{bkg}(\cos\theta_K)$	-0.111 ± 0.018	0.884 ± 0.012	0.187 ± 0.002
$c^2_{bkg}(\cos\theta_K)$	-0.057 ± 0.020	1.079 ± 0.015	0.160 ± 0.002

[1.10, 2.50]	pull mean	pull width	sensitivity
S_{1s}	-0.024 ± 0.019	1.029 ± 0.015	0.093 ± 0.001
S_3	0.038 ± 0.020	1.057 ± 0.015	0.152 ± 0.002
S_7	0.055 ± 0.019	1.026 ± 0.014	0.172 ± 0.002
F_S	0.002 ± 0.002	0.055 ± 0.019	0.000 ± 0.000
S_{S1}	-0.001 ± 0.020	1.031 ± 0.014	0.295 ± 0.004
S_{S4}	-0.039 ± 0.020	1.046 ± 0.015	0.175 ± 0.002
$f_{\rm sig}$	0.061 ± 0.017	0.921 ± 0.013	0.035 ± 0.000
m_{B^+}	0.000 ± 0.019	0.998 ± 0.014	3.055 ± 0.040
$\lambda_{\rm m}$	-0.060 ± 0.018	0.955 ± 0.014	0.001 ± 0.000
$c^2_{bkg}(\cos\theta_L)$	0.000 ± 0.019	1.004 ± 0.014	0.096 ± 0.001
$c^1_{bkg}(\cos\theta_K)$	-0.099 ± 0.017	0.748 ± 0.011	0.112 ± 0.001
$c^2_{bkg}(\cos\theta_K)$	-0.027 ± 0.018	0.968 ± 0.013	0.084 ± 0.001

[2.50, 4.00]	pull mean	pull width	sensitivity
S_{1s}	-0.052 ± 0.018	0.979 ± 0.013	0.096 ± 0.001
S_3	-0.002 ± 0.021	1.103 ± 0.016	0.170 ± 0.002
S_7	-0.006 ± 0.020	1.045 ± 0.015	0.188 ± 0.002
F_S	-0.003 ± 0.003	0.055 ± 0.019	0.000 ± 0.000
S_{S1}	-0.025 ± 0.020	1.008 ± 0.014	0.311 ± 0.004
S_{S4}	0.010 ± 0.020	1.047 ± 0.015	0.188 ± 0.002
$f_{\rm sig}$	0.025 ± 0.017	0.902 ± 0.013	0.029 ± 0.000
m_{B^+}	0.016 ± 0.019	1.021 ± 0.014	3.518 ± 0.046
$\lambda_{\rm m}$	-0.042 ± 0.018	0.942 ± 0.012	0.001 ± 0.000
$c^2_{bkg}(\cos\theta_L)$	0.023 ± 0.018	0.958 ± 0.014	0.067 ± 0.001
$c^1_{bkg}(\cos\theta_K)$	0.041 ± 0.018	0.960 ± 0.013	0.107 ± 0.001
$c^2_{bkg}(\cos\theta_K)$	-0.012 ± 0.018	0.971 ± 0.014	0.073 ± 0.001

[4.00, 6.00]	pull mean	pull width	sensitivity
S_{1s}	-0.032 ± 0.018	0.986 ± 0.014	0.075 ± 0.001
S_3	0.012 ± 0.020	1.057 ± 0.015	0.126 ± 0.002
S_7	-0.013 ± 0.019	0.989 ± 0.014	0.146 ± 0.002
F_S	-0.000 ± 0.001	0.056 ± 0.020	0.000 ± 0.000
S_{S1}	0.044 ± 0.019	1.008 ± 0.015	0.265 ± 0.003
S_{S4}	-0.013 ± 0.019	1.026 ± 0.015	0.150 ± 0.002
$f_{\rm sig}$	-0.001 ± 0.018	0.939 ± 0.012	0.028 ± 0.000
m_{B^+}	0.026 ± 0.018	0.982 ± 0.014	2.834 ± 0.037
$\lambda_{\rm m}$	-0.028 ± 0.019	0.999 ± 0.014	0.000 ± 0.000
$c^2_{bkg}(\cos\theta_L)$	0.085 ± 0.019	0.984 ± 0.013	0.079 ± 0.001
$c^1_{bkg}(\cos\theta_K)$	-0.012 ± 0.017	0.921 ± 0.013	0.089 ± 0.001
$c^2_{bkg}(\cos\theta_K)$	0.020 ± 0.019	1.016 ± 0.014	0.068 ± 0.001

[6.00, 8.00]	pull mean	pull width	sensitivity
S_{1s}	0.017 ± 0.019	1.029 ± 0.014	0.065 ± 0.001
S_3	-0.026 ± 0.019	1.019 ± 0.014	0.107 ± 0.001
S_7	-0.012 ± 0.019	0.999 ± 0.014	0.126 ± 0.002
F_S	-0.001 ± 0.001	0.055 ± 0.020	0.000 ± 0.000
S_{S1}	-0.017 ± 0.019	1.018 ± 0.014	0.221 ± 0.003
S_{S4}	0.011 ± 0.019	1.017 ± 0.014	0.126 ± 0.002
$f_{\rm sig}$	0.009 ± 0.018	0.962 ± 0.013	0.028 ± 0.000
m_{B^+}	-0.026 ± 0.018	0.994 ± 0.013	2.256 ± 0.029
$\lambda_{\rm m}$	0.028 ± 0.018	0.975 ± 0.014	0.000 ± 0.000
$c^2_{bkg}(\cos\theta_L)$	0.030 ± 0.019	1.001 ± 0.014	0.084 ± 0.001
$c^1_{bkg}(\cos\theta_K)$	-0.215 ± 0.018	0.529 ± 0.011	0.073 ± 0.001
$c^2_{bkg}(\cos\theta_K)$	-0.021 ± 0.018	0.962 ± 0.013	0.058 ± 0.001

[11.00, 12.50]	pull mean	pull width	sensitivity
S_{1s}	0.065 ± 0.019	1.035 ± 0.014	0.063 ± 0.001
S_3	0.010 ± 0.019	1.000 ± 0.015	0.109 ± 0.001
S_7	-0.010 ± 0.018	0.986 ± 0.013	0.122 ± 0.002
F_S	0.002 ± 0.002	0.055 ± 0.019	0.000 ± 0.000
S_{S1}	-0.048 ± 0.019	1.014 ± 0.014	0.200 ± 0.003
S_{S4}	0.027 ± 0.018	0.994 ± 0.014	0.134 ± 0.002
$f_{\rm sig}$	0.054 ± 0.018	0.975 ± 0.014	0.033 ± 0.000
m_{B^+}	-0.046 ± 0.018	0.984 ± 0.013	2.088 ± 0.027
$\lambda_{\rm m}$	-0.033 ± 0.019	0.993 ± 0.014	0.001 ± 0.000
$c^2_{bkg}(\cos\theta_L)$	0.035 ± 0.019	0.997 ± 0.014	0.113 ± 0.001
$c^1_{bkg}(\cos\theta_K)$	0.001 ± 0.018	0.987 ± 0.014	0.124 ± 0.002
$c^2_{bkg}(\cos\theta_K)$	0.004 ± 0.021	1.103 ± 0.015	0.106 ± 0.001

[15.00, 17.00]	pull mean	pull width	sensitivity
S_{1s}	0.063 ± 0.020	1.058 ± 0.015	0.062 ± 0.001
S_3	-0.018 ± 0.019	1.031 ± 0.015	0.118 ± 0.002
S_7	-0.016 ± 0.019	1.017 ± 0.014	0.123 ± 0.002
F_S	0.003 ± 0.002	0.055 ± 0.019	0.000 ± 0.000
S_{S1}	-0.032 ± 0.019	0.994 ± 0.015	0.188 ± 0.002
S_{S4}	0.009 ± 0.019	0.995 ± 0.014	0.142 ± 0.002
$f_{\rm sig}$	0.037 ± 0.019	0.991 ± 0.013	0.039 ± 0.001
m_{B^+}	0.005 ± 0.019	1.022 ± 0.015	2.510 ± 0.032
$\lambda_{\rm m}$	0.013 ± 0.018	0.956 ± 0.013	0.001 ± 0.000
$c^2_{bkg}(\cos\theta_L)$	0.025 ± 0.019	0.964 ± 0.013	0.167 ± 0.002
$c^1_{bkg}(\cos\theta_K)$	0.026 ± 0.019	1.024 ± 0.015	0.167 ± 0.002
$c^2_{bkg}(\cos\theta_K)$	0.032 ± 0.021	1.106 ± 0.016	0.149 ± 0.002

[17.00, 19.00]	pull mean	pull width	sensitivity
S_{1s}	0.096 ± 0.020	1.072 ± 0.014	0.091 ± 0.001
S_3	-0.030 ± 0.020	1.040 ± 0.014	0.180 ± 0.002
S_7	-0.042 ± 0.020	1.056 ± 0.015	0.180 ± 0.002
F_S	-0.000 ± 0.001	0.056 ± 0.020	0.000 ± 0.000
S_{S1}	0.019 ± 0.019	0.992 ± 0.013	0.267 ± 0.003
S_{S4}	-0.000 ± 0.019	1.004 ± 0.014	0.207 ± 0.003
$f_{\rm sig}$	0.001 ± 0.019	1.009 ± 0.014	0.053 ± 0.001
m_{B^+}	-0.012 ± 0.019	1.026 ± 0.014	3.500 ± 0.045
$\lambda_{\rm m}$	-0.026 ± 0.019	1.003 ± 0.014	0.001 ± 0.000
$c^2_{bkg}(\cos\theta_L)$	0.003 ± 0.019	0.979 ± 0.015	0.208 ± 0.003
$c^1_{bkg}(\cos\theta_K)$	0.046 ± 0.020	1.062 ± 0.015	0.222 ± 0.003
$c^2_{bkg}(\cos\theta_K)$	0.013 ± 0.021	1.084 ± 0.016	0.207 ± 0.003

Table 97: Results from the toy event studies with number of events equal to estimations in Table 19. Angular folding 4 is used. All eight q^2 bins are shown.

[0.10, 0.98]	pull mean	pull width	sensitivity
S_{1s}	0.022 ± 0.020	1.046 ± 0.014	0.071 ± 0.001
S_3	-0.052 ± 0.019	1.024 ± 0.014	0.111 ± 0.001
S_8	-0.003 ± 0.019	1.031 ± 0.014	0.157 ± 0.002
F_S	0.002 ± 0.002	0.055 ± 0.019	0.000 ± 0.000
S_{S4}	0.001 ± 0.019	1.011 ± 0.014	0.135 ± 0.002
$f_{\rm sig}$	0.058 ± 0.017	0.940 ± 0.013	0.044 ± 0.001
m_{B^+}	-0.005 ± 0.019	1.018 ± 0.014	2.373 ± 0.031
$\lambda_{\rm m}$	-0.000 ± 0.018	0.959 ± 0.013	0.001 ± 0.000
$c^2_{bkg}(\cos\theta_L)$	-0.060 ± 0.019	1.005 ± 0.014	0.137 ± 0.002
$c^2_{bkg}(\cos\theta_K)$	-0.028 ± 0.020	1.056 ± 0.015	0.165 ± 0.002

[1.10, 2.50]	pull mean	pull width	sensitivity
S_{1s}	-0.049 ± 0.019	1.037 ± 0.015	0.095 ± 0.001
S_3	-0.013 ± 0.020	1.057 ± 0.015	0.144 ± 0.002
S_8	0.005 ± 0.020	1.049 ± 0.015	0.220 ± 0.003
F_S	0.004 ± 0.003	0.055 ± 0.019	0.000 ± 0.000
S_{S4}	0.006 ± 0.020	1.067 ± 0.015	0.175 ± 0.002
$f_{\rm sig}$	0.054 ± 0.017	0.908 ± 0.012	0.035 ± 0.000
m_{B^+}	-0.030 ± 0.019	1.015 ± 0.014	3.236 ± 0.042
$\lambda_{\rm m}$	-0.038 ± 0.019	0.982 ± 0.013	0.001 ± 0.000
$c^2_{bkg}(\cos\theta_L)$	-0.017 ± 0.018	0.984 ± 0.014	0.097 ± 0.001
$c^2_{bkg}(\cos\theta_K)$	-0.028 ± 0.018	0.940 ± 0.013	0.089 ± 0.001

[2.50, 4.00]	pull mean	pull width	sensitivity
S_{1s}	-0.017 ± 0.018	0.981 ± 0.014	0.098 ± 0.001
S_3	0.014 ± 0.020	1.085 ± 0.015	0.166 ± 0.002
S_8	-0.009 ± 0.019	1.038 ± 0.015	0.222 ± 0.003
F_S	-0.002 ± 0.002	0.055 ± 0.019	0.000 ± 0.000
S_{S4}	-0.004 ± 0.020	1.078 ± 0.015	0.187 ± 0.002
$f_{\rm sig}$	0.028 ± 0.017	0.913 ± 0.012	0.030 ± 0.000
m_{B^+}	0.004 ± 0.020	1.047 ± 0.015	3.614 ± 0.047
$\lambda_{\rm m}$	0.021 ± 0.018	0.955 ± 0.013	0.001 ± 0.000
$c^2_{bkg}(\cos\theta_L)$	0.033 ± 0.018	0.960 ± 0.013	0.068 ± 0.001
$c^2_{bkg}(\cos\theta_K)$	-0.001 ± 0.018	0.981 ± 0.013	0.075 ± 0.001

[4.00, 6.00]	pull mean	pull width	sensitivity
S_{1s}	0.046 ± 0.018	0.995 ± 0.014	0.076 ± 0.001
S_3	0.014 ± 0.019	1.026 ± 0.015	0.124 ± 0.002
S_8	-0.017 ± 0.019	1.025 ± 0.015	0.167 ± 0.002
F_S	-0.000 ± 0.001	0.056 ± 0.020	0.000 ± 0.000
S_{S4}	0.005 ± 0.020	1.056 ± 0.015	0.150 ± 0.002
$f_{\rm sig}$	-0.013 ± 0.018	0.921 ± 0.013	0.028 ± 0.000
m_{B^+}	-0.005 ± 0.019	1.028 ± 0.014	3.055 ± 0.039
$\lambda_{\rm m}$	-0.011 ± 0.018	0.952 ± 0.014	0.000 ± 0.000
$c^2_{bkg}(\cos\theta_L)$	0.032 ± 0.019	1.004 ± 0.014	0.080 ± 0.001
$c^2_{bkg}(\cos\theta_K)$	-0.031 ± 0.019	1.013 ± 0.015	0.071 ± 0.001

[6.00, 8.00]	pull mean	pull width	sensitivity
S_{1s}	0.013 ± 0.019	1.028 ± 0.015	0.065 ± 0.001
S_3	-0.010 ± 0.019	1.010 ± 0.014	0.106 ± 0.001
S_8	0.009 ± 0.018	0.992 ± 0.013	0.136 ± 0.002
F_S	-0.003 ± 0.002	0.055 ± 0.019	0.000 ± 0.000
S_{S4}	-0.005 ± 0.018	0.986 ± 0.014	0.125 ± 0.002
$f_{\rm sig}$	-0.004 ± 0.018	0.973 ± 0.013	0.028 ± 0.000
m_{B^+}	-0.034 ± 0.019	1.018 ± 0.014	2.431 ± 0.031
$\lambda_{\rm m}$	0.051 ± 0.018	0.971 ± 0.012	0.000 ± 0.000
$c^2_{bkg}(\cos\theta_L)$	0.042 ± 0.018	0.980 ± 0.013	0.083 ± 0.001
$c^2_{bkg}(\cos\theta_K)$	0.021 ± 0.018	0.981 ± 0.013	0.067 ± 0.001

[11.00, 12.50]	pull mean	pull width	sensitivity
S_{1s}	0.051 ± 0.020	1.070 ± 0.014	0.066 ± 0.001
S_3	0.033 ± 0.019	1.027 ± 0.015	0.112 ± 0.001
S_8	0.011 ± 0.019	1.031 ± 0.015	0.132 ± 0.002
F_S	-0.002 ± 0.002	0.055 ± 0.020	0.000 ± 0.000
S_{S4}	-0.020 ± 0.019	1.032 ± 0.015	0.137 ± 0.002
$f_{\rm sig}$	0.033 ± 0.018	0.981 ± 0.013	0.033 ± 0.000
m_{B^+}	-0.019 ± 0.019	0.994 ± 0.013	2.103 ± 0.027
$\lambda_{\rm m}$	-0.021 ± 0.019	0.977 ± 0.014	0.001 ± 0.000
$c^2_{bkg}(\cos\theta_L)$	0.028 ± 0.019	0.994 ± 0.014	0.114 ± 0.001
$c^2_{bkg}(\cos\theta_K)$	-0.018 ± 0.020	1.087 ± 0.015	0.106 ± 0.001

[15.00, 17.00]	pull mean	pull width	sensitivity
S_{1s}	0.001 ± 0.020	1.079 ± 0.016	0.063 ± 0.001
S_3	-0.027 ± 0.019	0.999 ± 0.014	0.112 ± 0.001
S_8	-0.008 ± 0.020	1.044 ± 0.016	0.133 ± 0.002
F_S	0.001 ± 0.001	0.055 ± 0.020	0.000 ± 0.000
S_{S4}	0.018 ± 0.019	1.010 ± 0.015	0.143 ± 0.002
$f_{\rm sig}$	0.038 ± 0.019	1.000 ± 0.015	0.039 ± 0.001
m_{B^+}	0.021 ± 0.019	1.009 ± 0.014	2.455 ± 0.032
$\lambda_{\rm m}$	-0.012 ± 0.018	0.975 ± 0.014	0.001 ± 0.000
$c^2_{bkg}(\cos\theta_L)$	0.012 ± 0.019	0.999 ± 0.014	0.167 ± 0.002
$c^2_{bkg}(\cos\theta_K)$	-0.005 ± 0.020	1.088 ± 0.015	0.149 ± 0.002

[17.00, 19.00]	pull mean	pull width	sensitivity
S_{1s}	0.058 ± 0.021	1.067 ± 0.015	0.089 ± 0.001
S_3	-0.013 ± 0.019	1.031 ± 0.015	0.175 ± 0.002
S_8	0.017 ± 0.020	1.079 ± 0.016	0.196 ± 0.003
F_S	0.000 ± 0.001	0.056 ± 0.020	0.000 ± 0.000
S_{S4}	-0.001 ± 0.019	1.033 ± 0.014	0.216 ± 0.003
$f_{\rm sig}$	0.060 ± 0.019	0.995 ± 0.013	0.053 ± 0.001
m_{B^+}	0.006 ± 0.019	1.000 ± 0.014	3.464 ± 0.045
$\lambda_{\rm m}$	-0.019 ± 0.018	0.971 ± 0.013	0.001 ± 0.000
$c^2_{bkg}(\cos\theta_L)$	0.007 ± 0.019	0.966 ± 0.014	0.211 ± 0.003
$c^2_{bkg}(\cos\theta_K)$	0.038 ± 0.020	1.091 ± 0.016	0.205 ± 0.003

A.13 Toy study results in standard deviations from nominal values

In addition to the absolute differences from the nominal values 1(0) for the width(mean) of the pull distribution in toy event studies as shown in Section 4.4.2, this section shows the same tables as Figs. 48 to 50 but color coded by the number of standard deviations of which the resulting values of the pull distribution differ from the nominal values.
For this color code, the markers of the mean position (pull width) are indicated by full circles (filled squares). Similar to the absolute difference to the nominal value, as explained in Fig. 44, the following tables use the color coding as follows:

$$\begin{aligned} &\bullet < 1\sigma \\ &\bullet < 2\sigma \\ &\bullet < 3\sigma \\ &\bullet < 4\sigma \\ &\bullet > 4\sigma \end{aligned} \tag{47}$$

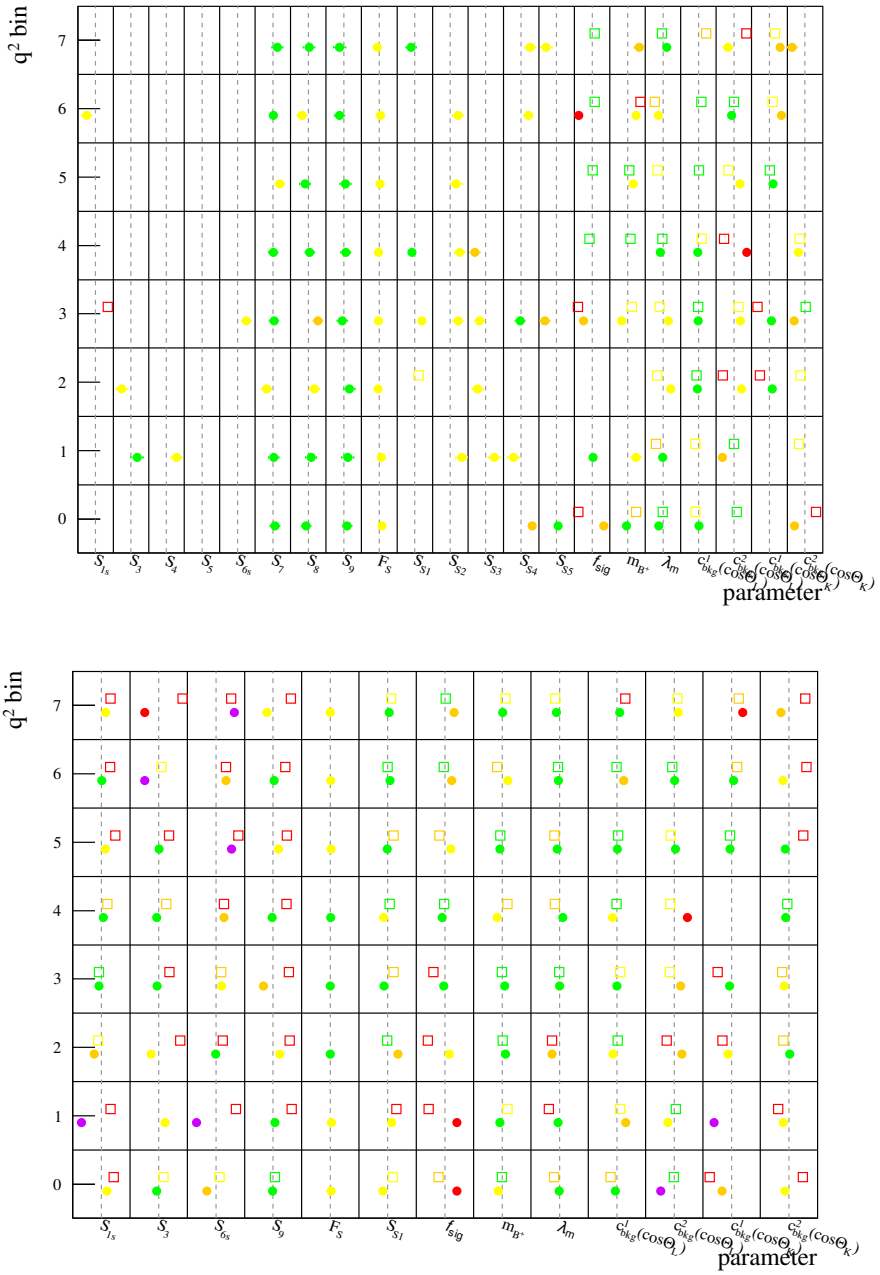

Figure 165: Toy event studies with no angular folding (top) and folding 0 (bottom) using 2597 (see Table 19) toy events per fit. The top plot clearly shows, that a full angular fit does not work on the expected number of signal events. Hence, angular folding is applied. The summary of the pull distributions for all free parameters in all q^2 bins. Each cell contains two markers, the hollow squares indicate the width of the pull distribution from toy studies, while the filled circles show the mean position of the pull distribution. The dashed line in each cell indicates the designated positions 0 (1) for the mean (width). See Eq. (47) for explanations on the color code.

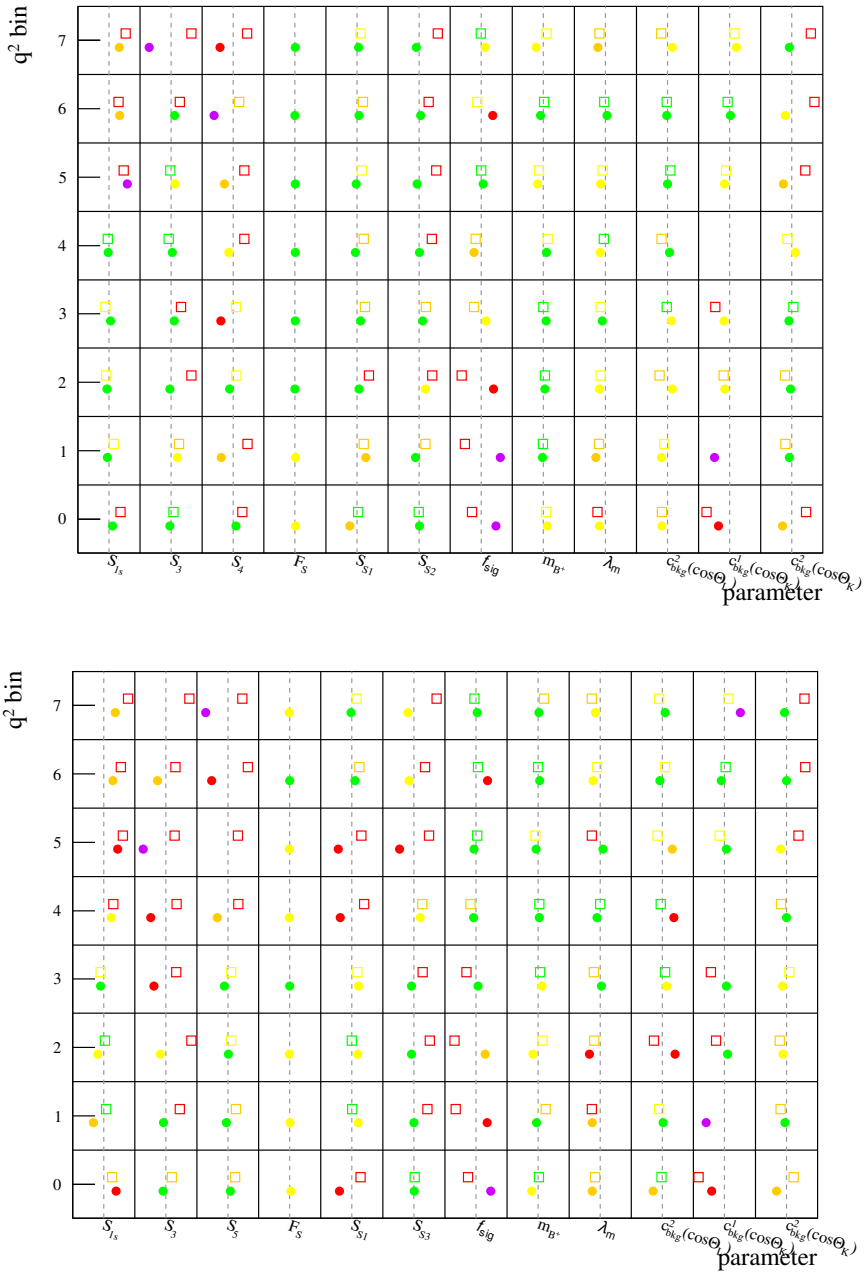

Figure 166: Toy event studies for angular folding 1 (top) and 2 (bottom) using 2597 (see Table 19) toy events per fit. Summary of the pull distributions for all free parameters in all q^2 bins. Each cell contains two markers, the hollow squares indicate the width of the pull distribution from toy studies, while the filled circles show the mean position of the pull distribution. The dashed line in each cell indicates the designated positions 0 (1) for the mean (width). See Eq. (47) for explanations on the color code.

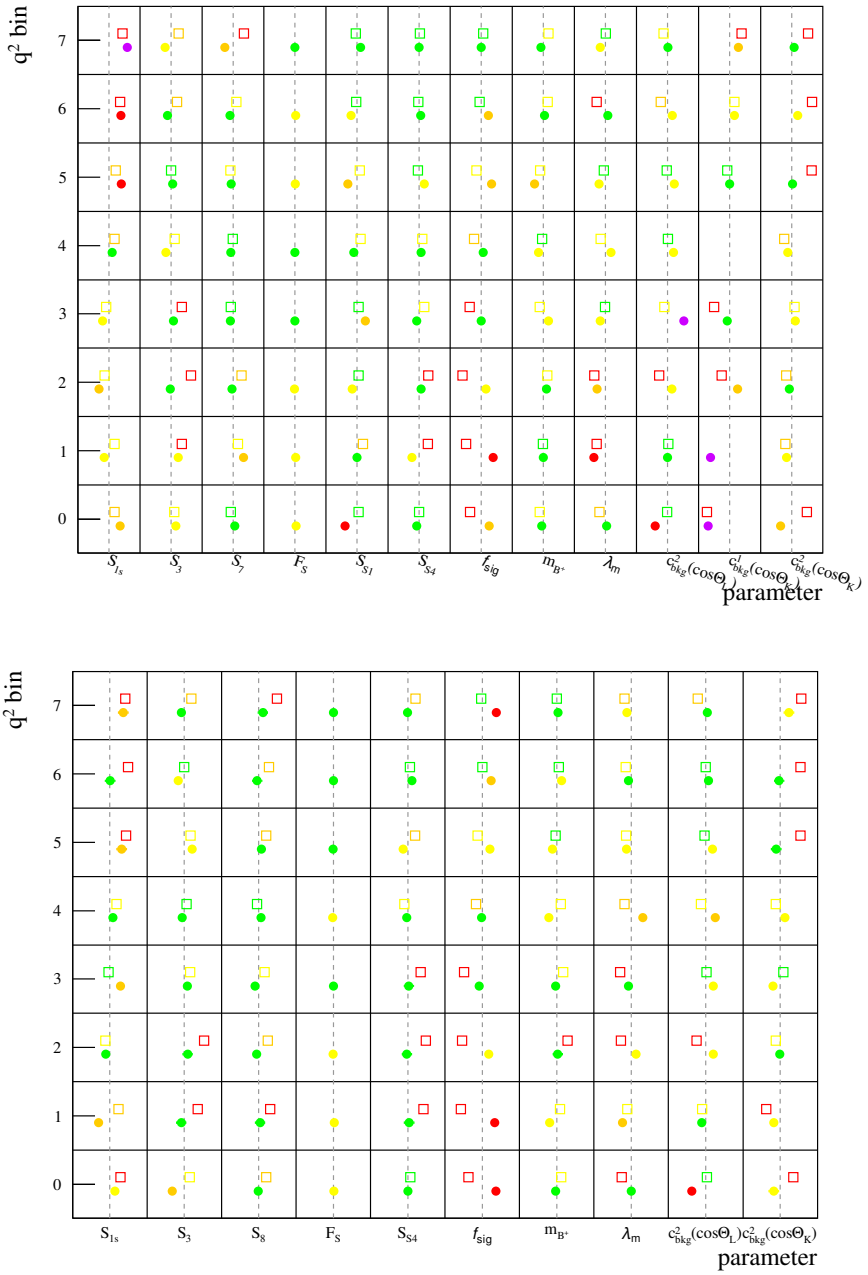

Figure 167: Toy event studies for angular folding 3 (top) and 4 (bottom) using 2597 (see Table 19) toy events per fit. Summary of the pull distributions for all free parameters in all q^2 bins. Each cell contains two markers, the hollow squares indicate the width of the pull distribution from toy studies, while the filled circles show the mean position of the pull distribution. The dashed line in each cell indicates the designated positions 0 (1) for the mean (width). See Eq. (47) for explanations on the color code.

A.14 Toy studies for P observables with fit configuration as in the final fit

Repeating the toy event studies from Section 4.4.6 for the angular observables of the P basis. The observed bias in the different start value scenarios is assigned as a systematic uncertainty in Table 140 in Appendix A.21. Due to the observed poor coverage - the widths of many pull distributions is not compatible with 1.0 - Feldman-Cousins scans are performed to determine the confidence level. The method is explained in Section 4.6.
In addition to the toy studies with the estimated signal and background event numbers, studies with toy samples of the size of 4000 events per q^2 bin are performed to validate the functionality of the fitter and the PDF determinations. The results of these additional tests are given in Tables 104 and 105, small biases in the mean positions of the pull distributions can be seen in Table 104, which is a result of the constraint on the S-wave fraction F_S: the line shape of the K^{*+} peak is q^2 dependent (see Eq. (33)) and taking the central value in a large q^2 bin does not fully compensate the different shapes generated using the finer q^2 binning. However, the resulting bias is negligible small compared to the precision achieved in the fits to data events, as it is shown in mean positions of the residuals from the fits to the large toy samples in Table 106.

Table 98: Mean values of the pull distributions from toy event studies with P basis observables using the SM values for the generation of toy events. The results are obtained using the 2D+4D fit method as described in Section 4.2 with angular folding. Values for F_L and P_1 are obtained from folding 4.

q^2 bin	0	1	2	3
F_L	0.1625 ± 0.0341	-0.0720 ± 0.0332	0.0987 ± 0.0314	-0.1835 ± 0.0296
P_1	-0.0627 ± 0.0325	-0.0232 ± 0.0326	0.1096 ± 0.0315	0.0423 ± 0.0320
P_2	-0.0520 ± 0.0319	0.5016 ± 0.0338	0.3270 ± 0.0327	-0.1432 ± 0.0333
P_3	0.0518 ± 0.0336	0.0780 ± 0.0312	0.0098 ± 0.0308	0.0202 ± 0.0316
P_4'	-0.0229 ± 0.0311	-0.0463 ± 0.0335	0.0742 ± 0.0320	0.0412 ± 0.0325
P_5'	0.0376 ± 0.0318	-0.0618 ± 0.0321	0.1377 ± 0.0315	0.1578 ± 0.0324
P_6'	-0.0337 ± 0.0350	0.0321 ± 0.0325	0.0126 ± 0.0324	-0.0012 ± 0.0334
P_8'	-0.0161 ± 0.0301	-0.0108 ± 0.0320	0.0341 ± 0.0320	0.0229 ± 0.0328
q^2 bin	4	5	6	7
F_L	-0.1470 ± 0.0299	-0.1551 ± 0.0325	-0.1557 ± 0.0347	-0.1135 ± 0.0340
P_1	0.0474 ± 0.0329	0.0777 ± 0.0317	0.0538 ± 0.0330	0.0465 ± 0.0324
P_2	-0.1980 ± 0.0330	-0.2170 ± 0.0323	-0.0804 ± 0.0337	0.0262 ± 0.0337
P_3	0.0018 ± 0.0315	0.0696 ± 0.0309	0.0071 ± 0.0317	0.0320 ± 0.0360
P_4'	-0.0036 ± 0.0340	0.0112 ± 0.0338	-0.0249 ± 0.0340	-0.0593 ± 0.0344
P_5'	0.0219 ± 0.0304	0.0937 ± 0.0322	-0.0097 ± 0.0328	-0.0329 ± 0.0345
P_6'	0.0183 ± 0.0341	0.0007 ± 0.0320	0.0455 ± 0.0317	-0.0044 ± 0.0345
P_8'	0.0172 ± 0.0316	0.0182 ± 0.0328	-0.0234 ± 0.0347	0.0238 ± 0.0348

Table 99: The widths of pull distribution from toy event studies with P basis observables using the SM values for the generation of toy events. The results are obtained using the 2D+4D fit method as described in Section 4.2 with angular folding. Values for F_L and P_1 are obtained from folding 4.

q^2 bin	0	1	2	3
F_L	0.9620 ± 0.0241	1.3813 ± 0.0235	1.5241 ± 0.0222	0.8703 ± 0.0210
P_1	0.9249 ± 0.0230	0.8071 ± 0.0230	0.7318 ± 0.0223	0.8030 ± 0.0226
P_2	1.0116 ± 0.0226	0.8739 ± 0.0239	0.7710 ± 0.0232	0.8293 ± 0.0236
P_3	0.9622 ± 0.0238	0.7514 ± 0.0221	0.7503 ± 0.0218	0.7431 ± 0.0224
P'_4	1.0623 ± 0.0220	0.9257 ± 0.0237	0.8866 ± 0.0226	0.9914 ± 0.0230
P'_5	0.9761 ± 0.0225	0.9255 ± 0.0227	0.8909 ± 0.0223	0.9351 ± 0.0229
P'_6	1.0301 ± 0.0248	0.8576 ± 0.0230	0.8502 ± 0.0229	0.8917 ± 0.0236
P'_8	1.0089 ± 0.0213	0.9407 ± 0.0227	0.9084 ± 0.0226	0.9190 ± 0.0232
q^2 bin	4	5	6	7
F_L	0.8786 ± 0.0211	1.1108 ± 0.0230	1.1644 ± 0.0246	1.1707 ± 0.0241
P_1	0.8703 ± 0.0233	0.9275 ± 0.0224	0.9581 ± 0.0233	0.9889 ± 0.0229
P_2	0.8935 ± 0.0233	0.8996 ± 0.0229	0.9770 ± 0.0238	1.0334 ± 0.0238
P_3	0.8684 ± 0.0223	0.9393 ± 0.0219	1.0163 ± 0.0224	1.0550 ± 0.0255
P'_4	1.0084 ± 0.0241	0.9475 ± 0.0239	1.0449 ± 0.0241	1.0333 ± 0.0243
P'_5	0.8885 ± 0.0215	0.9842 ± 0.0228	1.0249 ± 0.0232	1.0784 ± 0.0244
P'_6	0.9872 ± 0.0241	0.9776 ± 0.0227	0.9954 ± 0.0224	0.9925 ± 0.0244
P'_8	1.0031 ± 0.0223	0.9777 ± 0.0232	1.0505 ± 0.0245	1.0445 ± 0.0247

Table 100: Mean values of the pull distributions from toy event studies with P basis observables using theoretically predicted values for a new physics scenario of a Wilson coefficient $C_9 = -1$ for the generation of toy events. The results are obtained using the 2D+4D fit method as described in Section 4.2 with angular folding. Values for F_L and P_1 are obtained from folding 4.

q^2 bin	0	1	2	3
F_L	0.2292 ± 0.0316	0.0071 ± 0.0330	-0.1171 ± 0.0312	-0.2207 ± 0.0306
P_1	-0.0348 ± 0.0311	-0.0826 ± 0.0314	-0.0370 ± 0.0308	0.0613 ± 0.0325
P_2	-0.0367 ± 0.0350	0.4174 ± 0.0329	0.2934 ± 0.0338	-0.0447 ± 0.0323
P_3	-0.0239 ± 0.0326	0.0099 ± 0.0307	0.0125 ± 0.0308	-0.0060 ± 0.0306
P_4'	-0.0239 ± 0.0318	0.0405 ± 0.0341	-0.0218 ± 0.0339	-0.0053 ± 0.0328
P_5'	-0.0672 ± 0.0325	-0.0894 ± 0.0311	0.0850 ± 0.0313	0.0559 ± 0.0307
P_6'	0.0314 ± 0.0340	-0.0062 ± 0.0339	0.0132 ± 0.0330	0.0189 ± 0.0325
P_8'	-0.0151 ± 0.0308	0.0046 ± 0.0321	0.0305 ± 0.0321	-0.0272 ± 0.0317
q^2 bin	4	5	6	7
F_L	-0.1629 ± 0.0304	-0.1511 ± 0.0346	-0.0536 ± 0.0331	-0.0760 ± 0.0354
P_1	0.0661 ± 0.0319	0.0739 ± 0.0310	0.0809 ± 0.0310	0.1050 ± 0.0320
P_2	-0.0765 ± 0.0347	-0.1288 ± 0.0327	-0.0405 ± 0.0343	-0.0329 ± 0.0350
P_3	-0.0257 ± 0.0320	0.0046 ± 0.0316	0.0346 ± 0.0340	-0.0127 ± 0.0349
P_4'	-0.0852 ± 0.0323	-0.0066 ± 0.0347	0.0319 ± 0.0335	-0.0362 ± 0.0338
P_5'	0.0479 ± 0.0324	0.0853 ± 0.0322	0.0325 ± 0.0318	-0.0299 ± 0.0333
P_6'	-0.0115 ± 0.0322	0.0341 ± 0.0314	-0.0016 ± 0.0331	0.0461 ± 0.0340
P_8'	0.0212 ± 0.0324	-0.0179 ± 0.0308	-0.0098 ± 0.0329	0.0305 ± 0.0340

Table 101: The widths of pull distribution from toy event studies with P basis observables using theoretically predicted values for a new physics scenario of a Wilson coefficient $C_9 = -1$ for the generation of toy events. The results are obtained using the 2D+4D fit method as described in Section 4.2 with angular folding. Values for F_L and P_1 are obtained from folding 4.

q^2 bin	0	1	2	3
F_L	0.9282 ± 0.0224	1.1666 ± 0.0233	1.1965 ± 0.0221	0.9228 ± 0.0216
P_1	0.9704 ± 0.0220	0.8493 ± 0.0222	0.7970 ± 0.0218	0.7905 ± 0.0230
P_2	1.0635 ± 0.0247	0.8131 ± 0.0233	0.8053 ± 0.0239	0.8125 ± 0.0228
P_3	0.9620 ± 0.0230	0.7837 ± 0.0217	0.7123 ± 0.0218	0.8236 ± 0.0216
P_4'	1.0583 ± 0.0225	0.9246 ± 0.0241	0.9394 ± 0.0240	0.9803 ± 0.0232
P_5'	0.9561 ± 0.0230	0.9101 ± 0.0220	0.8298 ± 0.0221	0.9139 ± 0.0217
P_6'	1.0000 ± 0.0241	0.8658 ± 0.0240	0.9396 ± 0.0233	0.8905 ± 0.0230
P_8'	1.0238 ± 0.0218	0.9485 ± 0.0227	0.9212 ± 0.0227	0.9569 ± 0.0224
q^2 bin	4	5	6	7
F_L	0.9331 ± 0.0215	1.1690 ± 0.0245	1.2258 ± 0.0234	1.1575 ± 0.0250
P_1	0.8948 ± 0.0225	0.9116 ± 0.0219	0.9659 ± 0.0219	1.0019 ± 0.0226
P_2	0.9452 ± 0.0246	0.8675 ± 0.0232	0.9579 ± 0.0242	1.0269 ± 0.0248
P_3	0.8804 ± 0.0226	0.9272 ± 0.0224	1.0332 ± 0.0241	1.0275 ± 0.0247
P_4'	1.0479 ± 0.0229	0.9981 ± 0.0246	1.0254 ± 0.0237	1.1009 ± 0.0239
P_5'	0.9861 ± 0.0229	0.9796 ± 0.0227	1.0394 ± 0.0225	1.0255 ± 0.0236
P_6'	1.0055 ± 0.0228	0.9866 ± 0.0222	0.9986 ± 0.0234	1.0402 ± 0.0241
P_8'	1.0302 ± 0.0229	1.0255 ± 0.0218	0.9755 ± 0.0233	1.0195 ± 0.0241

Table 102: Mean values of the pull distributions from toy event studies with P basis observables using the final fit values for the generation of toy events. The results are obtained using the 2D+4D fit method as described in Section 4.2 with angular folding. Values for F_L and P_1 are obtained from folding 4.

q^2 bin	0	1	2	3
F_L	0.2410 ± 0.0332	-0.0157 ± 0.0340	0.2470 ± 0.0353	-0.2174 ± 0.0311
P_1	-0.0085 ± 0.0305	-0.4820 ± 0.0327	0.0518 ± 0.0306	0.4124 ± 0.0313
P_2	-0.0539 ± 0.0338	0.2047 ± 0.0324	-0.0090 ± 0.0335	0.1872 ± 0.0341
P_3	-0.0012 ± 0.0331	0.0514 ± 0.0295	0.1367 ± 0.0315	-0.2861 ± 0.0314
P_4'	-0.0705 ± 0.0315	-0.1306 ± 0.0328	-0.0351 ± 0.0321	0.0650 ± 0.0328
P_5'	0.0319 ± 0.0324	-0.0201 ± 0.0321	0.2433 ± 0.0312	-0.0045 ± 0.0309
P_6'	-0.0454 ± 0.0346	0.0208 ± 0.0347	0.0894 ± 0.0324	0.0143 ± 0.0324
P_8'	0.0253 ± 0.0329	0.0025 ± 0.0321	-0.0332 ± 0.0315	0.0094 ± 0.0326
q^2 bin	4	5	6	7
F_L	-0.1527 ± 0.0347	-0.2114 ± 0.0341	-0.0927 ± 0.0338	0.0093 ± 0.0362
P_1	0.1598 ± 0.0321	0.0825 ± 0.0311	0.1762 ± 0.0328	0.0736 ± 0.0321
P_2	0.0885 ± 0.0353	-0.7402 ± 0.0321	-0.1395 ± 0.0332	-0.0593 ± 0.0349
P_3	-0.1229 ± 0.0315	0.3029 ± 0.0300	0.0880 ± 0.0331	-0.0699 ± 0.0346
P_4'	-0.0960 ± 0.0323	-0.0286 ± 0.0411	-0.0281 ± 0.0352	0.0250 ± 0.0341
P_5'	-0.0181 ± 0.0322	0.1248 ± 0.0297	-0.0494 ± 0.0319	-0.0998 ± 0.0334
P_6'	0.0724 ± 0.0320	0.0210 ± 0.0315	0.0950 ± 0.0313	0.0349 ± 0.0340
P_8'	0.0047 ± 0.0326	-0.0417 ± 0.0350	0.0370 ± 0.0340	0.0016 ± 0.0347

Table 103: The widths of pull distribution from toy event studies with P basis observables using the final fit values for the generation of toy events. The results are obtained using the 2D+4D fit method as described in Section 4.2 with angular folding. Values for F_L and P_1 are obtained from folding 4.

q^2 bin	0	1	2	3
F_L	0.9665 ± 0.0235	1.0068 ± 0.0241	1.0494 ± 0.0249	0.9273 ± 0.0220
P_1	0.9303 ± 0.0215	0.9998 ± 0.0231	0.9342 ± 0.0216	0.8555 ± 0.0222
P_2	1.0260 ± 0.0239	0.9289 ± 0.0229	0.9542 ± 0.0237	0.8407 ± 0.0241
P_3	0.9364 ± 0.0234	0.8538 ± 0.0209	0.9041 ± 0.0223	0.8702 ± 0.0222
P_4'	1.0678 ± 0.0223	1.0352 ± 0.0232	1.0525 ± 0.0227	1.0475 ± 0.0232
P_5'	0.9979 ± 0.0229	0.9620 ± 0.0227	0.9832 ± 0.0221	0.9437 ± 0.0219
P_6'	1.0085 ± 0.0245	0.9746 ± 0.0245	0.9997 ± 0.0229	0.9191 ± 0.0229
P_8'	1.0778 ± 0.0233	1.0159 ± 0.0227	0.9206 ± 0.0223	0.9733 ± 0.0230
q^2 bin	4	5	6	7
F_L	1.2354 ± 0.0246	1.2946 ± 0.0241	1.0893 ± 0.0239	1.1041 ± 0.0257
P_1	0.9541 ± 0.0227	0.9502 ± 0.0220	0.9401 ± 0.0232	1.0202 ± 0.0227
P_2	0.9795 ± 0.0250	1.1776 ± 0.0227	1.0292 ± 0.0235	1.0003 ± 0.0247
P_3	0.9795 ± 0.0223	1.0194 ± 0.0212	1.0481 ± 0.0234	1.0056 ± 0.0245
P_4'	1.0483 ± 0.0228	1.0261 ± 0.0294	1.0357 ± 0.0249	1.0521 ± 0.0241
P_5'	1.0112 ± 0.0227	0.9934 ± 0.0210	1.0356 ± 0.0225	1.0382 ± 0.0236
P_6'	1.0057 ± 0.0227	1.0089 ± 0.0223	1.0265 ± 0.0222	1.0100 ± 0.0241
P_8'	1.0144 ± 0.0231	0.9945 ± 0.0248	1.0508 ± 0.0241	1.0353 ± 0.0246

Table 104: Mean values of the pull distributions from toy event studies with P basis observables using the SM values for the generation of toy events. Other than in the previous toy event studies, here 4000 events per q^2 bin are generated and fitted. The results are obtained using the 2D+4D fit method as described in Section 4.2 with angular folding. Values for F_L and P_1 are obtained from folding 4.

q^2 bin	0	1	2	3
F_L	0.1627 ± 0.0513	0.1146 ± 0.0513	-0.0455 ± 0.0438	-0.0729 ± 0.0371
P_1	-0.0104 ± 0.0521	0.0312 ± 0.0466	-0.0688 ± 0.0455	-0.0588 ± 0.0501
P_2	-0.1186 ± 0.0450	0.1800 ± 0.0486	0.1607 ± 0.0424	-0.1189 ± 0.0453
P_3	0.0070 ± 0.0464	0.0057 ± 0.0457	0.0732 ± 0.0430	0.0277 ± 0.0427
P_4'	-0.1508 ± 0.0469	-0.0883 ± 0.0441	0.0285 ± 0.0469	0.0173 ± 0.0472
P_5'	-0.0920 ± 0.0469	0.0517 ± 0.0477	0.1364 ± 0.0485	0.0836 ± 0.0468
P_6'	0.0032 ± 0.0490	0.0932 ± 0.0462	0.0119 ± 0.0472	-0.0009 ± 0.0471
P_8'	0.0630 ± 0.0504	0.0974 ± 0.0506	0.0455 ± 0.0497	0.0186 ± 0.0505
F_S	0.1988 ± 0.0504	0.1761 ± 0.0505	-0.0627 ± 0.0463	-0.0149 ± 0.0468
q^2 bin	4	5	6	7
F_L	-0.0655 ± 0.0445	-0.1098 ± 0.0520	0.0598 ± 0.0555	0.0874 ± 0.0520
P_1	0.0226 ± 0.0490	0.0992 ± 0.0483	0.1486 ± 0.0502	0.1687 ± 0.0516
P_2	-0.1568 ± 0.0419	-0.0837 ± 0.0399	-0.0938 ± 0.0439	-0.0953 ± 0.0439
P_3	-0.0064 ± 0.0452	0.0373 ± 0.0465	0.0388 ± 0.0451	0.0232 ± 0.0450
P_4'	0.0482 ± 0.0459	0.0838 ± 0.0447	0.0977 ± 0.0432	0.0858 ± 0.0466
P_5'	0.1097 ± 0.0481	0.0342 ± 0.0469	0.1037 ± 0.0511	0.0043 ± 0.0496
P_6'	0.0535 ± 0.0489	0.0408 ± 0.0502	0.0306 ± 0.0534	0.0527 ± 0.0467
P_8'	0.0020 ± 0.0532	0.0267 ± 0.0520	0.0488 ± 0.0509	-0.0590 ± 0.0497
F_S	-0.0181 ± 0.0484	-0.1464 ± 0.0527	-0.2973 ± 0.0488	-0.1788 ± 0.0477

Table 105: The widths of pull distribution from toy event studies with P basis observables using the SM values for the generation of toy events. Other than in the previous toy event studies, here 4000 events per q^2 bin are generated and fitted. The results are obtained using the 2D+4D fit method as described in Section 4.2 with angular folding. Values for F_L and P_1 are obtained from folding 4.

q^2 bin	0	1	2	3
F_L	1.0202 ± 0.0363	1.0211 ± 0.0363	0.8721 ± 0.0310	0.8388 ± 0.0262
P_1	1.0368 ± 0.0368	0.9268 ± 0.0329	0.9048 ± 0.0321	0.9970 ± 0.0354
P_2	0.9817 ± 0.0319	1.0600 ± 0.0344	0.9246 ± 0.0300	0.9877 ± 0.0320
P_3	1.0120 ± 0.0328	0.9951 ± 0.0323	0.9370 ± 0.0304	0.9305 ± 0.0302
P_4'	1.0232 ± 0.0332	0.9603 ± 0.0312	1.0225 ± 0.0332	1.0287 ± 0.0334
P_5'	0.9640 ± 0.0331	0.9809 ± 0.0337	0.9979 ± 0.0343	0.9629 ± 0.0331
P_6'	0.9756 ± 0.0346	0.9213 ± 0.0327	0.9412 ± 0.0334	0.9387 ± 0.0333
P_8'	1.0022 ± 0.0356	1.0067 ± 0.0358	0.9898 ± 0.0352	1.0042 ± 0.0357
F_S	1.0028 ± 0.0357	1.0042 ± 0.0357	0.9214 ± 0.0327	0.9321 ± 0.0331
q^2 bin	4	5	6	7
F_L	0.8864 ± 0.0315	1.0339 ± 0.0367	1.1034 ± 0.0392	1.0341 ± 0.0368
P_1	0.9761 ± 0.0347	0.9607 ± 0.0341	0.9999 ± 0.0355	1.0260 ± 0.0365
P_2	0.9129 ± 0.0296	0.8687 ± 0.0282	0.9573 ± 0.0311	0.9578 ± 0.0311
P_3	0.9861 ± 0.0320	1.0132 ± 0.0329	0.9829 ± 0.0319	0.9811 ± 0.0318
P_4'	1.0000 ± 0.0324	0.9750 ± 0.0316	0.9406 ± 0.0305	1.0150 ± 0.0329
P_5'	0.9892 ± 0.0340	0.9639 ± 0.0331	1.0516 ± 0.0362	1.0208 ± 0.0351
P_6'	0.9753 ± 0.0346	1.0004 ± 0.0355	1.0636 ± 0.0378	0.9303 ± 0.0330
P_8'	1.0581 ± 0.0376	1.0356 ± 0.0368	1.0136 ± 0.0360	0.9889 ± 0.0351
F_S	0.9632 ± 0.0342	1.0481 ± 0.0373	0.9711 ± 0.0346	0.9495 ± 0.0338

Table 106: Mean values of the residual distributions from toy event studies with P basis observables using the SM values for the generation of toy events. Other than in the previous toy event studies, here 4000 events per q^2 bin are generated and fitted. The results are obtained using the 2D+4D fit method as described in Section 4.2 with angular folding. Values for F_L and P_1 are obtained from folding 4. This table shows that the observed bias in the mean position observed in Table 104 results in a negligible small bias for all observables, as discussed in the text.

q^2 bin	0	1	2	3
F_L	0.0137 ± 0.0009	0.0080 ± 0.0017	-0.0040 ± 0.0020	-0.0040 ± 0.0014
P_1	-0.0007 ± 0.0035	0.0090 ± 0.0155	-0.0587 ± 0.0242	-0.0222 ± 0.0151
P_2	-0.0025 ± 0.0010	0.0016 ± 0.0048	-0.0017 ± 0.0061	-0.0045 ± 0.0032
P_3	0.0003 ± 0.0015	0.0012 ± 0.0072	0.0215 ± 0.0111	0.0027 ± 0.0063
P_4'	-0.0095 ± 0.0029	-0.0394 ± 0.0051	-0.0003 ± 0.0068	-0.0001 ± 0.0049
P_5'	-0.0045 ± 0.0024	0.0074 ± 0.0048	0.0206 ± 0.0066	0.0041 ± 0.0050
P_6'	0.0002 ± 0.0025	0.0092 ± 0.0047	0.0012 ± 0.0063	0.0001 ± 0.0047
P_8'	0.0039 ± 0.0031	0.0107 ± 0.0060	0.0060 ± 0.0075	0.0022 ± 0.0053
F_S	0.0082 ± 0.0005	0.0038 ± 0.0011	-0.0015 ± 0.0011	-0.0003 ± 0.0010
q^2 bin	4	5	6	7
F_L	-0.0043 ± 0.0013	-0.0018 ± 0.0011	0.0027 ± 0.0009	0.0032 ± 0.0009
P_1	0.0023 ± 0.0088	0.0097 ± 0.0052	0.0109 ± 0.0039	0.0278 ± 0.0040
P_2	-0.0049 ± 0.0018	-0.0042 ± 0.0010	-0.0046 ± 0.0007	-0.0068 ± 0.0008
P_3	-0.0003 ± 0.0040	0.0019 ± 0.0024	0.0013 ± 0.0016	0.0008 ± 0.0017
P_4'	0.0038 ± 0.0036	0.0053 ± 0.0028	0.0102 ± 0.0022	0.0204 ± 0.0025
P_5'	0.0147 ± 0.0037	0.0139 ± 0.0030	0.0143 ± 0.0025	0.0199 ± 0.0025
P_6'	0.0044 ± 0.0037	0.0027 ± 0.0032	0.0016 ± 0.0028	0.0029 ± 0.0026
P_8'	-0.0001 ± 0.0042	0.0016 ± 0.0035	0.0026 ± 0.0029	-0.0035 ± 0.0029
F_S	-0.0004 ± 0.0009	-0.0037 ± 0.0013	-0.0111 ± 0.0008	-0.0080 ± 0.0007

A.15 Toy studies in two larger bins fit configuration as in the final fit

The two larger bins (see Section 3.1) are evaluated in toy studies in the same way as the nominal binning scheme. Again, the biases observed for the toy studies with Standard Model values (as shown in Table 108 for S and P observables) are assigned to the systematic uncertainty due to the S-wave fraction, F_S. Biases in the fit with final fit results as start values (see Table 111) are assigned to the general bias systematic uncertainty. The systematic uncertainties are listed in Appendix A.22.

Table 107: Mean values of the pull distributions from toy event studies with S (left) and P (right) basis observables using the SM values for the generation of toy events in the two extra large q^2 bins of $[1.1-6.0]\,\mathrm{GeV}^2/c^2$ and $[15.0-19.0]\,\mathrm{GeV}^2/c^2$. The results are obtained using the 2D+4D fit method as described in Section 4.2 with angular folding. Values for S_{1s}, S_3, F_L and P_1 are obtained from folding 4.

q^2 bin	[1.1-6.0]	[15.0-19.0]
S_{1s}	0.0944 ± 0.0288	0.0083 ± 0.0329
S_3	-0.0119 ± 0.0321	0.0947 ± 0.0319
S_4	-0.0813 ± 0.0315	-0.0838 ± 0.0326
S_5	0.1105 ± 0.0313	0.2415 ± 0.0315
S_{6s}	0.0428 ± 0.0311	0.1014 ± 0.0322
S_7	-0.0269 ± 0.0318	-0.0846 ± 0.0321
S_8	0.0550 ± 0.0325	-0.0400 ± 0.0314
S_9	0.0235 ± 0.0308	-0.0247 ± 0.0306
q^2 bin	[1.1-6.0]	[15.0-19.0]
F_L	-0.1430 ± 0.0288	-0.0732 ± 0.0329
P_1	0.0583 ± 0.0321	0.1096 ± 0.0319
P_2	-0.0364 ± 0.0315	0.0880 ± 0.0326
P_3	0.0102 ± 0.0313	0.0036 ± 0.0315
P_4'	-0.1642 ± 0.0311	-0.0775 ± 0.0322
P_5'	0.0261 ± 0.0318	0.1471 ± 0.0321
P_6'	0.0164 ± 0.0325	-0.0844 ± 0.0314
P_8'	0.0078 ± 0.0308	-0.0261 ± 0.0306

Table 108: The widths of the pull distributions from toy event studies with S (left) and P (right) basis observables using the SM values for the generation of toy events in the two extra large q^2 bins of $[1.1-6.0]\,\mathrm{GeV}^2/c^2$ and $[15.0-19.0]\,\mathrm{GeV}^2/c^2$. The results are obtained using the 2D+4D fit method as described in Section 4.2 with angular folding. Values for S_{1s}, S_3, F_L and P_1 are obtained from folding 4.

q^2 bin	[1.1-6.0]	[15.0-19.0]
S_{1s}	0.9110 ± 0.0204	1.0408 ± 0.0233
S_3	1.0137 ± 0.0227	1.0093 ± 0.0226
S_4	0.9957 ± 0.0223	1.0299 ± 0.0230
S_5	0.9898 ± 0.0221	0.9950 ± 0.0223
S_{6s}	0.9831 ± 0.0220	1.0194 ± 0.0228
S_7	1.0048 ± 0.0225	1.0152 ± 0.0227
S_8	1.0263 ± 0.0230	0.9923 ± 0.0222
S_9	0.9736 ± 0.0218	0.9670 ± 0.0216
q^2 bin	[1.1-6.0]	[15.0-19.0]
F_L	0.8698 ± 0.0204	1.1244 ± 0.0233
P_1	0.8999 ± 0.0227	1.0030 ± 0.0226
P_2	0.9060 ± 0.0223	0.9655 ± 0.0230
P_3	0.8263 ± 0.0221	0.9908 ± 0.0223
P_4'	0.9698 ± 0.0220	1.0749 ± 0.0228
P_5'	0.9512 ± 0.0225	1.0219 ± 0.0227
P_6'	0.9441 ± 0.0230	0.9768 ± 0.0222
P_8'	0.9670 ± 0.0218	1.0479 ± 0.0216

Table 109: Mean values of the pull distributions from toy event studies with S (left) and P (right) basis observables using theoretically predicted values for a new physics scenario of a Wilson coefficient $C_9 = -1$ for the generation of toy events in the two extra large q^2 bins of $[1.1 - 6.0]\,\mathrm{GeV}^2/c^2$ and $[15.0 - 19.0]\,\mathrm{GeV}^2/c^2$. The results are obtained using the 2D+4D fit method as described in Section 4.2 with angular folding. Values for S_{1s}, S_3, F_L and P_1 are obtained from folding 4.

q^2 bin	[1.1-6.0]	[15.0-19.0]
S_{1s}	0.1122 ± 0.0291	-0.0453 ± 0.0327
S_3	0.0095 ± 0.0311	0.1036 ± 0.0316
S_4	-0.0861 ± 0.0307	-0.0588 ± 0.0351
S_5	0.0813 ± 0.0322	0.1714 ± 0.0318
S_{6s}	0.0055 ± 0.0323	0.1535 ± 0.0316
S_7	-0.0047 ± 0.0325	-0.0519 ± 0.0317
S_8	-0.0087 ± 0.0318	-0.0050 ± 0.0324
S_9	-0.0290 ± 0.0315	0.0468 ± 0.0324
q^2 bin	[1.1-6.0]	[15.0-19.0]
F_L	-0.1721 ± 0.0269	-0.0468 ± 0.0343
P_1	-0.0387 ± 0.0285	0.1407 ± 0.0313
P_2	-0.0888 ± 0.0296	0.0413 ± 0.0313
P_3	-0.0056 ± 0.0285	0.0271 ± 0.0316
P'_4	-0.1760 ± 0.0305	-0.0958 ± 0.0336
P'_5	0.1267 ± 0.0309	0.1819 ± 0.0325
P'_6	-0.0220 ± 0.0298	-0.0416 ± 0.0306
P'_8	0.0190 ± 0.0305	0.0264 ± 0.0323

Table 110: The widths of the pull distributions from toy event studies with S (left) and P (right) basis observables using theoretically predicted values for a new physics scenario of a Wilson coefficient $C_9 = -1$ for the generation of toy events in the two extra large q^2 bins of $[1.1 - 6.0]\,\mathrm{GeV}^2/c^2$ and $[15.0 - 19.0]\,\mathrm{GeV}^2/c^2$. The results are obtained using the 2D+4D fit method as described in Section 4.2 with angular folding. Values for S_{1s}, S_3, F_L and P_1 are obtained from folding 4.

q^2 bin	[1.1-6.0]	[15.0-19.0]
S_{1s}	0.9207 ± 0.0206	1.0345 ± 0.0231
S_3	0.9826 ± 0.0220	0.9994 ± 0.0223
S_4	0.9706 ± 0.0217	1.1092 ± 0.0248
S_5	1.0189 ± 0.0228	1.0059 ± 0.0225
S_{6s}	1.0207 ± 0.0228	1.0001 ± 0.0224
S_7	1.0292 ± 0.0230	1.0024 ± 0.0224
S_8	1.0049 ± 0.0225	1.0251 ± 0.0229
S_9	0.9973 ± 0.0223	1.0231 ± 0.0229

q^2 bin	[1.1-6.0]	[15.0-19.0]
F_L	0.8520 ± 0.0191	1.0852 ± 0.0243
P_1	0.9017 ± 0.0202	0.9912 ± 0.0222
P_2	0.9350 ± 0.0209	0.9899 ± 0.0221
P_3	0.9013 ± 0.0202	0.9991 ± 0.0223
P_4'	0.9632 ± 0.0215	1.0624 ± 0.0238
P_5'	0.9763 ± 0.0218	1.0292 ± 0.0230
P_6'	0.9405 ± 0.0210	0.9688 ± 0.0217
P_8'	0.9631 ± 0.0215	1.0202 ± 0.0228

Table 111: Mean values of the pull distributions from toy event studies with S (left) and P (right) basis observables using the final fit values for the generation of toy events in the two extra large q^2 bins of $[1.1 - 6.0]\,\mathrm{GeV}^2/c^2$ and $[15.0 - 19.0]\,\mathrm{GeV}^2/c^2$. The results are obtained using the 2D+4D fit method as described in Section 4.2 with angular folding. Values for S_{1s}, S_3, F_L and P_1 are obtained from folding 4.

q^2 bin	[1.1-6.0]	[15.0-19.0]
S_{1s}	0.0183 ± 0.0316	0.0463 ± 0.0334
S_3	-0.0001 ± 0.0327	0.1884 ± 0.0304
S_4	-0.0720 ± 0.0333	0.6249 ± 0.0314
S_5	0.0950 ± 0.0310	-0.0141 ± 0.0317
S_{6s}	0.0203 ± 0.0315	-0.6517 ± 0.0342
S_7	0.0357 ± 0.0305	-0.0289 ± 0.0303
S_8	0.0335 ± 0.0326	0.0323 ± 0.0319
S_9	0.0127 ± 0.0314	-0.0684 ± 0.0323
q^2 bin	[1.1-6.0]	[15.0-19.0]
F_L	-0.1046 ± 0.0285	-0.0310 ± 0.0350
P_1	0.0486 ± 0.0302	0.1639 ± 0.0307
P_2	0.0496 ± 0.0296	-0.5625 ± 0.0313
P_3	-0.0014 ± 0.0303	0.0330 ± 0.0320
P'_4	-0.0793 ± 0.0317	0.4867 ± 0.0327
P'_5	0.0253 ± 0.0307	-0.0391 ± 0.0328
P'_6	0.0202 ± 0.0312	-0.0819 ± 0.0315
P'_8	-0.0308 ± 0.0327	0.0264 ± 0.0332

Table 112: The widths of the pull distributions from toy event studies with S (left) and P (right) basis observables using the final fit for the generation of toy events in the two extra large q^2 bins of $[1.1 - 6.0]\,\mathrm{GeV}^2/c^2$ and $[15.0 - 19.0]\,\mathrm{GeV}^2/c^2$. The results are obtained using the 2D+4D fit method as described in Section 4.2 with angular folding. Values for S_{1s}, S_3, F_L and P_1 are obtained from folding 4.

q^2 bin	[1.1-6.0]	[15.0-19.0]
S_{1s}	0.9977 ± 0.0223	1.0556 ± 0.0236
S_3	1.0344 ± 0.0231	0.9616 ± 0.0215
S_4	1.0542 ± 0.0236	0.9926 ± 0.0222
S_5	0.9815 ± 0.0219	1.0029 ± 0.0224
S_{6s}	0.9965 ± 0.0223	1.0821 ± 0.0242
S_7	0.9643 ± 0.0216	0.9592 ± 0.0214
S_8	1.0302 ± 0.0230	1.0085 ± 0.0226
S_9	0.9934 ± 0.0222	1.0209 ± 0.0228
q^2 bin	[1.1-6.0]	[15.0-19.0]
F_L	0.9006 ± 0.0201	1.1067 ± 0.0248
P_1	0.9553 ± 0.0214	0.9700 ± 0.0217
P_2	0.9363 ± 0.0209	0.9893 ± 0.0221
P_3	0.9587 ± 0.0214	1.0113 ± 0.0226
P_4'	1.0037 ± 0.0224	1.0327 ± 0.0231
P_5'	0.9695 ± 0.0217	1.0365 ± 0.0232
P_6'	0.9863 ± 0.0221	0.9949 ± 0.0222
P_8'	1.0343 ± 0.0231	1.0490 ± 0.0235

A.16 Method of moments result tables for signal MC

In addition to the plots in Fig. 67, all numbers for the Method of Moments comparison with the likelihood fit for signal channel MC events are given in the following two tables, Tables 113 and 114.

Table 113: Comparison of Method of Moments and the likelihood fit for the first 4 angular observables in all 8 q^2 bins for signal channel MC. No S-wave is included in neither method nor data and the events are signal only without background pollution. The results are plotted in Fig. 67.

S_{1s}	fit	MoM	GenLvl
$[0.1, 1.0]$	0.509 ± 0.011	0.510 ± 0.007	0.512 ± 0.002
$[1.1, 2.5]$	0.189 ± 0.008	0.172 ± 0.008	0.180 ± 0.002
$[2.5, 4.0]$	0.136 ± 0.005	0.114 ± 0.008	0.137 ± 0.002
$[4.0, 6.0]$	0.182 ± 0.004	0.177 ± 0.006	0.193 ± 0.002
$[6.0, 8.0]$	0.257 ± 0.004	0.254 ± 0.006	0.275 ± 0.002
$[11.0, 12.5]$	0.389 ± 0.004	0.379 ± 0.006	0.417 ± 0.002
$[15.0, 17.0]$	0.474 ± 0.004	0.467 ± 0.005	0.484 ± 0.002
$[17.0, 19.0]$	0.482 ± 0.005	0.478 ± 0.007	0.503 ± 0.002
S_3	fit	MoM	GenLvl
$[0.1, 1.0]$	0.052 ± 0.009	0.052 ± 0.009	-0.000 ± 0.004
$[1.1, 2.5]$	-0.002 ± 0.008	-0.009 ± 0.010	0.002 ± 0.004
$[2.5, 4.0]$	-0.006 ± 0.007	-0.004 ± 0.010	-0.008 ± 0.004
$[4.0, 6.0]$	-0.014 ± 0.006	-0.013 ± 0.008	-0.012 ± 0.003
$[6.0, 8.0]$	-0.029 ± 0.005	-0.024 ± 0.008	-0.024 ± 0.003
$[11.0, 12.5]$	-0.053 ± 0.005	-0.058 ± 0.009	-0.062 ± 0.003
$[15.0, 17.0]$	-0.143 ± 0.006	-0.141 ± 0.009	-0.152 ± 0.003
$[17.0, 19.0]$	-0.222 ± 0.007	-0.215 ± 0.012	-0.233 ± 0.004
S_4	fit	MoM	GenLvl
$[0.1, 1.0]$	0.067 ± 0.022	0.070 ± 0.014	0.087 ± 0.004
$[1.1, 2.5]$	0.051 ± 0.023	0.010 ± 0.017	0.004 ± 0.005
$[2.5, 4.0]$	-0.102 ± 0.012	-0.084 ± 0.016	-0.108 ± 0.005
$[4.0, 6.0]$	-0.183 ± 0.008	-0.183 ± 0.012	-0.195 ± 0.004
$[6.0, 8.0]$	-0.249 ± 0.006	-0.246 ± 0.010	-0.251 ± 0.003
$[11.0, 12.5]$	-0.268 ± 0.005	-0.277 ± 0.010	-0.277 ± 0.003
$[15.0, 17.0]$	-0.292 ± 0.005	-0.294 ± 0.009	-0.290 ± 0.003
$[17.0, 19.0]$	-0.301 ± 0.007	-0.301 ± 0.013	-0.304 ± 0.003
S_5	fit	MoM	GenLvl
$[0.1, 1.0]$	0.273 ± 0.014	0.275 ± 0.010	0.244 ± 0.004
$[1.1, 2.5]$	0.069 ± 0.019	0.082 ± 0.015	0.095 ± 0.005
$[2.5, 4.0]$	-0.155 ± 0.011	-0.160 ± 0.015	-0.159 ± 0.005
$[4.0, 6.0]$	-0.308 ± 0.008	-0.300 ± 0.012	-0.305 ± 0.004
$[6.0, 8.0]$	-0.413 ± 0.006	-0.412 ± 0.010	-0.414 ± 0.003
$[11.0, 12.5]$	-0.445 ± 0.006	-0.455 ± 0.009	-0.421 ± 0.003
$[15.0, 17.0]$	-0.345 ± 0.006	-0.338 ± 0.008	-0.340 ± 0.003
$[17.0, 19.0]$	-0.252 ± 0.008	-0.252 ± 0.011	-0.249 ± 0.003

Table 114: Comparison of Method of Moments and the likelihood fit for the last 4 angular observables in all 8 q^2 bins for signal channel MC. No S-wave is included in neither method nor data and the events are signal only without background pollution. The results are plotted in Fig. 67.

S_{6s}	fit	MoM	GenLvl
$[0.1, 1.0]$	-0.107 ± 0.020	-0.095 ± 0.019	-0.127 ± 0.004
$[1.1, 2.5]$	-0.220 ± 0.015	-0.233 ± 0.013	-0.207 ± 0.003
$[2.5, 4.0]$	-0.090 ± 0.008	-0.080 ± 0.011	-0.086 ± 0.003
$[4.0, 6.0]$	0.088 ± 0.006	0.100 ± 0.008	0.095 ± 0.003
$[6.0, 8.0]$	0.293 ± 0.005	0.287 ± 0.008	0.302 ± 0.003
$[11.0, 12.5]$	0.489 ± 0.006	0.481 ± 0.008	0.514 ± 0.003
$[15.0, 17.0]$	0.551 ± 0.005	0.558 ± 0.009	0.557 ± 0.003
$[17.0, 19.0]$	0.451 ± 0.009	0.467 ± 0.012	0.470 ± 0.004
S_7	fit	MoM	GenLvl
$[0.1, 1.0]$	-0.000 ± 0.013	0.003 ± 0.010	-0.006 ± 0.004
$[1.1, 2.5]$	0.044 ± 0.023	0.035 ± 0.014	-0.010 ± 0.005
$[2.5, 4.0]$	0.006 ± 0.012	0.012 ± 0.015	-0.003 ± 0.005
$[4.0, 6.0]$	0.010 ± 0.009	0.008 ± 0.012	0.002 ± 0.004
$[6.0, 8.0]$	-0.006 ± 0.008	-0.011 ± 0.011	0.003 ± 0.004
$[11.0, 12.5]$	0.008 ± 0.008	0.015 ± 0.010	-0.002 ± 0.004
$[15.0, 17.0]$	-0.017 ± 0.008	-0.014 ± 0.010	-0.002 ± 0.004
$[17.0, 19.0]$	0.019 ± 0.011	0.013 ± 0.013	0.005 ± 0.005
S_8	fit	MoM	GenLvl
$[0.1, 1.0]$	0.016 ± 0.020	0.008 ± 0.013	0.001 ± 0.004
$[1.1, 2.5]$	0.007 ± 0.028	0.007 ± 0.017	-0.003 ± 0.005
$[2.5, 4.0]$	-0.018 ± 0.012	-0.020 ± 0.016	-0.004 ± 0.005
$[4.0, 6.0]$	0.005 ± 0.010	0.008 ± 0.012	-0.003 ± 0.004
$[6.0, 8.0]$	-0.012 ± 0.008	-0.031 ± 0.011	-0.001 ± 0.004
$[11.0, 12.5]$	0.003 ± 0.008	0.007 ± 0.010	0.003 ± 0.004
$[15.0, 17.0]$	0.009 ± 0.008	-0.000 ± 0.010	-0.001 ± 0.004
$[17.0, 19.0]$	0.012 ± 0.011	0.012 ± 0.014	0.003 ± 0.005
S_9	fit	MoM	GenLvl
$[0.1, 1.0]$	-0.021 ± 0.009	-0.022 ± 0.009	-0.002 ± 0.004
$[1.1, 2.5]$	0.005 ± 0.008	-0.003 ± 0.010	0.000 ± 0.004
$[2.5, 4.0]$	-0.001 ± 0.007	0.004 ± 0.010	0.002 ± 0.004
$[4.0, 6.0]$	-0.007 ± 0.006	-0.024 ± 0.008	0.004 ± 0.003
$[6.0, 8.0]$	0.005 ± 0.006	0.003 ± 0.008	-0.002 ± 0.003
$[11.0, 12.5]$	-0.003 ± 0.006	-0.003 ± 0.009	-0.001 ± 0.003
$[15.0, 17.0]$	0.009 ± 0.006	0.007 ± 0.009	-0.001 ± 0.003
$[17.0, 19.0]$	0.002 ± 0.010	0.005 ± 0.012	0.001 ± 0.005

A.17 Correlation matrices for 2D mass fits

The fit in the two mass dimensions of the invariant masses of B^+ and K^{*+} are used to obtain the S-wave fraction, F_S. To prevent biases in the *double usage* of the the data, the correlation between F_S and other parameters have to be considered. A potential large correlation should be fed into the consecutive 4D fit to not introduce biases or warps in the statistical uncertainty determination. In Table 115 the correlation matrices for the three bins are given.

F_S has significant correlations with the width of the K^{*+} mass shape, Γ. However, any K^{*+} related parameters are not present in the 4D fit to the B^+ mass and the angular distributions. Other than that, the correlation of F_S to the signal fraction (or here N_{sig} and N_{bkg}) as well as the background parameter, λ_m, are at an acceptable level, given that both the signal fraction and the background parameter are free to float in the 4D fit.

Table 115: Correlation matrices for all three large bins, which are used to determine the S-wave fraction F_S.

$[1.1-8.0]$	F_S	N_{sig}	N_{bkg}	$m(B^+)$	λ_m	$\Gamma(K^{*+})$	$m(K^{*+})$	$c^1_{bkg}(m_{K\pi})$
F_S	1.000	0.228	-0.144	0.052	0.106	-0.566	0.012	-0.034
N_{sig}		1.000	-0.303	-0.007	0.235	0.020	-0.011	0.007
N_{bkg}			1.000	0.004	-0.148	-0.013	0.007	-0.004
$m(B^+)$				1.000	-0.032	-0.028	-0.015	0.007
λ_m					1.000	0.011	-0.004	0.002
$\Gamma(K^{*+})$						1.000	-0.058	0.049
$m(K^{*+})$							1.000	-0.101
$c^1_{bkg}(m_{K\pi})$								1.000

$[11.0-12.5]$	F_S	N_{sig}	N_{bkg}	$m(B^+)$	λ_m	$\Gamma(K^{*+})$	$m(K^{*+})$	$c^1_{bkg}(m_{K\pi})$
F_S	1.000	0.226	-0.193	0.072	0.125	-0.546	-0.291	-0.077
N_{sig}		1.000	-0.287	0.028	0.204	-0.023	-0.020	-0.040
N_{bkg}			1.000	-0.024	-0.174	0.020	0.017	0.034
$m(B^+)$				1.000	-0.018	-0.011	-0.072	0.012
λ_m					1.000	-0.013	-0.002	-0.026
$\Gamma(K^{*+})$						1.000	0.356	0.013
$m(K^{*+})$							1.000	-0.088
$c^1_{bkg}(m_{K\pi})$								1.000

$[15.0-19.0]$	F_S	N_{sig}	N_{bkg}	$m(B^+)$	λ_m	$\Gamma(K^{*+})$	$m(K^{*+})$	$c^1_{bkg}(m_{K\pi})$
F_S	1.000	0.118	-0.121	0.020	0.103	-0.648	-0.201	-0.092
N_{sig}		1.000	-0.232	0.037	0.202	0.018	-0.014	-0.050
N_{bkg}			1.000	-0.038	-0.207	-0.019	0.014	0.052
$m(B^+)$				1.000	0.006	0.008	-0.013	-0.004
λ_m					1.000	0.017	-0.011	-0.044
$\Gamma(K^{*+})$						1.000	0.246	0.027
$m(K^{*+})$							1.000	-0.086
$c^1_{bkg}(m_{K\pi})$								1.000

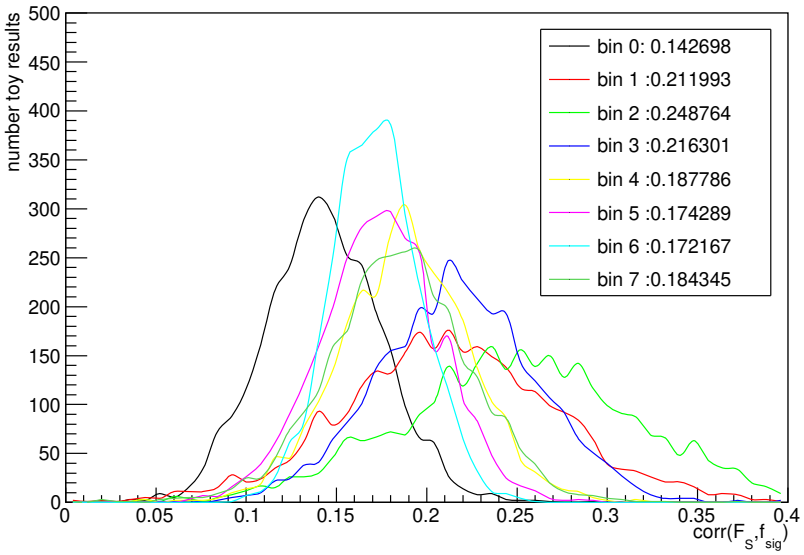

Figure 168: Distribution of the correlation between F_S and f_{sig} that arise from the 2D mass fit toy studies (see Section 4.4.5). No correlation was specifically generated with the toy event creation. For more details on why this result on the correlations is important, see text.

The correlation between the S-wave fraction F_S and the signal fraction f_{sig} (or N_{sig}/N_{bkg} in Table 115) might potentially be a cause for biases, as the correlations are not passed from the 2D mass fits to the 4D angular fits (see Section 4.2). However, the toys of the final fit configuration (see Section 4.4.6) cover this potential issue, because the studies also miss passing on any correlation from the 2D to the 4D fit.
As it turns out, the correlations between F_S and f_{sig} in the toy studies of the pure 2D fit (see Section 4.4.5), show very similar correlations as Table 115, even though no correlation was specifically generated with the generation of the toy samples. The resulting distribution of the correlations for all eight q^2 bins along with their mean values can be seen in Fig. 168. We therefore conclude, that the lack of correlation transport between the 2D and 4D fit are tested by the toy studies and clearly do not impact the results of the angular observables.

A.18 Correlation matrices of the fits to the reference channel

In addition to the mean values and statistical uncertainties from the fits to the reference channel in Table 26, the correlation matrices from these fits are given in Tables 116 to 121.

Table 116: Correlation matrix of the full angular fit to the reference channel.

	S_{1s}	S_3	S_4	S_5	S_{6s}	S_7	S_8	S_9	F_S	S_{S1}	S_{S2}	S_{S3}	S_{S4}	S_{S5}
S_{1s}	1.000	0.001	-0.011	-0.007	-0.003	0.000	-0.002	-0.034	-0.215	0.033	0.010	-0.008	0.001	-0.056
S_3		1.000	-0.095	-0.002	0.000	-0.002	0.028	-0.000	-0.002	-0.015	0.005	-0.021	0.001	0.041
S_4			1.000	-0.004	-0.012	-0.002	-0.055	0.004	-0.207	-0.016	-0.059	0.009	0.003	-0.023
S_5				1.000	-0.162	-0.058	-0.001	0.001	-0.006	0.008	0.005	-0.078	-0.003	0.003
S_{6s}					1.000	-0.046	-0.007	0.002	-0.004	0.001	-0.003	0.008	-0.060	-0.001
S_7						1.000	-0.008	-0.009	0.003	-0.005	0.004	-0.014	-0.053	-0.002
S_8							1.000	-0.085	-0.046	-0.037	-0.016	0.004	-0.002	-0.046
S_9								1.000	-0.169	-0.011	-0.045	-0.005	0.006	-0.007
F_S									1.000	-0.004	-0.002	-0.006	-0.002	0.003
S_{S1}										1.000	-0.140	-0.006	0.001	-0.042
S_{S2}											1.000	-0.011	-0.000	-0.072
S_{S3}												1.000	-0.100	-0.000
S_{S4}													1.000	-0.009
S_{S5}														1.000

Table 117: Correlation matrix of the fit to the reference channel using folding 0.

	S_{1s}	S_3	S_{6s}	S_9	F_S	S_{S1}
S_{1s}	1.000	0.004	-0.002	-0.031	-0.220	0.033
S_3		1.000	0.001	-0.001	-0.000	-0.014
S_{6s}			1.000	0.001	-0.006	0.000
S_9				1.000	-0.164	-0.010
F_S					1.000	-0.006
S_{S1}						1.000

Table 118: Correlation matrix of the fit to the reference channel using folding 1.

	S_{1s}	S_3	S_4	F_S	S_{S1}	S_{S2}
S_{1s}	1.000	0.001	-0.011	-0.212	0.031	0.013
S_3		1.000	-0.091	-0.000	-0.016	0.009
S_4			1.000	-0.207	-0.012	-0.049
F_S				1.000	-0.005	-0.002
S_{S1}					1.000	-0.137
S_{S2}						1.000

Table 119: Correlation matrix of the fit to the reference channel using folding 2.

	S_{1s}	S_3	S_5	F_S	S_{S1}	S_{S3}
S_{1s}	1.000	0.004	-0.004	-0.220	0.032	-0.005
S_3		1.000	-0.004	0.000	-0.014	-0.021
S_5			1.000	-0.006	0.006	-0.067
F_S				1.000	-0.006	-0.004
S_{S1}					1.000	-0.005
S_{S3}						1.000

Table 120: Correlation matrix of the fit to the reference channel using folding 3.

	S_{1s}	S_3	S_7	F_S	S_{S1}	S_{S4}
S_{1s}	1.000	0.004	0.001	-0.216	0.032	0.002
S_3		1.000	-0.004	0.003	-0.014	-0.003
S_7			1.000	0.003	-0.004	-0.044
F_S				1.000	-0.005	0.001
S_{S1}					1.000	0.001
S_{S4}						1.000

Table 121: Correlation matrix of the fit to the reference channel using folding 4.

	S_{1s}	S_3	S_8	F_S	S_{S4}
S_{1s}	1.000	0.003	-0.001	-0.216	0.003
S_3		1.000	0.022	0.000	-0.003
S_8			1.000	-0.047	-0.002
F_S				1.000	0.001
S_{S4}					1.000

A.19 Correlation matrices from the validation of the bootstrapping method

To validate the BOOTSTRAPPING method to extract the correlation matrix, seven samples of each 8000 toy events have been used to compare the correlation matrix from the full angular fitter and the BOOTSTRAPPING method. More details are given in Section 4.9.1. In the following, the seven pairs of correlation matrices are given in Tables 122 to 128.

Table 122: Correlation matrix obtained from the full angular fit (top) and the BOOTSTRAPPING method (bottom) of toy sample #1.

bin 0	S_{1s}	S_3	S_4	S_5	S_{6s}	S_7	S_8	S_9
S_{1s}	1.000	−0.002	0.044	−0.018	−0.054	−0.047	−0.037	−0.018
S_3		1.000	0.020	0.112	0.036	0.019	0.018	0.006
S_4			1.000	0.074	0.098	−0.007	−0.029	−0.009
S_5				1.000	−0.002	−0.066	−0.004	−0.050
S_{6s}					1.000	−0.012	−0.036	−0.001
S_7						1.000	−0.063	0.127
S_8							1.000	0.035
S_9								1.000

bin 0	S_{1s}	S_3	S_4	S_5	S_{6s}	S_7	S_8	S_9
S_{1s}	1.000	0.006	0.019	0.021	−0.041	−0.032	−0.026	−0.028
S_3		1.000	0.060	0.081	−0.038	0.002	−0.018	−0.042
S_4			1.000	−0.053	0.041	−0.030	−0.041	−0.052
S_5				1.000	−0.078	−0.034	−0.053	0.011
S_{6s}					1.000	−0.007	0.081	−0.062
S_7						1.000	−0.160	0.121
S_8							1.000	−0.013
S_9								1.000

Table 123: Correlation matrix obtained from the full angular fit (top) and the BOOTSTRAPPING method (bottom) of toy sample #2.

bin 0	S_{1s}	S_3	S_4	S_5	S_{6s}	S_7	S_8	S_9
S_{1s}	1.000	0.097	0.207	0.178	−0.170	−0.002	−0.014	0.031
S_3		1.000	0.156	0.229	−0.003	0.019	0.009	0.042
S_4			1.000	0.231	0.063	−0.003	−0.044	0.025
S_5				1.000	−0.026	−0.037	0.005	0.045
S_{6s}					1.000	−0.010	−0.007	−0.032
S_7						1.000	−0.102	0.130
S_8							1.000	0.101
S_9								1.000

bin 0	S_{1s}	S_3	S_4	S_5	S_{6s}	S_7	S_8	S_9
S_{1s}	1.000	0.090	0.009	−0.079	−0.045	−0.085	−0.081	−0.003
S_3		1.000	0.062	0.170	−0.055	0.040	−0.040	0.056
S_4			1.000	0.016	0.092	−0.097	0.004	−0.083
S_5				1.000	0.033	−0.037	−0.026	0.007
S_{6s}					1.000	−0.030	0.073	−0.069
S_7						1.000	−0.118	0.173
S_8							1.000	−0.000
S_9								1.000

Table 124: Correlation matrix obtained from the full angular fit (top) and the BOOTSTRAPPING method (bottom) of toy sample #3.

bin 0	S_{1s}	S_3	S_4	S_5	S_{6s}	S_7	S_8	S_9
S_{1s}	1.000	0.025	0.142	0.382	−0.318	−0.029	−0.076	0.081
S_3		1.000	0.093	0.171	−0.026	0.036	0.045	0.021
S_4			1.000	0.100	0.086	0.005	0.021	−0.013
S_5				1.000	−0.229	−0.024	−0.137	0.078
S_{6s}					1.000	−0.001	0.024	−0.043
S_7						1.000	−0.155	0.185
S_8							1.000	0.042
S_9								1.000

bin 0	S_{1s}	S_3	S_4	S_5	S_{6s}	S_7	S_8	S_9
S_{1s}	1.000	0.004	0.047	−0.027	−0.130	0.029	0.002	0.148
S_3		1.000	−0.024	0.047	−0.009	0.032	0.049	0.045
S_4			1.000	−0.047	0.229	−0.078	0.059	0.013
S_5				1.000	0.004	−0.077	−0.185	−0.096
S_{6s}					1.000	−0.054	0.168	−0.030
S_7						1.000	−0.148	0.103
S_8							1.000	0.130
S_9								1.000

Table 125: Correlation matrix obtained from the full angular fit (top) and the BOOTSTRAPPING method (bottom) of toy sample #4.

bin 0	S_{1s}	S_3	S_4	S_5	S_{6s}	S_7	S_8	S_9
S_{1s}	1.000	−0.018	0.193	0.244	−0.344	0.019	−0.053	−0.101
S_3		1.000	0.055	0.083	0.035	−0.013	0.021	0.018
S_4			1.000	0.128	−0.031	0.049	−0.041	−0.100
S_5				1.000	−0.199	0.040	−0.059	−0.100
S_{6s}					1.000	−0.057	0.003	0.081
S_7						1.000	−0.145	0.105
S_8							1.000	0.103
S_9								1.000

bin 0	S_{1s}	S_3	S_4	S_5	S_{6s}	S_7	S_8	S_9
S_{1s}	1.000	−0.030	−0.014	−0.079	−0.183	−0.102	−0.005	−0.034
S_3		1.000	0.059	0.029	0.037	−0.031	0.096	0.021
S_4			1.000	0.052	−0.021	−0.085	−0.022	−0.024
S_5				1.000	0.100	0.103	−0.069	−0.078
S_{6s}					1.000	−0.025	0.034	0.026
S_7						1.000	−0.021	0.025
S_8							1.000	0.093
S_9								1.000

Table 126: Correlation matrix obtained from the full angular fit (top) and the BOOTSTRAPPING method (bottom) of toy sample #5.

bin 0	S_{1s}	S_3	S_4	S_5	S_{6s}	S_7	S_8	S_9
S_{1s}	1.000	0.027	0.099	0.127	−0.233	−0.020	−0.026	0.026
S_3		1.000	0.065	0.143	−0.009	0.020	−0.002	−0.001
S_4			1.000	0.054	0.083	−0.022	0.003	0.006
S_5				1.000	−0.114	−0.070	−0.013	0.019
S_{6s}					1.000	0.027	0.024	−0.012
S_7						1.000	−0.100	0.157
S_8							1.000	0.110
S_9								1.000

bin 0	S_{1s}	S_3	S_4	S_5	S_{6s}	S_7	S_8	S_9
S_{1s}	1.000	0.038	−0.030	0.005	−0.064	0.029	−0.005	0.013
S_3		1.000	0.085	−0.022	0.002	0.032	−0.060	−0.010
S_4			1.000	−0.052	0.033	−0.079	−0.033	−0.056
S_5				1.000	−0.076	−0.050	0.050	−0.048
S_{6s}					1.000	−0.077	0.016	0.031
S_7						1.000	−0.270	0.163
S_8							1.000	0.055
S_9								1.000

Table 127: Correlation matrix obtained from the full angular fit (top) and the BOOTSTRAPPING method (bottom) of toy sample #6.

bin 0	S_{1s}	S_3	S_4	S_5	S_{6s}	S_7	S_8	S_9
S_{1s}	1.000	0.005	0.064	−0.005	−0.184	−0.006	−0.030	−0.001
S_3		1.000	0.064	0.128	0.001	0.009	0.010	−0.009
S_4			1.000	−0.000	0.088	0.008	−0.003	−0.048
S_5				1.000	−0.071	−0.061	−0.023	−0.028
S_{6s}					1.000	−0.020	0.015	0.057
S_7						1.000	−0.097	0.124
S_8							1.000	0.038
S_9								1.000

bin 0	S_{1s}	S_3	S_4	S_5	S_{6s}	S_7	S_8	S_9
S_{1s}	1.000	0.044	0.135	−0.046	−0.012	0.070	−0.029	0.010
S_3		1.000	0.033	0.133	0.005	−0.021	−0.011	−0.002
S_4			1.000	0.010	−0.045	0.032	−0.039	−0.033
S_5				1.000	0.070	−0.140	−0.046	−0.034
S_{6s}					1.000	−0.062	0.032	0.039
S_7						1.000	−0.099	0.103
S_8							1.000	−0.022
S_9								1.000

Table 128: Correlation matrix obtained from the full angular fit (top) and the BOOTSTRAPPING method (bottom) of toy sample #7.

bin 0	S_{1s}	S_3	S_4	S_5	S_{6s}	S_7	S_8	S_9
S_{1s}	1.000	0.029	−0.011	−0.111	−0.112	−0.088	−0.038	0.022
S_3		1.000	0.015	0.209	−0.008	0.006	−0.039	0.006
S_4			1.000	−0.099	0.143	−0.056	−0.017	0.050
S_5				1.000	−0.120	0.055	0.147	−0.031
S_{6s}					1.000	0.032	−0.065	0.003
S_7						1.000	−0.007	0.102
S_8							1.000	−0.020
S_9								1.000

bin 0	S_{1s}	S_3	S_4	S_5	S_{6s}	S_7	S_8	S_9
S_{1s}	1.000	0.048	0.239	0.294	−0.132	−0.313	−0.126	0.076
S_3		1.000	0.044	0.170	−0.045	−0.007	−0.035	−0.050
S_4			1.000	0.171	−0.024	−0.135	−0.126	0.085
S_5				1.000	−0.146	−0.217	−0.029	−0.010
S_{6s}					1.000	0.144	−0.012	−0.031
S_7						1.000	−0.077	0.105
S_8							1.000	−0.105
S_9								1.000

A.20 Fitting the reference channel with a forced symmetric acceptance in $\cos\theta_L$

The forced symmetry in the acceptance correction coefficients for $\cos\theta_L$ has been tested on a fit to the reference channel. Results are presented in the Table 129.

Table 129: Results to the reference channel when using a forced symmetry in the acceptance of $\cos\theta_L$.

observable	value
S_{1s}	0.318 ± 0.002
S_3	-0.003 ± 0.003
S_4	-0.266 ± 0.003
S_5	-0.003 ± 0.003
S_{6s}	0.000 ± 0.002
S_7	-0.001 ± 0.003
S_8	-0.060 ± 0.003
S_9	-0.082 ± 0.003

A.21 Systematic studies for angular observables in $P_x^{(\prime)}$ basis

Identical to the different sections in Section 5, all studies on systematic uncertainties are repeated for the angular observables in the $P_x^{(\prime)}$ basis. In the following, the resulting tables are given with a reference to the section discussing the systematic study in the S basis.

Table 130: The width of the result distributions for all parameters due to fluctuating the PHSP MC weights for angular acceptance correction parametrization is assigned as a systematic uncertainty of this PHSP MC reweighting. More details on this systematic study are given in Section 5.1.

q^2 bin	0	1	2	3	4	5	6	7
F_L	0.0373	0.0091	0.0261	0.0161	0.0036	0.0161	0.0068	0.0105
P_1	0.0101	0.1021	0.1271	0.0513	0.0433	0.0724	0.0398	0.0224
P_2	0.0181	0.0624	0.0306	0.0564	0.0493	0.0395	0.0223	0.0223
P_3	0.0104	0.1437	0.1653	0.1244	0.0355	0.0262	0.0074	0.0074
P_4'	0.0823	0.0937	0.0350	0.0380	0.0146	0.0550	0.0557	0.0900
P_5'	0.0311	0.0503	0.0497	0.0615	0.0303	0.0332	0.0374	0.0544
P_6'	0.0543	0.0687	0.0463	0.0423	0.0234	0.0187	0.0063	0.0191
P_8'	0.0781	0.0063	0.0571	0.0410	0.0030	0.0330	0.0393	0.0574

Table 131: The statistical power of the PHSP MC sample is determined using the BOOTSTRAPPING method. 500 random subsets with equal size to the original PHSP MC set are taken, acceptance correction determined for each and the width of the signal parameter distribution is equal to the systematic uncertainty. More details on this systematic study are given in Section 5.2.

q^2 bin	0	1	2	3	4	5	6	7
F_L	0.0193	0.0209	0.0096	0.0106	0.0091	0.0106	0.0105	0.0167
P_1	0.0529	0.0544	0.0587	0.0355	0.0262	0.0200	0.0246	0.0461
P_2	0.0242	0.0240	0.0218	0.0118	0.0055	0.0023	0.0031	0.0088
P_3	0.0377	0.0059	0.0072	0.0044	0.0025	0.0014	0.0016	0.0054
P_4'	0.0774	0.0398	0.0378	0.0313	0.0169	0.0191	0.0225	0.0321
P_5'	0.0616	0.0387	0.0337	0.0298	0.0180	0.0180	0.0200	0.0330
P_6'	0.0260	0.0171	0.0128	0.0110	0.0063	0.0091	0.0065	0.0210
P_8'	0.0396	0.0319	0.0167	0.0193	0.0077	0.0154	0.0131	0.0351

Table 132: The absolute value of the difference in the mean values of all signal parameters between a fit with acceptance correction using the nominal order of polynomials and one fit of where the acceptance is parametrized by two additional orders per dimension. The absolute value of the difference is considered as an estimation of the systematic uncertainty for the PHSP MC parametrization. More details on this systematic study are given in Section 5.3.

q^2 bin	0	1	2	3	4	5	6	7
F_L	0.0345	0.0076	0.0126	0.0193	0.0114	0.0204	0.0118	0.0300
P_1	0.0878	0.0611	0.0686	0.0317	0.0460	0.0276	0.0393	0.0739
P_2	0.0006	0.0002	0.0141	0.0004	0.0015	0.0012	0.0013	0.0007
P_3	0.0027	0.0075	0.0155	0.0035	0.0066	0.0021	0.0027	0.0044
P_4'	0.0229	0.0157	0.0207	0.0116	0.0121	0.0049	0.0206	0.0073
P_5'	0.0924	0.0404	0.0227	0.0260	0.0134	0.0156	0.0130	0.0351
P_6'	0.0064	0.0022	0.0156	0.0023	0.0021	0.0006	0.0052	0.0135
P_8'	0.0106	0.0194	0.0028	0.0107	0.0093	0.0012	0.0097	0.0014

Table 133: Due to the large uncertainty on the Gaussian constraint of F_S, the toy study results of the final fit configuration with SM values show a bias, as shown in Table 20. The bias disappears when a stronger Gaussian constraint is applied for F_S. Here, the resulting values are not given relative to the statistical uncertainty as in Table 20, but the absolute values of the shift are given. These values are assigned as a systematic uncertainty. More details on this systematic study are given in Section 5.4.

q^2 bin	0	1	2	3	4	5	6	7
F_L	0.0192	0.0065	0.0191	0.0043	0.0058	0.0026	0.0067	0.0061
P_1	0.0225	0.0046	0.1286	0.0295	0.0069	0.0162	0.0001	0.0097
P_2	0.0073	0.1343	0.1029	0.0110	0.0148	0.0040	0.0056	0.0362
P_3	0.0099	0.0421	0.0019	0.0036	0.0058	0.0171	0.0037	0.0020
P'_4	0.0013	0.0374	0.0101	0.0324	0.0197	0.0155	0.0268	0.0825
P'_5	0.0257	0.0084	0.0339	0.0027	0.0308	0.0132	0.0312	0.0512
P'_6	0.0076	0.0139	0.0083	0.0002	0.0078	0.0077	0.0131	0.0002
P'_8	0.0038	0.0014	0.0328	0.0052	0.0035	0.0087	0.0070	0.0052

Table 134: The toy events are generated with the nominal double-sided Crystal Ball model for the B meson signal peak. Then these events are fitted with a single Gaussian bell shape and the mean value of the $x - x_0$ distributions is assigned as the systematic uncertainty for the mass model. More details on this systematic study are given in Section 5.5.

q^2 bin	0	1	2	3	4	5	6	7
F_L	0.0028	0.0023	0.0007	0.0027	0.0017	0.0021	0.0033	0.0012
P_1	0.0054	0.0329	0.0517	0.0383	0.0207	0.0115	0.0069	0.0134
P_2	0.0010	0.0047	0.0099	0.0015	0.0054	0.0035	0.0056	0.0024
P_3	0.0052	0.0076	0.0020	0.0086	0.0090	0.0032	0.0032	0.0010
P'_4	0.0027	0.0052	0.0030	0.0143	0.0035	0.0064	0.0091	0.0126
P'_5	0.0109	0.0054	0.0084	0.0058	0.0010	0.0121	0.0112	0.0091
P'_6	0.0002	0.0003	0.0058	0.0003	0.0023	0.0068	0.0041	0.0023
P'_8	0.0068	0.0023	0.0116	0.0118	0.0052	0.0013	0.0078	0.0038

Table 135: The angular background model is increased by an additional polynomial order compared to the nominal orders ($\cos\theta_K$: 2, $\cos\theta_L$: 2 and ϕ : 0) with an amplitude of 0.1 for the new order. The events are then fitted with the nominal background model and the difference to fit to a nominal background sample are compared. More details on this systematic study are given in Section 5.7.

q^2 bin	0	1	2	3	4	5	6	7
F_L	0.0037	0.0017	0.0024	0.0001	0.0000	0.0034	0.0042	0.0029
P_1	0.0028	0.0223	0.0561	0.0299	0.0183	0.0010	0.0019	0.0139
P_2	0.0033	0.0155	0.0041	0.0060	0.0117	0.0045	0.0038	0.0019
P_3	0.0106	0.0932	0.1129	0.0604	0.0331	0.0164	0.0111	0.0103
P'_4	0.0015	0.0064	0.0038	0.0065	0.0075	0.0034	0.0109	0.0073
P'_5	0.0086	0.0147	0.0139	0.0004	0.0165	0.0112	0.0059	0.0064
P'_6	0.0035	0.0008	0.0028	0.0052	0.0000	0.0036	0.0063	0.0025
P'_8	0.0043	0.0092	0.0035	0.0072	0.0006	0.0009	0.0036	0.0061

Table 136: By removing a Gaussian shaped hole from the upper mass side-band during the generation of toy events, the veto against $B^0 \to K^0_S \mu^+ \mu^-$ plus a random π^+ decays are simulated. In the fit, only the nominal background model is applied. More details on this systematic study are given in Section 5.6.

q^2 bin	0	1	2	3	4	5	6	7
F_L	0.0021	0.0003	0.0022	0.0021	0.0017	0.0054	0.0012	0.0032
P_1	0.0058	0.0366	0.0515	0.0613	0.0591	0.0211	0.0011	0.0011
P_2	0.0023	0.0098	0.0164	0.0032	0.0012	0.0005	0.0002	0.0005
P_3	0.0030	0.0318	0.0032	0.0052	0.0013	0.0097	0.0024	0.0014
P'_4	0.0046	0.0042	0.0198	0.0403	0.0265	0.0192	0.0229	0.0160
P'_5	0.0036	0.0037	0.0001	0.0166	0.0351	0.0267	0.0201	0.0118
P'_6	0.0004	0.0007	0.0071	0.0078	0.0012	0.0026	0.0030	0.0055
P'_8	0.0030	0.0003	0.0105	0.0009	0.0017	0.0050	0.0055	0.0074

Table 137: Results of the systematic effects of the angular resolutions on the angular observables. The angular resolutions have been determined using the TRUE information on MC, which is presented in Appendix A.6. For this study, the generated angles of all toy events have been repeatedly varied within their resolution. The width of the result distribution from all fits is given in this table and assigned as an systematic uncertainty. More details on this systematic study are given in Section 5.8.

q^2 bin	0	1	2	3	4	5	6	7
F_L	0.0008	0.0012	0.0007	0.0005	0.0006	0.0005	0.0003	0.0003
P_1	0.0027	0.0026	0.0037	0.0034	0.0023	0.0015	0.0011	0.0011
P_2	0.0015	0.0017	0.0012	0.0009	0.0005	0.0004	0.0002	0.0003
P_3	0.0006	0.0022	0.0024	0.0016	0.0014	0.0008	0.0005	0.0006
P'_4	0.0038	0.0034	0.0021	0.0019	0.0015	0.0011	0.0012	0.0012
P'_5	0.0033	0.0020	0.0015	0.0015	0.0010	0.0010	0.0007	0.0011
P'_6	0.0033	0.0021	0.0015	0.0014	0.0011	0.0010	0.0007	0.0009
P'_8	0.0066	0.0038	0.0023	0.0019	0.0014	0.0012	0.0010	0.0012

Table 138: The differences in the L0Muon trigger line efficiency (see Fig. 13) is used for an alternative determination of the angular acceptance correction coefficients. Toy studies are performed by generating events with the nominal acceptance and fitted with the alternative acceptance correction. This table presents the observed absolute values of the bias in the result distribution, which is assigned as a systematic uncertainty to the L0Muon trigger efficiency difference in data and MC events. More details on this systematic study are given in Section 5.10.

q^2 bin	0	1	2	3	4	5	6	7
F_L	0.0014	0.0009	0.0041	0.0042	0.0039	0.0003	0.0017	0.0005
P_1	0.0039	0.0000	0.0219	0.0187	0.0042	0.0064	0.0012	0.0058
P_2	0.0011	0.0070	0.0149	0.0077	0.0093	0.0001	0.0033	0.0027
P_3	0.0006	0.0107	0.0104	0.0026	0.0178	0.0036	0.0042	0.0039
P'_4	0.0074	0.0015	0.0215	0.0075	0.0027	0.0056	0.0020	0.0044
P'_5	0.0019	0.0001	0.0038	0.0225	0.0051	0.0009	0.0018	0.0023
P'_6	0.0016	0.0041	0.0031	0.0052	0.0043	0.0008	0.0028	0.0112
P'_8	0.0044	0.0134	0.0013	0.0075	0.0115	0.0020	0.0000	0.0006

Table 139: The non-flat ratio between MC and data DD tracks events in K^0_S p_T are used to weight the PHSP MC events prior to the determination of the angular acceptance correction coefficients. With the alternative coefficients, as well as with the nominal coefficients, toy events have been fitted repeatedly. The shift in the mean position of the difference distribution is assigned as an systematic uncertainty. More details on this systematic study are given in Section 5.11.

q^2 bin	0	1	2	3	4	5	6	7
F_L	0.0017	0.0016	0.0000	0.0012	0.0037	0.0021	0.0059	0.0006
P_1	0.0052	0.0530	0.0000	0.0015	0.0222	0.0028	0.0009	0.0010
P_2	0.0018	0.0011	0.0020	0.0032	0.0015	0.0011	0.0032	0.0043
P_3	0.0005	0.0061	0.0033	0.0014	0.0019	0.0060	0.0033	0.0007
P'_4	0.0015	0.0062	0.0033	0.0200	0.0001	0.0021	0.0042	0.0114
P'_5	0.0094	0.0004	0.0124	0.0126	0.0117	0.0070	0.0038	0.0103
P'_6	0.0003	0.0083	0.0044	0.0104	0.0025	0.0090	0.0029	0.0032
P'_8	0.0034	0.0248	0.0013	0.0117	0.0049	0.0067	0.0050	0.0056

Table 140: The observed bias in toy studies with values equal final fit results are assigned as a general systematic uncertainty to the unknown bias of the likelihood fit. More details on this systematic study are given in Section 5.12.

q^2 bin	0	1	2	3	4	5	6	7
F_L	0.0278	0.0229	0.0255	0.0127	0.0041	0.0067	0.0028	0.0059
P_1	0.0081	0.2782	0.0026	0.2690	0.0324	0.0113	0.0353	0.0098
P_2	0.0097	0.0054	0.0006	0.0195	0.0058	0.0169	0.0091	0.0018
P_3	0.0212	0.0029	0.0325	0.0566	0.0187	0.0257	0.0059	0.0084
P'_4	0.0266	0.0233	0.1260	0.0495	0.0462	0.0378	0.0117	0.0286
P'_5	0.0232	0.0689	0.0519	0.0315	0.0122	0.0119	0.0159	0.0893
P'_6	0.0109	0.0372	0.0126	0.0060	0.0035	0.0018	0.0107	0.0165
P'_8	0.0233	0.0128	0.0119	0.0050	0.0068	0.0054	0.0056	0.0248

A.22 Systematic studies in the two larger q^2 bins

In addition to the eight nominal q^2 bins (see Table 15), two larger bins are fitted in addition. For these bins, the systematic uncertainty is evaluated in the same way as for the nominal binning scheme. All systematic studies are listed in the following section, for both angular observable bases, the S- and $P^{(\prime)}$ observables.
Note that due to the larger q^2 bins, no scaling of the S-wave fraction F_S (see Appendix A.8) is required and therefore, no systematic uncertainty is assigned to this effect. The quadratic summation of all these systematic uncertainties is then combined in Table 51 in Section 5.15.

Table 141: The width of the result distributions for all parameters due to fluctuating the PHSP MC weights for angular acceptance correction parametrization is assigned as a systematic uncertainty of this PHSP MC reweighting. More details on this systematic study are given in Section 5.1.

q^2 bin	[1.1-6.0]	[15.0-19.0]	q^2 bin	[1.1-6.0]	[15.0-19.0]
S_{1s}	0.0021	0.0008	F_L	0.0028	0.0011
S_3	0.0014	0.0014	P_1	0.0093	0.0042
S_4	0.0032	0.0017	P_2	0.0041	0.0045
S_5	0.0019	0.0016	P_3	0.0105	0.0007
S_{6s}	0.0025	0.0013	P'_4	0.0178	0.0037
S_7	0.0007	0.0005	P'_5	0.0039	0.0039
S_8	0.0013	0.0013	P'_6	0.0016	0.0012
S_9	0.0007	0.0007	P'_8	0.0028	0.0028

Table 142: The statistical power of the PHSP MC sample is determined using the BOOTSTRAPPING method. 500 random subsets with equal size to the original PHSP MC set are taken, acceptance correction determined for each and the width of the signal parameter distribution is equal to the systematic uncertainty. More details on this systematic study are given in Section 5.2.

q^2 bin	[1.1-6.0]	[15.0-19.0]	q^2 bin	[1.1-6.0]	[15.0-19.0]
S_{1s}	0.0180	0.0092	F_L	0.0240	0.0123
S_3	0.0075	0.0083	P_1	0.0463	0.0249
S_4	0.0250	0.0214	P_2	0.0416	0.0097
S_5	0.0161	0.0147	P_3	0.0330	0.0046
S_{6s}	0.0293	0.0138	P'_4	0.0549	0.0459
S_7	0.0111	0.0052	P'_5	0.0348	0.0306
S_8	0.0212	0.0080	P'_6	0.0242	0.0111
S_9	0.0063	0.0031	P'_8	0.0450	0.0172

Table 143: The absolute value of the difference in the mean values of all signal parameters between a fit with acceptance correction using the nominal order of polynomials and one fit of where the acceptance is parametrized by two additional orders per dimension. The absolute value of the difference is considered as an estimation of the systematic uncertainty for the PHSP MC parametrization. More details on this systematic study are given in Section 5.3.

q^2 bin	[1.1-6.0]	[15.0-19.0]	q^2 bin	[1.1-6.0]	[15.0-19.0]
S_{1s}	0.0034	0.0183	F_L	0.0018	0.0165
S_3	0.0018	0.0231	P_1	0.0255	0.0395
S_4	0.0013	0.0063	P_2	0.0004	0.0037
S_5	0.0045	0.0102	P_3	0.0067	0.0010
S_{6s}	0.0092	0.0169	P'_4	0.0072	0.0392
S_7	0.0033	0.0042	P'_5	0.0087	0.0132
S_8	0.0075	0.0055	P'_6	0.0232	0.0084
S_9	0.0037	0.0010	P'_8	0.0247	0.0064

Table 144: Due to the large uncertainty on the Gaussian constraint of F_S, the toy study results of the final fit configuration with SM values show a bias, as shown in Table 20. The bias disappears when a stronger Gaussian constraint is applied for F_S. Here, the resulting values are not given relative to the statistical uncertainty as in Table 20, but the absolute values of the shift are given. These values are assigned as a systematic uncertainty. More details on this systematic study are given in Section 5.4.

q^2 bin	0	1	q^2 bin	0	1
S_{1s}	0.0016	0.0002	F_L	0.0031	0.0016
S_3	0.0007	0.0059	P_1	0.0023	0.0167
S_4	0.0062	0.0061	P_2	0.0075	0.0043
S_5	0.0068	0.0159	P_3	0.0016	0.0007
S_{6s}	0.0028	0.0053	P'_4	0.0230	0.0079
S_7	0.0014	0.0066	P'_5	0.0136	0.0146
S_8	0.0045	0.0038	P'_6	0.0071	0.0129
S_9	0.0013	0.0023	P'_8	0.0027	0.0053

Table 145: The toy events are generated with the nominal double-sided Crystal Ball model for the B meson signal peak. Then these events are fitted with a single Gaussian bell shape and the mean value of the $x - x_0$ distributions is assigned as the systematic uncertainty for the mass model. More details on this systematic study are given in Section 5.5.

q^2 bin	[1.1-6.0]	[15.0-19.0]
S_{1s}	0.0007	0.0006
S_3	0.0016	0.0026
S_4	0.0016	0.0063
S_5	0.0060	0.0020
S_{6s}	0.0048	0.0036
S_7	0.0033	0.0015
S_8	0.0013	0.0047
S_9	0.0021	0.0028

q^2 bin	[1.1-6.0]	[15.0-19.0]
F_L	0.0004	0.0041
P_1	0.0408	0.0054
P_2	0.0067	0.0011
P_3	0.0009	0.0037
P'_4	0.0109	0.0115
P'_5	0.0061	0.0155
P'_6	0.0057	0.0046
P'_8	0.0115	0.0095

Table 146: The angular background model is increased by an additional polynomial order compared to the nominal orders ($\cos\theta_K$: 2, $\cos\theta_L$: 2 and ϕ : 0) with an amplitude of 0.1 for the new order. The events are then fitted with the nominal background model and the difference to fit to a nominal background sample are compared. More details on this systematic study are given in Section 5.7.

q^2 bin	[1.1-6.0]	[15.0-19.0]
S_{1s}	0.0009	0.0022
S_3	0.0015	0.0027
S_4	0.0014	0.0038
S_5	0.0032	0.0005
S_{6s}	0.0046	0.0006
S_7	0.0033	0.0043
S_8	0.0004	0.0011
S_9	0.0111	0.0197

q^2 bin	[1.1-6.0]	[15.0-19.0]
F_L	0.0016	0.0040
P_1	0.0119	0.0182
P_2	0.0049	0.0011
P_3	0.0250	0.0314
P'_4	0.0052	0.0011
P'_5	0.0119	0.0172
P'_6	0.0073	0.0131
P'_8	0.0097	0.0138

Table 147: By removing a Gaussian shaped hole from the upper mass side-band during the generation of toy events, the veto against $B^0 \to K^0_S \mu^+ \mu^-$ plus a random π^+ decays are simulated. In the fit, only the nominal background model is applied. More details on this systematic study are given in Section 5.6.

q^2 bin	[1.1-6.0]	[15.0-19.0]	q^2 bin	[1.1-6.0]	[15.0-19.0]
S_{1s}	0.0004	0.0003	F_L	0.0018	0.0001
S_3	0.0021	0.0030	P_1	0.0080	0.0043
S_4	0.0013	0.0077	P_2	0.0110	0.0006
S_5	0.0034	0.0023	P_3	0.0034	0.0046
S_{6s}	0.0033	0.0004	P'_4	0.0090	0.0091
S_7	0.0002	0.0005	P'_5	0.0022	0.0182
S_8	0.0045	0.0017	P'_6	0.0015	0.0135
S_9	0.0018	0.0019	P'_8	0.0012	0.0005

Table 148: Results of the systematic effects of the angular resolutions on the angular observables. The angular resolutions have been determined using the TRUE information on MC, which is presented in Appendix A.6. For this study, the generated angles of all toy events have been repeatedly varied within their resolution. The width of the result distribution from all fits is given in this table and assigned as an systematic uncertainty. More details on this systematic study are given in Section 5.8.

q^2 bin	[1.1-6.0]	[15.0-19.0]	q^2 bin	[1.1-6.0]	[15.0-19.0]
S_{1s}	0.0006	0.0003	F_L	0.0007	0.0003
S_3	0.0004	0.0004	P_1	0.0028	0.0011
S_4	0.0008	0.0006	P_2	0.0012	0.0002
S_5	0.0006	0.0004	P_3	0.0020	0.0005
S_{6s}	0.0007	0.0004	P'_4	0.0018	0.0014
S_7	0.0006	0.0004	P'_5	0.0013	0.0009
S_8	0.0009	0.0006	P'_6	0.0013	0.0008
S_9	0.0005	0.0003	P'_8	0.0019	0.0013

Table 149: The differences in the L0Muon trigger line efficiency (see Fig. 13) is used for an alternative determination of the angular acceptance correction coefficients. Toy studies are performed by generating events with the nominal acceptance and fitted with the alternative acceptance correction. This table presents the observed absolute values of the bias in the result distribution, which is assigned as a systematic uncertainty to the L0Muon trigger efficiency difference in data and MC events. More details on this systematic study are given in Section 5.10.

q^2 bin	[1.1-6.0]	[15.0-19.0]
S_{1s}	0.0029	0.0011
S_3	0.0038	0.0037
S_4	0.0012	0.0001
S_5	0.0016	0.0037
S_{6s}	0.0011	0.0032
S_7	0.0029	0.0020
S_8	0.0010	0.0026
S_9	0.0010	0.0002

q^2 bin	[1.1-6.0]	[15.0-19.0]
F_L	0.0061	0.0010
P_1	0.0110	0.0038
P_2	0.0072	0.0004
P_3	0.0069	0.0032
P'_4	0.0030	0.0029
P'_5	0.0105	0.0025
P'_6	0.0028	0.0037
P'_8	0.0011	0.0012

Table 150: The non-flat ratio between MC and data DD tracks events in K^0_S p_T are used to weight the PHSP MC events prior to the determination of the angular acceptance correction coefficients. With the alternative coefficients, as well as with the nominal coefficients, toy events have been fitted repeatedly. The shift in the mean position of the difference distribution is assigned as an systematic uncertainty. More details on this systematic study are given in Section 5.11.

q^2 bin	[1.1-6.0]	[15.0-19.0]
S_{1s}	0.0018	0.0002
S_3	0.0003	0.0001
S_4	0.0031	0.0007
S_5	0.0000	0.0025
S_{6s}	0.0027	0.0007
S_7	0.0037	0.0009
S_8	0.0054	0.0018
S_9	0.0010	0.0025

q^2 bin	[1.1-6.0]	[15.0-19.0]
F_L	0.0064	0.0043
P_1	0.0220	0.0245
P_2	0.0019	0.0005
P_3	0.0046	0.0048
P'_4	0.0014	0.0066
P'_5	0.0054	0.0004
P'_6	0.0110	0.0015
P'_8	0.0301	0.0048

Table 151: The observed bias in toy studies with values equal final fit results are assigned as a general systematic uncertainty to the unknown bias of the likelihood fit. More details on this systematic study are given in Section 5.12.

q^2 bin	0	1	q^2 bin	0	1
S_{1s}	0.0017	0.0015	F_L	0.0027	0.0005
S_3	0.0017	0.0132	P_1	0.0202	0.0305
S_4	0.0066	0.0518	P_2	0.0002	0.0330
S_5	0.0068	0.0019	P_3	0.0055	0.0040
S_{6s}	0.0007	0.0469	P'_4	0.0166	0.0835
S_7	0.0012	0.0027	P'_5	0.0032	0.0092
S_8	0.0028	0.0029	P'_6	0.0019	0.0149
S_9	0.0003	0.0046	P'_8	0.0050	0.0050

A.23 Results from method of moments

In Section 4.8 the likelihood fit is evaluated to be superior over the method of moments for the determination of the Wilson coefficients of the underlying effective field theory. Therefore, the values from the method of moments are determined but then only used to cross-check the likelihood fits. In Table 152 the values obtained by the method of moments are listed but will not be published. The final results of this analysis can be found in Table 59 for the S_x observables.

Table 152: Values of the S_x observables as determined by the Method of Moments. No systematic uncertainties are evaluated. These measurements have only been used to cross-check the likelihood fit method in Section 7.1 and will not be published. See Table 59 for the results from the likelihood fit.

q^2 bin	S_{1s}	S_3	S_4	S_5
0	0.629 ± 0.742	0.243 ± 0.159	-0.003 ± 0.246	0.117 ± 0.180
1	0.390 ± 0.757	0.008 ± 0.270	0.203 ± 0.529	0.114 ± 0.357
2	0.351 ± 0.587	-0.361 ± 0.497	-0.147 ± 0.638	-0.924 ± 0.611
3	0.326 ± 0.046	-0.146 ± 0.160	-0.549 ± 0.281	-0.193 ± 0.213
4	0.432 ± 0.347	-0.311 ± 0.177	-0.060 ± 0.240	0.012 ± 0.206
5	0.423 ± 0.256	-0.120 ± 0.134	-0.312 ± 0.163	-0.390 ± 0.153
6	0.439 ± 0.061	-0.243 ± 0.099	-0.184 ± 0.111	-0.057 ± 0.106
7	0.486 ± 0.071	-0.067 ± 0.138	-0.362 ± 0.180	-0.200 ± 0.161
q^2 bin	S_{6s}	S_7	S_8	S_9
0	0.000 ± 0.230	0.011 ± 0.160	0.281 ± 0.218	0.361 ± 0.171
1	-0.161 ± 0.512	-0.553 ± 0.497	0.089 ± 0.675	-0.316 ± 0.348
2	-0.202 ± 0.647	0.418 ± 0.592	0.529 ± 0.760	0.229 ± 0.456
3	0.066 ± 0.252	-0.033 ± 0.213	-0.115 ± 0.245	-0.065 ± 0.144
4	-0.293 ± 0.213	-0.212 ± 0.240	-0.345 ± 0.283	-0.200 ± 0.174
5	0.674 ± 0.170	-0.084 ± 0.141	0.101 ± 0.157	0.088 ± 0.113
6	0.466 ± 0.105	-0.250 ± 0.117	-0.156 ± 0.119	0.182 ± 0.108
7	0.374 ± 0.177	0.004 ± 0.147	0.167 ± 0.175	0.027 ± 0.144

References

[1] LHCb collaboration, R. Aaij *et al.*, *Differential branching fractions and isospin asymmetries of $B \to K^* \mu^+ \mu^-$ decays*, JHEP **06** (2014) 133, arXiv:1403.8044.

[2] Belle Collaboration, J.-T. Wei *et al.*, *Measurement of the Differential Branching Fraction and Forward-Backward Asymmetry for $B \to K^{(*)} l^+ l^-$*, Phys. Rev. Lett. **103** (2009) 171801.

[3] BABAR Collaboration, B. Aubert *et al.*, *Angular distributions in the decay $B \to K^* l^+ l^-$*, Phys. Rev. D **79** (2009) 031102.

[4] LHCb collaboration, R. Aaij *et al.*, *Angular analysis of the $B^0 \to K^{*0} \mu^+ \mu^-$ decay using $3\,fb^{-1}$ of integrated luminosity*, JHEP **02** (2016) 104, arXiv:1512.04442.

[5] T. Blake *et al.*, *Differential branching fractions and isospin asymmetries of $B \to K^{(*)} \mu^+ \mu^-$ decays*, LHCb-ANA-2013-090. Linked to paper LHCB-PAPER-2014-006.

[6] A. Puig, *The LHCb trigger in 2011 and 2012*, LHCb-PUB-2014-046.

[7] E. A. Smith, *Run 2 update of the angular analysis of $B_d \to K^* \mu^+ \mu^-$*, LHCb-ANA-2017-055.

[8] F. Dettori, *Hlt2DiMuonDetached bug in Run 2*, Indico link.

[9] S. Neubert, *AALLSAMEBPV LoKi bug*, https://indico.cern.ch/event/692140/#22-aallsamebpv-loki-bug, Apr, 2018. Accessed: 2019-05-15.

[10] *LoKi functor bug affecting trigger (inc. Topo) and stripping*, https://indico.cern.ch/event/715191/contributions/2960112/attachments/1630170/2598205/TuesdayMeeting-180410.pdf, Apr, 2018. Accessed: 2019-05-15.

[11] *TISTOS summary*, https://indico.cern.ch/event/668057/contributions/2731438/attachments/1531580/2397375/ConorFitzpatrick_PPG280917.pdf, Sep, 2017. Accessed: 2019-08-15.

[12] *TISTOS problems in Run 2*, https://indico.cern.ch/event/663863/contributions/2718530/attachments/1521815/2377767/TuesdayMeeting-170912.pdf, Sep, 2017. Accessed: 2019-08-15.

[13] Particle Data Group, C. Patrignani *et al.*, *Review of particle physics*, Chin. Phys. **C40** (2016) 100001.

[14] W. D. Hulsbergen, *Decay chain fitting with a Kalman filter*, Nucl. Instrum. Meth. **A552** (2005) 566, arXiv:physics/0503191.

[15] T. Skwarnicki, *A study of the radiative cascade transitions between the Upsilon-prime and Upsilon resonances*, PhD thesis, Institute of Nuclear Physics, Krakow, 1986, DESY-F31-86-02.

[16] LHCb collaboration, R. Aaij *et al.*, *Differential branching fractions and isospin asymmetries of $B \to K^{(*)}\mu^+\mu^+$ decays*, arXiv:1403.8044. LHCB-PAPER-2014-006. CERN-PH-EP-2014-055. Comments: 23 pages, 4 figures, 7 tables.

[17] M. Clemencic *et al.*, *The LHCb simulation application, Gauss: Design, evolution and experience*, J. Phys. Conf. Ser. **331** (2011) 032023.

[18] I. Belyaev *et al.*, *Handling of the generation of primary events in Gauss, the LHCb simulation framework*, J. Phys. Conf. Ser. **331** (2011) 032047.

[19] D. Gerick, *What can go wrong with GenCutTool*, `https://indico.cern.ch/event/793409/#9-what-can-go-wrong-with-gencu`, Jan, 2019. Accessed: 2019-05-15.

[20] A. Poluektov, *Correction of simulated particle identification response in LHCb using transformation of variables*, Tech. Rep. LHCb-INT-2017-007, CERN, Geneva, Apr, 2017.

[21] V. Gligorov, *The BackgroundCategory tool for background classification*, Oct, 2013. Accessed: 2019-08-07.

[22] M. T. Alexander, *Run 1&2 Performance: news & update on VELO errors issue*, `https://indico.cern.ch/event/941777/#41-run-12-performance-news-upd`, Sep, 2020. Accessed: 2020-09-29.

[23] A. Hoecker *et al.*, *TMVA: Toolkit for Multivariate Data Analysis*, PoS **ACAT** (2007) 040, `arXiv:physics/0703039`.

[24] LHCb Collaboration, R. Aaij *et al.*, *Measurement of the branching fraction and CP asymmetry in $B^+ \to J/\psi\rho^+$ decays*, Eur. Phys. J. C **79** (2018) 537. 21 p.

[25] T. Blake *et al.*, *Angular analysis of $B^0 \to K^{*0}\mu^+\mu^-$ decays using 3 fb^{-1} of integrated luminosity*, LHCb-ANA-2013-097.

[26] A. Bharucha, D. M. Straub, and R. Zwicky, *$B \to V\ell^+\ell^-$ in the Standard Model from light-cone sum rules*, Journal of High Energy Physics **2016** (2016) .

[27] LHCb collaboration, R. Aaij *et al.*, *Differential branching fraction and angular analysis of the decay $B^0 \to K^{*0}\mu^+\mu^-$*, JHEP **08** (2013) 131, `arXiv:1304.6325`.

[28] LHCb collaboration, R. Aaij *et al.*, *Measurement of form-factor-independent observables in the decay $B^0 \to K^{*0}\mu^+\mu^-$*, Phys. Rev. Lett. **111** (2013) 191801, `arXiv:1308.1707`.

[29] S. Descotes-Genon, T. Hurth, J. Matias, and J. Virto, *Optimizing the basis of $B \to K^*\ell^+\ell^-$ observables in the full kinematic range*, Journal of High Energy Physics **2013** (2013) .

[30] T. Blake *et al.*, *Angular analysis of $B^0 \to K^{*0}\mu^+\mu^-$ at LHCb with 1 fb^{-1}*, LHCb-ANA-2012-051. Linked to LHCB-PAPER-2013-019.

[31] B. Efron, *Bootstrap Methods: Another Look at the Jackknife*, Ann. Statist. **7** (1979) 1.

[32] C. Langenbruch, *Differential branching fraction and angular analysis of the decay* $B_s^0 \to \phi\mu^+\mu^-$, LHCb-ANA-2012-099.

[33] F. Beaujean, M. Chrzaszcz, N. Serra, and D. van Dyk, *Extracting angular observables without a likelihood and applications to rare decays*, Phys. Rev. D **91** (2015) 114012.

[34] T. Nikodem, *Angular analysis of* $B^0 \to K^{(*0)}\mu^+\mu^-$ *decays using* 3fb^{-1} *of integrated luminosity at lhcb*, Dec, 2015.

[35] D. M. Straub, *flavio: a Python package for flavour and precision phenomenology in the Standard Model and beyond*, 2018.

[36] D. Aston, *et al.*, *A study of* $K^-\pi^+$ *scattering in the reaction* $K^-p \to K^-\pi^+n$ *at* $11\,\text{GeV}/c$, Nuclear Physics B **296** (1988), no. 3 493 .

[37] J. Bressieux *et al.*, *Evidence for the resonant character of the* $Z(4430)^- \to \psi(2S)\pi^-$ *mass peak observed in* $B^0 \to \psi(2S)K^+\pi^-$ *decays, and determination of the* $Z(4430)^-$ *spin-parity*, LHCb-ANA-2013-053.

[38] K. Chilikin *et al.*, *Experimental constraints on the spin and parity of the* $Z(4430)^+$, Physical Review D **88** (2013) .

[39] J. P. Grabowski, M. De Cian, and S. Esen, *Branching fraction and CPV measurements in* $B^+ \to J/\psi\rho^+$ *decays*, LHCb-ANA-2018-006.

[40] A. Ali, P. Ball, L. T. Handoko, and G. Hiller, *Comparative study of the decays* $B \to (K, K^*)\ell^+\ell^-$ *in the standard model and supersymmetric theories*, Physical Review D **61** (2000) .

[41] Belle, R. Itoh *et al.*, *Studies of CP violation in B —¿ J/psi K* decays*, Phys. Rev. Lett. **95** (2005), no. BELLE-PREPRINT-2005-15, KEK-PREPRINT-2005-7 091601, arXiv:hep-ex/0504030.

[42] BaBar, B. Aubert *et al.*, *Measurement of decay amplitudes of* $B \to J/\psi K^*, \psi(2S)K^*$, *and* $\chi_{c1}K^*$ *with an angular analysis*, Phys. Rev. **D76** (2007), no. SLAC-PUB-12430, BABAR-PUB-07-009 031102, arXiv:0704.0522.

[43] LHCb collaboration, R. Aaij *et al.*, *Measurement of the polarization amplitudes in* $B^0 \to J/\psi\, K^*(892)^0$ *decays*, Phys. Rev. **D88** (2013) 052002, arXiv:1307.2782.

[44] G. J. Feldman and R. D. Cousins, *Unified approach to the classical statistical analysis of small signals*, Physical Review D **57** (1998) 38733889.

[45] F. Beaujean, M. Chrzaszcz, N. Serra, and D. van Dyk, *Extracting angular observables without a likelihood and applications to rare decays*, Physical Review D **91** (2015) .

[46] S. Descotes-Genon, L. Hofer, J. Matias, and J. Virto, *Global analysis of* $b \to s\ell\ell$ *anomalies*, JHEP **06** (2016) 92, arXiv:1510.04239.

[47] LHCb collaboration, R. Aaij *et al.*, *Measurement of the S-wave fraction in* $B^0 \to K^+\pi^-\mu^+\mu^-$ *decays and the* $B^0 \to K^*(892)^0\mu^+\mu^-$ *differential branching fraction*, JHEP **11** (2016) 047, Erratum ibid. **04** (2017) 142, arXiv:1606.04731.